This work was performed for the Jet Propulsion Laboratory, California Institute of Technology, sponsored by the National Aeronautics and Space Administration under Contract NAS7-100.

Surveyor Spacecraft System

SURVEYOR III FLIGHT PERFORMANCE FINAL REPORT

JPL Contract 950056/July 1967

SSD 68189-3

K C Beall for
J. D. CLOUD
Manager
System Engineering and Analysis Laboratory

T B Van Horne
T. B. VAN HORNE
Manager
Analysis Department

W McIntyre for
R. H. LEUSCHNER
Head
Post Flight Analysis Section

CONTENTS

1.0 SCOPE AND PURPOSE

At 07:05 GMT (11:05 PDT) on 17 April 1967, the third Surveyor spacecraft was launched from Cape Kennedy into a temporary parking orbit and then into a near-perfect translunar trajectory by the Atlas/Centaur launch vehicle. At 00:04:18 GMT on 20 April 1967 after a 64-hour, 59-minute journey through space, the spacecraft bounced to a successful touchdown. During the multiple touchdown, engineering telemetry was impaired; however, successful TV camera operations and digging with the soil mechanics/surface sampler (SM/SS) were performed. Many pictures of the lunar surface have been received, and indications of soil texture have been reported.

The basic purpose of this report is to document the actual performance of this third spacecraft throughout the mission, compare its performance with that predicted by spacecraft design, and recommend any changes or modifications that should be made in the spacecraft design. The report is based on both real-time and postmission data analysis.

2.0 DESCRIPTION OF SURVEYOR SYSTEM

The Surveyor spacecraft is designed and built by the Hughes Aircraft Company under the direction of the California Institute of Technology Jet Propulsion Laboratory for the National Aeronautics and Space Administration. It has been conceived and designed to effect a transit from earth to the moon, perform a soft landing, and transmit to earth basic scientific and engineering data relative to the moon's environment and characteristics. A brief description of the Surveyor vehicle design is given in the "Surveyor I Final Performance Report" (Reference 1).

2.1 SURVEYOR III MISSION OBJECTIVES

The basic objectives of the Surveyor III spacecraft system, as defined in Reference 2, were as follows:

1) Primary objectives

   a) Accomplish a soft landing on the moon at a site east of the Surveyor I landing site.

   b) Demonstrate spacecraft capability to soft land on the moon with an oblique approach angle not greater than 35 degrees.

   c) Obtain postlanding television pictures.

   d) Obtain data on radar reflectivity, thermal characteristics, touchdown dynamics, and other measurements of the lunar surface through the use of various payload equipment, including the SM/SS.

2) Secondary objective – Demonstrate the capability of DSS-61 (Robledo, Spain) to support future Surveyor missions.

Surveyor III met the foregoing primary and secondary objectives. Soft landing occurred east of the Surveyor I landing site at an approach angle of 23.6 degrees. Television pictures were transmitted from the lunar surface, and extensive use was made of the SM/SS. Due to a telemetry anomaly at the time of the second touchdown, all spacecraft analog data except TV were

impaired; however, corrective calibration has made almost all data usable at a low bit rate (17.2 bps). In addition, DSS-61 supported the mission.

2.2 SURVEYOR III FLIGHT CONFIGURATION

For a summary description of the major Surveyor functions and design mechanization, consult the "Surveyor I Final Performance Report" (Reference 1). The major differences in the SC-3 configuration, compared with that of the second spacecraft, are detailed in Table 2-1. For completeness, the major differences of SC-2 and the first spacecraft are given in Table 2-2. A complete list of SC-3 control items, separated by subsystem or function, is given in Table 2-3. Table 2-2 details only items in Reference 3.

2.3 REFERENCES

1) "Surveyor I Flight Performance Final Report," Hughes Aircraft Company, SSD 68189R, October 1966.

2) "Space Flight Operations Plan, Surveyor Mission C," Jet Propulsion Laboratory, EPD-180-S/MC, 20 February 1967.

3) "SC-3 Consent-to-Launch," Hughes Aircraft Company, SSD 74042, Vol. I, April 1967.

TABLE 2-1. SC-3 MAJOR CONFIGURATION CHANGES

Item	Description
Spacecraft	
1) Add two special viewing mirrors	On SC-3, enables TV survey camera to view as much as possible in area of crushable blocks and vernier engines.
2) Add new crushable block ballast details	Required to compensate for different launch windows.
3) Change ballast on leg 3 footpad from 0.25 to 0.8 pound	Limit deceleration loads transmitted to shock absorber.
4) Landing gear kickout springs	Add kickout spring to overcome initial static friction during initial leg deployment.
5) Ground SM/SS compartment	Prevents possible buildup of electrical charges.
6) Electrical bonding of shocks	Provide a grounding path of low impedance from the squibs to the spaceframe. Prevent premature squib firing which would cause landing gear shock absorber lock.
7) Install new retro	High impulse main retro installed in spacecraft
8) Shock absorber clearance	Because of differential thermal expansion/ contraction of dissimilar materials, clearance is changed to prevent binding under worst-case conditions of parking orbit trajectory.
9) Mirror installation	Due to dissimilar material of mirrors and their shims: 1) washers added under nut to maintain minimum dimensions, 2) torque reduced on nuts, 3) dry lube eliminated on washers. This was done to eliminate excessive loading in the mirror studs at extreme temperature conditions.
Accelerometers	
10) Coax cables – stake connectors	Change system test specification, as well as review other engineering and staking procedures.

Table 2-1 (continued)

Item	Description
A/SPP	
11) Pin pullers	A/SPP pin pullers redesigned.
FCSG	
12) Remove silicone grease from Canopus o-ring	To increase star window temperature and reduce or eliminate internal fogging.
13) Torque all connectors	Torque requirements specified for connectors on flight control unit to ensure proper seating and secureness after assembly.
Omnidirectional Antenna Mechanism	
14) Add loctite after final adjustment	Better locking conditions.
Retro Motor	
15) Increase propellant	Change in retro weight according to spacecraft weight changes and requirements.
Retro Motor Harness	
16) Provide category A squib firing circuits, shielding	Revised harnesses and attaching hardware to comply with AFETR safety requirements.
17) Wrap all external wiring harness connectors with aluminum foil	Connector extending retaining nut has sharp internal edges.
RF Cables	
18) Bond at chamfer of connector	To prevent connectors from loosening during vibration.
Roll Actuator	
19) Change pin puller screw torque	To prevent cracking of the fiberglass electrical washers under the heads of the pin puller screws.
RADVS SDC	
20) Sidelobe frequency discrimination	SC-3 only. Antenna sidelobe skewing of 2.0 instead of 0.2 degree necessitated crosscoupled sidelobe logic modification since rejection logic circuitry was designed for a frequency rejection criteria based upon 0.2 degree.

Table 2-1 (continued)

Item	Description
21) Addition of spacer to waveguide -93 support	Spacer controls clamping pressure at required torque without any significant permanent deformation to bracket.
Shock Absorber	
22) Install new shock absorber	Modify A-24 shock absorber design to meet A-21 lower weight requirement.
23) New squibs	Improve lock landing gear squib firing condition.
Solar Panel	
24) Seal bumper adjustments	Add loctite on the damper adjustment threads during final adjustment prior to launch.
Wiring Harness – Compartments A and B	
25) Compartment A harness	Notch out strain relief to eliminate interference.
26) Compartment B harness	Addition of zener diode limiter to V_x and V_y outputs to prevent possible erroneous readings in other telemetry channels.
Payload	
27) SM/SS added	Approach camera TV-4 replaced with simplified SM/SS subsystem.
28) Addition of sun bonnet on TV camera	Sun shade added to mirror assembly to prevent direct sunlight from entering mirror hood at sun angles from zenith to 45 degrees.

TABLE 2-2. SC-2 MAJOR CONFIGURATION DIFFERENCES WITH SC-1

Item	Description
1) Boost regulator overload trip circuit	In SC-1, the overload trip circuit in the boost regulator had to be disabled because it would trip with a 2-millisecond transient. The SC-2 boost regulator has an overload trip circuit that does not trip unless the transient is 20 to 30-milliseconds.
2) a) Filter chokes on input to ESP and AESP b) Filter on A/D converter 2 nulling amplifier in CSP	Both of these design improvements eliminate the large variations in temperature readouts on telemetry which were present on SC-1.
3) Telemetry of flight control return signal	In SC-2 the flight control return signal is telemetered so that varying harness voltage drops can be corrected to provide more accurate data on flight control telemetry signals.
4) A/SPP pin pullers	A/SPP pin puller modules were redesigned to simplify installation at AFETR.
5) A/SPP drive motor	All SC-2 drive motors on the A/SPP have roller detents instead of ball detents used in all but the SC-1 roll axis. This is a design improvement.
6) Omnidirectional antenna latch and release mechanism	SC-2 release mechanisms for omnidirectional antennas A and B have been redesigned to prevent the deployment problem that occurred in the SC-1 flight. The clevis opening has been broadened, and a kickout spring has been added.
7) Command assignments	SC-2 engineering mechanisms auxiliary had been modified to combine functions of two commands so that two command channels would be made available for fuel and oxidizer dump. It has since been determined that fuel and oxidizer dump are not necessary, but the engineering mechanisms auxiliary change had already been accomplished.
	SC-1 / Command / SC-2
	Roll actuator unlock / 0605 / Roll actuator unlock and pressurize VPS
	Pressurize VPS / 0607 / Spare
	Unlock roll-(lunar) / 0633 / Unlock elevation and roll (lunar)
	Unlock elevation / 0634 / Spare
8) Boost regulator flight control regulator filter	SC-2 boost regulator has a new filter on the flight control regulator to eliminate oscillations that would sometimes occur, causing an overload on the shunt regulator. SC-1 did not have this filter, but apparently did not need it.
9) Vx and Vy gain in flight control sensor group	Vx and Vy radar attitude loop gains have been reduced in SC-2 to eliminate a potential instability problem at velocities greater than 535 fps.
10) Solder splash in ESP and AESP	All SC-2 units have had the Kit 10 modification performed to eliminate the solder splash problem (except the spare central command decoder).
11) RADVS sidelobe rejection logic	Two resistors in the SC-2 signal data converter were removed in order to lower the point at which the sidelobe signals are rejected from 28 to 25 db.
12) Canopus sun reference filter change	SC-1 had a Canopus sun filter with a reduction of 50 percent (filter factor of 1.5) to compensate for any possible fogging of Canopus sensor window, in accordance with recent measurements of Canopus brightness at Tucson. SC-2 has a filter factor of 1.2. This has been reduced from 1.5 to 1.2 because the fogging problem did not materialize at the Canopus sensor temperature of 79°F for the SC-1 flight.
13) Canopus window	The O-rings on the Canopus window were changed for SC-2 in an effort to prevent possible fogging of the Canopus filter.
14) A/SPP pulse duration	Battery charge regulator was changed to reduce A/SPP stepping current pulse duration from 65 to 40 milliseconds. This change reduced the power dissipation in the battery charge regulator and in the A/SPP drive motors.
15) Quick disconnects	Q3 and Q4 were replaced on SC-2 by changing valves CV3 and CV4.
16) Auxiliary battery cover paint pattern	The paint pattern of the auxiliary battery container was changed to increase the temperature of this unit, which became too low during Coast Mode II for SC-1.

TABLE 2-3. SPACECRAFT UNIT CONFIGURATION AT LAUNCH

Part Name, Number, S/N	Part Name, Number, S/N
Flight Control	Shock absorber, leg 3, 264300, S/N 6
Flight control sensor group, 235000-5, S/N 1	Landing gear, 261278, S/N 5
Inertial reference unit, 235100-1, S/N 5	Landing gear, 261279, S/N 4
Roll actuator, 235900-3, S/N 9	Landing gear, 261280, S/N 5
Gas supply, attitude jet, 235600-2, S/N 3	Accelerometer amplifier, 239011, S/N 5
Jet, attitude, 235700-3, S/N 3	Strain gage amplifier, 238930, S/N 2
Jet, attitude, 235700-2, S/N 11	SM/SS Subsystem
Jet, attitude, 235700-2, S/N 6	SM/SS auxiliary, 3024536, S/N 1
Secondary solar sensor, 235450-1, S/N 5	SM/SS mechanism, 3024700, S/N 1
Thermal Control	Harness
Thermal switch A, 238810-4, S/N 5	Wiring harness compartment B, 286998, S/N 1
Thermal switch A, 238810-3, S/N 32, 4, 9, 13, 14, 19, 20, and 24	Wiring harness compartment A, 286980, S/N 1
Thermal switch B, 238811-3, S/N 4	Wiring harness basic bus 1, 292191, S/N 1
Thermal switch B, 238811-2, S/N 2, 3, 6, 7, and 9	Wiring harness TV camera, 292259, S/N 1
Thermal shell, compartment A, 286459, S/N 5	Wiring harness basic bus 2, 286240, S/N 1
Thermal shell, compartment B, 286460, S/N 5	Wiring harness auxiliary battery, 264100, S/N 6
Thermal tray, compartment A, 264334-1, S/N 2	Wiring harness retro motor, 286984, S/N 1
Thermal tray, compartment B, 276935, S/N 3	Wiring harness battery cell volt, 302515, S/N 4
Mechanisms	Wiring harness separation squibs, 286926, S/N 1
Spaceframe, 264178-2, S/N 1	Wiring harness A/SPP, 286417, S/N 6
Mech. antenna omnidirectional A, 3028000-1, S/N 4	Cable retro igniter, 286927, S/N 1
Mech. antenna omnidirectional B, 273880-1, S/N 2	Rel. mech. retro rocket, 230069-1, S/N 10, 11, and 12
A/SPP, 287580, S/N 3	Telecommunications
Leg position pots, 988684, S/N 989063, 989064, and 989065	Transmitter A, 263220-4, S/N 18
Separation sensing and arming device, 293400, S/N 10, 11, and 12	Transmitter B, 263220-4, S/N 17
Shock absorber, leg 1, 264300, S/N 4	Command receiver A, 231900-3, S/N 22
Shock absorber, leg 2, 264300, S/N 5	Command receiver B, 231900-3, S/N 23
	Omnidirectional antenna A, 232400, S/N 25
	Omnidirectional antenna B, 232400, S/N 9
	TM buffer amplifier A, 290780-1, S/N 11
	TM buffer amplifier B, 290780-1, S/N 12
	Planar array antenna, 232300, S/N 16

Table 2-3 (continued)

Part Name, Number, S/N	Part Name, Number, S/N
Telecommunication (continued)	Electrical Power
Low pass filter A, 233466, S/N 8	Main battery, 237900, S/N 90
Low pass filter B, 233466, S/N 18	Auxiliary battery, 232921, S/N 59
RF switch SPDT, 283983, S/N 15	Thermal container and heater A, 232210-1, S/N 11
RF switch transfer, 283984, S/N 12	Thermal container and heater B, 232210-2, S/N 16
Television	Boost regulator filter, unregulated bus, 290080, S/N 16
Survey camera, 284312-7, S/N 13	Boost regulator, 274200-12, S/N 12
Signal Processing	Boost regulator input choke, 290390, S/N 15
Signal processing auxiliary, 232540-1, S/N 2	Auxiliary battery control, 273000-2, S/N 11
Central command decoder, 232000-5, S/N 4	Battery charge regulator, 274100-4, S/N 13
Low data rate auxiliary, 264875-2, S/N 6	Solar panel, 237760-3, S/N 3
Engineering signal processor, 233350-5, S/N 3	Main power switch, 254112, S/N 8
Auxiliary engineering signal processor, 264900-5, S/N 1	Engineering mechanisms auxiliary, 263500-6, S/N 11
Central signal processor, 232200-8, S/N 3	Propulsion
TV auxiliary, 232106-5, S/N 14	Oxidizer tank, 287119, S/N 3
Radar	Oxidizer tank, 287120, S/N 4
Altitude marking radar, 283827-1, S/N 15	Oxidizer tank, 287121, S/N 1
KPSM (RADVS), 232909, S/N 9	Fuel tank, 287117, S/N 5
SDC (RADVS), 232908-5, S/N 10	Fuel tank, 287117, S/N 6
Altitude velocity sensor antenna (RADVS), 232910, S/N 8	Fuel tank, 287118, S/N 3
Velocity sensor antenna (RADVS), 232911-1, S/N 8	Helium tank and valve assembly, 262789-2, S/N 2
Waveguide assembly (RADVS), 232912-1, S/N 7	Thrust chamber assembly, 285063-4 (Hughes), S/N 563
	Thrust chamber assembly, 285063-5 (Hughes), S/N 554
	Thrust chamber assembly, 285063-6 (Hughes), S/N 559
	Main retro, 238612-1, S/N 2

3.0 SYSTEM SUMMARY

3.1 SUMMARY OF SIGNIFICANT ANOMALIES

The anomalies that occurred during Mission C are summarized in Table 3-1. For this report, an anomaly is defined as an unexpected occurrence that might be indicative of a spacecraft trouble or failure. The anomalies are discussed in greater detail in the sections noted in this table.

Currently, 19 spacecraft anomalies have been assigned to the SC-3 mission. None of them, as outlined in Table 3-1, prevented completion of the mission.

3.2 SYSTEM PERFORMANCE PARAMETERS

Performance parameters that could be directly determined through analysis of spacecraft telemetry are summarized in Table 3-2. Required or predicted values for these parameters are included in this summary for comparative purposes.

3.3 CONCLUSIONS AND RECOMMENDATIONS

3.3.1 Conclusions

The Surveyor III flight was essentially uneventful. Following a near-perfect injection and an equally perfect transit phase and midcourse, the spacecraft successfully landed near the center of a small lunar crater. The soft multiple touchdown was due to failure of the doppler radar to turn off the vernier engines 14 feet above the lunar surface. The engines were manually commanded off. A partial failure in the spacecraft telemetry subsystem occurred during this bouncy landing, making it usable only at low bit rates. Other spacecraft subsystems operated normally.

3.3.2 Recommendations

Table 3-3 is a summary of the status of Surveyor III design recommendations.

TABLE 3-1. SPACECRAFT ANOMALIES

Number	Time		Anomaly	Cause	Effect on Mission	TFR Number	Disposition
	GMT, day:hr:min	From Launch, hr:min					
1	Prelaunch		Prelaunch roll actuator telemetry response indicated movement when roll actuator pinned (subsection 5.5.2.1)	Telemetry pickoff may move when roll actuator is pinned	Temporary hold of launch	None	Special test on SC-5 proved this effect was not peculiar to SC-3.
2	108:05:00	21:55	Unequal thrust telemetry indications at midcourse (subsections 4.3.1 and 5.6.4.3)	Probably due to inaccuracies in engine thrust calibration	None. Attitude stable during midcourse and touchdown, indicating proper system performance	18258	Closed 15 June 1967. Calibration data on TCAs on last ETR flow check prior to TCA installation will be used in future.
3	110:00:04	64:59	14-foot mark was not generated during terminal descent (subsections 4.3.2, 5.2.2.2, and 5.9.2.1)	Loss of lock of beam 3 tracker due to lunar reflectivity characteristics and RADVS CCSLL circuits	Vernier engines were not shut off, causing spacecraft to hop twice after first landing	18255	Closed 11 May 1967. Corrective action in effect. See ECA 113469 – disable CCSLL below 1000 feet.
4	110:00:04	64:59	Scrambled analog telemetry data (subsections 4.3.2 and 5.4.2)	Multiple failure of a commutator switch in both ESP and AESP	Confused post-touchdown spacecraft assessment. Subsequent (except TV) operations restricted to low bit rate (17.2 bps).	18256	Closed 8 June 1967. Possibly due to high voltage arc in KPSM caused by plasma effect from vernier engines.
5	110:00:04	64:59	KPSM turnoff at touchdown (subsections 4.3.2 and 5.9.2.2)	Possible plasma effect from vernier engines causing high-voltage arcing	KPSM turnoff has no effect. Arcing is probably the cause of anomaly 4.	–	Since this is a nonstandard condition resulting from anomaly 3, no corrective action will be taken.
6	110:00:04	64:59	Unexpected low reading on leg 1 strain gage at second touchdown	Lunar surface had small depression at point footpad 1 hit, causing reduced force levels	None	–	
7	110:00:04	64:59	Inadvertent switching of ABC unit at second touchdown (subsection 5.2.2)	Spurious command resulting from transient at second landing	None. Spacecraft subsequently commanded into desired mode	18261	Closed 26 May 1967
8	110:00:04	64:59	RADVS range value large at relock after first touchdown (subsection 5.9.2.3)	Possibly due to KPSM arcing	Unknown. Spacecraft landed	None	Closed
9	110:00:10	65:05	Delayed RADVS turnoff after RADVS off command sent (subsection 5.9.2.4)	Analog telemetry already scrambled, possibly due to KPSM arcing	Unknown. Spacecraft landed	None	Closed
10	Transit	–	Temperature reading in SM/SS auxiliary lower than predicted from STV data (subsections 5.1.2.1 and 5.1.4.2)	STV environment was identical to actual environment, resulting in erroneous prediction	None. Temperatures reached during transit were well within survival limits	18257	Closed 16 May 1967

Table 3-1 (continued)

Number	Time		Anomaly	Cause	Effect on Mission	TFR Number	Disposition
	GMT, day:hr:min	From Launch, hr:min					
11	114:04	164	Auxiliary battery failure (subsection 5.2.2)	Telemetry indicates a short to the spaceframe	None – main battery and solar panel provided sufficient power for lunar operation	18260	Corrective action not required as auxiliary battery not needed after landing. Closed 11 May 1967
12	End of lunar day 1	–	Thermal switch malfunction (subsection 5.1.2.2)	Switch contact adhesion. This is a recognized design problem	Reduced operation after lunar sunset	18259	Closed 18 May 1967. ECR 329570 (ECA 112830) provides fix on SC-4 and subsequent spacecraft
13	Lunar day 1	–	SM/SS operation took about twice as many commands to step the SM/SS as expected	High motor temperature increased motor resistance	Operation essentially unhampered	None	Closed
14	Transit	–	Helium transducer zero shift at midcourse	–	After helium was dumped on lunar surface, telemetry read zero bcd shift, which is consistent with calibration curve	None	Closed
15	Lunar day 1	–	Filter wheel telemetry indicated improper operation. Telemetry did not correspond with verified position of the filter wheel. Proper operation of filter wheel drive verified by imagery (subsection 5.13.2)	Probably set screw in the gear on the potentiometer shaft worked loose	Loss of filter wheel telemetry, not filter wheel operation	27669	Closed 22 June 1967. The manufacturing process has been changed. The staking material was changed from locktite to epoxy
16	Lunar day 1	–	Camera mirror assembly failed to respond to step right and left commands. Difficulty more noticeable during rapid temperature changes (subsection 5.13.2)	Increased torque in bearing due to high thermal gradients caused excessive motor loading. This, coupled with motor degradation due to accumulated number of steps, caused step failures	Greatly reduced rate of picture taking	27670	Closed 26 May 1967. A motor of improved design has been incorporated into SC-4 and SP-1 cameras
17	Lunar day 1	–	Vidicon temperature readout (TV-9) and electronics temperature readout (TV-10) indicated camera operating approximately 40° F hotter than equivalent SC-1 time period (subsection 5.13.2)	Had old telemetry conversion coefficients in ground computer	Restricted operation until coefficients were corrected	27671	Closed 26 May 1967. Action taken to assure proper transmittal of coefficients
18	Lunar day 1		Camera mirror assembly failed to respond to step-down commands (subsection 5.13.2)	Probably elevation motor wearout	Greatly reduces rate of picture taking	27672	Closed 26 May 1967. A motor of improved design has been incorporated on the other TV cameras
19	Lunar day 1		Severe loss of picture contrast ratio (masking of low light picture information). Effect most severe at low sun angles when the mirror surface or filter wheel was directly illuminated (subsection 5.13.2)	Combination of dust on mirrors and high reflectivity from surrounding parts of spacecraft	Could not use mirrors to view surface under spacecraft	27673	Closed 26 May 1967. Launch specification 224564 for SC-4 has been modified to include launching with the mirror closed

TABLE 3-2. SYSTEM PERFORMANCE DETAILS AND MISSION EVENTS

Performance Details						
Item	Description	Actual	Reference	Predicted or Specified	Reference	Comments
	Launch to Acquisition Summary					
1	Dynamic Flight Environment					
	Ignition-liftoff	0	Flight path analysis and command	0	Preflight nominal trajectory	0 second is 107:07:05:01.059 GMT in seconds referenced to launch
	Booster engine cutoff	142.5		142.9		
	Booster jettison	145.5		146.0		
	Insulation panel jettison	176.2		176.9		
	Nose fairing jettison	203.5		203.9		
	Sustainer engine cutoff	237.7		236.4		
	Atlas/Centaur separation	239.6		238.4		
	Centaur main engine cutoff 1	569		574.9		
	Centaur main engine cutoff 2	2028.8		2021.7		
	Surveyor:					
	Extend landing gear	2051.8		2047.7		
	Extend omnidirectional antenna	2061.8		2058.2		
	Transmitter to high power	2072.5		2078.7		
	Electrical disconnect from Centaur	2087.8		2084.2		
	Centaur separation	2093.4		2089.7		
2	Powered Flight Vibration Environment		5.10.4.2			
	Launch +	3.3 g 0 to peak				Single spike 0 to 0.2 second
	Booster engine cutoff	1.75 g 0 to peak				0.8 second
	Insulation panel jettison	10 g 0 to peak				Decay in 0.08 second
	Sustainer engine cutoff	>0.5 g 0 to peak				Single pulse
	Atlas/Centaur separation	>10 g 0 to peak				High-frequency transient
3	Spacecraft Attitude Change During Nulling of Rates		5.5.4.2			
	Pitch	-0.50 degree				
	Yaw	-1.30 degrees				
	Roll	+0.90 degree				
	Time to null rates to 0.1 deg/sec		5.5.4.2			
	Pitch					
	Yaw	<11 seconds		Within 50 seconds	224510E	
	Roll					
4	Centaur Retro Maneuver Time	L + 2355.5	Flight path analysis and command	L + 2329.7	Nominal	
5	Solar Axis Deployment Time	358 seconds	5.11.4.3	358 seconds	Preflight test	

Table 3-2 (continued)

Performance Details						
Item	Description	Actual	Reference	Predicted or Specified	Reference	Comments
	Launch to Acquisition Summary (continued)					
6	Spacecraft Weight	2281.31 pounds	IDC-3.4.159			Spacecraft weight, cg, and moments of inertia at separation
7	Spacecraft cg Location					
	X	0.058 inch				
	Y	0.179 inch				
	Z	58.93 inches				
8	Spacecraft Moment of Inertia					
	I_{xx}	202 slug-ft^2				
	I_{yy}	198 slug-ft^2				
	I_{zz}	223 slug-ft^2				
	Coast Summary					
	Sun Acquisition		5.5.4.3		224510E (3.4.1)	Roll maneuver until activation of acquisition sun sensor and then a yaw maneuver until primary sun sensor illumination
1	Roll angle	-181 degrees				
2	Yaw angle	+38 degrees				
3	Total time	438.2 seconds		18 minutes maximum		
	Star Acquisition		5.5.4.4		224510E (3.4.2)	
4	Proper acquisition and Canopus verification	Automatic				
5	Roll angle from beginning of maneuver to Canopus	+205 degrees				
6	Objects identified	Canopus, moon, Jupiter, earth, Procyon, Adhara, and Altair				
7	Mean roll rate during star map phase	0.5011 deg/sec		0.5 deg/sec	224510E (3.4.2.1.1)	
8	Effective gain of Canopus sensor	1.03-1.22 x Canopus			Design	Normally the gain setting is 1 x Canopus
9	Time from start of star acquisition to midcourse firing	12:50		2 hours maximum	224510E (3.4.2)	
	Attitude Orientation					
10	Average error from sunline		5.5	Within 0.2 degree	224510E (4.3.1.1)	Sensor group roll axis shall be held within 0.2 degree of sun-spacecraft line.
	Pitch	0				
	Yaw	+0.02				
	Roll	-0.06				

Table 3-2 (continued)

Performance Details						
Item	Description	Actual	Reference	Predicted or Specified	Reference	Comments
			Coast Summary (continued)			
11	Average error from Canopus line of sight		5.5	Within 0.2 degree	(4.3.1.2)	Angle between sensor group roll-pitch plane and projection of Canopus-spacecraft line on sensor group pitch-yaw plane.
	Pitch	0				
	Yaw	+0.02				
	Roll	-0.06				
12	Limit Cycle Optical Mode		5.5.4.5			
	Average amplitude-roll	0.55 degree		±0.30 degree	224510E	
	Average amplitude-pitch	0.51 degree			(4.3.1.1.2)	
	Average amplitude-yaw	0.54 degree				
	Average period	68.5 seconds				
13	Limit Cycle Inertial Mode		5.5.4.5			
	Average amplitude-roll	0.46 degree		±0.30 degree	224510E	
	Average amplitude-pitch	0.48 degree			(4.3.1.1.2)	
	Average amplitude-yaw	0.50 degree				
	Average period	68.5 seconds				
14	Gyro Drift		5.5.4.9			
	Roll	+1.1 deg/hr		≤1 deg/hr	224510E	Non g sensitive
	Pitch	+0.6 deg/hr			(4.3.1.5)	
	Yaw	-0.8 deg/hr				
			Midcourse Summary			
1.0	Total Magnitude Errors (RSS)	0.19	5.5.4.8			
1.1	Errors proportional to maneuver magnitude:		5.5.4.8			
	Accelerometer accuracy	0.17		1.1 percent	234632C	
	Reference signal			0.5 percent	234600E	
	FCE null			0.15 percent	234600E	
	Thrust bias variation			0.09 percent	287105	
	Control channel gain variation			0.07 percent	234600E	
	Accelerometer misalignment			0.06 percent	234600E	
	Total proportional errors: (RSS)			0.17 percent		
1.2	Errors independent of maneuver magnitude:		5.5.4.8			
	Shutdown impulse dispersion	-0.012		±0.63 lb-sec	287015	
	Hysteresis limit cycle	0.035		3 milli-amperes	287105	
	Ignition transient	0		—		
	Timing granularity	-0.07	5.5.4.8	0.05		
	Total independent errors: (RSS)	0.08				

Table 3-2 (continued)

Performance Details						
Item	Description	Actual	Reference	Predicted or Specified	Reference	Comments
		Midcourse Summary (continued)				
2.0	Total Attitude Errors (RSS)	0.184 degree	5.5.4.6	±0.7 degree	244510E (363)	Attitude error prior to ignition (0.1-degree uncertainty)
2.1	Initial position errors:					
	Sensor group roll axis to sun spacecraft line	Pitch = 0.013 degree Yaw = 0.13 degree		0.2 degree	(4.3.1.1)	
	Pitch/yaw limit cycle	0.08 degree		0.3 degree	(4.3.1.1)	
	Sensor group roll-pitch plane to Canopus-spacecraft line	0.05 degree		0.2 degree	(4.3.1.1)	
	Roll limit cycle	-0.306 degree		0.3 degree	(4.3.1.2)	
2.2	Rotational magnitude errors:					
	Gyro torquer scale factor	0.2 percent		0.05 percent	234633	
	Precession current accuracy			0.13 percent	234610	
	Precession current circuit drift			0.1 percent		
	Timing source accuracy	Roll = 0.075 degree Pitch = 0.116 degree		0.2 percent	(4.4.2.2.1)	
2.3	Rotational axis error:					
	Gyro alignment to FCSG, roll axis	Pitch = 0.017 degree Yaw = 0.067 degree		0.14 degree	234630 (4.2.4.3)	
2.4	Final position errors:					
	Reference axis drift, gyro non-g drift	Roll = 0.24 degree Yaw = -0.2 degree Pitch = 0.09 degree		<1 deg/hr	224510E (4.3.1.4)	
	Midcourse maneuver duration	4.245 seconds	5.5.4.8	4.278 seconds	Command	
3.0	Midcourse ΔV	4.0139 m/sec	5.5.4.8	4.19 m/sec	SSD 74073	
4.0	Midcourse ΔV Error	0.176 m/sec	5.5.4.8	0.178 m/sec	SSD 74075	
5.0	Peak Attitude Transient at Engine Ignition					
	Roll	-1.0 degree				
	Pitch	-0.125 degree				
	Yaw	+0.3 degree				
6.0	Peak Angular Error at Shutdown		5.5.4.8			
	Roll	+0.58 degree				
	Pitch	+0.96 degree				
	Yaw	+1.97 degree				

Table 3-2 (continued)

Performance Details						
Item	Description	Actual	Reference	Predicted or Specified	Reference	Comments
	Midcourse Summary (continued)					
7.0	Roll Actuator Position					
	Peak at ignition	-0.8	5.5.4.8			
8.0	Engine Shutoff Impulse		5.5.4.8	<5 lb-sec per engine	(4.2.2.7)	
	Engine 1	-0.31 lb-sec				
	Engine 2	+0.42 lb-sec		Δ impulse		
	Engine 3	-0.11 lb-sec		<0.66 lb-sec		
9.0	Shut Down Angular Rate:					
	Pitch	+0.25 deg/sec				
	Yaw	+0.53 deg/sec				
	Terminal Descent Summary					
1	Initial Time of First Maneuver	109:23:23:30	TM		Command	Before AMR mark
2	Retro Phase Initial Conditions (Vernier Ignition)		5.12.4.1		SSD 74075	Six Degree of Freedom Program Prediction
	Time	110:00:01:17.9				
	Attitude	22.94 degrees		22.94 degrees		
	Slant range	271,334 feet		273,170 feet		
	Velocity	8617.5 fps		8617.5 fps		
3	Retro Burnout Conditions (2.15 seconds after retro eject)		5.12.4.1			
	Slant range	36,158 feet		34,734 feet	SSD 74075	
	Longitudinal velocity	462 ft/sec		445.2 fps		
	Lateral velocity	171 ft/sec		116.6 fps		
	Attitude	3.8 degrees		9.2 degrees		
4	Misalignment During Burn	In plane, 0.34 degree Out of plane, 0.02 degree	5.12.4.1	0	Predict	
5	Time Between AMR Mark and Vernier Ignition	5.09 seconds	Table 4.1	5.070 seconds	SSD 74075	
6	Retro Thrust to CG Offset During Burning	0.024	5.7.3	<0.18 inch	224510E (4.1.3.3)	Total value
7	Retro Action Time (T3500)	41.02 ± 0.1 seconds	5.7.3	41.09 seconds	5.7.3	
8	Maximum Retro Thrust	9550 pounds	5.7.3	9600 pounds	QA firing date	
9	Peak Attitude Transient at Retro Ignition		5.5.1.6			
	Roll	-0.22 degree				
	Pitch	-0.10 degree				

Table 3-2 (continued)

Performance Details						
Item	Description	Actual	Reference	Predicted or Specified	Reference	Comments
	Terminal Descent Summary (continued)					
10	Descent Segment Intercept Time	110:00:02:33	5.5.1.6			
	Slant range	22,300				
	Velocity	495 ft/sec (V_z)				
11	1000-foot Mark Conditions		5.12.4.1			
	Time	110:00:03:53				
	Velocity	103.27 fps		106.45 fps		
	Attitude	0.51 degree		1.09 degree		
12	10-fps Mark Conditions		5.12.4.1			
	Slant range	46 feet		43 feet		
	Time	110:00:04:10				
	Attitude	0.025 degree		0.01 degree		
13	Engine Cutoff Conditions		5.12.4.1		224510E	
	Slant range	Did not occur		14 ± 4.5 feet	(3.10.3.1)	
	Velocity	–		5 ± 1.5 fps	(3.10.3.2)	
	Attitude	–		0 ± 4.8 deg	(3.10.3.5)	
14	Touchdown Conditions (No. 1)		5.5			
	Longitudinal velocity	6 to 8 fps	5.5.1.6	<15 fps	(3.11.2.1)	
	Lateral velocity	~0	5.10.3	<5.0 fps	(3.11.2.2)	
	Attitude	~0		<7 degrees	(3.11.2.3)	

TABLE 3-3. SURVEYOR III RECOMMENDATIONS SUMMARY

Number	Subsection	Recommendations
1	5.5.3.2	Add a telemetry signal to monitor the sidelobe logic rejection circuit to indicate when a forced break lock occurs.
2	5.5.3.2	Investigate the use of touchdown switches to permit the vernier engines to burn down to the lunar surface.
3	5.5.3.2	Supply pitch and yaw calibration data over the range of 0 to 5 telemetry volts to include the nonlinear regions at the end points.
4	5.8.3	Additional preflight calibration at longer pulse lengths for proper AGC interpretation in the AMR.
		Implemented Recommendations
1	5.5.3.2 5.6.3	Continue to provide more realistic calibration of the telemetered vernier engine thrust commands in conjunction with flow bench tests.
2	5.5.3.2	Use the same sun filter for the SC-4 mission as was used for the Surveyor III.
3	5.9.3 5.6.3	Engineering change proposal (ECP-23) has been added to provide complete rejection of any and all crosscoupled sidelobes in all gain state combinations, at any approach angle, and at any burnout velocity where system capability otherwise exists.
4	5.9.3	CCSL rejection logic (ECP-23) will be disabled by the 1000-foot mark.
5	5.9.3	CRO steering will not be disabled until the 1000-foot mark.

4.0 SYSTEM PERFORMANCE ANALYSIS

4.1 GENERAL MISSION SUMMARY

Surveyor III was launched by the Atlas/Centaur booster from pad 36B at AFETR at 07:05:01.06 GMT on Monday, 17 April, after a 50-minute hold in the count to resolve an apparent spacecraft roll actuator anomaly. After a near-perfect injection (the uncorrected impact point was only 480 km from the aim point) and an equally perfect transit phase and midcourse correction (the actual landing point was only 5 km from the aim point), the spacecraft landed successfully near the center of a small (100-km diameter) crater. The landing was complicated by the failure of the doppler radar to turn off the vernier engines 14 feet above the surface. As a result, the spacecraft bounced twice after the initial contact before finally coming to rest after the engines were manually commanded off, probably causing a partial failure in the spacecraft telemetry system which made it usable at very low bit rates only. All other spacecraft equipment performed normally. A major event history for the transit phase is shown in Table 4-1.

After landing, the spacecraft solar panel and planar array were positioned on the sun and earth, respectively. During the ensuing days, several thousand TV pictures were taken and the soil mechanics/surface sampler was successfully exercised in digging and manipulating the lunar surface. Successful lunar operation continued until shortly after lunar sunset. All spacecraft operations for the first lunar day were terminated at 00:00 GMT on day 124. All attempts to reactivate the spacecraft on the second lunar day failed.

The earth track traced by Surveyor III is shown in Figure 4-1. Specific events such as sun and Canopus acquisition, midcourse correction, and touchdown, are also shown. The Surveyor and Centaur trajectory in the earth's equatorial plane is shown in Figure 4-2. The predicted view periods for the tracking stations are given in Table 4-2.

Details of spacecraft performance during each phase of the mission are presented in the following paragraphs. Most of the material has been extracted from the mission operation reports (References 1 and 2) with additions derived from postmission analysis.

TABLE 4-1. SURVEYOR III TRANSIT MISSION MILESTONES

Event	GMT, day:hr:min:sec
Launch	107:07:05:01.059
Injection	107:07:38:49
Separation – electrical	107:07:39:50*
Separation – mechanical	107:07:39:54*
Automatic sun acquisition completed	107:07:47:58*
ASPP solar panel unlocked	107:07:39:53.846±1.188*
ASPP solar panel locked in transit position	107:07:45:51.456±1.2*
ASPP roll axis locked in transit position	107:07:50:05.238*
Spacecraft visibility at Tidbinbilla (one-way)	107:07:55:10*
Initial DSS acquisition (two-way lock) confirmed	107:08:01:30*
First ground command sent to spacecraft	107:08:09:48
Canopus verification begins	107:16:09:12.7*
Canopus lockon	107:16:27:50.8*
First premidcourse attitude maneuver initiated	108:04:46:51
Midcourse thrust executed	108:05:00:03.433±0.025*
Sun reacquired	108:05:04:37*
Canopus reacquired	108:05:08:11*
Initiation of yaw maneuver	109:23:23:30*
Initiation of pitch maneuver	109:23:30:17*
Initiation of roll maneuver	109:23:34:35*
Retro sequence mode on	109:23:55:15.491*
AMR on	109:23:56:35.258*
Thrust phase power on	109:23:57:35.156*
AMR enable	109:23:59:35.252*
AMR mark	110:00:01:12.829 ± 0.05*
Vernier ignition	110:00:01:17.914 ± 0.025*
Retro ignition	110:00:01:19.011 ± 0.05*
RADVS on	110:00:01:19.889 ± 0.6*
Retro burnout	110:00:02:00.578 ± 0.05*
Retro eject	110:00:02:12.527 ± 0.05*

Table 4-1 (continued).

Event	GMT, day:hr:min:sec
Start RADVS controlled descent	110:00:02:14.627 ± 0.05*
1000-foot mark	110:00:03:53.023 ± 0.05*
10-fps mark	110:00:04:10.623 ± 0.05*
14-foot mark	Did not occur
Touchdown 1	110:00:04:18.05**
Touchdown 2	110:00:04:42.03**
Thrust phase power off	110:00:04:53.59*
Touchdown 3	110:00:04:54.42**
RADVS off (command)	110:00:10:35.9
Flight control power off	110:00:10:40.02*
First 200-line TV picture	110:01:02:32*
Earth/sun acquisition completed	110:08:15:00*
First 600-line TV picture	110:08:42:00*

*DSS received time.

**Strain gage data – leg 2 makes first contact – received time.

4.1.1 Spacecraft Transit Phase Command Log

A detailed list of spacecraft commands sent during the transit phase is presented in Table 4-3, including the time the command was sent as well as the tracking station originating the command.

The significant changes in procedure from the prepared standard mission sequence documented in Engineering Planning Document (EPD) 180 are summarized in Table 3-3 of Reference 1. Also included in this table are the reasons for each deviation. Briefly, the sequence changes resulted from the following:

1) DSS report that modulation of the subcarrier on the carrier was not normal, resulting in a special nonstandard sequence for investigating this problem. (The report proved to be incorrect.)

2) Desire to obtain maximum possible sampling rate during star verification, resulting in selection of 4400 bits/sec for this sequence.

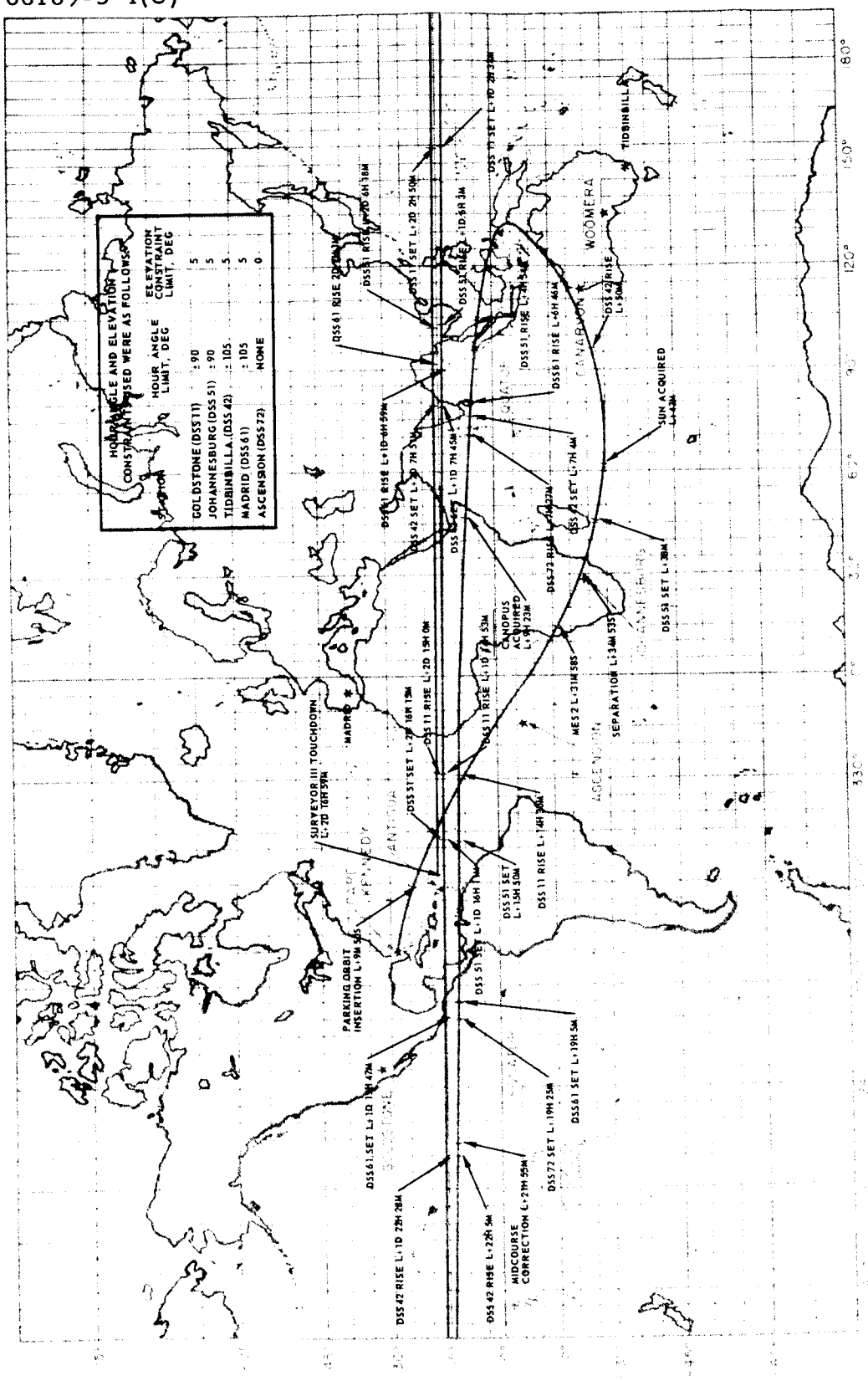

Figure 4-1. Surveyor III Earth Track

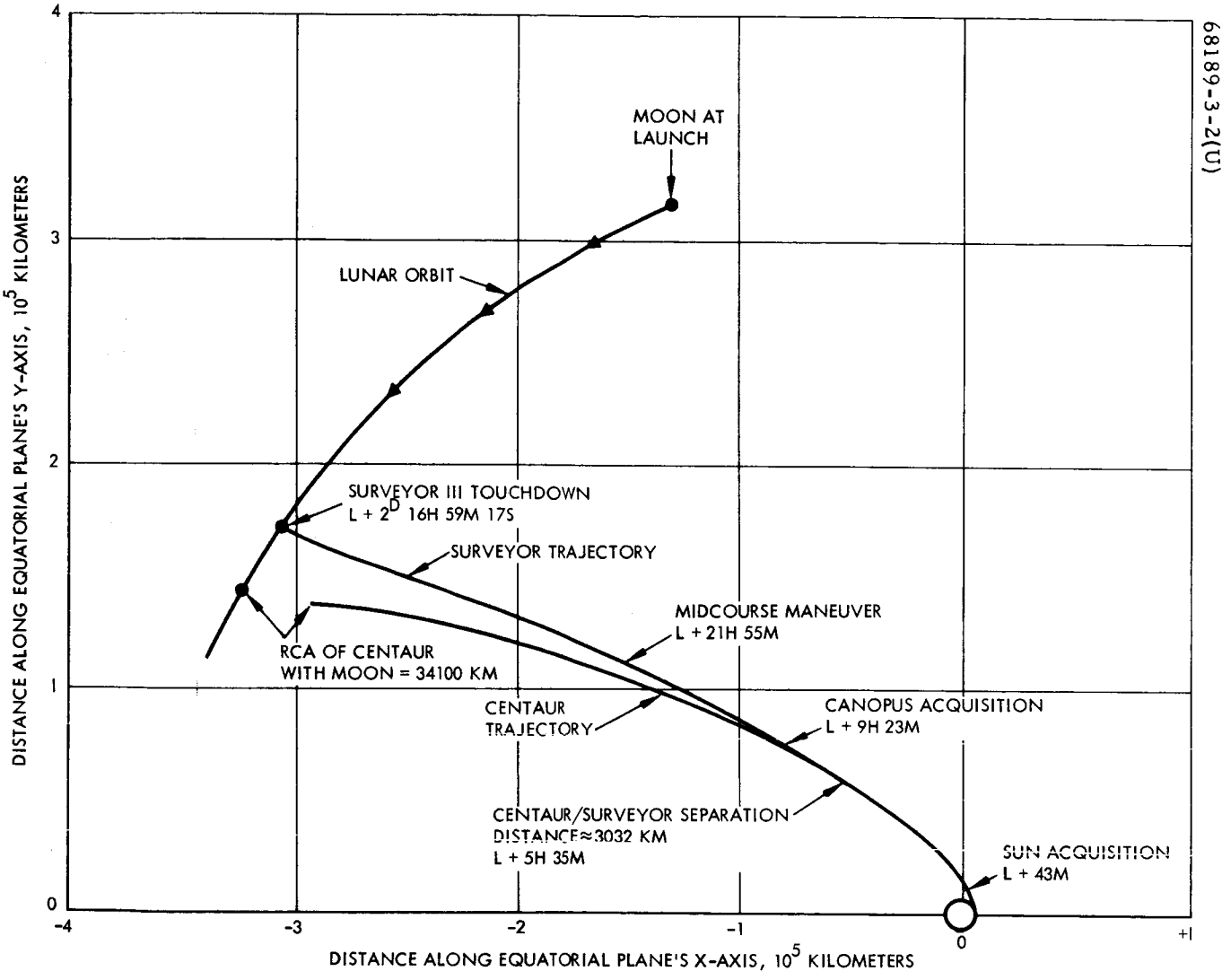

Figure 4-2. Surveyor and Centaur Trajectory in Earth's Equatorial Plane

TABLE 4-2. PREDICTED VIEW PERIOD SUMMARY

Station	Event, degrees	GMT		
		April 1967	Hour	Minute
DSS 51 Johannesburg	270 hour angle set	17	7	42
DSS 42 Tidbinbilla	5 elevation rise	17	7	55
DSS 51 Johannesburg	5 elevation rise	17	11	59
DSS 61 Madrid	5 elevation rise	17	13	51
DSS 42 Tidbinbilla	5 elevation set	17	14	9
DSS 72 Ascension	0 elevation rise	17	14	32
DSS 11 Goldstone	270 hour angle rise	17	21	35
DSS 51 Johannesburg	5 elevation set	17	22	55
DSS 61 Madrid	5 elevation set	18	2	11
DSS 72 Ascension	0 elevation set	18	2	31
DSS 42 Tidbinbilla	5 elevation rise	18	5	10
DSS 11 Goldstone	90 hour angle set	18	9	39
DSS 51 Johannesburg	5 elevation rise	18	13	8
DSS 61 Madrid	5 elevation rise	18	14	4
DSS 42 Tidbinbilla	5 elevation set	18	14	50
DSS 11 Goldstone	270 hour angle rise	18	21	58
DSS 51 Johannesburg	5 elevation set	18	23	16
DSS 61 Madrid	5 elevation set	19	2	46
DSS 42 Tidbinbilla	5 elevation rise	19	5	33
DSS 11 Goldstone	90 hour angle set	19	9	55
DSS 51 Johannesburg	5 elevation rise	19	13	23
DSS 61 Madrid	5 elevation rise	19	14	6
DSS 42 Tidbinbilla	5 elevation set	19	14	56
DSS 11 Goldstone	270 hour angle rise	19	22	5
DSS 51 Johannesburg	5 elevation set	19	23	20
DSS 61 Madrid*	6.5 elevation set	20	02	53
DSS 42 Tidbinbilla*	10.2 elevation rise	20	06	16
DSS 11 Goldstone*	9.7 elevation set	20	10	10

*View periods of moon's center.

TABLE 4-3. SURVEYOR III MISSION EVENTS

Command Sequence				
Command Number	Description	Time (GMT), hr:min:sec	Mode	Bit Rate
		Day 107-DSS-42		
0107	Xmtr Hi Volt Off	08:09:48.2	5	550
0110	Xmtr Fil Pwr Off	09:57.9		
0130	Xfer Sw B Lo Pwr	09:58.4		
0623	Accel Amp 1-4 Off	11:05.0		
0316	SP Deploy Logic Off	11:05.5		
0522	Prop S-Gage Pwr Off	11:06.0		
0512	Accel Amp 5-8 Off	11:06.5		
0516	TD S-Gage Pwr Off	11:07.0		
0126	Xfer Sw A Lo Pwr	11:07.5		
0402	Step SP Minus X 10	12:12.5		
0401	Step SP Plus X 5	12:18.0		
0405	Step Roll Axis Plus X 10	13:07.5		
0406	Step Roll Axis Minus X 5	13:13.0	5	
0510	AESP Off	14:08.0		
0226	Mode 1 On	14:13.5	1	
0237	Low Mod SCO Off	14:45.5		
0216	7.35 Kc SCO On	14:46.0		550
0205	1100 bps	14:46.5		1100
0231	Mode 4 On	16:41.5	4	
0227	Mode 2 On	19:22.5	2	
0232	ESP Off	21:14.1		
0507	Mode 6 On	21:20.1	6	
0506	Mode 5 On	23:25.0	5	
0704	Cruise Mode On	10:52:48.5	5	
0220	7.35 Kc SCO Off	13:07:03.6		
0217	33 Kc SCO On	07:04.1		
0206	4400 bps	07:04.6		4400
0205	1100 bps	09:46.0		1100
0220	33 Kc SCO Off	09:46.5		1100
0216	7.35 Kc SCO On	09:47.0		1100
0503	550 bps	31:55.5		550
0204	A/D Coast φ Rates	32:16.5		
0220	7.35 Kc SCO Off	32:26.0		
		Day 107-DSS-61		
0215	3.9 Kc SCO On	13:32:35.3		
0203	A/D Conv Pwr Off	14:07:18.0		
0201	A/D Conv Pwr On (No. 1)	12:23.2	5	
0510	AESP Off	15:42:49.6		
0231	Mode 4 On	42:57.3	4	
0227	Mode 2 On	47:01.3	2	550

Table 4-3 (continued).

Command Sequence				
Command Number	Description	Time (GMT), hr:min:sec	Mode	Bit Rate
		Day 107-DSS-61		
0226	Mode 1 On	15:49:48.8	1	550
0232	ESP Off	54:20.3		
0506	Mode 5 On	54:27.2	5	
0105	Xmtr B Fil Pwr On	16:00:41.2		
0127	Xfer-Sw B Hi Pwr	02:24.2		
0106	Xmtr B Hi Volt On	02:24.7		
0220	3.9 Kc SCO Off	03:30.2		
0217	33 Kc SCO On	03:46.2		550
0206	4400 bps	04:05.1		4400
0124	Xpdr Pwr Off	05:52.2		
0704	Cruise Mode On	06:54.2		
0715	Man Delay Mode On	06:54.7		
0710	Pos Angle Maneuver	06:55.2		
0714	Sun and Roll	09:12.2		
0703	Sun-Star Acq Mode On	27:35.1		
0704	Cruise Mode On	30:27.6		
0123	Xpdr B Pwr On	31:25.6		4400
0205	1100 bps	36:26.6		1100
0220	33 Kc SCO Off	37:29.5		
0216	7.35 Kc SCO On	37:40.0		
0107	Xmtr Hi Volt Off	39:28.3		
		Day 107-DSS-42		
0110	Xmtr Fil Pwr Off	16:39:49.5		
0130	Xfer-Sw B Lo Pwr	39:50.0		
0700	Inertial Mode On	17:29:17.7		
0704	Cruise Mode On	19:16:32.3		
		Day 107-DSS-51		
0700	Inertial Mode On	19:23:35.2		
0700	Inertial Mode On	20:06:44.0	5	
		Day 107-DSS-61		
0510	AESP Off	21:19:47.5		
0231	Mode 4 On	19:55.4	4	
0227	Mode 2 On	22:22.4	2	
0232	ESP Off	26:04.0	2	
0506	Mode 5 On	26:10.9	5	
0704	Cruise Mode On	41:54.3	5	1100

Table 4-3 (continued).

Command Sequence				
Command Number	Description	Time (GMT), hr:min:sec	Mode	Bit Rate
		Day 107-DSS-11		
0702	Sun Acq Mode On	23:11:20.6	5	1100
0510	AESP Off	53:26.0	5	
0231	Mode 4 On	53:36.8	4	
0227	Mode 2 On	58:14.8	2	
		Day 108-DSS-11		
0232	ESP Off	00:00:33.8		
0506	Mode 5 On	00:00:43.2	5	
0704	Cruise Mode On	02:11:21.1	5	
0510	AESP Off	54:34.9	5	
0231	Mode 4 On	54:41.4	4	
0227	Mode 2 On	56:19.6	2	
0226	Mode 1 On	57:51.8	1	
0232	ESP Off	59:42.7	1	
0506	Mode 5 On	59:48.7	5	
0220	7.35 Kc SCO Off	03:01:49.8		
0221	Gyro Spd Sig Pro On	01:50.3		
0222	Next Gyro	02:50.3		
0222	Next Gyro	03:46.3		
0222	Next Gyro	04:13.3		
0223	Gyro Spd Sig Pro Off	04:48.8		
0216	7.35 Kc SCO On	04:49.3	5	
0510	AESP Off	04:12:54.2		
0231	Mode 4 On	13:00.2	4	
0227	Mode 2 On	16:00.4	2	
0226	Mode 1 On	17:55.9	1	
0105	Xmtr B Fil Pwr On	19:09.9		
0127	Xfer Sw B Hi Pwr	20:47.9		
0106	Xmtr B Hi Volt On	20:48.4		
0220	7.35 Kc SCO Off	21:30.4		
0217	33 Kc SCO On	21:30.9		1100
0206	4400 bps	21:31.4		4400
0704	Cruise Mode On	29:59.7		
0710	Pos Angle Maneuver	30:00.2		
3617	Interlock	30:00.7		
M1034	Magnitude (284 BCD) (56.8°)	30:01.2		
0714	Sun and Roll	46:49.8		
0702	Sun Acq Mode On	49:27.2		
3617	Interlock	49:27.7		
M0604	Magnitude (196 BCD) (-39.2°)	49:28.2		
0712	Pitch	50:08.2	1	4400

Table 4-3 (continued).

Command Sequence				
Command Number	Description	Time (GMT), hr:min:sec	Mode	Bit Rate
		Day 108-DSS-11		
0227	Mode 2 On	04:52:36.2	2	4400
0226	Mode 1 On	54:00.7	1	
0521	Prop S-Gage Pwr On	54:29.2		
0700	Inertial Mode On	54:29.7		
0720	Reset-Set IV Outputs	54:41.6		
0135	SMSS Aux Htr Off	55:18.3		
0604	AMR Htr Off	55:18.8		
0613	VL2FT2 Ther Pwr Off	55:19.3		
0616	VL1OT2 Ther Pwr Off	56:19.8		
0621	VL3OT3 Ther Pwr Off	55:20.3		
3617	Interlock	55:20.8		
0605	Unlk Roll Act, Press VPS	55:21.3		
0727	FC T -φ Pwr On	57:03.2		
3617	Interlock	57:23.7		
M0226	Magnitude (86 BCD)(4.3 sec.)	57:24.2		
3617	Interlock	05:00:01.7		
0721	Vernier Ignition	00:02.2		
0735	Emer Vernier Eng Off	00:09.1		
0735	Emer Vernier Eng Off	00:10.1		
0737	FC T -φ Pwr Off	00:30.2		
0737	FC T -φ Pwr Off	00:31.7		
0522	Prop S-Gage Pwr Off	00:49.7		
0512	Accel Amp 5-8 Off	00:50.2		
0516	TD S-Gage Pwr Off	00:50.7	1	
0232	ESP Off	01:10.2		
0506	Mode 5 On	01:15.7	5	
0611	VL2 Ther Pwr On	01:52.2		
0614	VL1 Ther Pwr On	01:52.7		
0617	VL3 Ther Pwr On	01:53.2		
0624	AMR Htr On	01:54.2		
0136	SMSS Aux Htr On	01:54.7		
0710	Pos Angle Maneuver	02:33.0		
3617	Interlock	02:33.5		
M0604	Magnitude (196 BCD)(39.2°)	02:34.0		
0712	Pitch	03:18.7		
0702	Sun Acq Mode On	05:11.7		
3617	Interlock	05:46.2		
M1034	Magnitude (284 BCD)(-56.8°)	05:46.7		
0714	Sun and Roll	06:17.7		
0704	Cruise Mode On	09:04.1	5	
0510	AESP Off	10:45.9		
0227	Mode 2 On	10:52.4	2	
0231	Mode 4 On	12:14.1	4	4400

Table 4-3 (continued).

Command Sequence				
Command Number	Description	Time (GMT), hr:min:sec	Mode	Bit Rate
		Day 108-DSS-11		
0232	ESP Off	05:15:03.1		
0506	Mode 5 On	15:09.1	5	4400
0205	1100 bps	15:28.7		1100
0220	33 Kc SCO Off	15:37.0		
0216	7.35 Kc SCO On	15:43.5		
0107	Xmtr Hi Volt Off	16:08.6		
0110	Xmtr Fil Powr Off	16:14.6		
0130	Xfer Sw B Lo Pwr	16:15.1	5	
0510	AESP Off	07:03:03.6		
0231	Mode 4 On	03:13.4	4	
0227	Mode 2 On	07:40.4	2	
0232	ESP Off	11:39.9		
0506	Mode 5 On	11:49.4	5	
0700	Inertial Mode On	35:58.1		1100
		Day 108-DSS-12		
0503	550 bps	08:49:13.5		550
0204	A/D Coast φ Rates	49:38.1		
0220	7.35 Kc SCO Off	49:52.1		
0215	3.9 SCO On	50:08.6		
0704	Cruise Mode On	09:43:45.8	5	
		Day 108-DSS-51		
0507	Mode 6 On	15:08:22.3	6	
0510	AESP Off	12:59.5	6	
0231	Mode 4 On	13:07.5	4	
0227	Mode 2 On	17:58.5	2	
0232	ESP Off	21:05.0		
0506	Mode 5 On	21:12.4	5	
0700	Inertial Mode On	17:31:25.8		
		Day 108-DSS-61		
0702	Sun Acq Mode On	19:31:50.1		
0700	Inertial Mode On	37:26.6		
0510	AESP Off	20:02:49.1	5	
0231	Mode 4 On	02:56.9	4	
0227	Mode 2 On	09:07.9	2	
0232	ESP Off	12:06.0		
0506	Mode 5 On	12:14.3	5	
0704	Cruise Mode On	22:34.8		
0700	Inertial Mode On	27:20.3		
0704	Cruise Mode On	22:50:04.8		
0702	Sun Acq Mode On	54:00.2	5	550

Table 4-3 (continued).

Command Sequence				
Command Number	Description	Time (GMT), hr:min:sec	Mode	Bit Rate
		Day 109-DSS-61		
0510	AESP Off	00:52:24.9		550
0231	Mode 4 On	52:33.3	4	
0227	Mode 2 On	59:52.3	2	
0232	ESP Off	01:07:11.8		
0506	Mode 5 On	07:19.7	5	
0704	Cruise Mode On	15:43.7		
0700	Inertial Mode On	23:35.7		
		Day 109-DSS-11		
0704	Cruise Mode On	03:36:31.7		
0702	Sun Acq Mode On	57:26.1	5	
0510	AESP Off	05:24:53.6		
0231	Mode 4 On	25:03.0	4	
0227	Mode 2 On	32:02.1	2	
0232	ESP Off	39:11.6		
0506	Mode 5 On	39:20.9	5	
0317	Aux Batt Mode On	06:01:18.9		
0322	Hi Curr Mode On	11:59.8		
0320	Restore MB Mode	13:43.3		
		Day 109-DSS-42		
0704	Cruise Mode On	06:45:13.7		
0700	Inertial Mode On	48:52.7		
0615	VOT2 Ther Pwr On	07:03:55.3		
		Day 109-DSS-11		
0704	Cruise Mode On	09:09:21.4		550
		Day 109-DSS-42		
0504	137.5 bps	57:13.3		137.5
0220	3.9 Kc SCO Off	57:24.8		
0500	Coast φ I SCO On	57:36.3		
0510	AESP Off	10:02:48.3	5	
0231	Mode 4 On	02:56.8	4	
0232	ESP On	13:19.9		
0507	Mode 6 On	10:13:32.8	6	
0506	Mode 5 On	19:44.4	5	
0702	Sun Acq Mode On	21:22.9		
0317	Aux Batt Mode On	59:59.5		
0323	Hi Curr Mode Off	11:07:53.0		
0320	Restore MB Mode	08:15.6		
0322	Hi Curr Mode On	13:33.6	5	137.5

Table 4-3 (continued).

Command Sequence				
Command Number	Description	Time (GMT), hr:min:sec	Mode	Bit Rate
		Day 109-DSS-42		
0704	Cruise Mode On	12:41:23.8	5	137.5
0510	AESP Off	47:57.4		
0231	Mode 4 On	48:05.3	4	
0227	Mode 2 On	50:52.4	2	
0232	ESP Off	53:17.4		
0506	Mode 5 On	53:25.8	5	
		Day 109-DSS-61		
0700	Inertial Mode On	14:28:07.4		
0124	Xpdr Pwr Off	15:59:51.9		
0123	Xpdr B Pwr On	16:05:25.4		
0704	Cruise Mode On	55:52.6		
0702	Sun Acq Mode On	17:05:59.9	5	
0510	AESP Off	17:03.5		
0231	Mode 4 On	17:12.9	4	
0227	Mode 2 On	21:57.9	2	
0232	ESP Off	24:11.1		
0506	**Mode 5 On**	**24:20.9**	5	
		Day 109-DSS-51		
0317	Aux Batt Mode On	18:14:20.6		
0323	Hi Curr Mode Off	19:24.1		
0320	Restore MB Mode	20:25.0		
0322	Hi Curr Mode On	26:24.5		
		Day 109-DSS-61		
1136	Sur Camera ETC On	18:51:47.4		
0507	Mode 6 On	19:43:09.2	6	
0510	AESP Off	46:35.6	6	
0231	Mode 4 On	46:45.1	4	
0227	Mode 2 On	48:37.6	2	
0232	ESP Off	54:27.1		
0506	Mode 5 On	54:36.0	5	
0700	Inertial Mode On	20:50:50.8		
0704	Cruise Mode On	56:12.8		
0510	AESP Off	21:24:39.6	5	
0231	Mode 4 On	24:48.5	4	
0227	Mode 2 On	26:43.1	2	
0226	Mode 1 On	28:16.6	1	
0232	ESP Off	29:57.1		
0506	Mode 5 On	30:05.0	5	
0502	Coast φ SCOs Off	31:57.1		137.5

Table 4-3 (continued).

Command Sequence				
Command Number	Description	Time (GMT), hr:min:sec	Mode	Bit Rate
		Day 109-DSS-61		
0221	Gyro Spd Sig Pro On	32:17.6	5	137.5
0222	Next Gyro	34:41.1		
0222	Next Gyro	35:24.5		
0222	Next Gyro	35:50.0		
0223	Gyro Spd Sig Pro Off	36:30.5		
0500	Coast φ I SCO On	36:51.0	5	
0124	Xpdr Pwr Off	40:23.5		
0123	Xpdr B Pwr On	41:40.0		
		Day 109-DSS-11		
0507	Mode 6 On	23:01:55.8	6	
0510	AESP Off	05:53.3		
0231	Mode 4 On	06:00.7	4	
1133	Sur Camera VTC On	07:40.7		
0105	Xmtr B Fil Pwr On	07:59.2		
0127	Xfer SW B Hi Pwr	09:40.2		
0106	Xmtr B Hi Volt On	23:09:90.7		
0502	Coast φ SCOs Off	10:33.7		137.5
0216	7.35 Kc SCO On	10:33.7		
0205	1100 bps	10:40.2		1100
0214	Sum Amps Off	11:30.8		
0211	Phase Sum Amp B On	11:31.3	4	
0227	Mode 2 On	12:09.8	2	
0232	ESP Off	13:09.7		
0506	Mode 5 On	13:17.2	5	
0521	Prop S-Gage Pwr On	17:01.2		
0515	TD S-Gage Pwr On	17:45.2		
0517	TD S-Gage D-Ch On	17:46.2		
0124	Xpdr Pwr Off	19:21.2		
0704	Cruise Mode On	21:26.8		
3617	Interlock	21:27.3		
M3026	Magnitude (790 BCD)(-158°)	21:27.8		
0713	Yaw	23:29.7		
3617	Interlock	29:15.6		
M1400	Magnitude (384 BCD)(-76.8°)	29:16.1		
0712	Pitch	30:17.2		
3617	Interlock	33:22.6		
M1200	Magnitude (320 BCD)(-64°)	33:23.1		
0711	Roll	34:35.2		
0723	Reset Nom Thr Bias	38:35.3		
3617	Interlock	39:38.1	5	1100

Table 4-3 (continued).

Command Sequence				
Command Number	Description	Time (GMT), hr:min:sec	Mode	Bit Rate
		Day 109-DSS-11		
M0306	Magnitude (102 BCD) (5.1 sec.)	23:39:39.1	5	1100
0507	Mode 6 On	46:26.0	6	
0720	Reset-Set IV Outputs	52:20.8		
3617	Interlock	55:12.5		
0724	Retro Seq Mode On	55:13.0		
0613	VL2FT2 Ther Pwr Off	55:44.0		
0616	VL1OT2 Ther Pwr Off	55:45.0		
0621	VL3OT3 Ther Pwr Off	55:45.5		
0135	SMSS Aux Htr Off	55:46.0		
1134	Sur Camera VTC Off	55:46.5		
1137	Sur Camera ETC Off	55:47.0		
0604	AMR Htr Off	55:48.0		
0625	AMR Pwr On	56:32.8		
0727	FC T-φ Pwr On	57:32.8		
0626	AMR Enable	59:32.9		
		Day 110-DSS-11		
0730	Emer AMR Signal	00:01:11.9		
0730	Emer AMR Signal	01:12.4		
0730	Emer AMR Signal	01:12.9		
0207	Pre Sum Amp On	02:32.7		
0737	FC T-φ Pwr Off	04:51.4		
0737	FC T-φ Pwr Off	04:52.4		
0737	FC T-φ Pwr Off	06:51.9		
0737	FC T-φ Pwr Off	06:53.4		
0737	FC T-φ Pwr Off	07:26.9		
0737	FC T-φ Pwr Off	07:28.4	6	1100

3) Additional gyro drift checks obtained during coast phase I and coast phase II to obtain the best estimate of the drift of each gyro for use in terminal descent computations.

4) Normal acquisition of the sun and star following the reverse midcourse maneuvers resulting in a decision by the Space Flight Operations Director to eliminate the postmidcourse star verification sequence.

5) Reduction in bit rate from 550 to 137.2 bits/sec caused by bit error rate exceeding maximum allowable 3×10^{-3} rate.

6) Request of the flight path analysis and command group to perform an additional voltage controlled crystal oscillator frequency check, resulting in an additional check approximately 8 hours prior to touchdown.

7) Decision to combine the last two preterminal descent engineering interrogations.

8) Additional sampling of mode 6 data.

9) Delay in commanding the survey camera vidicon temperature control on until mode 4 was selected to permit verification that the temperature was greater than specified (i.e., >-20°F) for turnon.

4.1.2 Prelaunch Countdown

The prelaunch systems readiness test, started at 17:45 GMT (12:45 EST) on Sunday afternoon 16 April, was completed at 24:00 GMT. The countdown was then started at 03:55 GMT with a target launch time of 06:14 GMT. Because of a question regarding the spacecraft roll actuator performance, the count was held at T-5 minutes for approximately 1 hour while the question was resolved by performing a verification test on SC-5 at El Segundo. This test showed performance to be normal and the count was restarted, resulting in Atlas ignition and liftoff at 07:05:01.059 GMT on 17 April with a launch azimuth of 100.809 degrees.

It had been noted during the prelaunch system readiness test that the roll actuator position telemetry signal had changed approximately 13 BCD when thrust phase power was turned on, indicating the possibility that the roll actuator was not pinned as desired, but was actually free to move. A special test was run which turned on thrust phase power and precessed the roll gyro to create an error in the roll loop. The resulting roll actuator position was then observed. Test results showed that the roll actuator telemetry did indicate a change of approximately 2 degrees when the roll gyro was precessed 10 degrees.

While test results were being analyzed and a special AFETR-directed test was being set up on SC-5 to determine if the performance observed on Surveyor III was characteristic of a normal system, the countdown continued until T-5 minutes without any further problems. At T-5 minutes, the normal built-in hold was extended until the SC-5 roll actuator test could be completed.

This special SC-5 test confirmed that Surveyor III behavior was not anomalous. The apparent movement of the roll actuator was attributed to internal movement of the position pickoff due to structural compliance of the components under torquer command. The decision was therefore made to launch, and the countdown was continued. Liftoff occurred at 07:05:01.059 GMT, some 51 minutes later than the originally scheduled launch time, at a launch azimuth of 100.809 degrees.

4.1.3 Launch, Injection, and Separation

4.1.3.1 Launch Trajectory Profile

Surveyor III was launched using a General Dynamics/Convair (CD/C) Atlas/Centaur (AC-12) boost vehicle. The launch had been held 51 minutes because a spacecraft roll actuator problem was indicated. Liftoff occurred at 07:05:01.059 GMT. Two seconds after liftoff, the launch vehicle began a 13-second programmed roll that oriented the vehicle from a pad-aligned azimuth of 115 degrees to a launch azimuth of 100.809 degrees. At 15 seconds, a programmed pitch maneuver was initiated. The nominal and actual mark times for the Atlas/Centaur boost phase events are summarized in Table 4-4. Times for mark events 12, 16, 17, 19, and 23 were never made available during the mission. All mark times were nominal with the exception of events 10 and 11, but there was some question of the validity of these mark times. Postflight data showed that the times received for events 10 and 11 were in error and were, in fact, nominal. The launch phase ascent trajectory profile is illustrated in Figure 4-3.

Separation of Surveyor from Centaur occurred at 07:39:54.5 GMT on 17 April at an approximate geocentric latitude and longitude of -24 and 30 degrees, respectively. The spacecraft was in the earth's shadow during the first 16.5 minutes of the ascent phase and parking orbit, but left the earth's shadow prior to separation and remained out of the shadow during the transit trajectory.

4.1.3.2 Spacecraft Performance

The boost phase was normal, with the Atlas roll and pitch programs, as well as the normal opening and closing of the spacecraft inertia switch, being confirmed by spacecraft telemetry. In addition, secondary sun sensor signals showed that the spacecraft remained in the earth's shadow approximately 17 minutes. After remaining in a parking orbit for 24 minutes, the Centaur reignited its engines and injected the spacecraft on a trajectory which was nearly perfect and which ensured that a landing at the target area could be achieved. Subsequent to injection and just prior to its separation from the spacecraft, the Centaur issued the necessary preprogrammed commands for accomplishing the spacecraft operations required for the post-separation phase – namely, extend landing gears, extend omnidirectional antennas, and transmitter high power on. The poor quality of the data received in the spacecraft performance and analysis command (SPAC) area prevented confirmation of these events by spacecraft telemetry as they occurred, but they were verified along with spacecraft separation from the Centaur at approximately 07:40:09 GMT (L+35M8S), when the received SPAC data quality improved.

Following separation, solar panel stepping was automatically initiated. Also, the spacecraft cold gas jets were enabled, and the flight control subsystem nulled out the tipoff rates and initiated the roll-yaw sequence to acquire the sun. At 07:48:00 GMT, primary sun sensor lockon was observed

TABLE 4.4 MARK EVENTS

Number	Event	Nominal Time, seconds	Actual Time, seconds
	Liftoff (2-inch motion)(07:05:01.059 GMT)	L + 0.0	
1	Atlas BECO	142.9	142.5
2	Atlas booster engine jettison	146.0	145.5
3	Centaur insulation panel jettison	176.9	176.2
4	Centaur nose fairing jettison	203.9	203.5
5	Atlas SECO and VECO	236.4	237.7
6	Atlas/Centaur separation	238.4	239.6
7	Centaur MES1	247.9	249.2
8	Centaur MECO1	574.9	569
9	100-pound thrust on	574.9	589.7
10	100-pound thrust off	650.9	665.2
11	6-pound thrust on	650.9	665.2
12	100-pound thrust on	1873.6	1877.34
13	Centaur MES1 engine C2	1913.6	1977.33
14	Centaur MES1 engine C1	1913.6	1918.7
15	Centaur MECO2	2021.7	2028.7
16	Extend landing gear	2047.7	2051.8
17	Unlock omnidirectional antenna	2058.2	2061.8
18	Surveyor high power transmitter on	2078.7	2072.5
19	Centaur/Surveyor electrical disconnect	2084.2	2087.83
20	Spacecraft separate	2089.7	2093.35
21	Begin Centaur turn around maneuver	2094.7	2095.7
22	Start Centaur lateral thrust	2134.7	2151.7
23	End Centaur lateral thrust	2154.7	N.A.
24	Start Centaur tank blowdown	2329.7	2333.5
25	End Centaur tank blowdown	2579.7	2583.8
26	Power changeover switch	2679.7	2683.5

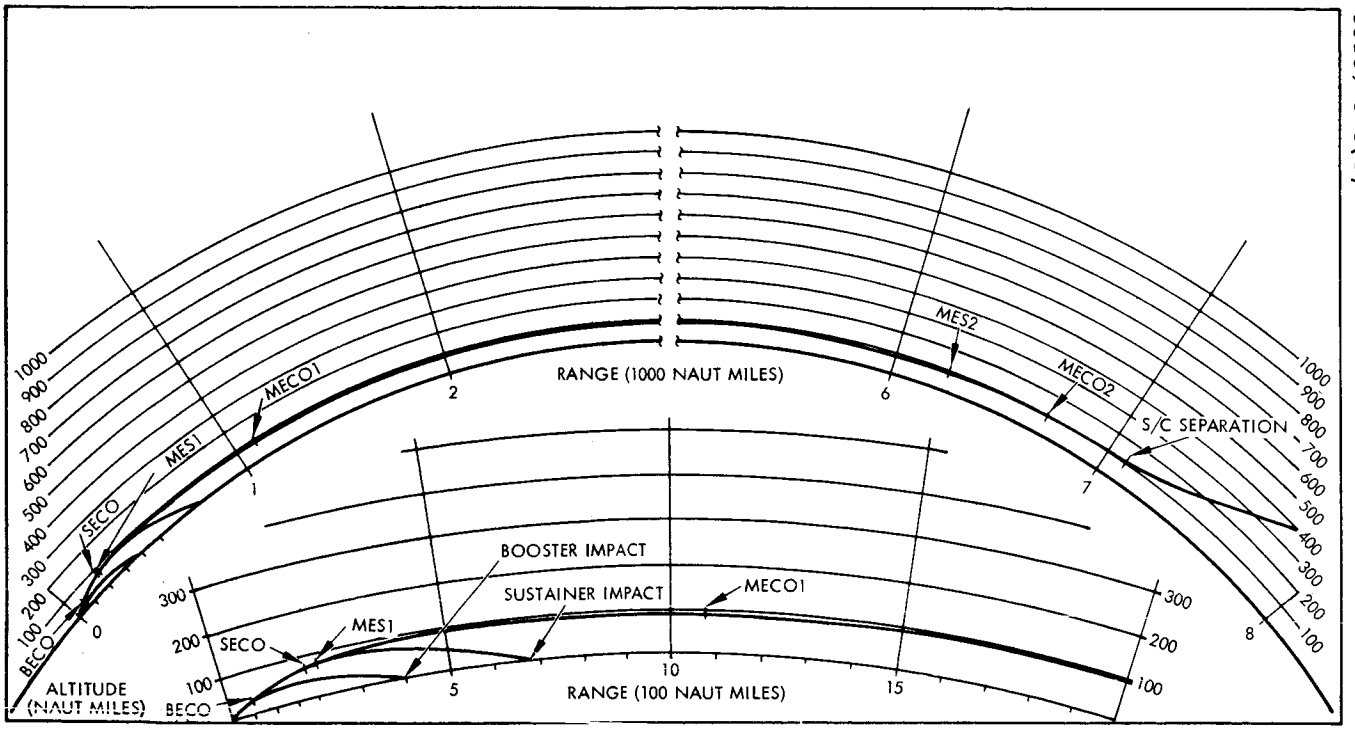

Figure 4-3. Al-12 Launch Phase Trajectory Profile

following a minus roll of approximately 181 degrees and a positive yaw of 38 degrees. Concurrent with the sun acquisition sequence, the antenna/solar panel positioner (A/SPP) was completing its solar-panel and roll-axis deployment and, at 07:50:05 GMT, the solar panel was in its proper transit position (Table 4-5).

Spacecraft separation and sun acquisition performance are presented in Table 4-6. The launch, separation, and acquisition time sequence is shown in Figure 4-4.

4.1.4 DSIF Acquisition

4.1.4.1 Initial Two-Way Acquisition at DSS 42

Predictions indicated a Surveyor III rise at DSS 42 (Canberra) at 07:54:57 GMT on 17 April. DSS 42 reported good one-way doppler data at 07:55:42 (rise + 00:45), auto-track on the acquisition-aide antenna at 07:57:50 (rise + 2:53), auto-track on the subcarrier modulator (SCM) (antenna main beam) at 08:00:44 GMT (rise + 5:47), and good two-way doppler data at 08:01:52 GMT (rise + 6:55). The current acquisition procedure does not allow transfer to the SCM and up-link (two-way) acquisition search to begin until the spacecraft is 10 degrees above the local horizon, which in this case occurred at 07:58:10 GMT (rise + 03:13). In light of this, the initial acquisition at DSS 42 can be considered quite smooth and close to optimum.

4.1.4.2 Initial Spacecraft Operations

The first ground-controlled sequence (initial spacecraft operations) was initiated at L+1H4M47S. Commands were sent to the spacecraft to turn off equipment required only for the launch-to-Deep Space Instrumentation Facility acquisition phase (e.g., transmitter power off, accelerometer amplifiers off, etc.), to seat the solar panel and roll-axis locking pins securely, i.e., by rocking the axis back and forth, to increase the telemetry bit rate to 1100 bits/sec, and to interrogate telemetry commutator modes so that the overall spacecraft condition could be assessed. All spacecraft responses to commands were normal. Because of a high value of star intensity signal (indicating the presence of the earth in the Canopus sensor field of view), it was decided that the cruise mode on command should be delayed and that the flight control subsystem be kept in sun mode. In addition, it was determined that there would be no need to implement the "if required" sequence for permitting receiver A to lock on to the ground transmitter signal since the signal was already well within the receiver passband (i.e., receiver A automatic frequency control telemetry indicated only 2 kHz error).

4.1.5 Coast Phase I (Including Canopus Acquisition)

The spacecraft continued to coast normally with its pitch-yaw attitude controlled to track the sun and with its roll axis held inertially fixed. Tracking and telemetry data were being obtained by the use of transponder B

TABLE 4-5. SPACECRAFT SEPARATION EVENTS

Events Completed	Time GMT, day:hr:min:sec
Centaur separation – electrical	107:07:39:50
Centaur separation – mechanical	39:54
Solar panel deployed	45:51
ASPP to roll transit position	50:05
Sun acquisition	47:58

TABLE 4-6. SPACECRAFT SEPARATION AND ACQUISITION PERFORMANCE

Performance	Units	Actual	Predicted	
			Value	Source
Time to remove separation rates	Seconds	<11	<51	Specification
Solar panel deployment time	Seconds	357	357	Preflight test
ASPP roll positioning time	Seconds	254	259	Preflight test
Sun acquisition maneuver				
Roll	Degrees	181		
Yaw	Degrees	38		
Time	Seconds	438.2	1080	Specification

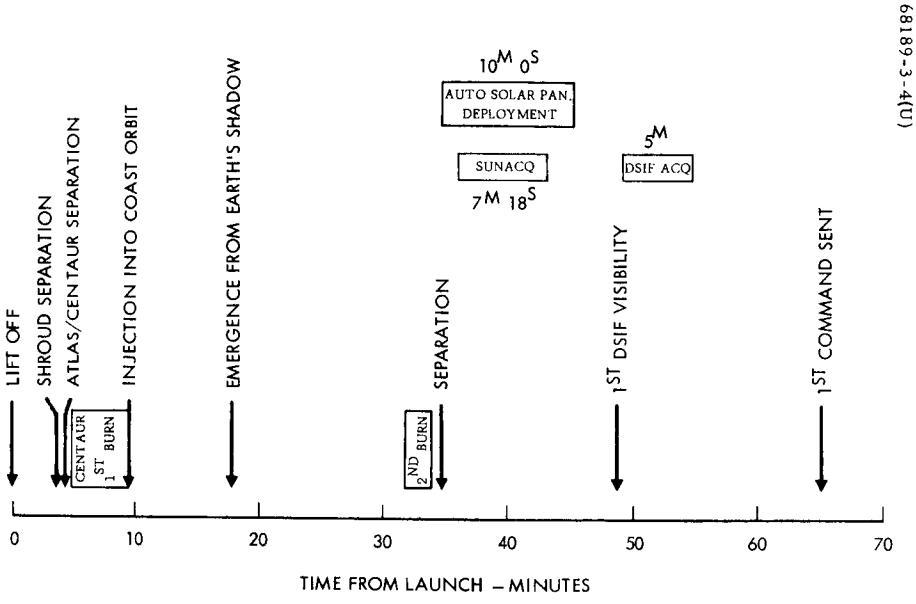

Figure 4-4. Launch, Separation, and Acquisition Timing

operating in low power. At L+2H45M, it was recommended that the star verification and acquisition sequence be initiated at approximately L+9H, based upon DSS 61 acquiring the vehicle at L+8H45M and upon the availability of a prepared star map for this time.

By L+3H35M, the star intensity signal had decreased to a low level (i.e., 0.5 volt), and had remained steady for over 30 minutes. This indication that the earth was no longer in the Canopus sensor field of view resulted in the decision to command cruise mode on to ensure that the attitude control system would revert to inertial mode in case sun lock was inadvertently lost. This was accomplished and verified at L+3H48M.

At L+4H5M, DSS 42 reported that a measurement of sideband energy had shown that this energy level was approximately 5 to 6 db lower than expected compared to the carrier power. The possibility was suggested that the modulation index for the subcarrier modulating the carrier was incorrect. Since transfer to DSS 51 was imminent, it was decided to delay initiation of any nonstandard procedures for investigating this problem until DSS 51 could confirm the problem by making the same sideband energy measurement that DSS 42 had made. Using the same procedure as DSS 42, DSS 51 obtained the same results.

At L+6H2M, a nonstandard sequence was initiated to determine whether the problem was due to: 1) the 7.35 kHz subcarrier oscillator output voltage (so that the 1100 bits/sec only would be affected), or 2) the modulator for the subcarrier modulation of the carrier (so that all bit rates would be affected on one transmitter), or 3) the measurement technique of the DSS stations. Changes in bit rate were commanded and resulted in the proper change of carrier power, but the subcarrier power measurement still indicated too low a value. It was then decided to interrupt the modulation of the data on the subcarrier to see if the DSS measurements of sideband power were being affected. This was accomplished by turning the analog-to-digital converter off at L+7H2M. The DSS measurements of sideband and carrier power verified that the modulation index was correct and that the problem was not in the spacecraft, but in the technique of measuring sideband power when the data are modulating the subcarrier oscillator signal (i.e., only part of the sideband power was being measured). The analog-to-digital converter was turned back on at L+7H7M.

At approximately L+8H, the performance analysis group completed its analysis for accomplishing star verification and acquisition. It was recommended that the star map be obtained by making one complete roll using omnidirectional antenna B with coast mode commutator data being transmitted at 4400 bits/sec. It was predicted that the spacecraft would roll through a deep null which could cause loss of data from 40 to 60 seconds for the worst case and from 15 to 20 seconds for the nominal case. It was also predicted that two-way lock could probably be maintained, but that there was some slight risk that spacecraft rotation through the deep null might cause a loss of lock. Consequently, since the flight path and analysis command group indicated that loss of two-way data for 30 to 45 minutes would not be serious, it was decided to do the verification sequence in one-way lock.

After completion of an engineering interrogation initiated at L+8H37M, the spacecraft roll sequence for obtaining the star map and for locking on to Canopus was begun at L+9H4M. During the first revolution, star intensity signals from Canopus, Procyon, Adhara, Altair, the moon, Jupiter, and the earth were identified, with Canopus being observed after 205 degrees of roll. The roll maneuver predicted by the trajectory group was 205.3 degrees. It was also noticed that signals from two objects which appeared after 68 and 172 degrees of roll, respectively, did not appear on the preprepared map and that a Canopus lock signal did appear when Canopus was in the star sensor field of view. As the spacecraft continued to roll (on its way to achieving Canopus lockon), it was noticed that the two signals which could not be identified on the first revolution did not appear, indicating that the signals were probably due to particles that had moved through the field of view during the first rotation. The star acquisition mode on command for achieving automatic lockon was sent at L+9H22M34S after passing the star Adhara for the second time. Canopus was automatically acquired at L+9H22M50S. This was the first automatic acquisition for any Surveyor mission. The star map is described in Table 4-7.

Prior to the flight, it was predicted that the star intensity signal (FC-14) would read approximately 3.8 volts with Canopus in the field of view. The actual inflight reading was approximately 4.2 volts, which is within the tolerance on the signal. The fact that automatic lockon was obtained confirms the fact that the intensity fell within the upper and lower intensity gates. No change in sensor gain is planned for SC-4.

Transponder B was commanded back on at L+9H26M and two-way lock reestablished. Transmitter high power was commanded off at L+9H34M, and the vehicle returned to its coasting as before, but with its roll attitude controlled so that the star sensor remained locked to Canopus. Continuous engineering data were obtained at 1100 bits/sec with transmitter low power throughout this phase. Coast mode commutator data were transmitted at all times except during an engineering interrogation of commutator modes 4 and 2 at L+16H48M for thermal assessment, during the two premidcourse interrogations of modes 4, 2, and 1 (at L+19H49M and L+21H7M), and during the gyro speed check at L+19H57M. Two full gyro drift checks (pitch, yaw, roll) and one roll-only drift check were conducted from L+10H24M to L+12H11M, from L+12H18M to L+14H37M, and from L+16H6M to L+19H6M, respectively.

During this coast phase, only one anomaly was noted. The soil mechanics/surface sampler (SM/SS) auxiliary temperature dropped below its design thermal control temperature of -4°F, even though its heater was full on, to a low of approximately -35°F. Spacecraft drift during the full gyro drift checks was such that the SM/SS temperature increased to as much as -15°F.

4.1.6 Midcourse Correction

The first spacecraft rotation (a positive roll) of 56.75 degrees was initiated at 4:46:48 GMT on 18 April. Upon its completion, a negative pitch rotation of 39.13 degrees was effected to align the spacecraft Z-axis along the

TABLE 4-7. DESCRIPTION OF SURVEYOR III STAR MAP

Roll Angle From Start of Maneuver, degrees	Object in Star Sensor Field of View	Comments
0		Start of maneuver
68	Reflection from a particle	Does not appear on second revolution
120	Moon	
128	Jupiter	
144	Procyon (Alpha Canis Minoris)	
172	Reflection from a particle	Does not appear on second revolution
179	Adhara (Epsilon Canis Majoris)	
205	Canopus	
315	Earth	
337	Altair (Alpha Aquilae)	
480	Moon	
488	Jupiter	
504	Procyon (Alpha Canis Minoris)	
539	Adhara (Epsilon Canis Majoris)	
565	Canopus	Automatically acquired

midcourse velocity vector. At 05:00 GMT, the spacecraft was commanded to ignite the vernier engines for 4.278 seconds (4.19 m/sec). Telemetry indicated a burn time of 4.3 ± 0.1 second during which 3.58 pounds of vernier propellant were consumed. The 4.278-second engine burn time was the computed critical plane correction necessary to correct the 480-km miss on the lunar surface. The 3σ dispersions on the surface about the aim point, as a result of expected midcourse execution and tracking errors, were estimated to be: semimajor axis = 15.1 km, semiminor axis = 10.6 km. Orbit determination following the midcourse correction placed the soft landing site 5 km short of the desired landing site. This is equivalent to an engine burn time of 4.233 seconds (an error of 0.045 second).

The final landing site, a shallow crater, has tentatively been determined by inspection of Lunar Orbiter high resolution photographs taken prior to the flight. The location is 2.94°S latitude and 23.34°W longitude. This site is 2.77 km short of the aim point, which is analogous to a midcourse burn time error of 0.025 second.

Following engine burn, the spacecraft was commanded to perform a positive pitch of 39.13 degrees to acquire the sun and a negative roll of 56.75 degrees to acquire Canopus. This confirmed that the gyros had retained their inertial reference during the vernier engine shutdown. Also, the need to perform a postmidcourse star verification to ensure lockon to the proper star was eliminated.

Table 4-8 shows the salient data points concerning the midcourse maneuver, and Table 4-9 lists some of the midcourse performance parameters. Table 4-10 lists the target and landing site locations.

During midcourse correction, three vernier engine thrust command signals were different, indicating an apparent imbalance in thrust levels. A subsequent investigation revealed the following:

1) Sum of the three thrust commands was within 3 pounds of the total thrust which would have been required to achieve the commanded midcourse thrusting level (i.e., the level required to maintain the spacecraft acceleration at 0.1 g).

2) Observed doppler shift in the received DSS signal produced by the midcourse thrust was almost exactly as predicted, thereby verifying that total thrust magnitude and thrust direction were proper.

3) Possible causes for the observed imbalance in vernier engine 1 and 2 thrust command signals were reduced to the following:

   a) Center-of-gravity offset of approximately 1 inch

   b) Broken engine 2 nozzle

TABLE 4-8. MIDCOURSE DATA

Velocity magnitude, m/sec	4.19
Critical plane, m/sec	4.19
Noncritical direction, m/sec	0
Propellant weight, pounds	3.58
First rotation, roll, degrees	+56.75
Second rotation, pitch, degrees	-39.13
Omnidirectional antenna	B-B
Engine burn time, seconds	4.278
Mechanization plus tracking errors, 3σ on the surface:	
Semimajor axis, km	15.1
Semiminor axis, km	10.6
Theta, degrees (position from B·TQ toward B·RQ)	-64.4
Miss on surface before midcourse, km	480
Miss on surface after midcourse, km	5

c) Misalignment of engine 2

d) Change in engine 2 transfer function

e) Incorrect engine 2 calibration data and/or telemetry uncertainties

4) Large center of gravity shift of approximately 1 inch appeared to be impossible (e.g., it would require moving a 100-pound weight approximately 2 feet, or would require a shift of the retro engine by approximately 1.5 inches, neither of which appear possible).

5) There were no special in-flight checks which could be devised to verify or correct any of the possible causes with the exception of obtaining additional telemetry data at other commanded thrust levels. Those checks would have required that added risks be taken which could have jeopardized the mission (e.g., putting the

TABLE 4-9. MIDCOURSE MANEUVER PARAMETERS

Parameters	Commanded		Obtained	
	Angle, degrees	Time	Angle, degrees	Time
First maneuver roll	+56.74	113.4	≈56.775	≈113.55
Second maneuver pitch	-39.13	78.2	≈39.215	≈ 78.43
Engine ignition time	05:00:00		05:00:03	
Engine burn time	4.278 seconds		4.245 ± 0.03 second	
M/C velocity change	4.19 meters/second		4.073 meters/second from orbit determination 4.215 meters/second from lunar orbiter 4.162 meters/second from spacecraft telemetry	

Peak angular errors	Ignition, degrees	Shutdown, degrees
Roll	-1.0	+0.58
Pitch	-0.125	+0.96
Yaw	+0.30	+1.97

Engine shutdown impulse variations from the average	
Engine 1	-0.31 lb-sec
Engine 2	+0.42 lb-sec
Engine 3	-0.11 lb-sec

TABLE 4-10. SURVEYOR III LANDING SITES

	Latitude, south	Longitude, west
Premission aim point	3.33	23.17
Uncorrected impact	10.08	36.98
Midcourse aim point	2.92	23.25
Final orbit determination	3.00	23.43
Tentative lunar orbiter determination	2.94	23.34

vehicle in a postretro separation condition, with the risk of actually ejecting the retro engine, or commanding the 150-pound thrust level initially during the actual terminal and then commanding the proper 200-pound level with the risk that the proper level would not be obtained during this crucial period).

The most likely cause of the problem was determined to be the uncertainty in the engine 2 calibration and/or telemetry uncertainties. Because of the minimal value of the additional telemetry data and the high risk associated with the only possible additional action which could be taken, the normal sequence was used and no special tests were run.

4.1.7 Coast Phase II

The postmidcourse coasting phase (coast phase II) was begun and continued until initiation of the terminal descent maneuvers. Throughout this period, data were transmitted continuously using the low-power transmitter (at 1100 bits/sec until L+25H45M, at 550 bits/sec from L+25H45M to L+50H52M, and at 137.5 bits/sec from L+50H52M until the start of the terminal descent operations). During this interval, nine additional gyro drift measurements (i.e., seven measurements of drift in all three axes, plus two measurements of roll drift only) were made, and these were the basis for recommending to the flight path analysis and command group that the following drift rates be compensated for during the terminal descent: +1.1 deg/hr for roll, +0.6 deg/hr for pitch, and -0.8 deg/hr for yaw.

Eight engineering interrogations of modes 2 and 4 for thermal assessments of the spacecraft performance, plus the final two preterminal descent interrogations, were also conducted during this period. Other completed sequences included: 1) power mode cycling checks to determine the percentage of electrical load which would be supplied by each spacecraft battery (main and auxiliary) during the terminal descent when both batteries are placed directly on the bus (at L+46H56M, L+51H55M, and L+59H14M); 2) turn on of the vernier oxidizer tank 2 heater at L+47H58M; and 3) turn on of the survey TV electronic thermal control at L+60H47M and survey TV vidicon temperature control at L+64H2M.

4.1.8 Terminal Descent Phase

Terminal descent closely followed design and predicted performance except for failure to generate the 14-foot mark and shut off the vernier engine prior to touchdown. This problem is discussed in greater detail in the following paragraphs. As in the Surveyor I flight, the altitude marking radar mark was obtained, vernier ignition was smooth, and the pitch/yaw disturbance during the retro phase was small, indicating excellent alignment between the vehicle center of gravity and the retro thrust vector. Retro separation was smooth, vernier descent contour acquisition was obtained, and vernier descent control was normal.

Event times and important performance parameters are given in Table 4-11. The touchdown events, including anomalous operation, are shown in chart form in Figure 4-5.

TABLE 4-11. SURVEYOR III TERMINAL DESCENT PERFORMANCE PARAMETERS

Terminal Descent Time Profile		
Event	Desired, day:hr:min:sec	Sent (DSS) day:hr:min:sec
Initiation of yaw maneuver	109:23:23:16	109:23:23:30
Initiation of pitch maneuver	23:30:32	23:30:17
Initiation of roll maneuver	23:35:5	23:34:35
Radar power on	—	23:56:33
AMR enable	23:59:30	23:59:33
Event	Predicted	Estimated Occurrence at the Spacecraft
Radar mark	110:00:01:11.52	110:00:01:11.60 (±0.05)
AMR backup	00:01:13.25	00:01:12.21 (±0.0)
Ignition (vernier)	00:01:16.59	00:01:16.70 (±0.05)
Ignition (retro)	00:01:17.69	00:01:17.80 (±0.05)
3.5 g level	00:01:59.04	00:01:59.10 (±0.05)
Retro eject	00:02:11.04	00:02:11.27 (±0.025)
Vernier phase start	00:02:13.19	00:02:13.42 (±0.6)
Descent segment intercept	00:02:43.20	00:02:32.60 (±0.11)
1000-foot mark	00:03:55.20	00:03:51.79 (±0.05)
10-fps mark (8.6)	00:04:12.90	00:04:09.39 (±0.05)
14-foot mark	00:04:18.40	None
Initial touchdown	00:04:20.10	00:04:16.83 (±0.11)

Terminal Attitude Maneuvers		
Maneuver	Attitude	Degrees
First	Yaw	-157.9
Second	Pitch	- 76.7
Third	Roll	- 63.9

Table 4-11 (continued)

Retro Burnout Conditions (2. 15 seconds after retro eject)			
Parameter	Predicted/Specified		
	3 σ dispersions	Expected value	Actual
Total velocity	±120 fps	461 fps	492 fps
Altitude	8250 feet	34,734 feet	36,158 feet
Flight path angle	—	9. 2 degrees	3.8 degrees
Retro phase total impulse variation	1 percent	—	<-0. 2 percent
Retro burn time	±1. 2 seconds	41.09 seconds	40.02 ± 0. 1 seconds
Apparent retro phase attitude error	1 degree	—	<0. 4 degree

Vernier Descent Phase Timing				
Phase	Predicted, seconds		Actual, seconds	
	Δ	Total	Δ	Total
Retro burnout (case eject + 2. 15 seconds)	0	0	0	0
First segment intercept	30. 0	30. 0	19. 2	19. 2
End first segment	19. 1	49. 1	24. 5	43. 7
End second segment	53. 7	102. 8	54. 6	98. 3
End third segment	7. 8	110. 6	8. 7	107
10-fps mark	9. 5	120. 1	8. 9	115. 9
First touchdown	6. 8	126. 9	7. 5	123. 4

Table 4-11 (continued)

Touchdown Location		
Location	Latitude, degrees south	Longitude, degrees west
Aim site	2.92	23.25
Actual site (from lunar orbiter photos)	2.94	23.34

Touchdown Conditions		
Conditions	Expected	Actual
Vertical velocity	≤15 fps	7 to 8 fps
Lateral velocity	< 5 fps	<1.5 fps
Angle to local vertical	< 7 degrees	≈0
Local slope	≤15 degrees	≈10 degrees

68189-34(U)

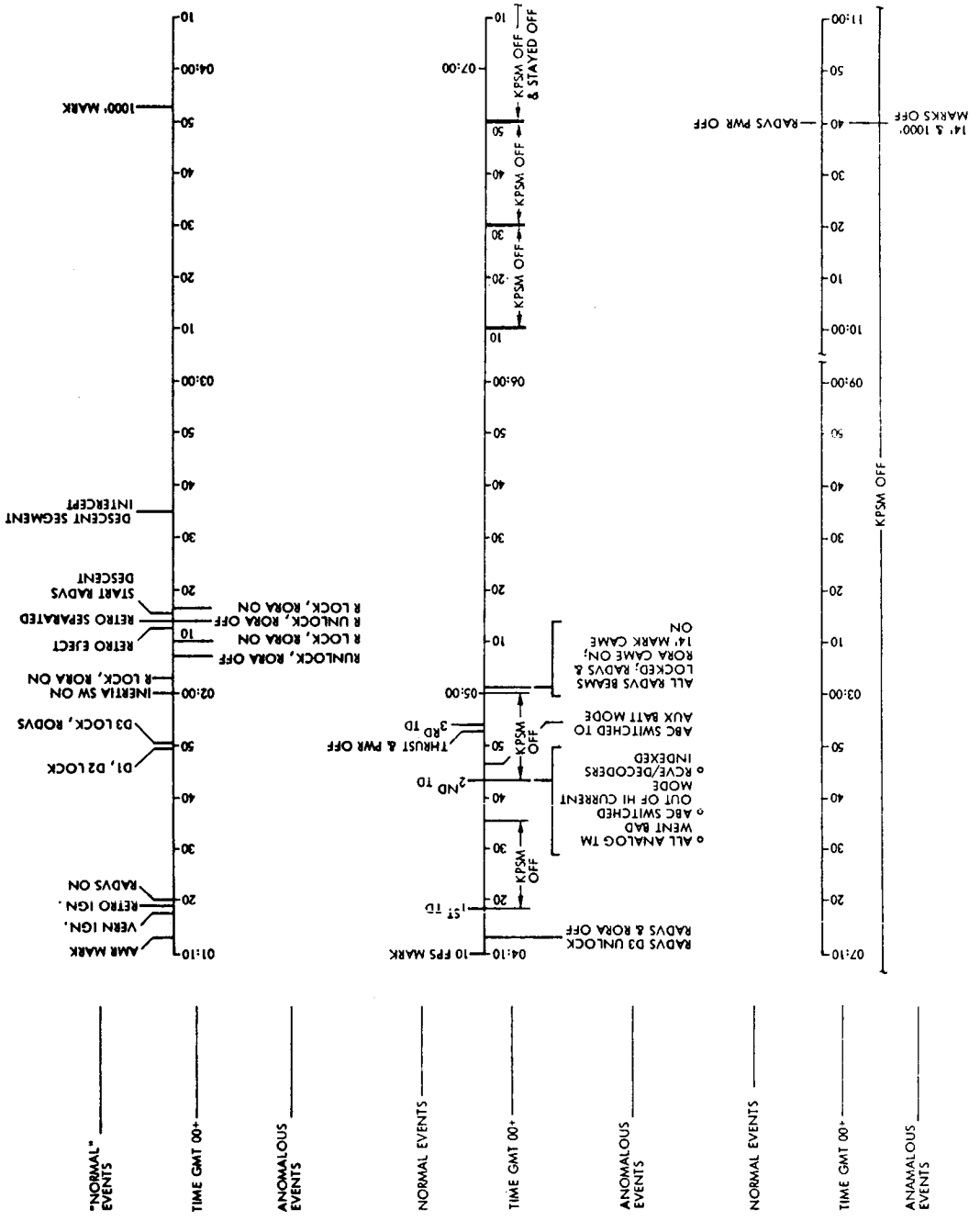

Figure 4-5. Touchdown Anomalous Events Chart

4.1.8.1 Spacecraft Performance

The terminal descent sequence was initiated at L+64H4M40S with turnon of the high power transmitter and performance of the last engineering interrogation. Terminal descent attitude maneuvers were initiated 38 minutes prior to the predicted retro ignition time (L+64H18M29S) to allow an additional 5 minutes for responding to any nonstandard situation that might arise. The first two maneuvers (a minus yaw of 157.9 degrees followed by a minus pitch of 79.8 degrees), which aligned the retro engine thrust axis to the desired direction, were completed at L+64H27M49S. A third maneuver (a minus roll of 63.9 degrees), which established the preferred spacecraft orientation at retro ignition to reduce the probability of the RADVS locking on to a cross-coupled sidelobe, was initiated at L+64H29M34S and completed at L+64H31M42S.

The three maneuvers, as well as other spacecraft operations (e.g., loading the proper altitude-mark-to-vernier-ignition delay quantity, establishing the retro sequence mode for ensuring that the automatic flight control sequences would occur in response to the altitude radar mark, establishing the proper vernier engine thrust level for the retro phase, turning on flight control thrust phase power, etc.) required before retro engine ignition, were executed on schedule without difficulty. In addition, the altitude marking radar was turned on at L+64H51M32S and was enabled at L+64H54M32S. Except for a single command (which was sent at L+64H57M32S) for obtaining the touchdown strain gage data, the spacecraft automatically accomplished the remaining operations until engine cutoff.

The automatic descent sequence was initiated by the altitude marking radar mark and confirmed on the ground at L+64H56M13.38S. Vernier engine ignition, retro engine ignition, RADVS initial turnon and application of high power after 18 seconds, retro burnout, and retro separation occurred normally. The moment disturbance produced by the retro engine firing was small (on the same order as Surveyor I), indicating no large cg offset (which was a possible explanation for the imbalance in engine thrust commands during midcourse). RADVS velocity and range acquisition and lockon were accomplished prior to retro burnout.

Although the altimeter apparently twice lost lock momentarily (the last time probably caused by the retro case separation), it was back in lock in one sweep time of the tracker. When the enable doppler control signal was generated 2 seconds after retro separation was initiated and after the RADVS had relocked, the doppler control phase was initiated. Realignment of the spacecraft Z-axis to the existing velocity vector was accomplished in 3 to 4 seconds, with the gyro error signals confirming that the spacecraft was being controlled normally during this phase.

The vernier engines, under RADVS control, kept the spacecraft on the desired range-V_Z contour, and the 1000-foot and 10-fps marks were generated as expected (telemetry confirmation received on the ground at L+64H58M54S and L+64H59M11S, respectively). However, approximately 2 to 3 seconds after generation of the 10-fps mark (or when the spacecraft was only approximately 30 feet above the lunar surface), RADVS beam 3

tracker lock telemetry indicated a loss of lock. At the same time, a loss of reliable operate doppler velocity sensor and reliable operate radar altimeter (RORA) occurred. Loss of RORA prevented generation of the 14-foot mark and, since this signal cuts off the vernier engines, the engines continued to thrust. The thrust level commanded was near minimum value (actually a level to maintain 0.9 lunar g) because of loss of RORA.

With the spacecraft in a near-weightless state due to the engine thrust and the lunar gravity being almost balanced, the spacecraft contacted a sloping lunar surface (later confirmed by earth initial acquisition and by subsequent tracking antenna/solar panel positioner to be 12.4 degrees in a near-westerly direction) and became airborne. It traveled approximately 24 seconds and reached an altitude of approximately 38 feet. The spacecraft again hopped in the downhill direction after the second contact, remaining airborne for approximately 12 seconds and reaching a height of approximately 11 feet.

Gyro error signals indicated that the spacecraft attitude was returned to the pretouchdown attitude by the flight control system in response to these signals, and that spacecraft attitude was stable during the hops. The ground command for turning off the flight control thrust phase power 33 seconds after the initial contact resulted in the vernier engines being turned off approximately 3 seconds before the end of the second hop. Thus, when the spacecraft contacted the surface for the third time, it only moved approximately 1 foot laterally before coming to rest (Figure 4-6). On all contacts with the surface, leg 2 impacted the surface first in the uphill direction, with legs 2 and 3 contacting the surface almost simultaneously (within 70 milliseconds of each other in the range of 250 to 440 milliseconds after the leg 2 contact for all contacts). The forces sensed by the touchdown strain gages indicated forces in the shock absorber were on the order of less than one-half that indicated on the Surveyor I touchdown, as would be expected for landings with the engines thrusting. These readings were consistent with touchdown velocities on the order of 6 to 7 fps and a slope of 12 degrees.

The first two impacts also affected other spacecraft subsystems. On the initial contact, the RADVS high voltage was turned off, which would normally indicate that a voltage transient on the order of 4 to 6 volts with a duration of 5 to 30 microseconds had occurred. This high voltage was reapplied after 18 seconds (during the first spacecraft hop) as it normally should. On the second touchdown, the RADVS high voltage was again turned off, the decoders indexed (from B to A), and the high current mode turned off. The power system reverted to the auxiliary battery mode shortly thereafter (within three frames of data), and all analog signals became erroneous (TFR 18256).

The erroneous analog data at first produced great concern that an acute power system problem existed since the indicated bus and battery voltages were low and the currents were high. Initial spacecraft operations were concerned with commanding off the high electrical loads, including the RADVS and flight control coast phase power off. In addition, nonstandard sequences for attempting to isolate the telecommunication problem were implemented (e.g., changing analog-to-digital converters, commutators,

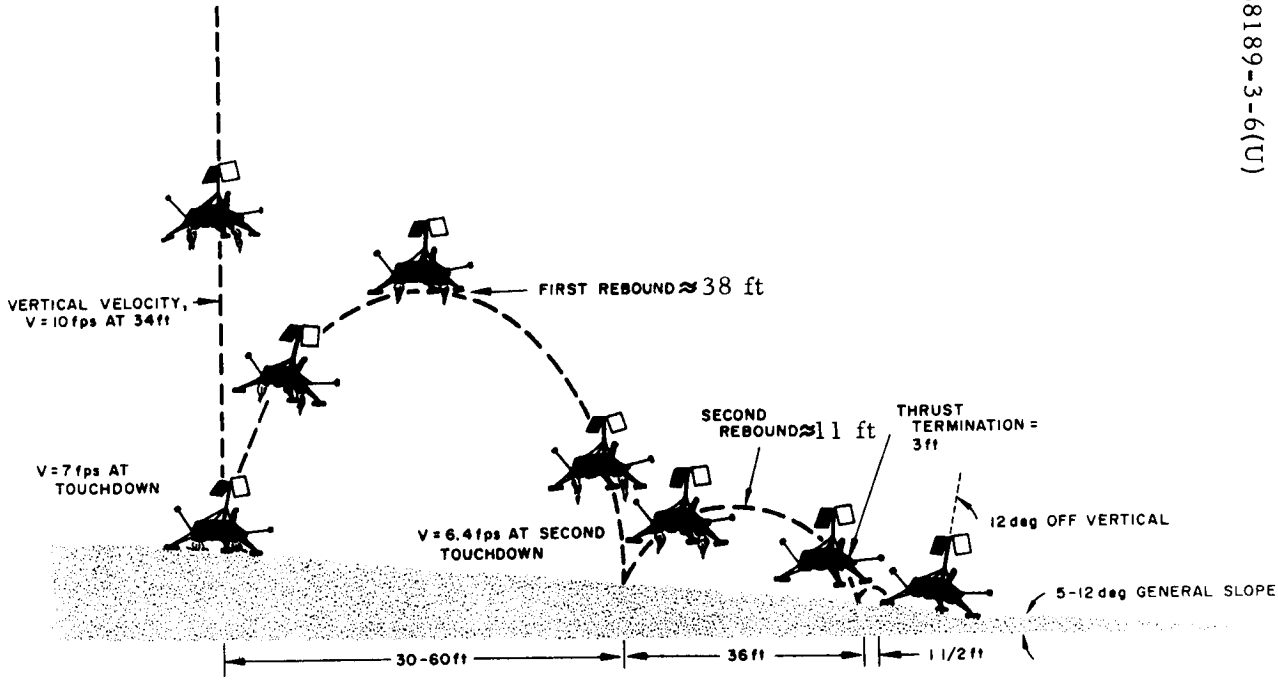

Figure 4-6. Surveyor III Landing Profile

transmitters, and checking data rates of 550 and 137 bits/sec in addition to 1100 bits/sec, etc.). The conclusions reached as a result of these sequences were: 1) all analog data were affected on all bit rates, but the effect at the lower bit rates was less for some signals (particularly the electrical currents and mechanism signals); and 2) all discrete signals were normal.

4.1.8.2 Touchdown Location

Based on orbit determination postflight analysis data, the computed Surveyor III landing site is 3°S latitude and 23.43°W longitude. This is only 3.1 km from the position determined from Lunar Orbiter pictures correlated with the Surveyor III pictures. While examining the Lunar Orbiter high resolution photographs of the general landing area, a likely looking crater was selected for closer examination. This scrutiny revealed several smaller enclosed craters that resembled those visible in the Surveyor photos. By using simple triangulation techniques, the exact landing spot of 2.94°S and 23.34°W was pinpointed. A sufficient number of recognizable landmarks was located to give a high degree of confidence in the selection. The actual site selected prior to the midcourse maneuver was 2.92°S latitude and 23.25°W longitude. This gives a miss of only 2.76 km or 1.65 miles (based on Lunar Orbiter photos).

A summary of landing site computations is as follows:

	Degrees	
	South	West
Final aim point	2.92	23.25
Orbit determination unbraked impact	2.97	23.22
Computed touchdown point	3.00	23.43
Actual touchdown (Lunar Orbiter photos)	2.94	23.34
Miss (error) 2.76 km; 1.65 miles	0.02	0.09

4.1.9 Postlanding Lunar Operations

4.1.9.1 Operations Summary

Although initial postlanding operations were complicated by the telemetry system malfunction, all lunar operations requirements were met. Table 4-12 summarizes initiation times for the major lunar operations events.

The initial spacecraft operations were concerned with commanding off the high electrical loads, including the RADVS and flight control coast phase power. Nonstandard sequences were then initiated to attempt to isolate the telecommunications problem. The conclusion reached as a result of these sequences was that all analog data were affected for all bit rates, but the effect at the lower bit rates was less for some signals. It was also observed that all discrete signals were normal. The engineering investigation was interrupted so that the 200-line TV picture sequence could be initiated. It was noted that the TV frame identification data were normal. The 200-line TV operations were normal, providing a total of about 54 pictures and meeting the design requirements.

Following the completion of the 200-line TV survey, the positioning of the planar array and solar panel were initiated. Due to the difficulty with the spacecraft telemetry after touchdown, the positioning procedures were slightly complicated but were still completed within a 2-hour period. The stepping sequences employed are tabulated in Table 4.13 and the resultant earth track through the planar array field pattern is shown in Figure 4-7.

During the second posttouchdown Canberra control period, it was determined that the secondary sun sensor center cell would indicate sun position. The peak reading obtained was 1.7 volts instead of the expected 3.0 volts; however, in this case, the signal pattern rather than the absolute value is the important factor. One sun/earth sighting was performed during this period; three additional sightings were performed during the next Canberra control period. Details of spacecraft attitude determination are presented in subsection 4.1.9.2.

Although all attitude calculations were performed from a cumulative step count rather than telemetry, indications are that the attitude determination is accurate. Confirmations from operations based on this attitude determination include:

1) Venus was photographed at the exact camera position predicted.

2) During a thermal experiment involving ASPD shading calculated from attitude data, moving the shadow from positions 4 to 3 and 2 to 1 had no effect on sensor V-23, yet the 3.5-degree solar panel motion calculated as being required to move the shadow from position 3 to position 2 resulted in V-23 increasing more than 10° F. (See Figure 4-8.)

TABLE 4-12. POSTLANDING MISSION MILESTONES

Item	Date	GMT, hr:min:sec	Time from Touchdown
Initial 200-line TV picture	April 20	01:02:32	57M39S
Earth/sun acquisition initiated	April 20	06:32:28	6H27M35S
Earth/sun acquisition completed	April 20	08:15:00	8H10M7S
Initial 600-line TV picture	April 20	08:42:00	8H37M7S
Initial checkout of the SM/SS extension mechanism	April 21	09:59	1D8H55M
Initial bearing strength test made by SM/SS on surface (scoop closed)	April 22	05:14	2D5H9M
SM/SS trenching operations initiated	April 22	09:14	2D9H9M
			Day:Hr:Min
Helium dumped	April 24	20:35	4:20:30
Fine positioning of planar array	April 25	04:57	5: 4:52
Special thermal experiment to measure thermal response of compartments by variation in ASPP shading.	April 26	04:00	6: 3:55
RF and signal processing assessment	April 27	15:25	7:15:20
Planar array gain/ temperature sensitivity	April 27	16:48	7:16:43
Special telemetry assessment	April 29	03:00	9: 2:55

Table 4-12 (continued)

Item	Date	GMT, hr:min:sec	Time from Touchdown, hr:min:sec
Axial ratio experiment	May 1	10:04	11: 9:59
Final positioning of solar panel	May 3	10:08	13:10: 3
Sunset on the solar panel and start of temperature decay experiment	May 3	18:38	13:18:33
Spacecraft power off	May 4	00:02	13:23:57

TABLE 4-13. SUN AND EARTH ACQUISITION SEQUENCE

Item	Stepping, degrees	Time	GMT, hr:min:sec
Nominal sun acquisition	Solar axis -154.50	Begun	06:32:28
	Polar axis + 75.00		
	Roll axis +131.75		
Nominal earth acquisition	Polar axis +4.00		
	Elevation axis +3.50	Completed	07:27:02
Detect lobe center	Elevation axis +3.50		
	Elevation axis +3.50		
	Elevation axis -1.50	Completed	07:37:34
	Polar axis +1.80		
	Polar axis -4.25	Completed	07:43:26
Identify lobe	Polar axis +7.5		
	Polar axis +7.5	Completed	07:59:24
Step to mainlobe	Polar axis -7.5		
	Polar axis -7.5		
	Polar axis -7.5	Completed	08:15:30

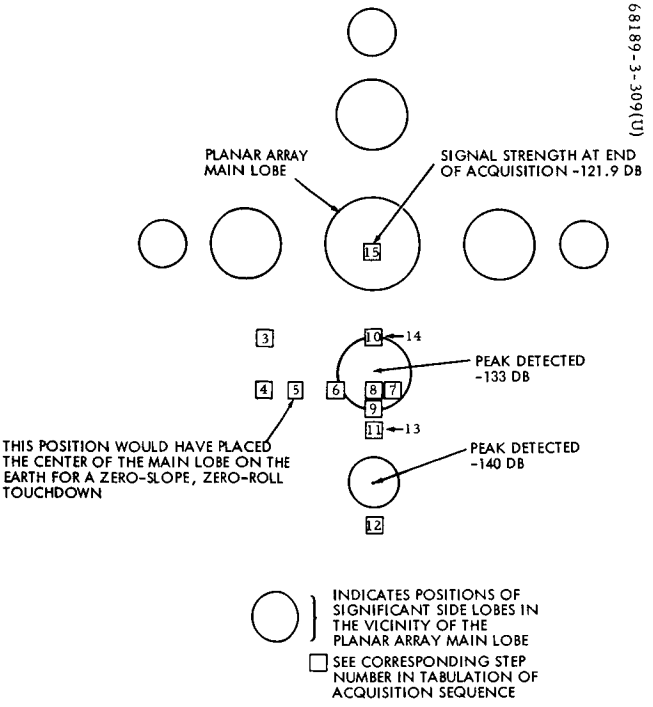

Figure 4-7. Stepping Sequence

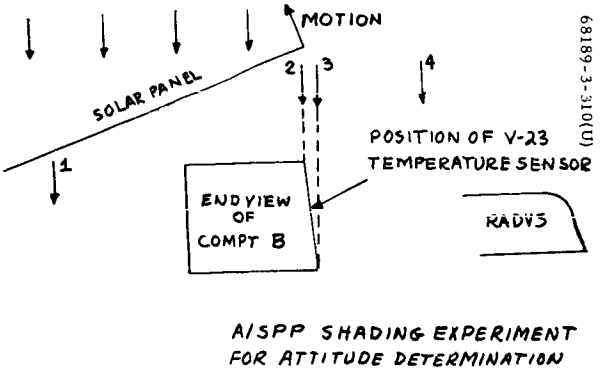

Figure 4-8. A/SPP Shading Experiment for Attitude Determination

Television pictures in the 600-line TV mode were initiated at 08:42 GMT on April 20 and continued throughout the first lunar day. A total of 6315 pictures of the lunar environment were taken and sent to earth. These pictures include lunar survey of the landing sight, examination of footpad impressions from the initial landings, assessment of spacecraft components, monitoring of surface sampler operations, photographs of stars from the moon, pictures of earth during lunar eclipse, and shadow pictures during sunset on the first lunar day. Television frame identification data were excellent during the mission, and, although several problems developed during TV operation, the performance was satisfactory and the TV camera met its design requirements in the 600-line mode.

Soil mechanics/surface sampler (SM/SS) operations were initiated at 09:59 GMT on April 21 and continued throughout the first lunar day. SM/SS operations were monitored by the TV camera and were satisfactory. Experiments included trench digging, depositing soil on footpad 2, and conducting impact and bearing tests.

4.1.9.2 Spacecraft Attitude Determination

The normal attitude determination procedure utilized by the spacecraft performance analysis and command (SPAC) attitude analysts requires that the sun and earth directions in the spacecraft system be determined by peaking the secondary sun sensor voltages and planar array AGC, respectively. The two vectors thus obtained in the spacecraft system in terms of the ASPP gimbal angles, M-3 through M-7, are likewise known in selenographic or lunar coordinates. This information is sufficient to establish the rotation matrix required to transform between systems.

From premission testing and analysis, the calibration curves of optical angles versus ASPP drive telemetry signals are obtained. By the error analysis described in Reference 3, 3σ estimates of the uncertainties in the spacecraft tilt and roll can be determined when spacecraft orientation is established from these ASPP sightings. However, due to the Surveyor III telemetry anomaly, the calibrations of optical angle versus telemetry were invalidated for the ASPP drives, as was the associated error analysis.

Spacecraft attitude estimates were still accomplished from ASPP positionings by maintaining a complete command count record for the gimbal drives. Since an error analysis was not performed for this mode of operation, estimates of spacecraft tilt and roll variances are not available based on analysis; however, engineering estimates are given.

Four sun and earth fine positionings were performed for attitude determination purposes. The individual and combined results of these sightings are given in Tables 4-14 and 4-15, respectively.

In addition, the spacecraft attitude can also be determined from star and planet sightings with the TV camera; however, an error analysis is likewise unavailable for this method of attitude determination. The tilt

TABLE 4-14. ATTITUDE PARAMETERS FROM INDIVIDUAL ASPP SIGHTINGS

Sighting Number	Angle Between $X_{S/C}$ and Local Vertical, degrees	Angle Between $Y_{S/C}$ and Local Vertical, degrees	Angle Between $X_{S/C}$ and Lunar East, degrees
1	80.30	97.45	43.96
2	79.84	97.62	44.03
3	79.87	98.52	43.70
4	80.03	96.60	42.56
Combined	80.14	97.52	43.86

TABLE 4-15. COMBINED ASPP DETERMINED ATTITUDE

Slope Magnitude 12.45 Degrees	Downhill Slope Direction 6.4 Degrees North of West	Roll Orientation in Tangent Plane $X_{S/C}$ South of East 43.8 Degrees
X slope -9.94 degrees	Y slope 7.64 degrees	Attitude Matrix 0.41056 0.60749 -0.67970 -0.41690 -0.53754 -0.73277 -0.81020 0.58585 0.03259

and roll results obtained from three Venus sightings and one earth sighting are given in Table 4-16; the results obtained from a combination of these sightings are given in Table 4-17.

It can be seen from Tables 4-15 and 4-17 that the lunar slopes determined using the ASPP and TV camera systems agree within 1 degree in both magnitude and direction. An equally weighted combination of the final combined ASPP and TV camera matrices yields the results plotted in Figure 4-9 (Reference 4).

TABLE 4-16. ATTITUDE PARAMETERS FROM INDIVIDUAL TV CAMERA SIGHTINGS

Sighting Number	Angle Between $X_{S/C}$ and Local Vertical, degrees	Angle Between $Y_{S/C}$ and Local Vertical, degrees	Angle Between $X_{S/C}$ and East, degrees
1	80.79	96.89	44.92
2	80.84	96.96	44.75
3	80.89	97.03	44.56
Combined	80.83	96.95	44.78

TABLE 4-17. COMBINED TV CAMERA DETERMINED ATTITUDE

Slope Magnitude 11.54 degrees	Downhill Slope Direction 7.5 Degrees North of West	Roll Orientation in Tangent Plane $X_{S/C}$ South of East 44.7 Degrees
X slope -9.24 degrees	Y slope 7.04 degrees	Attitude Matrix 0.39502 0.60259 -0.69343 -0.41288 -0.55784 -0.71996 -0.82066 0.57072 0.02844

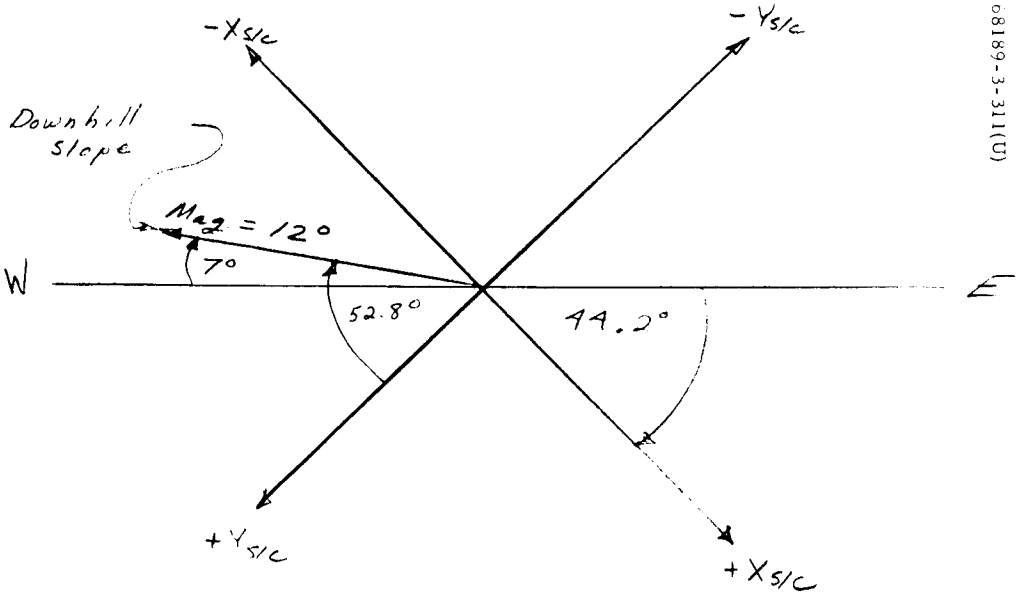

Figure 4-9. Spacecraft Attitude From Combined A/SPP and TV Camera Sighting

4.2 RELIABILITY ANALYSIS

4.2.1 SC-3 Reliability Estimates

4.2.1.1 System and Subsystem Reliability. The final reliability point estimate for Surveyor III is 0.75. This estimate is based upon SC-3 flight and landing mission data available as of 1 May 1967, SC-3 systems test data, and applicable SC-1 and SC-2 system test and flight experience.

At the 80 percent confidence level, SC-3 reliability is 0.71. This value is based upon application of the binomial distribution.

Final reliability point estimates for each subsystem are given in Table 4-18.

TABLE 4-18. SUBSYSTEM FINAL RELIABILITY POINT ESTIMATES

Subsystem	Reliability Estimates
Telecommunications	0.965
Vehicle mechanisms	0.907
Propulsion	0.968
Electrical power	0.935
Flight controls	0.971
Spacecraft	0.770
(System interaction reliability factor)	0.967

Spacecraft reliability (0.967)(0.770) = 0.75

4.2.1.2 Summary of Data Base for SC-3 Reliability Estimates. The primary source of data for reliability estimates is the time and cycle information experienced by SC-3 units during systems tests and the accumulated reliability relevant failures provided by TFRs. Data from SC-1 and SC-2 test and flight experience are included where there are no significant design differences between the units. A failure is considered relevant if it affects equipment reliability and could occur during a mission (References 5 and 6). Relevance of failures is based on a joint reliability-systems engineering decision. In addition, relevant failures are weighted as follows:

1.0 Critical – Would normally cause a safety hazard, mission abort, or failure of mission objective

0.6 Major – Would significantly degrade system performance but not cause mission abort or failure

0.1 Minor – Would not significantly affect ability of system to function as designed

A summary data base for SC-3 reliability estimates is presented in Table 4-19.

4.2.1.3 Time/Cycle/Reliability History for All SC-1 and SC-2 Units. Table 4-20 presents a history of time/cycle/reliability data for each major control item for SC-1 and SC-2.

4.2.2 Future Reliability Predictions

4.2.2.1 Reliability Trends. Surveyor spacecraft have realized a steady growth in reliability. This can be readily seen from Table 4-21 which gives the reliability history for each subsystem from SC-1 through SC-4. Unit level growth can also be verified by review of the data presented in Tables 4-19 and 4-20. Of particular interest is the relatively large decrease in the telecommunications subsystem reliability between SC-3 and SC-4. This decrease is a direct reflection of a failure in the low data rate auxiliary. In particular, module assembly 264886, S/N 10, failed. Detail failure analysis indicates failure was due to a broken weld on either transistor Q3 or Q4. Analysis of historical data on weld failures in systems test indicates an 0.007 probability of this failure occurring during a mission. Module assembly, S/N 10 has been downgraded to Class III, but no additional corrective action was deemed necessary.

4.2.2.2 Unit Type Permitting Greatest Improvement in SC-4 Reliability. Table 4-22 lists those units which, with reliability improvement, would have the greatest effect on SC-4 reliability. In particular, Table 4-22 shows the resulting percent increase in SC-4 reliability if the listed unit type attained its specification reliability value in place of its current data-based value.

4.2.2.3 Surveyor SC-4 Reliability. Estimated reliability for SC-4 at flight for the flight and landing mission, including parking orbit, is 0.75. This projected estimate is based upon SC-4 systems test data as of 1 May 1967, and applicable SC-1, SC-2, and SC-3 flight and test experience. At the 80 percent confidence level, the SC-4 reliability is 0.69. This estimate is based upon application of the binomial distribution.

JPL specification 30240 requires a demonstrated reliability of 0.75 at the 80 percent confidence level prior to the fourth spacecraft flight. The figure 0.69 given above assumes a broad application of the binomial distribution and represents a very rough estimate. In direct response to JPL Specification 30240, a reliability measurement involving refined engineering,

Table 4-19. SUMMARY OF DATA BASE FOR SC-3 RELIABILITY ESTIMATES

Units	Total Weighted Relevant Failures	Test Time (hours) or Cycles	SC-3 Reliability
Receiver-decoder select	0	5602.1	1.0
Central decoder	0.6	5602.1	0.990
Subsystem decoder	0	28010.5	1.0
Engineering signal processor	0.8	1711.8	0.960
Auxiliary engineering signal processor	2.8	2290.4	0.901
Signal processing auxiliary	0	530.4	1.0
Central signal processor	1.3	4661.7	0.977
Low data rate auxiliary	0.1	1484.3	0.994
Omnidirectional antenna	0	2075.5	1.0
Omnidirectional mechanisms	0	663 cycles	1.0
Diplexer	0	8948.9	1.0
Transmitter	2.4	3685.9	0.942
Low pass filter	0	9880.2	1.0
TM buffer amplifier	0	8160.7	1 0
Receiver	0.1	10355.3	0.999
Transponder	0	1663.2	1.0
RF transfer switch	0	3685.9	1.0
SPDT switch	0	3685.9	1.0
Thermal sensors	0	104180.8	1.0
Passive controls	0	2358.2	1.0
Thermal control and heater assembly	0	2359.7	1.0
Thermal switch	1.2	35373.0	0.958
Thermal shell	0	4716.4	1.0
Space frame	0	16 mission cycles	1.0
Landing gear structure	0	160 mission cycles	1.0
Compartment A thermal tray	0	17 mission cycles	1.0
Compartment B thermal tray	0	17 mission cycles	1.0
Auxiliary battery compartment	0.1	17 mission cycles	0.994
Wiring harness			
Wiring harness separation squibs	0	493.0	1.0
Wiring harness compartment A	0	3332.9	1.0
Wiring harness compartment B	0	3332.9	1.0
Wiring harness basic bus 1	2.1	5870.1	0.970

Table 4-19 (continued)

Units	Total Weighted Relevant Failures	Test Time (hours) or Cycles	SC-3 Reliability
Wiring harness separation squibs (cont)			
Wiring harness basic bus 2	1.0	5870.1	0.986
Wiring harness A/SPP	0	1121.2	1.0
Wiring harness auxiliary battery	0	1440.2	1.0
Wiring harness TV camera	0	1492.5	1.0
Wiring harness RF cabling	0	5601.0	1.0
Wiring harness retro motor	0	1070.8	1.0
Nitrogen lines	0	2814.7	1.0
Retro rocket release	0	578 trials	1.0
Engineering mechanism auxiliary	0	4887.3	1.0
Antenna/solar panel positioner*	1.1 roll	Roll: 259424 cycles	0.998
	0.3 solar	Solar: 223022 cycles	0.999
SS and A device*	0	178 actuations	1.0
Retro rocket system	0	15 mission cycles	1.0
Solar panel	0	467.7	1.0
Battery charge regulator	0.7	4600.7	0.987
Boost regulator	1.4	6004.8	0.982
Auxiliary battery control	0.7	5526.7	0.998
Main power switch	0	4883.3	1.0
Main battery	0	2685.5	1.0
Auxiliary battery	0.6	248.5	0.962
Boost regulator input choke	0	4152.6	1.0
Boost regulator unregulated bus filter	0	4156.6	1.0
Flight control sensor group	0	2815.1	1.0
Altitude marking radar	0	106.3	1.0
RADVS*			
SDC	11.1	1131.7	0.989
KPSM	5.9	921.0	0.993
AVSA	4.4	823.9	0.994
VSA	2.2	652.5	0.996
Wave guide	0	424.2	1.0
Roll actuator	0	148.6	1.0
Attitude jet system	0.1	370756 cycles	0.998

Table 4-19 (continued)

Units	Total Weighted Relevant Failures	Test Time (hours) or Cycles	SC-3 Reliability
Pin puller*	0	16092 cycles	1.0
Pin puller cartridge*	0	16441 equiv. firings	1.0
Helium tank and valves assembly*	0.1	34 mission cycles	0.997
Propellant tank assembly*			
Fuel tank	0	52 mission cycles	1.0
Oxidizer tank	0	70 mission cycles	1.0
Lines and fittings	0.1	66 mission cycles	0.998
Thrust chamber assembly (JPL supplied)			
Propellant shutoff valve	0	7953 cycles	1.0
Throttle valve	2.0	697 cycles	0.997
Thrust chamber and injector assembly	1.0	259 cycles	0.996
Helium release valves*	0	15 firings	1.0
Valve cartridge*	0	16063 equiv. firings	1.0
Shock absorber*	0	400 cycles	1.0
Chrushable structure*	0	70 cycles	1 0
Secondary sun sensor	0	145.5	1.0
System**	0.6	1528.7	0.967

*Includes unit flight acceptance and type approval test data.

**Based on receiver operating time in system test.

TABLE 4-20. TIME/CYCLE/RELIABILITY HISTORY FOR ALL SC-1 AND SC-2 UNITS

Units	Time (hours) or Cycles	SC-1 Failures	Reliability	Time (hours) or Cycles	SC-2 Failures	Reliability
Receiver-decoder select	2137.3	0	1.0	4073.4	0	1.0
Central decoder	2137.3	0.6	0.972	4073.4	0.6	0.987
Subsystem decoder	10686.5	0	1.0	20367.0	0	1.0
Engineering signal processor	691.3	2.2	0.752	1300.5	2.3	0.861
Auxiliary engineering processor	838.0	1.0	0.893	1478.2	2.4	0.870
Signal processor auxiliary	292.7	0	1.0	461.8	0	1.0
Central signal processor	1828.3	0.7	0.960	3133.0	1.4	0.963
Low data rate auxiliary	449.9	0	1.0	847.1	0	1.0
Omnidirectional antenna	716.7	0	1.0	1068.4	0	1.0
Omnidirectional mechanism	42.0 cycles	0	1.0	510.0	0.2	0.999
Diplexer	2173.8	0	1.0	5891.5	0	1.0
Transmitter	1019.1	2.3	0.874	2373.0	1.0	0.961
Low pass filter	3176.6	0	1.0	6822.8	0	1.0
TM buffer amplifier	1874.4	0	1.0	5103.3	0	1.0
Receiver	3580.2	0.2	0.995	7297.9	0.2	0.998
Transponder	529.1	0	1.0	1153.4	0	1.0
RF transfer switch	1019.1	0	1.0	2373.0	0	1.0
SPDT switch	1019.1	0	1.0	2373.0	0	1.0
Thermal sensors	40953.8	0	1.0	76038.0	0	1.0
Thermal control and heater assembly	1455.9	0	1.0	1591.7	0	1.0
Thermal switch	14755.5	0	1.0	26196.0	1.2	0.943
Thermal shell	1967.4	0	1.0	3492.8	0	1.0
Space frame	8.0 cycles	0	1.0	11.0 cycles	0	1.0
Landing gear structure	21.0 cycles	0	1.0	139.0 cycles	0	1.0
Thermal tray compartment A	8.0 cycles	0	1.0	11.0 cycles	0	1.0

Table 4-20 (continued)

Units	Time (hours) or Cycles	SC-1 Failures	Reliability	Time (hours) or Cycles	SC-2 Failures	Reliability
Thermal tray compartment B	8.0 cycles	0	1.0	11.0 cycles	0	1.0
Auxiliary battery compartment	8.0 cycles	0	1.0	11.0 cycles	0	1.0
Wire harness compartment A	2587.2	1.0	0.963	1868.5	0	1.0
Wire harness compartment B	2587.2	0.1	0.997	1868.5	0	1.0
Wire harness basic buss 1	2537.2	0.1	0.996	4405.7	2.1	0.960
Wire harness basic buss 2	2537.2	1.0	0.962	4405.7	2.0	0.962
Wire harness A/SPP	1063.9	0	1.0	1111.7	0	1.0
Wire harness auxiliary battery	1129.1	0	1.0	1333.8	0	1.0
Wire harness RF cabling	2601.3	0.1	0.996	4227.5	0	1.0
Wire harness retro motor	1053.2	0	1.0	1059.5	0	1.0
Nitrogen lines	1147.0	0	1.0	1963.0	0	1.0
Retro rocket release	540.0 cycles	0	1.0	575.0 cycles	0	1.0
Engineering mechanism auxiliary	1576.3	0	1.0	3358.6	0	1.0
Antenna/solar panel positioner	240504 cycles	22.7	0.891	511506 cycles	1.4	0.995
Separation sensing and arming device	75.0 cycles	0	1.0	72.0 cycles	0	1.0
Retro rocket systems	13.0 cycles	0	1.0	14.0 cycles	0	1.0
Solar panel	357.1	0	1.0	402.7	0	1.0
Battery charge regulator	1128.4	0.1	0.989	3072.0	0.7	0.980
Boost regulator	2457.8	0.8	0.968	4476.1	1.4	0.974
Auxiliary battery control	1929.3	0	1.0	3998.0	0.6	0.998

Table 4-20 (continued)

Units	Time (hours) or Cycles	SC-1 Failures	Reliability	Time (hours) or Cycles	SC-2 Failures	Reliability
Main power switch	1475.4	0	1.0	3354.6	0	1.0
Main battery	1037.4	1.0	0.882	1553.8	0.1	0.994
Auxiliary battery	90.7	0.6	0.880	113.6	0.6	0.924
Boost regulator input choke	937.2	0	1.0	2623.9	0	1.0
Boost regulator unregulated bus filter	937.2	0	1.0	2627.9	0	1.0
Flight control sensor group	1147.2	0	1.0	1963.2	2.0	0.917
Altitude marking radar	62.9	0	1.0	92.9	0	1.0
RADVS signal data converter	595.1	6.5	0.982	987.1	10.3	0.989
Klystron power supply modulator	311.5	5.4	0.981	725.7	5.9	0.991
Altitude and velocity sensing antenna	295.9	2.2	0.992	522.7	2.2	0.996
Velocity sensing antenna	266.6	0	1.0	424.1	1.6	0.996
RADVS waveguide	194.1	0	1.0	278.0	0	1.0
Roll actuator	56.6	0	1.0	98.1	0	1.0
Attitude jet system	147381 cycles	0.1	0.995	269576 cycles	0.1	0.998
Pin pullers	16071 cycles	0	1.0	16080 cycles	0	1.0
Pin puller cartridges	16071 cycles	0	1.0	16429	0	1.0
Helium tank and valve assembly	30.0 cycles	0	1.0	33.0 cycles	0.1	0.997
Fuel tanks	46.0 cycles	0	1.0	49.0 cycles	0	1.0
Oxidizer tanks	64.0 cycles	0	1.0	67.0 cycles	0	1.0
Lines and fittings	54.0 cycles	0	1.0	60.0 cycles	0.1	0.998
Propellant shutoff valve	7944.0 cycles	0	1.0	7947.0 cycles	0	1.0
Throttle valve	693.0 cycles	2.0	0.997 cycles	694.0	2.0	0.997
Thrust chamber and injector assembly	255.0 cycles	0	1.0	256.0 cycles	1.0	0.996

Table 4-20 (continued)

Units	Time (hours) or Cycles	SC-1 Failures	Reliability	Time (hours) or Cycles	SC-2 Failures	Reliability
Helium release valves	13.0 cycles	0	1.0	14.0 cycles	0	1.0
Valve cartridges	16061 cycles	0	1.0	16062 cycles	0	1.0
Shock absorber	391.0	0.2	0.999	391.0	0	1.0
Crushable structures	61.0 cycles	0	1.0	61.0 cycles	0	1.0
System	1717.1	5.0	0.736	1013.2	0.6	0.949

TABLE 4-21. SURVEYOR SPACECRAFT RELIABILITY GROWTH

Subsystem	SC-1	SC-2	SC-3	SC-4
Telecommunication	0.925	0.944	0.965	0.924
Vehicle mechanisms	0.816	0.868	0.907	0.937
Propulsion	0.991	0.991	0.968	0.968
Electrical power	0.869	0.958	0.935	0.951
Flight controls	0.952	0.889	0.971	0.972
Systems interaction factor	0.736	0.949	0.967	0.967
Spacecraft	0.456	0.658	0.745	0.750

TABLE 4-22. UNITS HAVING GREATEST EFFECT ON SC-4 RELIABILITY

Unit Type	Unit Data-Based Reliability	Unit Specification Reliability	Percent Increase in SC-4 Reliability If Unit Specification Is Attained	Reliability of SC-4 If Unit Specification Is Attained
LDRA	0.948	0.999	5.4	0.79
RADVS	0.974	0.998	2.4	0.77
Central signal processor	0.980	0.998	1.9	0.76
Wiring harness	0.973	0.987	1.3	0.76
Boost regulator	0.983	0.988	0.5	0.75

as well as mathematical, analysis is being accomplished. Results of this analysis will be published as a formal report prior to the fourth spacecraft flight.

4.2.2.4 Reliability Estimate Basis. The estimates reported herein are based on equipment failure data and operating time and cycle data generated during spacecraft missions and spacecraft systems testing which are combined in accordance with the "Reliability Math Model Surveyor Spacecraft A-21, "SSD 64002-2R, 24 October 1966. The model describes the spacecraft system in terms of block diagrams, mission profile, time/cycle data, and probabilistic equations appropriate to the functional interaction of all spacecraft units. For convenience, the spacecraft is referred to at three basic levels: 1) subsystem, 2) set, and 3) control item or unit. Two mission phases, flight and landing and lunar 80-hour, are considered. For these phases, reliability is defined as follows:

1) Reliability of the A-21 Surveyor spacecraft for the flight and landing (F&L) phase is the probability that the spacecraft equipment will operate successfully as required from launch through soft landing. Successful soft landing is assumed if two-way communication is established and there is no apparent damage to spacecraft equipment required to support intended lunar operations.

2) Reliability of the A-21 Surveyor spacecraft for the lunar 80-hour (L-80) phase is the probability that the spacecraft equipment will operate successfully as required for 80 hours on the lunar surface given that the spacecraft has successfully soft landed.

In the derivation of the model, the following general assumptions were made:

1) No human errors will occur which will cause failure.

2) All equipment inspection and test procedures are perfect and comprehensive, and all equipment will be used only in applications within the boundaries of its design parameters.

3) Only standard operating procedures are considered.

4) Every performance characteristic is verified up to the instant of no return in launch operations, and the launch will be aborted if fault exists.

5) All parts and designs are used in applications proven by test.

6) All scheduled changes to improve reliability of performance have been physically incorporated and tested prior to launch.

7) Natural hazards, such as meteorites and deep lunar dust, are nonexistent.

4.3 MIDCOURSE AND TOUCHDOWN ANOMALIES

4.3.1 Anomaly Observed During Midcourse Correction

During the midcourse velocity correction, an apparent anomaly was observed in the thrust command for engine 1. The thrust level for this engine calculated from the observed thrust command current was about 6.2 pounds higher than the expected thrust level based on premidcourse predictions. Postmidcourse analysis of the problem indicates that the difference is probably due to inaccuracies in thrust chamber assembly (TCA) calibration data used to convert the observed thrust command current to thrust level.

One possible cause of the observed differences considered in the analysis was a change in the spacecraft geometry, such as a shift in the spacecraft center of mass. However, to match the observed data (assuming calibration was correct) an improbable shift of mass of nearly an inch would be required. Therefore it was concluded the actual thrust levels were not as calculated from the thrust command currents. This conclusion was supported by the fact that the spacecraft was stable during the thrust period and velocity correction was as predicted.

The signal used to determine thrust levels for the engines is a measure of the thrust command difference current (referred to as delta-milliampere in the calibration data). The telemetry circuits that measure thrust command for the engines were redesigned for Surveyor III and to date reflect a fairly accurate measure of thrust command current. Reference 7 indicates the accuracy to be ±2 percent (3 sigma) which relates to a thrust level variation of about ±0.62 pounds. However, to relate thrust command current to engine thrust level requires two further calibrations. The thrust command current is used to control fluid flow rates to the engines. The actual thrust provided by the engine is dependent on the fluid flow rate and the engine construction. Therefore, the accuracy of relating thrust command data to actual engine thrust level is dependent on the accuracy of the engine calibration data. It has been observed that TCA calibration data do vary with time and test setup.

TCA calibration data have been obtained from three sources: 1) RMD hot firing data obtained several months before launch, 2) RMD engine flow bench data obtained several months before launch, and 3) ETR flow bench data. The RMD hot firing data were used to provide the thrust level versus delta-milliampere calibration used in the initial Surveyor III thrust level calculations. However, in order to check calibration accuracy, hot firing and flow bench data were plotted as total flow rate (i.e. sum of fuel flow and oxidizer flow) versus delta-milliamperes for 21 engines. From these plots the following observations were made:

1) In most cases the original hot firing data and the RMD engine flow bench data checked very closely.

2) When the original hot firing data were compared to the ETR flow bench data taken about 6 months later, variations of up to ± 5 percent were observed.

It is felt that these variations can be explained by two effects: 1) test instrumentation inaccuracies introduced because the two sets of data were taken on different test setups, and 2) actual shifts in TCA calibration due to aging, handling, and normal usage. That the latter effects could be significant is indicated by the fact that TCA operation involves mechanical valve operation and fluid flow. The actual thrust provided as a function of fluid flow is also dependent on engine geometry. Variations in the engine such as cleaning, firing, changing parts, and aging will have an effect (even if slight) on the amount of thrust produced by the thrust command current. Thus, while the engine will still operate properly on the spacecraft, the thrust command current will not give an accurate measure of thrust. Reference 8 indicates that thrust calculations based on thrust command data can be in error by as much as ± 5 pounds.

To improve thrust command calibrations on future spacecraft, the ETR flow bench data will be used in conjunction with the RMD hot fire data (for details see Section 5.6.4). While this procedure does not eliminate inaccuracies due to test instrumentation, it will reduce calibration shifts caused by handling and normal usage of the TCAs.

4.3.2 Touchdown Anomalies

Although the terminal descent and landing can ultimately be called successful, there were several anomalous events that occurred. These events, as well as the probable cause of the events, are discussed briefly in the following paragraphs. More detailed discussions may be found in the subsystem reports and the referenced documents.

The primary cause of all these events was the loss of lock in the RADVS beam 3 tracker at approximately 5 seconds prior to touchdown. This locked out the generation of the 14-foot mark and thus the vernier engines were not automatically shut off. The spacecraft then continued its descent with the engines thrusting at 0.9 lunar g's and the spacecraft touched down at approximately 7 to 8 fps with the engines still thrusting. As the spacecraft settled onto the sloping surface, the attitude control system, in trying to keep the spacecraft Z-axis vertical, caused the thrust on engines 1 and 3 (the downhill engines) to increase, thereby causing the spacecraft to rise back off the lunar surface aided by the rebounding of the landing gear. On becoming horizontal again, the engines throttled back down to 0.9 lunar g's and the spacecraft vertical rise slowed to a stop, then accelerated back toward the lunar surface with an acceleration of 0.1 lunar g's (≈ 0.53 ft/sec^2). It contacted the lunar surface again 24 seconds after the first touchdown and the above hopping procedure repeated. Just prior to the third touchdown (about 12.5 seconds after the second) the engines were commanded off via a ground command and the spacecraft remained on the surface at the third touchdown.

The following spacecraft conditions were observed concurrently with the second touchdown: anomalous telemetry data from both commutators (post-analysis), inadvertent switching of the battery logic out of high current mode into the main battery mode, and the indexing of the receiver/decoder combination. Three seconds after switching to the main battery mode, the battery control logic automatically switched to the auxiliary battery mode, which is probably a normal occurrence for the state of battery charge existing at the time.

Concurrent with both the first and second touchdown, as well as three times subsequently, the RADVS high-voltage power supply inadvertently switched off. Four of these times it timed back in and came on as it should in 18 seconds. The fifth time, it stayed off and did not come back on. The high-voltage power supply did not switch off on the third touchdown as it was already off.

4.3.2.1 Probable Causes of RADVS Break Lock

Loss of lock in the RADVS beam 3 tracker which locked out the generation of the 14-foot mark was probably caused by the cross-coupled sidelobe logic circuits operating in the presence of a weaker than expected signal strength in all beams. Detailed analysis leading to this conclusion is presented in Reference 9 as well as in the RADVS subsystem discussion, subsection 5.9.2.

The sidelobe logic in Surveyor III existed only between beams 2 and 3. The purpose of this logic is to reject a beam lock condition determined to be a false lock resulting from sidelobes from the adjacent beam transmitter. Once the reject signal is generated, the channel having a false lock-on will go into search mode and presumably acquire the mainlobe. However, due to an inherent characteristic of the DVS trackers, it is virtually impossible for the radar to reacquire if the spacecraft velocity is low (10 fps or less). Analysis of the telemetry data indicates that all of the conditions required for break lock were probably satisfied due to the geometry of the approach. Therefore, the break lock probably occurred normally and not as a result of some component failure or other system malfunction.

Since the probability of either a sidelobe acquisition or a main beam break lock below 1000-foot altitude is extremely remote, the sidelobe logic is no longer needed after the 1000-foot mark. Therefore, in SC-4 and up, the sidelobe logic will be disabled by the 1000-foot mark, avoiding the problem which occurred on Surveyor III.

4.3.2.2 Probable Cause of Touchdown Anomalies

The anomalies observed at touchdown (in particular, the KPSM shutdown and the erratic PCM data) were probably a result of the vernier engines continuing to operate down to the lunar surface rather than being shut off at 14 feet above the surface. A possible cause of the failures is high-voltage sparking induced by exhaust gases from the engines impinging

on the landing vehicle. This effect is analyzed in detail in References 10 and 11 and apparently accounts for the klystron power supply modulator (KPSM) high-voltage shutdown. High-voltage sparking in the KPSM or some other unit may also account for the anomalous telemetry data. Reference 2 concludes that it is improbable that a static discharge to the lunar surface occurred at touchdown. Therefore static discharge does not appear to be the cause of the failures. It also appears, from analysis of strain gage and TV data, that the anomalies cannot be ascribed to the severity of landing loads at touchdown.

4.3.2.3 KPSM Shutdown Anomaly

In discussing the KPSM shutdown, Reference 11 considers the possibility that the exhaust gases from the engines strike the lunar surface and a fraction rebounds to impinge on the landing vehicle, creating a gas pressure about the high-voltage supply. At a critical condition given by experimental Paschen curves of striking voltage versus the product of pressure and electrode separation, the gas breaks down. Reference 11 concludes that at an altitude above 10 feet it is impossible for the KPSM to become inoperable because of glow discharge. With a reasonable fractional ionization of between 10^{-4} and 10^{-5}, it is concluded that the system would break down at 3 ± 2 feet. The inaccuracies arise from the very complicated fluid flow pattern which provides the pressure of the gas at the vehicle versus altitude and the uncertainty in the fractional ionization of this gas.

It is likely that the reverse flow of the vernier engines at and near touchdown impinged on the KPSM box (and other boxes) and entered the box chiefly through the downward-facing overlap of the microwave plumbing flange (Reference 2). The stagnation pressure here may have been about the average value of 0.25 to 0.6 mm Hg for low or high thrust. The gas pressure in the box would rise until the flow outward equaled the flow inward. This would be a fraction of the pressure against the overlap, perhaps as much as a quarter of a tenth in the more accessible spaces in the box. The pressure in some parts of the box may have risen to as much as 1/10 mm. The 2100 volts would spark at a pressure of 1/100 mm for a distance of 4 inches, and at less pressure at greater distances. The ratio of the pressure required for sparking and the likely pressure in the unit is about 10:1.

Thus, while the analysis cannot be exact, it appears likely that sparking of the KPSM high voltage did occur. Since KPSM power supply recycles subsequent to the third touchdown were abortive (i.e., the circuit would not stay on even in the absence of back flow from the engines), the sparking evidently damaged some insulation, causing further circuit failure. The high-voltage sparking may also be directly or indirectly responsible for the telemetry failure at second touchdown. Analysis of the problem, including special arcing tests, is continuing at the time of this report to obtain more understanding of the failure mode.

4.3.2.4 Telemetry Anomaly*

At the time of the second touchdown of Surveyor III, the telemetry data became severely degraded, indicating some malfunction of the spacecraft signal processing system. Several investigations were begun immediately following touchdown (References 12, 13, and 14). Special commutator assessments were made during the first lunar day to obtain additional information about the nature of the anomaly. Analysis of the data from the commutator assessments indicated the following characteristics:

1) Digital words were not affected by the commutator anomaly.

2) The analog data were erroneous regardless of which A/D converter was being used to convert the data from analog to digital.

3) The analog data at the higher bit rate had a large number of erroneous readings containing consecutive ones and zeros (i.e., 511, 512, etc., BCD units).

4) The analog data showed a dependency on the value of the preceding word of any given assessment.

5) The analog data at 17.2 bps were within 10 to 20 percent of expected values, and the data from the AESP commutator were consistently lower than the same data sampled with the ESP commutator.

6) The data from the TV commutator were not affected by the anomaly.

The data characteristics noted above indicate that the most likely failure made would be a short in one or more commutator switches in both the ESP and AESP. The result of these shorts is an additional resistor-capacitor load connected at the input to the A/D converter. At low bit rates the effect of the capacitor is minimized, making it possible to determine the value of the load resistor introduced by the shorted switches. The value of the resistive load on the ESP and AESP was determined to be 19,500 and 9850 ohms, respectively. With these resistive loads determined, correction factors for certain data channels at the 17.2-bps rate were derived so that telemetry data at this bit rate could be used to control lunar operations and also to analyze spacecraft performance during these operations.

*A more detailed discussion of the telemetry anomaly is contained in subsection 5.4, "Signal Processing Subsystem."

4.4 REFERENCES

1. "Surveyor Mission C Space Flight Operations Report," Hughes Aircraft Company, SSD 74071, May 1967.

2. "Surveyor III Flight Path Analysis and Command Operations Report," Hughes Aircraft Company, SSD 74075, May 1967.

3. "Error Analysis of the SC-3 Spacecraft Attitude on the Lunar Surface," Hughes IDC 2292/246.

4. "SC-3 Attitude Matrix and Sun/Earth Positions," Hughes IDC 2292/322.

5. "Weighting of Surveyor Relevant TFR's," Hughes IDC 2258.2/201, 21 June 1965.

6. "Reliability Relevant Failures," Hughes IDC 2258.2/328, 24 February 1966.

7. R.O. Crook, "FCEU Thrust Command TM Circuit – Accuracy of," Hughes IDC 2223/2858, 11 May 1967.

8. T.S. Davis, "Thrust-Signal Accuracy of the Surveyor TCA," Hughes IDC 2227.1/2009, 9 May 1967.

9. O.N. Hertzmann, "SC-3 RADVS Performance Evaluation," Hughes IDC 2223/2891, 8 May 1967.

10. J.M. Hansen, "SC-3 Plasma and Sparking," Hughes IDC 2294.1/129, 31 May 1967.

11. J.F. Cashen, et al, "SC-3 PSM Failure," Hughes IDC 2245.10/49, 15 June 1967.

12. J.P. Stringham, "Correction of SC-3 Commutator Data During Lunar Operation," Hughes IDC 2294.2/129, 13 June 1967.

13. W. Herold, R. Lucey, "Post Touchdown Telemetry Data Failure on SC-3," Hughes IDC 2951/5, 23 June 1967.

14. D. Hersey, K. Kimball, "Investigation of the SC-3 Signal Processing Failure," JPL IOM 273-B-848.

4.5 ACKNOWLEDGEMENTS

The material in Sections 1, 2, 3 and 4 was coordinated (and in many cases originated or compiled) by G.A. Young and W. McIntyre. Mention is also due the following people:

L. M. Bronstein, for gathering information on the telemetry anomaly.

R. L. Lackman, for information concerning postlanding attitude determination.

L. K. Cooley, for the excellent reliability analysis in subsection 4. 2.

G. A. Young, for midcourse and touchdown anomaly summaries in Section 4. 3.

Much of the data in subsection 4. 1 was compiled from the mission operations reports (References 1 and 2).

5.0 PERFORMANCE ANALYSIS

5.1 THERMAL CONTROL SUBSYSTEM

5.1.1 INTRODUCTION

5.1.1.1 Surveyor Thermal Control Techniques

The Surveyor thermal design uses a variety of temperature control techniques. Both active and passive systems are employed to provide the required temperature control throughout the transit and lunar phases of the mission. Each spacecraft subsystem is individually controlled, and the thermal coupling between subsystems is minimized by using conduction and radiation isolation wherever advantageous. Subsystem analyses are accomplished by evaluating in detail the thermal environment for each subsystem, with consideration being given to all significant interactions between the subsystems whenever a high degree of isolation is not possible.

The following temperature control techniques are used on the Surveyor spacecraft:

1) Passive thermal control utilizing combinations of paints and metal processes to provide solar absorptance and infrared emittance characteristics that produce required subsystem temperatures.

2) Active thermal control systems utilizing heaters to provide energy in cases where sufficient solar illumination is not available.

3) High conduction and radiation isolation utilizing superinsulation for systems having a large heat capacity. Such systems never reach equilibrium conditions and therefore depend on their stored heat capacity.

4) Bimetallically activated thermal switches that control the temperature of the electronics compartments during transit and lunar operations.

Combinations of the above techniques are used on many of the subsystems to optimize the temperature control system.

5.1.2 THERMAL ANOMALIES

5.1.2.1 Soil Mechanics/Surface Sampler (SM/SS) Electronics Compartment (SS-12)

During Mission C the SM/SS auxiliary electronic compartment temperature ran 10° to 30°F below the nominal transit predicted value of -5°F and the heater thermostatic control point of -4°F. The compartment heater was operating continuously throughout. A predictability of ±15°F was associated with the nominal. The steady-state coast phase temperature of the unit was -35°F. The effects of gyro drift maneuvers resulted in periodic warmups to -15°F. During the transit phase of the mission the allowable temperature range of the unit is -67° to +185°F. Thus the flight performance of the compartment remained within its survival range but below the heater control point. This discrepant performance was documented in TFR 18257.

The published SM/SS prediction was based solely upon solar thermal vacuum (STV) test results. No attempts were made to develop an analytical model and account for differences between chamber and space environments which include determination of the relative contributions of direct solar loading, reflections from the spacecraft, and decollimation effects. It had been noted (and published) that an average of about 30 percent of a solar constant was incident upon the radiator in STV tests. Thus it is felt that the predication for the SM/SS compartment was in error.

The large temperature oscillations of the SM/SS electronic compartment can be attributed to the fact that in transit most of the radiator is shadowed and temperature levels are very sensitive to shadow line variations.

The TFR was closed as the unit remained well above the -67°F limit in transit. There are no changes to the SM/SS compartment thermal system for SC-4.

5.1.2.2 Failure of Thermal Switches to Open

One of the most significant thermal problems was the malfunction of the thermal switches. Only one switch was observed to have opened throughout lunar operations, whereas there were three occasions on which thermal switches should have opened (15 to 25 hours after touchdown, lunar eclipse, and after lunar sunset).

5.1.3 SUMMARY

The performance of the spacecraft thermal control system was excellent. The actual spacecraft temperatures were close to the nominal prediction in most cases. Of the 75 temperature sensors on the spacecraft, 43 were within ±5°F of their predicted values, 16 were within ±10°F, 7 were within ±15°F, 8 were within ±20°F, and one, the SM/SS electronics auxiliary, was 30°F lower than the predicted nominal value.

The temperatures of the following units exceeded their premission prediction range:

Upper and lower thermal trays of compartment B were 2°F below the prediction range

SM/SS was 15°F below lower prediction bound

Oxidizer tank 3 was 2°F higher than upper bound prediction value from 37-hour mission time until touchdown.

However, no problems were evidenced during the mission.

Although the temperatures in compartment B were outside the prediction tolerance, they were more advantageous from an equipment utilization standpoint. The SM/SS auxiliary temperature was below the control point of the thermostat (-5°F minimum), although the heater remained full on throughout the flight. The steady-state temperature of this unit when the vehicle was in normal transit attitude was -35°F with the heater operating continuously.

A short summary of events significant to the thermal subsystem is given in Table 5.1-1. A summary of the actual and predicted transit steady-state temperatures is shown in Table 5.1-2, which also presents equilibrium temperatures observed during Missions A, B, and C. Table 5.1-3 gives a summary of maximum quasi-steady-state temperatures and minimum temperatures on the lunar surface. Plots of all spacecraft temperatures in transit are given in Figures 5.1-15 to 5.1-88. Temperatures throughout the lunar day (corrected for the telemetry problem) are presented in Figures 5.1-89 to 5.1-115.

Only thermal performance which is unique or of special interest is discussed in detail. For those units whose temperature is consistent with previous missions, the steady-state temperature summary and the transit and lunar temperature history plots should be sufficient. The SM/SS temperature and stuck thermal switch anomalies are discussed in detail. Thermal performance is presented for prelaunch, parking orbit and earth shadow, midcourse, coast and terminal phases and lunar day on a selective basis.

A sun trace is shown which indicates the orientation of the sun relative to the spacecraft in the parking orbit. Transient performance of the vernier engines, solar panel, and planar array are analyzed for the cooldown in earth shadow and for the parking orbit and sun acquisition phase. Vernier engine temperatures are correlated to sun orientation in the parking orbit. It is shown that some units are influenced substantially by aerodynamic heating. The transient response of all spacecraft temperatures in the illuminated phase of the parking orbit is summarized.

Engine temperatures as a result of the midcourse thrusting are indicated. Coast phase temperature performance is analyzed for the compartment system, auxiliary battery, flight control sensor group, and the vernier propulsion system.

TABLE 5. 1-1. MISSION THERMAL EVENT LOG FOR SURVEYOR III TRANSIT MISSION

Day	GMT Time Hr:Min	Mission Time Hr:Min	Event
107 17 April	07:05	0	Launch and enter earth shadow
	07:15	00:10	MECO 1
	02:21	00:16	Exit from 16-minute shadow period due to parking orbit
	07:40	00:35	Separation
	07:50	00:45	Sun acquisition complete
	08:09	01:04	High power off
	09:28	02:22	Vernier line 2 heater cycling
	16:09	09:04	Star acquisition sun and roll
	16:11	09:06	Transmitter B high power On (HP On)
	16:28	09:23	Star acquisition complete
	16:39	09:34	Transmitter B high power OFF (HP Off)
	17:29	10:24	Gyro drift check (roll, pitch, yaw) = (R, P, Y)
	19:17	12:12	End gyro drift check
	19:24	12:19	R, P, Y gyro drift check
	21:42	14:37	End gyro drift check
	23:11	16:07	Roll gyro drift check
108 18 April	02:11	19:06	End gyro drift check
	03:02	19:57	In mode 5 at 1100 bps
	04:13	21:08	Mode 4 On
	04:16	21:11	Mode 2 On
	04:18	21:13	Mode 1 On
	04:21	21:16	Transmitter B high power On
	04:22	21:17	4400 bps
	04:30	21:25	Position angle maneuver
	04:47	21:42	Sun and roll +57 degrees
	04:50	21:45	Pitch -39. 4 degrees

Table 5. 1-1 (continued)

Day	GMT Time Hr:Min	Mission Time Hr:Min	Event
	04:53	21:48	Mode 2 On
	04:54	21:49	Mode 1 On
	04:55	21:50	SM/SS auxiliary heater Off AMR heater Off Heaters Off: V Line 2, 1, 3 Tanks: fuel 2, oxid 2, 3
	04:57	21:52	Thrust phase power On
	05:00	21:55	MIDCOURSE 3. 9 second burn
	05:01	21:56	Thrust phase power Off
	05:01	21:56	Mode 5 On
	05:02	21:57	Thermal power On for: V Lines 1, 2, 3 Heaters On for: AMR, SM/SS auxiliary
	05:03	21:58	Pos. angle maneuver pitch (reverse)
	05:06	22:01	Sun and roll (reverse)
	05:11	22:06	Mode 2 On
	05:12	22:07	Mode 4 On
	05:15	22:10	Mode 5 On 1100 bps
	05:16	22:11	Transmitter B high power Off
	07:03	23:58	Mode 4 On
	07:08	24:03	Mode 2 On
	07:12	24:07	Mode 5 On
	07:36	24:31	R, P, Y gyro drift check
	08:49	25:44	550 bps
	09:43	26:38	End gyro drift check
	17:31	34:26	R, R, Y gyro drift check
	19:32	36:27	End P, Y gyro drift check
	20:23	37:18	End R gyro drift check
	20:27	37:22	R, P, Y gyro drift check
	22:50	39:45	End gyro drift check
	22:54	39:49	Roll gyro drift check

Table 5. 1-1 (continued)

Day	GMT Time Hr:Min	Mission Time Hr:Min	Event
109 19 April	01:16	42:11	End gyro drift check
	01:24	42:19	R, P, Y gyro drift check
	03:37	44:32	End gyro drift check
	03:57	44:52	Roll gyro drift check
	06:01	46:56	Auxiliary battery Mode On
	06:14	47:09	High current mode On
	06:45	47:40	End gyro drift check
	06:49	47:44	R, P, Y gyro drift check
	07:04	48:00	Ox 2 tank heater On
	09:09	50:04	End gyro drift check
	09:57	50:52	137 bps
	10:21	51:16	Roll gyro drift check
	11:08	52:03	High current mode Off, auxiliary battery mode Off
	11:13	52:08	High current mode On
	11:26	52:21	Power verified ox line 3 heater On
	12:45	53:40	End gyro drift check
	14:28	55:23	R, P, Y gyro drift check
	16:57	57:51	End gyro drift check
	17:06	58:01	Roll gyro drift check
	18:14	59:09	Auxiliary battery mode On
	18:27	59:22	High current mode On
	18:52	59:47	TV heater On
	20:51	61:46	R, P, Y gyro drift check On (Inadvertantly set)
	20:56	61:51	End gyro drift check
	23:08	64:03	Vidicon heater On
	23:09	64:04	Transmitter B high power On
	23:23:27	64:18	Yaw -157. 9 degrees
	23:28:55	64:24	End yaw
	23:30:15	64:25	Pitch -76. 8 degrees

Table 5. 1-1 (continued

Day	GMT Time Hr:Min	Mission Time Hr:Min	Event
	23:33	64:28	End pitch
	23:34:33	64:30	Roll -63. 9 degrees
	23:37:00	64:32	End roll
	23:55:47	64:50	Heaters Off V. line 2, 1, fuel tank 2 AMR, SM/SS, survey com. Elect and vidicon
	23:56:40	64:52	AMR On
	23:57:31	64:53	Thrust phase power On
	23:59:31	64:55	AMR enable
110 20 April	00:01:16	64:56	Retro ignition
	00:02:17	64:57	Retro ejection
	00:04:20	64:59	Touchdown
	00:10:32	65:06	RADVS Off
	00:13	65:08	Restore main battery mode auxiliary battery Off
	00:26	65:21	Transmitter B high power Off
	00:50	65:45	Transmitter A high power On

Several changes were made in thermal systems of Surveyor III as compared to Surveyor II. Thermal switch closure temperatures were set at 35° ± 10°F for all switches on both compartments A and B. Previously compartment A had a mixture of four 40°F closure temperature switches and five 65°F closure temperature switches and compartment B had all 50°F closure temperature switches. The flight control electronics power supply was redesigned so that the electronic dissipation was reduced by 50 percent. TV auxiliary viewing mirrors were added to the spaceframe adjacent to leg 1 propellant tanks.

The influence of gyro drift checks and heater duty cycles for all heated thermal systems are indicated. Thermal performance was very nominal for the terminal phase of the mission.

Subsequent to touchdown a signal processing problem made the engineering telemetry unintelligible. It was necessary to adjust all the lunar data in accordance with a correction supplied by the signal processing group to evaluate and present the lunar data given here.

Shadowing of compartment A and the TV kept temperatures of these systems from overheating at lunar noon. It was shown that the computer model for the solar panel and planar array correlates well with the lunar phase data. Thermal requirements for a Surveyor III lunar surface liftoff and translation were analyzed. The temperature of the lunar surface at the Surveyor III landing site was determined from spacecraft thermal data.

TABLE 5.1-2. COMPARISON OF STEADY-STATE TEMPERATURES IN MISSIONS A, B, AND C

Flight Sensor Location by Subsystem		Actual Steady-State Temperature, °F						Operation Allowable Limits
		Mission A Transit		Mission B Premidcourse		Mission C Transit		
		Actual	Predicted	Actual	Predicted	Actual	Predicted	
Vehicle and mechanisms								
Compartment A								
Upper tray	V-15	70	78	74	73	49	49	140/0
Lower tray	V-16	93	98	94	94	70	72	125/0
Transmitter A	D-13	68	76	71	72	49	47	210/0
Transmitter B	D-14	68	78	73	73	48	48	210/0
Main battery	EP-8	97	98	99	99	69	75	125/40
Battery charge regulator	EP-34	123	125	118	120	94	100	185/0
Radiators								
No. 5	V-20	42	36	31	42	30	25	150/-300
No. 8	V-25	44	30	28	35	36	32	150/-300
No. 2	V-47	35	30	34	36	19	15	150/-300
Thermal shell inside	V-17	92	102	92	91	68	72	120/0
Thermal shell outside	V-18	-85	-110	-82	-90	-84	-90	
Thermal switch No. 5 inside	V-19	66	79	69	69	47	47	150/-300
Compartment B								
Upper tray	V-21	93	97	99	106	76	93	125/0
Lower tray	V-22	98	102	103	111	81	98	125/0
Boost regulator	EP-13	115	110	128	123	94	110	185/0
Radiators								
No. 4	V-24	67	75	70	77	55	67	150/-300
No. 1	V-45	73	71	84	91	61	74	150/-300
No. 5	V-46	66	71	70	78	56	72	150/-300
Thermal shell outside	V-23	-70	-78	-72	-65	-64	-70	
Thermal switch No. 4 inside	V-26	88	93	93	101	74	88	125/0
Wiring harness	V-29	88		91	94	72	88	125/0
Auxiliary battery	EP-26	35	60	64*	66	54	60	130/20
Auxiliary battery compartment	V-48	-2		9*	28	12	5	130/30
Landing gear assembly								
Leg 2	V-31	83	85	74	55	77	70	160/-140
Crushable block	V-44	-62	-50	-48	-51	-63	-60	160/-140
Shock absorber								
No. 1	V-30	84	90	76	84	74	84	125/-20
No. 2	V-32	72	88	73	82	76	72	125/-20
No. 3	V-33	82	90	82	84	79	84	125/-20
Antenna/solar panel positioner mechanism								
Solar panel drive	M-10	60	40	45	60	51	47	165/-225
Elevation axis drive	M-12	1	-86	-17	-8	-11	-7	165/-225
Solar cell array	EP-12	109	118	111	110	112	110	165/-200
Planar array	M-8	-50	-60	-50	-50	-50	-50	280/-280
A/SPP mast	V-34	-84	-114	-88	-86	-88	-86	160/-140
Spaceframe and substructure								
Upper spaceframe								
Near leg 1	V-27	60	73	53	65	57	56	160/-140
Near leg 2	V-35	-79	-70	-81	-75	-82	-81	160/-140
Lower spaceframe								
Under compartment B	V-28	48	46	42	50	43	45	160/-140
Under compartment A	V-36	-27	-21	-24	-24	-32	-25	160/-140

Table 5.1-2 (continued)

Flight Sensor Location by Subsystem		Actual Steady-State Temperature, °F						Operation Allowable Limits
		Mission A Transit		Mission B Premidcourse		Mission C Transit		
		Actual	Predicted	Actual	Predicted	Actual	Predicted	
Retro attach points								
Leg 1	V-37	39	46	44	46	42	44	160/-140
Leg 2	V-38	-36	-21	-32	-24	-52	-50	160/-140
Leg 3	V-39	44	46	44	50	46	46	160/-140
Propulsion								
Vernier engine thrust chamber assembly								
No. 1	P-7	59	76	54	65	58	60	125/20
No. 2	P-10	72	81	84	80	81	85	140/20
No. 3	P-11	59	62	63	70	69	66	130/20
Propellant tanks								
Oxidizer 1	P-15	75/41†	74/45†	76/50††	49	76/41@	33@	100/0
Fuel 1	P-13	76/52†	73/48†	77/57††	58	76/55@	48@	100/0
Oxidizer 2	P-16	77/24†	79/35†	75/35††	38	75/18@	17@	100/15
Fuel 2	P-5	75/34†	74/30†	83/47††	44	74/33@	19@	100/15
Oxidizer 3	P-6	79/40†	73/45†	75/46††	50	77/30@	17@	100/15
Fuel 3	P-14	76/53†	73/51†	75/53††	57	76/52@	42@	100/0
Propellant lines								
Leg 1	P-8	23 to 29	35	18 to 28	18 to 28	30	19	100/0
Leg 2	P-4	21 to 26	20 to 27	20 to 27	20 to 27	19 to 22	19 to 24	100/0
Leg 3	P-9	21 to 26	30	20 to 27	20 to 27	19 to 24	19 to 24	100/0
Helium tank	P-17	60	75	72	75	73	75	100/100
Main retro								
Upper case	P-3	73/67†	74/67†	72/73††	72	73/64@	65@	70/40
Lower case	P-12	74/46†	74/36†	76/59††	60	78/41@	42@	70/25
Nozzle	P-22	-124	74/-222†	-118	-120	-130	-120	
Flight control								
Flight control electronics								
Chassis board 1	FC-44	90	100	90	100	71	65	165/0
Chassis board 6	FC-45	124	135	137	138	60	55	190/0
Canopus sensor	FC-47	78	90	85	89	74	75	130/-20
Roll gyro	FC-46	170**	178**	175**	177	173**	177	185/175
Pitch gyro	FC-54	175**	175**	175**	174	172**	173	185/170
Yaw gyro	FC-55	180**	177**	174**	177	172**	177	185/170
Roll actuator	FC-71	79	98	82	88	83	90	200/0
Nitrogen tank	FC-48	45	71	40	52	50	45	115/-10
Radars	FC-70	88	87	86	77	105	90	160/-50
RADVS								
KPSM	R-8	12	22	11	15	17	20	100/-22
SDC	R-9	56	53	63	63	55	59	140/-18
VS preamplifier	R-10	22	32	14	11	16	13	112/-42
A/VS preamplifier	R-13	33	45	20	10	27	26	110/-20
Altitude marking radar								
Electronics	R-7	14 to 16	20 to 22	18	16	14 to 19	18 to 22	120/-5
Antenna dish	R-6	-12	0	-14	-12	3	-15	135/-20
Edge of dish	R-27	-185	-160	-191	-185	-202	-180	200/-300
Television and SM/SS								
TV 3 mirror	TV-17	-120	-162	-120	-117	-120	-135	180/-50
TV 3 ECU	TV-16	-134	-150	-128	-123	-128	-134	150/-20
TV 4	T-3	-124	-140	-103	-116	—	—	165/-20
Auxiliary electronics	SS12	—	—	—	—	-35	-5	158/-4

*Not at steady state.
**Corrected for bit rate error.
†Launch + 63 hours.
††Launch + 15 hours.
@Launch + 65 hours.

TABLE 5.1-3. MAXIMUM QUASI-STEADY-STATE TEMPERATURES AND MINIMUM TEMPERATURES ON LUNAR SURFACE

Sensor and Location		Maximum Temperature, F°		Surveyor III Minimum Temperature, F°	
		Surveyor I	Surveyor III	Eclipse	Spacecraft Shutdown*
D-13	Transmitter A	185	118	47	17
D-14	Transmitter B	106	110	43	12
EP-8	Main battery	118	116	74	60
EP-12	Solar panel	217	220	-185	-215
EP-13	Boost regulator	132	132	32	
EP-26	Auxiliary battery	155	166	140	-24
EP-34	Battery charge regulator	142	125	72	36
FC-44	Flight control electronics	192	202	53	-79
FC-45	Flight control electronics	200	201	-3	-67
FC-46	Roll gyro	167	198	11	-35
FC-47	Canopus	180	194	-20	-79
FC-48	Nitrogen tank	173	165	—	-137
FC-54	Pitch gyro	188	—	—	—
FC-55	Yaw gyro	170	—	—	—
FC-70	Attitude jet 2	205	210	-52	-182
FC-71	Roll actuator	224	239	-16	-61
M-8	Planar array	228	230	-140	-195
M-10	Solar motor	218	230	-43	-156
M-12	Elevation motor	190	201	14	-123
P-4	Oxidizer line 2	203	203	76	-9
P-5	Fuel line 2	164	197	165	110
P-6	Oxidizer tank 3	154	179	108	—
P-7	Vernier engine 1	244	256	-12	-52
P-8	Oxidizer line 1	221	202	8	-7
P-9	Oxidizer line 3	184	200	62	14
P-10	Vernier engine 2	229	256	36	-106
P-11	Vernier engine 3	227	232	22	-65
P-13	Fuel tank 1	190	208	83	162
P-14	Fuel tank 3	171	188	137	121
P-15	Oxidizer tank 1	173	183	96	99
P-16	Oxidizer tank 2	166	185	153	51
P-17	Helium tank	145	178	21	-112
R-8	Klystron power supply modulator	225	214	23	-9
R-9	Signal data converter	149	168	8	15

Table 5.1-3 (continued)

Sensor and Location		Maximum Temperature, F°		Surveyor III Minimum Temperature, F°	
		Surveyor I	Surveyor III	Eclipse	Spacecraft Shutdown*
R-10	Doppler preamplifier	235	260	-33	-18
R-13	Altitude preamplifier	214	232	2	-42
SS-12	Surface sampler electronics	–	144	-18	-28
TV-16	TV electronics	127	140	-10	-7
TV-17	TV hood	124	148	-12	0
V-15	A tray top	110	109	41	11
V-16	A tray bottom	118	117	68	34
V-17	Compartment A shell, retainer	–	120	69	34
V-18	Compartment A shell, cannister	–	108	-170	-202
V-19	Compartment A switch 5, base	–	112	45	10
V-20	Compartment A switch 5, radiator	78	101	18	-16
V-21	B tray top	118	117	21	-1
V-22	B tray bottom	124	122	29	10
V-23	Compartment B shell, cannister	111	152	-154	–
V-24	Compartment B switch 4, radiator	99	100	-16	-26
V-25	Compartment A switch 8, radiator	88	100	13	-13
V-26	Compartment B switch 4, base	–	114	21	-5
V-27	Upper spaceframe	138	156	-75	-147
V-28	Lower spaceframe	190	186	-32	-116
V-29	Thermal tunnel	–	115	47	28
V-30	Shock absorber 1	193	190	-51	-130
V-31	Leg 2 upper web	148	158	–	-105
V-32	Shock absorber 2	171	183	-57	-140
V-33	Shock absorber 3	175	186	-35	-128
V-34	Antenna solar panel positioner mast	130	142	-102	-172
V-35	Upper spaceframe	125	154	-70	-143
V-36	Lower spaceframe	166	179	-45	-129
V-37	Retro bolt 1	222	202	-2	-100
V-38	Retro bolt 2	175	227	32	-121
V-39	Retro bolt 3	185	200	-11	-100
V-44	Crushable block 3 heat shield	189	193	-29	-130
V-45	Compartment B switch 1, radiator	104	105	-95	-143
V-46	Compartment B switch 5, radiator	96	100	-5	-17
V-47	Compartment A switch 2, radiator	–	104	18	-18

*Last available temperature recorded.

5.1.4 THERMAL PERFORMANCE IN TRANSIT

5.1.4.1 Prelaunch Phase

All prelaunch thermal constraints were satisfied. The various spacecraft component heaters were properly configured prior to launch as follows:

SM/SS heater	Enabled
Vernier line heaters	Enabled
AMR heater	Enabled
Survey TV electronics heater	Not enabled
Survey TV vidicon heater	Not enabled
Propellant tank heaters	Not enabled
Compartment A heater	Not enabled, and off
Compartment B heater	Not enabled, and off

Prelaunch air-conditioning was provided as required. Conditioned air was provided and maintained at 75°F until 2-1/2 hours prior to launch, whereupon it was increased to 85°F and maintained there until launch.

5.1.4.2 Thermal Performance From Launch to Sun Acquisition

Some of the most interesting environmental conditions and flight temperature conditions are encountered in the launch through sun acquisition phases of the mission. In this period the vehicle is in darkness until 16M20S after launch, at which time the vehicle exits from the earth's shadow. From this time until sun lockon at launch +45M the spacecraft is in the sun but not in a normal transit attitude. During the period from exit shadow to sun lock, some spacecraft units continue to cool because of shadowing by other parts of the vehicle and other units are heated to temperatures in excess of their transit steady-state temperature due to off normal solar irradiation. In addition to the varying solar heating conditions, the vehicle is subjected to aerodynamic heating from Centaur shroud jettison (L+3M23S) to spacecraft separation at L+35M. This includes part of the ascent trajectory and parking orbit.

When the vehicle exited from the earth shadow at L+980 seconds, the Centaur/Surveyor vehicle had rolled approximately 71 degrees and acquired the vehicle-sun attitude shown in Figure 5.1-1. As the spacecraft traveled along its flight trajectory prior to lunar injection (thrust vector parallel to the earth's surface) the vehicle thrust vector-sun vector attitude changed continuously. Subsequent to vehicle exit from the earth shadow, the spacecraft continued to roll at 0.17 deg/sec. Spacecraft components in the proximity of Surveyor landing legs 2 and 3 were illuminated as the vehicle exited from the shadow. As the parking orbit phase of the mission progressed, spacecraft subsystems in the proximity of Surveyor leg 3 moved

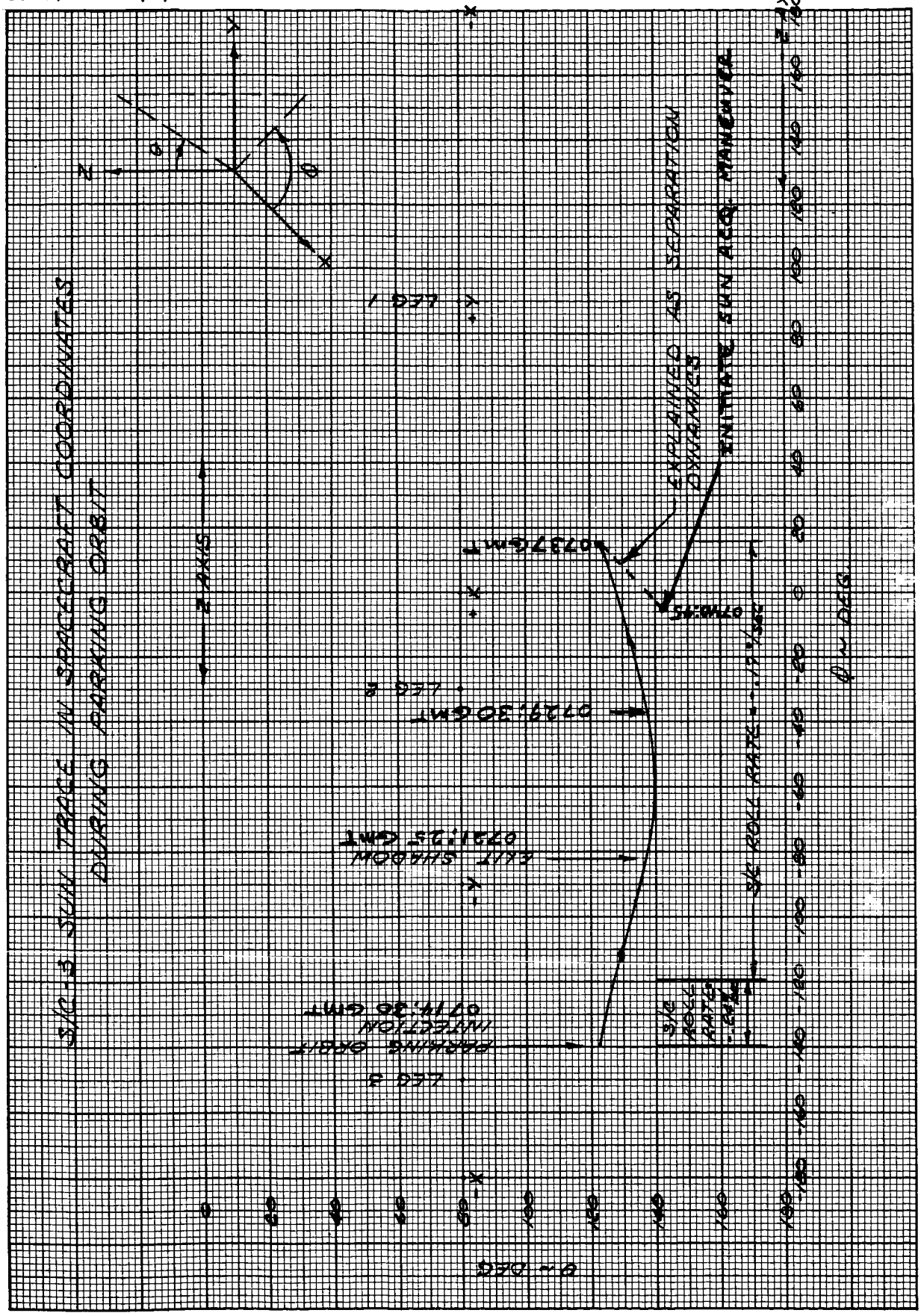

Figure 5.1-1. SC-3 Sun Trace in Spacecraft Coordinates During Parking Orbit

out of the sun direct field of view and subsystems in the proximity of leg 1 moved in direct view of the sun. Thermal data indicate that Surveyor subsystems adjacent to leg 2 were illuminated throughout the parking orbit phase of the mission.

Vernier Engines

The thermal performance of the Surveyor vernier engines was as expected during the launch, earth shadow, and parking orbit mission phases; however, the peak temperature of vernier engine 2 exceeded its maximum predicted temperature subsequent to the Centaur/Surveyor exit from the earth shadow. Predictions indicated a peak temperature of 95°F; vernier engine 2 reached a peak temperature of 103°F during this period.

The Surveyor SC-3 mission presented thermal analysts the first opportunity to compare initial flight eclipse data and thermal data obtained during the rapid chilldown period in STV testing. SC-3 STV test data are not available in sufficient quantity to make a comparison of units tested with the SC-3 flight units. However, thermal data are available from the SC-5 STV flight acceptance test. A comparison of the cooldown rates exhibited by SC-3 vernier engines during flight in the earth shadow period and the cooldown rates exhibited by the SC-5 vernier engines during the rapid chilldown STV mission phase are tabulated in Table 5.1-4.

TABLE 5.1-4. SURVEYOR III FLIGHT AND SC-5 TEST COOLDOWN RATES

Units	Surveyor III, °F/minute	SC-5 Test, °F/minute
TCA-1	1.08	0.78
TCA-2	1.08	0.82
TCA-3	0.78	0.87

The comparison of Surveyor III flight/SC-5 test data presented in Table 5.1-4 indicates that the rapid chilldown phase of STV tests is a good simulation of the vernier engine thermal behavior during earth shadow periods.

Analytical studies have demonstrated that the three Surveyor vernier engines should cool at approximately the same rate when subjected to the same thermal environment (earth shadow) following launch. An investigation of the thermal data indicates that TCA-1 and TCA-2 had identical cooling rates from launch to launch +13M as shown in Figure 5.1-2.

Thermal test data prior to the Surveyor I flight indicated that the thermal transient capability (TTC) of the vernier engines was 88 minutes

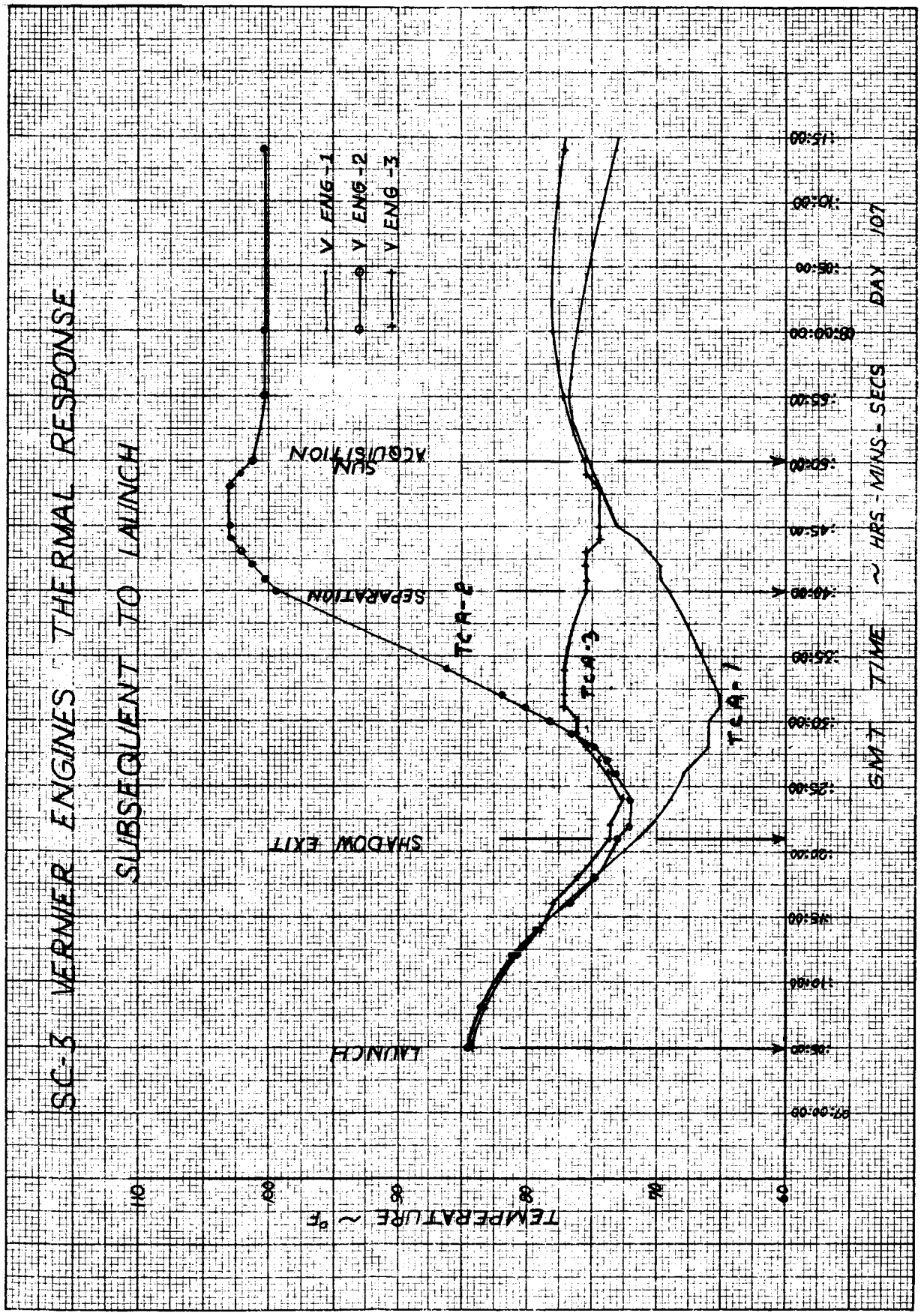

Figure 5.1-2. SC-3 Vernier Engines Thermal Response Subsequent to Launch

during earth shadow periods. The minimum thermal transient capability of the Surveyor III TCAs may be determined from the cooldown rates exhibited by TCA-1 and TCA-2 and assuming a linear cooldown (which is a worst case). Hence, the minimum TTC of the Surveyor III vernier engines was 79 minutes, based on a launch temperature of 85°F.

Solar thermal vacuum tests and analytical studies have verified the conservatism of the previous linear cooldown assumption. Analytical studies and STV test have shown that at lower temperatures (0° to 30°F range) the cooling rate exhibited by vernier engines is less than 1°F/minute. Therefore the analytically derived TTC for vernier engines is probably indicative of vernier engine thermal behavior during earth shadow periods.

Subsequent to launch plus 13 minutes (07:18 GMT) the cooldown rates for TCA-1, TCA-2, and TCA-3 started to diverge (Figure 5.1-2). At this time spacecraft subsystems in the proximity of Surveyor leg 2 entered the earth's penumbra. The cooling rate exhibited by TCA-2 began decreasing as a result of partial solar illumination. Subsequent to vehicle exit from the shadow at 16M20S (07:21:20 GMT), TCAs 2 and 3 showed temperature increases while TCA-1 continued to cool. At approximately launch plus 26M40S (07:31:40 GMT) TCA-3 exhibited a temperature decrease and TCA-1 showed an increase, indicating that TCAs 1 and 3 had moved into and out of the sun field of view, respectively.

Flight data indicate that TCA-2 exhibited a temperature rise rate of 2.2°F/minute during the parking orbit mission phase, subsequent to spacecraft exit from the earth shadow. Thermal analyses have shown that the TCAs can experience even larger temperature rise rates during periods of off-axis solar heating. However, the probability of the spacecraft maintaining an attitude that results in vernier engine overheating is small. While it is possible to establish a spacecraft attitude with respect to the sun vector that results in the TCAs receiving maximum direct insolation, it is very difficult to establish the spacecraft attitude that results in maximum TCA heating because of difficulties in defining the indirect insolation component. This component may be less than, equal to, or greater than the direct insolation component and in general is unpredictable for spacecraft attitudes that differ from the nominal transit attitude.

Vernier Propellant Lines

The vernier propellant lines cooled as expected during the earth shadowed phase of the mission. However, line temperatures were relatively constant during the period bounded by earth shadow exit and sun acquisition (Figures 5.1-34, 5.1-39, and 5.1-40). Vernier line 1 continued to cool subsequent to exit from the shadow; however, vernier line 1 showed a slight temperature increase at approximately launch plus 35 minutes. The temperature of vernier lines 2 and 3 remained constant throughout the parking orbit phase subsequent to exit from the shadow.

The thermal transit capability of the vernier propellant lines cannot be deduced from the SC-3 flight data because flight sensor readings probably

do not reflect the maximum rate at which line temperatures are decreasing. Long unheated sections of line are expected to experience larger temperature drops than those exhibited by the flight sensor for the same environmental conditions.

Solar Panel and Planar Array

The A/SPP and planar array temperature profiles were analyzed for the initial phase of the mission which consists of launch to Centaur-Surveyor separation. The flight temperature profiles of the solar panel and planar array during this time period when the vehicle is in the earth's shadow and the parking orbit are shown in Figure 5.1-3. It is clear that the solar panel and planar array temperatures are responsive to a change in environment.

When the vehicle is in the shadow of the earth, the temperatures of the solar panel and planar array are independent of the vehicle orientation since this equipment receives no solar energy. The temperature cooldown is shown in Figure 5.1-3. To understand the response of the solar panel and planar array temperature trend after exit from the earth's shadow, it is necessary to know the orientation of the vehicle with respect to the sun vector. The orientation of the sun vector with respect to the vehicle and the path of the sun relative to the vehicle from earth shadow exit to Centaur-Surveyor separation is shown in Figure 5.1-4. The sun vector trace as shown in Figure 5.1-4 is defined in spacecraft coordinates with θ and φ-angles defining the position of the sun vector relative to the spacecraft. Also illustrated in Figure 5.1-4 are the relative positions of the sun vector with respect to the solar panel and planar array in their stowed positions. The sun vector trace as seen from the figure indicates that upon exit from earth shadow to spacecraft separation the solar panel is illuminated by the sun. As a consequence, the solar panel temperature increases and continues to rise until separation occurs. The planar array upon exit from the shadow continues to decrease in temperature since the sun does not illuminate the back side of the planar array enough to overcome the radiation loss to space. However, as the vehicle moves with respect to the sun vector (Figure 5.1-4), the solar irradiation to the back side of the solar panel increases. Although the planar array increases in temperature, the rate of increase is slower than that of the solar panel as a result of only partial solar illumination.

Upon separation from the Centaur, the vehicle with solar panel begins to maneuver to acquire the transit configuration. As a result, the solar panel is positioned away from the sun, temporarily causing a drop in temperature. Finally the solar panel temperature increases again when the transit configuration is attained as shown in Figure 5.1-3.

From the solar panel and planar array flight temperature data the existing analytical model shown in Figure 5.1-5 was used to determine whether correlation with actual flight data could be obtained. The A/SPP thermal model as it existed originally was correlated to agree with Surveyor I transit temperature data. This existing model was then imposed on earth-orbit conditions for only the earth shadow phase of the mission. The results of

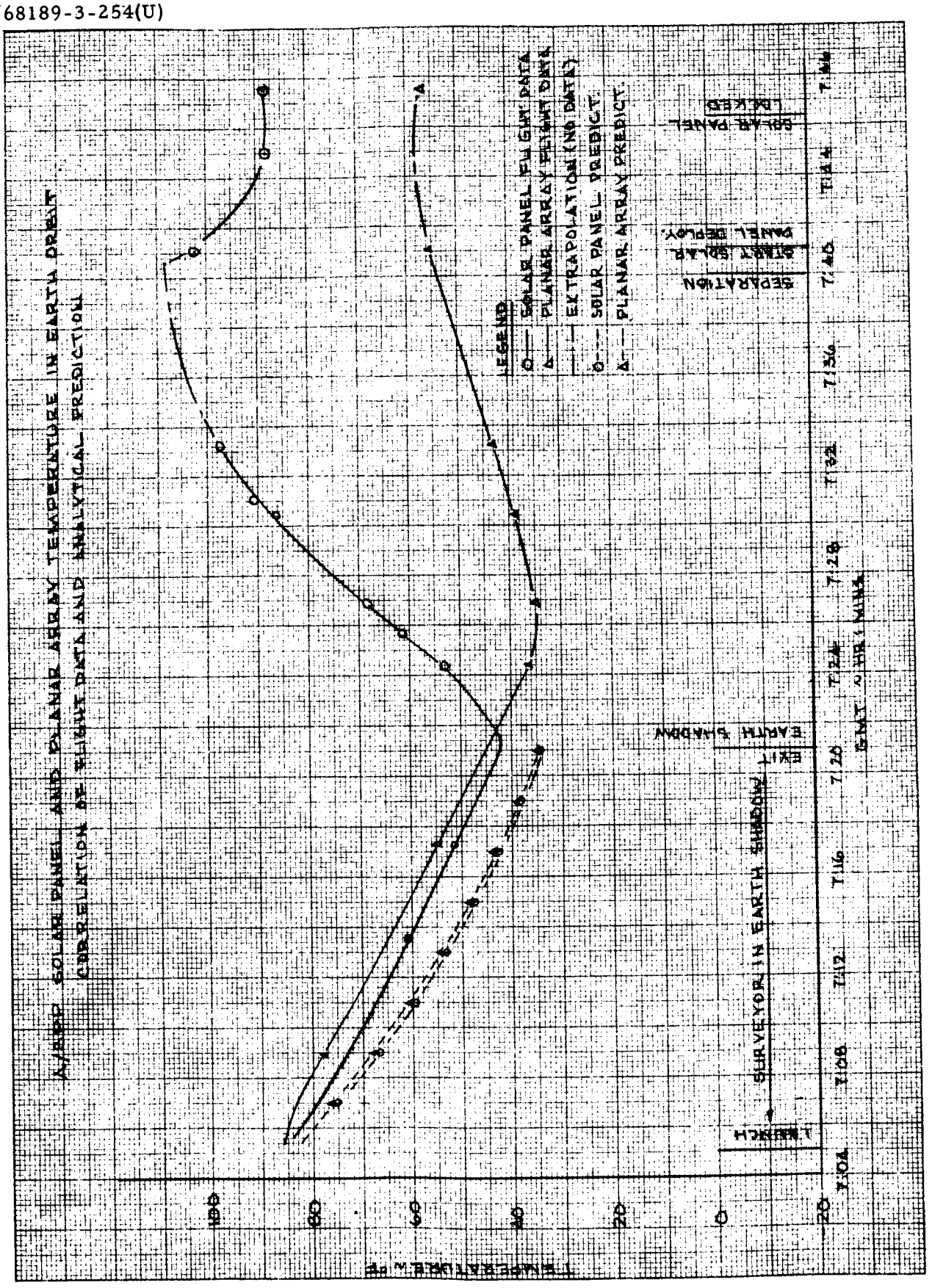

Figure 5.1-3. A/SPP Solar Panel and Planar Array Temperature in Earth Orbit Correlation of Flight Data and Analytical Prediction

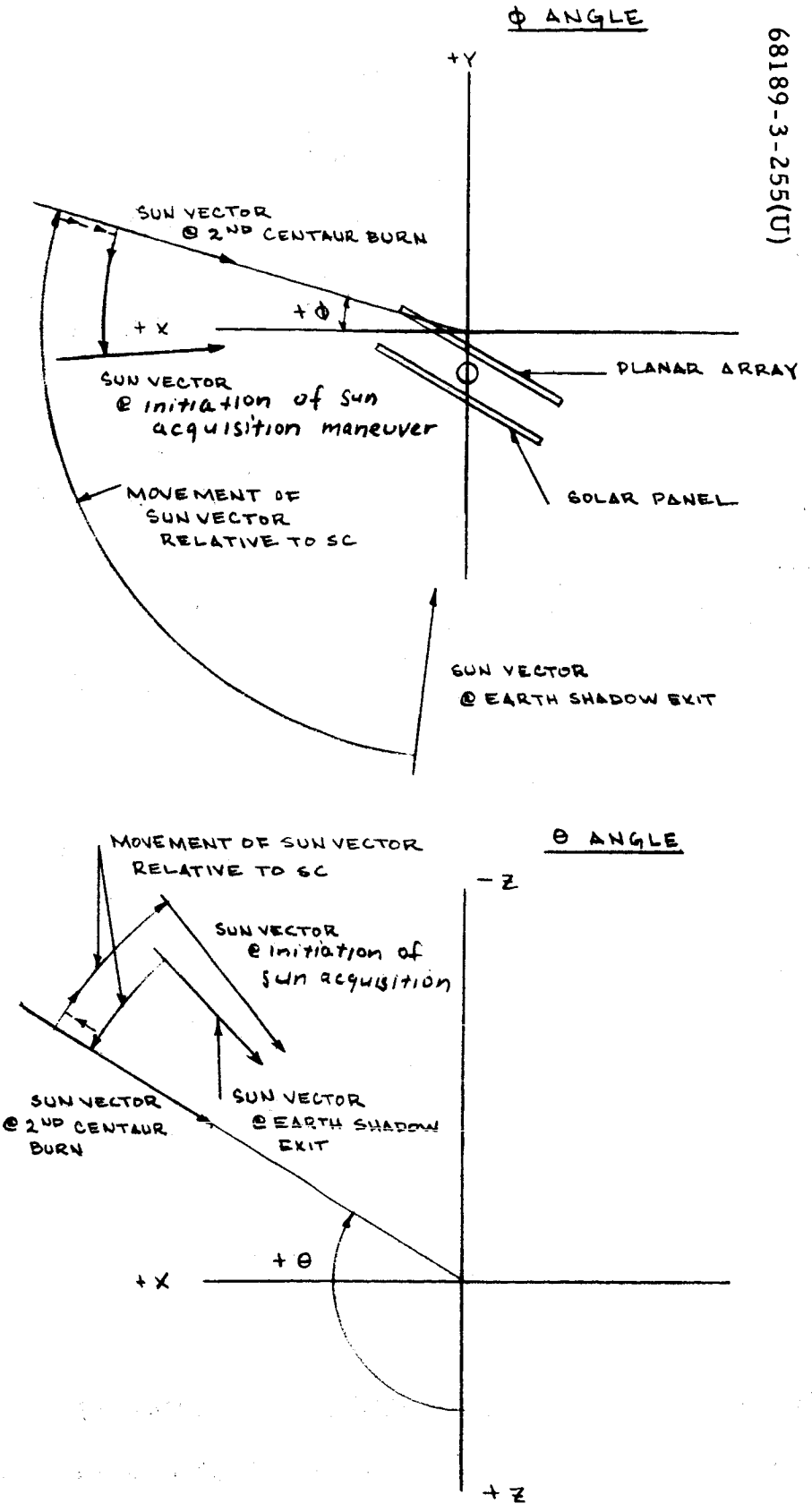

Figure 5.1-4. Sun Vector Trace During Parking Orbit Denoted by φ and θ Angles

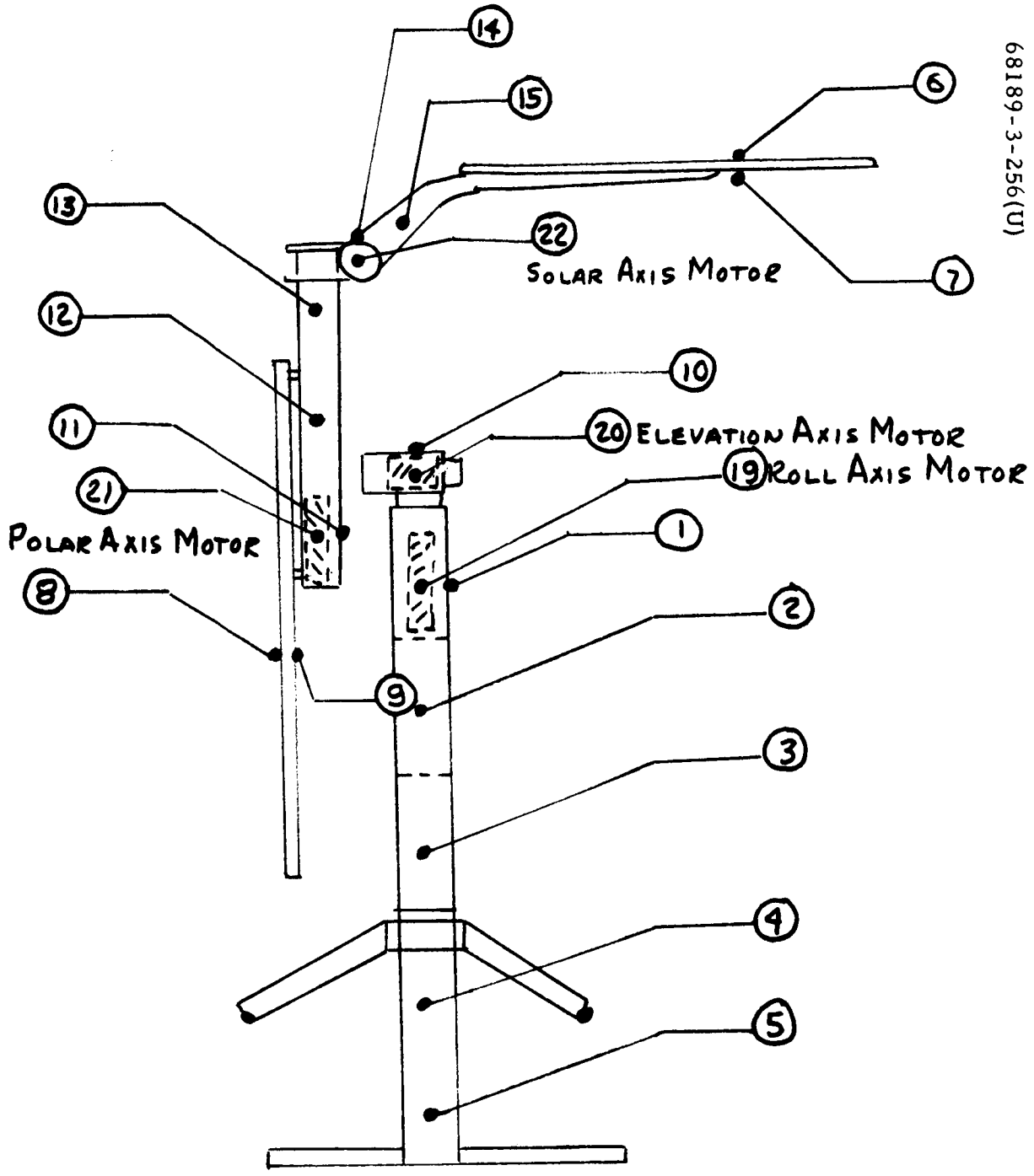

(X) INDICATES THERMAL MODEL NODE NUMBER

CROSS HATCHED AREA INDICATES DRIVE MOTORS

Figure 5.1-5. A/SPP Thermal Model

the analytical temperature response of the solar panel and planar array are shown in Figure 5.1-6. Because of the large deviation of 52 degrees between actual and analytical temperature results, it was reasoned that the deviation must be a consequence of aerodynamic heating. The model was then adjusted to account for aerodynamic heating and the temperature results are shown in Figure 5.1-6. The justification for aerodynamic heating is that the additional heat required cannot be accounted for by inaccuracies in the model, since the model agreed with Surveyor I transit data. The aerodynamic heating load used to obtain the temperature profile of the solar panel and planar array is approximately 48 Btu/hr-ft^2. Aerodynamic heating loads have been computed in Reference 1 and indicate that for the particular altitude in which Surveyor orbited, the nominal heating load is 55.5 Btu/hr-ft^2. As a result, it appears that aerodynamic heating in parking orbit does play a contributing role in the temperature response of the planar array and solar panel. The thermal model temperature prediction was not continued after earth shadow exit because of the difficulty in determining solar heat loads when the vehicle is rolling about its axis during the parking orbit.

Compartment System

Temperature data during launch and the parking orbit periods are influenced by the magnitude of aeroheating experienced by the spacecraft. The compartment A and B thermal switch radiators are prime examples of the aeroheating effects and each experienced a temperature rise of approximately 20°F during the parking orbit (Figures 5.1-65, 5.1-69, 5.1-70, and 5.1-86 through 5.1-88). Internal compartment A and B temperatures were not affected by the aeroheating. This data corresponds to a heating rate equal to or less than that expected from the nominal trajectory.

Other Thermal Systems

The thermal behavior of Surveyor III subsystems subsequent to vehicle exit from the earth shadow and prior to Centaur-Surveyor separation are presented in Table 5.1-5. The effect of the 16M20S earth shadow, subsequent off-axis solar illumination and aerodynamic heating in the parking orbit (separation at L+35M), and random solar illumination until sun acquisition (L+44M) may be seen in many of the thermally passive units. Examples of this behavior are found in the vernier engines, flight control sensor group, roll actuator, leg and shock 2, RADVS, helium tank, vernier lines, A/SPP, SM/SS, and the spaceframe.

Thermal data indicate that the solar panel (EP-12), vernier engine 2 (P-10), compartment A canister (V-18), landing leg 2 (V-31), and the auxiliary battery container (V-48) experienced the largest temperature increases during the illuminated phase of the parking orbit. The AMR antenna dish (R-27) exhibited the largest temperature decrease during the parking orbit.

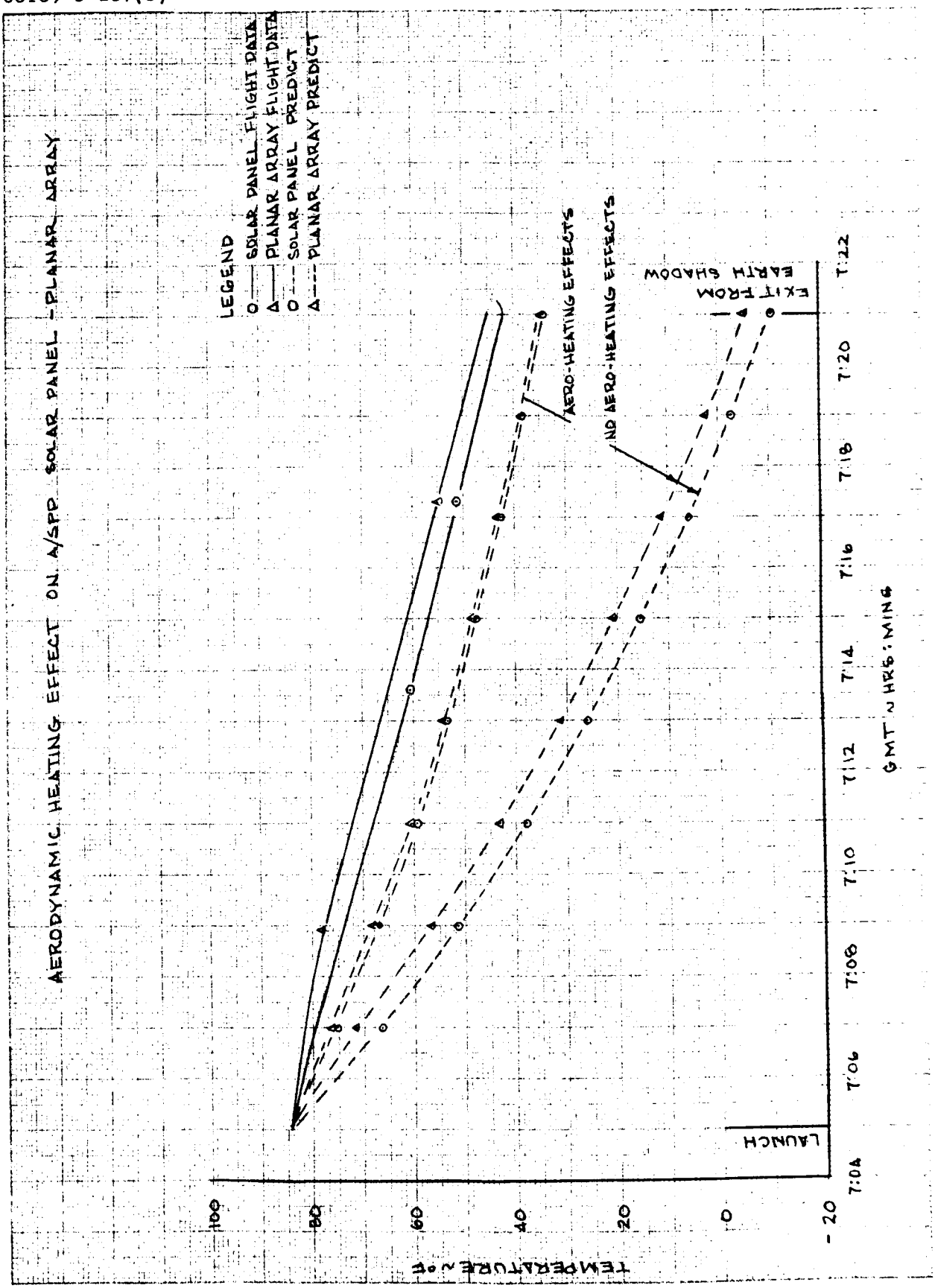

Figure 5.1-6. Aerodynamic Heating Effect on A/SPP Solar Panel Planar Array

TABLE 5.1-5. THERMAL RESPONSE OF THE SURVEYOR III SUBSYSTEMS DURING ILLUMINATED PHASE OF PARKING ORBIT

Sensor	Temperature, ~°F		Sensor	Temperature, ~°F		Sensor	Temperature, ~°F	
	At Exit Shadow	After Exit		At Exit Shadow	After Exit		At Exit Shadow	After Exit
D-13	83	7	P-14	75	0	V-38	75	5
D-14	82	18	P-15	73	0	V-44	46	-10
EP-8	82	1	P-16	74	-1	V-45	71	20
EP-12	49	54	P-17	56	34	V-46	70	16
EP-13	108	6	P-22	68	-18	V-47	67	18
EP-26	78	1	R-7	75	-5	V-48	62	46
EP-34	71	4	R-8	72	8			
FC-45	93	-1	R-9	78	3			
FC-46	172	3	R-10	79	-1			
FC-47	86	5	R-13	79	13			
FC-48	82	6	R-27	-18	-40			
FC-54	172	1	SS-12	76	5			
FC-55	172	3	TV-17	60	-2			
FC-70	81	14	V-15	83	14			
FC-71	82	5	V-16	82	2			
M-8	37	20	V-18	-12	68			
M-10	75	16	V-20	68	19			
P-6	74	1	V-21	92	5			
P-7	72	-7 +4	V-22	91	1			
			V-24	66	21			
P-8	74	-6 +2	V-25	65	21			
			V-27	60	21			
P-9	74	-5	V-28	75	-1			
P-10	72	27	V-29	81	1			
P-11	73	+4	V-31	52	58			
P-12	77	0	V-32	68	15			
P-13	75	-1						

Launch to Sun Acquisition

A qualitative description of the general spacecraft attitude can be infe inferred from an examination of the thermal data. The Surveyor III Centaur-Surveyor attitude with respect to the sun vector for the period bounded by earth shadow exit and Centaur-Surveyor separation has been established in a quantitative sense. This information will aid analytical efforts in assessing the thermal effects of the random orientation/parking orbit period on spacecraft subsystems during Missions E, F, and G. Mission 4 is a direct ascent (no parking orbit) mission.

The Centaur-Surveyor roll magnitude, rate, and direction are undefined and will not be available prior to launch. However, flight trajectories are available. Studies are in progress to bound the sun-vector/spacecraft-thrust-vector attitude during the parking orbit phases of Missions 5, 6, and 7. Surveyor III flight data will be superimposed on analytical data for Missions 5, 6, and 7 in an effort to bound the thermal behavior of spacecraft subsystems during subsequent parking orbits.

5.1.4.3 Midcourse Phase

Spacecraft thermal performance during midcourse was nominal. All heaters excluding the gyro heaters were commanded off for approximately 7 minutes during midcourse. All thermostatically controlled components apparently remained well within operational limits despite the 7-minute loss of temperature control.

Temperature stratification in the propellant tanks was evidenced during midcourse, as on previous spacecraft. All six propellant tank temperature sensors experienced an increase as shown in Figures 5.1-36, 5.1-37, and 5.1-44 through 5.1-47. This phenomenon is discussed in detail in subsection 5.1.4.4.

The Surveyor III vernier engines operated at a thrust level of approximately 76 pounds for 4 seconds during the midcourse correction maneuver. The maximum temperatures indicated by the thermal flight sensors were 166°, 267°, and 208°F for TCA-1 (P-7), TCA-2 (P-10), and TCA-3 (P-11), respectively. Midcourse TCA temperatures were within the predicted range.

5.1.4.4 Coast Phases

Compartment System

The compartment system thermal performance was well within the design limits throughout the transit mission. (Figures 5.1-15 through 5.1-21 and Figures 5.1-60 through 5.1-71.) Equilibrium temperatures on the compartment A thermal tray main battery and battery charge regulator were all within 6°F of the predicted value. However, the time to reach equilibrium was longer than predicted. During high power periods, the transmitter traveling-wave tube (TWT) temperature response was greater than predicted, but did not constitute a problem. The predicted transient temperature response of the TWT was based primarily on Surveyor I

flight data, whereas the use of STV test data for determining the TWT transient response would have resulted in a more accurate TWT temperature prediction during transmitter high power operations.

Compartment B transit equilibrium temperatures were 17°F lower than predicted. The lower temperatures are desirable operationally; however, the temperature uncertainty assigned to the compartment B thermal tray (±15°F) was violated by 2°F. Although compartment B temperatures in the Surveyor I flight were approximately 20°F higher than in Surveyor I low-sun-STV-test, phase 6B, the Surveyor III compartment B flight temperatures were very nearly the same as in the Surveyor III STV low sun tests.

The Surveyor III boost regulator thermal dissipation was approximately 4.4 watts less than in Surveyor I and II due to the redesigned flight control unit which requires less power. By merely adjusting the Surveyor I or SC-2 compartment B equilibrium flight temperatures to account for the 4.4 watt reduction in boost regulator thermal dissipation, and seasonal solar intensity variations, temperatures very nearly the same as those observed in the Surveyor III flight can be achieved. Consequently the compartment thermal performance appears to be reproducible in the space environment but not in an STV test environment. Vernier oxidizer lines 1, 2, and 3 were at temperatures of 48°, 35°, and 23°F at the initiation of the 4-second midcourse vernier thrusting period, respectively. Oxidizer lines 1, 2, and 3 reached peak temperatures of 55°, 56°, and 34°F, respectively, as a result of propellant flow.

Gyro Drift Checks

Several of the spacecraft temperatures are influenced by gyro drift checks, notably vernier engine 2 and the SM/SS electronics auxiliary compartment. The nominal drift angles were ±1.0 degree pitch, -2.0 degree yaw, and +2.2 degree roll. The times and types of gyro drift maneuvers are found in Table 5.1-6, the thermal sequence of events. The negative yaw drift caused the solar panel shadow to move away from the Y-Y axis. The positive pitch drift caused the solar panel shadow to move toward leg 1. As a result the SM/SS auxiliary compartment was exposed to more solar radiation and vernier engine 2 received less solar illumination. During gyro drift checks the SM/SS compartment temperature rose to as high as -14°F. After cruise mode was restored, the temperature decreased asymptotically at a rate of 3° to 5°F/hour until either the next drift check was initiated or the steady-state temperature was obtained. Vernier engine 2 temperature decreased to as low as 46°F during a yaw drift. The temperature responses to gyro drift checks of the nitrogen tank, the altimeter velocity preamplifier, compartment A radiators, leg 2 retro bolt, crushable block, vernier line 3, and survey camera electronics may be seen on their respective plots.

Performance and Duty Cycles of Heater Controlled Components

The thermal behavior of the vernier lines was well within the tolerances that were predicted. The cyclic bands of the vernier line thermostats are 18° to 22°F for line 1 and 19° to 23°F for vernier lines 2 and 3 respectively. Line 1 (Figure 5.1-39) did not reach cycling range but came to steady state at 30°F. Line 3 temperature (Figure 5.1-40) remained several degrees above the thermostatic control point until 45 hours into the mission. At this time, heater cycling started and continued throughout the remainder of the mission. The oscillation in temperature prior to heater cycling is caused by gyro drift checks.

TABLE 5.1-6. SURVEYOR III VERNIER LINE 2 HEATER DUTY CYCLE

Day	Mission Time, hours	Mission C, percent	STV Retest Phase 4C, percent
108	L+21	27	—
108	L+37	31	29

Line 2 started to cycle 2-1/4 hours into the mission and it remained between 19° to 22°F (with the exception of midcourse) during the remainder of the mission (Figure 5.1-35). The duty cycle of line 2 was calculated on the basis of unregulated bus current and is discussed in the following paragraph.

The AMR began to cycle 9 hours into the mission. The duty cycle at 37 hours mission time was 60 percent based on power data. After it started cycling it remained between 14° to 18°F. The duty cycle for the gyro heaters at 4 hours after launch was 38 percent, 21 percent, and 27 percent for the pitch, roll, and yaw gyros respectively.

Sensitivity of High Accuracy Temperature Sensors to Bit Rate

High bit rates affected the readings on the high accuracy gyro temperature sensors. Some typical readings at different bit rates are tabulated in Table 5.1-7.

Auxiliary Battery

The auxiliary battery temperature increase during the high current mode of battery operation was approximately 25°F. This was a nominal temperature profile and resulted in an estimated 79°F auxiliary battery temperature at retro ignition. The equilibrium temperature of the auxiliary battery prior to initiation of high current mode was sufficiently high to make the use of auxiliary battery mode unnecessary.

TABLE 5.1-7. TEMPERATURE SENSORS VERSUS BIT RATE

Bit Rate	FC-46	FC-54	FC-55
1100	182	181	180
550	176	174	175
137.5	173	172	172

Flight Control Sensor Group

The flight control electronics temperatures were considerably lower (approximately 20°F) than observed on previous missions. This effect was due primarily to the electrical redesign of the flight control electronics (i.e., power supply circuit); Surveyor III and temperature predictions reflected this accordingly. Flight control sensor FC-45 readings were approximately 70°F lower than on previous missions, primarily due to the redesign of the flight control electronics and the relocation of the flight sensor from electronics board 6 to board 7.

Vernier Engines

Vernier engine thermal performance was as expected during the transit mission phase. Predicted temperatures for thrust chamber assemblies (TCAs) 1, 2, and 3 were 60°, 85°, and 66°F, respectively. TCAs 1 and 3 reached steady-state equilibrium temperatures of 57° and 67°F, respectively. The steady-state equilibrium temperature of TCAs 1 and 3 were 3° and 1°F below and above their respective nominal predicted values. Because of the multiple gyro drift checks, TCA-2 did not reach a steady-state temperature. However, an extrapolation of the flight data indicates that the steady-state equilibrium temperature for TCA-2 was approximately 82°F, or 3°F lower than the nominal prediction.

The thermal effects of the gyro drift checks on TCA-2 (sensor P-10) temperatures can be seen in Figure 5.1-41. TCA-2 (as indicated by sensor P-10) reached a minimum temperature of 45°F during the gyro drift check initiated at L+ 12H19M and terminated at approximately L+ 14H37M. Thermal analysis has shown that complete shadowing of TCA-2 can result in 76, 56, and 43°F temperature drops at the head end, middle of barrel (flight sensor), and bottom of barrel, respectively. TCA-2 is completely shadowed when the spacecraft sustains a negative yaw maneuver equal to or greater than 2 degrees. However, if the negative yaw remains within the attitude control specification limits, less than or equal to 2 degrees, TCA-2 will receive sufficient insolation from the solar reflector to remain above the lower temperature limit of 0°F.

Calculations have shown that the temperature of the TCA-2 solenoid and shutoff valves can be as low as 20°F during gyro drift check maneuvers. A solenoid valve temperature of 20°F is in violation of the proposed 45°F lower limit for SC-4 and subsequent spacecraft. The limits for these components have been changed accordingly for Mission D to allow SPAC and TFAG to terminate drift checks at the proper time. The thermal effects of the gyro drift checks on TCA-3 are small but finite. TCA-3 experienced a temperature increase of 3°F during the gyro drift check initiated at L+ 12H19M. TCA-3 is partially shadowed by the omnidirectional boom (B) mounting structure. TCA-3 may receive increased insolation as a result of negative yaw or pitch maneuvers. Similarly, TCA-3 receives less insolation as a result of positive pitch and yaw maneuvers.

Thermal data indicate that TCA-1 reached a steady-state equilibrium temperature of 57°F during coast phase I. The temperature of TCA-1 increased to 59°F during coast phase II. The 2°F increase in vernier engine 1 steady-state temperature is attributable to thermal finish (HP4-144, organic white paint) degradation in space.

Transit temperature profiles are presented in Figures 5.1-38, 5.1-41, and 5.1-42 for TCA-1, TCA-2, and TCA-3, respectively.

Helium Tank

Thermal performance of the Surveyor III helium tank was as expected. Thermal data indicate that the helium tank (temperature sensor P-17)

reached a steady-state temperature at 72°F during coast phase I. The predicted temperature for the helium tank thermal sensor was 75°F. The helium tank temperature increased to 74°F during coast phase II. The 2°F increase in helium tank temperature is attributable to thermal finish (HP4-135, inorganic white) degradation. Calculations indicate that increasing the inorganic white paint nominal solar absorptance value (0.18 ± 0.02) by 0.01 results in a 2°F increase in tank bulk temperature. Since the local temperature perturbation would be greater than the bulk temperature perturbation, thermal analyses indicates that the degradation exhibited by the helium tank is small. The exact degree of thermal finish degradation cannot be accurately determined from the data because of the small temperature perturbation and the complex nature of the analytical model.

Vernier Propulsion Propellant Tanks

The vernier engine propellant tank temperatures during the launch-to-midcourse phase of the mission was in agreement with preflight temperature predictions. The maximum temperature deviation between actual flight data and predicted tank temperature was 4 degrees. However, after midcourse, the flight temperature data diverged from the predicted temperature profiles as shown in Figures 5.1-36, 5.1-37, and 5.1-44 through 5.1-47. The actual tank temperatures were all higher than the nominal prediction. The maximum deviation between predicted and actual tank temperatures occurred on oxidizer tank 3 where the actual temperature went outside of the predicted upper bound and had a maximum difference from the predicted nominal temperature of 18 degrees. The discrepancy between actual and predicted tank temperatures may be attributed to the manner in which the predictions were obtained.

The preflight tank temperature predictions were obtained from the use of spacecraft solar thermal-vacuum (STV) test results. The nominal predicted temperature profile was obtained by averaging STV test data when the vehicle was exposed to the following solar intensity levels: 1) high sun (112 percent intensity) and 2) low sun (87 percent solar intensity). The upper and lower predicted temperature limits of 15 degrees from the nominal were obtained by taking into account variations in thermal performance of the tank superinsulation blanket. Apparently the use of STV test data to predict initial cooldown from launch to midcourse is justifiable based on a comparison of actual and predicted results. The reason for the agreement is that the initial temperature distribution of the spacecraft at launch and in STV are approximately the same. However, at midcourse and immediately after midcourse, thermal phenomena occur, making invalid the use of STV data to predict flight temperature response since STV thermal simulation of a midcourse maneuver is nonexistent.

The temperature of the tank sensor at midcourse increases due to either a combination of two mechanisms or the occurrence of each one separately. The two mechanisms are: 1) propellant slash creating a mixing of warmer propellant with colder propellant originally located near the bottom of tanks and 2) propellant stratification, where the temperature of the propellant increases from the bottom of the tank toward the top; therefore,

upon ignition, the depleted cold propellant is replaced by the warmer propellant. The adjacent structure around the tanks, however, are less sensitive to the midcourse maneuver and therefore continue to cool. Immediately after midcourse the tank temperature profile descends at a steeper rate than at launch as a result of the larger potential between tank temperature and adjacent structures. If the profile is continued, the effect of midcourse should dampen out and the profile should converge to a hypothetical curve obtained if midcourse was neglected and the temperature curve prior to midcourse was extrapolated. This is better illustrated by comparing actual tank temperature data obtained from Surveyor I, SC-2, and Surveyor III as shown in Figures 5.1-7 through 5.1-12.

As seen in Figures 5.1-7 through 5.1-12, the tank temperatures for the various spacecraft were quite similar. The maximum tank temperature deviation was 10 degrees and occurred on oxidizer tank 3.

Because of the close agreement between tank temperatures for the various spacecraft, the use of existing flight temperature data for future spacecraft tank temperature predictions appears valid with STV test data used to adjust for differences in tank thermal performance between spacecraft.

5.1.4.5 Terminal Mission Phase (Retro-57M to Touchdown)

Vernier Engines

TCA-2 cooled as expected during the terminal mission phase; however, the thermal behavior of TCA-1 and TCA-3 was contrary to predictions. Predictions indicated that TCA-1 would always be shadowed by the spacecraft from direct insolation subsequent to the completion of the terminal attitude maneuvers. Thermal data indicate that TCA-1 was not completely shadowed during the terminal maneuver; in fact, TCA-1 was always partially illuminated. The temperature of TCA-1 increased throughout the terminal attitude maneuvers (Figure 5.1-13). Subsequent to the completion of the roll maneuver, the temperature of TCA-1 decreased; however, STV test data and analytical studies indicate that the rate of decrease was substantially less than that exhibited by a completely shadowed TCA.

The temperature of TCA-3 was expected to decrease or remain constant during the terminal maneuver. TCA-3 exhibited a 21°F temperature increase. Thermal analysis assumed that TCA-3 would be predominantly shadowed by the helium tank. Thermal data indicate TCA-3 was not shadowed by the helium tank during the terminal maneuver.

Preflight predictions indicated that the most probable TCA solenoid valve (SOV) temperatures at terminal ignition would be 75, 90, and 90°F for TCA-1, TCA-2 and TCA-3, respectively. Postflight data evaluations indicate that the TCA SOV temperatures were approximately 85, 85, and 110°F for TCA-1, TCA-2, and TCA-3, respectively.

Preflight analysis indicated that SOV temperatures could range from 100 to 165°F at terminal shutdown. SOV temperatures at terminal shutdown

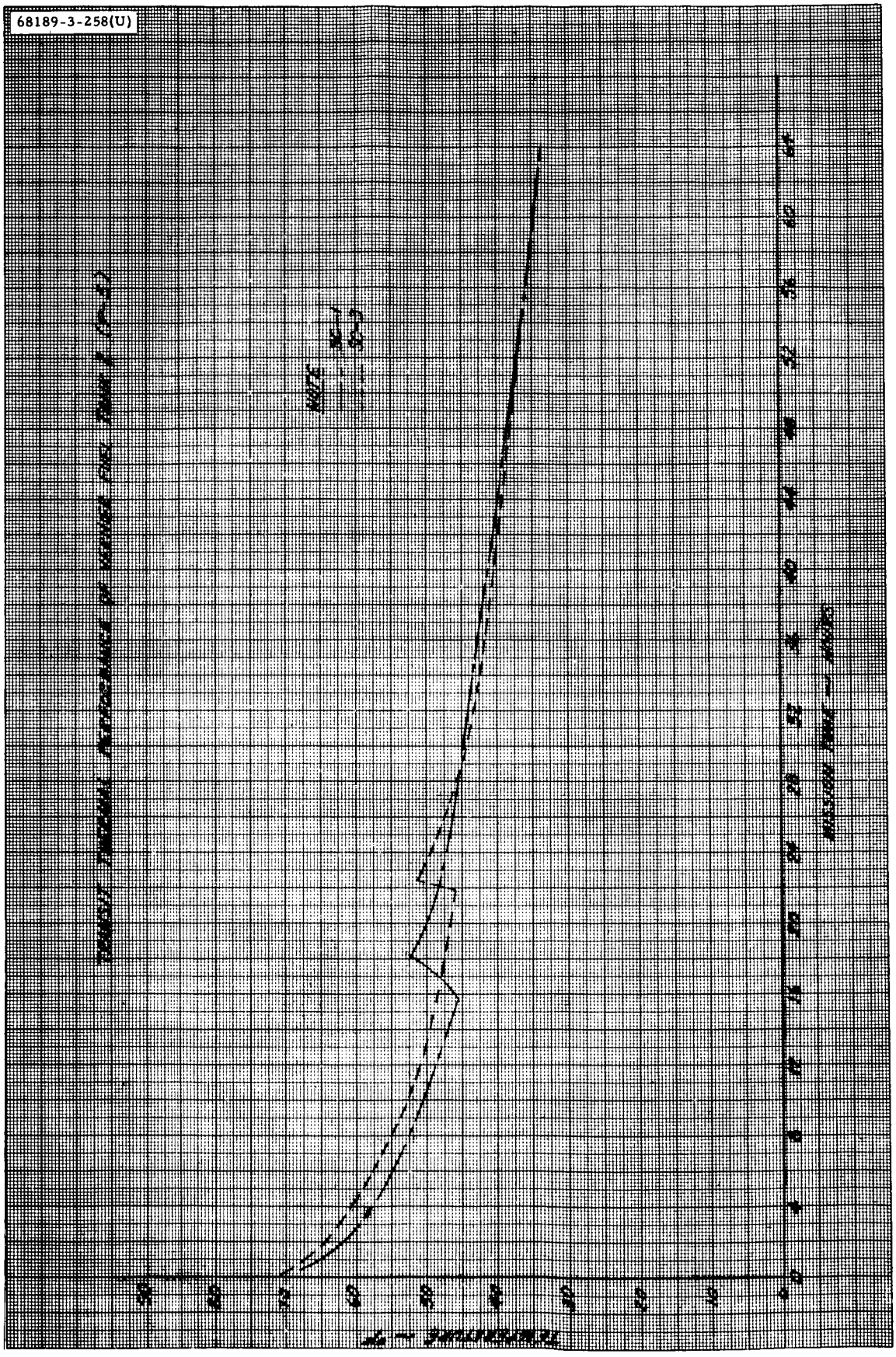

Figure 5.1-7. Transit Thermal Performance of Vernier Fuel Tank 2 (P-5)

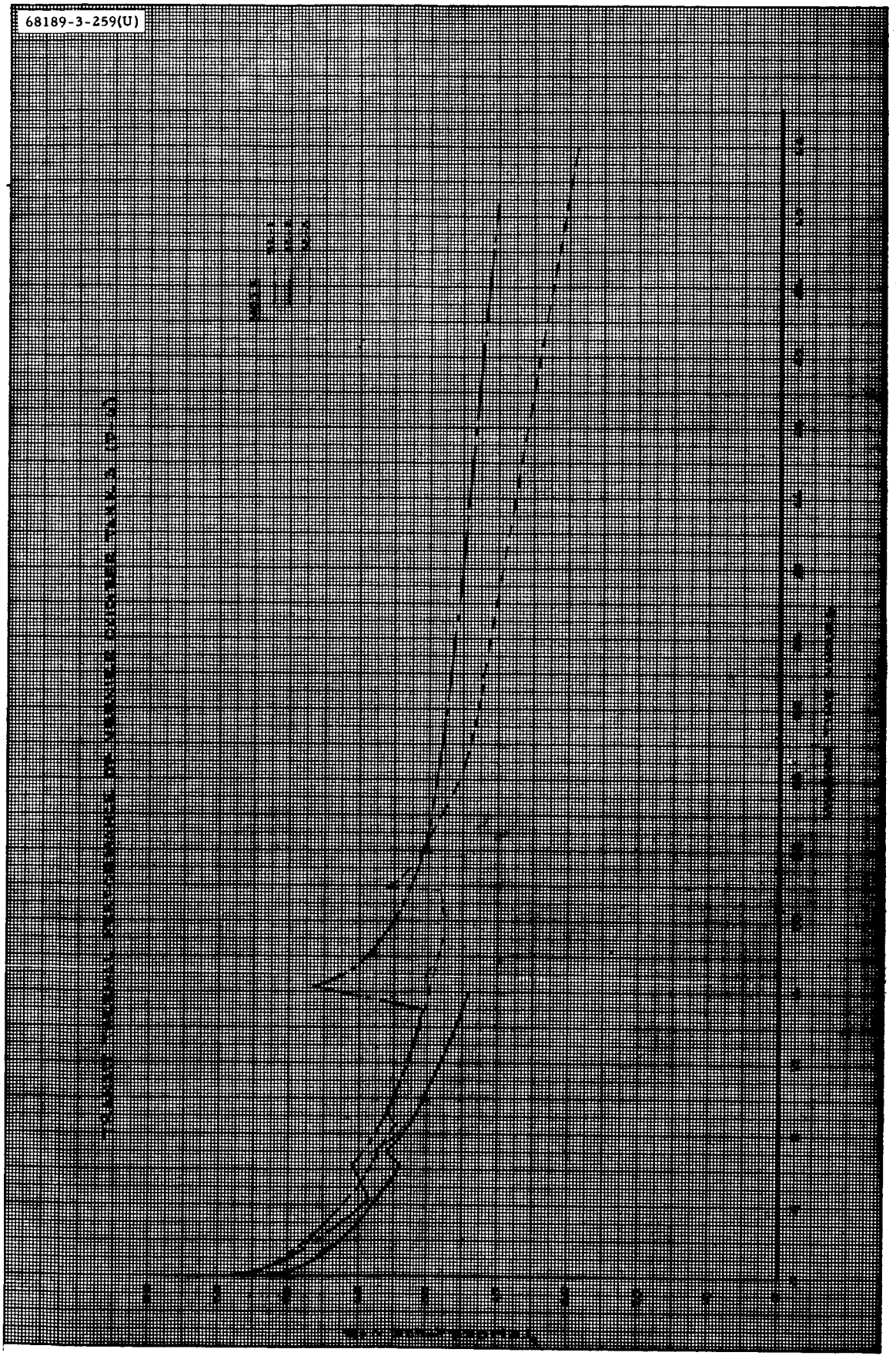

Figure 5.1-8. Transit Thermal Performance of Vernier Oxidizer Tank 3 (P-6)

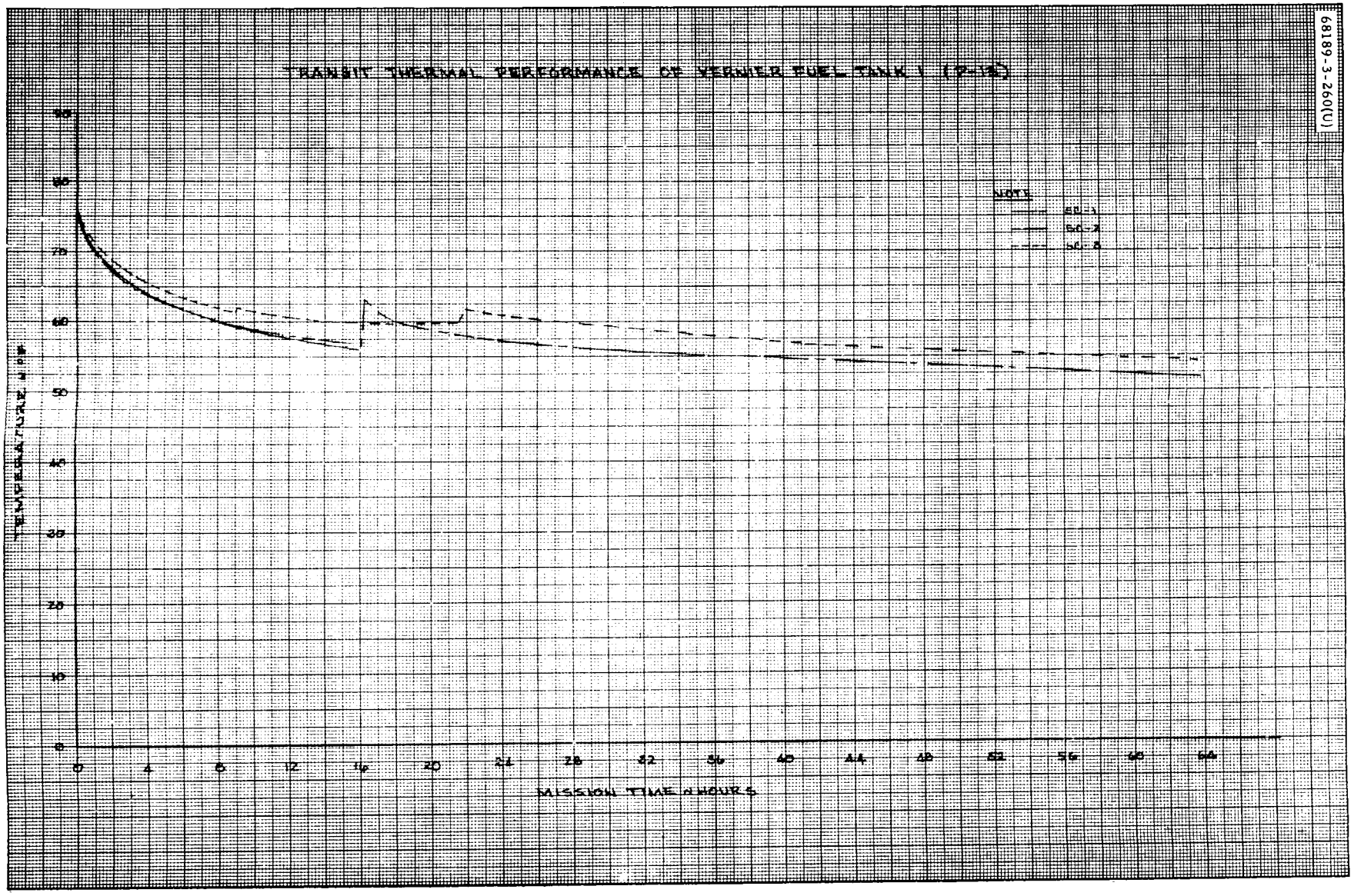

Figure 5.1-9. Transit Thermal Performance of Vernier Fuel Tank 1 (P-13)

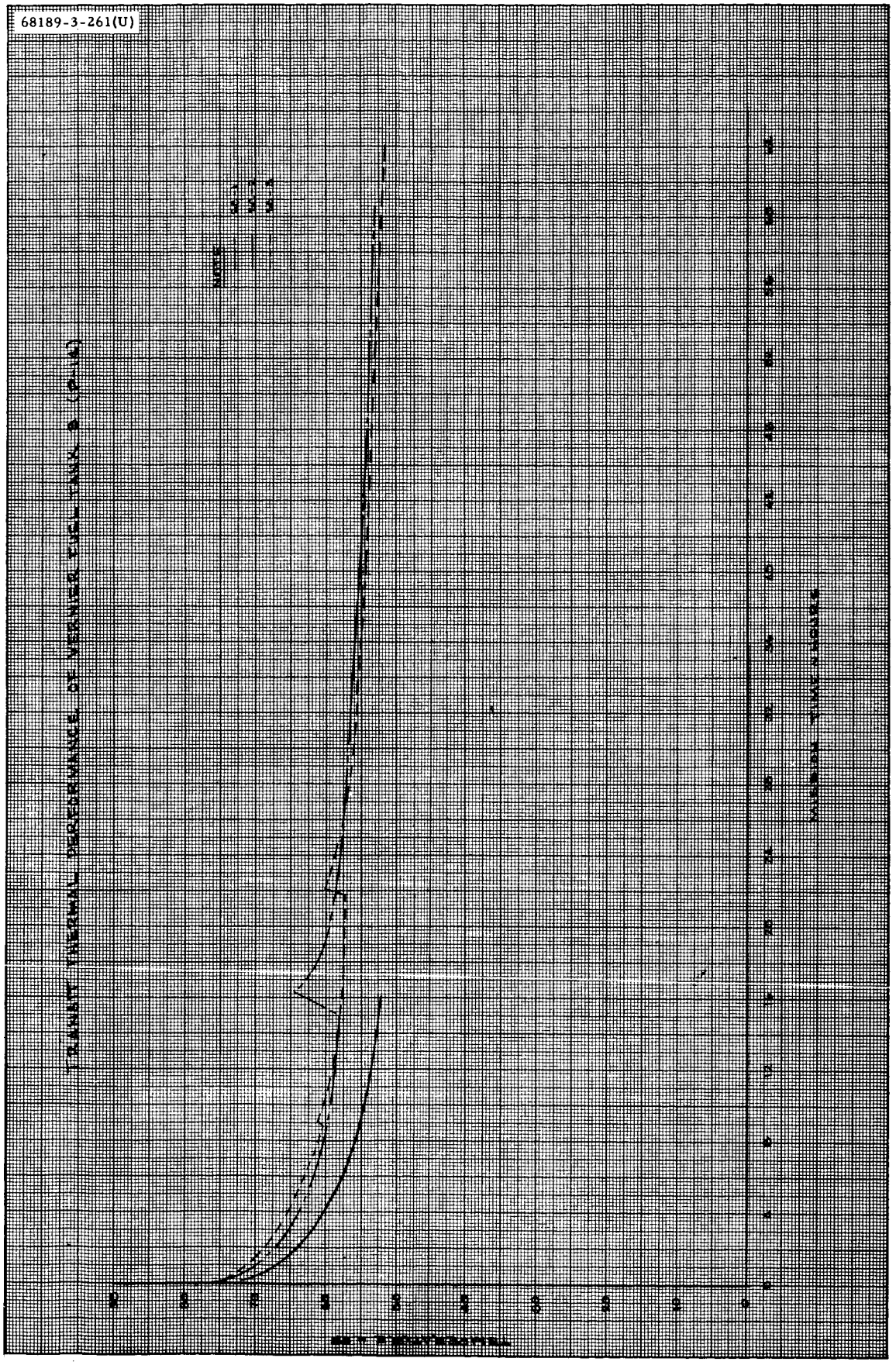

Figure 5.1-10. Transit Thermal Performance of Vernier Fuel Tank 3 (P-14)

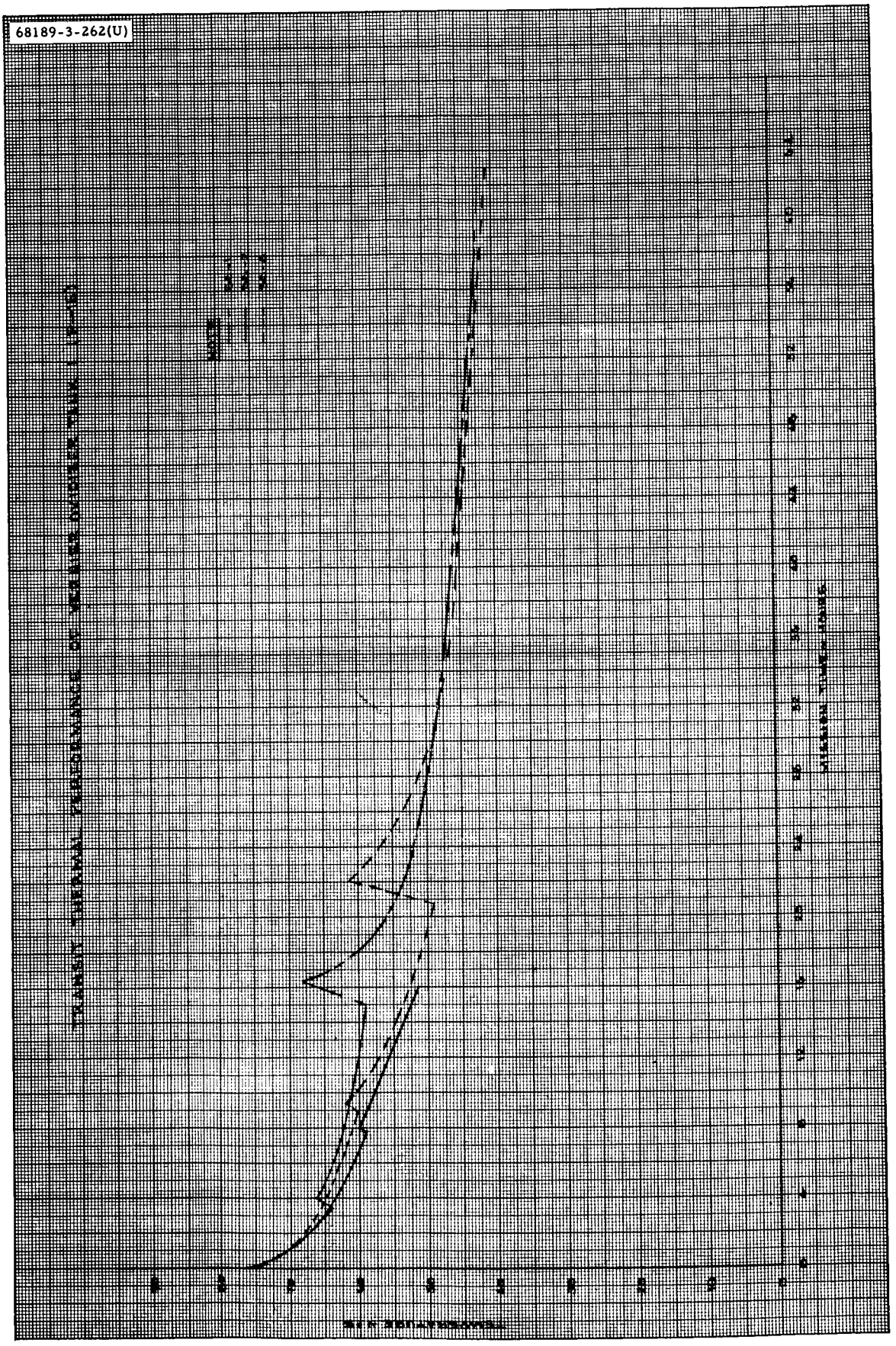

Figure 5.1-11. Transit Thermal Performance of Vernier Oxidizer Tank 1 (P-15)

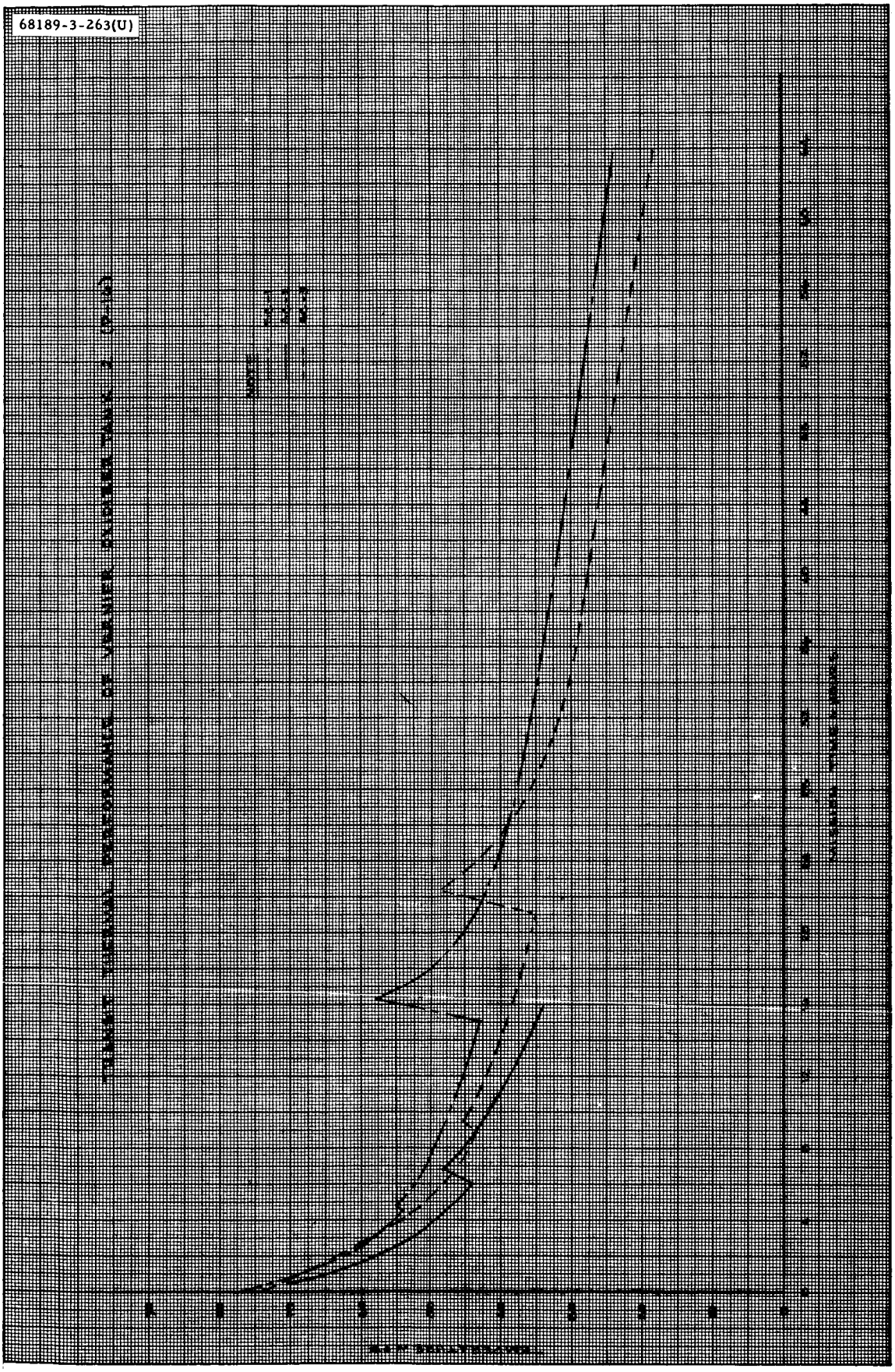

Figure 5.1-12. Transit Thermal Performance of Vernier Oxidizer Tank 2 (P-16)

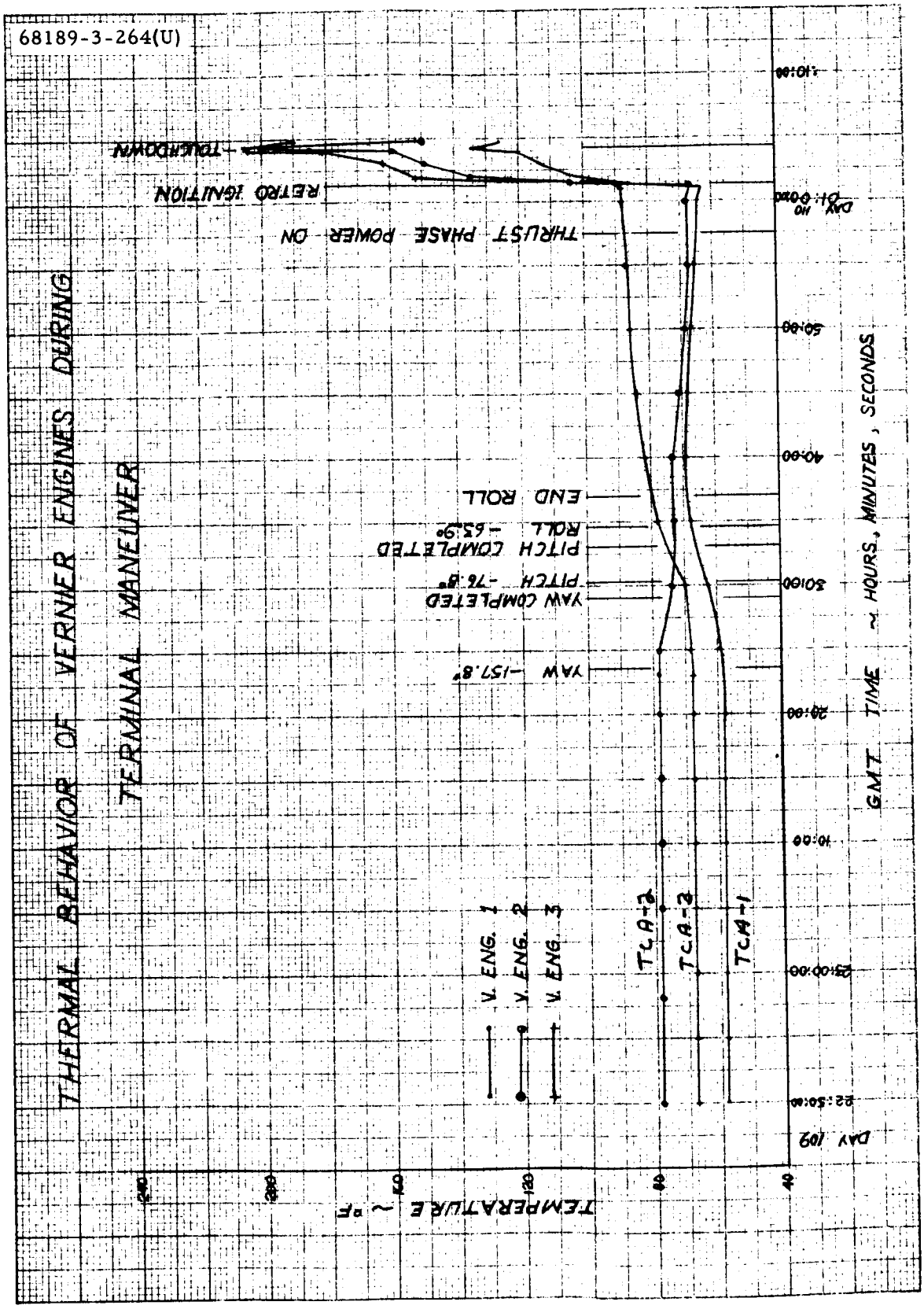

Figure 5.1-13. Thermal Behavior of Vernier Engines During Terminal Maneuver

are largely dependent on fuel supply temperatures, terminal burn duration, and a constant thermal parameter associated with each engine. Predicted SOV temperatures are tabulated in Table 5.1-8 as a function of fuel supply temperature.

TABLE 5.1-8. SURVEYOR III TCA SOLENOID VALVE TEMPERATURE PREDICTIONS

Fuel Supply	Temperature, °F		
	50	60	70
TCA-1 SOV	103	113	123
TCA-2 SOV	138	148	158
TCA-3 SOV	126	136	146

Flight data indicate that TCA-1 and TCA-3 had fuel supply temperatures of 60 and 55°F, respectively at terminal ignition. Therefore, predictions would indicate SOV temperatures of 113 and 131°F for vernier engines 1 and 3. Flight data are not available on TCA-2 fuel supply temperature; however, experience would indicate a temperature of approximately 50°F or a TCA-2 SOV temperature of 138°F.

Other Thermal Systems

Thermal performance in the terminal phase was nominal. The terminal maneuver was initiated (with the approval of SPAC) at R-38M which was 5 minutes sooner than specified in the transit sequence. No excessive cooldown or warmup of any unit occurred for this off-sun maneuver. The temperature of the following units increased during the maneuver: flight control electronics (FC-45), nitrogen tank (FC-48), planar array (M-8), retro nozzle (P-22), AMR dish (R-27), upper spaceframe near leg 1 (V-28), retro bolt 2 (V-38), crushable block (V-44), and compartment A radiator 2. The temperatures of the following units decreased during terminal maneuver: solar panel (EP-12), Canopus sensor (FC-47), attitude jet (FC-70), helium tank (P-17), SDC (R-9), upper spaceframe at leg 1 (V-27), legplate 2 (V-31), shock absorber 2 (V-32), compartment A radiator 8 (V-47), and compartment B radiators 1, 4, and 5 (V-45, V-24, V-46). All the compartment radiators are shadowed in the maneuver. The fact that all compartment B radiators (V-45, V-24, V-46), and compartment A radiator 2 (V-25) decrease in temperature indicates that the radiators are more sensitive to solar illumination than to the high power transmitter dissipation. By contrast, compartment A radiator 8 (V-47) is normally in the shadow of the solar panel during transit. As a result the temperature of this radiator increases during the terminal phase.

Temperatures of the electronics in Compartment A and B, the thermal trays, and main battery were nominal at touchdown as shown in Table 5.1-9. The time indicated is the last time for which data are available.

TABLE 5.1-9. SELECTED TEMPERATURES DURING TERMINAL DESCENT(*)

Sensor	Unit	Time, GMT	Temperature, °F
D-13	Transmitter A	109:23:46	66
D-14	Transmitter B	110:00:04	117
EP-8	Main battery	110:00:04	75
EP-13	Boost regulator	110:00:04	113
EP-34	Battery charge regulator	109:23:46	82
R-8	Klystron power supply modulator	**	18/13/85
V-15	Compartment A upper tray	109:23:40	78
V-16	Compartment A lower tray	109:23:40	73
V-21	Compartment B upper tray	109:23:40	79
V-22	Compartment B lower tray	109:23:40	84

*Touchdown 1 occurred at 110:00:04:18

**Indicates temperatures at steady state/minimum in maneuver/touchdown

The soil mechanics and surface sampler (SM/SS) auxiliary electronics temperature, whose potential cooldown in the terminal maneuver was of some concern, showed negligible temperature change.

5.1.5 LUNAR DAY THERMAL PERFORMANCE

The thermal response of the spacecraft during the lunar day was nominal and component temperature constraints were met with relative ease. The major difficulty encountered by the thermal subsystem was interpretation of the invalid data resulting from the spacecraft signal processing failure. All plots presented have been corrected for the telemetry system erroneous data problem according to corrections devised by the Signal Processing group.

5.1.5.1 Post Touchdown

All temperature control heaters (except gyro heaters) were command off just prior to retro ignition to eliminate the current fluctuations caused by these heaters when they cycle. The temperature data immediately following touchdown were erroneous; consequently, the spacecraft temperature status was unknown for several hours. The TV camera heaters and the SM/SS heater were not again commanded on until touchdown plus 2 hours, 24 minutes. After correcting and reviewing the 17.2 bps data, it was learned that the TV camera may have been operated at temperatures below the specified operating range. The SM/SS electronics may have reached temperatures as low as -94°F before the heater was commanded on. Although the SM/SS appears to have exceeded its lower survival limit, it performed within specifications when operated during the lunar day.

The post-touchdown data indicate that one of the thermal switches on compartment B (switch 1) opened when the thermal tray reached 0°F; however, all other instrumented switches on both compartments A and B were stuck. Since the switches were stuck closed, the temperatures on compartments A and B reached a minimum of 20 and 0°F, respectively, at touchdown plus 15 hours, as shown in Figures 5.1-92 and 5.1-93. The main battery reached a minimum temperature of 38°F during the post-touchdown period, as indicated in Figure 5.1-90.

5.1.5.2 Compartment System

The main battery was approaching its upper operational temperature limit toward the end of day 117 (8 days after touchdown). The solar panel was repositioned to shade compartment A and the TV at 2300 GMT, day 117. Subsequently, the temperature trend of compartment A was reversed and temperatures decreased as desired as shown in Figures 5.1-89 through 5.1-93 and 5.1-95.

Following the lunar sunset, the spacecraft was operated until the compartment B upper thermal tray reached a minimum of 0°F. This occurred approximately 3 hours after the end of sunset on the crater rim. Thermal switch on compartment B opened when the upper thermal tray reached approximately 20°F (Figures 5.1-93 and 5.1-94). Subsequent analysis has indicated that a maximum of two and three thermal switches on compartments A and B, respectively, were open at the time the spacecraft was shut down. The upper thermal tray temperatures on compartments A and B were 10 and 0°F, respectively, and the main battery temperature was 37°F at shutdown (see Figures 5.1-90, 5.1-91, and 5.1-93).

5.1.5.3 Solar Panel and Planar Array

The solar panel and planar array temperature profile on the lunar surface for the first 24 hours was correlated with the antenna and solar panel positioner (ASPP) thermal model. The results of the thermal model have been plotted against actual solar panel and planar array flight data as shown in Figure 5.1-14. Agreement between actual and predicted

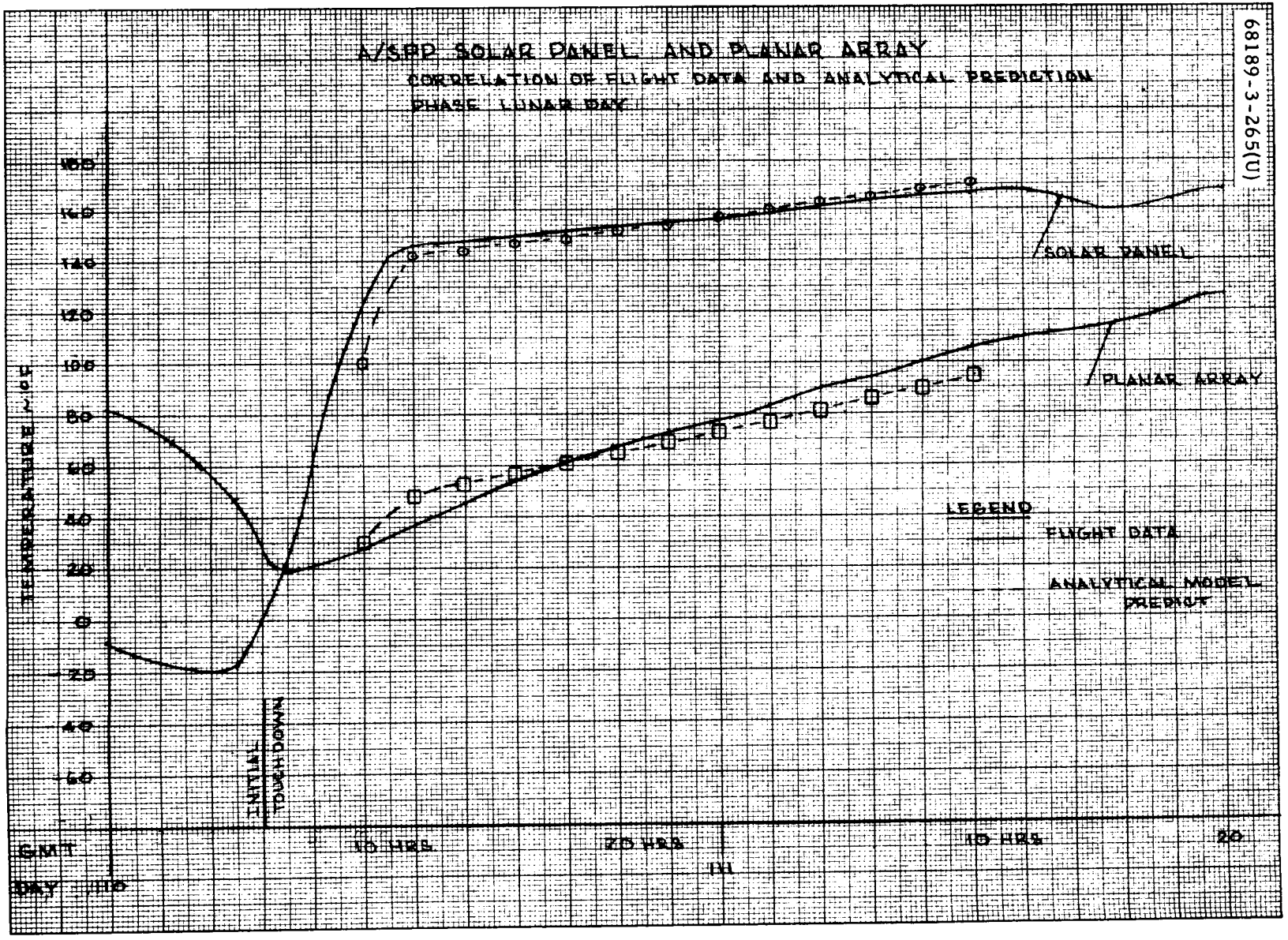

Figure 5.1-14. A/SPP Solar Panel and Planar Array – Correlation of Flight Data and Analytical Prediction Phase Lunar Day

temperature response is good. The maximum temperature deviation for the solar panel between predicted and actual is 20 degrees, which is probably due to slightly incorrect initial solar heat load. The maximum deviation for the planar array is 10 degrees and is probably a result of slightly incorrect solar heat loads.

The analytical model used to predict solar panel and planar array temperatures is the same one used for earth orbit correlations, except that the environmental boundary conditions have been changed.

Since the solar panel and planar array positions change with time as well as the solar elevation angle, the difficulty in determining heat loads caused the correlation to be continued for only the first 24 hours after touchdown. The spacecraft temperatures used for conduction and radiation to the ASPP thermal model are actual Surveyor III flight temperature data for the various spacecraft components.

The temperature profile of the planar array and solar panel for the entire lunar day are shown in Figure 5.1-96. A phenomenon which occurred during the lunar day is the earth eclipse. The eclipse occurred on GMT day 110 at 0948 and, as a result, the solar panel and planar array dropped in temperature (Figure 5.1-96). During this period the solar panel dropped from 203 to -185°F in a time period of 2 hours, 6 minutes. The planar array during this period dropped from 202 to -142°F. The high cooldown rates of the solar panel and solar array indicate the sensitivity of these components to changing environments.

5.1.5.4 Surveyor Liftoff and Translation on the Lunar Surface

The liftoff and translation of SC-3 from the lunar surface after its landing was planned but was not exercised. The thermal requirement for the liftoff and translation was analyzed and the optimum time and operational procedure were recommended. Although the planned liftoff and translation did not take place, much useful data were obtained which will provide a firmer basis for future liftoff activities. The purpose of this section is to present the pertinent thermal data for the liftoff and to analyze the data for future application.

The thermally critical components for liftoff are the vernier engines, flight control electronics, helium tank, roll actuator, and the shock absorbers. The temperature responses for these components are given in Figures 5.1-98 and 5.1-104. No direct comparison could be made during real time between the actual data and the predicted values because the intended roll orientation (-59 degrees) was different from the actual (-44 degrees). However, the actual temperature data were examined afterward based on the actual roll orientation, the actual shadow patterns, and the analytical models used for the predictions. The actual temperature data agreed with the analytical values except those of the helium tank as shown in Table 5.1-10. It can be seen from the temperature data that liftoff would be limited to the time prior to the sun elevation angle of 31 degrees. When vernier engine 2 had reached the limiting temperature of 220°F, the liftoff time interval is

TABLE 5.1-10. COMPARISON OF ACTUAL AND ANALYTICAL TEMPERATURE RESULTS FOR SURVEYOR III LUNAR LIFTOFF AND TRANSLATION

Unit	Sun Elevation			
	40 degrees		90 degrees	
	Actual, °F	Postflight Evaluation, °F	Actual, °F	Postflight Evaluation, °F
Engine 1	54	64	213	220
Engine 2	240	235	242	250
Engine 3	120	130	208	220
Flight control electronics	100	110	175	180
Helium tank	145	110	160	150
Roll actuator	45	44	200	200

shorter than the predicted solar elevation angle of 30 degrees and it is due primarily to the level of accuracy of the analytical models. With this relatively short liftoff time interval, it would be rather difficult to have the opportunity for the liftoff from the thermal consideration.

The generalized thermal responses for the liftoff components have been refined using Surveyor III data and are given in Figures 5.1-98 through 5.1-104. With these generalized thermal responses and the specific shadow patterns, temperature responses for future liftoff application can be obtained readily. Once the landed orientation of a spacecraft is known, the shadow patterns can be obtained from an available computer program. By knowing the temperature responses of the various components, the optimum liftoff time interval can be recommended.

Based on the actual temperature data from Surveyor I and III, together with the analytical work performed, it appears that the limiting components to liftoff are the vernier engines. Although the landed orientation is very important in governing the temperature responses of each vernier engine, its effect on liftoff time interval does not appear to be significant. Regardless of the roll orientation, one or all the vernier engines will reach the limiting operational temperature of 220°F at the time interval of 30 to 45 degrees sun elevation angle. It is expected that the liftoff time interval will be extended beyond the sun elevation angle of 45 degrees unless some changes are made such as increasing the operational temperature limit for the engines. It is recommended that the operational temperature limits for the engines be investigated. Any extension beyond 220°F will provide a longer liftoff time interval.

5.1.5.5 Determination of Lunar Surface Temperature

Lunar surface temperatures based on an emissivity value of the moon of 1.00 were calculated from the thermal data obtained from Surveyor III on the moon. Temperature sensors located on the outboard sides of compartments A and B were used to arrive at the lunar surface temperature. Using the identical method of calculation as with Surveyor I data, the computed lunar surface temperatures based on Surveyor III data are more scattered than Surveyor I. Due to the fact that Surveyor III did not land on a level plane on the lunar surface, the view factor from the sensor to the lunar surface is much more complicated to compute. Since the lunar surface temperature determination is a very strong function of this view factor, any uncertainty in it will cause scatter in the results. Keeping this in mind, the lunar surface temperatures were calculated based on several reasonable view factor values. The results of the lunar surface temperatures are given in Figure 5.1-115 using the most suitable view factors.

The data used for the determination are presented in Figure 5.1-112 through 5.1-115. These are the outboard sensor temperatures, the angle between the normal to the outboard sides and the sun vector, and the shadow patterns. The view factors from the sensor to the lunar surface used in the calculation are 0.32, 0.35, 0.375 and 0.40. The value of 0.32 is for the spacecraft landed on a level plane. Reviewing the Surveyor I lunar surface determination study and other analytical work, Surveyor III spacecraft must be landed in a position which gives a view factor greater than 0.32. In addition, the view factors from the two sensors to the lunar surface are not the same, which is a good indication that Surveyor III did not land on a level plane or that it was tilted with a level plane. Effort is continuing to obtain the particular view factors and to determine the lunar surface by using more accurate view factors.

5.1.5.6 Comparison of Surveyor I and Surveyor III Lunar Day Temperatures

A preliminary comparison of Surveyor I and Surveyor III lunar day temperatures indicates that there are no appreciable differences between these spacecraft. The data do not indicate any large thermal environment differences between the two landing sites. Surveyor III camera electronics was within 5°F of the Surveyor I electronics temperature during lunar noon when the camera was shaded on both spacecraft. This indicates that the thermal environment was the same in each case, since any solar absorptance differences between the two units is eliminated when the shaded period is used for comparison. Maximum lunar day temperatures for Surveyor I and Surveyor III are compared in Table 5.1-3.

5.1.6 REFERENCES

1. "Histories of Atlas/Centaur/Surveyor Heat Flux Parameter After Nose Fairing Jettison – Parking Orbit Ascent," GDC-BTD66-051, 21 April 1966.

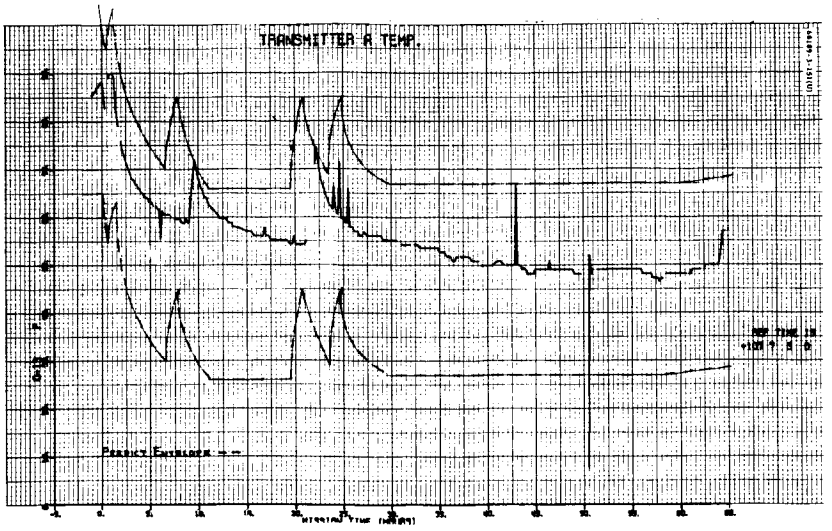

Figure 5.1-15. Transmitter A Temperature

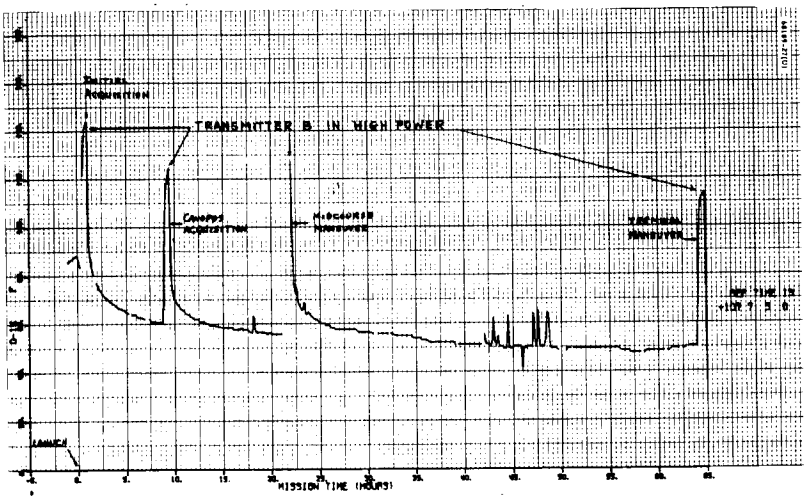

Figure 5.1-16. Transmitter B Temperature

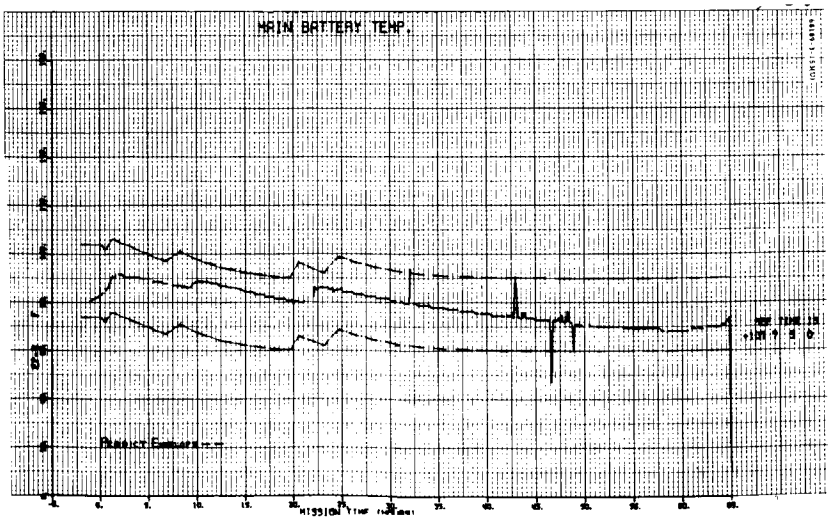

Figure 5.1-17. Main Battery Temperature

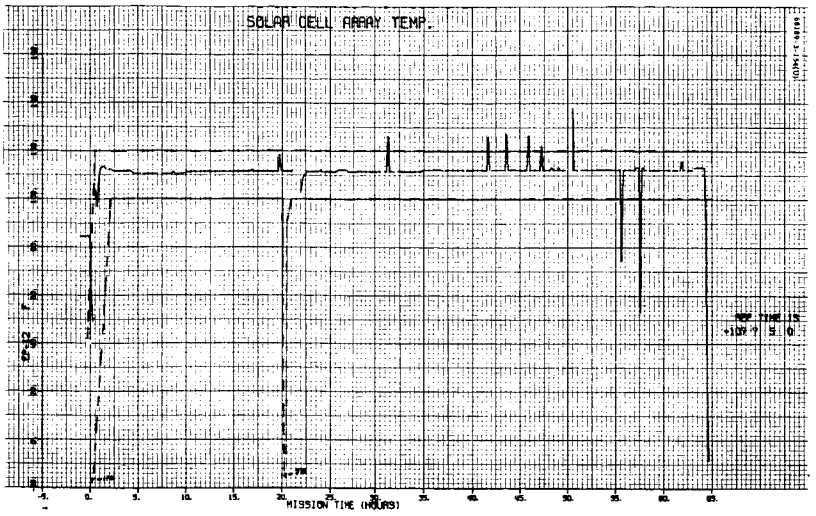

Figure 5.1-18. Solar Cell Array Temperature

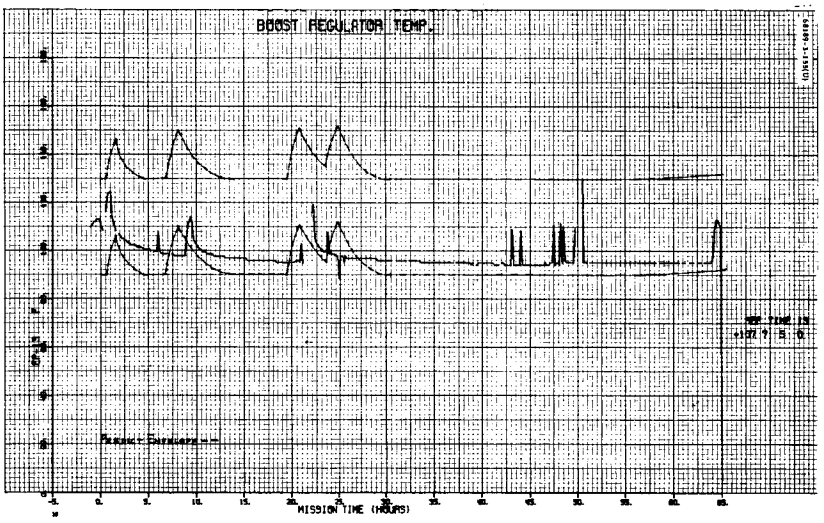

Figure 5.1-19. Boost Regulator Temperature

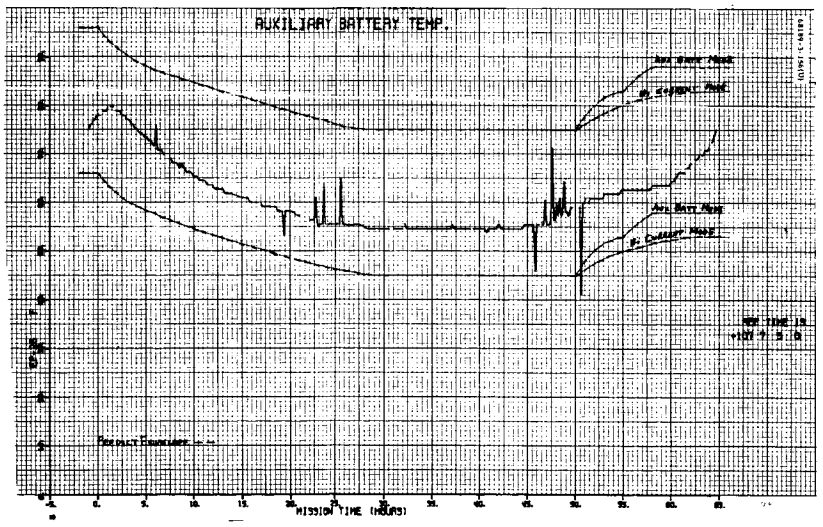

Figure 5.1-20. Auxiliary Battery Temperature

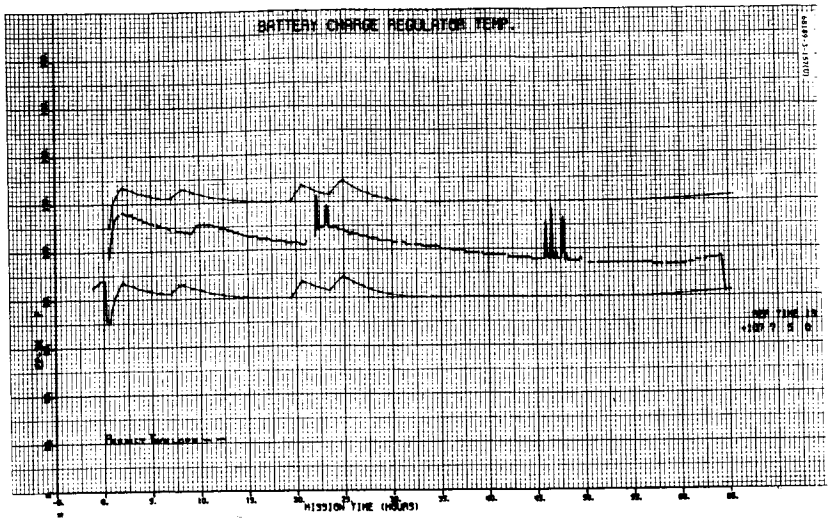

Figure 5.1-21. Battery Charge Regulator Temperature

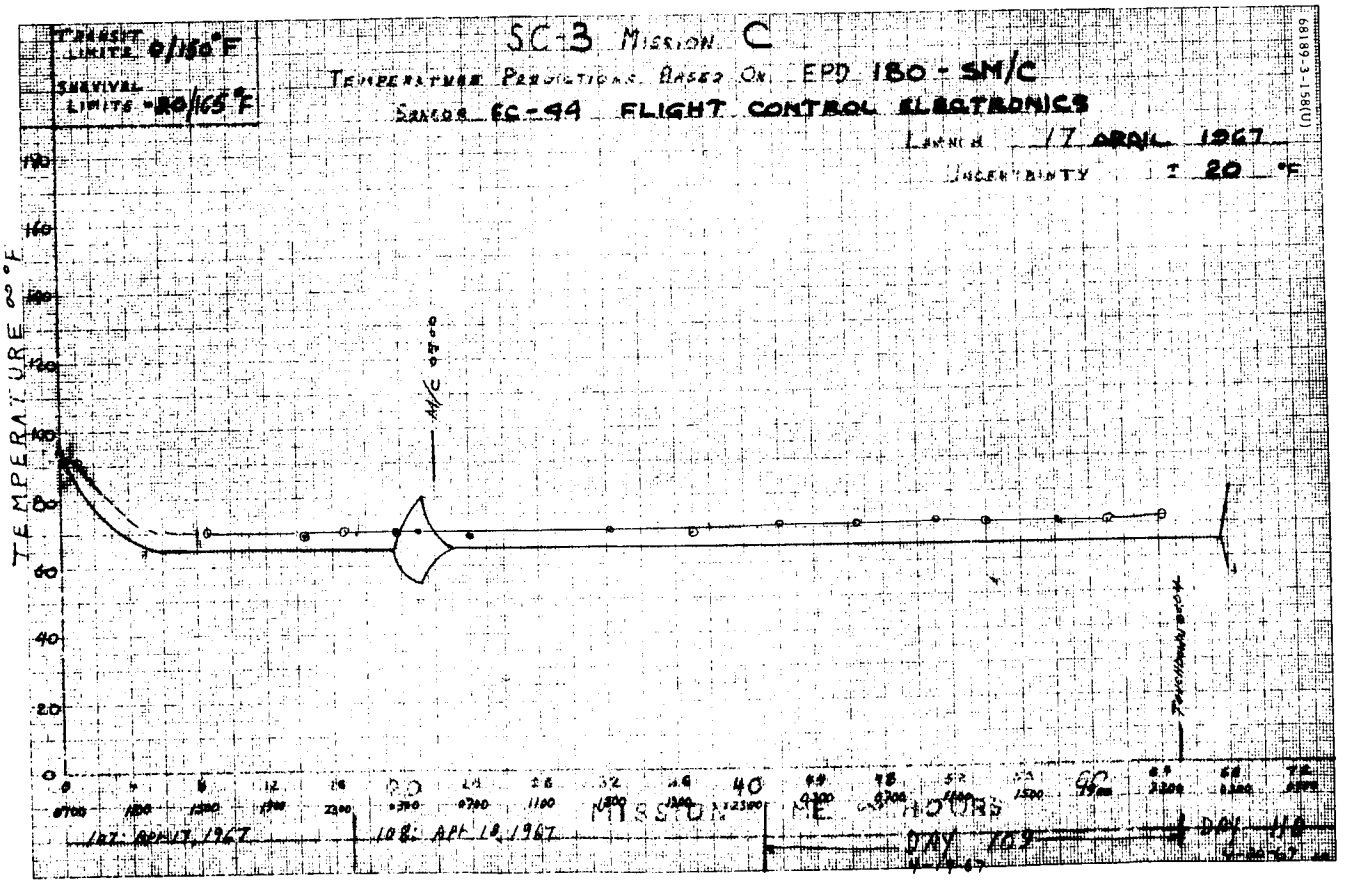

Figure 5.1-22. Sensor FC-44, Flight Control Electronics

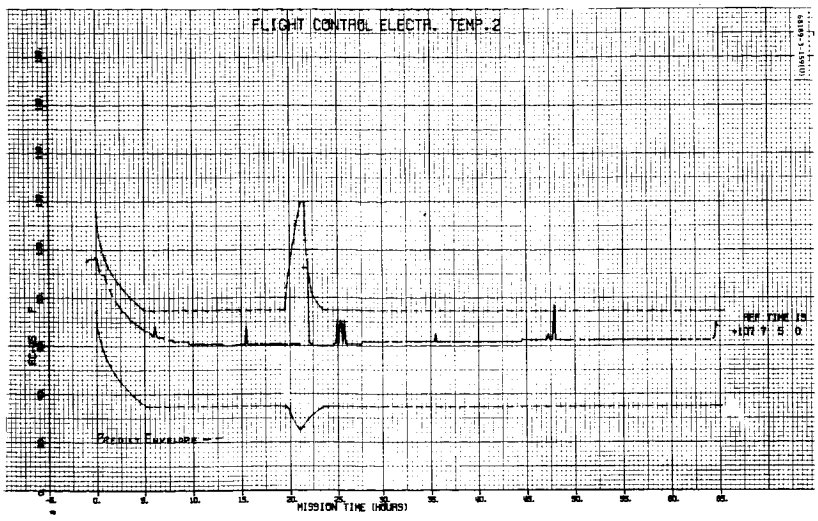

Figure 5.1-23. Flight Control Electronics Temperature

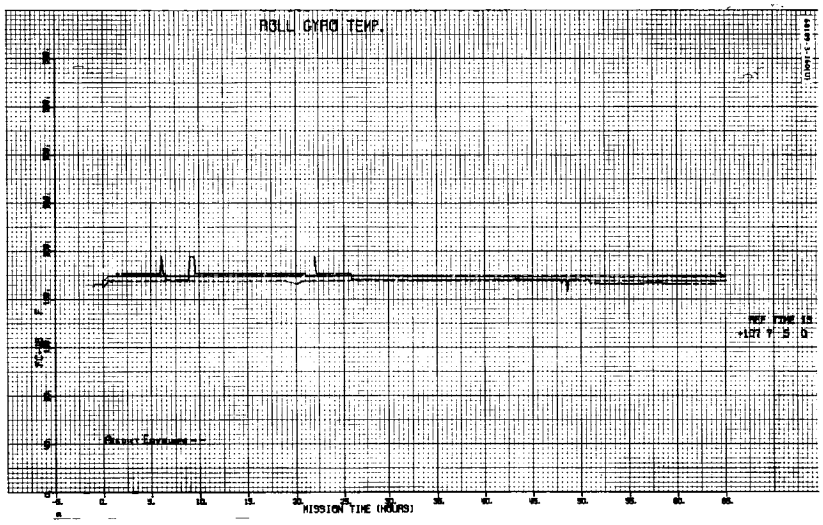

Figure 5.1-24. Roll Gyro Temperature

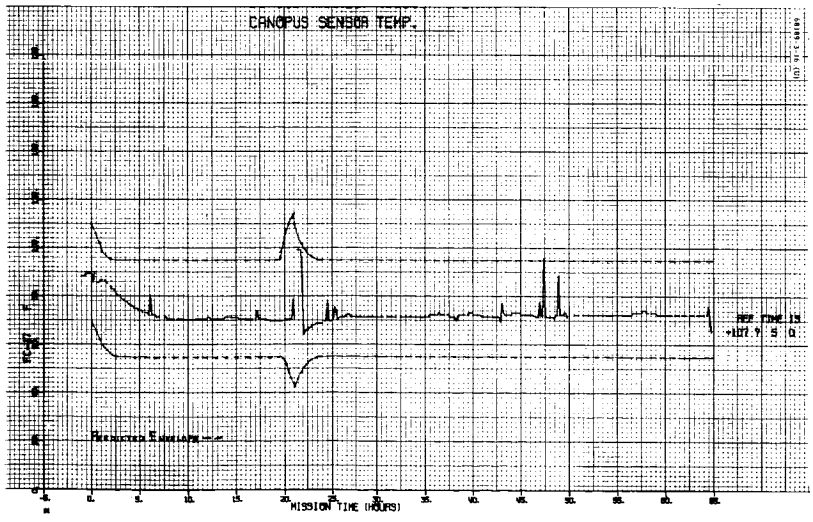

Figure 5.1-25. Canopus Sensor Temperature

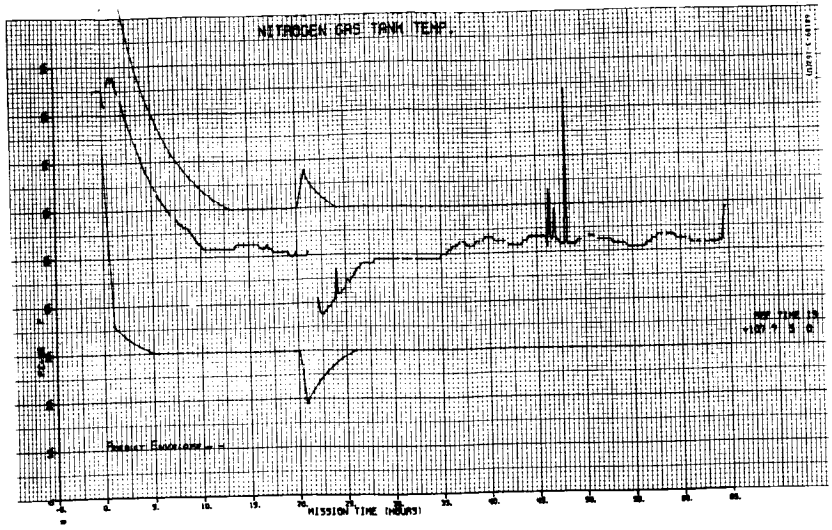

Figure 5.1-26. Nitrogen Gas Tank Temperature

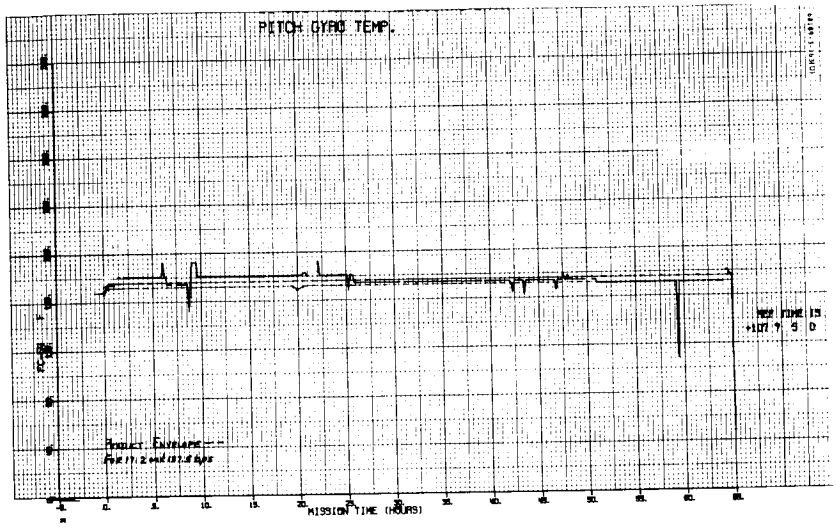

Figure 5.1-27. Pitch Gyro Temperature

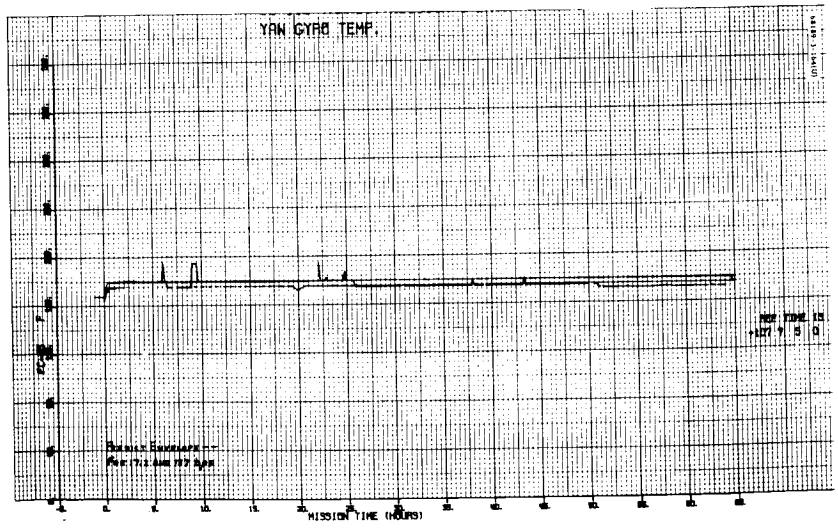

Figure 5.1-28. Yaw Gyro Temperature

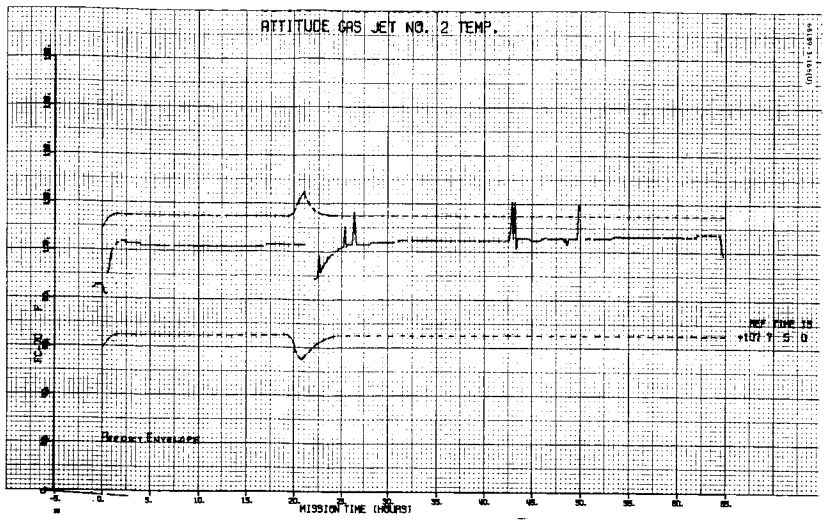

Figure 5.1-29. Attitude Gas Jet 2 Temperature

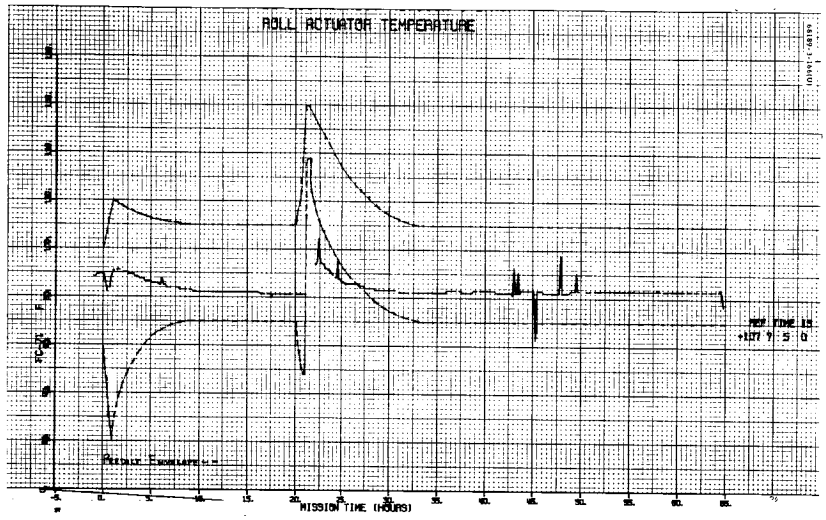

Figure 5.1-30. Roll Actuator Temperature

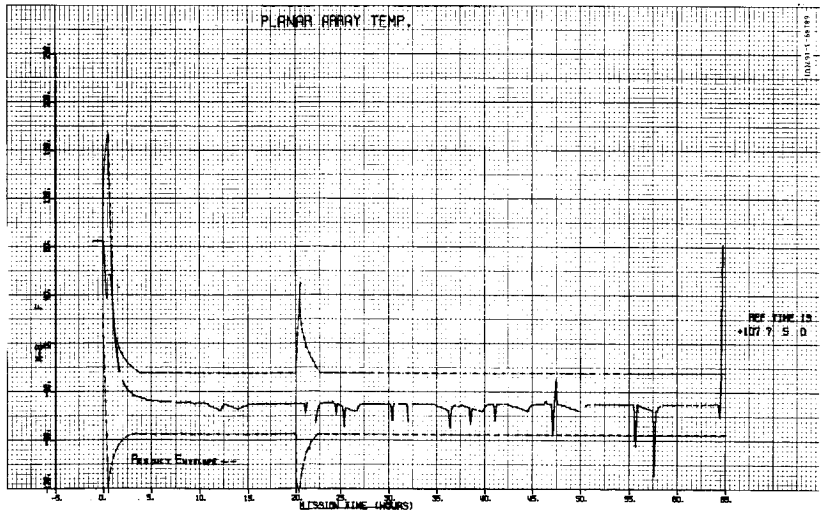

Figure 5.1-31. Planar Array Temperature

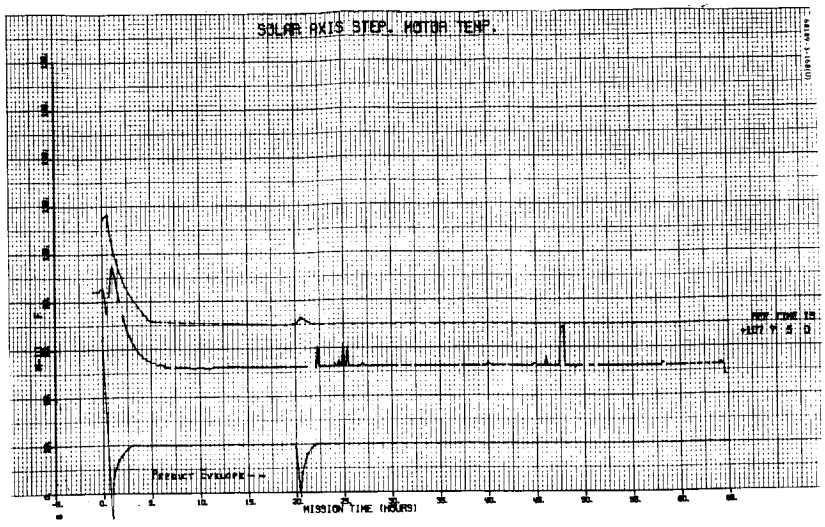

Figure 5.1-32. Solar Axis Stepping Motor Temperature

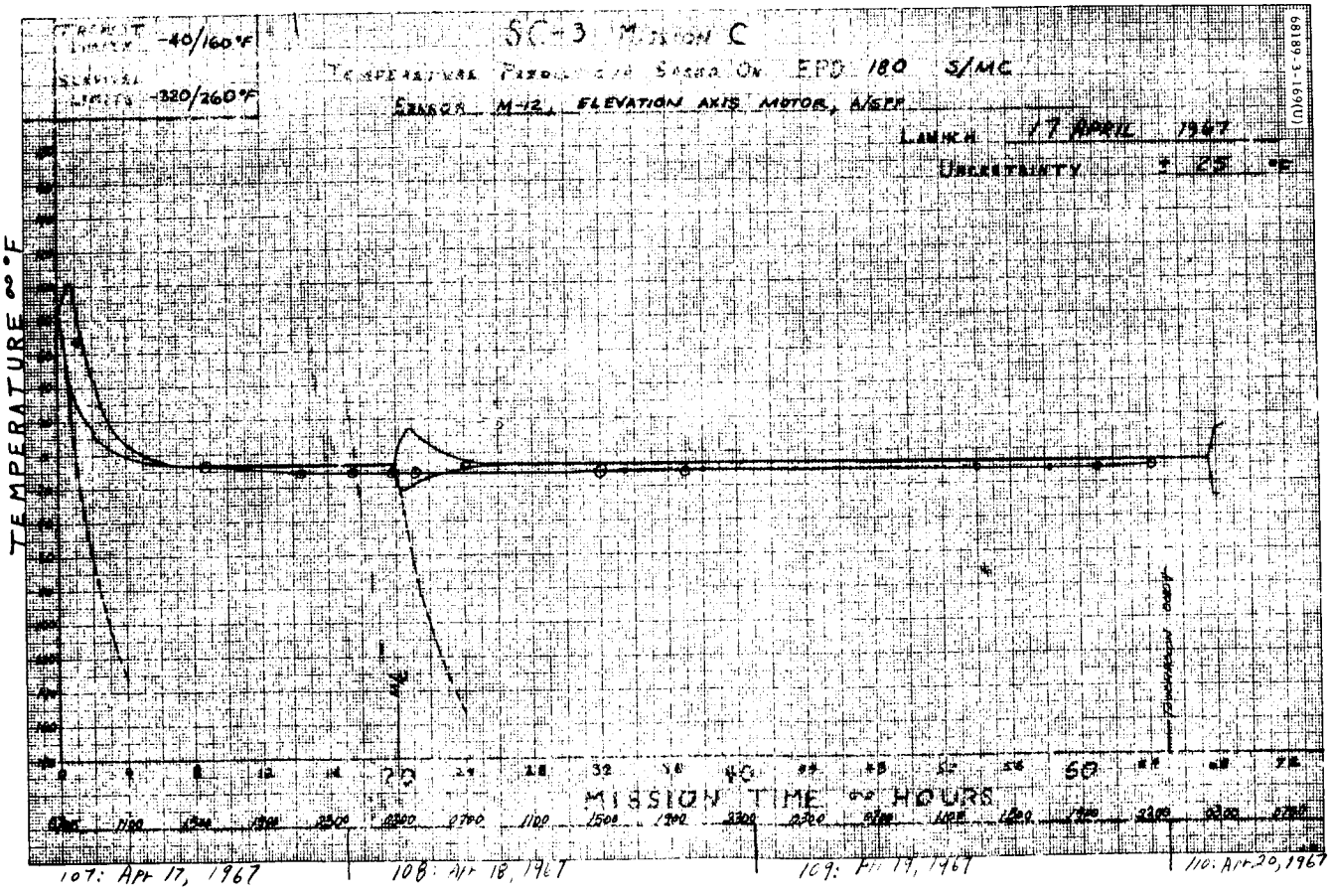

Figure 5.1-33. Sensor M-12, Elevation Axis Motor, A/SPP

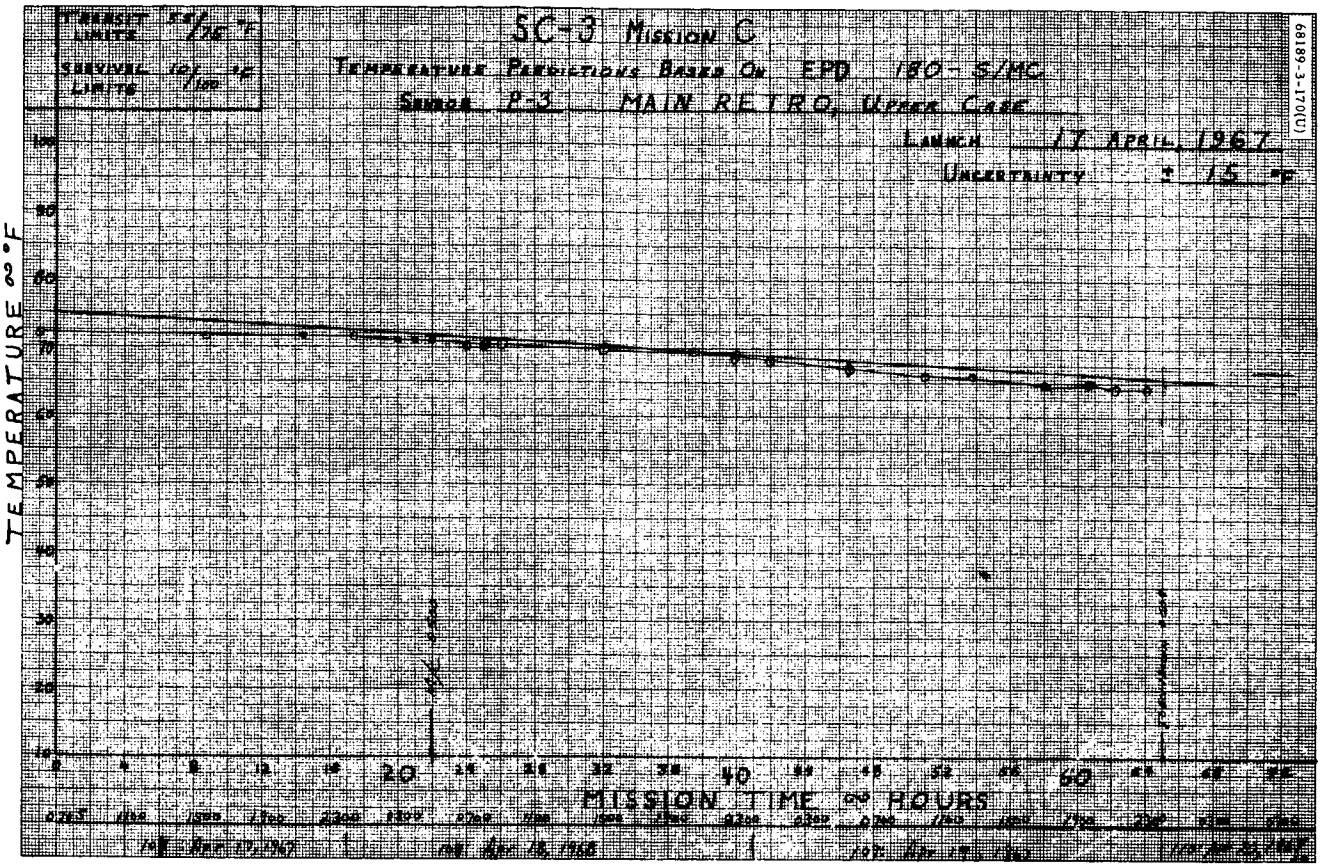

Figure 5.1-34. Sensor P-3, Main Retro, Upper Case

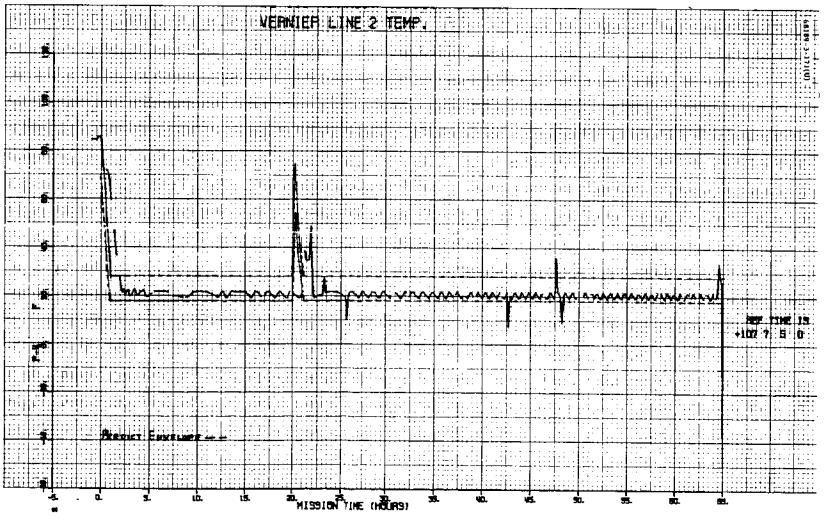

Figure 5.1-35. Vernier Line 2 Temperature

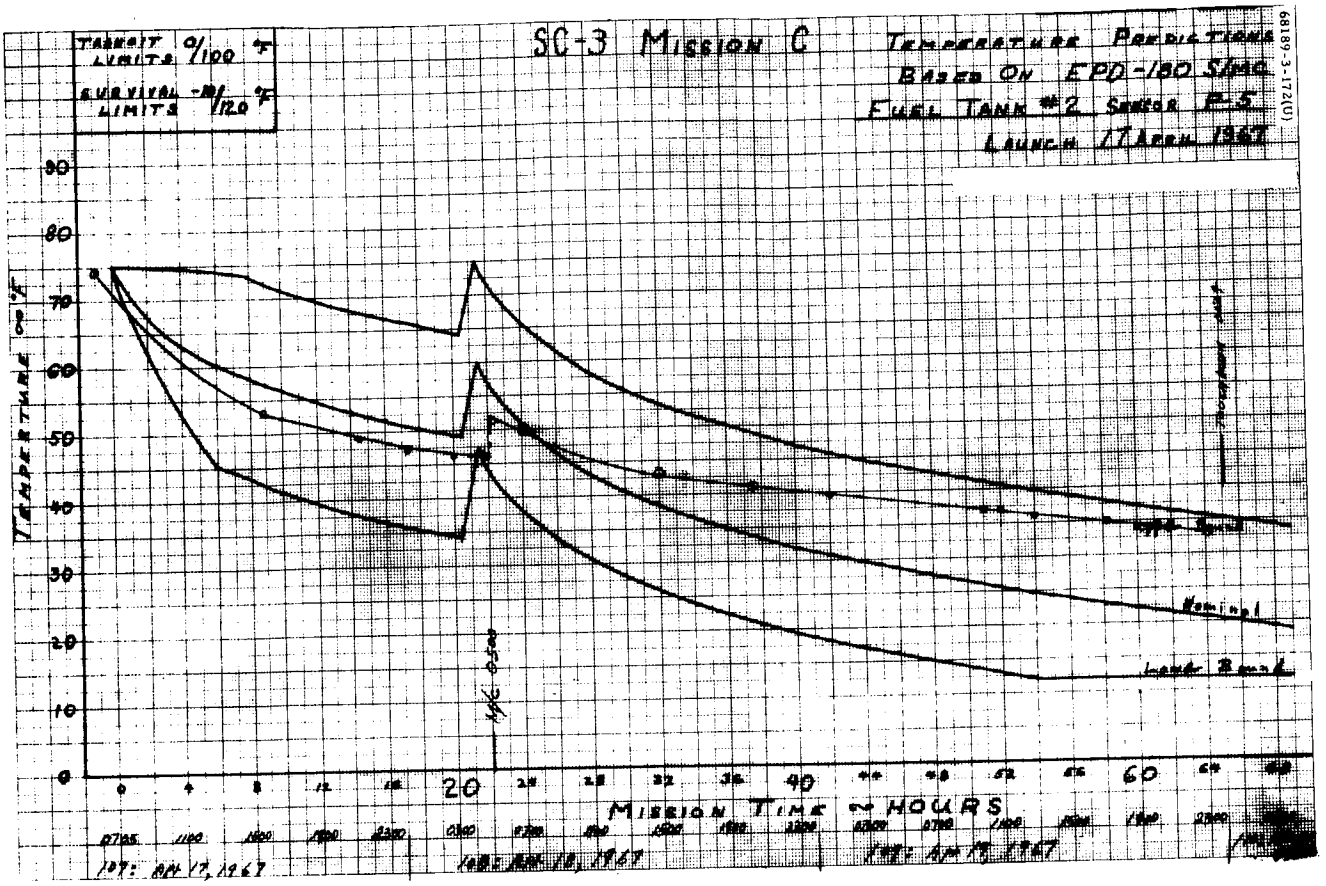

Figure 5.1-36. Sensor P-5, Fuel Tank No. 2

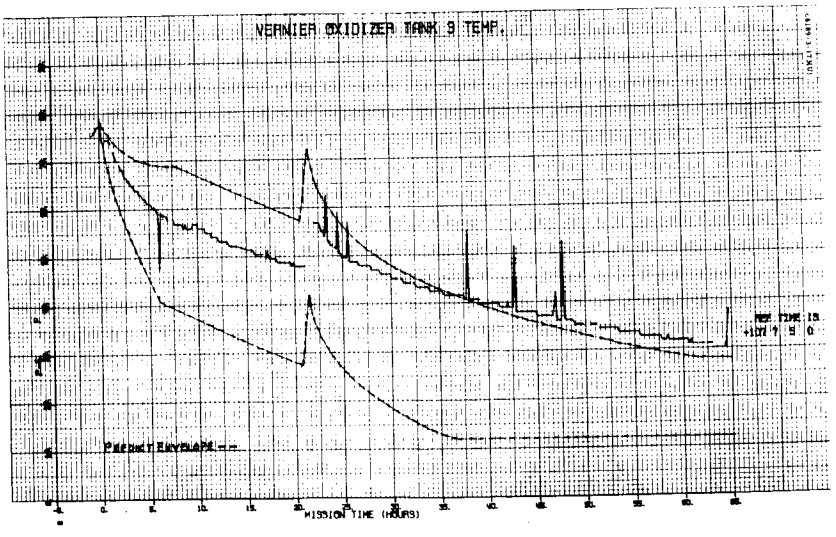

Figure 5.1-37. Vernier Oxidizer Tank 3 Temperature

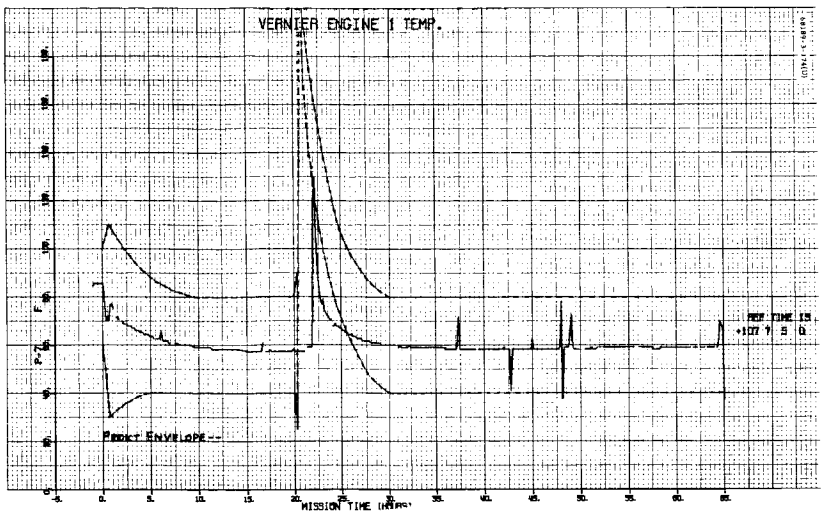

Figure 5.1-38. Vernier Engine 1 Temperature

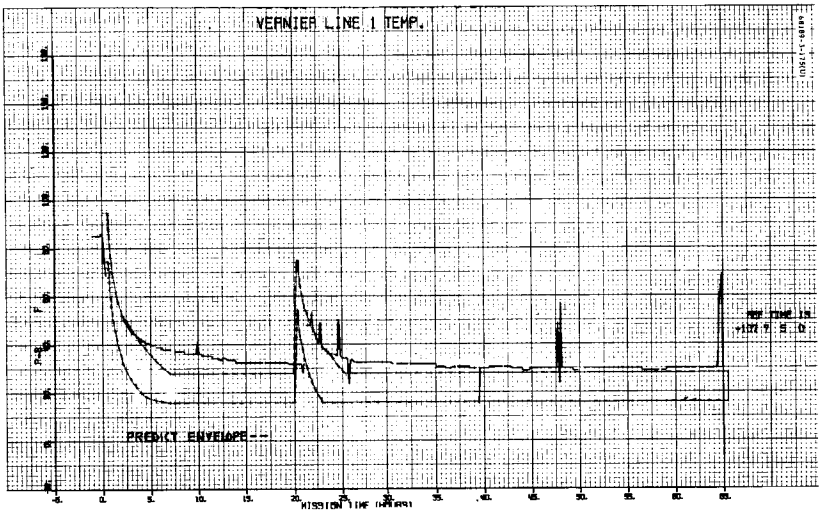

Figure 5.1-39. Vernier Line 1 Temperature

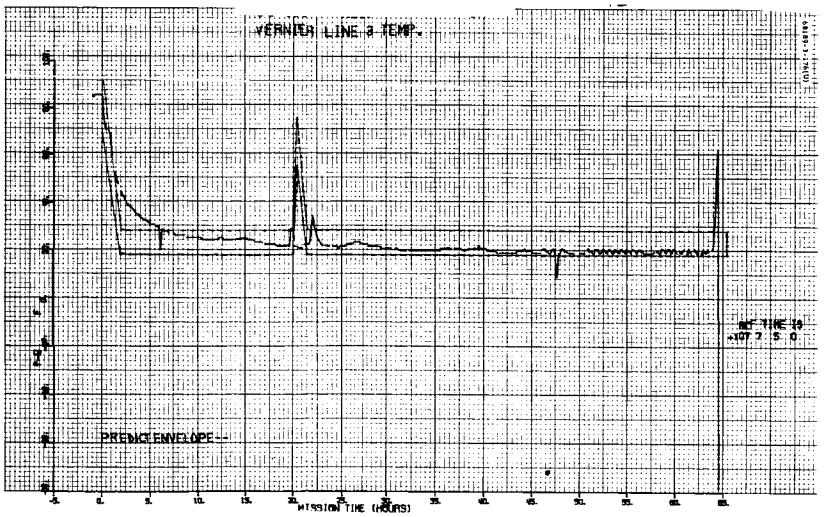

Figure 5.1-40. Vernier Line 3 Temperature

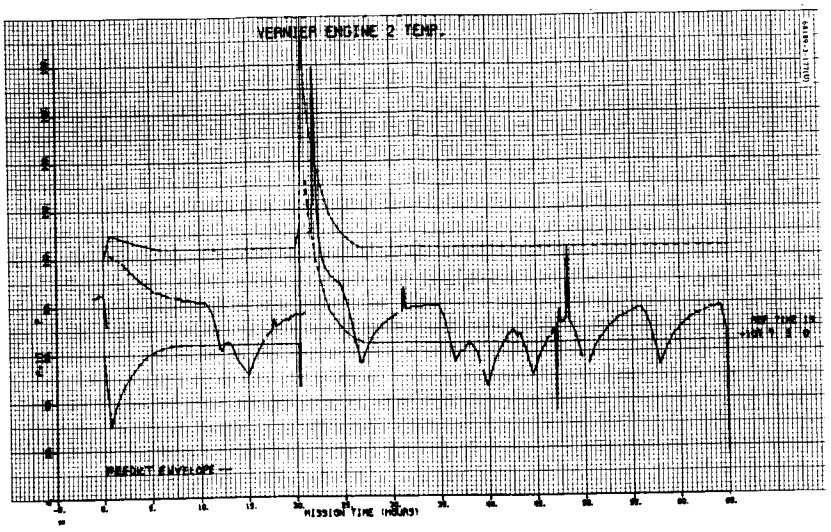

Figure 5.1-41. Vernier Engine 2 Temperature

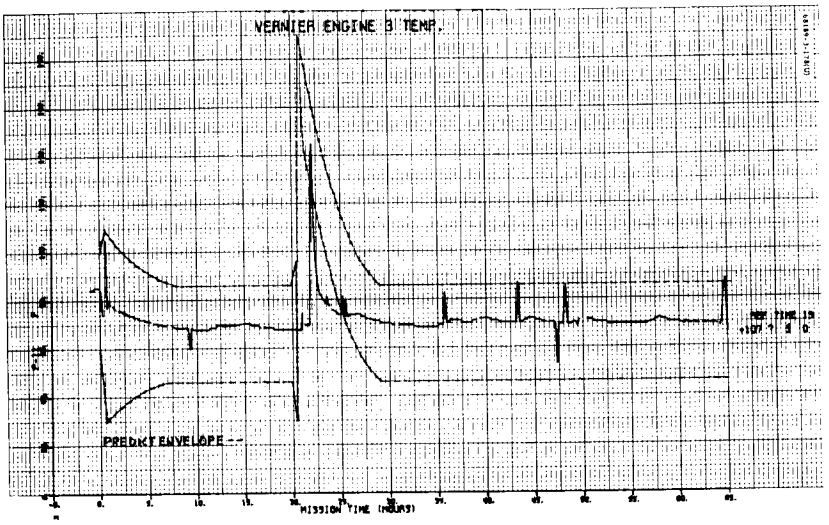

Figure 5.1-42. Vernier Engine 3 Temperature

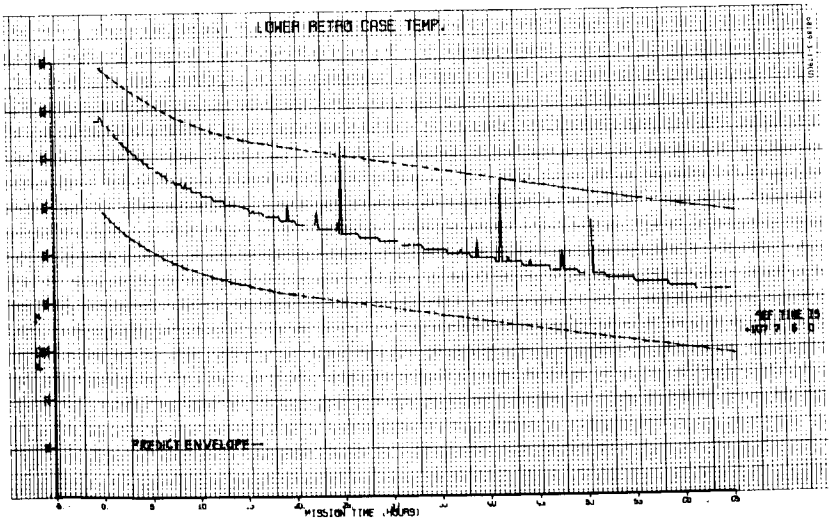

Figure 5.1-43. Lower Retro Case Temperature

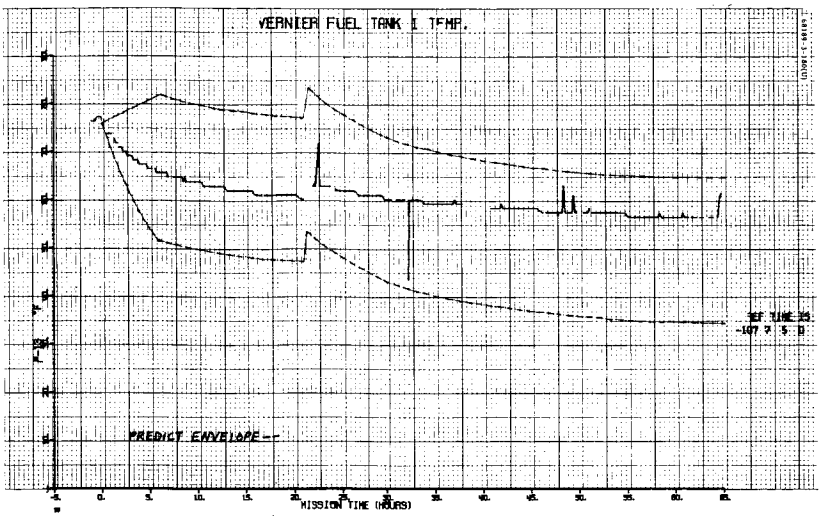

Figure 5.1-44. Vernier Fuel Tank 1 Temperature

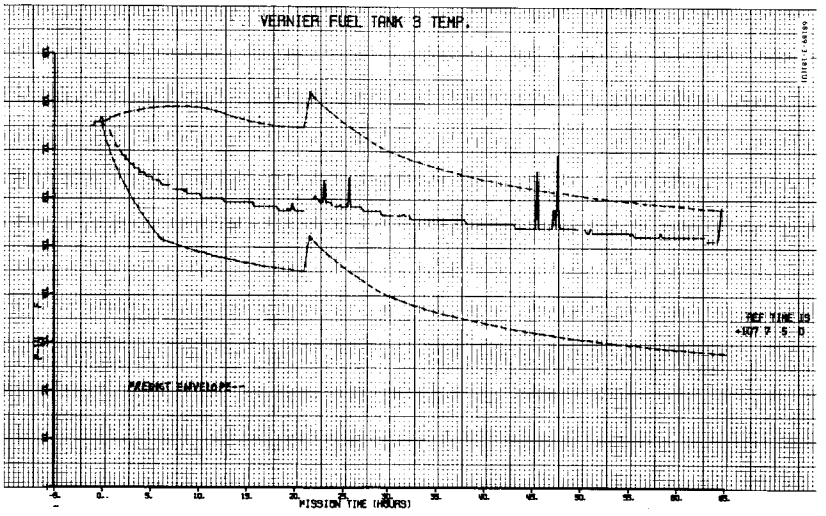

Figure 5.1-45. Vernier Fuel Tank 3 Temperature

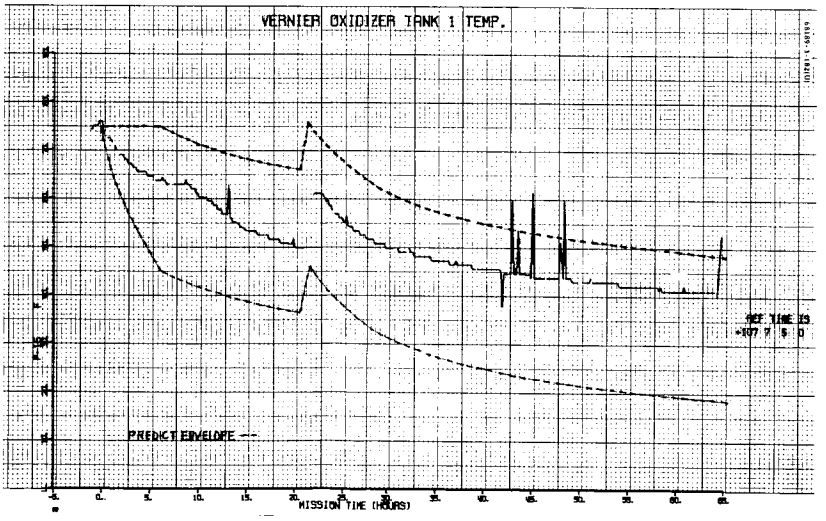

Figure 5.1-46. Vernier Oxidizer Tank 1 Temperature

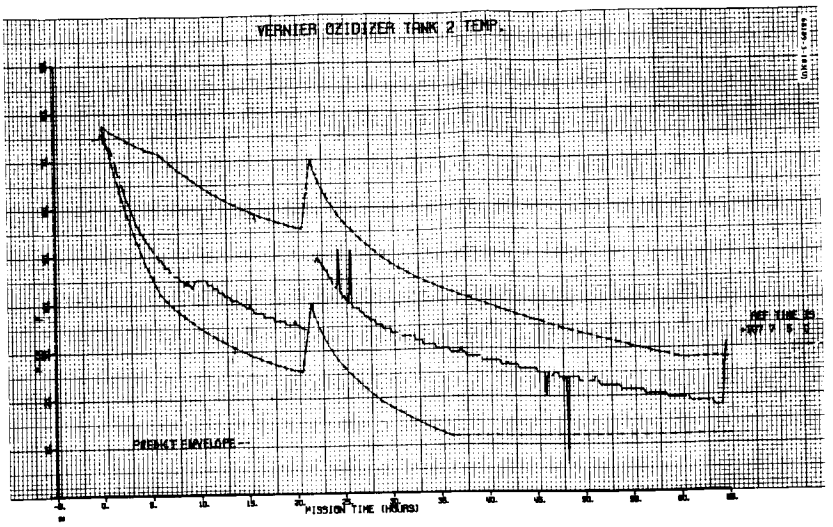

Figure 5.1-47. Vernier Oxidizer Tank 2 Temperature

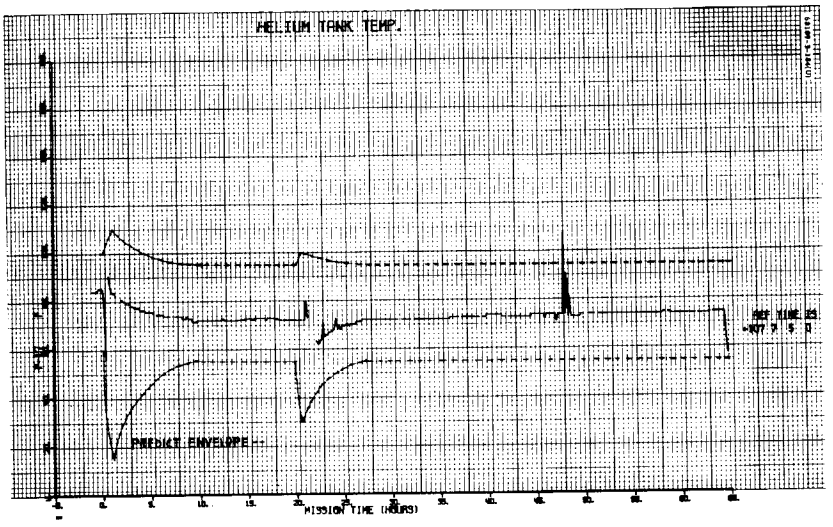

Figure 5.1-48. Helium Tank Temperature

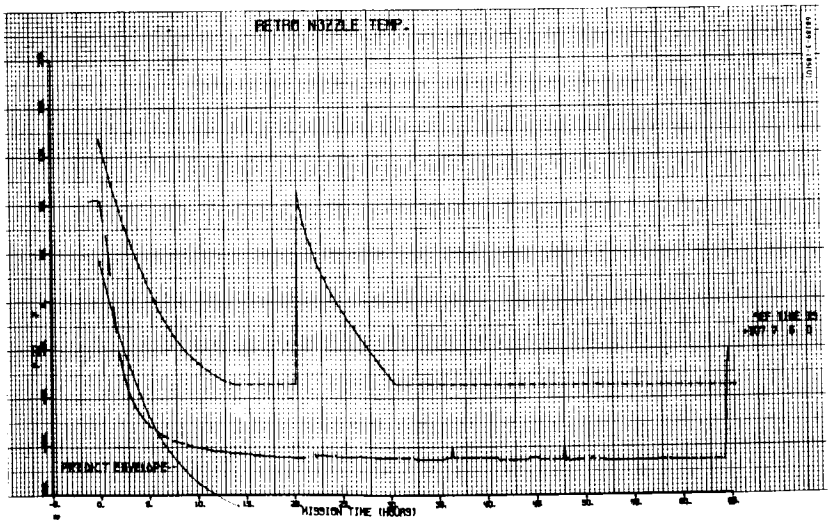

Figure 5.1-49. Retro Nozzle Temperature

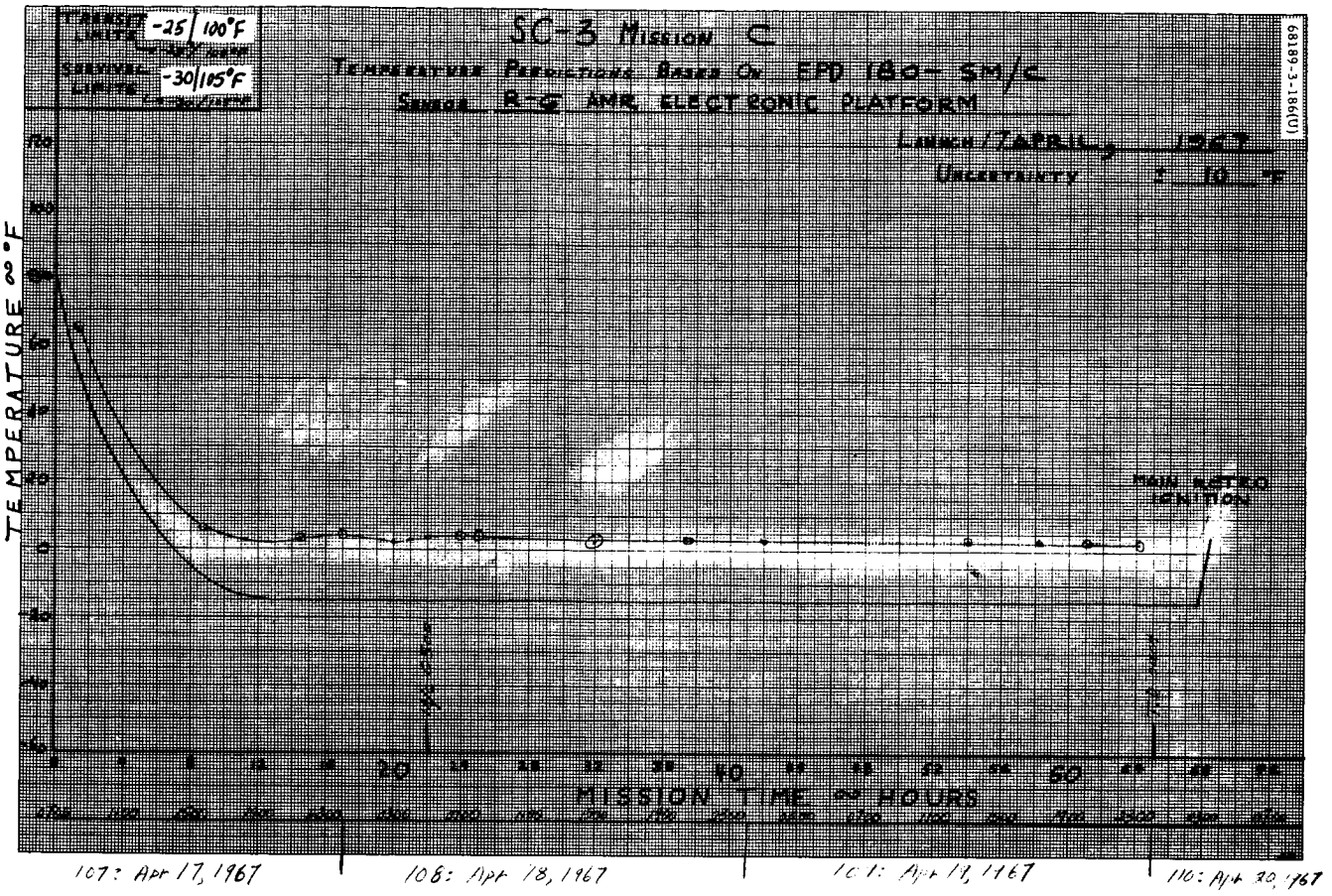

Figure 5.1-50. Sensor R-6, AMR Electronic Platform

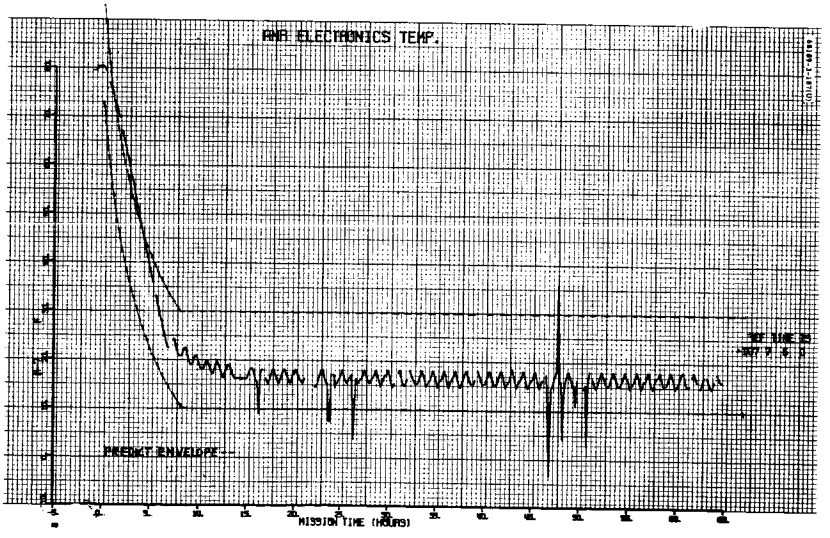

Figure 5.1-51. AMR Electronics Temperature

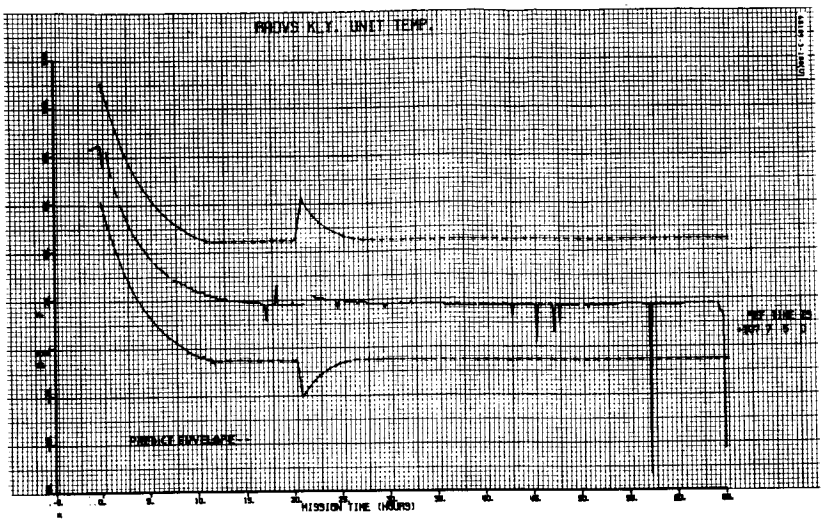

Figure 5.1-52. RADVS Klystron Unit Temperature

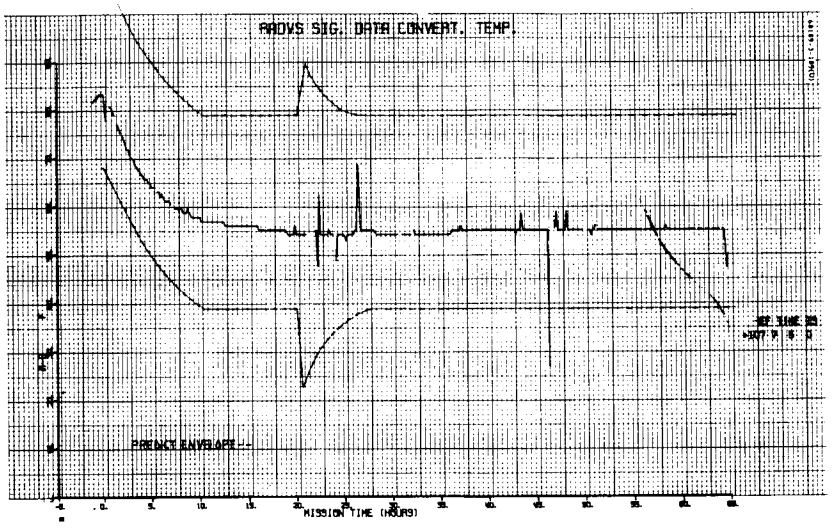

Figure 5.1-53. RADVS Signal Data Converter Temperature

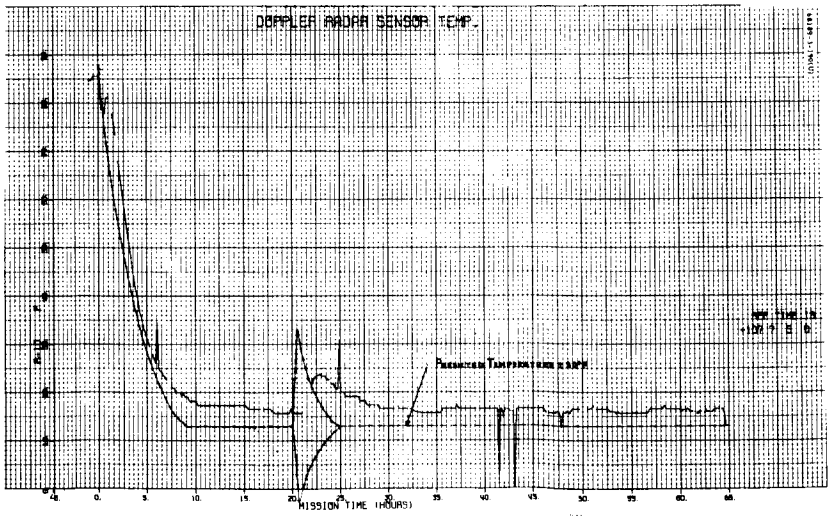

Figure 5.1-54. Doppler Radar Sensor Temperature

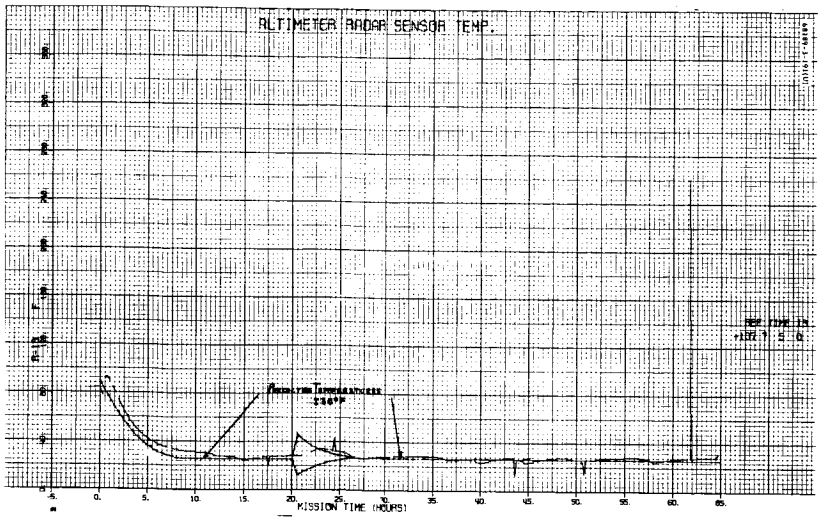

Figure 5.1-55. Altimeter Radar Sensor Temperature

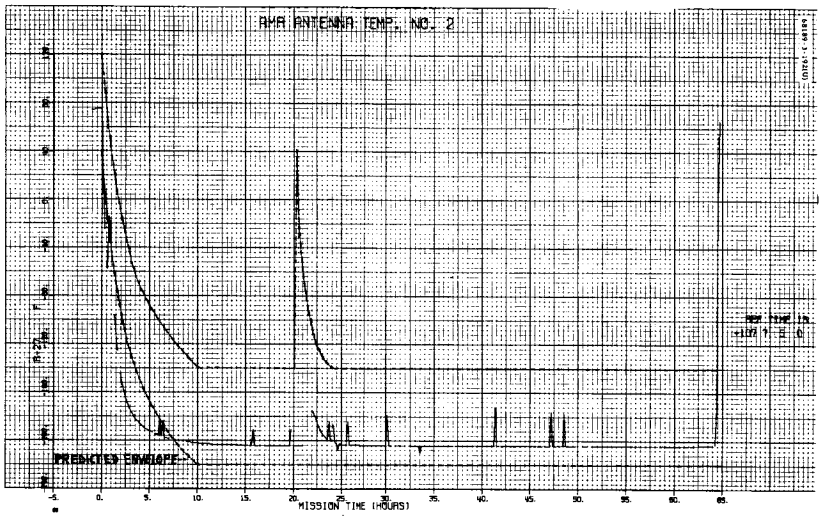

Figure 5.1-56. AMR Antenna Temperature No. 2

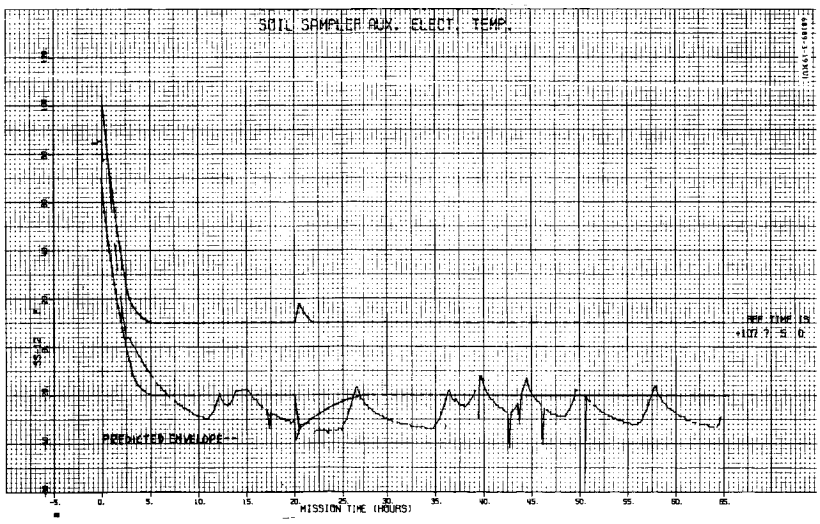

Figure 5.1-57. Soil Sampler Auxiliary Electronics Temperature

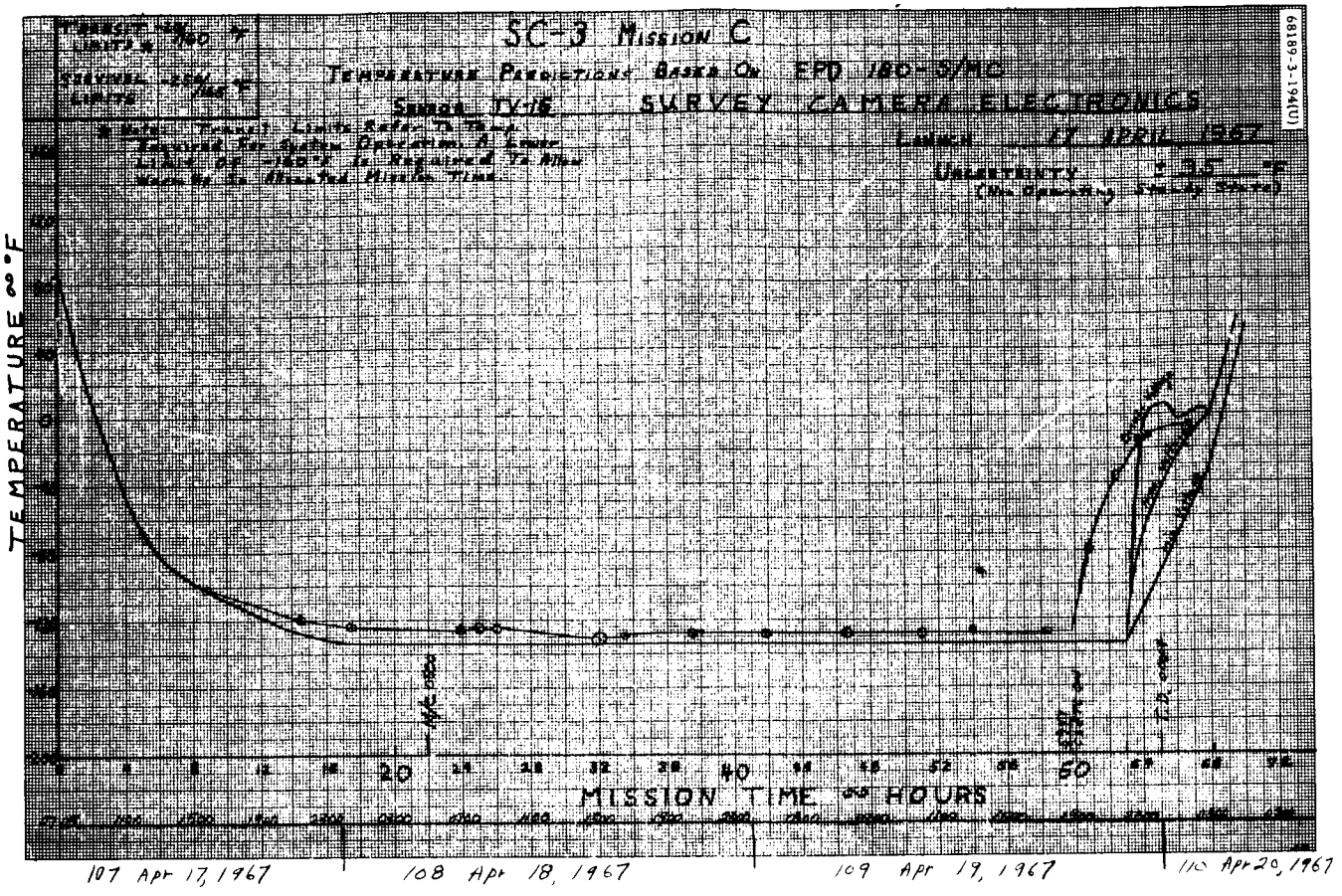

Figure 5.1-58. Sensor TV-16, Survey Camera Electronics

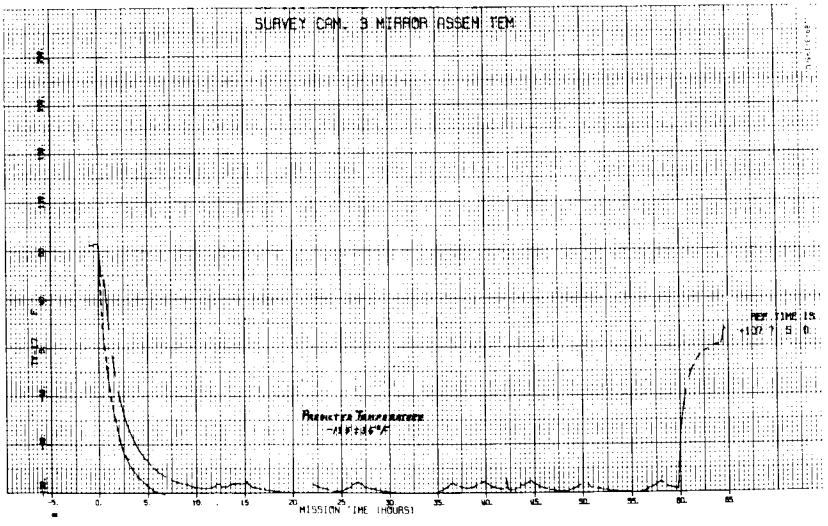

Figure 5.1-59. Survey Camera 3 Mirror Assembly Temperature

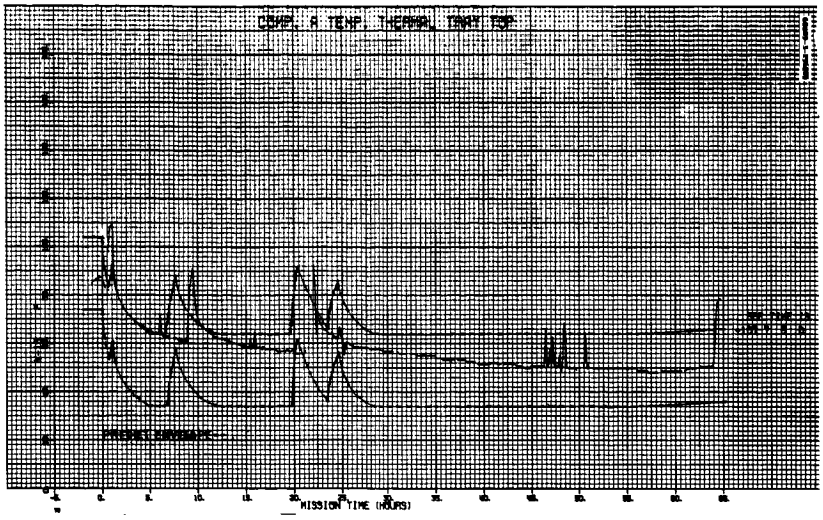

Figure 5.1-60. Compartment A Temperature Tray Top

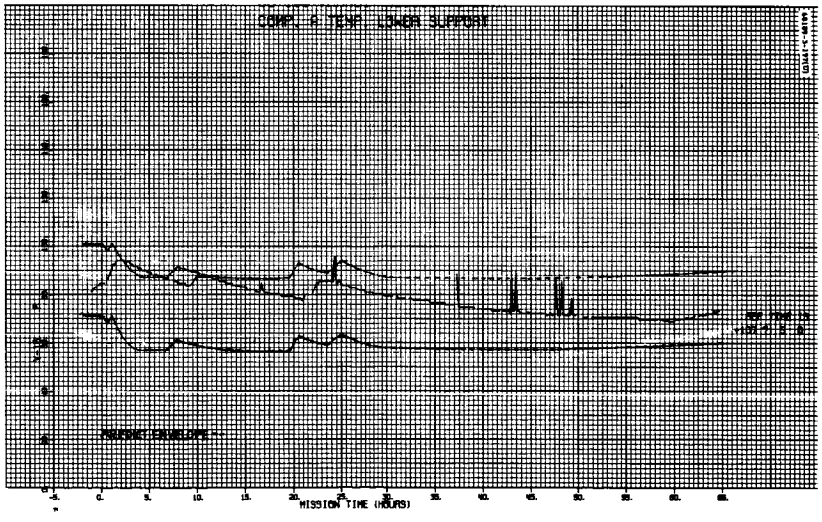

Figure 5.1-61. Compartment A Temperature Lower Support

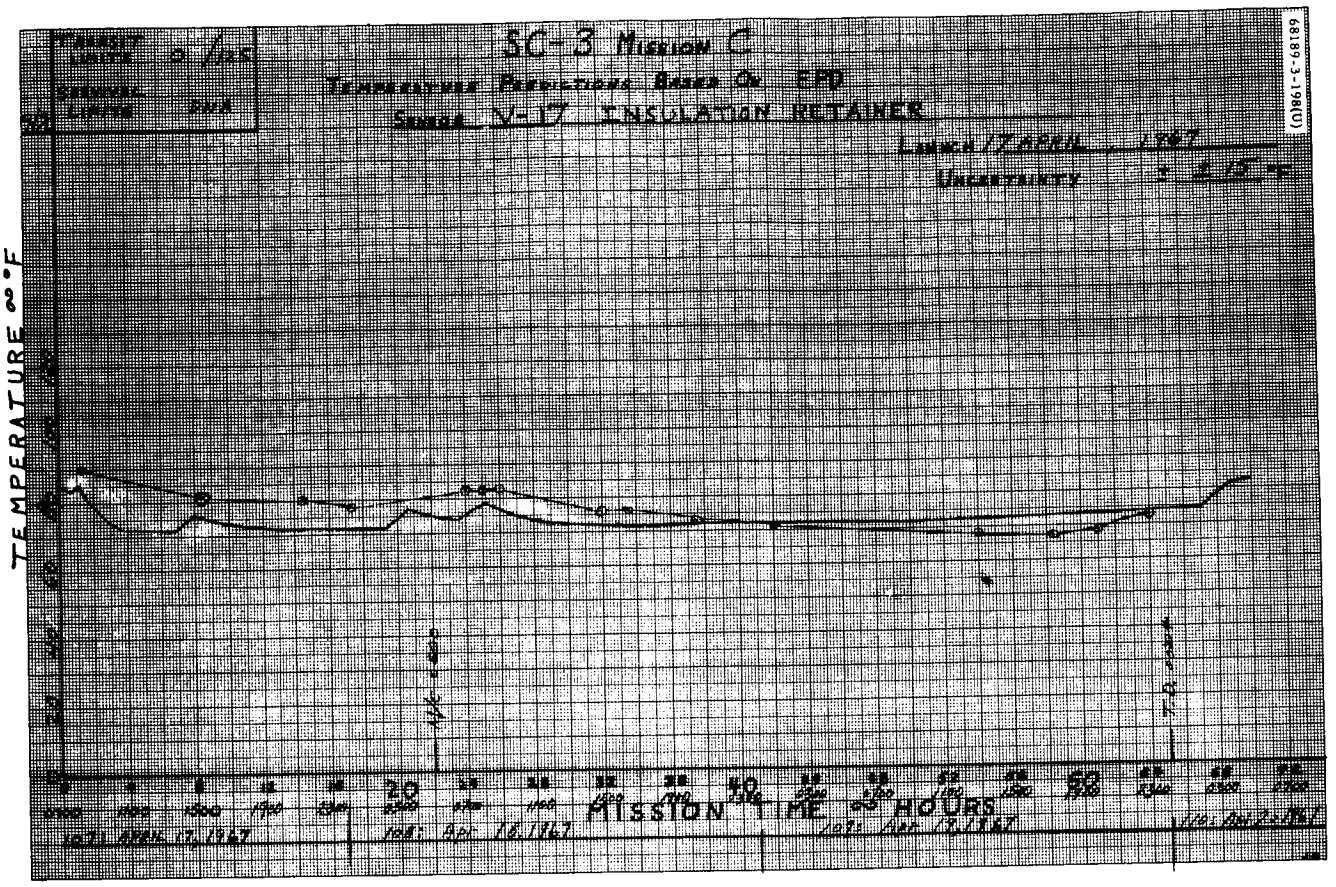

Figure 5.1-62. Sensor V-17, Insulation Retainer

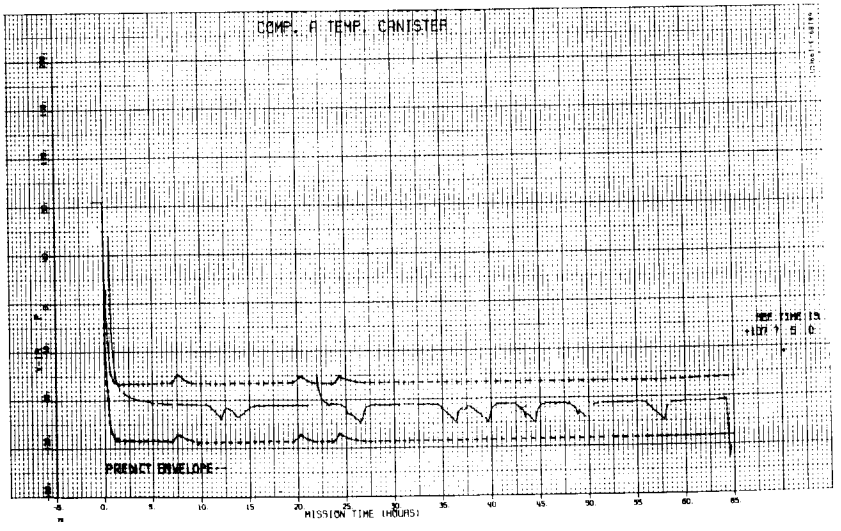

Figure 5.1-63. Compartment A Temperature Canister

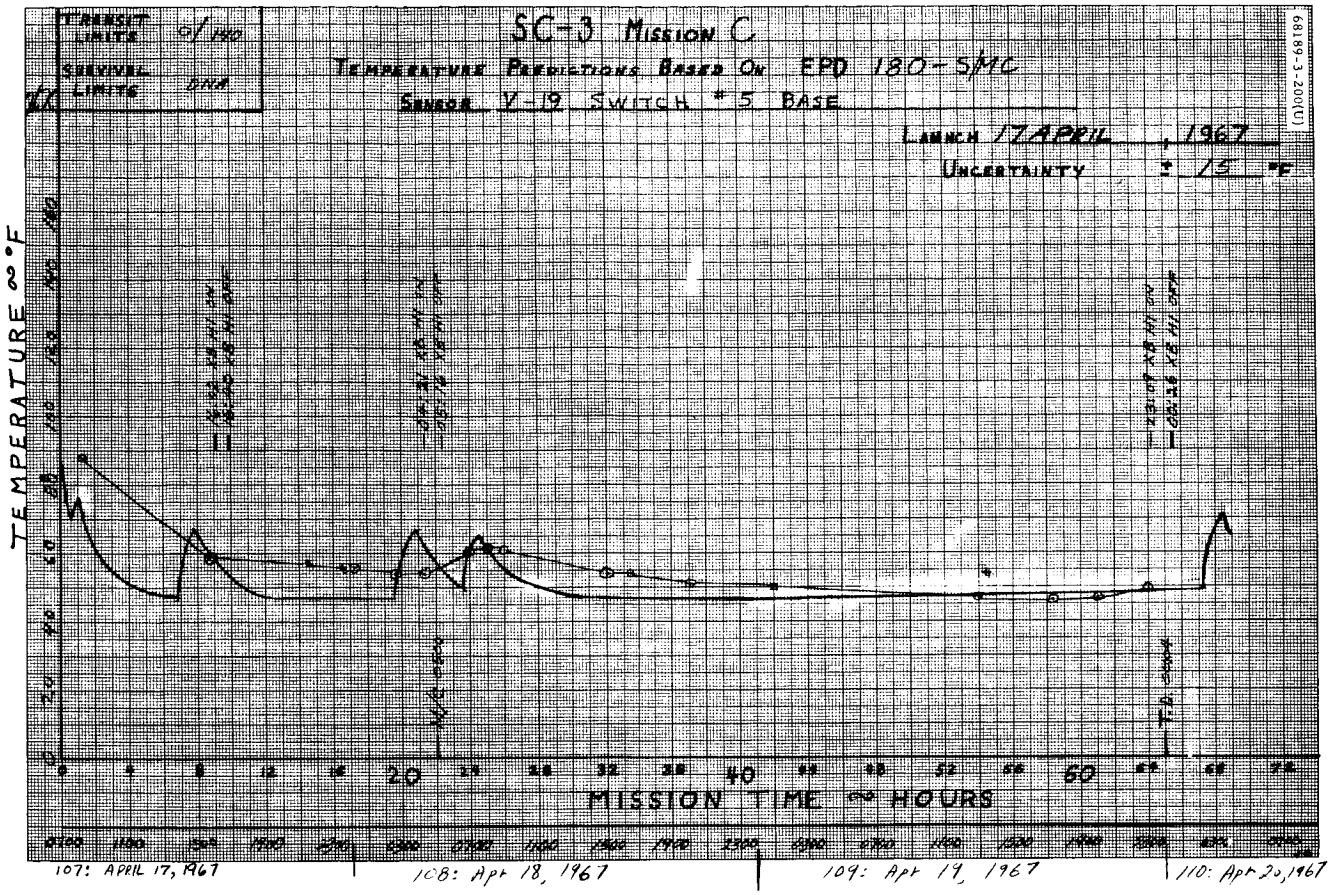

Figure 5.1-64. Sensor V-19, Switch No. 5 Base

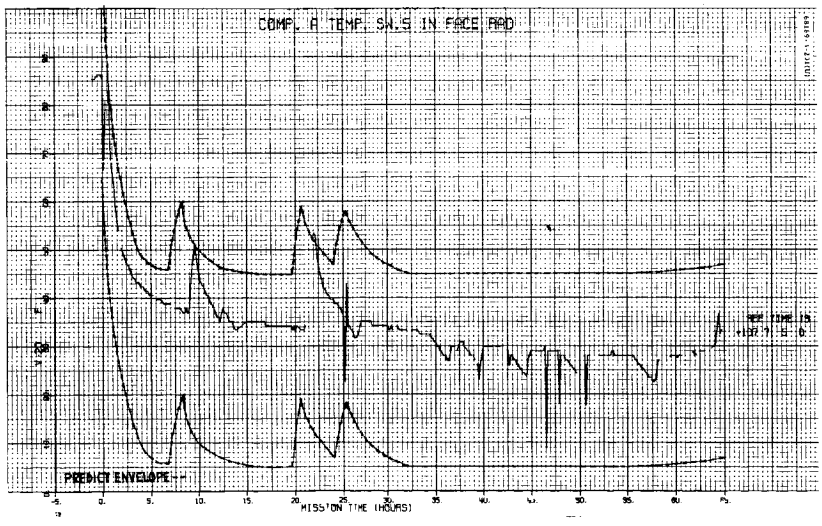

Figure 5.1-65. Compartment A Temperature Switch 5 in Face Radiator

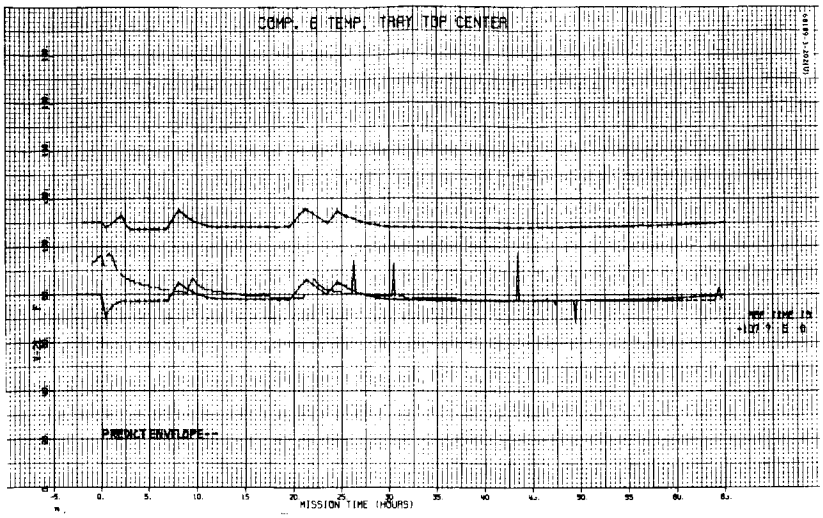

Figure 5.1-66. Compartment B Temperature Tray Top Center

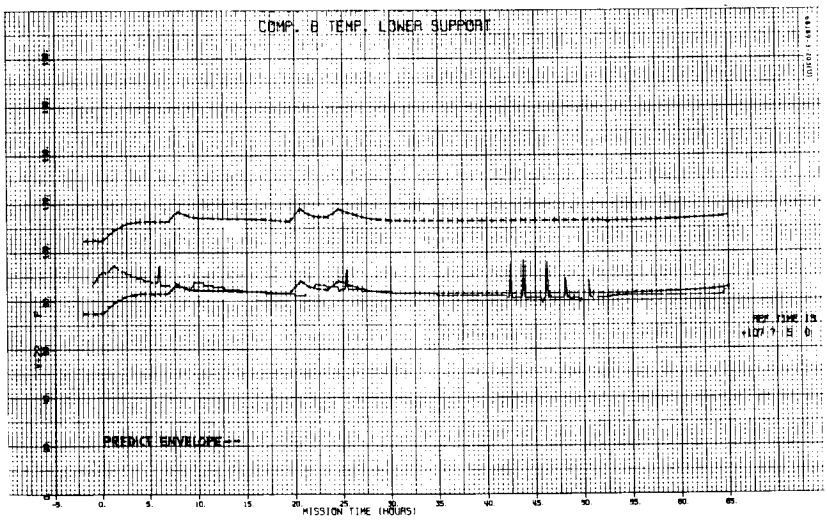

Figure 5.1-67. Compartment B Temperature Lower Support

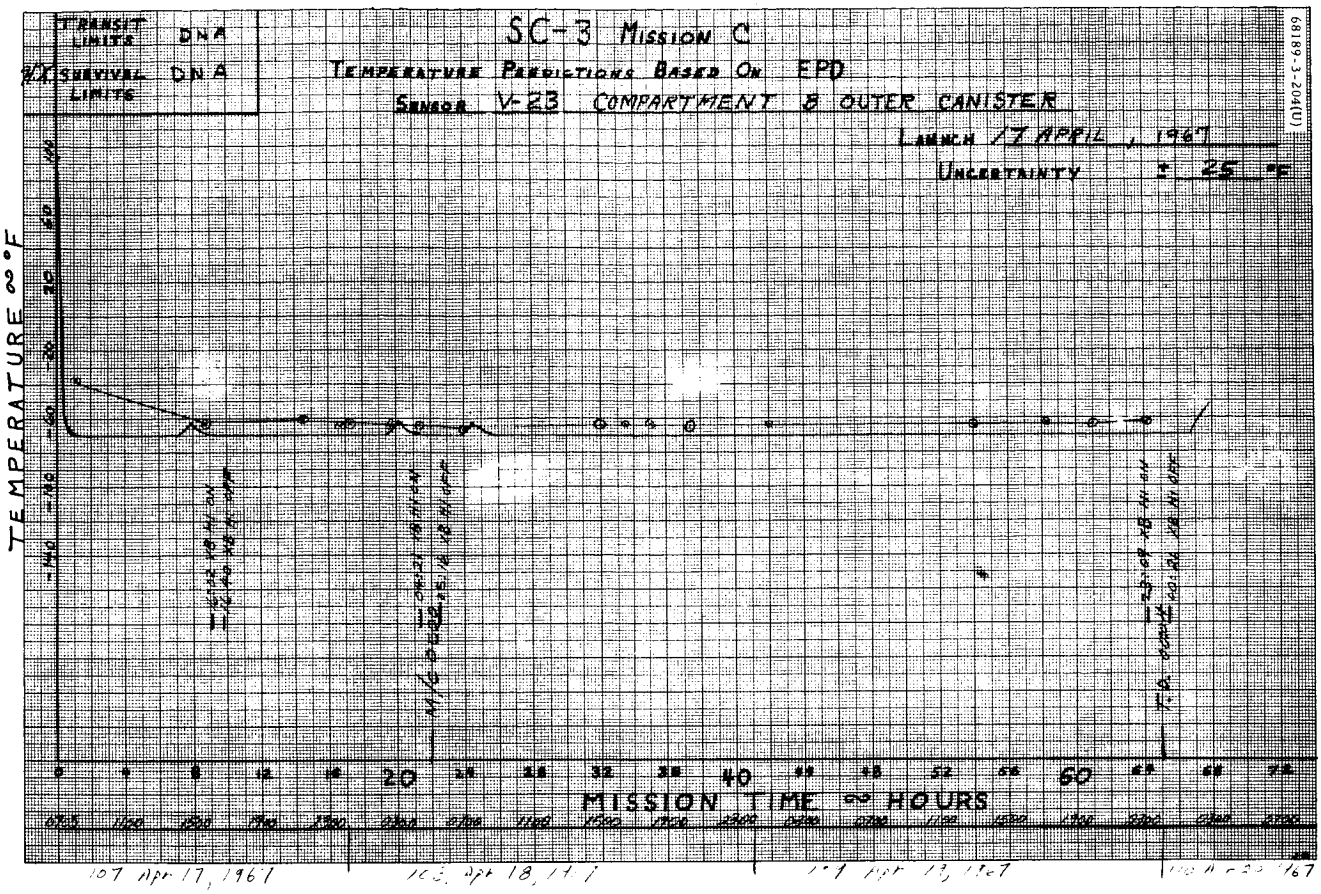

Figure 5.1-68. Sensor V-23, Compartment B Outer Canister

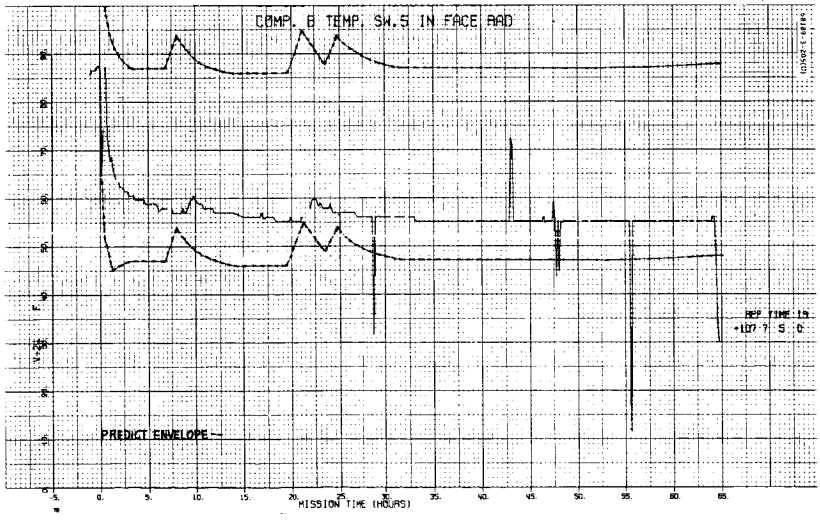

Figure 5.1-69. Compartment B Temperature Switch 5 in Face Radiator

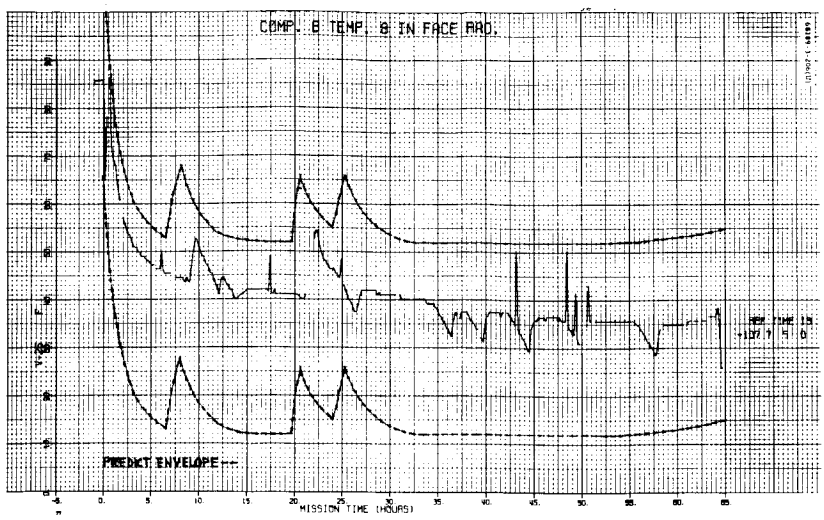

Figure 5.1-70. Compartment B Temperature 8 in Face Radiator

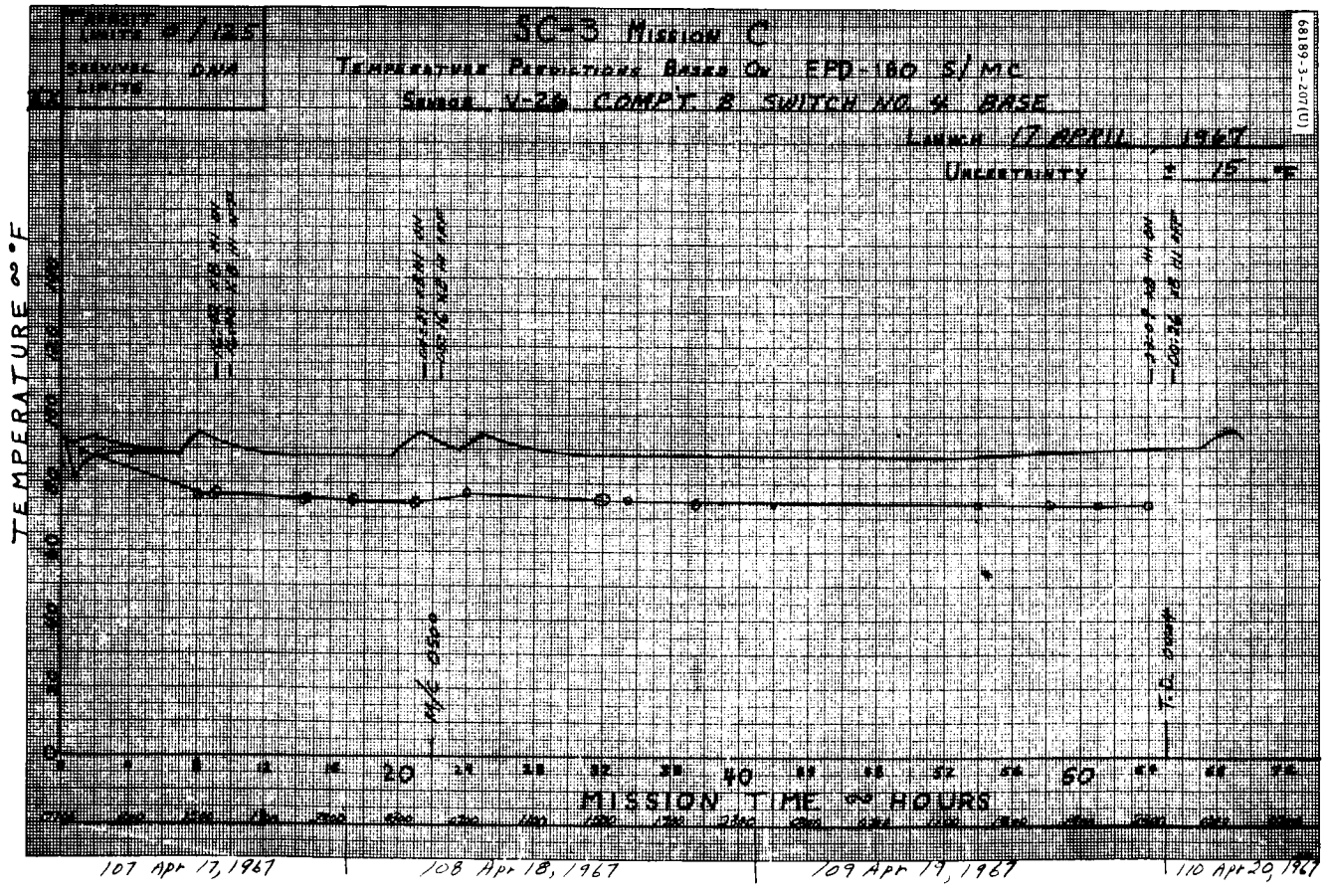

Figure 5.1-71. Sensor V-26, Compartment B Switch No. 4 Base

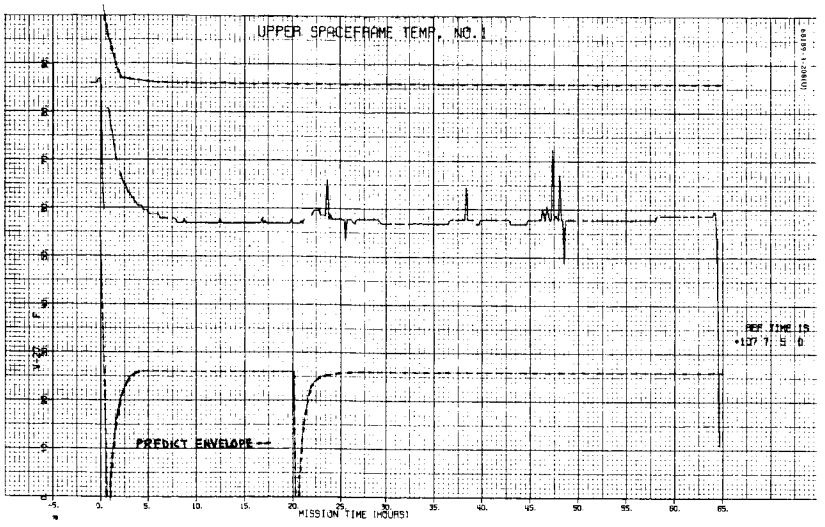

Figure 5.1-72. Upper Spaceframe 1 Temperature

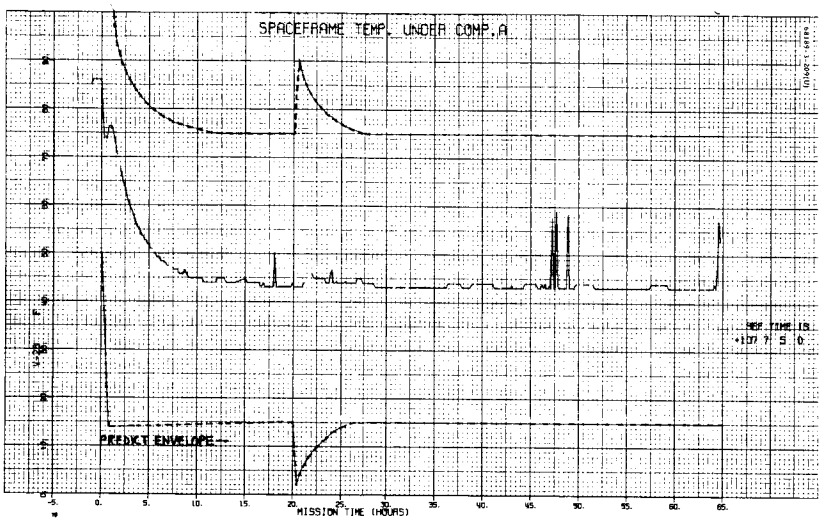

Figure 5.1-73. Spaceframe Temperature Under Compartment A

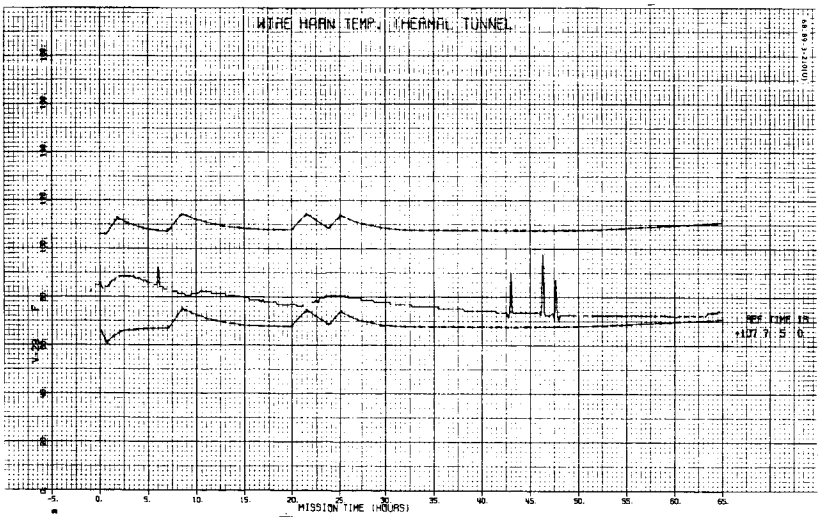

Figure 5.1-74. Wire Harness Temperature Thermal Tunnel

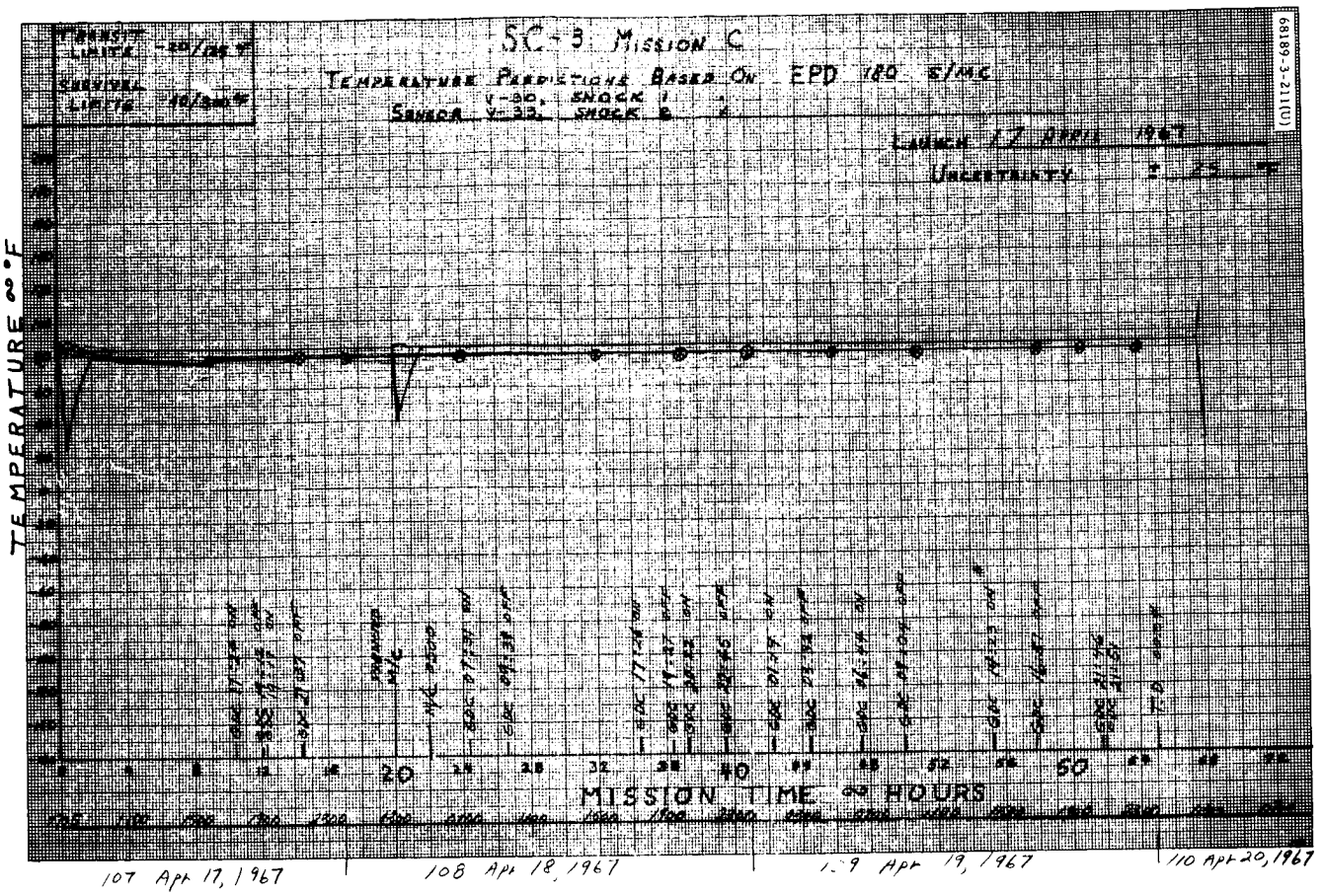

Figure 5.1-75. Sensor V-30, Shock 1
Sensor V-33, Shock 3

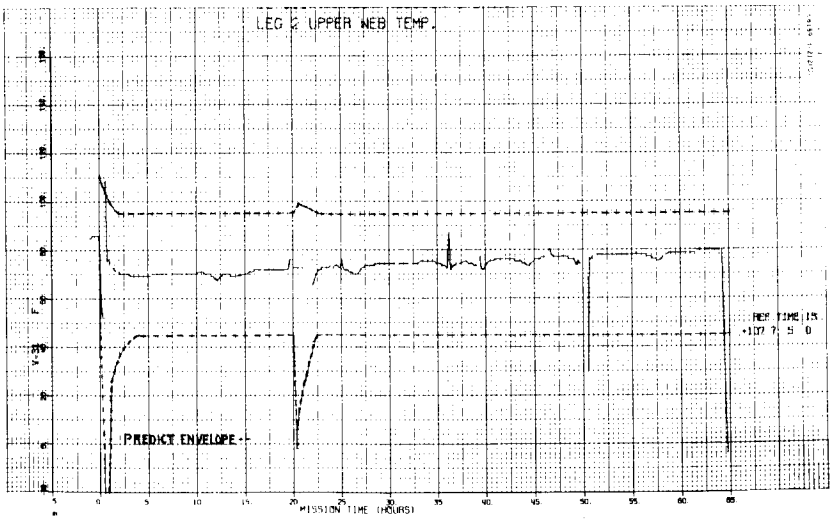

Figure 5.1-76. Leg 2 Upper Web Temperature

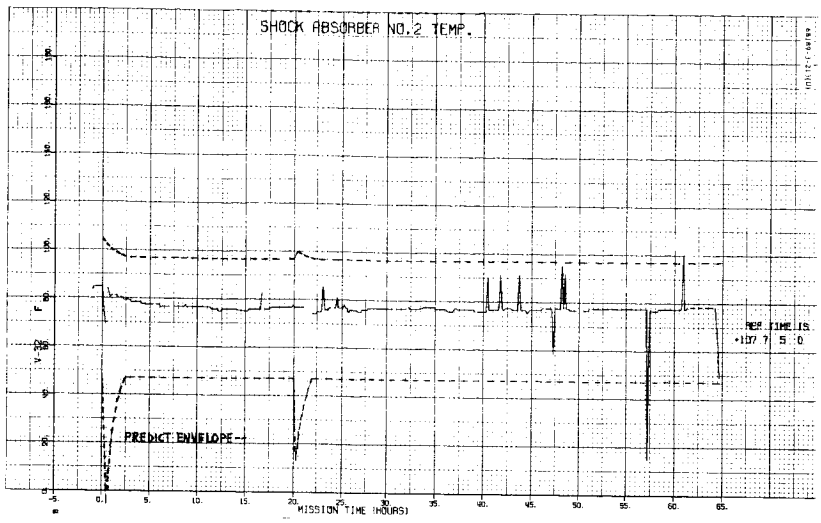

Figure 5.1-77. Shock Absorber 2 Temperature

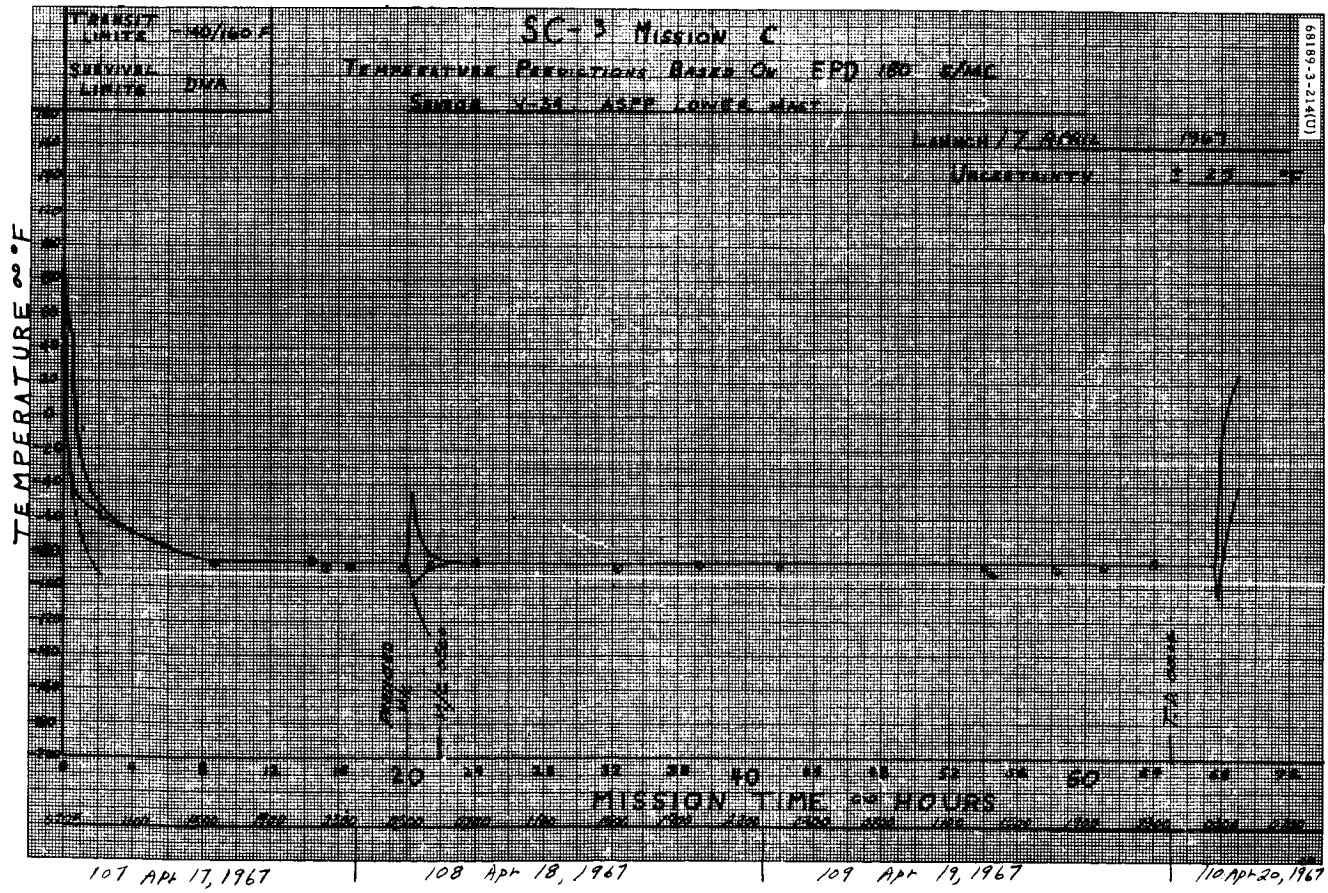

Figure 5.1-78. Sensor V-34, A/SPP Lower Mast

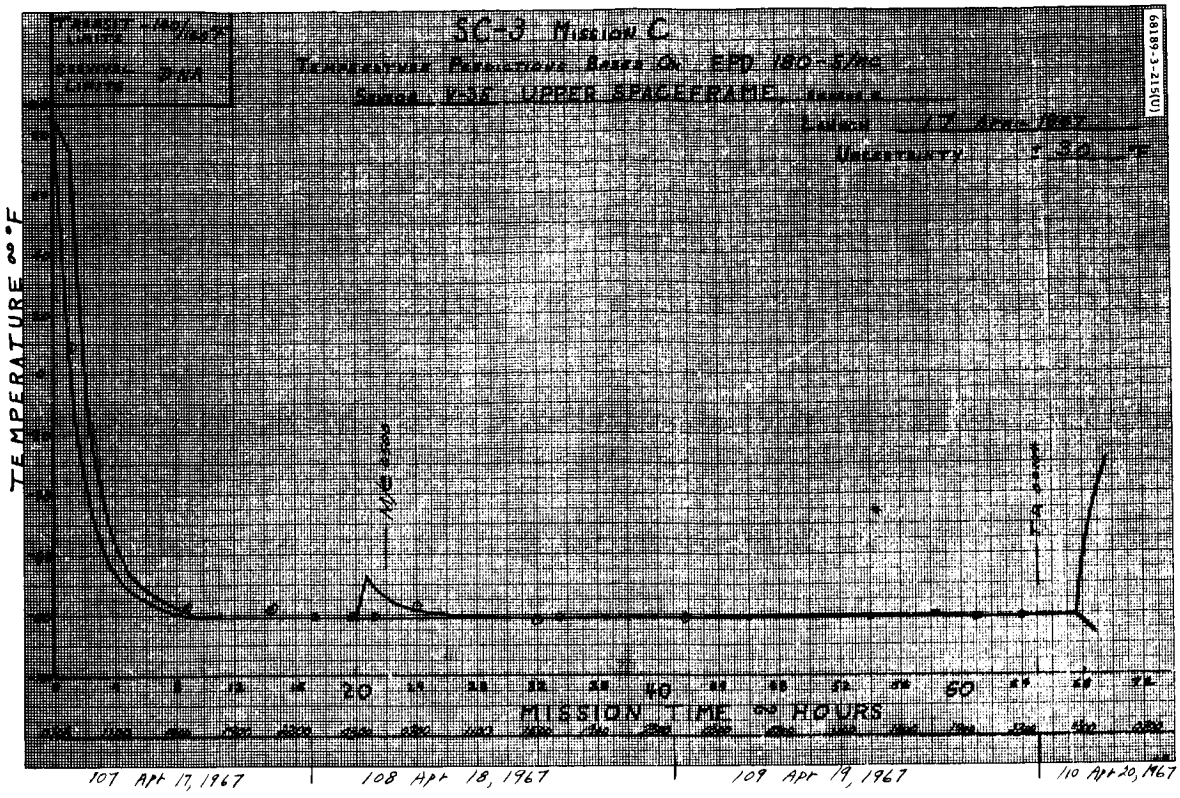

Figure 5.1-79. Sensor V-35, Upper Space Frame, Sensor 2

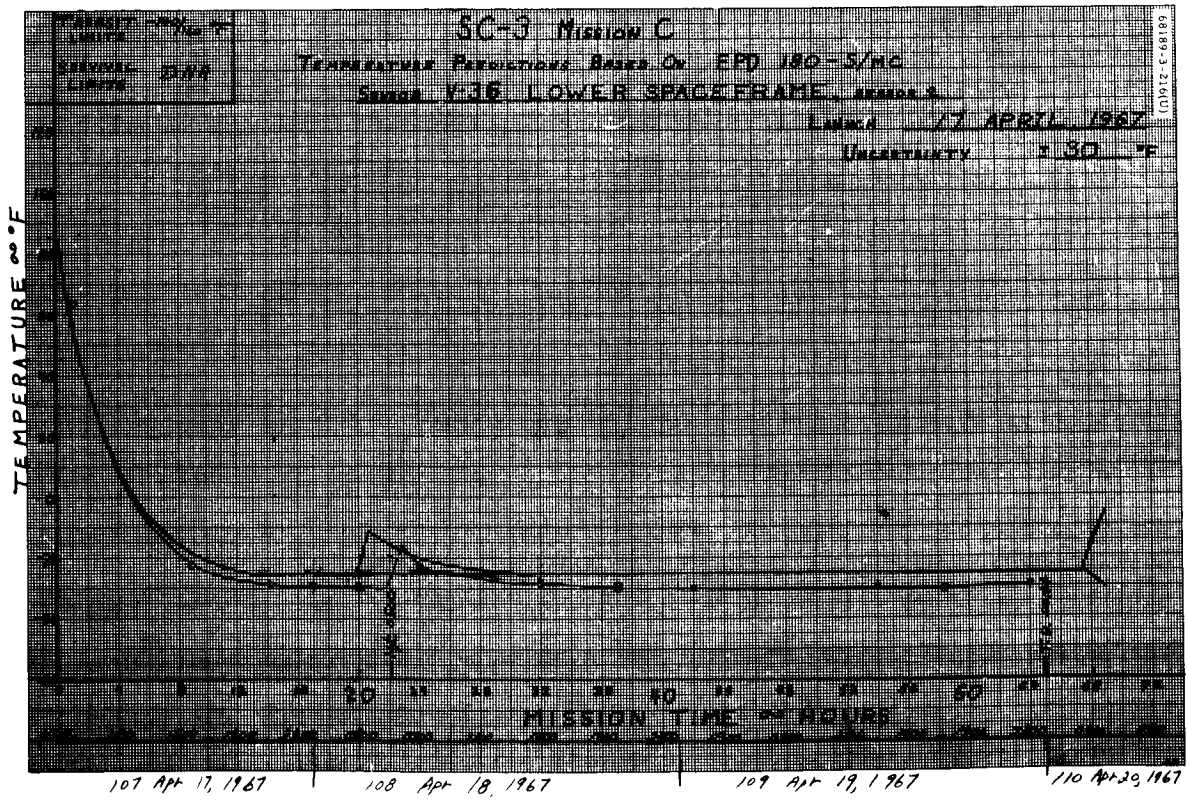

Figure 5.1-80. Sensor V-36, Lower Space Frame, Sensor 2

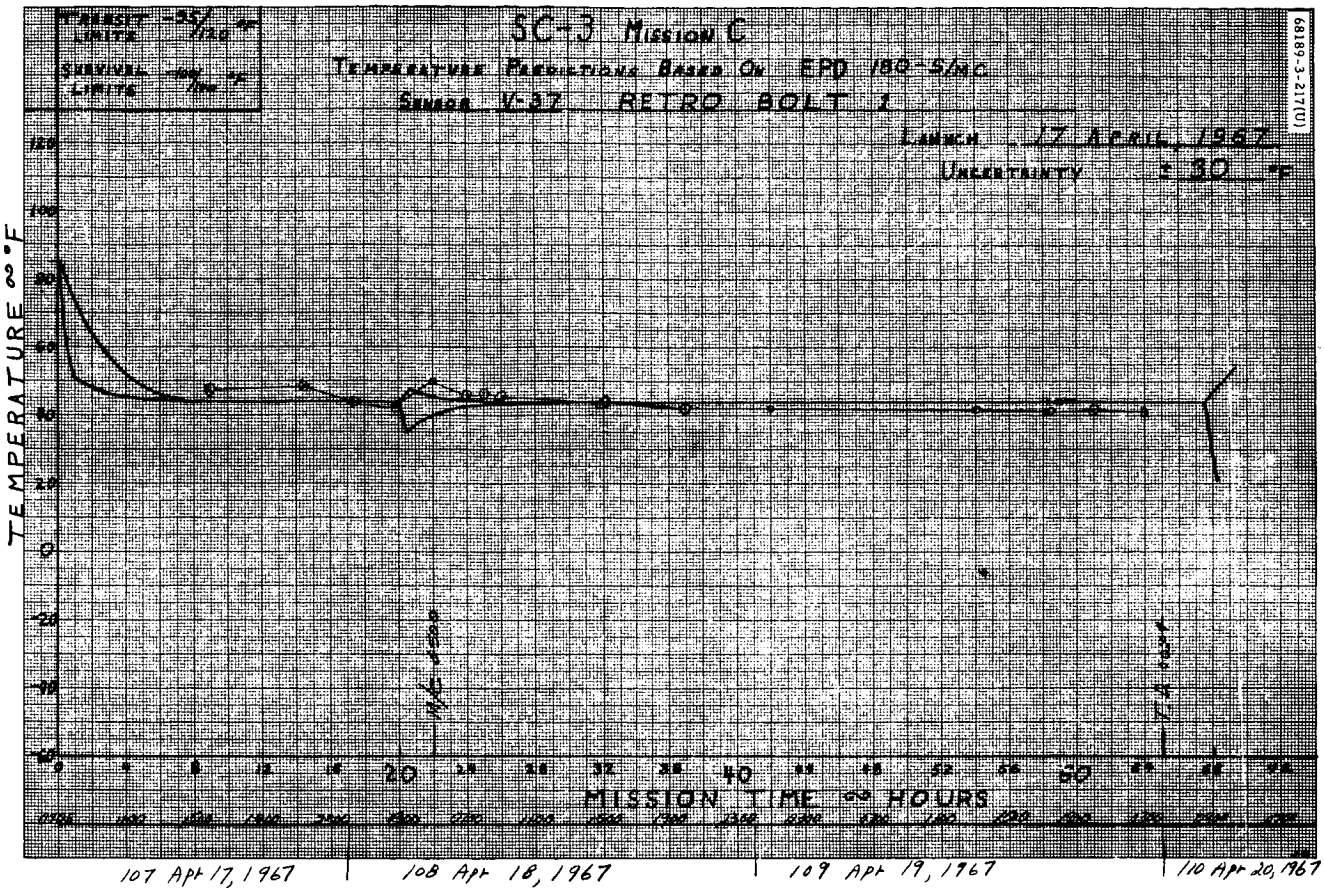

Figure 5.1-81. Sensor V-37, Retro Bolt 1

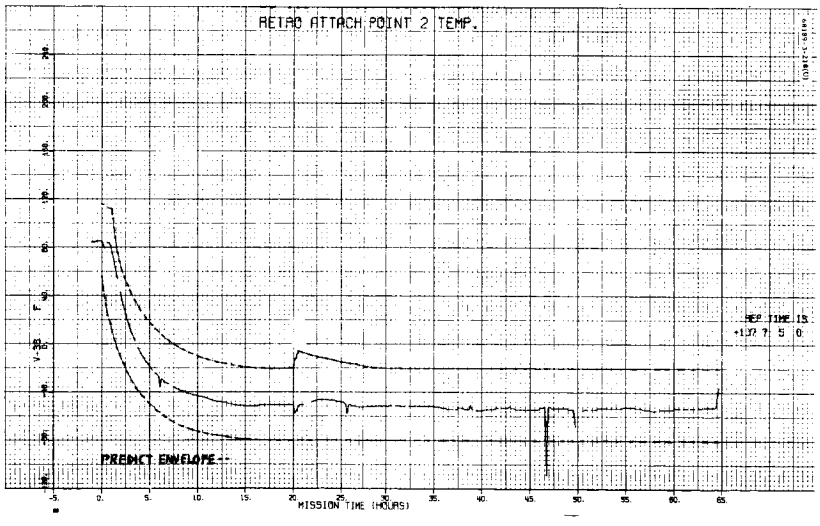

Figure 5.1-82. Retro Attach Point 2 Temperature

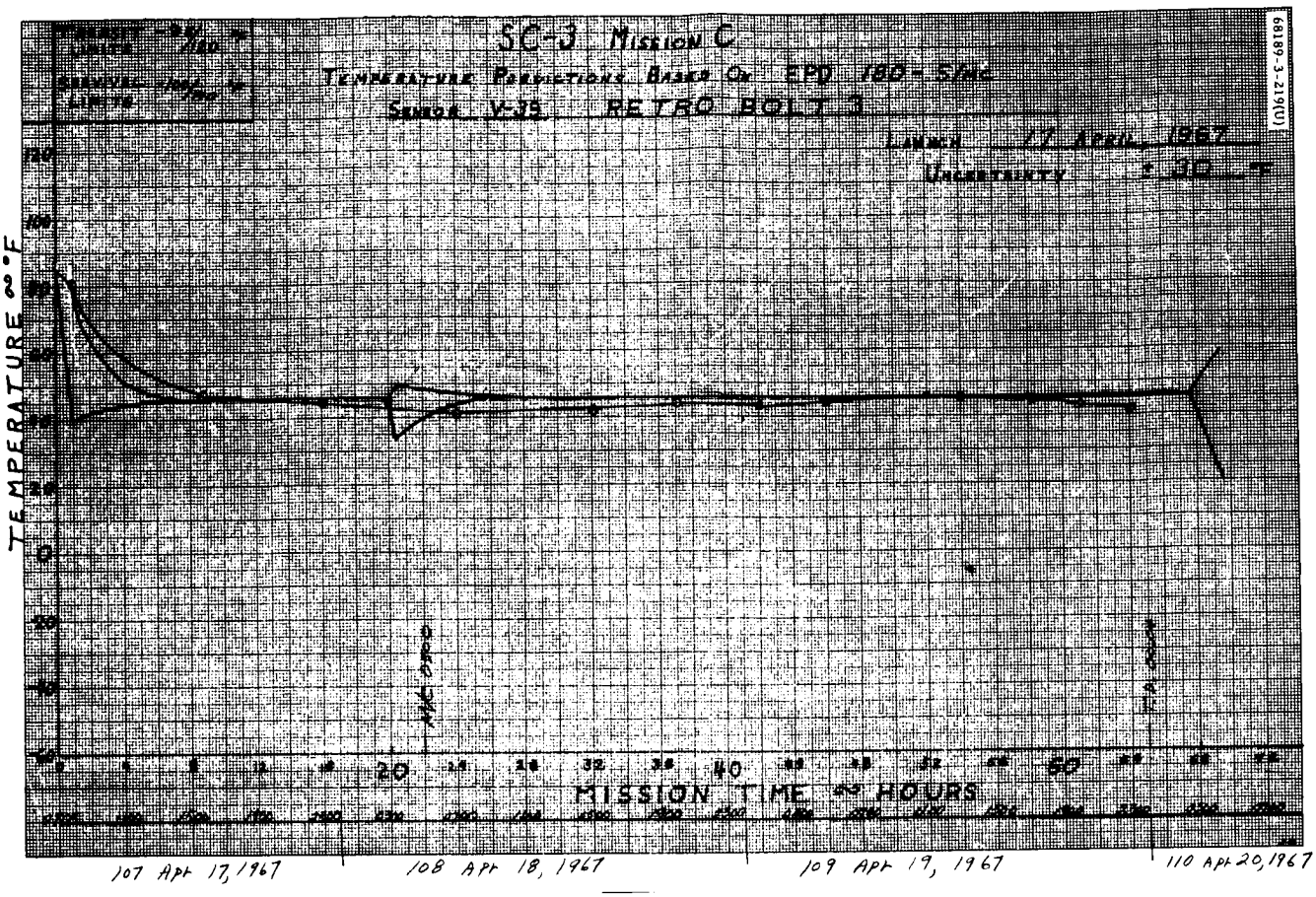

Figure 5.1-83. Sensor V-39, Retro Bolt 3

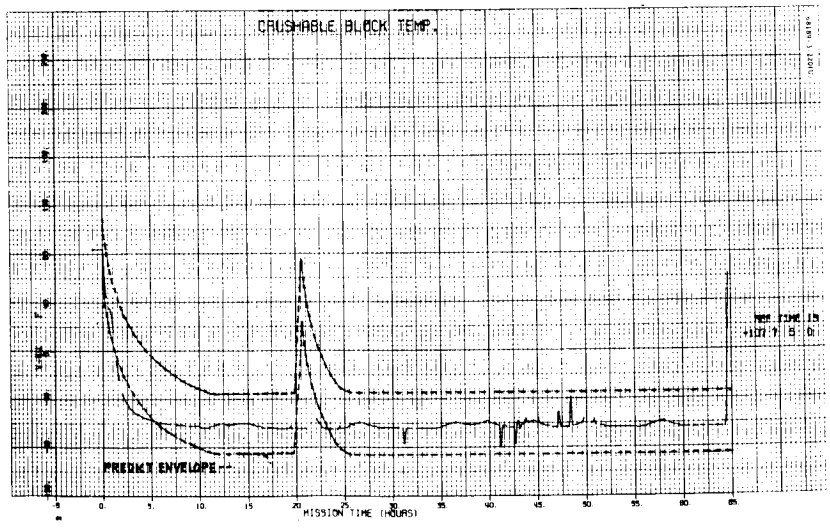

Figure 5.1-84. Crushable Block Temperature

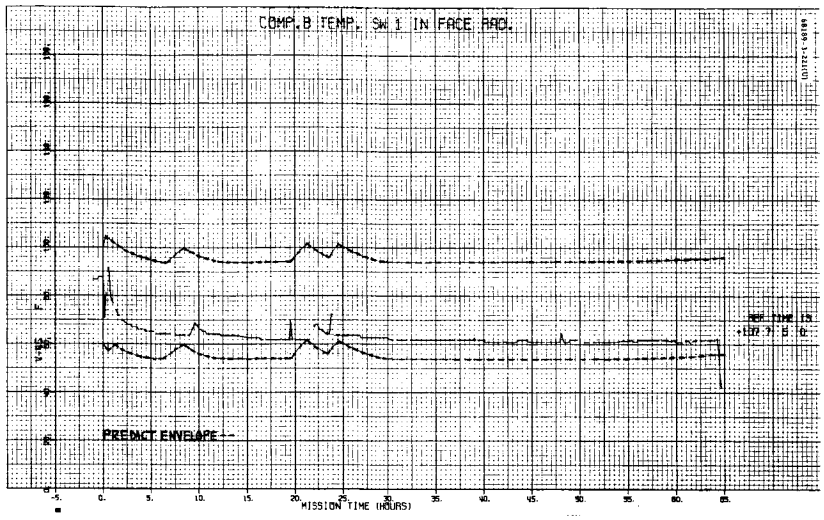

Figure 5.1-85. Compartment B Temperature Switch 1 in Face Radiator

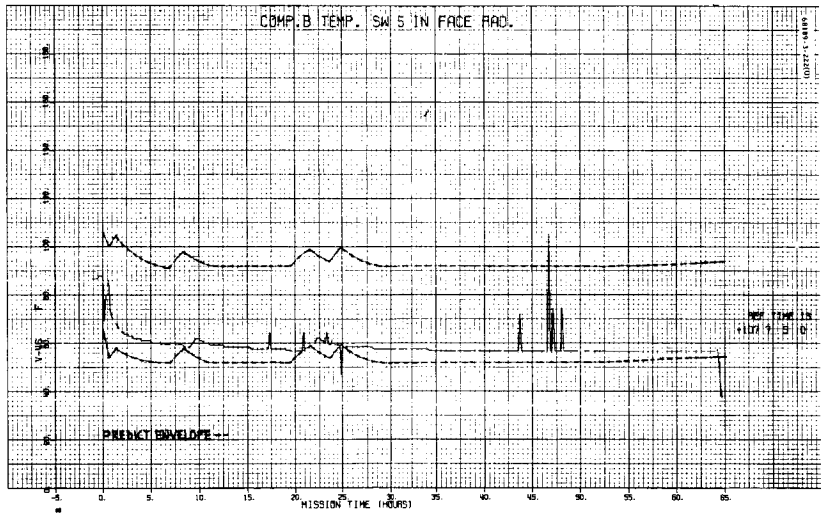

Figure 5.1-86. Compartment B Temperature Switch 5 in Face Radiator

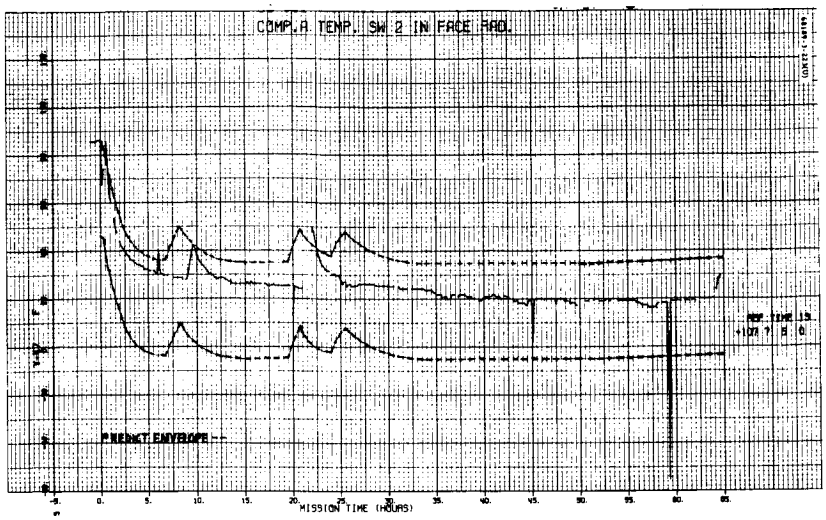

Figure 5.1-87. Compartment A Temperature Switch 2 in Face Radiator

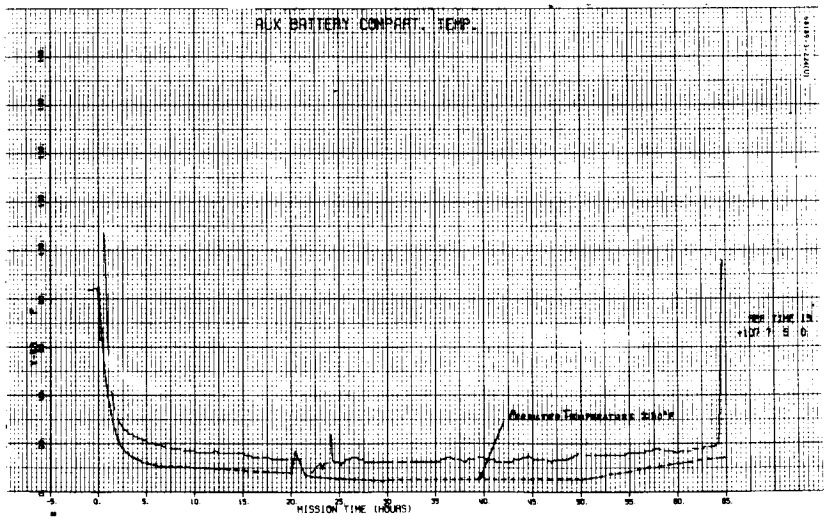

Figure 5.1-88. Auxiliary Battery Compartment Temperature

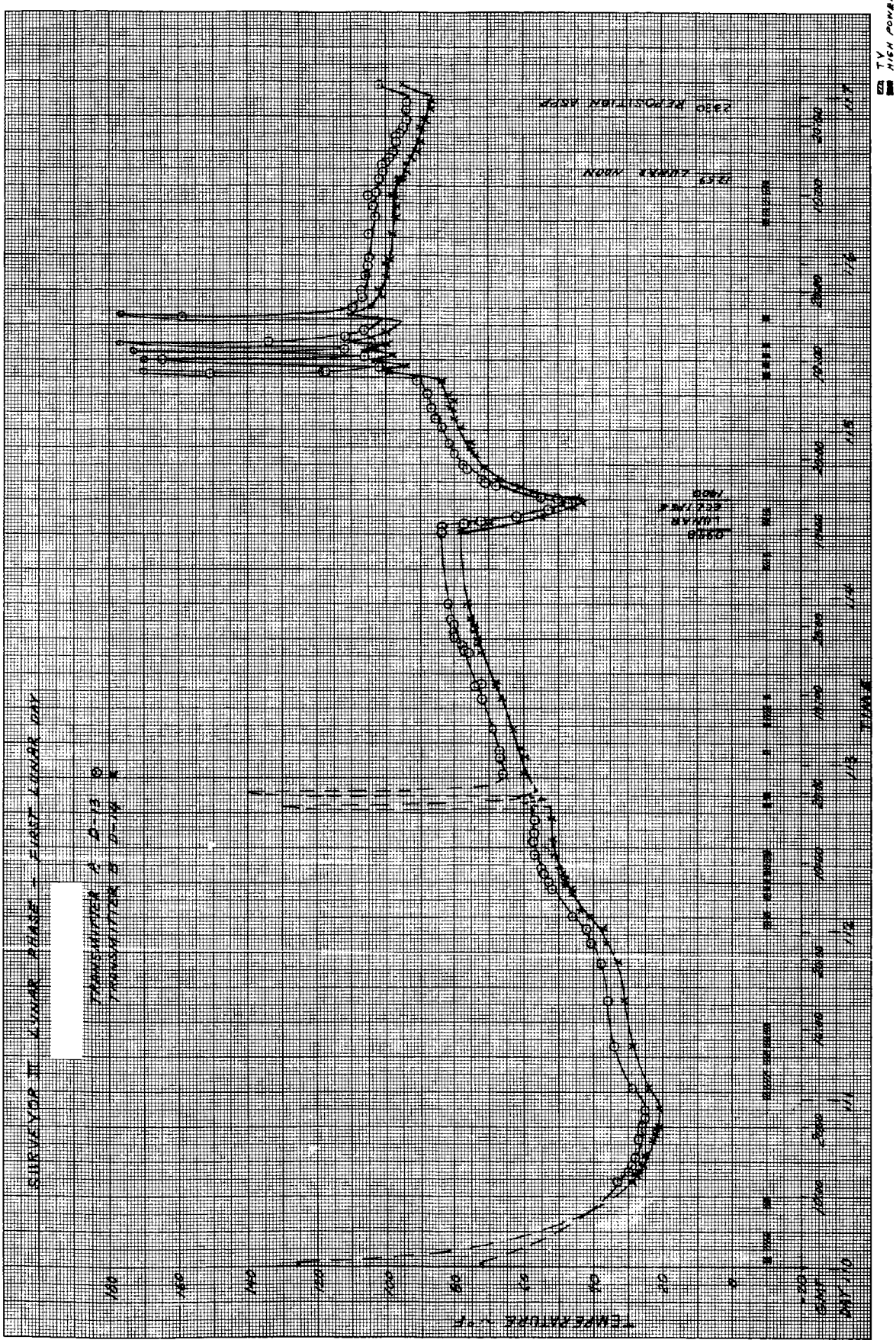

a) Day 110 to 117

Figure 5.1-89. Transmitter A and B Temperatures

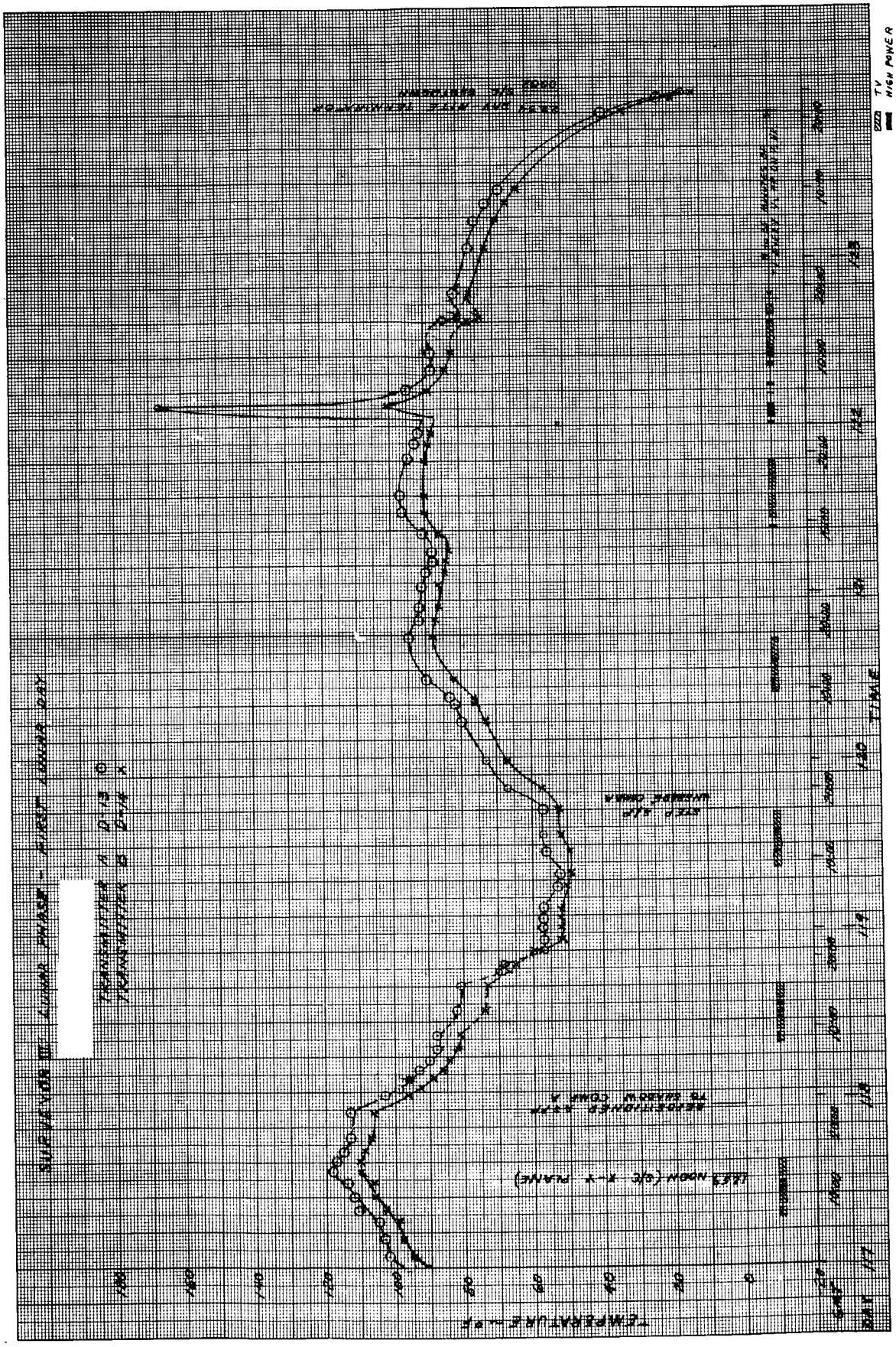

b) Day 117 to 124

Figure 5.1-89 (continued). Transmitter A and B Temperatures

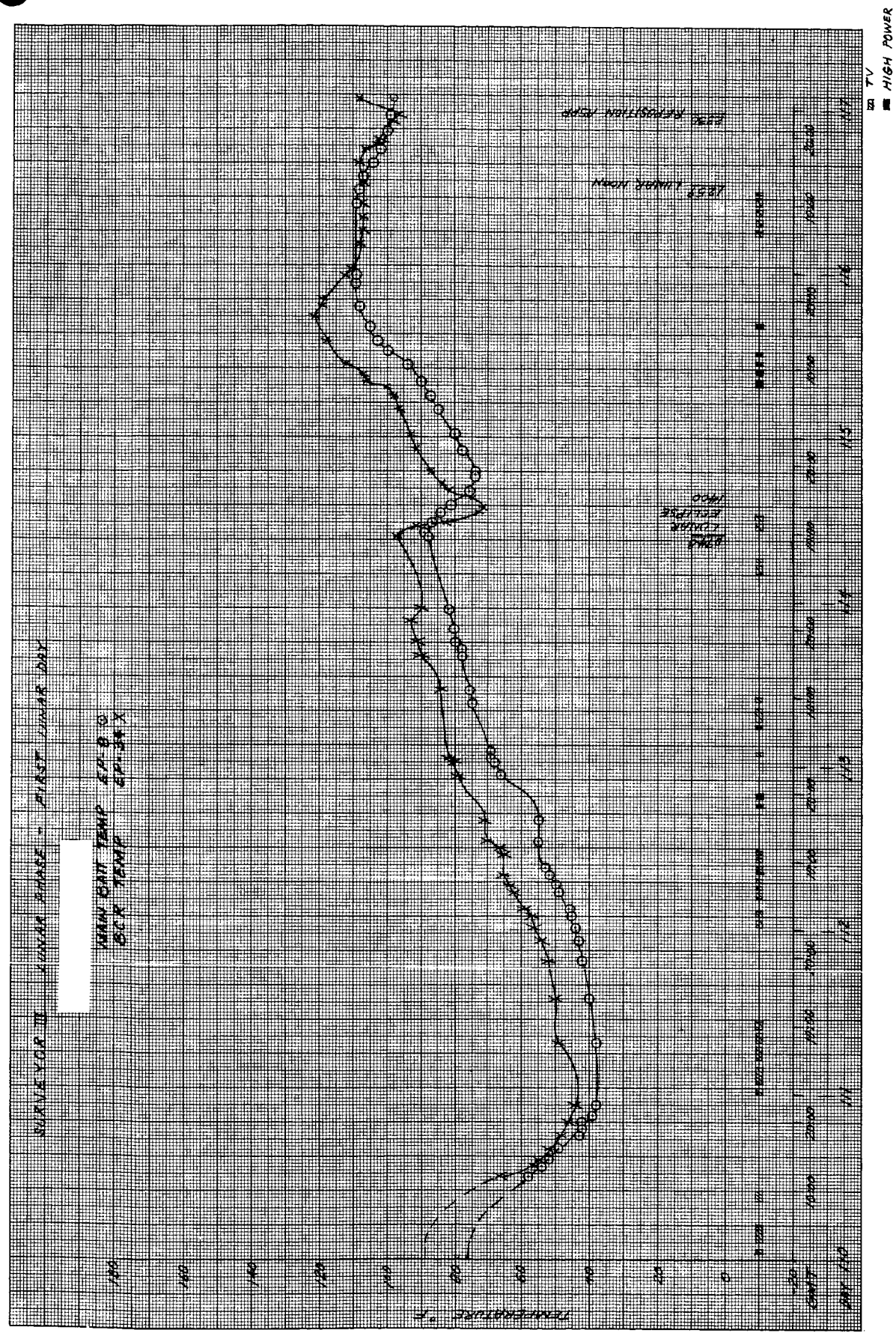

a) Day 110 to 117

Figure 5.1-90(continued). Battery and BCR Temperatures

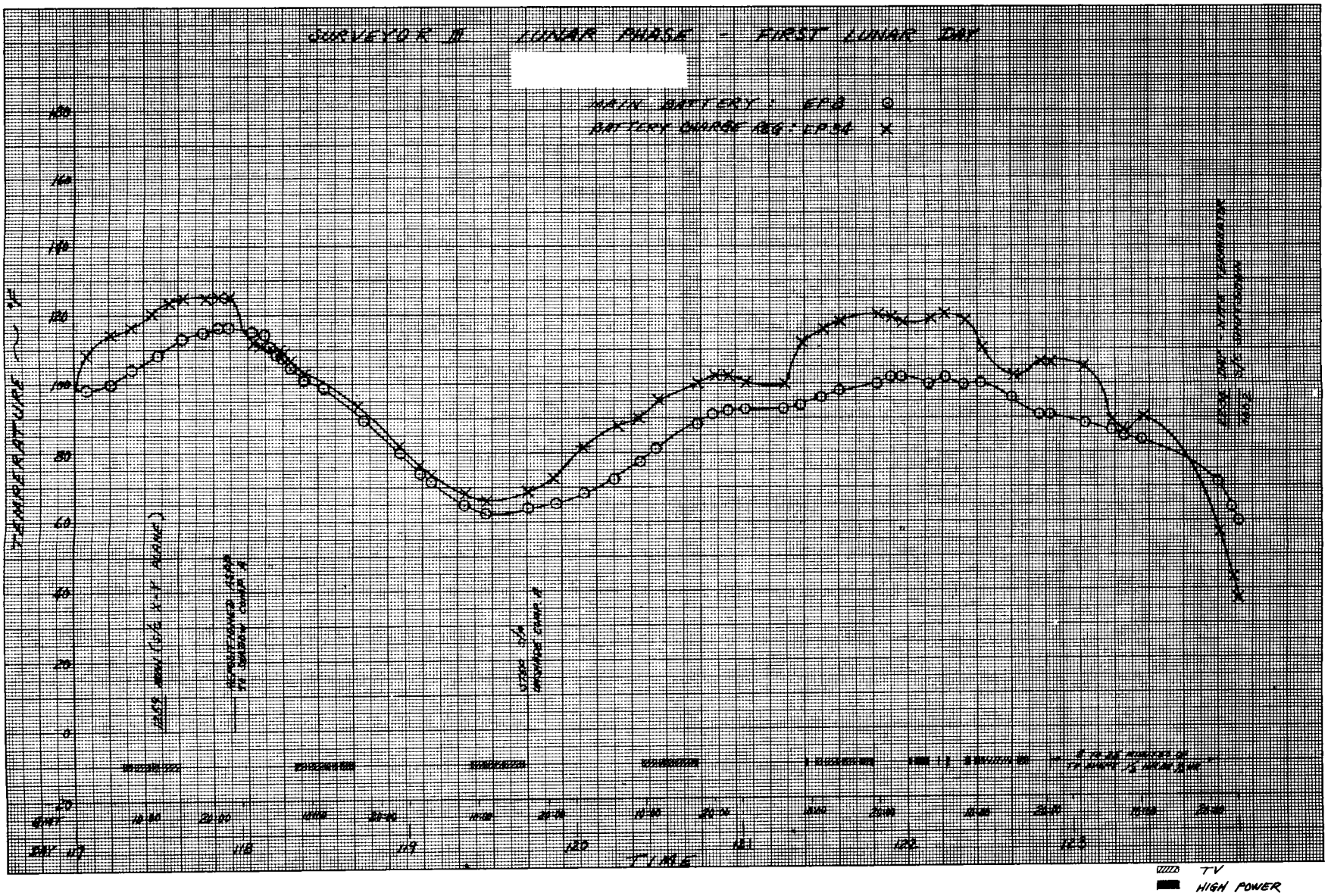

b) Day 117 to 124

Figure 5.1-90. Battery and BCR Temperatures

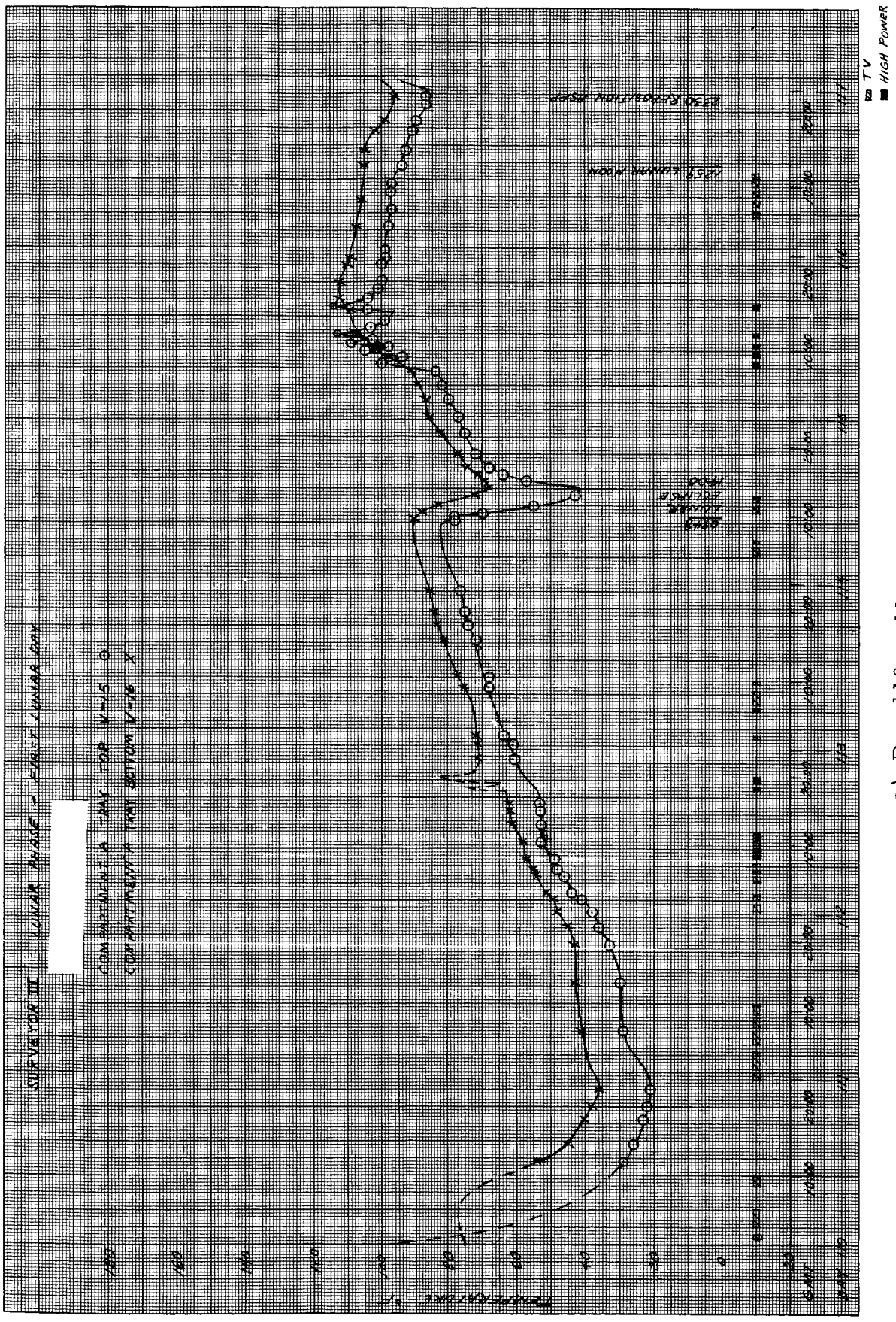

a) Day 110 to 117

Figure 5.1-91. A Tray Top and Bottom Temperatures

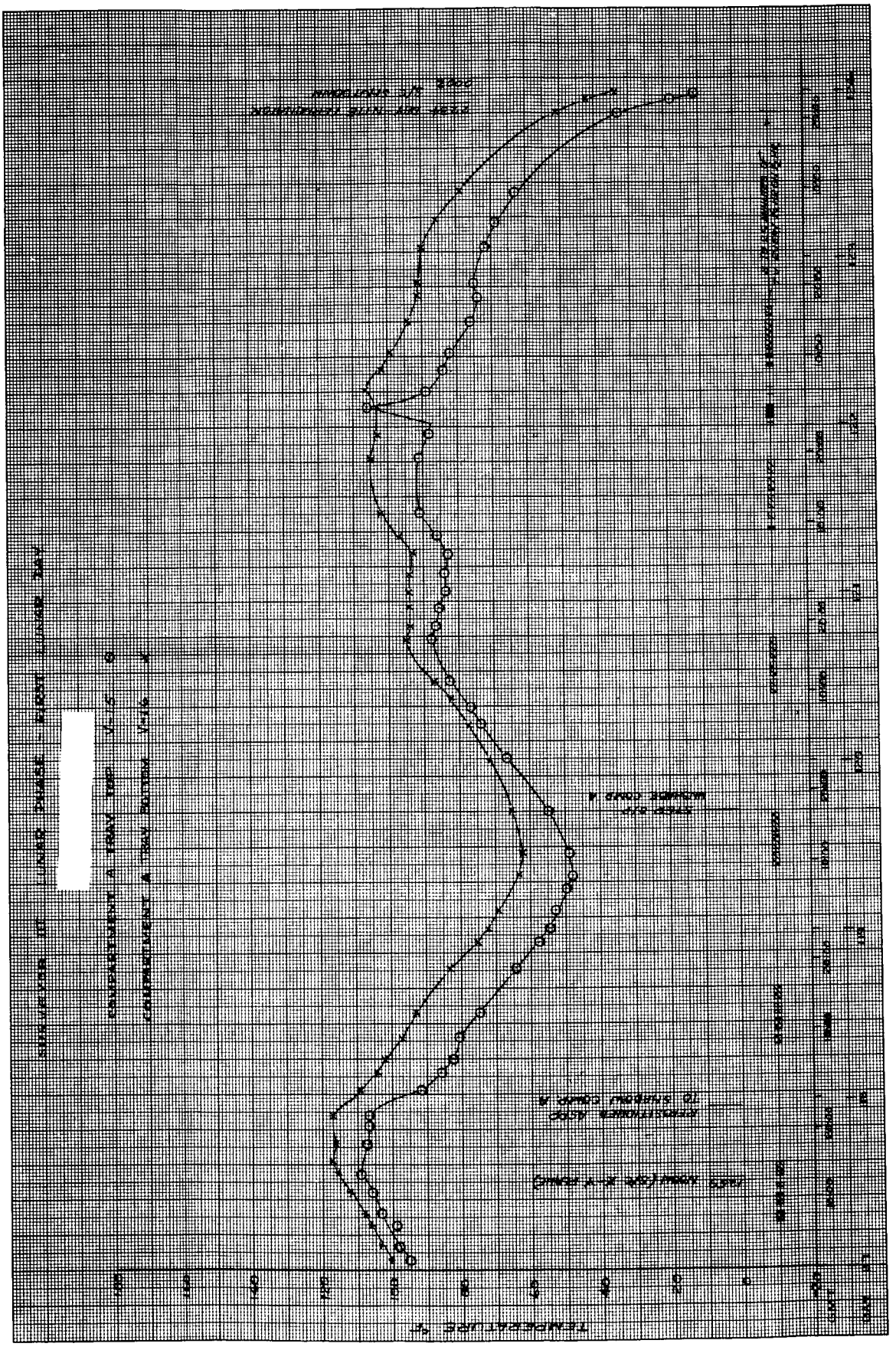

b) Day 117 to 124

Figure 5.1-91(continued). A Tray Top and Bottom Temperatures

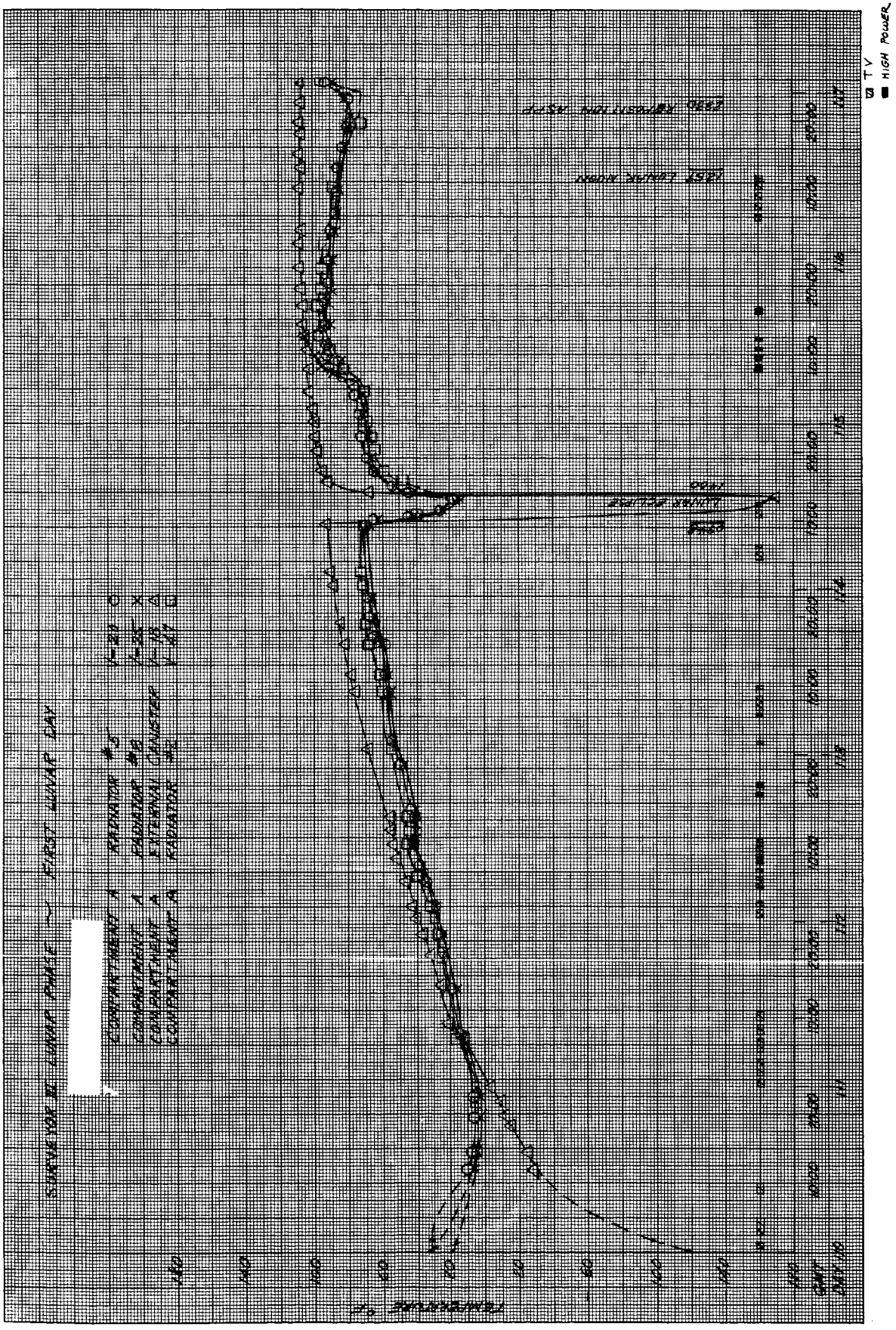

a) Day 110 to 117

Figure 5.1-92. Compartment A Temperatures

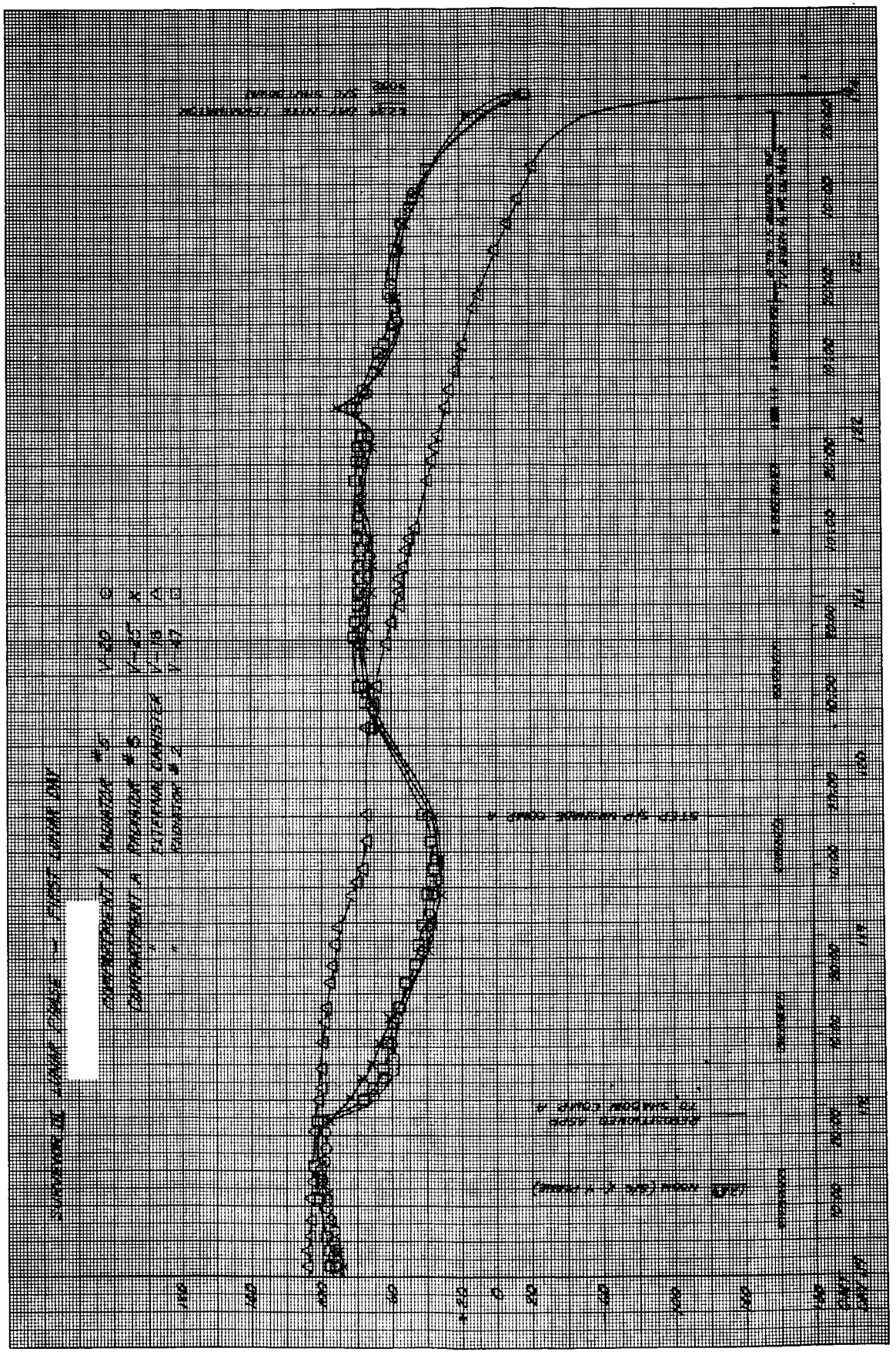

b) Day 117 to 124

Figure 5.1-92(continued). Compartment A Temperatures

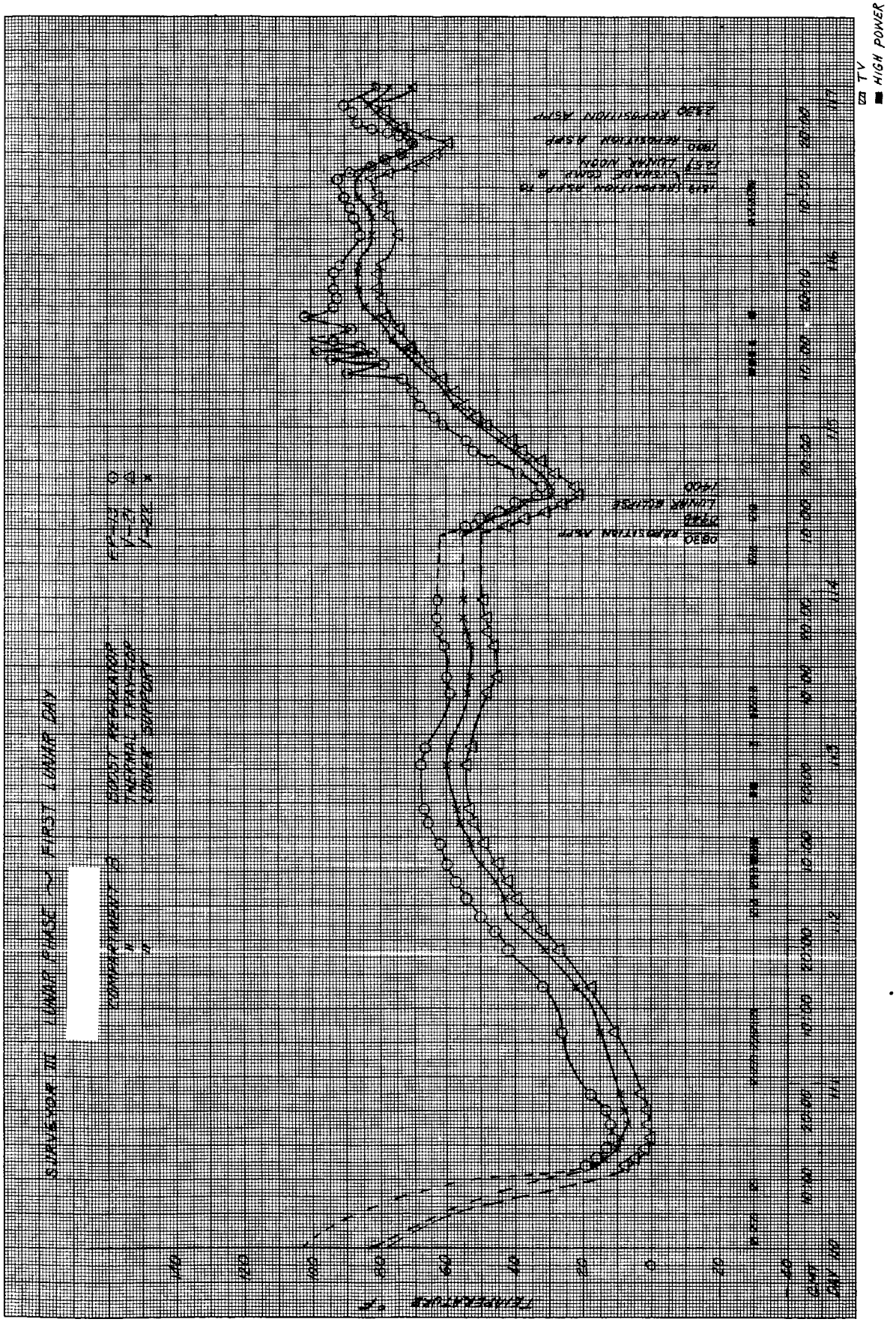

a) Day 110 to 117

Figure 5.1-93. Compartment B Temperatures I

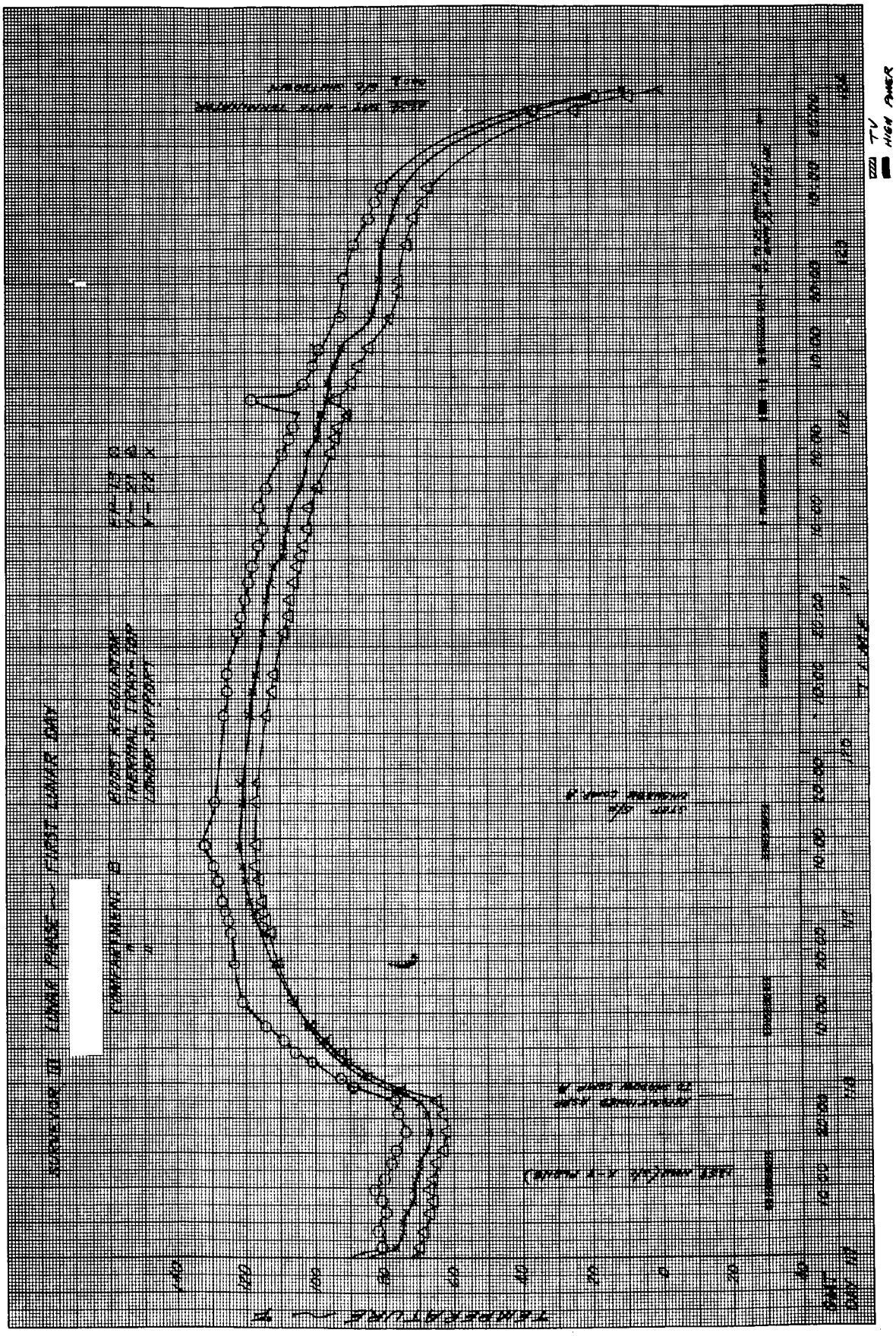

b) Day 117 to 124

Figure 5.1-93(continued). Compartment B Temperatures I

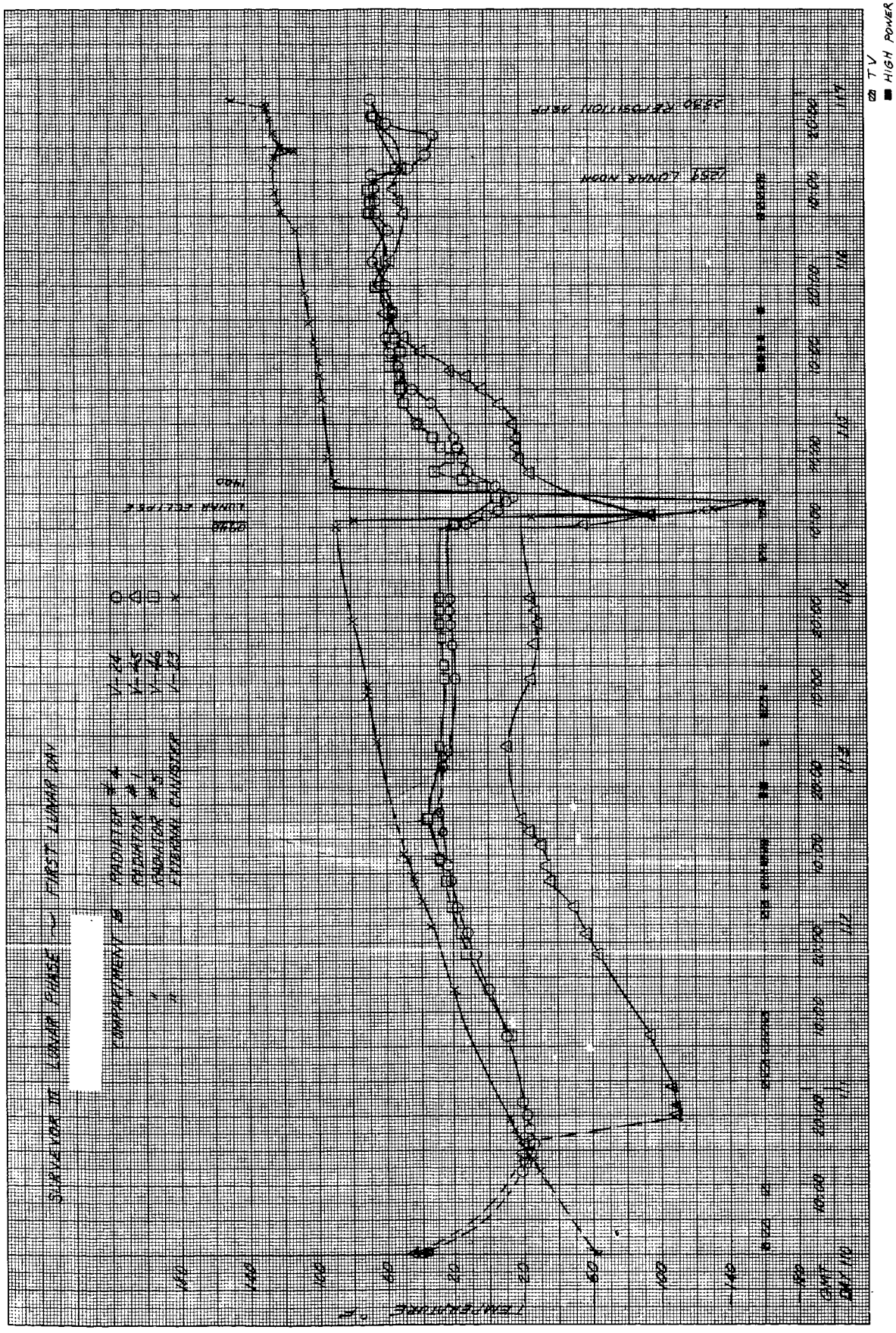

a) Day 110 to 117

Figure 5.1-94. Compartment B Temperatures II

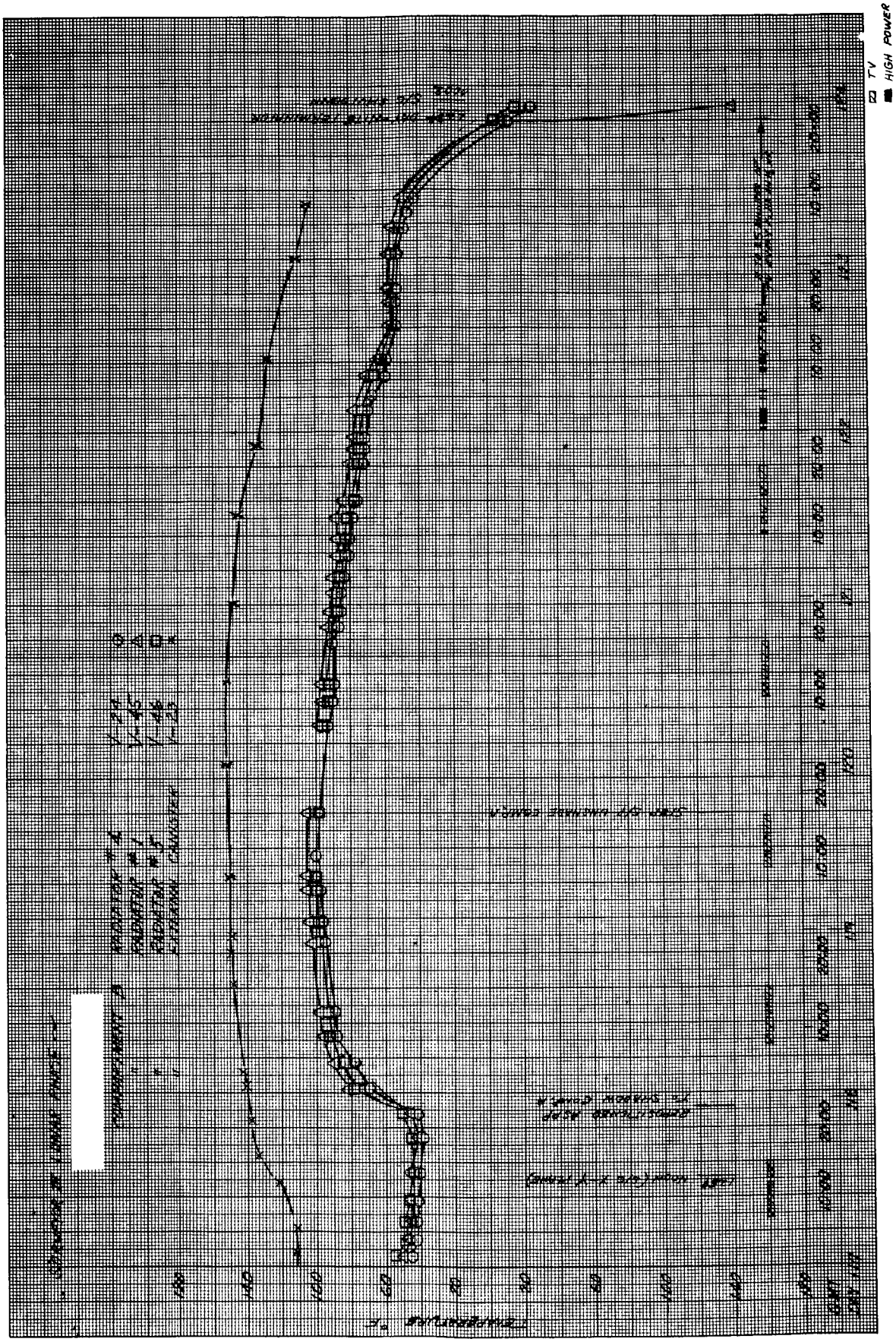

b) Day 117 to 124

Figure 5.1-94(continued). Compartment B Temperatures II

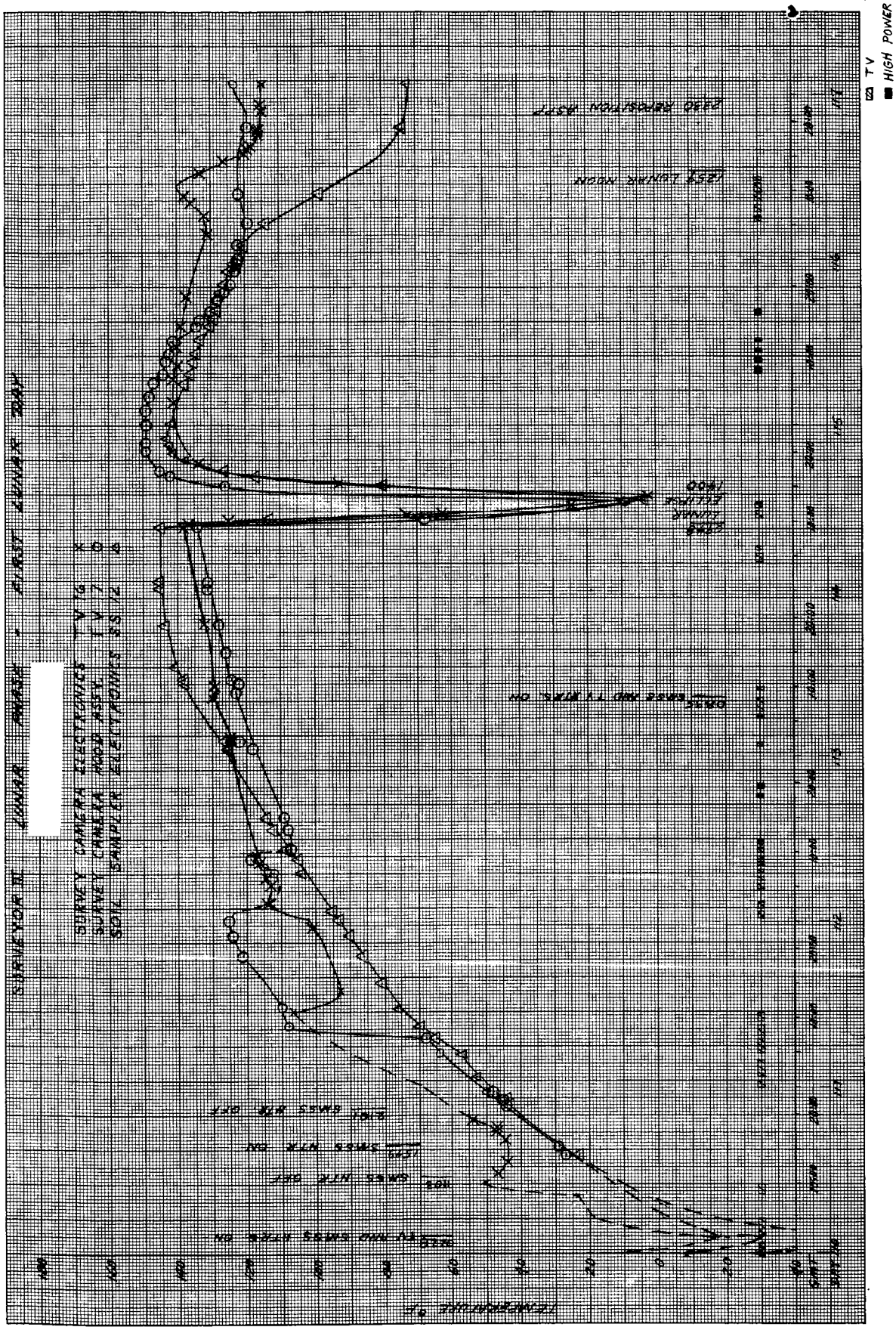

a) Day 110 to 117

Figure 5.1-95(continued). Surface Sampler and TV Camera Temperatures

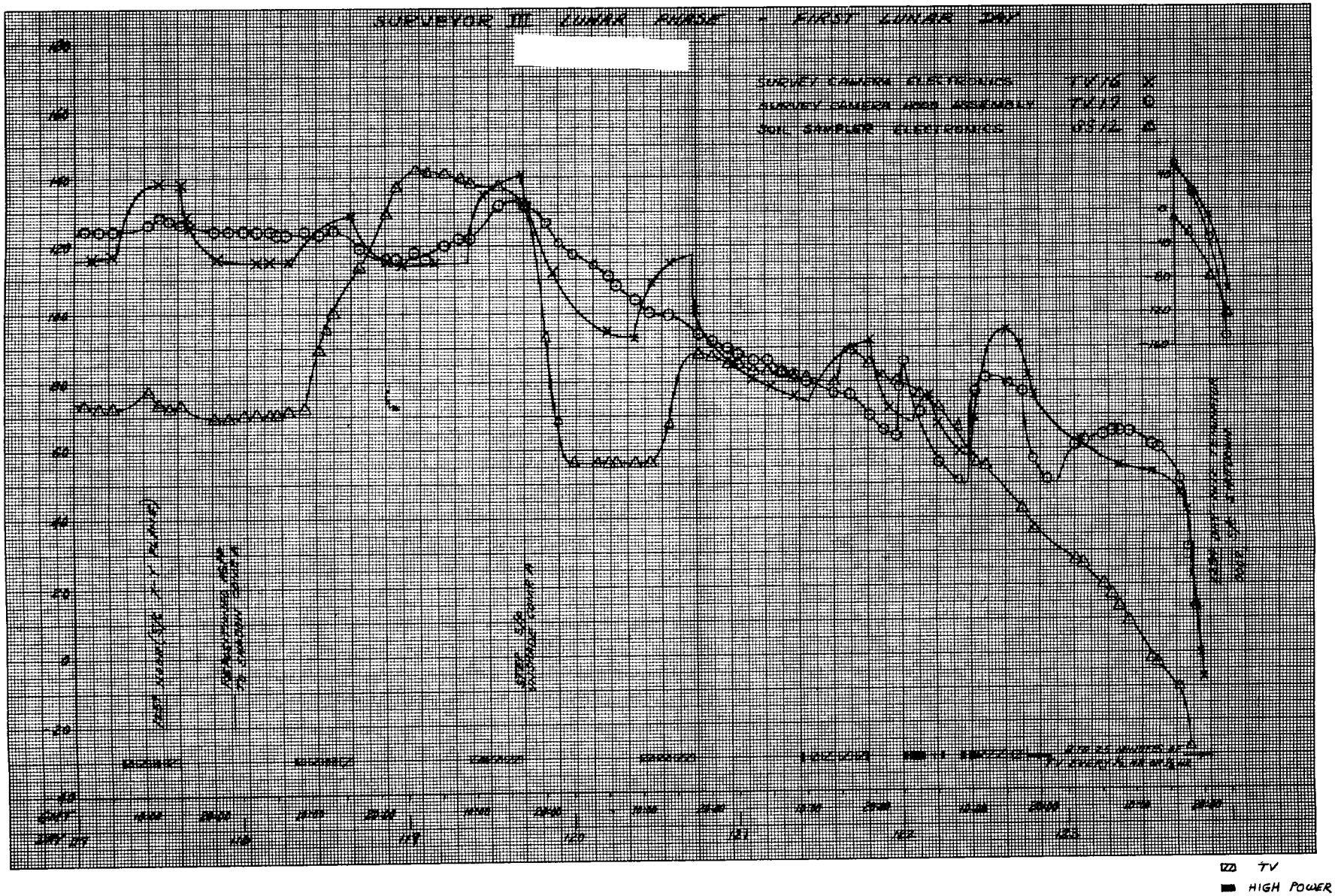

b) Day 117 to 124

Figure 5.1-95. Surface Sampler and TV Camera Temperatures

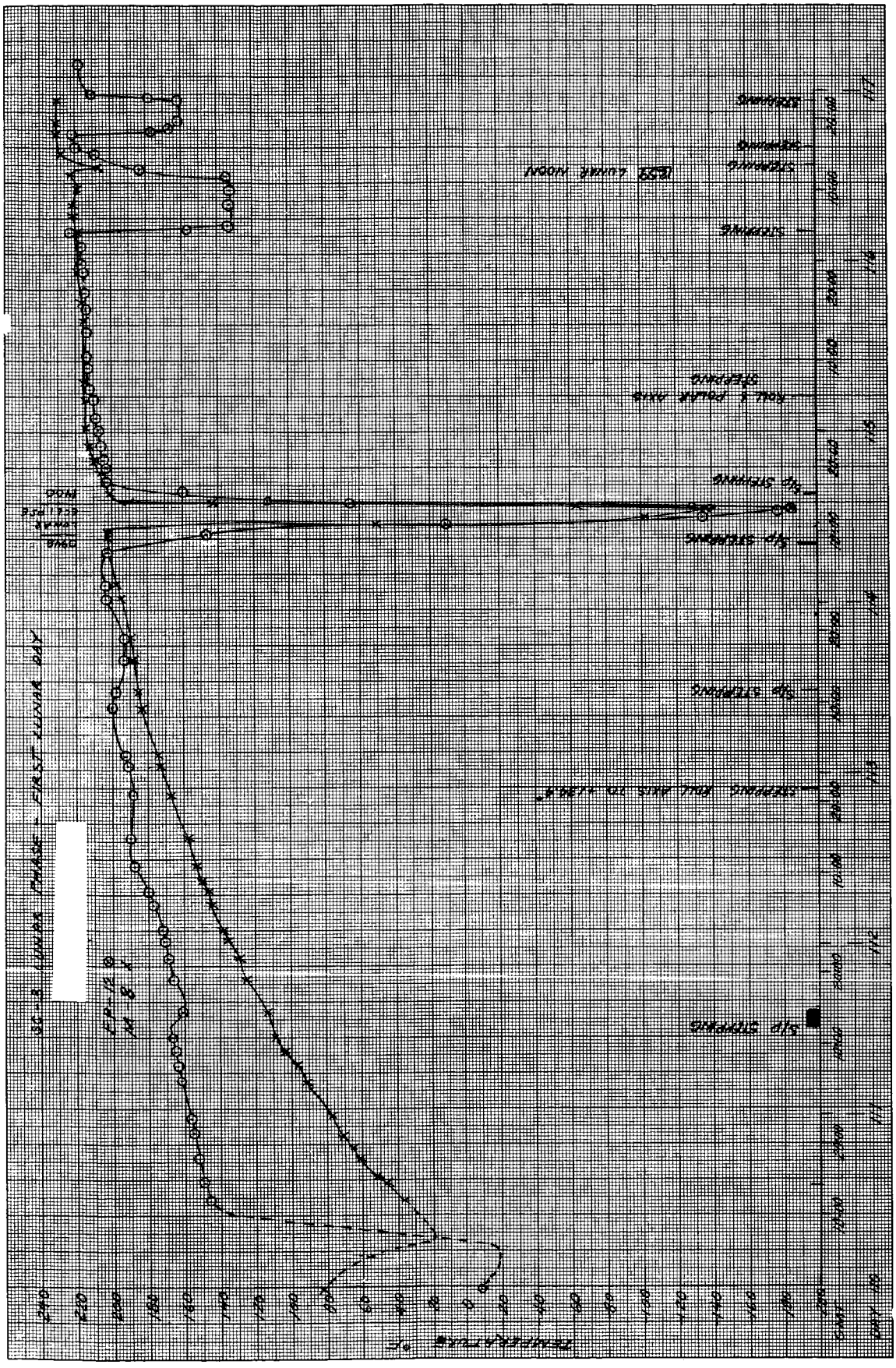

a) Day 110 to 117

Figure 5.1-96. Solar Panel and Planar Array Temperatures

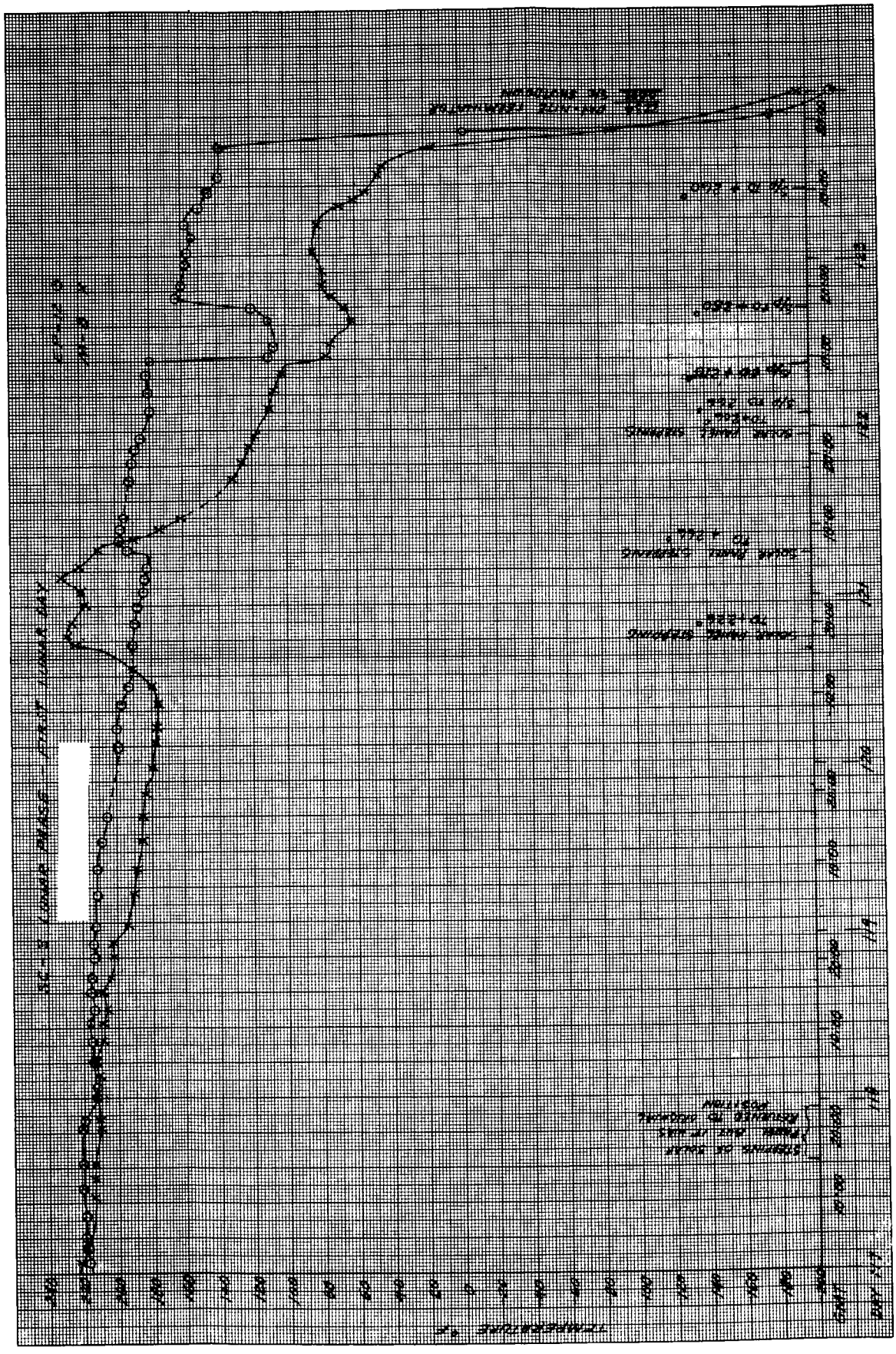

b) Day 117 to 124

Figure 5.1-96(continued). Solar Panel Planar Array Temperatures

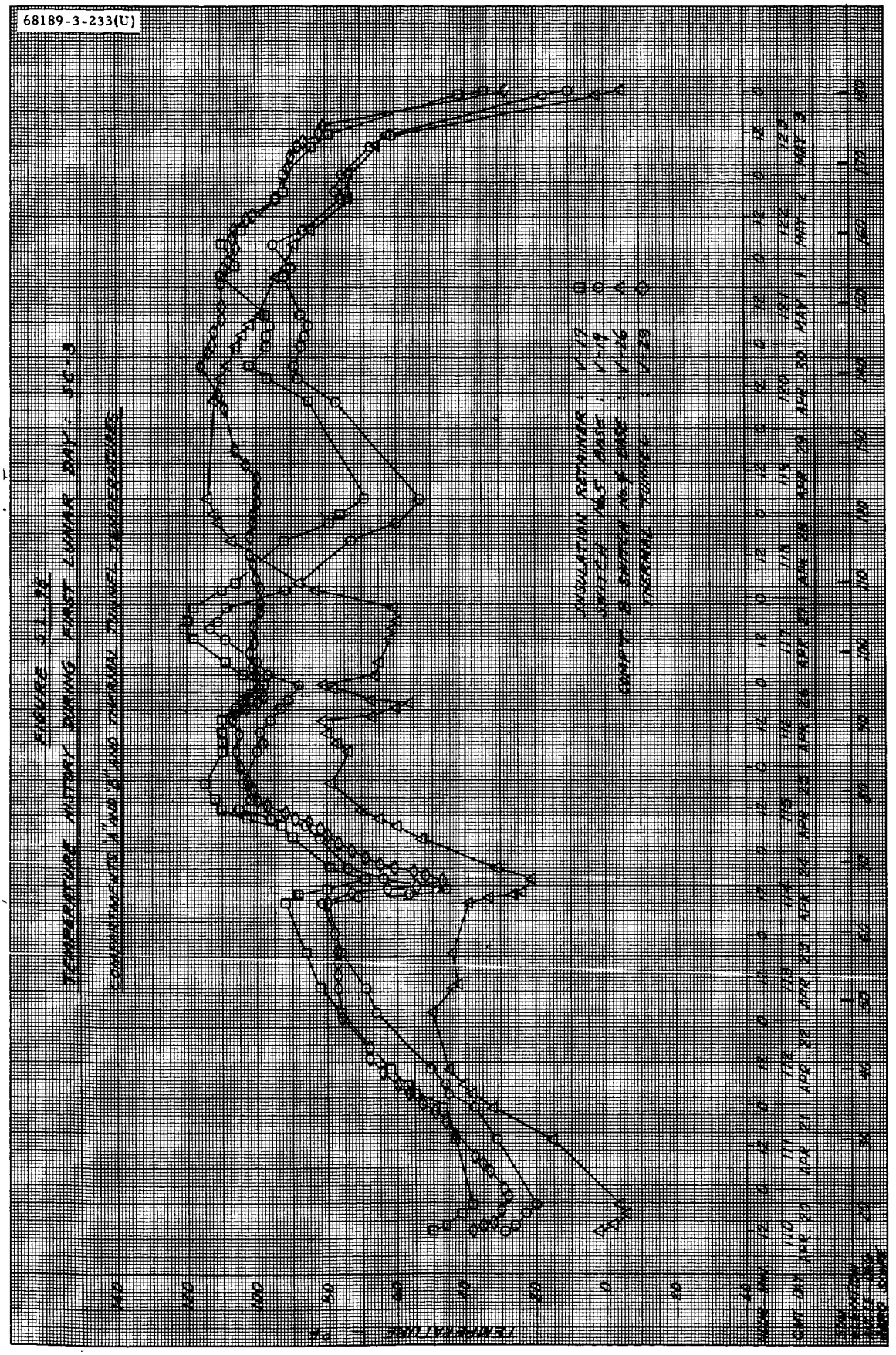

Figure 5.1-97. Compartments A and B and Thermal Tunnel Temperatures

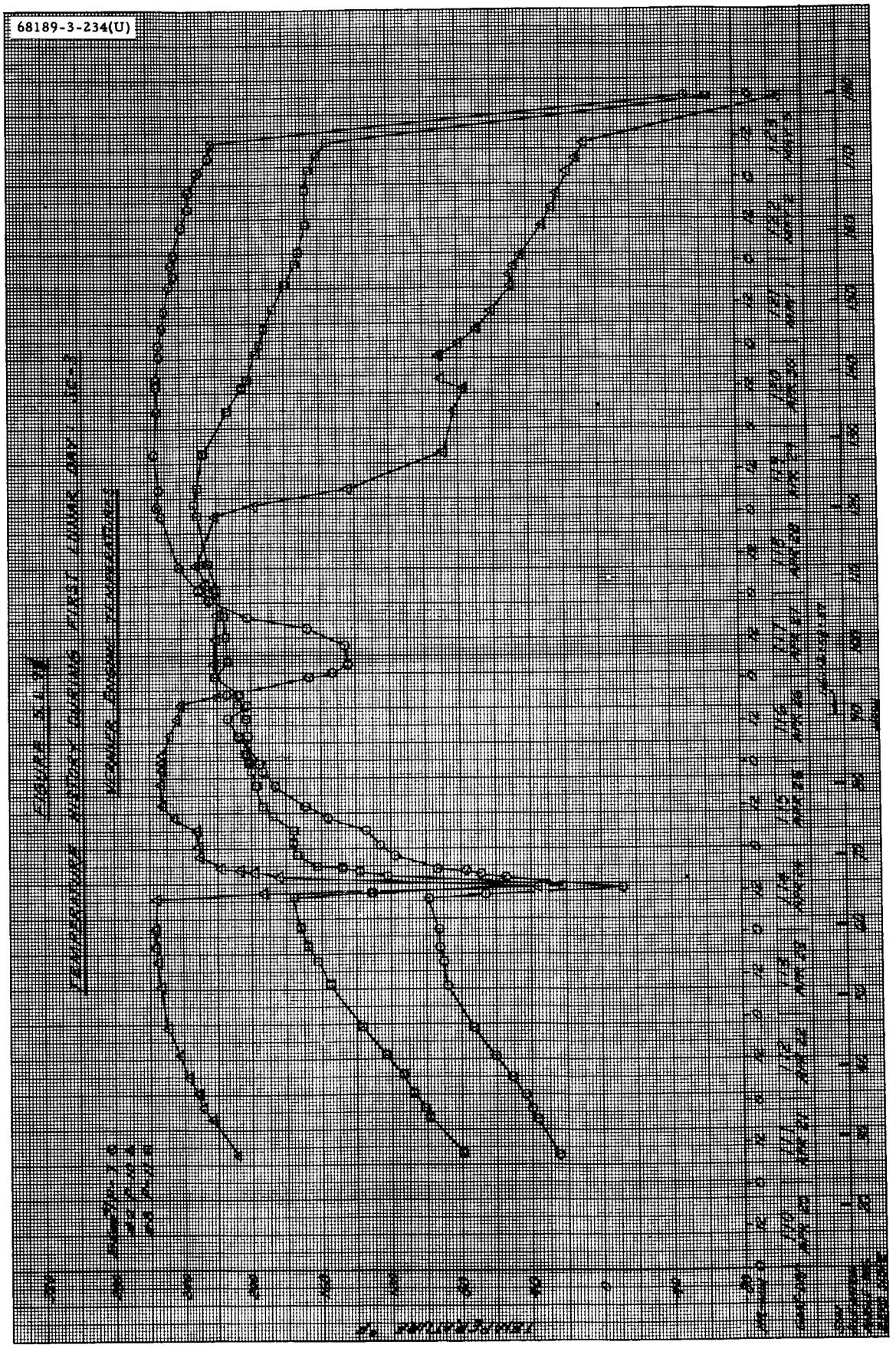

Figure 5.1-98. Vernier Engine Temperatures

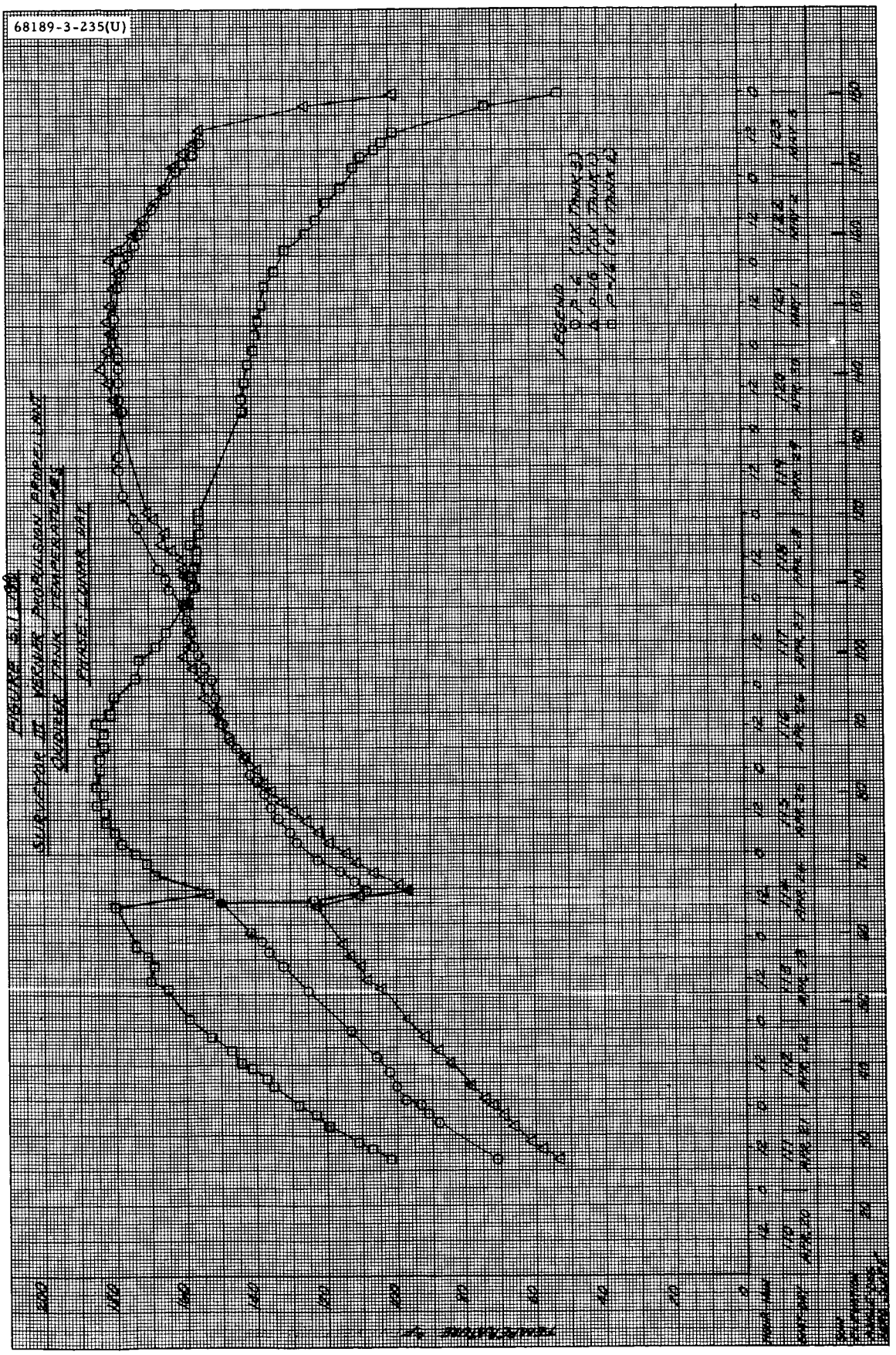

Figure 5.1-99. Vernier Propulsion Propellant Oxidizer Tank Temperatures

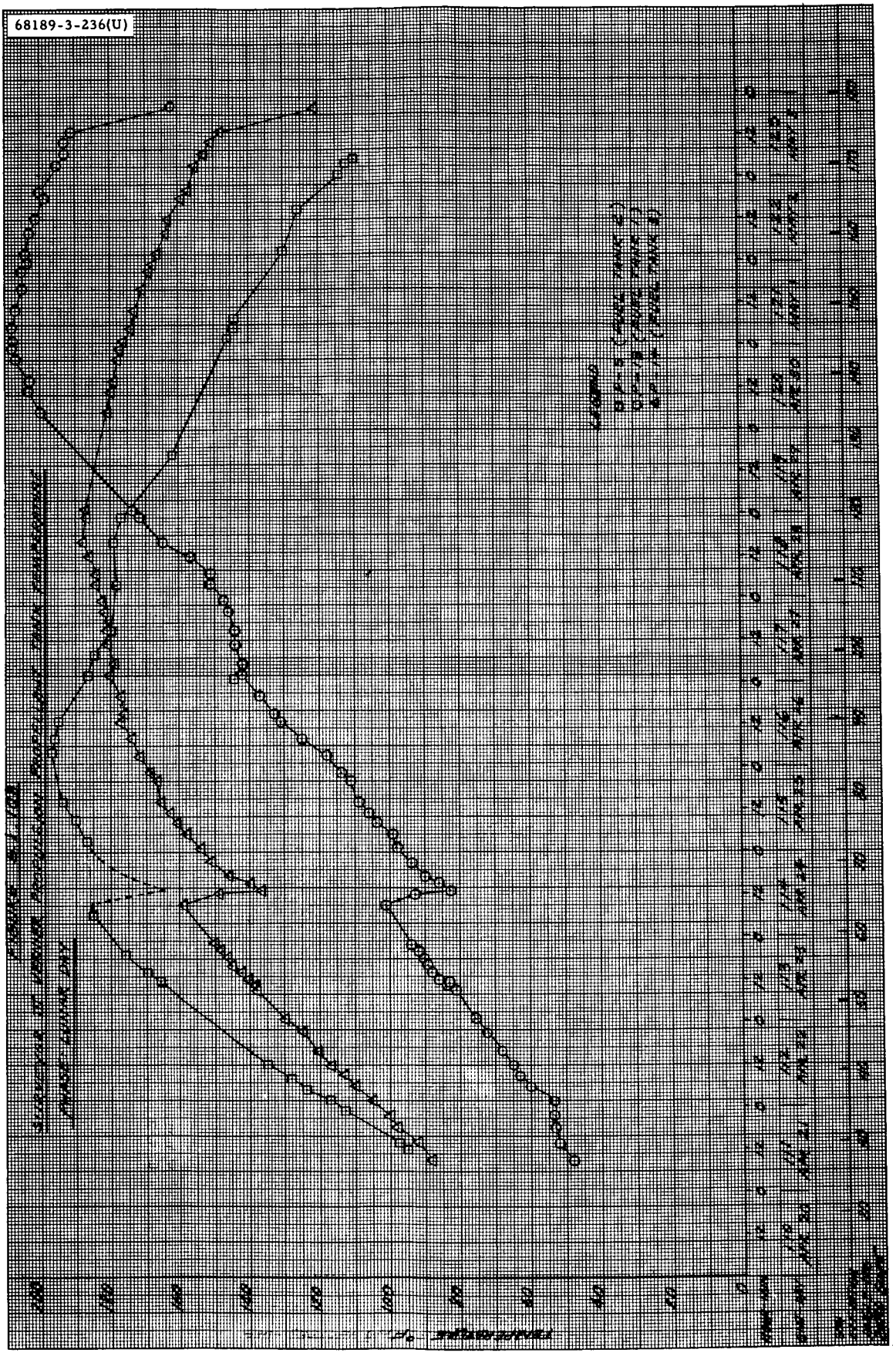

Figure 5.1-100. Vernier Propulsion Propellant Tank Temperature

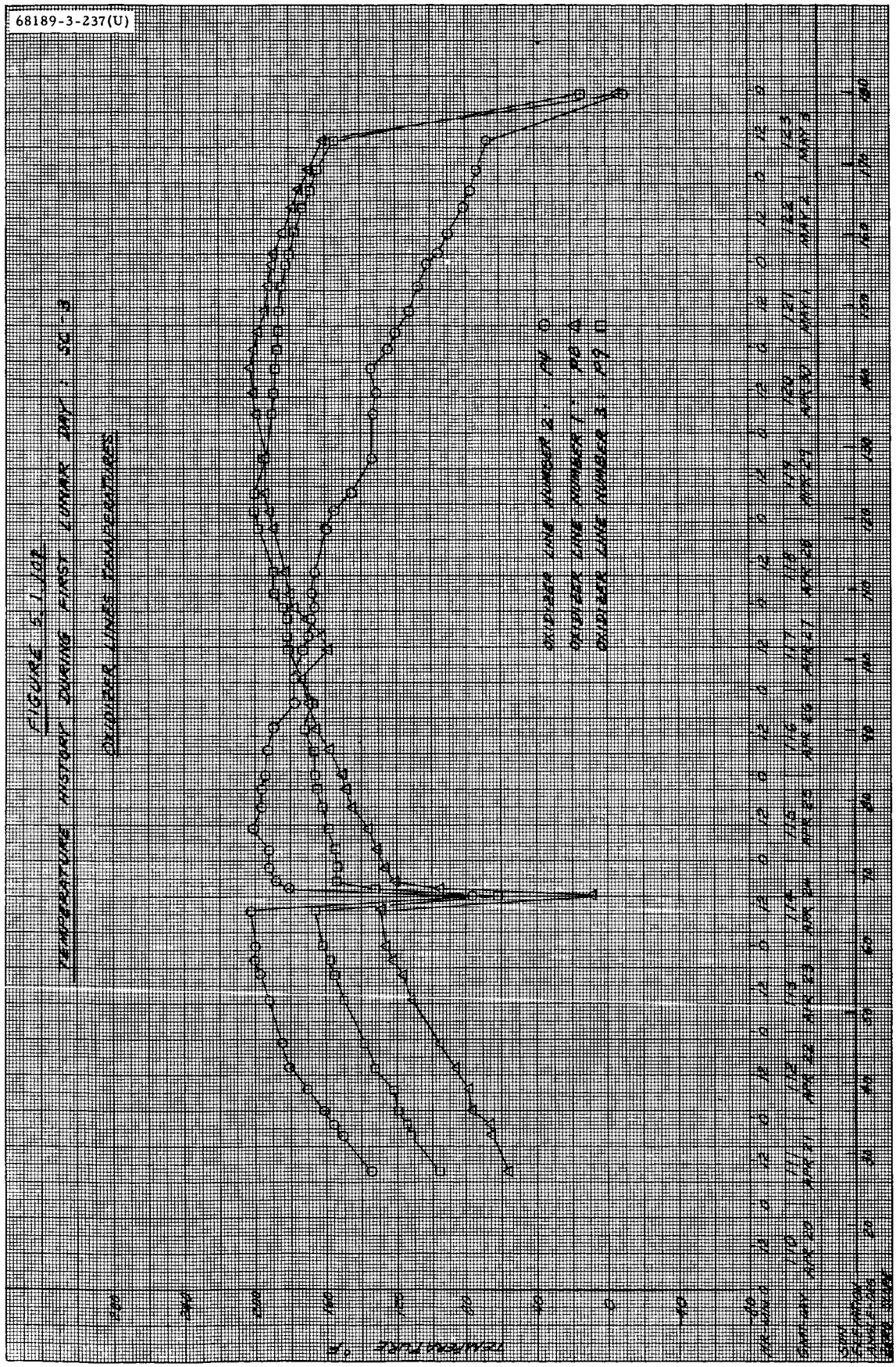

Figure 5.1-101. Oxidizer Lines Temperatures

68189-3-238(U)

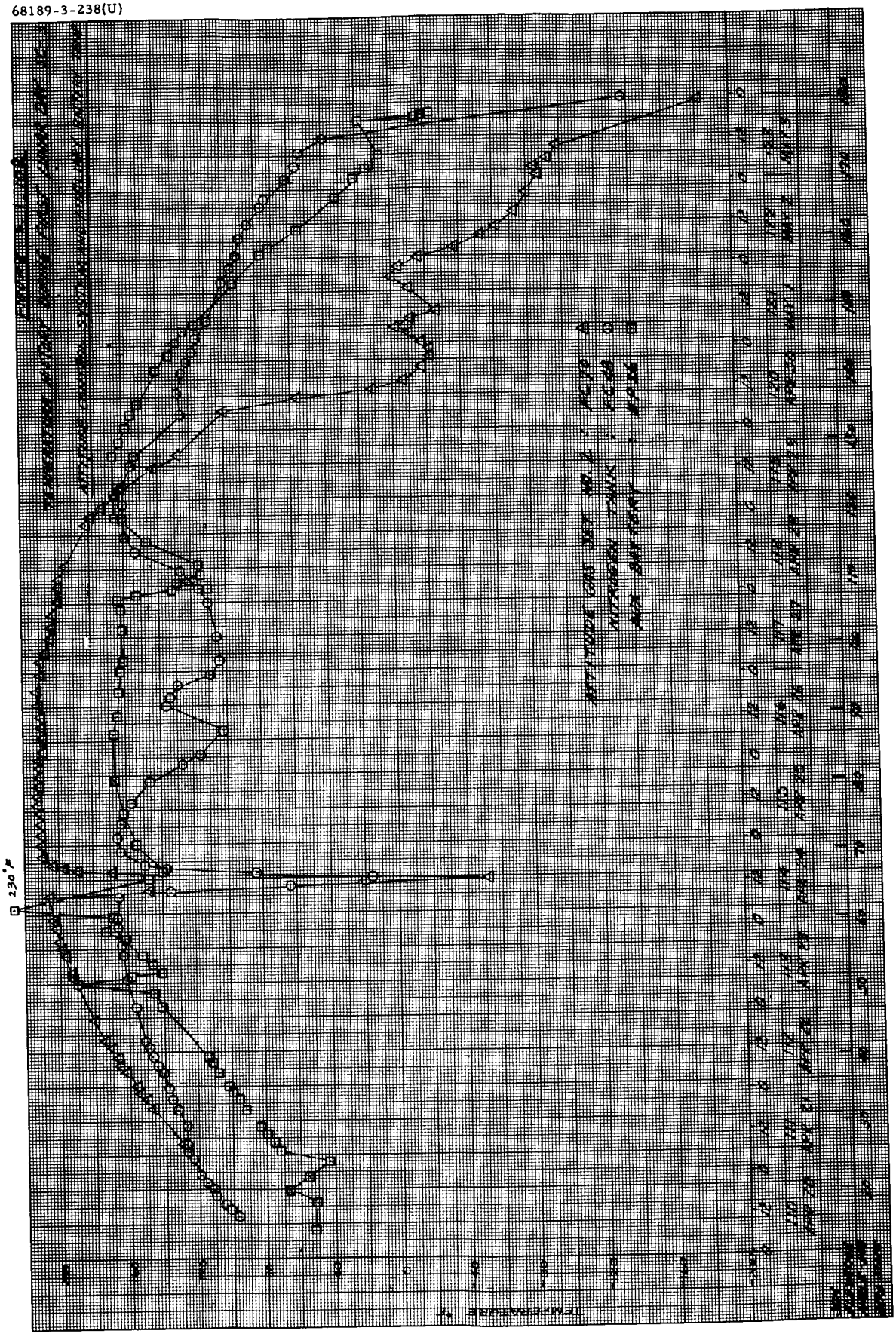

Figure 5.1-102. Attitude Control System and Auxiliary Battery Temperature

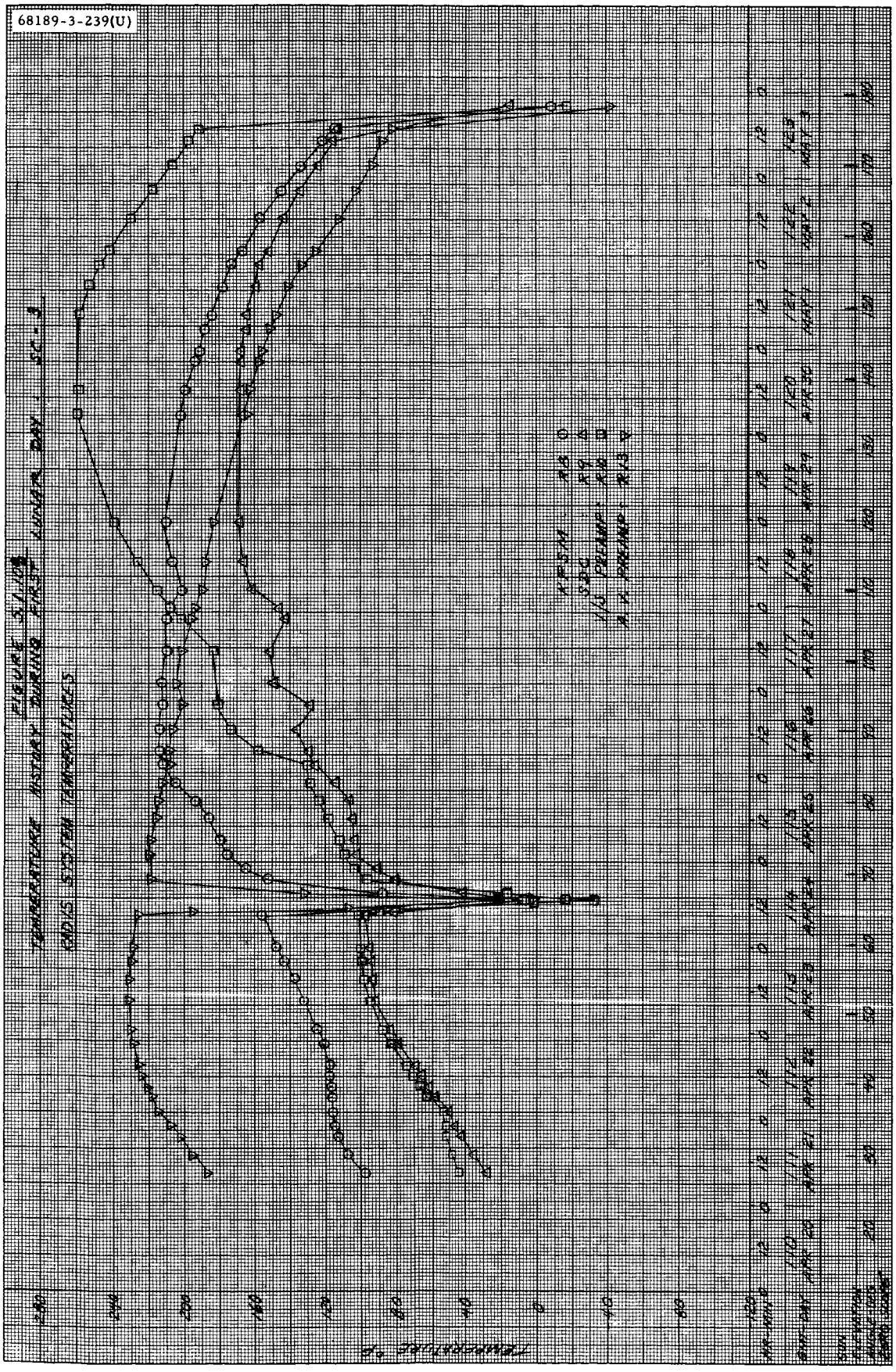

Figure 5.1-103. RADVS System Temperatures

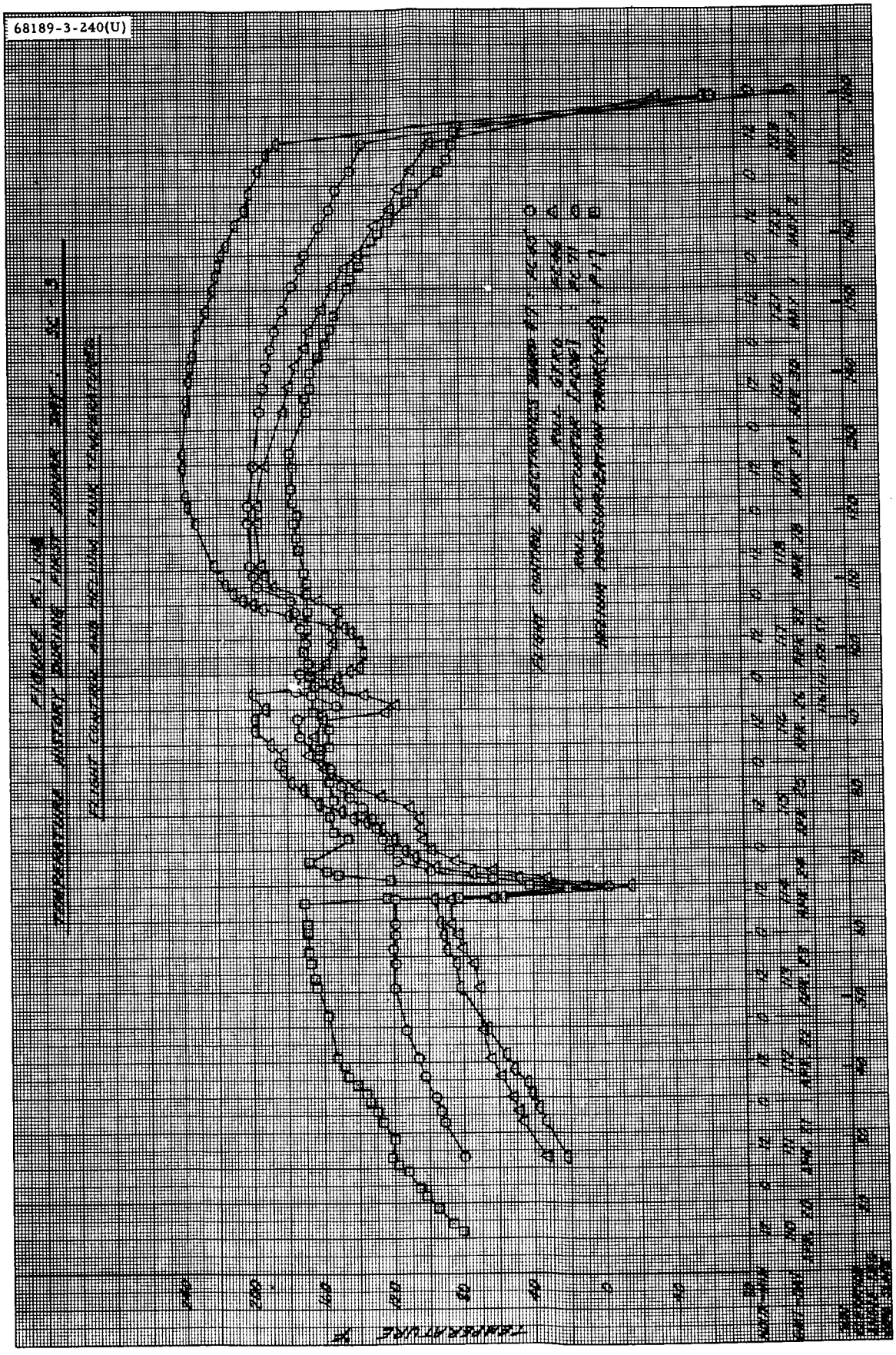

Figure 5.1-104. Flight Control and Helium Tank Temperatures

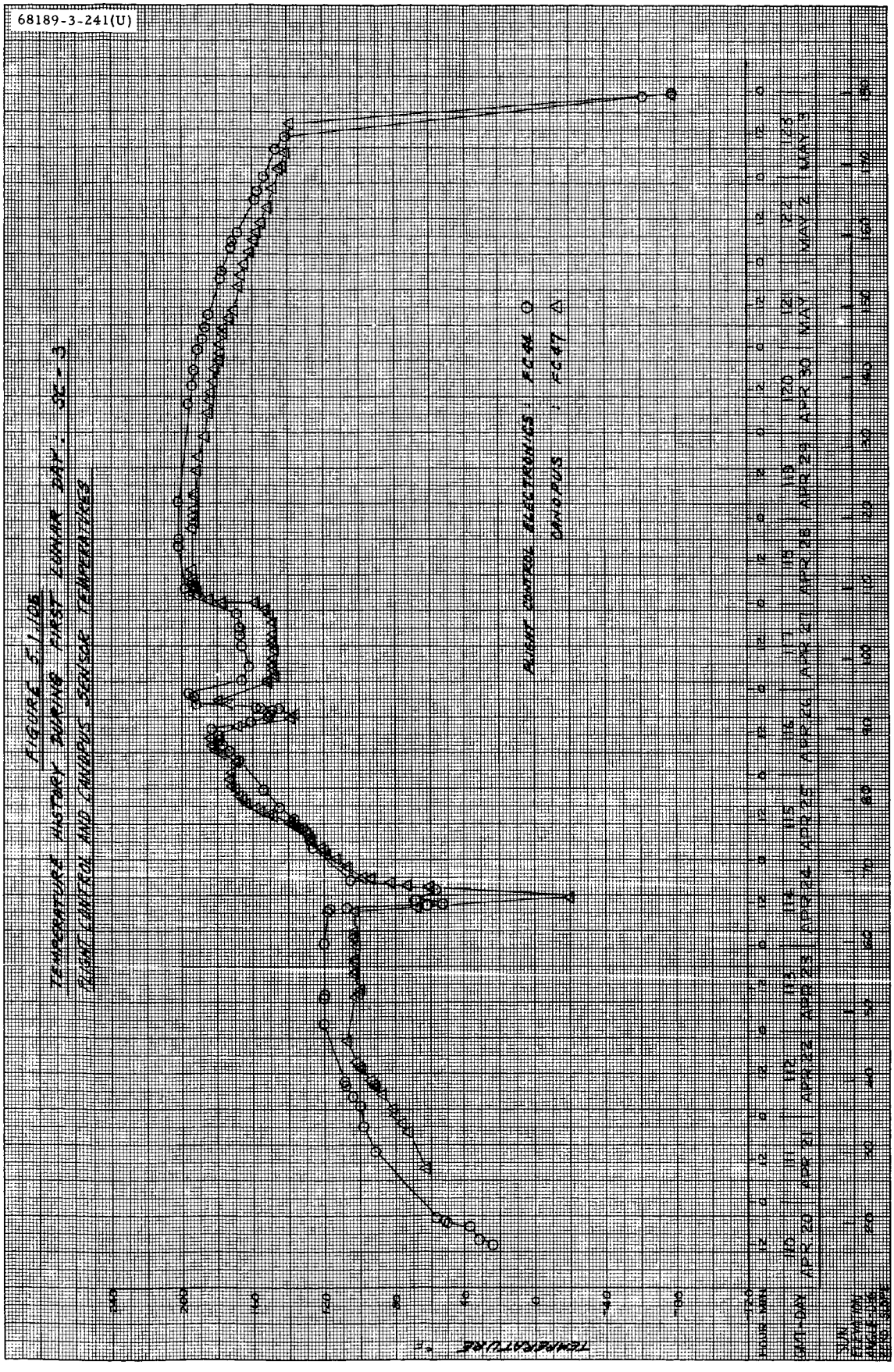

Figure 5.1-105. Flight Control and Canopus Sensor Temperatures

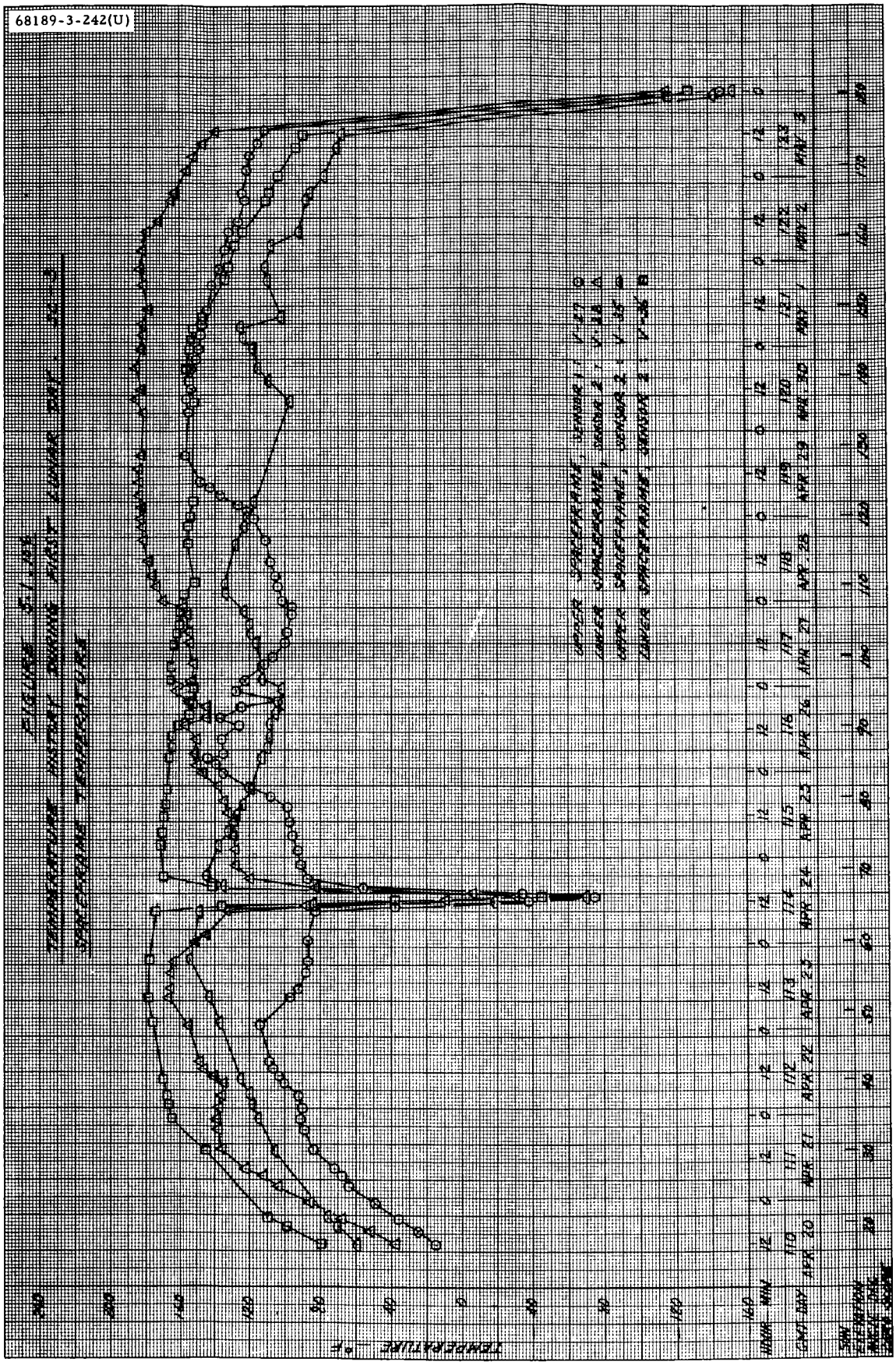

Figure 5.1-106. Spaceframe Temperatures

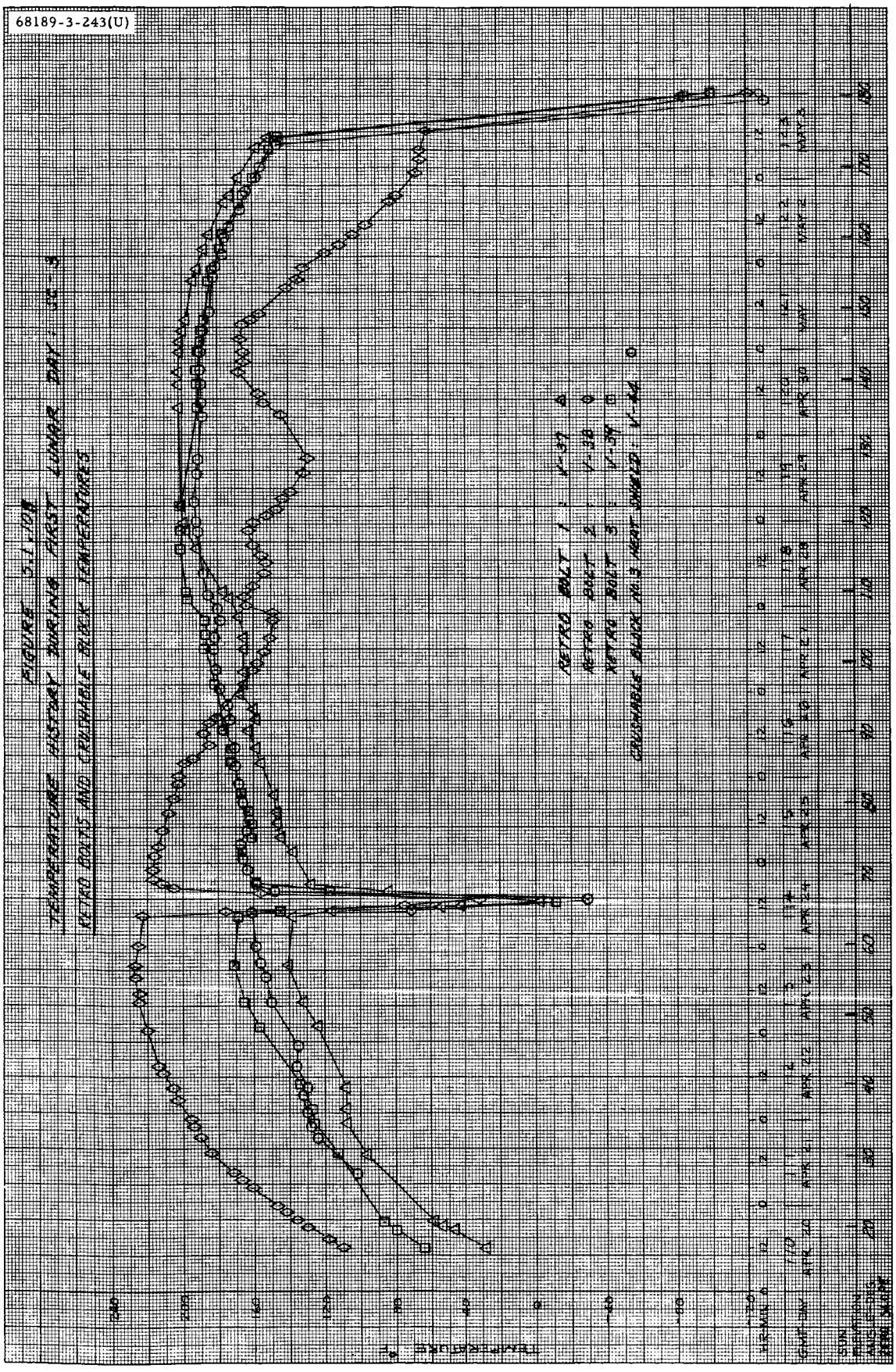

Figure 5.1-107. Retro Block and Crushable Block Temperatures

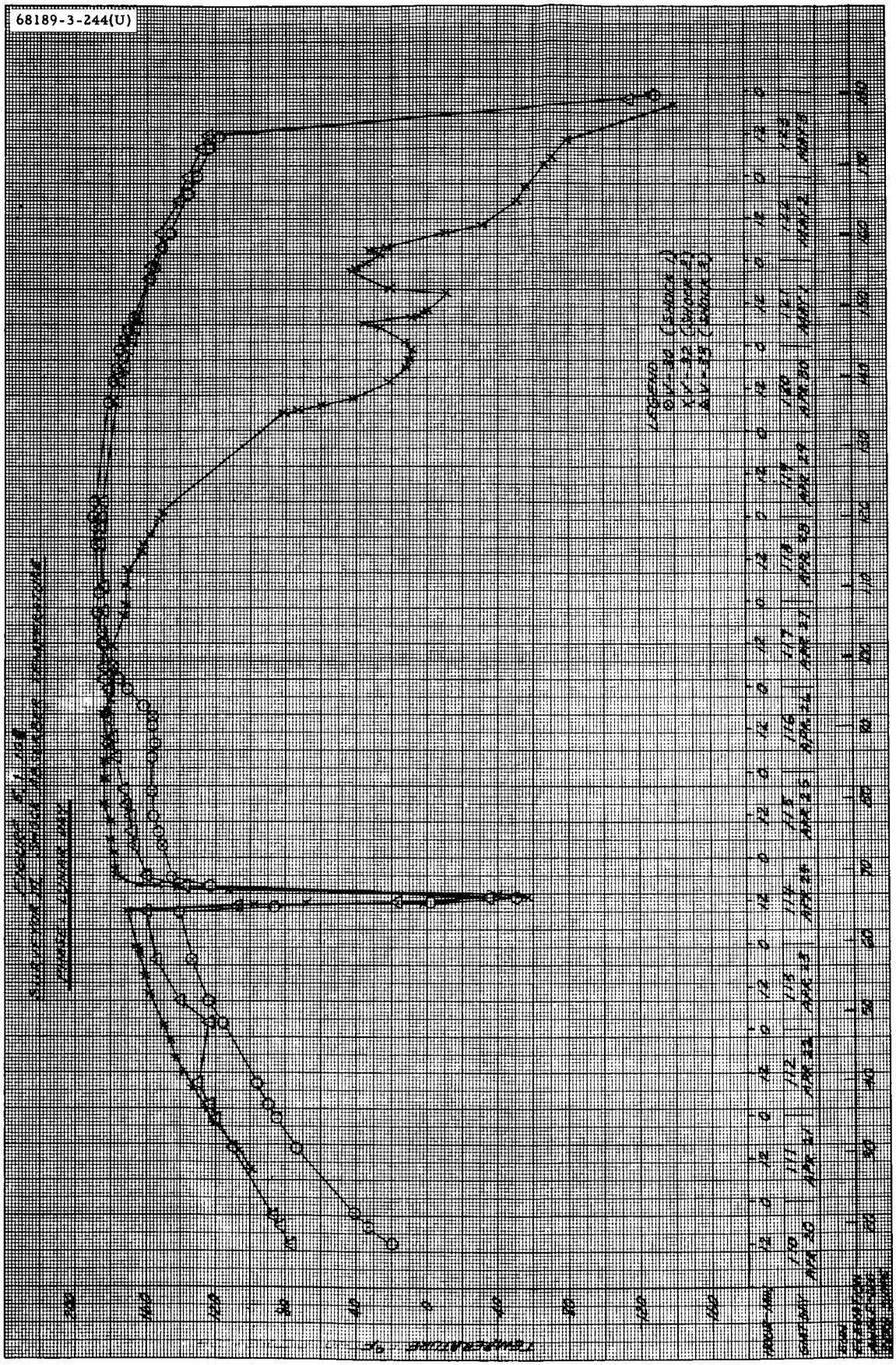

Figure 5.1-108. Shock Absorber Temperature

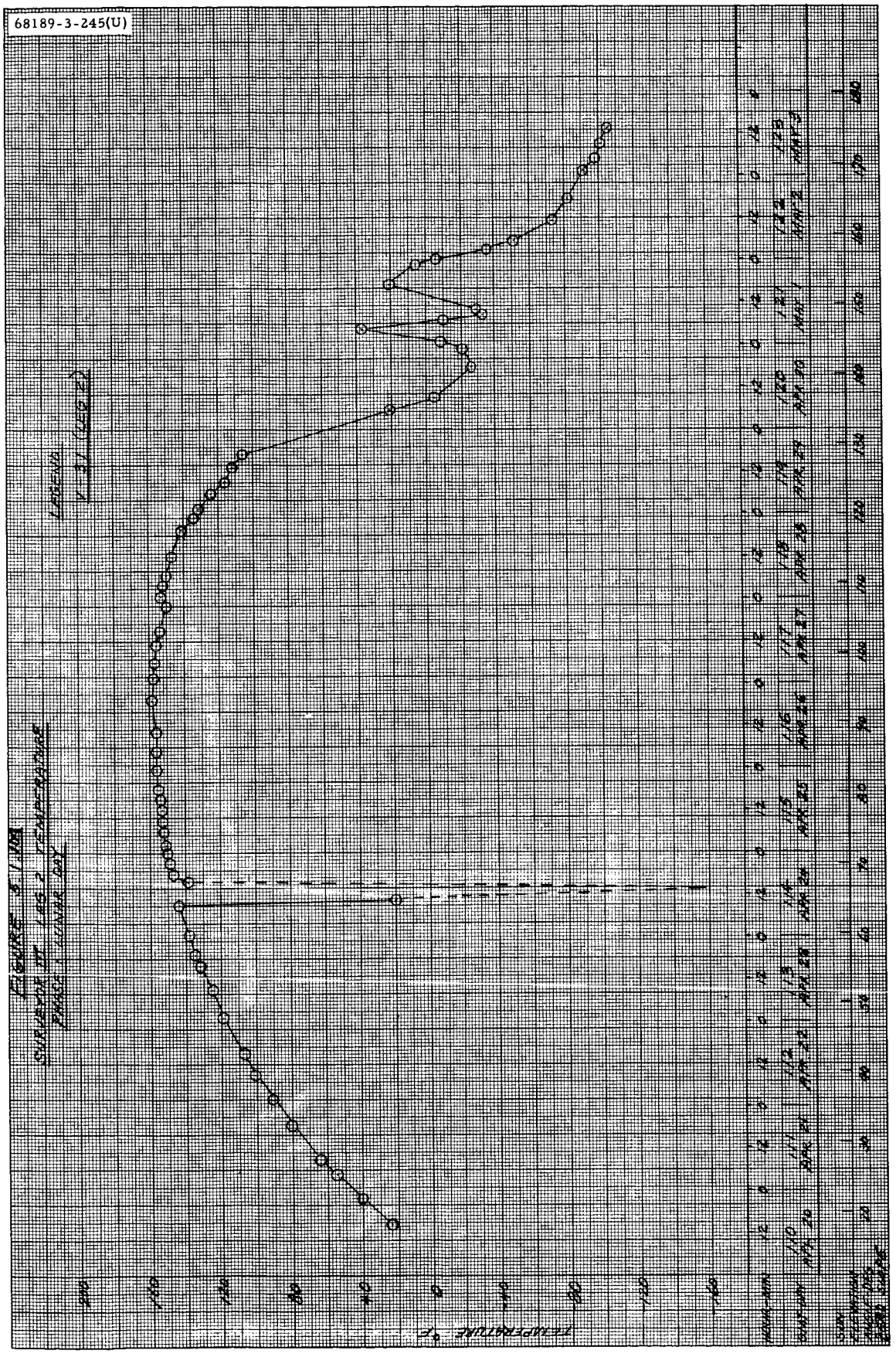

Figure 5.1-109. Leg 2 Temperature

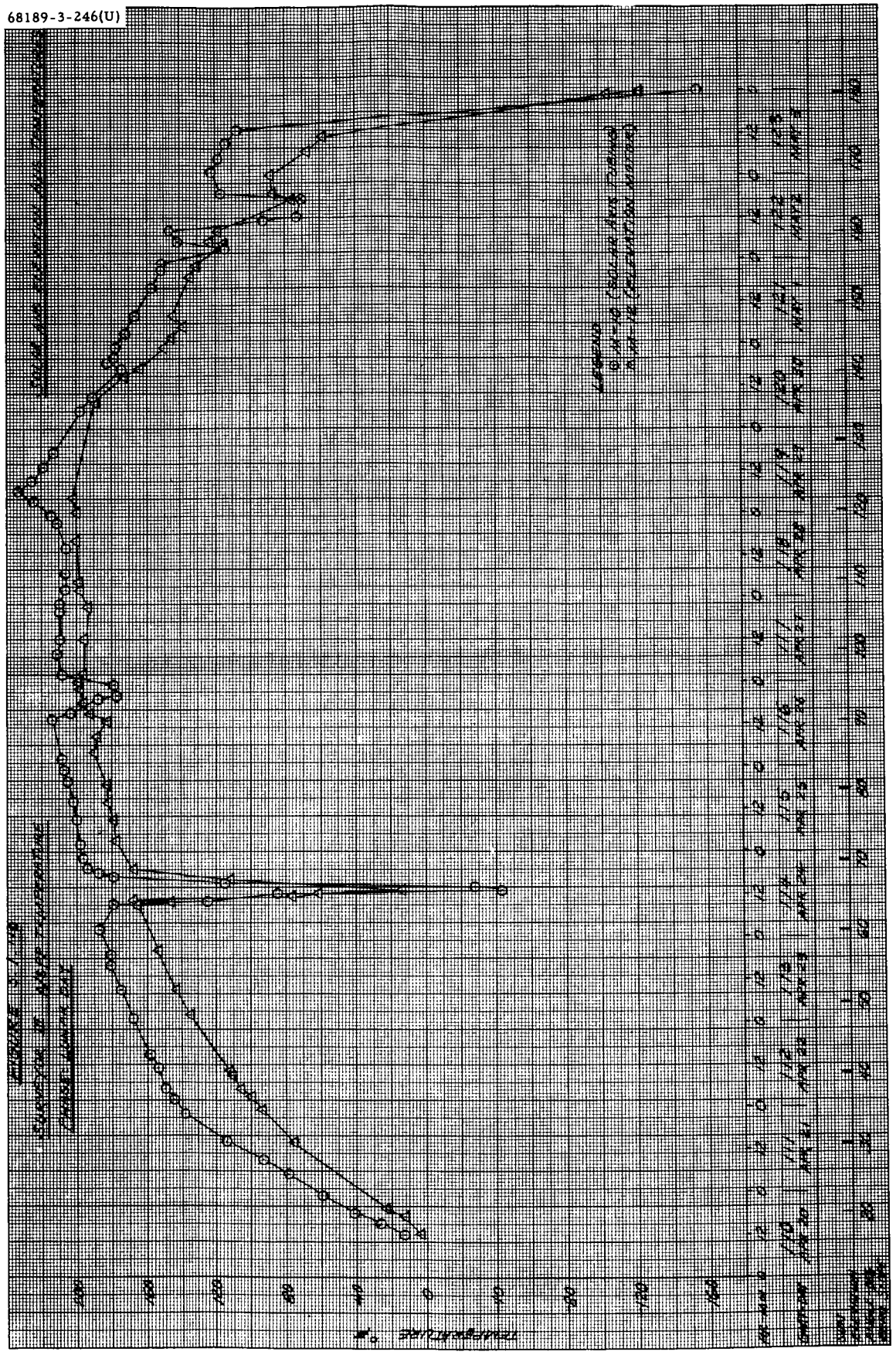

Figure 5.1-110. A/SPP Temperature

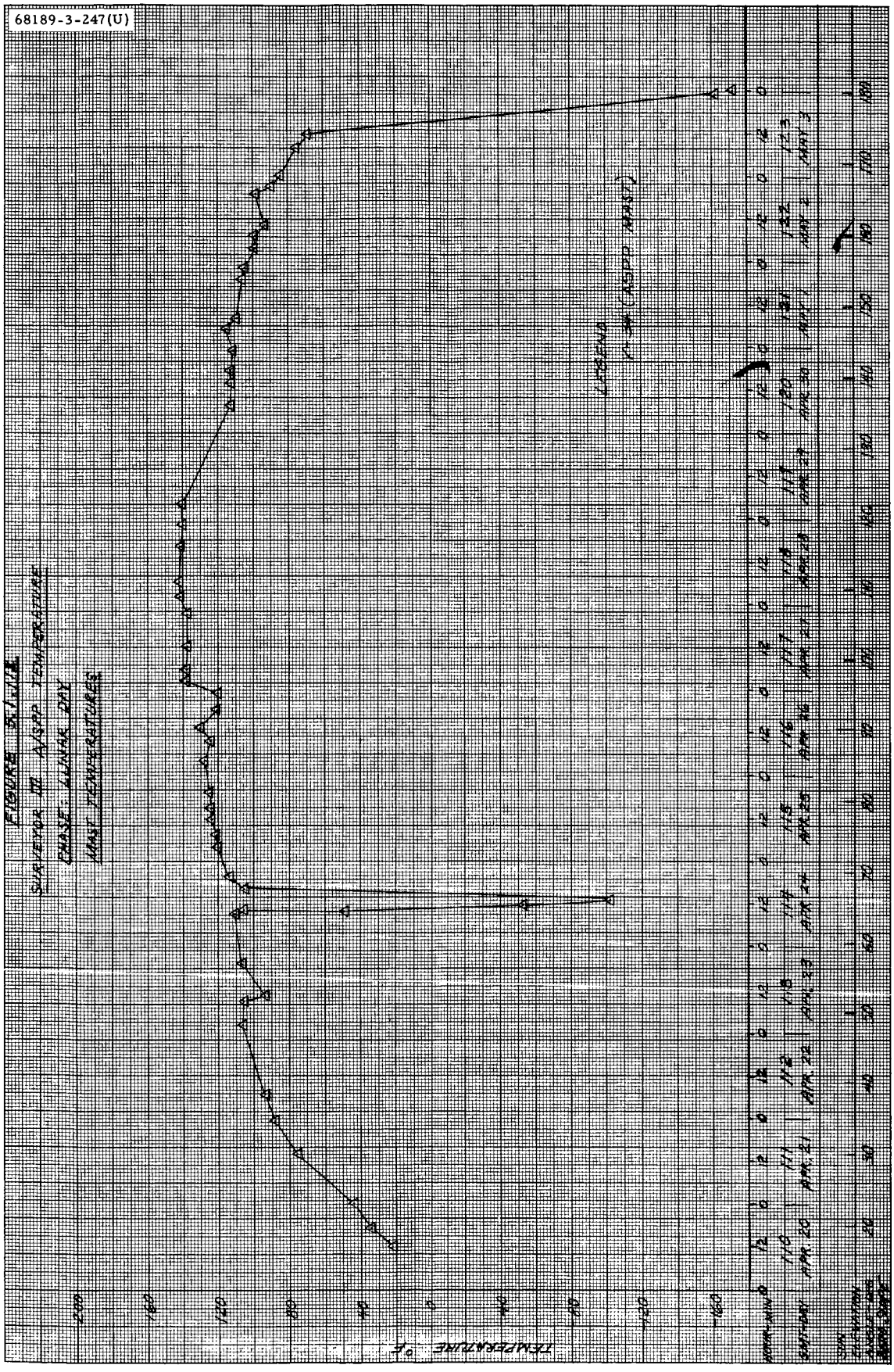

Figure 5.1-111. Mast Temperatures

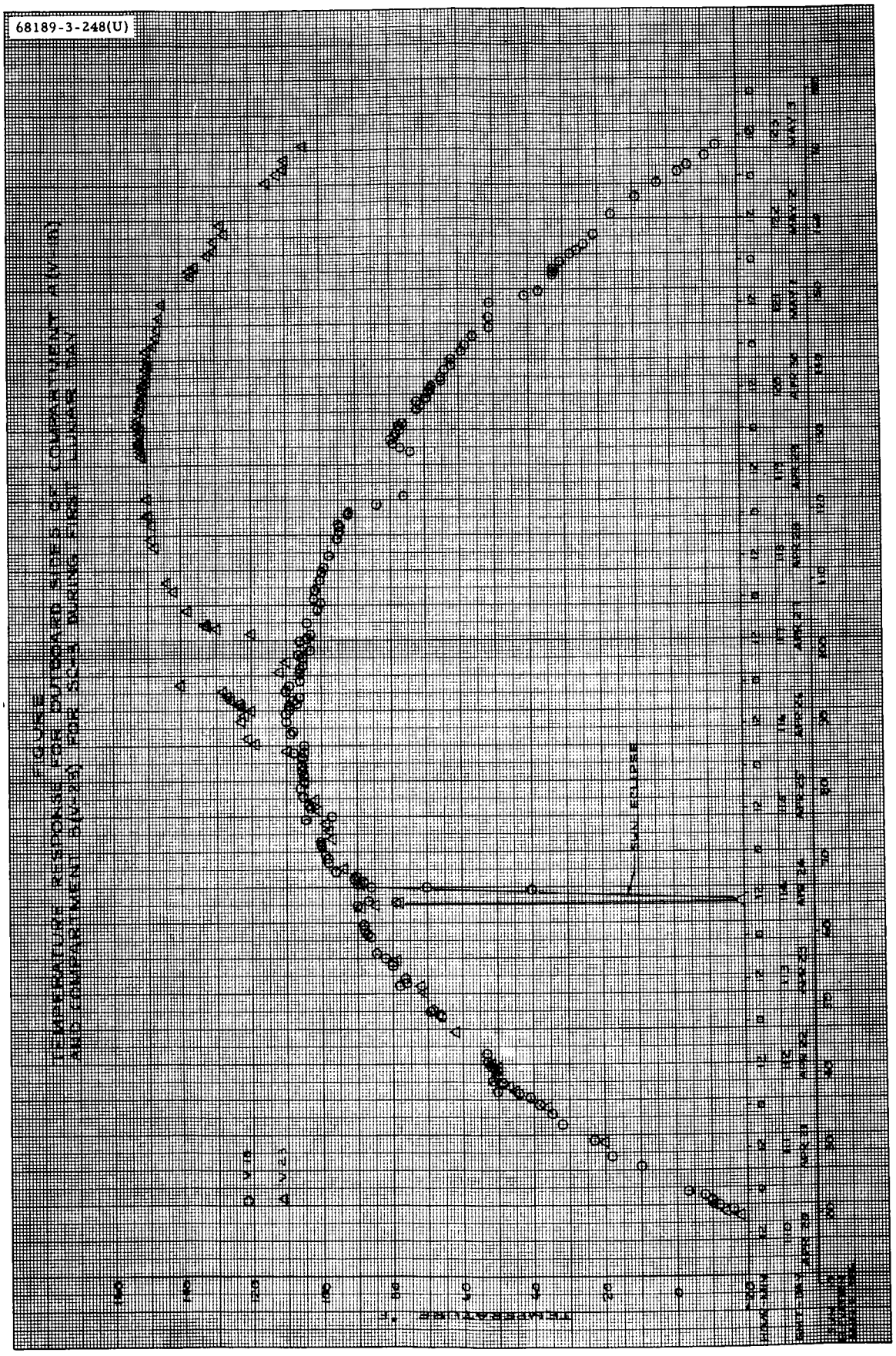

Figure 5.1-112. Compartment A and B Outboard Side Temperature

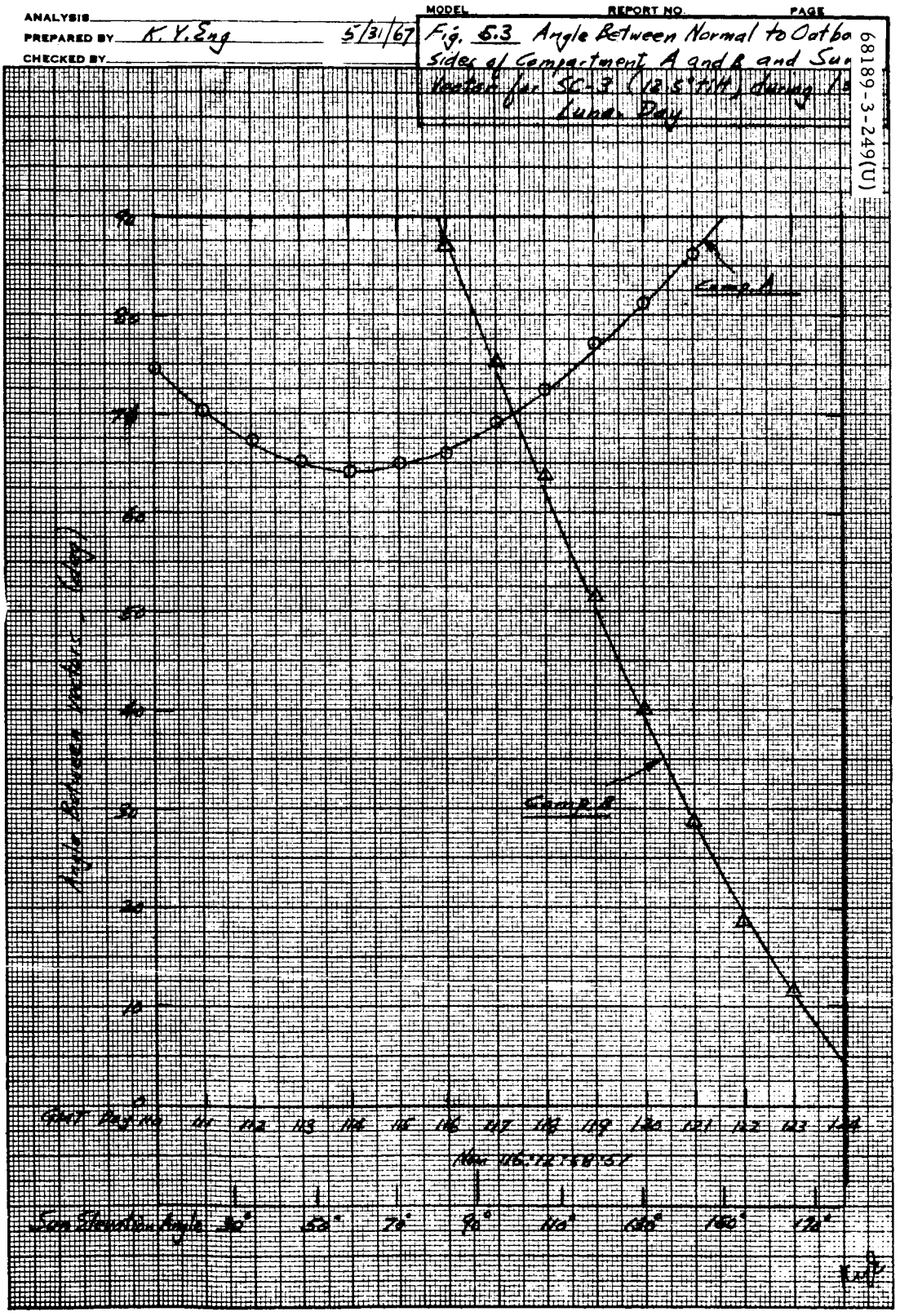

Figure 5.1-113. Angle Between Normal to Outboard Sides of Compartments A and B and Sun Vector (12.5 degree tilt)

ANALYSIS
PREPARED BY
CHECKED BY
MODEL
REPORT NO.
PAGE

68189-3-250(U)

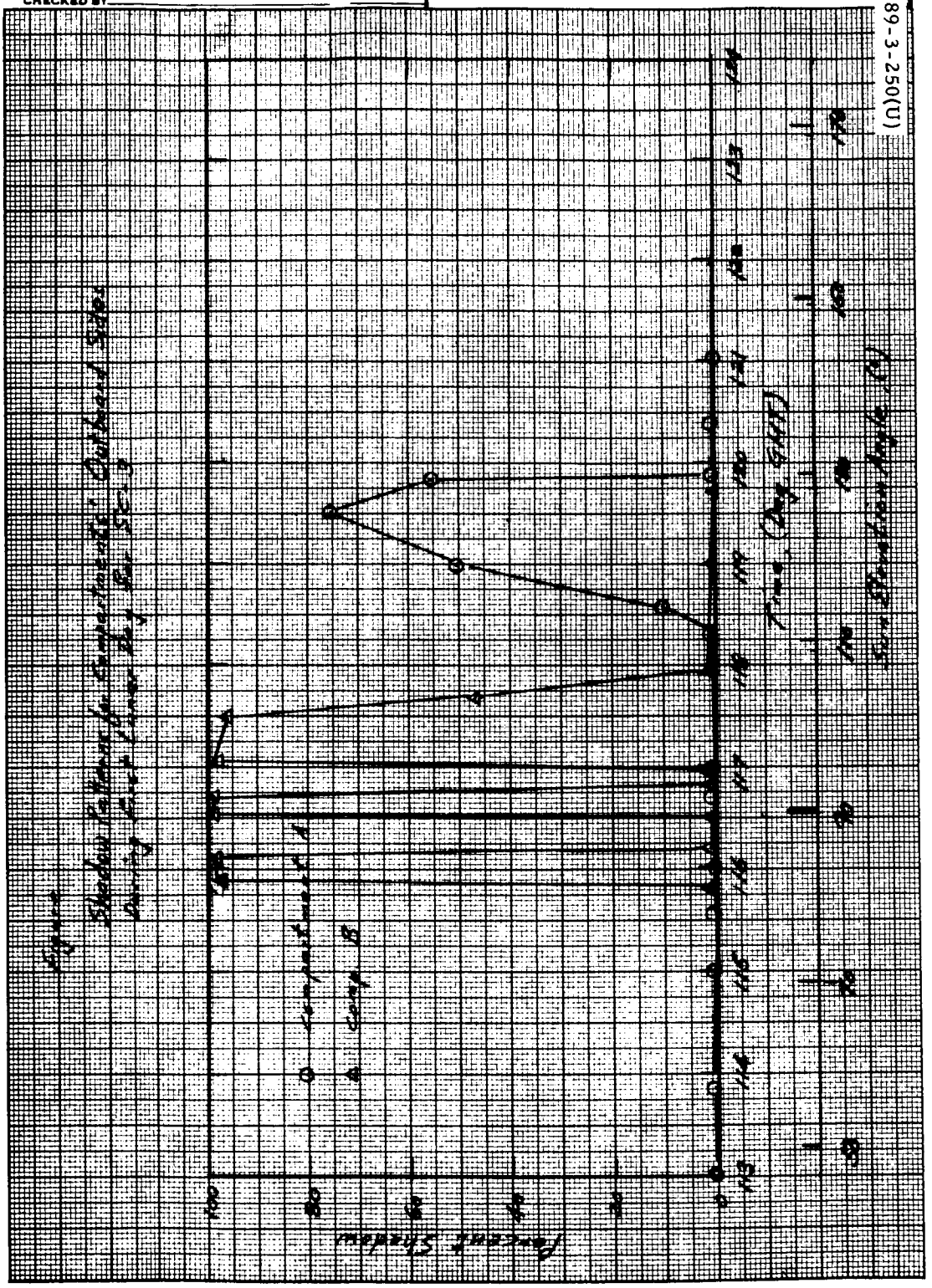

Figure 5.1-114. Shadow Patterns for Compartments' Outboard Sides

ANALYSIS
PREPARED BY
CHECKED BY
MODEL
REPORT NO.
PAGE

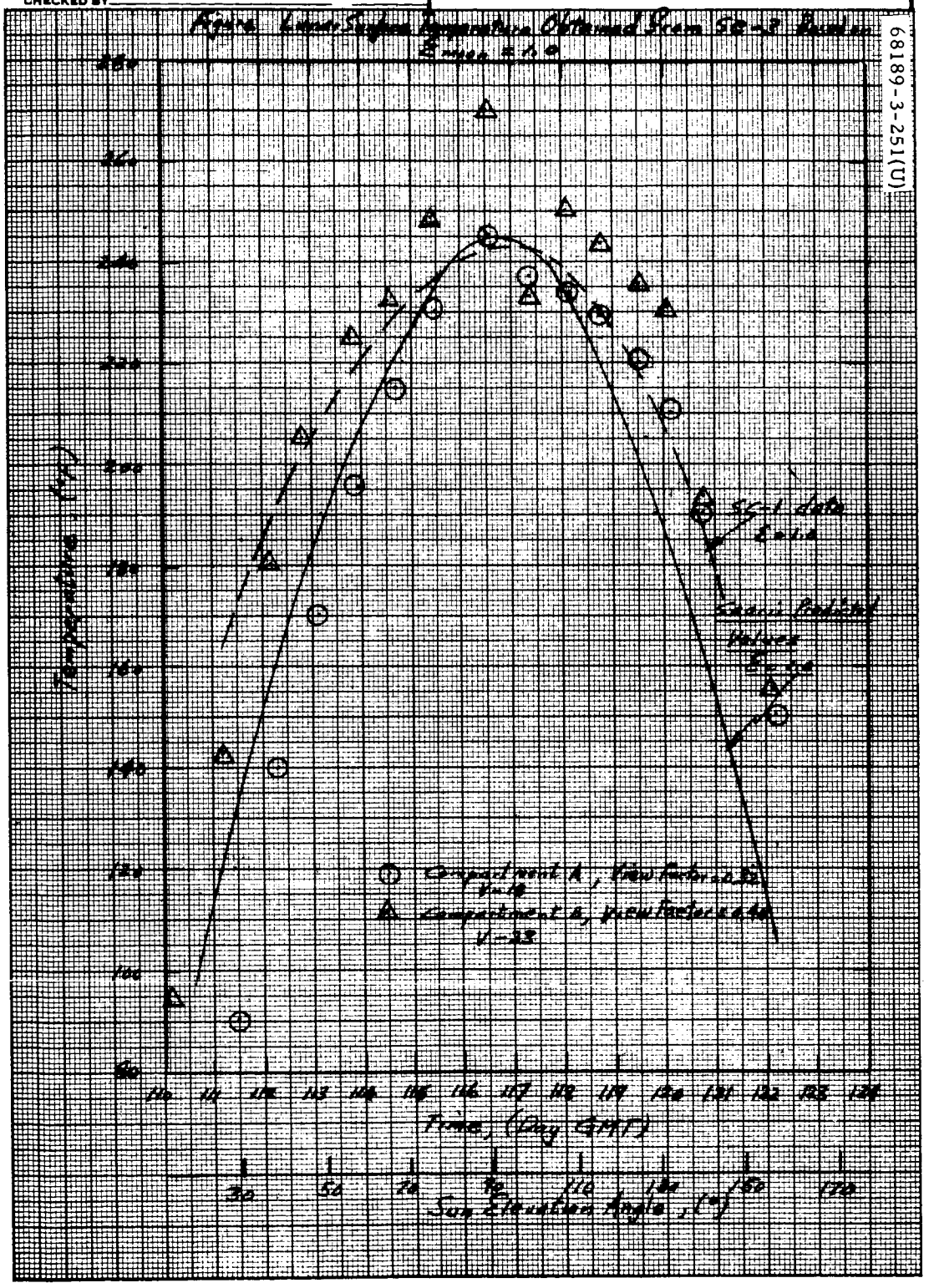

Figure 5.1-115. Lunar Surface Temperature, $\Sigma_{moon} = 1.0$

5.1.7 ACKNOWLEDGEMENTS

The efforts of the following individuals are acknowledged for contributing to the "Thermal Performance and Analysis" section.

Jay Tuchscher, Coordinator

Harlan Knudson

Ron McGrath

Jerry Lewis

Ray Mayikawa

5.2 ELECTRICAL POWER SUBSYSTEM

5.2.1 INTRODUCTION

The electrical power (EP) subsystem generates, stores, converts, and controls electrical energy for distribution to other spacecraft subsystems. There are two sources for this energy: 1) storage batteries and 2) radiant energy converted directly to electrical energy used for system loads or battery charging. During transit, the primary source of power is radiant energy via the solar panels. Figure 5.2-1 shows associated equipment groupings.

The performance of the EP subsystem during the Surveyor III flight was nominal as compared to test data and simulation analysis predictions. Subsequently, specific comparisons will be made in the body of this subsection.

Regarding the total system, various loads, solar panel input power, and regulator efficiencies are calculated from flight data. Analysis of specific loads, comparison to prediction, and explanation of discrepancies will be considered.

In Table 5.2-1, major events are presented with time in GMT for reference to various list information, i.e., commands and mission data processing (MDP) system processed data. In general, the divisions of Table 5.2-1 correspond to flight phases of importance to the EP subsystem and it may not correspond to flight phases in other subsections. Basically, the flight region is divided into times corresponding to significant changes in electrical loads. Load changes corresponding to these flight phases are partially illustrated by the regulated current (EP-14) and more completely by the battery discharge current (EP-9).

5.2.2 ANOMALY DESCRIPTION

No anomalies were detected in the electrical power subsystem during flight; however, anomalies were noted at the second touchdown (110:00:04:42.3).

1) At the second touchdown there was an inadvertent switching of the automatic battery control unit (TFR18261) resulting from a spurious command generated by a transient. There was no effect upon the mission since the spacecraft was subsequently commanded to the desired mode of battery operation.

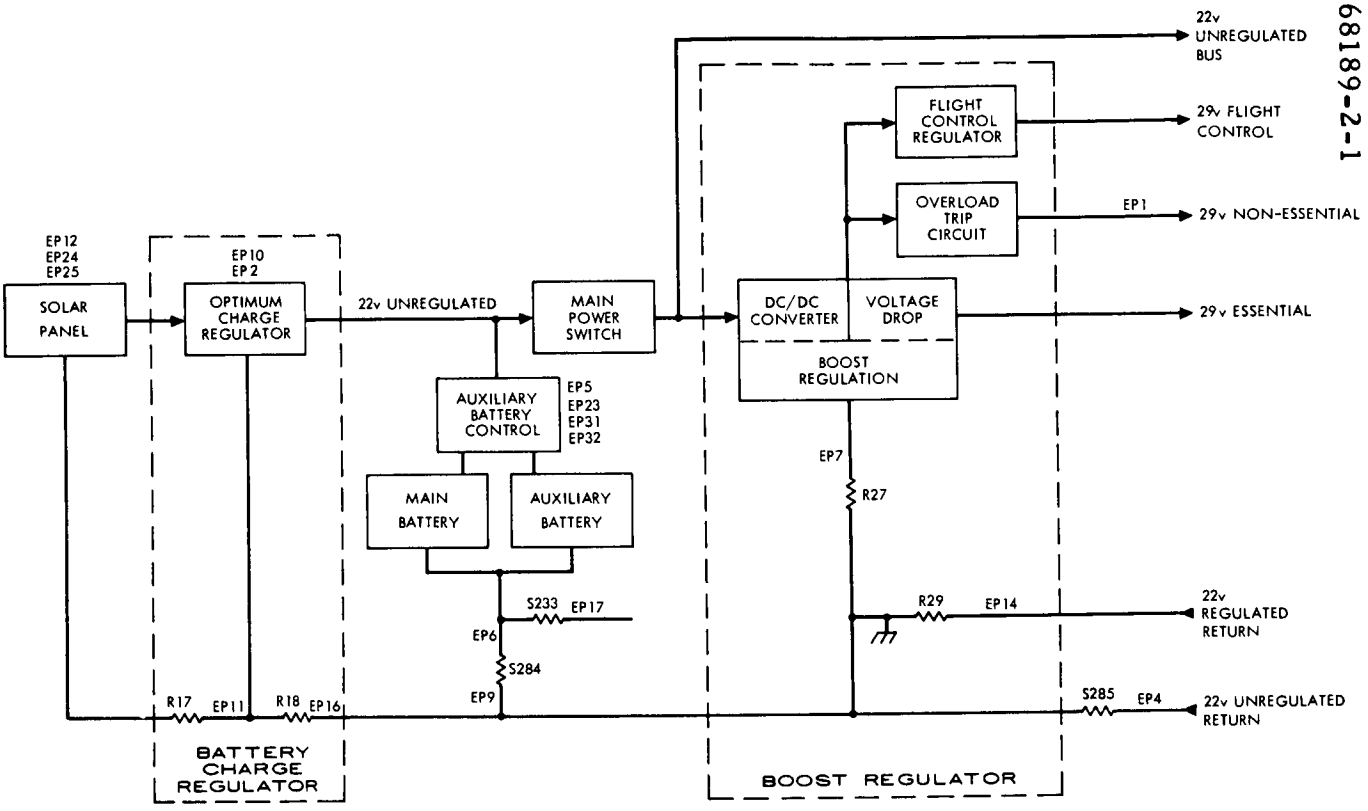

Figure 5.2-1. Electrical Power Schematic

TABLE 5.2-1. ELECTRICAL POWER EVENTS AND TIMES

Time, GMT* (day:hr:min:sec)		Comments
From	To	
107:07:05:00	107:07:48:00	Launch to sun acquisition
107:07:48:00	107:08:09:58	Transmitter high power
107:08:09:58	107:16:02:25	Coast
107:16:02:25	107:16:39:50	Coast, transmitter high power
107:16:39:50	108:04:20:48	Coast
108:04:20:48	108:04:57:03	Transmitter high power
108:04:57:03	108:05:00:32	Midcourse maneuver, transmitter high and FC thrust phase power on
108:05:00:32	108:05:16:15	Transmitter high power
108:05:16:15	109:06:01:19	Coast
109:06:01:19	109:06:13:43	Coast, power mode cycling, auxiliary battery on
109:06:13:43	109:10:59:59	Coast
109:10:59:59	109:11:13:34	Coast, power mode cycling, auxiliary battery on
109:11:13:34	109:18:14:20	Coast
109:18:14:20	109:18:26:24	Coast, power mode cycling, auxiliary battery on
109:18:26:24	109:23:09:40	Coast
109:23:09:40	109:23:56:35	Transmitter high power, preretro maneuvers
109:23:56:35	110:00:04:54	Transmitter high power, AMR on, terminal descent, touchdown, FC thrust phase power off

*Time referenced to when appropriate commands sent.

2) The auxiliary battery failed (TFR18260) on GMT day 114 due to a short to the spaceframe. There was no effect upon the mission since the main battery and solar panel provide sufficient power for lunar operation.

5.2.3 SUMMARY AND CONCLUSIONS

5.2.3.1 Summary

Table 5.2-2 presents a summary of flight data for Surveyor II compared to test data for the electrical power subsystem.

5.2.3.2 Conclusion

Operation of the electrical power subsystem was nominal throughout the spacecraft's flight except at the second touchdown. The anomalies at the second touchdown did not affect the ability of the electrical subsystem to supply power during the first lunar day.

5.2.4 ANALYSIS

The analysis considers six areas: mission telemetry plots, power loads and sources budget, comparison of flight loads and flight acceptance test (FAT) loads, and cyclic loads.

5.2.4.1 Mission Telemetry Plots

Figures 5.2-2 through 5.2-10 are selected mission plots which are pertinent to the electrical power subsystem. They represent line plots of the analog signals averaged at 1-minute intervals. Consequently, due to the scale of these plots and data averaging, they give excellent information for consideration of trends in data flow. Many annotations have been made on these plots related to commands and ground data processing.

5.2.4.2 Power Loads and Sources Budget

Energy Used

Figure 5.2-11 presents the remaining battery energy as a function of time. Table 5.2-3 compares energy expended as calculated from flight telemetry, an adjusted prediction (Reference 1), and specification values (Reference 2). Both the power management prediction and the telemetry deviations are very close to the specification value of 6462 ± 323 watt-hours for a 65-hour mission. Energy obtained from the solar panel is very close to specification (4542 ± 227 watt-hours) for a 65-hour mission.

TABLE 5.2-2. ELECTRICAL POWER SUMMARY

Item	Flight Data	Predicted or Specification
Boost regulator efficiency, percent	77	75 (minimum)
Optimum charge regulator efficiency	80	75 (minimum)
Optimum charge regulator output energy, w-hr	4521	4464
Battery energy used, w-hr	1943	1920 ± 395
Total energy used	6464	6462 ± 323
Selected loads		
Transmitter B high voltage, watts	60.6 ± 0.5	58.0
Transmitter B filament power, watts	2.9	2.9
FC thrust phase power on		
Regulated, watts	35.09 ± 0.58	34.22
Unregulated, watts	7.69 ± 0.05	10.34
AMR on, watts	37.4 ± 2.5	31.6
AMR enable, watts	33.0 ± 8.8	41.5
RADVS power on, watts	530 ± 8	551
Vernier ignition		
Midcourse, watts	36.8	39.6
Terminal descent, watts	37.8 ± 0.3	39.6
Vernier line 2 heater, watts	6.6	6.6
Altitude marking radar heater, watts	5.28	5.04
Gyro heater, watts	11	11

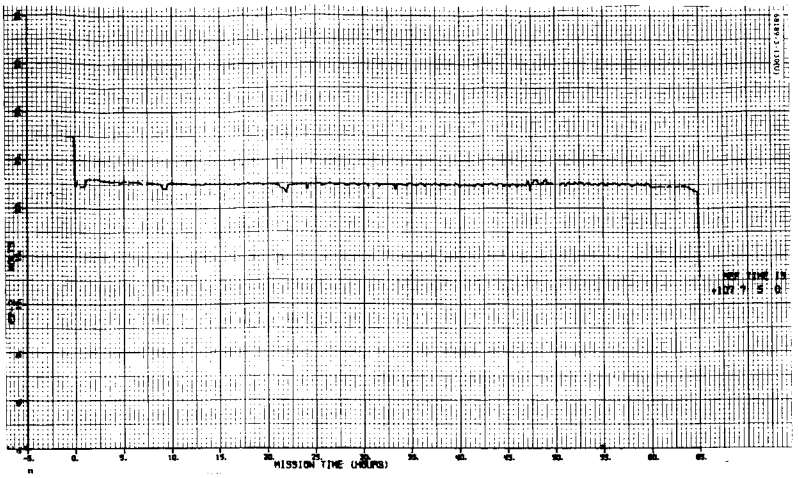

Figure 5.2-2. Unregulated Bus Voltage

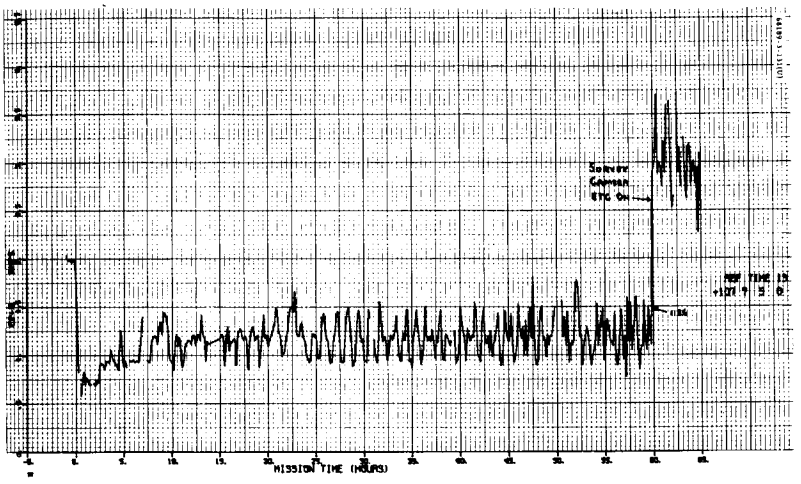

Figure 5.2-3. Unregulated Output Current

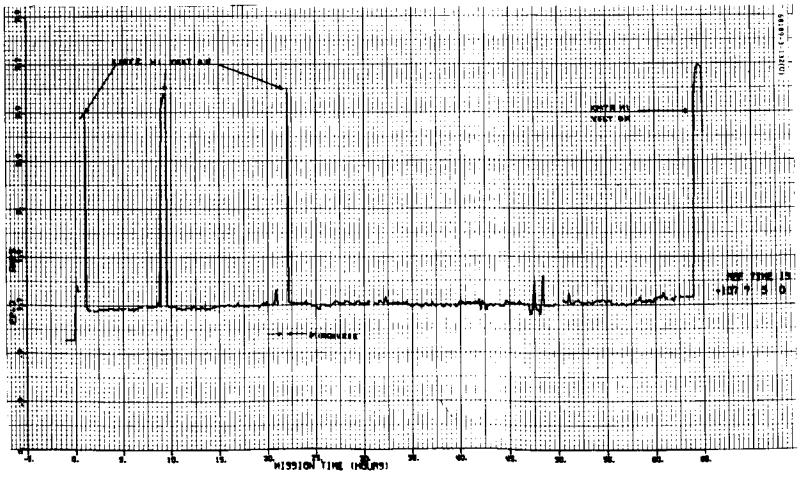

Figure 5.2-4. Boost Regulator Difference Current

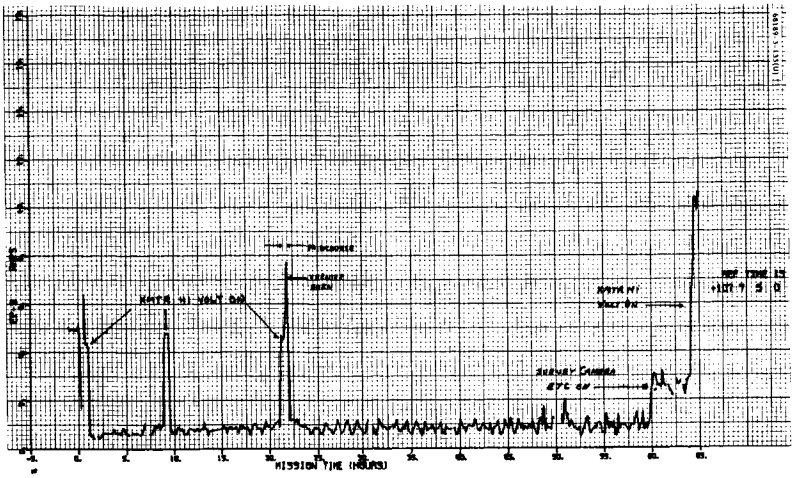

Figure 5.2-5. Battery Discharge Current

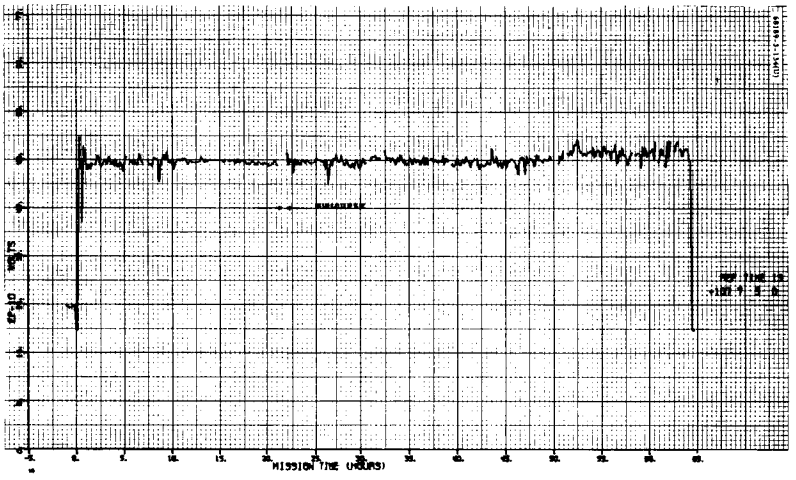

Figure 5.2-6. Solar Cell Array Voltage

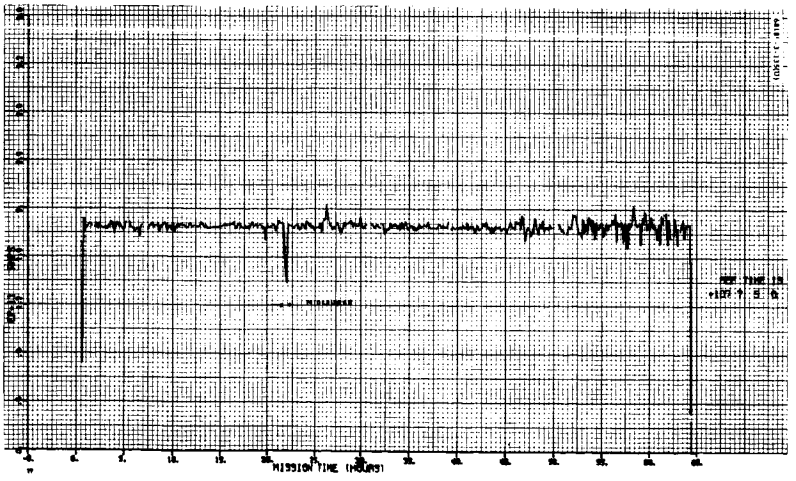

Figure 5.2-7. Solar Cell Array Current

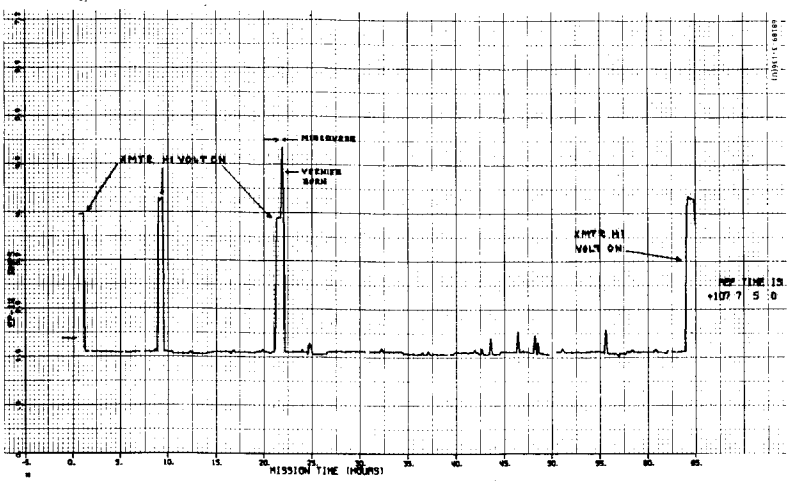

Figure 5.2-8. Regulated Output Current

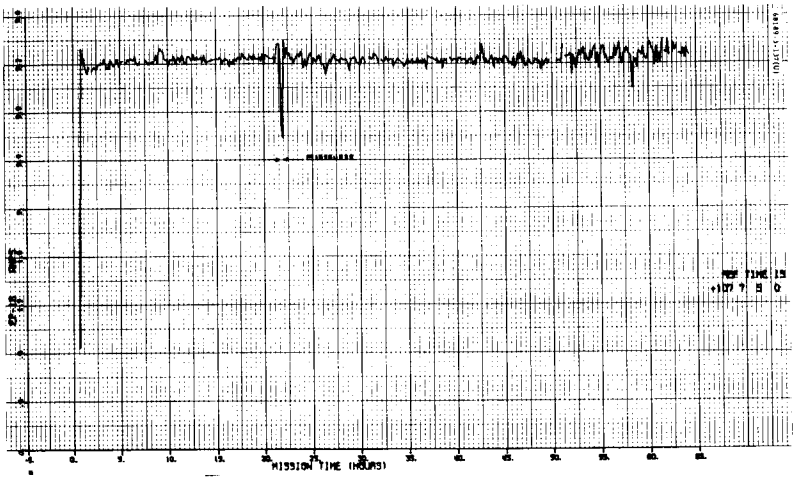

Figure 5.2-9. Optimum Charge Regulator Output Current

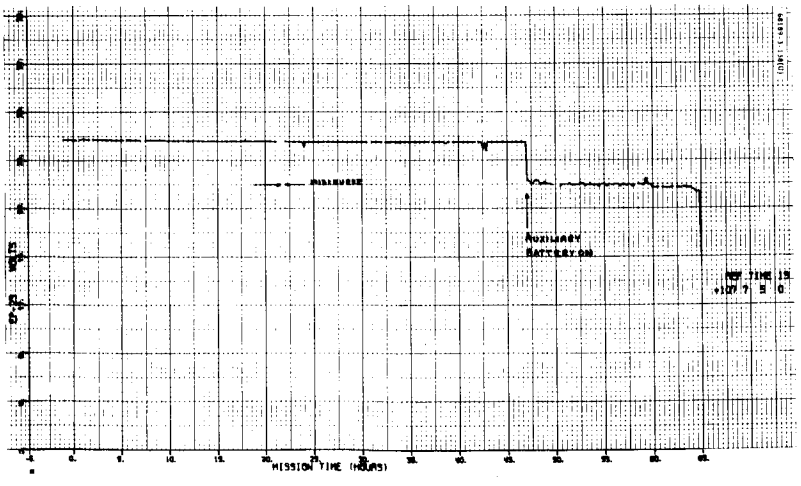

Figure 5.2-10. Auxiliary Battery Voltage

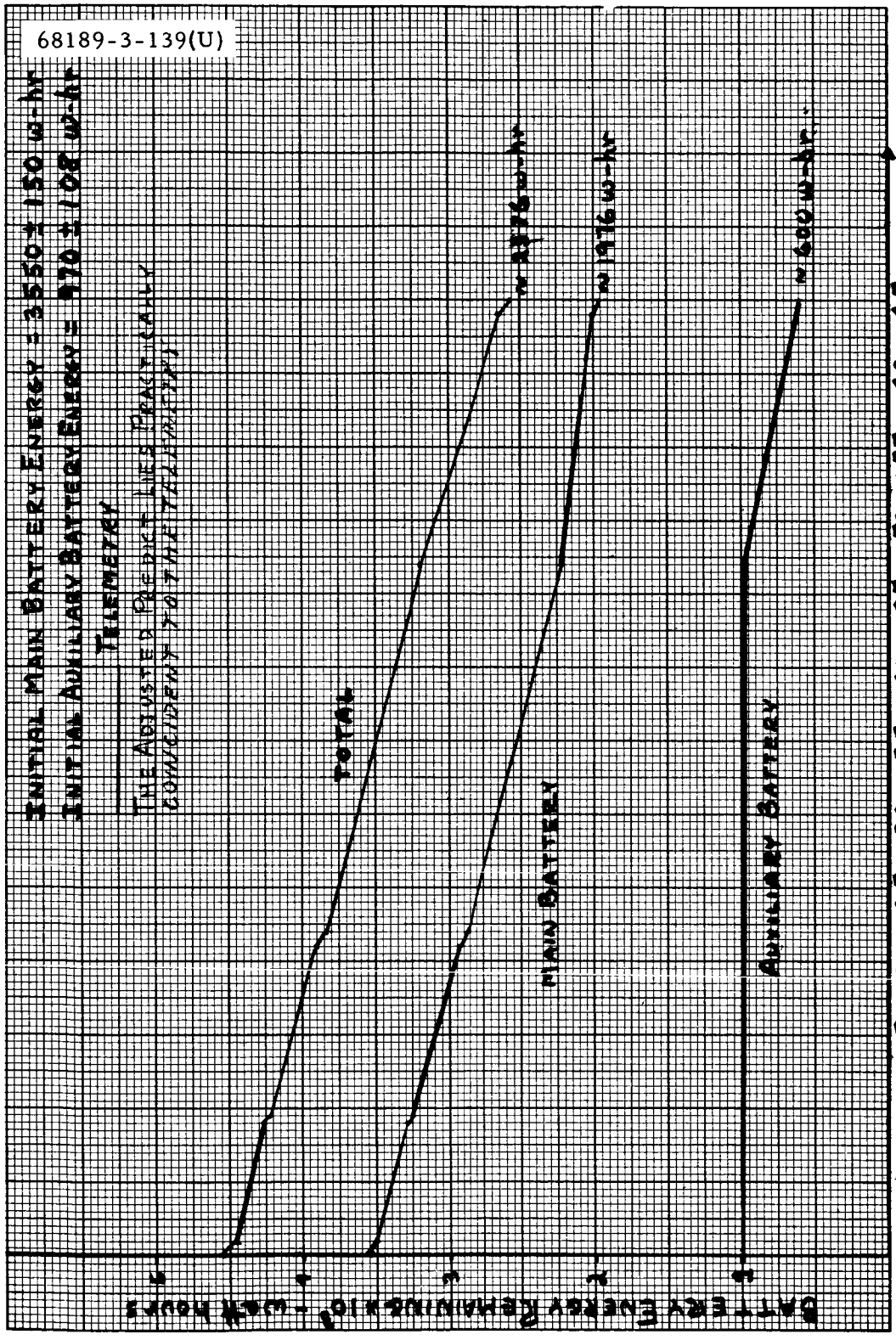

Figure 5.2-11. Battery Energy Remaining

TABLE 5.2-3. ENERGY USED

Source	Predict,* w-hr	Flight Data, w-hr	Specification, w-hr
Main battery	—	1574	—
Auxiliary battery	—	369	—
Total battery	2002 ± 300	1943	1920 ± 395
Solar panel	4464	4521	4542 ± 227
Total	6466 ± 300	6464	6462 ± 323

*Data adjusted to 65-hour mission (63.5-hour suntime).

Power Data

Figures 5.2-12 through 5.2-20 present various power parameters as calculated from flight data. The parameters are calculated directly from the following telemetry channels (averaged data):

1) Optimum charge regulator (OCR) efficiency = ((EP-2 * EP-16)/(EP-10 * EP-11)) * 100

2) Boost regulator efficiency = ((EP-1 * EP-14)/(EP-7 + EP-14) * (EP-2)) * 100

3) Shunt unbalance current = (EP-9 + EP-16 + EP-17) - (EP-4 + EP-14 + EP-7)

4) Regulated power = EP-1 * EP-14

5) Unregulated power = EP-2 * EP-4

6) Solar panel power = EP-10 * EP-11

7) Total loads = (EP-9 + EP-16 + EP-17) * EP-2

Figures 5.2-12 and 5.2-13 present mission plots of OCR and boost regulator efficiencies, respectively. The OCR efficiency is approximately 80 percent and the boost regulator efficiency, approximately 77 percent.

Figure 5.2-14 shows the shunt unbalance current throughout the flight. The current is generally biased at about +0.3 ampere.

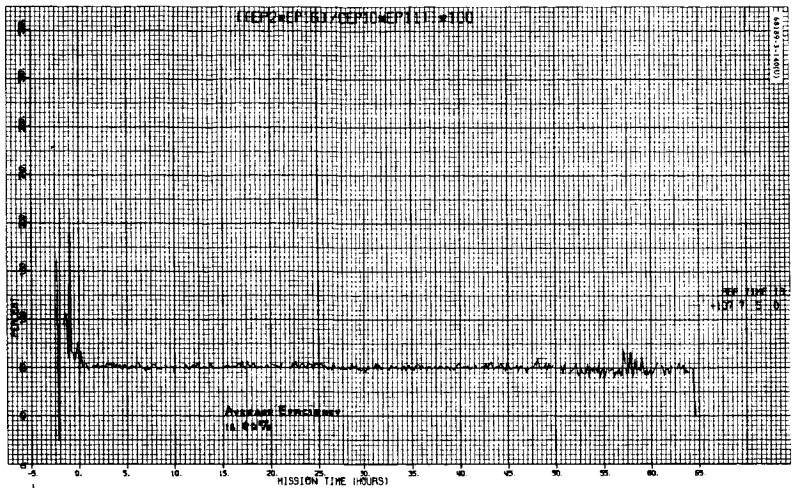

Figure 5.2-12. Optimum Charge Regulator Efficiency

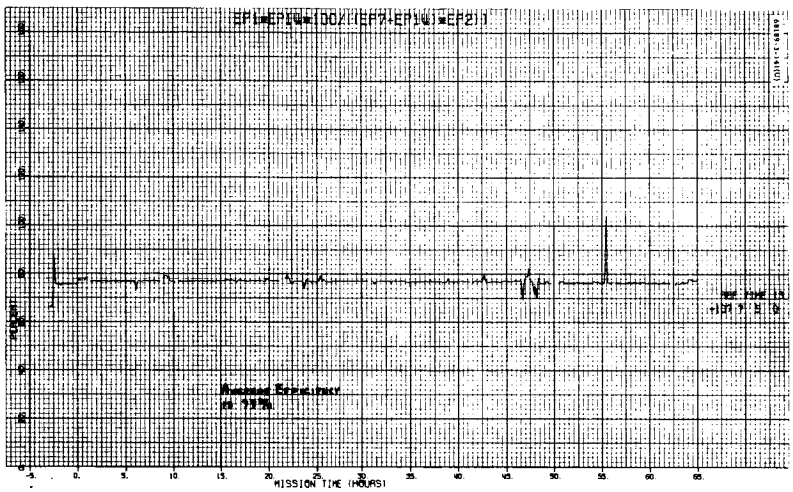

Figure 5.2-13. Boost Regulator Efficiency

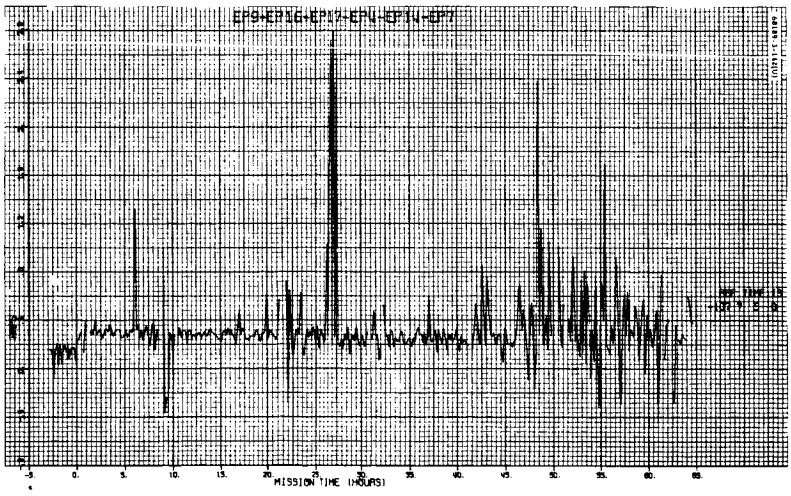

Figure 5.2-14. Shunt Unbalance Current

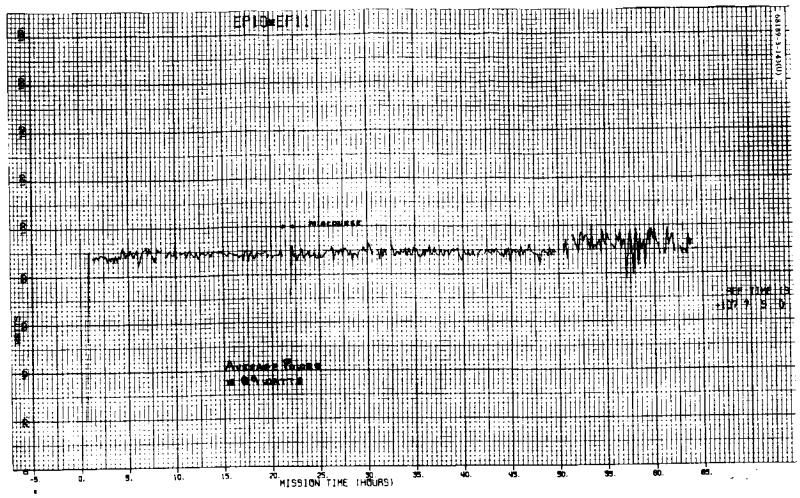

Figure 5.2-15. Solar Panel Power

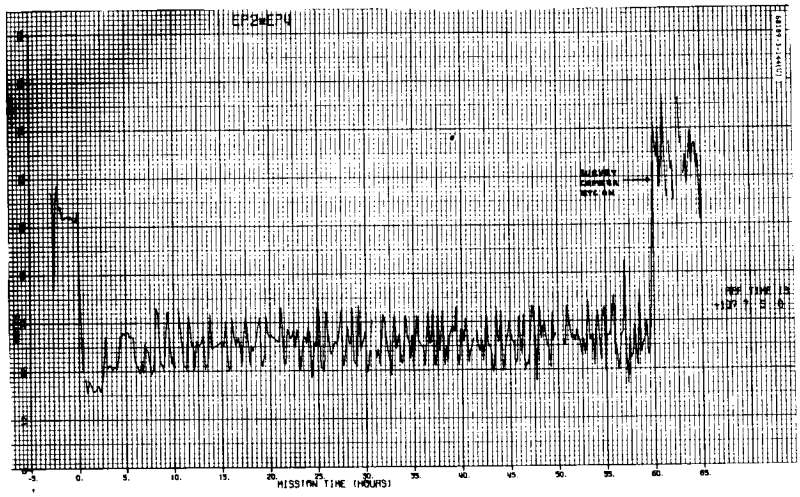

Figure 5.2-16. Unregulated Power

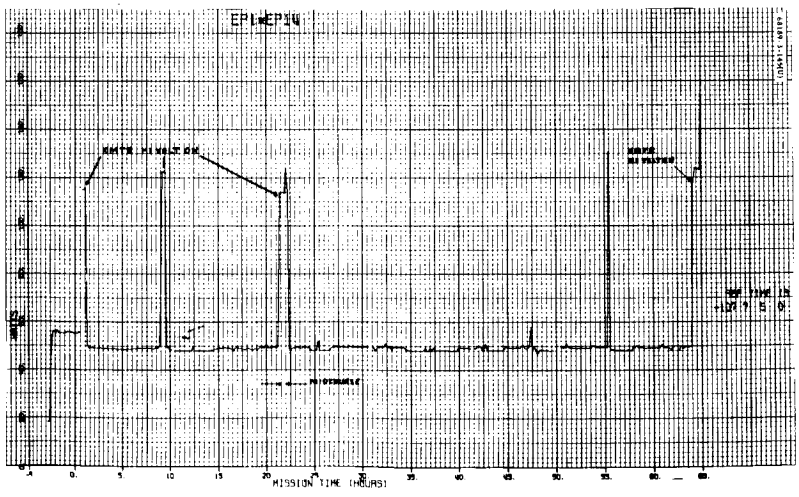

Figure 5.2-17. Regulated Power

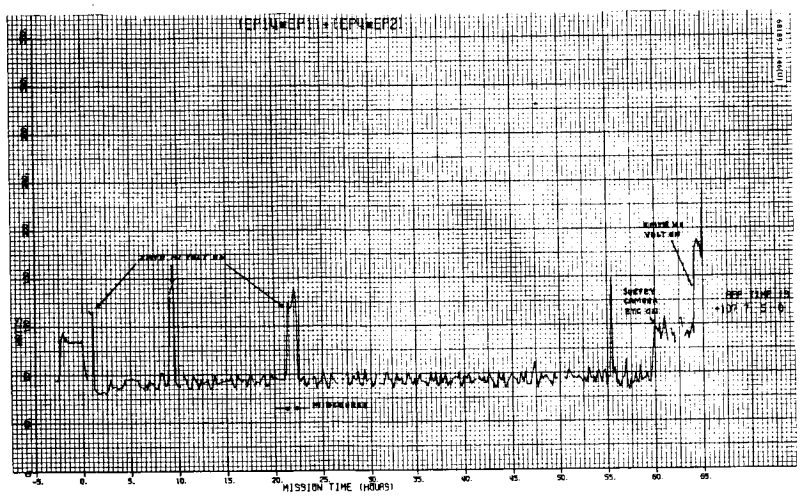

Figure 5.2-18. Total Power

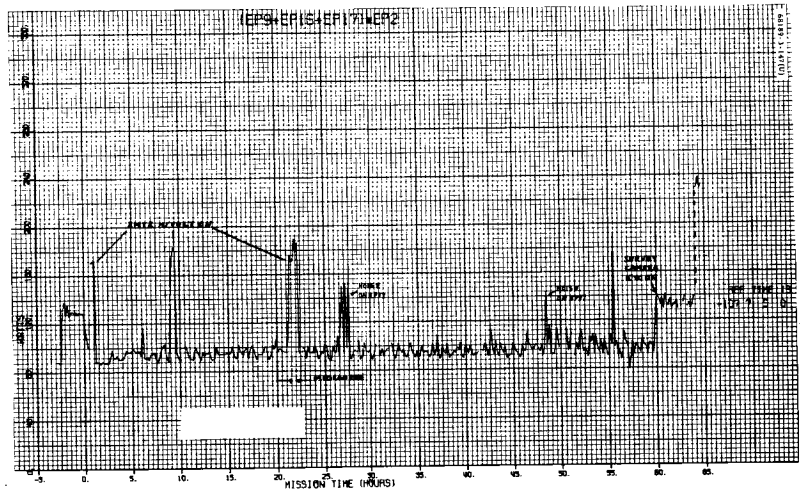

Figure 5.2-19. Total Loads

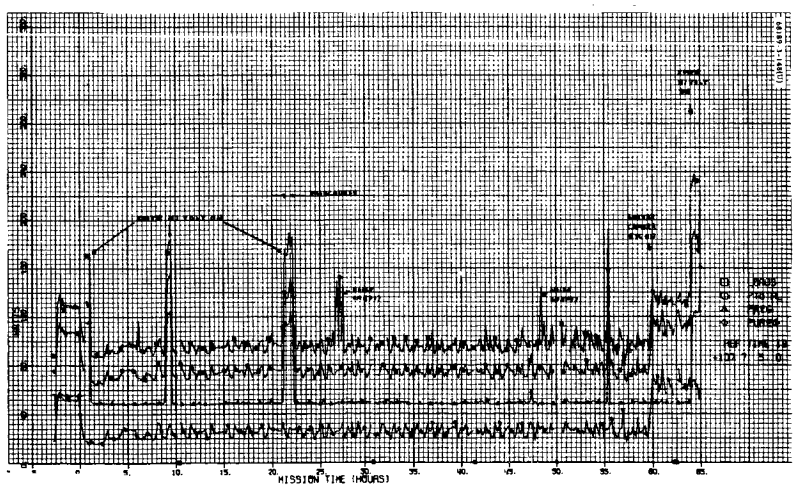

Figure 5.2-20. Power Consumed and Loads

Figure 5.2-15 is a plot of solar panel power received for 63.5 hours. This represents an energy input of approximately 4521 w-hr – average solar panel power of (89 watts) × (OCR efficiency of 80 percent) × (63.5 hours).

Figure 5.2-16 is a mission plot of unregulated power; Figure 5.2-17 is a similar plot of regulated power. Figure 5.2-18 is a sum of regulated and unregulated power.

Figure 5.2-19 shows the total loads for the electrical power subsystem for the entire Surveyor III flight. Total energy used during the flight can be estimated from this plot and this estimate is recorded in Table 5.2-3.

Figure 5.2-20 shows total power consumed as well as the sum of regulated and unregulated loads throughout the flight.

Comments on Load Sharing

During high current mode on condition, load sharing was assumed to be 1:1 without the diode. During auxiliary battery mode on, where the diode was between the main battery and unregulated bus, load sharing was assumed to be 3:2 (auxiliary to main). This is the same as for Surveyor II.

These assumptions are reflected in the construction of the plot of battery energy remaining in Figure 5.2-11 and the calculation of the values in Table 5.2-3.

5.2.4.3 Comparison of Flight Loads and FAT Loads

Comparison of telemetry-measured and FAT-measured loads (Reference 3) will be made for selected units, various heaters, and large current drains.

Selected Equipment Loads

Results of comparing flight and test specification selected equipment loads are presented in Table 5.2-4. The loads and equipments considered are as follows:

1) Transmitter High Voltage On/Off. Data are presented in Table 5.2-4. FAT data for the transmitters is taken from Reference 3.

2) Flight Control Thrust Phase Power On. 0727 commands is within specification.

3) RADVS Power On. Command 0637 applies power to the RADVS. The power consumed is close to that expected. Figure 5.2-21 (EP-17, radar and squib current) shows the current profile. The average value of EP-17 was about 26 amperes.

TABLE 5.2-4. SELECTED EQUIPMENT LOADS

Command(s)*	Command Time, GMT	Current, milliamperes		Power, watts	
	day:hr:min:sec	Flight	Specification Reference 3	Flight	Specification Reference 3
Transmitter B					
R 0107 HV off	107:08:09:48	2091 ± 17	2000	60.6 ± 0.5	58.0
R 0105 on	107:16:00:41	100	100	2.9	2.9
Flight control thrust phase power on					
R 0727	109:23:57:32	1210 ± 20	1180	35.09 ± 0.58	34.22
U 0727		350 ± 10	470	7.69 ± 0.05	10.34
Vernier ignition					
U 0721	108:05:00:03	1675	1800	36.85	39.6
U 0721	110:00:01:17	1720 ± 160	1800	37.8 ± 0.35	39.6
AMR on					
U 0626	109:23:56:35	1700 ± 100	1439	37.4 ± 2.5	31.6
AMR enable					
U 0625	109:23:59:35	1500 ± 400	1886	33 ± 8.8	41.5
RADVS power on					
U 0637	110:00:01:19	26200 ± 400	29000	530 ± 8	551

*R = regulated; U = unregulated.

5.2.4.4 Cyclic Loads

Gyro Heater

The periodic loading that occurs in EP-4 contains gyro heater effects. The gyro heaters have a short on-off cycle when compared to the altitude marking radar (AMR) and vernier line heaters. A dump of frame-by-frame nonaveraged telemetry was examined. Each gyro heater load is approximately 0.5 ampere, which compares favorably to the FAT data.

AMR and Vernier Line Heaters

Figure 5.2-22 is a plot of EP-4 at 20 min/in. Gyro heater effects are averaged out in this plot. The cyclic load effects of the AMR and

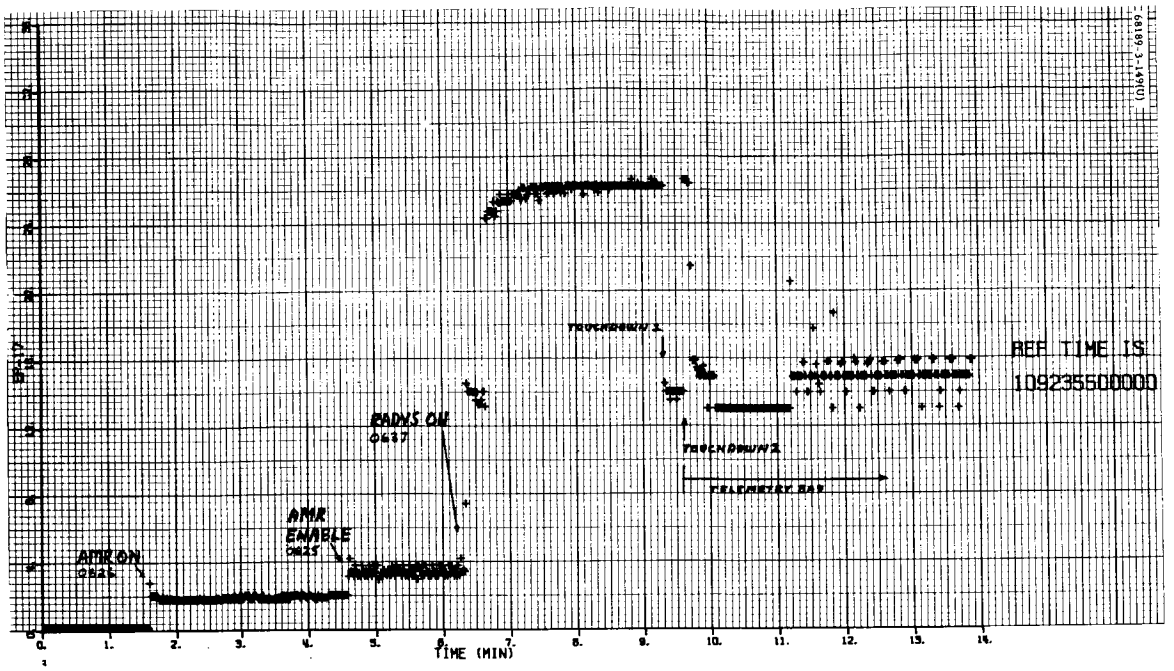

Figure 5.2-21. Radar and Squib Current (RADVS Power On)

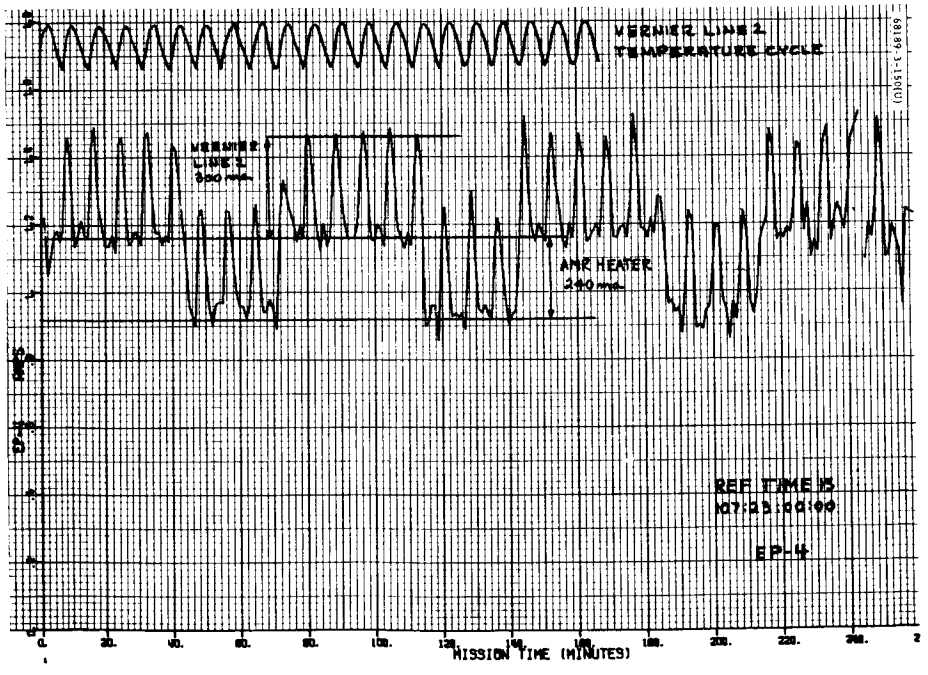

Figure 5.2-22. Unregulated Output Current — Coast I

vernier line 2 heaters are apparent. A trace of vernier line 2 temperature (P-4) has been placed above EP-4 in order to show how the middle frequency oscillation in EP-4 is associated with the vernier line heater. Only the AMR and vernier line 2 heaters are cyclic at this time. The vernier line 2 heater uses approximately 300 milliamperes, and the AMR heater draws about 240 milliamperes. This agrees favorably with test data, indicating that vernier line heater 2 should draw about 300 milliamperes and that the AMR heater should draw about 230 milliamperes.

5.2.5 REFERENCES

1. W. McIntyre, "SC-3 Mission Energy Prediction-Transit," Hughes Aircraft Company, IDC 2292/240, 28 March 1967.

2. "Surveyor Spacecraft Equipment Specification," Hughes Aircraft Company, No. 224832.

3. J. Mundy, "System Specification Power Management Data Summary SC-3 Spacecraft," Hughes Aircraft Company, No. 3023930, Revision A, 14 February 1967.

5.2.6 ACKNOWLEDGEMENTS

W. Mc Intyre, Technical coordinator and writer

J. Berger, Signal processing

S.F. McCormick, Loads analysis

5.3 RF DATA LINK SUBSYSTEM

5.3.1 INTRODUCTION

This section contains a summary and analysis of the performance of the data link subsystem during Surveyor Mission C.

The data link subsystem consists of the transmitters, transponders, receivers, command decoders, and antennas. It is the function of this subsystem to: 1) provide engineering data transmission from the spacecraft at bit rates compatible with specific mission phases, 2) provide analog data, such as that from television and strain gages, at signal levels high enough for proper discrimination, 3) provide phase coherent two-way doppler for tracking and orbit determination, and 4) provide command reception capability throughout the mission to allow for complete control of the spacecraft from the ground. A simplified block diagram of the communications subsystem is shown in Figure 5.3-1.

The pertinent subsystem units on the spacecraft during the mission are as follows:

Unit	Part Number	Serial Number
Receiver A	231900-3	22
Receiver B	231900-3	23
Transmitter A	263220-4	18
Transmitter B	263220-4	17
Command decoder unit	232000-5	4

Unlike most subsystems, individual data link subsystem parameters such as losses, threshold sensitivity, modulation index, etc., are not measured or individually determined from mission data. The composite effect of these parameters on the performance is measured as received signal power at the spacecraft and the tracking station (DSS) and as telemetry and command error rates. Consequently, it is impossible to compare individual link parameters to specified performance criteria. The best that can be done is to compare measured signal levels to predicted levels, and telemetry quality and command capability to predicted capabilities. To further cloud the analysis, omnidirectional antenna gain is a major contributor to the uncertainty in received signal levels. Accurate omnidirectional antenna gain

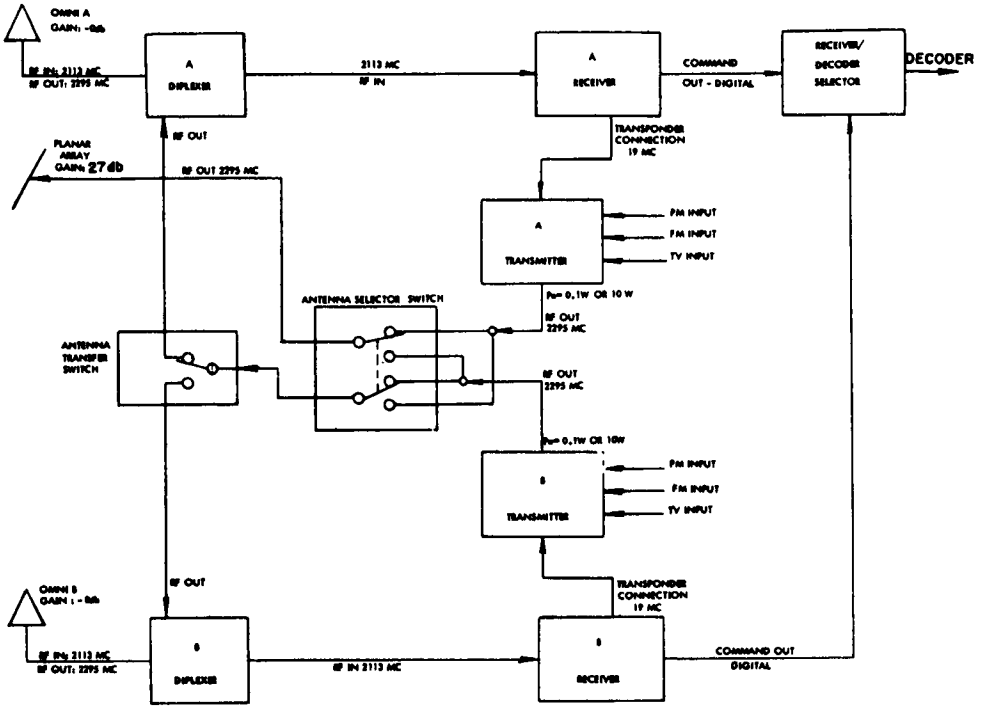

68189-2-134

Figure 5.3-1. Communications Subsystem Block Diagram

measurements are difficult to achieve and, in most cases, deviations from predictions can most likely be attributed to antenna gain uncertainty. Because of the problems outlined above, analysis of the data link subsystem performance will, in general, be a qualitative analysis of the performance of the entire subsystem rather than a quantitative assessment of the performance of the individual subsystem parameters. Equally as important as subsystem performance evaluation in this analysis is the qualitative assessment of the premission and real-time prediction techniques used during the mission, since future missions must rely on these techniques as guidelines during the real-time operation.

In general, the RF data link subsystem performed as expected. The single exception was the performance of receiver B, which, while still within the expected tolerance region, exhibited approximately a -2 db offset from the predicted nominal receiver signal level profile values. All other subsystem units performed very close to the nominal predictions.

The data contained in this report consist of spacecraft telemetered, DSS, and mission event time data. Where meaningful, the data are correlated to and compared with equipment specifications, previous test data, preflight predictions, and in-flight analysis predictions. Specifically, this section contains the following discussions which are shown with the appropriate subsection notation:

Anomaly Discussion (subsection 5. 3. 2) – This subsection primarily contains a discussion of the -2 db offset in receiver B received signal levels.

Summary and Conclusions (subsection 5. 3. 3) – This subsection contains a summary of subsystem performance with conclusions relative to performance and postflight analysis.

Subsystem Performance Analysis (subsection 5. 3. 4) – This subsection contains the following items:

1) General discussion of data, equations used, and path of the earth vector relative to omnidirectional antenna gain contours.

2) Discussion of subsystem performance during specific mission phases.

3) Discussion of pertinent subsystem telemetry signals plotted as a function of time from launch.

The major mission event times relative to the RF data link subsystem are tabulated in Tables 5. 3-1 and 5. 3-2. Table 5. 3-1 contains telemetry mode and bit rate, primary tracking station number, and station automatic gain control values as a function of time. Table 5. 3-2 contains a tabulation of the subsystem configuration as a function of time. Both tables cover the mission from launch to the time of initial solar panel/planar array positioning. Also, in some cases, the times in these tables are accurate only to the nearest minute.

TABLE 5. 3-1. TELEMETRY MODE SUMMARY

Time (GMT), hr:min:sec	Mode	Bit Rate	DSIF Station	DSIF AGC-DBM	TLM Margin, db	Comments
Day 107						
07:05:01.059	5	550				Launch – low mod index SCO on
07:48:58						Carnarvon has data lock
07:50:00				- 94		Carnarvon
07:55:10			42			In lock on SAA one-way
07:55:30				-120		On SAA
07:57:30				-122		Rcvr No. 2 on SAA (-9 degrees elevation)
07:57:50				-110		Auto track on SAA
07:59:10						Auto track on SCM (Rcvr No. 2)
07:59:46						Xmtr on
08:00:07						DSS loss of lock
08:00:30						Rcvr in lock – auto track SCM
08:01:30				>-90		Two-way lock confirmed
08:03:13						Cmd modulation on
08:09:38				>-90		DSS reports rcvr AGC saturated
08:10:10				-114.1		S/C xmtr low power at 08:09:58
08:13:45				-110.1		
08:14:14	1					
08:14:47		1100				
08:16:25				-114.5	+24.4	
08:16:42	4					
08:19:23	2					
08:21:20	6					
08:23:25	5					
08:28:00				-116.3	+22.6	
08:30:00				-117.0	+21.9	
08:43:00				-120.0	+18.9	
08:54:30				-121.0	+17.9	
09:00:00				-122.0	+16.9	
09:07:00				-127.0		
09:30:00				-125.2		
10:00:00				-129.0	+ 9.9	
10:40:00				-131.6	+ 7.3	
10:52:10				-132.8	+ 6.1	
11:18:00						DSS-42 reports results of S/B meas: 10-11 db below and 6.8 kc from carrier
11:48:00				-133.9	+ 5.0	
12:10:00						Cmd mod off – xfer to DSS-51
12:15:01						Three way with DSS-51
12:15:30			51			Two-way lock confirmed
12:17:45						Cmd modulation on
12:25:50				-133.3		
12:39:00	5	1100	51	-134.5		DSS-51 results of S/B meas: carrier 23.385276 – 134.5 dbm, upper S/B 23.385347 – 146.5 dbm, lower S/B 23.385205 – 147.0 dbm, S/B 6.816 kc from carrier

Table 5. 3-1 (continued)

Time (GMT), hr:min:sec	Mode	Bit Rate	DSIF Station	DSIF AGC-DBM	TLM Margin, db	Comments
Day 107 (continued)						
13:06:30				-133.5	+ 5.4	
13:07:05		4400				DSS-51 reports unable to find 33.0 kHz SCO; DSS-42 reports decom lock but experiencing high bit error rate
13:09:46		1100				
13:32:20		550		-134.5	+ 9.5	
13:44:00						DSS-51 report: carrier – 134.5 dbm, upper S/B – 145.5 dbm, lower S/B – 145.0 dbm
14:12:00						A/D converters off at 14:07:18; carrier – 136.0 dbm, upper S/B– 139.5 dbm, lower S/B– 139.5 dbm
14:30:02						Three-way with DSS-61
14:34:45			61			Cmd mod on
15:10:00				-138.3	+ 5.7	
15:42:56	4					
15:46:58	2					
15:49:46	1					
15:54:25	5					
16:00:00				-138.8	+ 5.2	
16:03:00				-119.3		Hi pwr Δ = 19.5 db
16:04:03		4400				
16:11:45						Loss of decom lock – approximately 5 seconds
16:37:39		1100				
16:38:30				-113.7		
16:40:15				-133.3	+ 5.6	Low pwr Δ = 19.6 db
16:55:00						Cmd mod off
16:59:00			51			Premature turn on at xmtr
17:00:01			51			Xmtr on (1 second late)
17:17:11						Two-way lock confirmed
17:22:00				-134.0	+ 4.9	
18:14:58				-133.2		
19:00:00				-134.0	+ 4.9	
19:41:00				-134.0	+ 4.9	
19:44:18	5	1100	51	-134.0		
20:30:02						Three-way with DSS-51
20:48:20			61	-134.2	+ 4.7	
21:00:00				-134.2	+ 4.7	
21:19:56	4					
21:22:23	2					
21:26:11	5					
21:33:53				-134.5	+ 4.4	
22:02:37			11	-136.8	+ 2.1	Three-way with DSS-61
22:05:42			61	-135.2	+ 3.4	
22:16:25			11			Two-way
22:50:40				-136.9		
23:52:56				-137.0		
23:53:37	4			-137.0		
23:58:15	2					

Table 5.3-1 (continued)

Time (GMT), hr:min:sec	Mode	Bit Rate	DSIF Station	DSIF AGC-DBM	TLM Margin, db	Comments
Day 108						
00:00:44	5					
00:30:41				-137.5	+ 1.4	
01:30:52				-137.3	+ 1.6	
02:11:20				-137.0		Before end of gyro drift
02:11:20				-138.3	+ 0.7	After terminate gyro drift
02:44:55				-138.3	+ 0.7	
02:54:35	4					
02:56:20	2					
02:57:52	1					
02:59:49	5					
03:01:48				-142.7		Gyro speed check
03:05:08				-138.2		
04:13:00	4					
04:16:00	2					
04:17:56	1					
04:19:08				-138.6		Low power
04:20:49				-117.5		High power; Δ = 21.1 db
04:21:32		4400		-121.8		
04:46:16				-121.8		
04:46:49						Premidcourse maneuver – roll
04:50:08						Premidcourse maneuver – pitch
04:52:36	2					
04:54:00	1					
05:01:16	5					
05:03:02				-120.0		
05:03:18						Postmidcourse maneuver – pitch
05:06:18						Postmidcourse maneuver – roll
05:10:53	2					
05:12:14	4	4400	11			
05:15:09	5					
05:15:44		1100				
05:16:33				-139.2		3×10^{-3} BER
05:39:00				-139.1		(T $\approx$ 45.90°K)
06:03:10				-139.8		3×10^{-3} BER
06:31:51				-139.1		
07:03:14	4					
07:07:41	2					
07:11:49	5					
07:36:45				-139.6		
08:13:10			42	-139.5		15×10^{-3} BER (T = 54°K)
08:13:30			11	-139.7		2.6×10^{-3} BER (T = 52°K)
08:33:52				-140.1		
08:48:31		1100	42	-140.5	- 1.4	(Nominal)
08:50:09		550		-141.7	+ 2.3	(Nominal)
09:32:51				-141.1		
10:01:18				-138.5		
10:34:49				-139.6		6×10^{-5} BER
11:00:47				-138.9		
11:33:05				-139.9		2×10^{-5} BER
12:00:00				-141.0		
12:34:44				-141.1		
13:00:00				-140.5		
13:30:00				-141.3		
13:35:00			51	-141.5		
13:55:00				-141.5		
14:00:00			42	-141.4		1×10^{-3} BER
14:05:00			51	-141.5		
14:46:00			61	-141.5		

Table 5. 3-1 (continued)

Time (GMT), hr:min:sec	Mode	Bit Rate	DSIF Station	DSIF AGC-DBM	TLM Margin, db	Comments
Day 108 (continued)						
15:08:23	6					
15:13:08	4					
15:17:59	2					
15:21:13	5					
15:36:00			61	-141.9		
16:06:00			61	-140.9		
16:06:00			51	-140.7		
17:00:00			51	-141.3		
17:00:00			61	-141.4		
17:55:00			61	-143.0		Gyro drift check in progress
18:23:00			51	-142.7		
18:23:00			61	-142.3		
18:57:00			61	-142.0		
19:30:00	5	550	61	-142.3		Terminate gyro drift check
19:31:00			61	-142.0		Terminate gyro drift check
20:02:57	4					
20:09:08	2					
20:12:14	5			-142.0		Terminate gyro drift check
20:26:20				-141.6		Terminate gyro drift check
21:47:44			11			Three-way
22:13:00			11	-145.0		
22:16:25			11			Two-way
22:42:00				-144.6		
23:52:00				-144.0		
Day 109						
00:52:34	4		61			
00:59:53	2					
01:07:20	5			-142.8		
01:54:13				-142.7		
02:14:00						Cmd mod off
02:20:02						Xmtr off
02:21:07			11			Confirms two-way
02:36:00				-145.4		
03:36:06				-144.0		Terminate gyro drift
03:36:32				-144.1		Terminate gyro drift
03:57:00				-144.0		
03:57:25						Start gyro drift check
04:23:40				-144.3		
05:17:55				-145.9		
05:24:04				-145.8		
05:25:03	4					
05:32:02	2					
05:39:21	5					
06:00:40				-146.1		
06:34:00			11			Cmd mod off
06:40:00			42			Two-way
06:44:59				-142.8		
06:46:46				-143.5		
06:50:44				-143.5		
07:01:00				-143.5		
07:07:07				-143.4		
07:30:00				-143.5		
08:00:00				-143.1		
08:20:50				-142.7		
08:28:28			11	-146.8		9.2×10^{-3} BER

Table 5. 3-1 (continued)

Time (GMT), hr:min:sec	Mode	Bit Rate	DSIF Station	DSIF AGC-DBM	TLM Margin, db	Comments
Day 109 (continued)						
09:08:50			11	-146.0		
09:10:24	5	550	11	-146.6		Terminate gyro drift test
09:45:02			42			8.8 - 8.7 x 10^{-3} BER
09:56:08				-143.8		
09:59:04		137.2		-146.0		
10:02:55	4					
10:05:14	2					
10:19:44	5					
10:21:00				-146.0	+ 7.4	
10:42:28				-146.2		
11:14:43				-146.2		
11:17:20				-145.6		
12:17:50				-145.5		No error count
12:37:50				-145.5		
12:41:23						End gyro drift check
12:42:30				-146.5		
12:47:56	4					
12:50:51	2					
12:53:25	5					
13:02:00				-146.3		
13:28:00				-146.5		
14:00:00				-146.6		
14:28:10			61	-147.1		
14:50:55				-147.5		Gyro drift check
15:40:30				-147.5		
16:01:00				-146.8		Xpndr pwr off at 15:59:51
16:05:23						Xpndr B pwr on
16:11:00				-147.1		
16:58:30				-146.8		End gyro drift check
17:17:12	4					
17:21:55	2					
17:24:20	5					
17:54:58						Cmd mod off – xfer to DSS-51
17:55:00						Started tuning
17:56:32						On XA – ready for xfer
18:00:38				-147.0	+ 6.4	Three-way with DSS-51
18:00:38			51			Two-way
18:45:00			61			Two-way
19:19:50				-146.4	+ 7.0	
19:43:10	6					
19:46:45	4					
19:48:38	2					
19:53:50				-146.1		
19:54:34	5	137.2	61			
21:00:00				-147.3	+ 6.1	
21:24:49	4					
21:26:43	2					
21:28:17	1					
21:30:05	5					
21:31:57						A/D SCOs off
21:32:18						Gyro spd sig process on
21:36:51	5					
21:40:24						Xpndr pwr off
21:41:40						Xpndr B pwr on
21:53:00				-147.3	+ 6.1	

Table 5.3-1 (continued)

Time (GMT), hr:min:sec	Mode	Bit Rate	DSIF Station	DSIF AGC-DBM	TLM Margin, db	Comments
Day 109 (continued)						
22:11:11			11			DSS-11 has decom lock
22:15:00						DSS-11 two-way
22:20:00				-147.6	+ 5.8	
22:46:15				-147.6	+ 5.8	
23:01:56	6					
23:04:00				-147.2		
23:06:00	4					
23:07:59						Xmtr B filament pwr
23:09:41						Xmtr B hi pwr
23:10:40		1100		-125.0		$\Delta P \doteq 22.2 - 3.35 \pm 18.9$ db
23:10:40						
23:12:10	2					
23:13:17	5					
23:13:50				-124.6		
23:17:46						TD strain gage pwr on
23:18:00				-124.6		
23:19:21						Xpndr pwr off
23:20:15				-124.4		
23:23:30						Start yaw maneuver
23:30:00						End yaw (approximately)
23:30:17						Start pitch maneuver
23:33:30						End pitch (approximate time)
23:34:35						Start roll maneuver
23:37:00						End roll (approximate time)
23:45:00			14	-116.5		
23:46:20	6					
Day 110						
00:02:32.7	6	1100	11			TD strain gages on — Pre sum amp on
00:04:18						Touchdown — DSS-11 and DSS-14 remained in lock at TD
00:04:50				-126.3		
00:09:33		550				Switched from A/D conv. 1 to conv. 2
00:09:38		1100				Re-established 1100 bps after A/D conv. switching
00:12:09						TD strain gage and propulsion strain gage pwr off
00:12:10				-125.0		
00:13:32	5					
00:16:13			14	-122.1		
00:18:52	2					
00:22:54		550		-123.0		
00:26:41				-143.6		Low power
00:28:11		137.5				
00:34:56						Xmtr B low power off
00:35:02						Xmtr A low power on
00:36:44						Xmtr B to planar array
00:37:45						Completed configuring xmtr A on omni B
00:38:20				-146.4		Low pwr xmtr A/omni B
00:49:51						Xmtr A hi pwr
00:50:48		1100				
00:55:17						ESP commutators off
00:55:32						Summing amps off
01:00:58	7					Start 200-line TV
01:30:41						Complete 200-line TV sequence
01:35:54	5					Hi pwr xmtr A
01:48:28	4					
01:54:43						A/D conv. 1 on
01:54:56		1100				

Table 5. 3-1 (continued)

Time (GMT), hr:min:sec	Mode	Bit Rate	DSIF Station	DSIF AGC-DBM	TLM Margin, db	Comments
Day 110 (continued)						
02:00:52						Xmtr A hi pwr off
02:02:08						ESP comm off, A/D conv. pwr
02:02:54						Off, SCOs off, sum amps off, xmtr low pwr off
02:03:06						Nonessential loads off
02:05:47						Xmtr A on low power
02:05:52						Narrow band VCXO on
02:14:53						PM sum amp A on
02:15:07						A/D conv. 2 on
02:16:22	4	137.5		-146.1		
02:31:48	5					
02:59:54						Xmtr A hi pwr
03:00:38				-126.1		
03:03:08						Summing amps off
03:05:00				-119.8		Hi pwr – no modulation
03:07:47						Start 200-line TV
03:52:00						Complete 200-line TV sequence
03:56:21						Xmtr A high power
03:57:08	5					
04:00:32	4					
04:16:23	7					Start TV sequence
05:00:59						End TV sequence
04:04:26						Xmtr A high pwr
05:05:07	5					
05:15:01	4					
05:19:13		137.5				
05:20:27						Xmtr high voltage off
06:30:00	5					
06:32:29						Start positioning solar panel, planar array
07:23:21						Xmtr A to planar array
07:27:03						Continue positioning planar array
08:15:30						Planar array positioning completed
08:18:57	4					
08:20:31		1100				
08:33:13						Xmtr A high pwr
08:33:47		4400				
08:40:36	7					Start TV sequence
10:01:58						End TV sequence
10:03:57						Xmtr high voltage off
10:04:33		1100				
10:04:38	4					
10:11:04			11	-119.1		
10:28:53						Xpndr A pwr on
10:36:30			42	-115.0		
10:48:00				-115.0		
10:49:56		550		-117.0		
10:59:18		137.5		-118.2		
11:08:14		17.2		-119.0		
13:18:12				-119.0		
14:09:45	5			-118.5		
14:13:03						Start planar array positioning
14:30:17						End planar array positioning
14:54:00				-119.3		

TABLE 5. 3-2. SPACECRAFT CONFIGURATION SHEET

Time (GMT), hr:min:sec	Major Sequence Title	Transmitter A/B	Transmitter Pwr H/L	Omni A/B	A/D Converter 1/2	Receiver A OL/AFC	Receiver A Transponder A	Receiver B ØL/AFC	Receiver B Transponder B	Command Dec A/B	Comments
Day 107											
07:05:01	Launch	B	Low	B	1	N/A	Off	N/A	On	B	
07:39:54	Mark 20		High			AFC		ØL			
08:00:07											DSS-42 acquired uplink
08:09:49			Low								Initial spacecraft operations
12:00:00											Command modulation off – DSS-42
12:17:45											
14:07:18					Both off						Command modulation on – DSS-51
											Troubleshooting sequence to verify proper carrier suppression
14:12:23					1						
14:25:00										A	Command modulation off – DSS-51
14:34:45											
16:02:25											Command modulation on – DSS-61
											Preparation for star identification acquisition sequence
16:05:53								AFC	Off		
16:31:26								ØL	On		
16:55:00											Command modulation off – DSS-61
17:00:02								AFC			DSS-51 experienced difficulty during transfer from DSS-61 to DSS-51
17:17:11											
18:40:20								ØL		B	Dec B observed to be on at time indicated. Time of occurrence unknown.
20:25:00										A	Command modulation off – DSS-51
20:35:00											Command modulation on – DSS-61 – approximate time
22:10:00											Command modulation off – DSS-61
22:20:00											Command modulation on – DSS-11
Day 108											
04:20:49	0043		High								
05:16:09	0043		Low								Midcourse correction preparation
08:35:00											Complete midcourse
08:45:00										B	Command modulation off – DSS-11
14:35:00											Command modulation on – DSS-42 – time approximate
14:45:00											Command modulation off – DSS-42
16:35:00											Command modulation on – DSS-61
16:43:00										A	Command modulation off – DSS-61
18:05:00											Command modulation on – DSS-51
18:15:00											Command modulation off – DSS-51
21:05:00											Command modulation on – DSS-61 – time approximate
21:15:00											Command modulation off – DSS-61
22:15:00											Command modulation on – DSS-51
22:25:00											Command modulation off – DSS-51
Day 109											Command modulation on – DSS-11 – time approximate
00:15:00											
00:25:00											Command modulation off – DSS-11
02:15:00											Command modulation on – DSS-61
02:25:00										B	Command modulation off – DSS-61
06:35:00											Command modulation on – DSS-11 – time approximate
06:45:00											Command modulation off – DSS-11
08:35:00											Command modulation on – DSS-42
08:45:00										A	Command modulation off – DSS-42
09:40:00											Command modulation on – DSS-11 – time approximate
09:50:00											Command modulation off – DSS-11
14:15:00											Command modulation on – DSS-42 – time approximate
14:25:00										B	Command modulation off – DSS-42
15:59:52								AFC	Off		Command modulation on – DSS-61
16:05:26									On		Special check – Receiver B AFC / SPE difference
16:07:55										A	
16:09:21											Command modulation off to reacquire downlink
17:54:58								ØL			
18:05:00											Command modulation off –DSS-61
18:40:00										B	Command modulation on –DSS-51
18:50:00											Command modulation off –DSS-51 (Receiver A)
21:40:24								AFC	Off		Command modulation on – DSS-61
21:41:40									On	A	Receiver B AFC/SPE offset check
21:43:30								ØL			
22:10:00											
22:20:00											
23:09:41			High								Command modulation off – DSS-61
23:19:21								AFC	Off		Command modulation on – DSS-11
23:39:00										B	Time approximate
Day 110											
00:09:33					2						
00:26:30			Low								
00:35:00		A	Low								
00:49:52			High								
01:51:43					1						
02:00:52			Low								
02:03:06		Both off	Off								Nonessential loads off
02:05:47		A	Low								
02:15:08					2						
02:59:54			High								
03:07:47											200-line TV
03:51:59											End TV sequence
03:56:21			High								
04:18:20											Start TV sequence
05:00:59											End TV sequence
05:20:27			Low								

5.3.2 ANOMALY DESCRIPTION

The only RF subsystem anomaly observed during the mission was a bias of approximately -2 db in receiver B performance. However, three other events occurred which caused the subsystem to be questioned and, in two of the cases, exercised in a nonstandard manner for troubleshooting purposes. These three situations are briefly summarized here even though no spacecraft RF subsystem anomaly existed in any case. For the most part, this section is concerned with the slight degradation in receiver B performance.

5.3.2.1 DSS Measurement of Sideband Power

During the pre-Canopus coast period, DSS 42 reported that the apparent sideband power with the spacecraft transmitting data at 1100 bits/sec was 10 to 11 db below the carrier level as opposed to an expected value of 5.5 db. Also, the sidebands were located 6.8 kHz, instead of 7.35 kHZ, from the carrier. These measurements were verified by DSS 51. When the spacecraft PCM data were eventually turned off and sideband power was again measured and found to be correct, it was concluded that no problem existed with the spacecraft carrier modulation indices and that the situation occurred as a result of the technique used by the ground stations for measuring sideband power. A discussion of the troubleshooting procedure is given in Reference 1.

5 3.2.2 Down Link Signal Decrease Prior to Midcourse

Prior to the midcourse maneuver, while in transmitter high power, the DSS automatic gain control recorder in the spacecraft performance/analysis/command (SPAC) area indicated a drop of approximately 10 db when or about the time thrust phase power was commanded on. The decrease in power lasted approximately 20 seconds and then returned to normal. DSS 11 recordings were checked, and indicated that receiver 1 showed a drop in signal level, but that receiver 2 did not. (The SPAC recorder is slaved to the receiver 1 output.) DSS 12, also tracking at the time, did not confirm a power drop off at their receiver. The conclusion was that no spacecraft problem had developed, but that a problem in receiver 1 at DSS 11 caused the signal level drop.

5.3.2.3 Anomalous Data After Touchdown

At touchdown, spacecraft subsystems began reporting anomalous data. Nonstandard exercising of the RF subsystem, as well as other spacecraft subsystems, followed. However, it was determined that the anomalous behavior was not due to the RF subsystem. Reference 1 describes the events that occurred as a result of this situation.

5.3.2.4 Degraded Receiver B Performance

During Mission C coast periods, deviations from the predicted received signal level curves were noted in both the up and down links. As

discussed in subsection 5.3.4.2, gyro drift checks performed during these periods accounted for omnidirectional antenna gain variations that were not taken into consideration when the predictions were generated. However, deviations in receiver B received signal levels, above those expected due to the gyro drifts, as well as deviations from predictions during maneuvering periods, indicated that an approximate -2 db bias existed in either the performance or calibration of the receiver.

The following discussion presents the data and conclusions relating to this anomaly. It should be pointed out that, during the mission, this degraded behavior was of no great concern since the combined effect of the gyro drift and receiver bias at no time caused the signal level to deviate below the region bounded by the negative tolerance of the predicted values.

Omnidirectional antenna B up-link gain variations during the transit phase of the mission are illustrated in Figure 5.3-2. This figure shows the earth vector variation superimposed on the omnidirectional antenna B up-link antenna gain contour map. For the most part, the mission was flown with the relative spacecraft/ground station attitude so that the antenna operated in a high gain region ($G \geq -3$ db). However, during the Canopus acquisition sequence, the required 360-degree spacecraft roll resulted in gains as low as -18 db. Figure 5.3-13 illustrates measured versus actual gain values for this maneuver and indicates an offset of approximately 2 db between the two sets of data. Figures 5.3-7 and 5.3-16 are similar presentations for the coast phases and midcourse phase, respectively, and indicate the same general bias. (Note: A 2-db compensation was made in the reduction of the mission data contained in Figure 5.3-7 to allow for data correlation in discussions that follow. It is therefore necessary to decrease all data points by 2 db to make this figure compatible with the arguments presented in this section.)

Point-by-point evaluation of the antenna pattern data, even in the high gain regions, has an uncertainty of ±2.5 db. Mapping many points within this region, of course, reduces this uncertainty but need not necessarily eliminate it entirely. From this standpoint, the significance of the Canopus data becomes apparent. Antenna gains are sampled throughout a region of high and low values where the uncertainty for any given point now varies as a function of the absolute value of that point. It is therefore unlikely that the bias seen in all the data can be attributed to any uncertainty in the antenna pattern data due to the consistency of the measured data throughout the wide range of sampled antenna gain values.

A second questionable area is the calibration data used to convert the spacecraft data to engineering units. Two sets of data were available for the conversion: one taken at the unit level and the other during solar thermal vacuum retest. The data chosen were those taken during the solar thermal vacuum retest since they were more representative of a space environment. The receiver calibration is quite sensitive to temperature at the low signal levels; however, for the range of values encountered during the mission (between -60 and -100 dbm), the sensitivity is not too significant. Also, for the temperatures encountered during the mission (approximately 75° F), the two sets of data essentially fall on top of each other, and the interpretation of mission data using either set yields the same general conclusions. (See References 2 and 3 for listings of these calibration data.)

Time constraints due to lunar experimentation and the anomalous conditions of the spacecraft analog data precluded any calibration attempt for Surveyor III during the first lunar day. Had this been performed, as it had on Surveyor I, additional insight into the reason for the observed -2 db bias in receiver B may have been gained. Therefore, it can only be concluded that the calibration had changed by 2 db or that the insertion loss value used for the predictions was in error.

Data relating to receiver B performance, except where noted, used in the remaining sections of this report will be compensated values having the 2-db bias removed.

5.3.3 SUMMARY AND CONCLUSIONS

Table 5.3-3 contains a summary of the measurable performance parameters compared with applicable requirements and premission predictions. Most subsystem parameters are not directly measurable, and those that are measurable are difficult to summarize due to time variability.

Received signal level, for example, is a function of time and spacecraft attitude. The summary for these parameters reflects wide tolerances, with corresponding wide variations in actual performance, in cases when the earth vector was in the omnidirectional antenna null. Performance and predictions outside the null are much more closely bounded. More detailed information is found in the subsections dealing with each mission phase.

The following conclusions can be drawn as a result of the foregoing analysis:

1) RF subsystem performed as expected with the exception of receiver B. In most cases, close to nominal performance was experienced in both the up and down links.

2) Receiver B performance was biased by -2 db from the predicted values. No operational problems resulted since the signal level at no time deviated below the region bounded by the negative tolerances of the predicted values.

(3) Mission C again verified the accuracy of the omnidirectional pattern data measured on the JPL range.

(4) RF subsystem premission predictions and real-time analysis techniques used during Mission C were relatively accurate.

5.3.4 SUBSYSTEM PERFORMANCE ANALYSIS

5.3.4.1 General Discussion

Before specific phases are discussed, a general treatment of the mission will be undertaken. Information application to all mission phases is included in this subsection.

Subsystem Parameters

Most quantitative estimates of performance are based on received signal levels which, in turn, are determined from individual link parameters. Those parameters used in the performance predictions and the subsystem analyses are tabulated in Table 5.3-4. Equations using these data are derived here; parameters discussed in later portions can be evaluated from these data. Tables 5.3-4 and 5.3-5 consist of measured data taken from flight acceptance (FAT), solar thermal vacuum (STV), and command and data handling console (CDC) tests or specification values where measurements were not available.

TABLE 5.3-3. RF PERFORMANCE PARAMETER SUMMARY

Parameter	Predicted Value	Requirement	Actual Performance
Transmitter frequency at acquisition	2294.995900 MHz	2295 MHz ± 23 kHz	2294.9935 MHz (2 minutes 37 seconds after one-way acquisition)
Receiver B frequency at acquisition	2113.315584 MHz	2113.31 MHz ± 21 kHz	2113.318944 MHz (at two-way acquisition)
Receiver A signal levels during coast phases*	Time variable predictions. Predicts are some nominal value ±10 db.	> - 114 dbm**	Level between +2 and -12 db of nominal and ≥ - 113 dbm
Receiver B signal levels during coast phases*	Time variable predictions. Predicts are some nominal value ±4 db.	> - 114 dbm**	Level between 0 -4 db of nominal and ≥ - 94.0 dbm
Receiver A signal levels during star maneuver	Time variable predictions. Predicts are some nominal value ±10 db.	> - 114 dbm**	Level between +5 and -6 db of expected and ≥ - 100 dbm
Receiver B signal levels during star maneuver	Time variable predictions. Predicts are some nominal value ±10 db.	> - 114 dbm**	Level between +2 and - 3 db of expected and ≥ - 97 dbm
Receiver A signal levels during postmidcourse maneuver	Time variable predictions. Predicts are some nominal value ±10 db.	> - 114 dbm**	Level between +5 and - 6 db of expected and > - 105 dbm
Receiver B signal levels during postmidcourse maneuver	Time variable predictions. Predicts are some nominal value ±3.0 db.	> - 114 dbm**	Level between +1.3 and - 3 db of expected and > - 92 dbm
Receiver A signal levels during terminal maneuver	Time variable predictions. Predicts are some nominal value ±10 db.	> - 114 dbm**	Level variations of 26.8 db and > - 123.7 dbm (predicted variations of 22 db)
Receiver B signal levels during terminal maneuver	Time variable predictions. Predicts are some nominal value ±3.4 db.	> - 114 dbm**	Level variations of 6.2 db and > - 99.7 dbm (predicted variations of 7.0 db)
DSS signal levels during coast phases*	Time variable predictions. Predicts are some nominal value ±6 db.	> - 157.7 dbm (carrier power) (17.2 bps threshold)	Level between +2 and - 4 db of nominal and > - 148 dbm at 137.5 bps
DSS signal levels during star maneuver	Time variable predictions. Predicts are some nominal value ±10 db.	None	Level between +6 and - 5 db of expected and ≥ - 146 dbm (carrier power at 4400 bps)
DSS signal levels during midcourse maneuver	Time variable predictions. Predicts are some nominal value ±3.0 db.	> - 136.4 dbm (carrier power at 4400 bps/high power)	Level between +2 and 0 db of expected and > - 121.5 dbm
DSS signal levels during terminal maneuver and descent	Time variable predictions. Predicts are some nominal value ±2.7 db.	> - 130.7 db (carrier power at 1100 bps/high power)	Level between 0 and -2 db of expected and > - 125 dbm (carrier at 1100 bps)

Table 5.3-3. (continued)

Parameter	Predicted Value	Requirement	Actual Performance
Transmitter A high power output	39.8 dbm $^{+0.2}_{-0.1}$ db	> 39.6 dbm	Not directly available due to telemetry anomaly
Transmitter A low power output	20.3 dbm $^{+0.7}_{-0.8}$ db	> 19.1 dbm	Not directly available due to telemetry anomaly
Transmitter B high power output	40.3 dbm ±0.1 db	> 39.6 dbm	Output between 40.3 and 40.5 dbm
Transmitter B low power output	21.0 dbm $^{+1.3}_{-1.2}$ db	> 19.1 dbm	Output between 19.2 and 21.7 dbm
Phase jitter 12 Hz bandwidth	< 36 degrees	< 36 degrees (3σ)	N/A
Phase jitter 152 Hz bandwidth (thrust phase)	< 22 degrees	< 22 degrees (3σ)	< 3 degrees at midcourse and touchdown
Command reject rate	< 1/2000	≤ 1/2000 at signal level > - 114 dbm	No known rejected commands in 23,435 sent at signal levels greater than -100 dbm***

*Gyro drift checks during coast phases caused antenna gain variations not taken into account in the predicted signal levels.

**Threshold value applies to command threshold and, as such, only requires one of the two receivers to be above -114 dbm at any one time.

***Number of commands does not include TV operations and covers through day 124.

N/A Not available.

Note: Receiver B values include correction for the - 2 db bias in measured flight data (see the anomalies discussion, subsection 5.3.2).

Computations Used

In this subsection, reference is made to received signal levels and quantities computed from these levels. The equations used are listed below and will not be derived again:

1) Spacecraft transmitter high power output is

$$P_{xmtr}(\text{dbm}) = 10 \log (P_{tm} \times 10^3) + L$$

where

P_{xmtr} = transmitter power (dbm) = P_{high}

P_{tm} = telemetered power output (watts)

L = loss from transmitter to power monitor. (Value for transmitter B/omnidirectional antenna B ≃ as determined from STV calibration data.)

TABLE 5.3-4. UPLINK PARAMETERS FROM FAT, STV, AND CDC TESTS

Description	Value
Transmitting system (DSS)	
RF power	$70.0\ ^{+0.5}_{-0.0}$ dbm
Antenna gain	
SAA	20.0 ± 2.0 db
SCM	51.0 (+1.0, -0.5) db
Circuit loss	
SAA	-0.5 ± 0.0 db
SCM	-0.4 ± 0.1 db
Receiving system (SC-3)	
Circuit loss	
Receiver A	-2.3 ± 0.3 db
Receiver B	-3.9 ± 0.3 db
Uplink carrier tracking loop	
Equivalent noise	
Bandwidth	240 ± 24 Hz
Threshold SNR	12 db
Uplink channel	
Threshold SNR	9 db
System noise	
Temperature	2700°K
Equivalent noise	
Bandwidth (predetection)	13430 Hz
Data/subcarrier modulation index	7.2
Subcarrier/carrier modulation index	1.6 ± 0.16

TABLE 5.3-5. DOWNLINK PARAMETERS FROM FAT, STV, AND CDC TESTS

Description	Value
Transmitting system (SC-3)	
RF power	
Transmitter A (low power)	20.3 (+0.7, -0.8) dbm
Transmitter B (low power)	21.0 (+1.3, -1.2) dbm
Transmitter A (high power)	39.8 (+0.2, -0.1) dbm
Transmitter B (high power)	40.3 (+0.1, -0.1) dbm
Planar array gain	27.0 ± 0.5 db
Circuit loss	
Transmitter A Omnidirectional antenna A	-3.1 (±0.3) db
Transmitter B Omnidirectional antenna A	-3.1 (±0.3) db
Transmitter A Omnidirectional antenna B	-3.2 (±0.3) db
Transmitter B Omnidirectional antenna B	-3.2 (±0.3) db
Planar array	-2.3 (+0.0, -0.2) db
Carrier frequency	2295 MHz
Receiving system (DSS)	
Antenna gain	
SAA (acquisition aid antenna)	21.0 ± 1.0 db
SCM (85-foot antenna)	53.0 (+1.0, -0.5) db

Table 5.3-5 (continued)

Description	Value
Circuit loss	
SAA	-0.5 ± 0.0 db
SCM	-0.18 ± 0.05 db
Effective noise temperature	
Maser	55 ± 10°K
Parametric amplifier (SAA antenna)	
All DSS except Johannesburg	270 ± 50°K
Johannesburg	320 ± 50°K
Lunar temperature	110 ± 25°K
Carrier channel	
Equivalent noise bandwidth for maneuvers (at threshold)	152 Hz
Equivalent noise bandwidth for coast mode (at threshold)	12 Hz
Threshold SNR	
Acquisition	9.0 db
Maneuvers	14.0 ± 1.0 db
Coast mode	11.4 db
SCO descriptions	
Equivalent predetection noise bandwidth, Hz ± 10 percent	
4400 bits/sec	4770
1100 bits/sec	1190
550 bits/sec	644
137.5 bits/sec	158.5
17.2 bits/sec	25.1
Strain gage 1	158
Strain gage 2	158
Strain gage 3	158
Reject/enable	377
Gyro speed	874

Table 5.3-5 (continued)

Description	Value
SCO center frequencies, kHz	
4400 bits/sec	33.0
1100 bits/sec	7.35
550 bits/sec	3.90
137.5 bits/sec	0.96
17.2 bits/sec	0.56
Strain gage 1	0.96
Strain gage 2	1.30
Strain gage 3	1.70
Reject/enable	2.3
Gyro speed	5.4
Threshold signal-to-noise ratio for telemetry data, ±1.0 db	
4400 bits/sec	10.0
1100 bits/sec	10.0
550 bits/sec	10.0
137.5 bits/sec	10.0
17.2 bits/sec	10.0
Strain gage 1	7.0
Strain gage 2	7.0
Strain gage 3	7.0
Reject/enable	10.0
Gyro speed	10.0
SCO modulation indices, ±10 percent	
4400 bits/sec	1.6
1100 bits/sec	0.935
550 bits/sec (acquisition)	0.3
550 bits/sec	1.15
137.5 bits/sec	1.45
17.2 bits/sec	1.45
Strain gage 1	0.65
Strain gage 2	0.65
Strain gage 3	0.65
Reject/enable	0.655
Gyro speed	1.600

2) Spacecraft transmitter low power output is

$$P_{low} = P_{high} - P_{DSS_H} + P_{DSS_L} \quad \text{(dbm)}$$

where

P_{low} = transmitter low power output

P_{high} = telemetered transmitter high power output

P_{DSS_H} = DSS received signal level at high power

P_{DSS_L} = DSS received signal level at low power

3) Spacecraft omnidirectional antenna gain (uplink) is

$$G_R = \frac{P_R}{P_T G_T \left(\frac{\lambda}{4\pi R}\right)^2 L}$$

where

G_R = received omnidirectional antenna gain (uplink gain)

P_R = received signal level (determined from spacecraft AGC)

P_T = DSS nominal transmitter power

G_T = DSS nominal antenna gain

λ = wavelength of uplink signal

R = slant range at time of computation

L = nominal spacecraft and DSS losses

(Note: For downlink gain, appropriate downlink parameters are inserted in a similar equation.)

When using these equations, attention must be given to the desired accuracy of the answer. Since several parameters are not measurable in flight, spacecraft telemetry, and DSS station reports are used, and consequently computed parameters have potentially large errors. Their validity is thus weighed against similar test data and/or is judged quite subjectively based on past experience. These equations are not used so much for their numerical results as for the total picture of subsystem performance generated. Any gross subsystem problems or computation errors will tend to be uncovered in this analysis, but subtle errors will not.

Omnidirectional Antenna Gain Maps

In order to better visualize and interpret the significance of the signal level data, traces of the earth vector on the omnidirectional antenna gain contour maps are presented. Figures 5.3-2 and 5.3-3 show the antenna up and down links. Since signal level variations are, for the most part, the result of increasing range (i.e., more space loss) and changing omnidirectional gain, these plots allow visualization of the expected signal level changes for comparison with plots of up-link and down-link signal levels versus time.

5.3.4.2 Mission Phase 1: Prelaunch to Spacecraft Acquisition

During the prelaunch phase, subsystem performance is assessed during the launch pad systems readiness test (SRT) and prelaunch countdown test. Next to assuring normal system performance prior to launch, the most important subsystem data taken during this phase are transmitter and receiver frequency data. Frequency data are used to predict the frequencies at initial acquisition and are transmitted from the Cape prior to launch. The DSS, in turn, uses these data to tune the DSS receiver for one-way lock and the DSS transmitter for eventual two-way lock.

The measured transmitter and receiver frequency data, as well as the corresponding predicted acquisition frequencies, are tabulated in Table 5.3-6. Compartment temperature during the prelaunch period was increasing, thus causing a frequency decrease, as expected. The temperature directly affecting the frequency is not actually measured, since the telemetered sensor is in the thermal tray and not at the voltage controlled crystal oscillator. Relative temperature versus frequency information is thus considered to be most reliable. Based on this judgment, the measured frequency data were consistent with previous SC-3 test data.

Acquisition frequencies were determined by extrapolating the measured values by essentially predicting the compartment temperature increase due to the high power operation from just prior to Centaur/Surveyor separation to the time of initial spacecraft acquisition. Figure 5.3-4 (obtained from Reference 4) illustrates test data results comparing transmitter B narrowband voltage controlled crystal oscillator frequency drift to time from initiation of high power operation. The original launch azimuth indicated that there would be 25 minutes of high power operation from separation to DSS 42 initial acquisition. Since the test illustrated in Figure 5.3-4 only

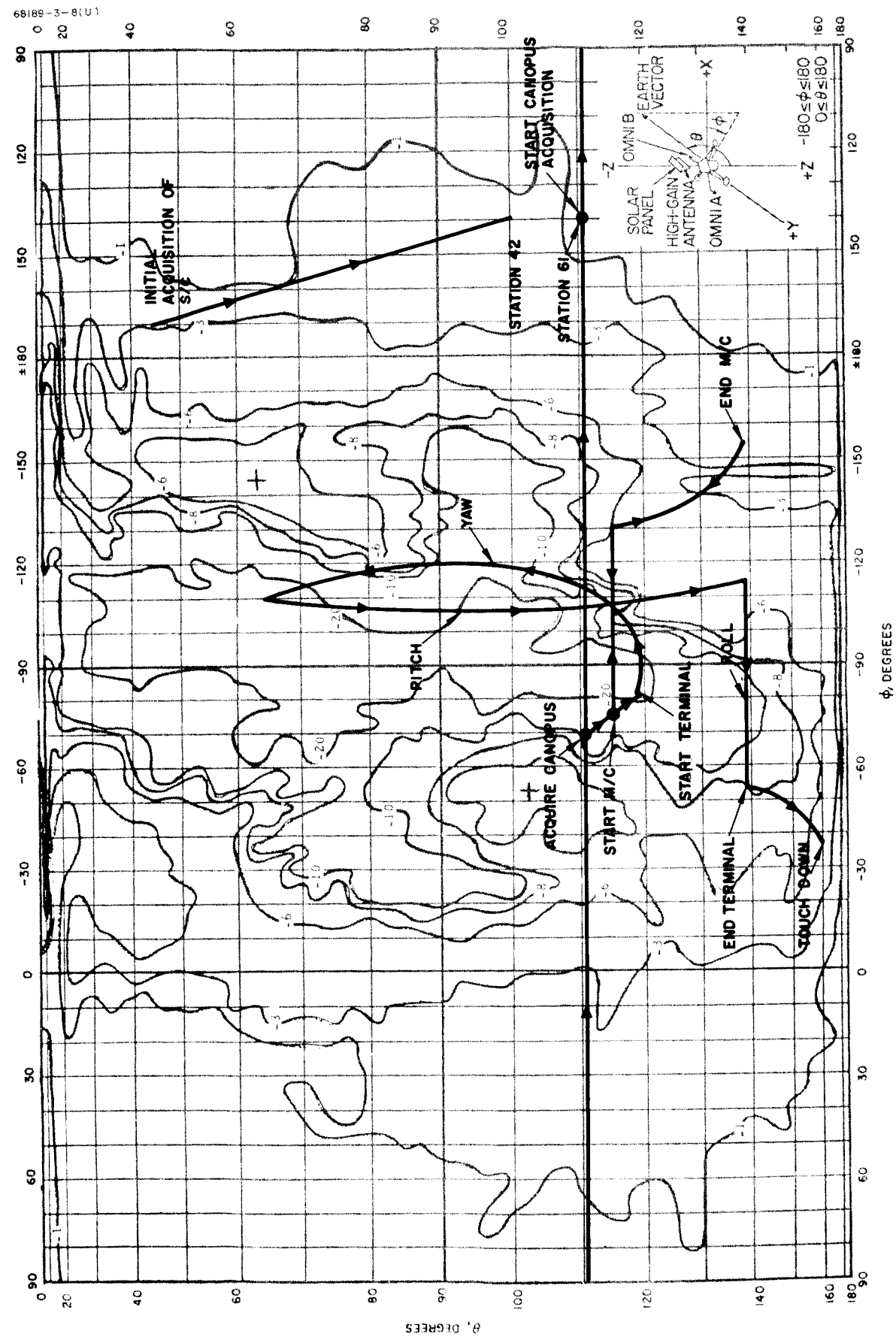

a) Omnidirectional Antenna A

Figure 5.3-2. Up-Link (2113 MHz) Omnidirectional Antenna Gain Map

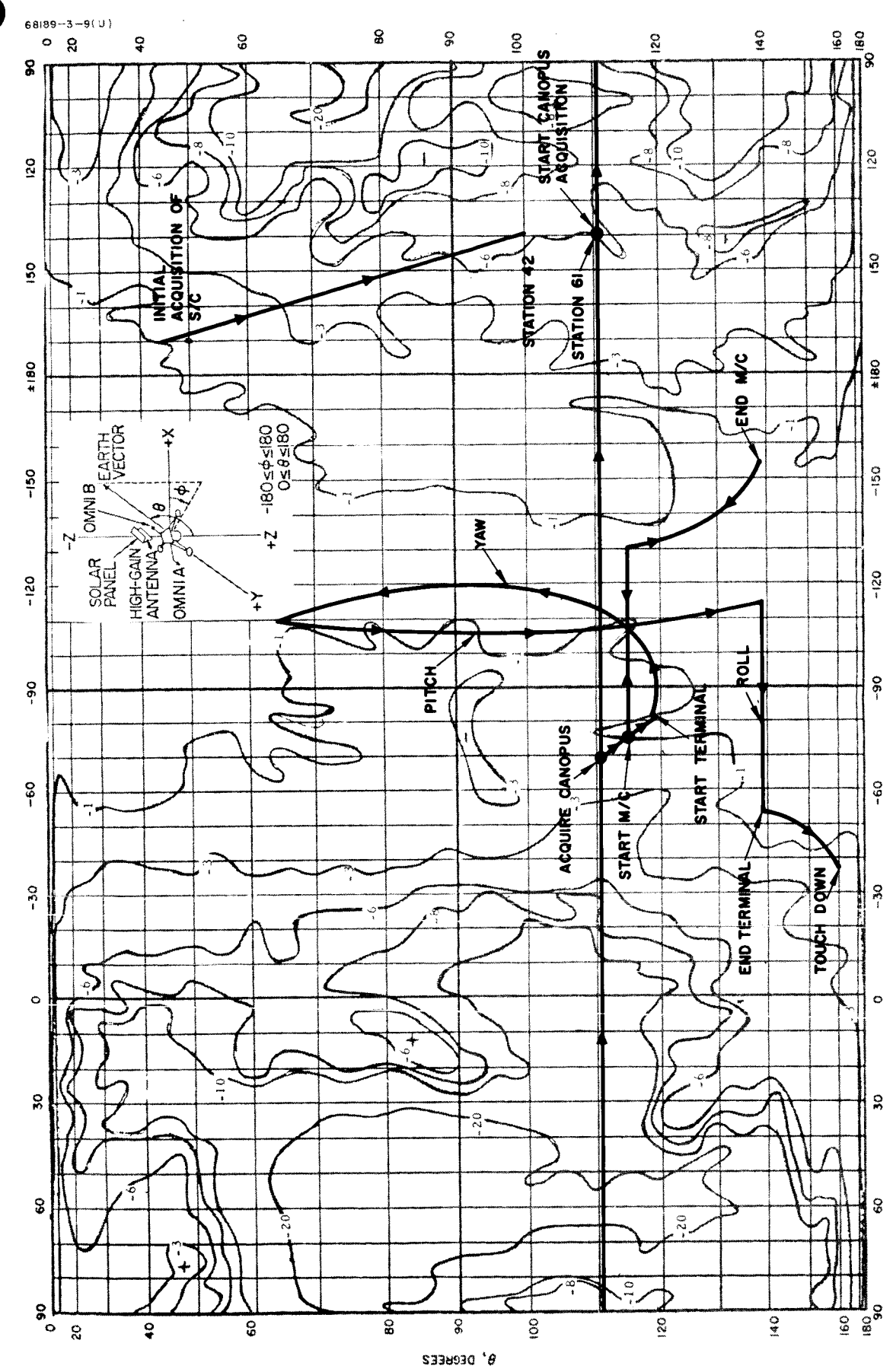

b) Omnidirectional Antenna B

Figure 5.3-2 (continued). Up-Link (2113 MHz) Omnidirectional Antenna Gain Map

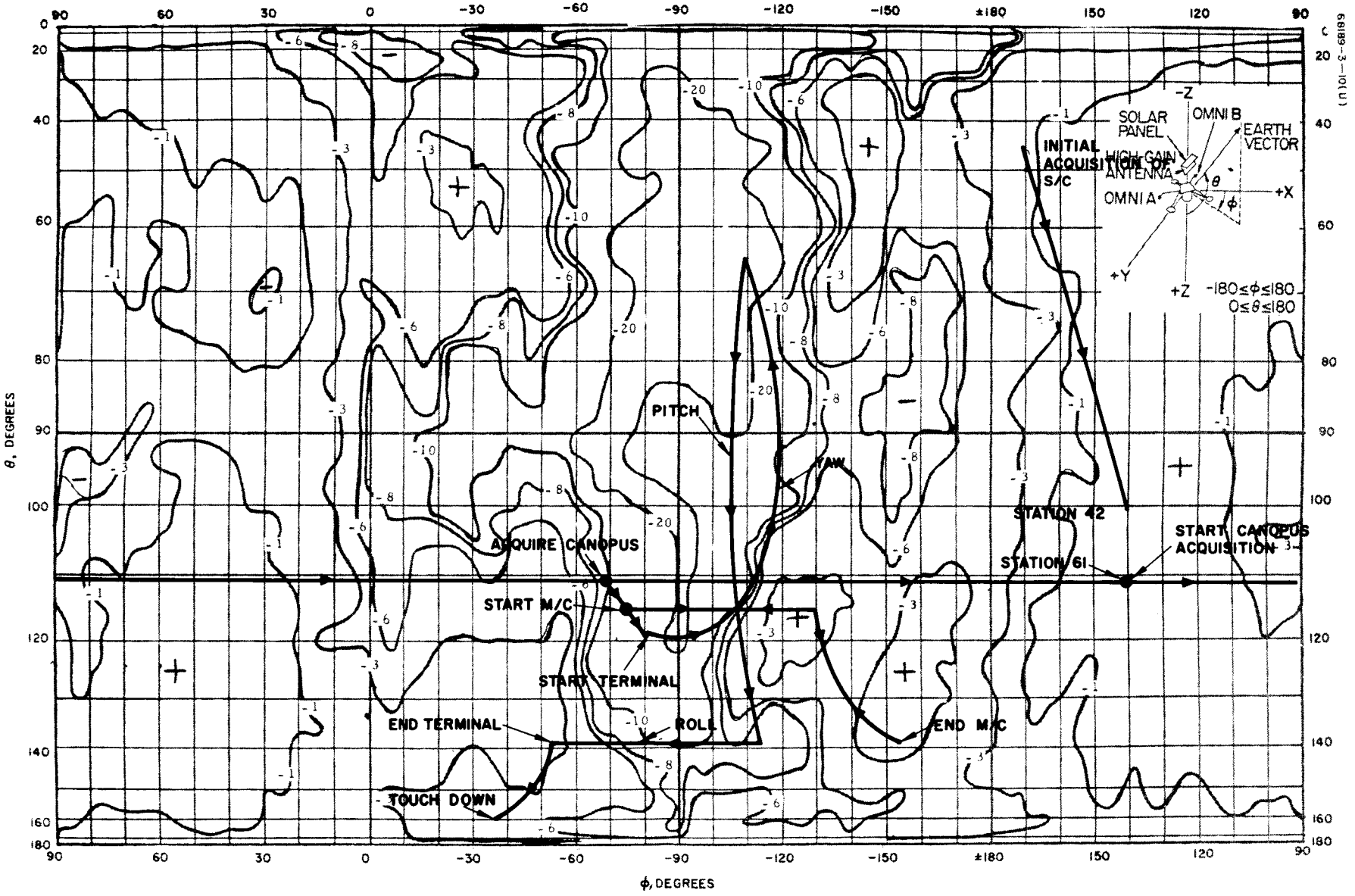

a) Omnidirectional Antenna A

Figure 5.3-3. Down-Link (2295 MHz) Omnidirectional Antenna Gain Map

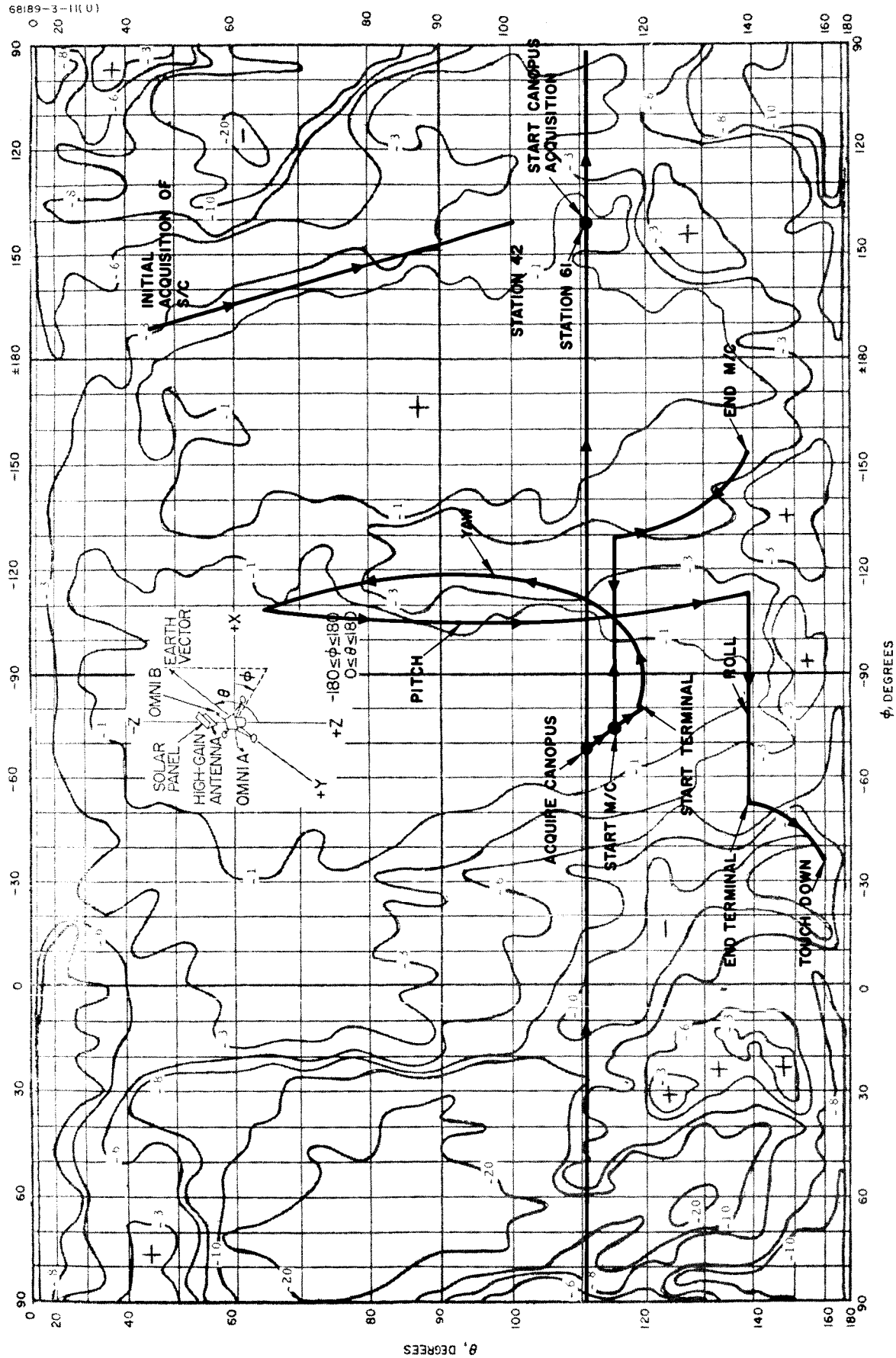

b) Omnidirectional Antenna B

Figure 5.3-3 (continued). Down-Link (2295 MHz) Omnidirectional Antenna Gain Map

TABLE 5.3-6. PRELAUNCH FREQUENCY SUMMARY*

Frequency Message, time in minutes	Measured Frequencies		Predicted Acquisition Frequencies		Lower Tray Temperature, °F
	One-way Narrowband Voltage Controlled Crystal Oscillator, mc	Best Lock, mc	One-way Narrowband Voltage Controlled Crystal Oscillator, mc	Best Lock, mc	
T-500 (Transmitter A)	2295.008502	2113.313008	2295.004502	2113.309008	72
T-400 (Transmitter B)	2295.003303	2113.321680	2294.999303	2113.317680	73
T-274 (Transmitter B)	2295.002811	2113.309344	2294.998811	2113.305344	79
T-90 (Transmitter B)	2295.003249	2113.323104	2294.999249	2113.319104	72
T-40 (Transmitter B)	2294.999900	2113.321776	2294.995900	2113.317776	75
T-20 (Transmitter B)	Not measured	2113.319584	–	2113.315584	80
T-5 (Transmitter B)	2294.995516	–	2294.991516	–	84

*Final frequencies used by Flight Performance/Analysis/Command for initial DSS 42 acquisition are: one-way, 2294.995900 MHz (T-40 report; two-way, 2113.315584 MHz (T-20 report).

covers approximately 20 minutes of high power operation, the expected frequency change was estimated, by extrapolating the test data, to be -4 kHz.

The final receiver prediction frequency was taken from the L-20 frequency message and the transmitter prediction frequency from the L-40 report. These frequencies represented the latest available data that could be formulated by the Trajectory Analysis group and transmitted to DSS 42 for use during initial acquisition.

The actual frequencies at initial acquisition were:

Transmitter (one-way) = 2294.993500 MHz

Receiver (two-way) = 2113.318944 MHz

The difference between predicted and actual was:

Transmitter = 2400 Hz

Receiver = 3360 Hz

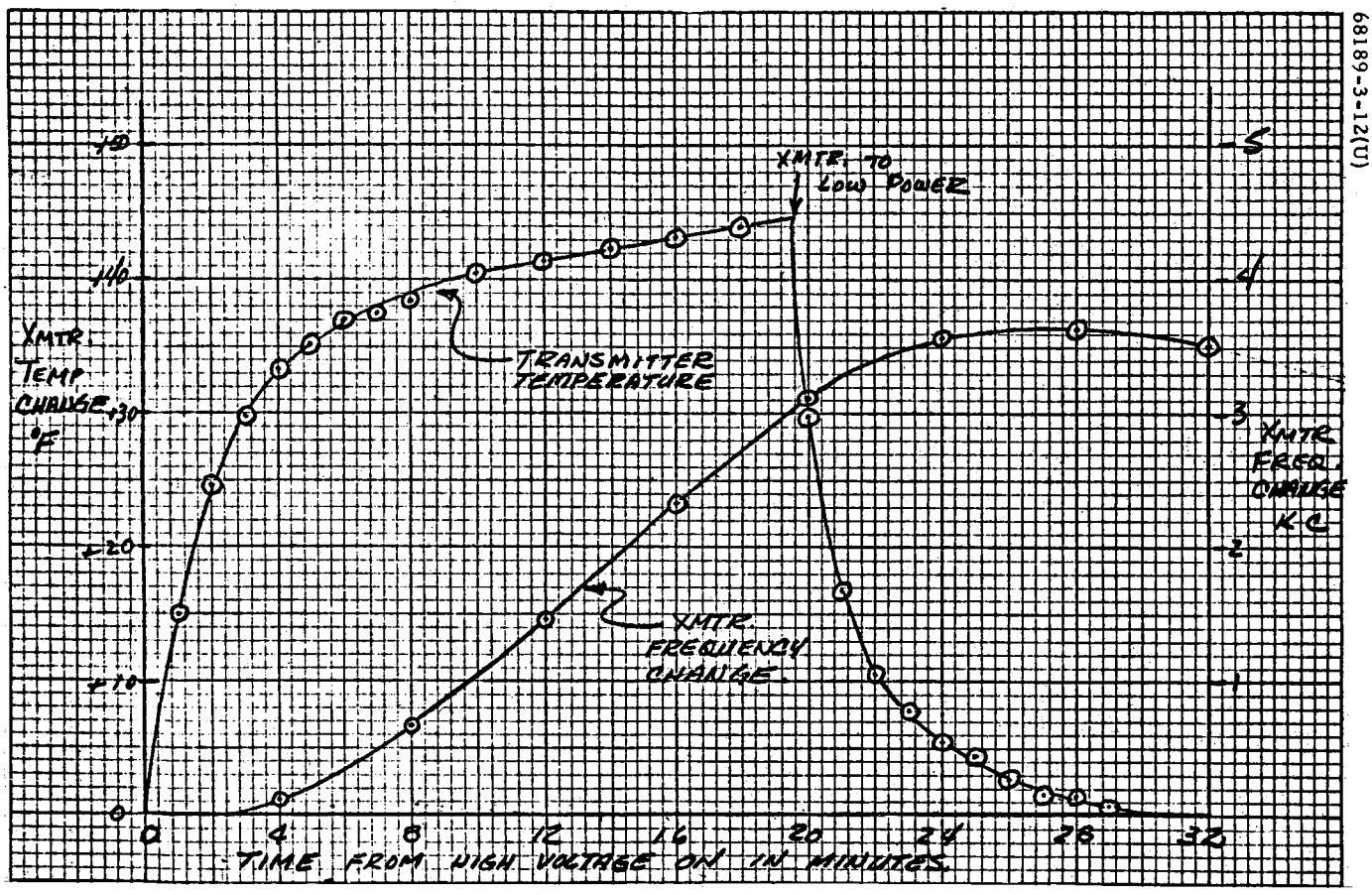

Figure 5.3-4. Transmitter B (S/N 17) Narrowband Voltage Controlled Crystal Oscillator Drift Rate

The T-5 hold was extended because of a suspected anomaly in the vernier engine 1 roll actuator. The alteration of the launch time caused a change in the launch azimuth which resulted in 16 minutes, rather than 25 minutes, of high power operation from separation to DSS 42 visibility. Had this been known and had operational time constraints allowed the use of the most current measured frequencies, the predicted acquisition frequencies would have been (see Table 5.3-6 and Figure 5.3-4):

Transmitter (one-way) T-5 report = 2294.993166 MHz

Receiver (two-way) T-20 report = 2113.317234 MHz

The difference between the predicted and actual frequencies would have been:

Transmitter = 334 Hz

Receiver = 1710 Hz

Table 5.3-7 is a summary of the significant events during initial RF acquisition at DSS 42 (Canberra). The spacecraft received signal levels for receivers A and B were -80 dbm and -60 dbm, respectively. One-way acquisition was accomplished 3 seconds later than the predicted first visibility, and two-way lock was accomplished in 5 minutes. Telemetry data indicated a signal in the passband of both spacecraft receivers at DSS transmitter turn on.

No problems were encountered during initial spacecraft acquisition. The spacecraft high power transmitter was turned off 30 minutes and 3 seconds after being commanded to high power by the Centaur. The maximum allowable time to accomplish turnoff is 1 hour.

5.3.4.3 Mission Phase Two: Coast

The coast phases consist of the following:

1) Pre-Canopus acquisition – Period from initial spacecraft acquisition until Canopus acquisition, during which time spacecraft attitude is uncertain in roll and the spacecraft -Z axis is pointed toward the sun.

2) Premidcourse – Period from Canopus acquisition until midcourse maneuvers.

3) Postmidcourse – Period from completion of midcourse maneuvers until terminal maneuvers.

Figures 5.3-5 and 5.3-6 are plots of DSS, receiver A, and receiver B signal levels from launch to touchdown. The premission predicted signal level after Canopus acquisition is shown in each figure. Since the spacecraft attitude in roll is uncertain to ±60 degrees about an estimated reference point prior to Canopus acquisition, no premission predictions are made for this period.

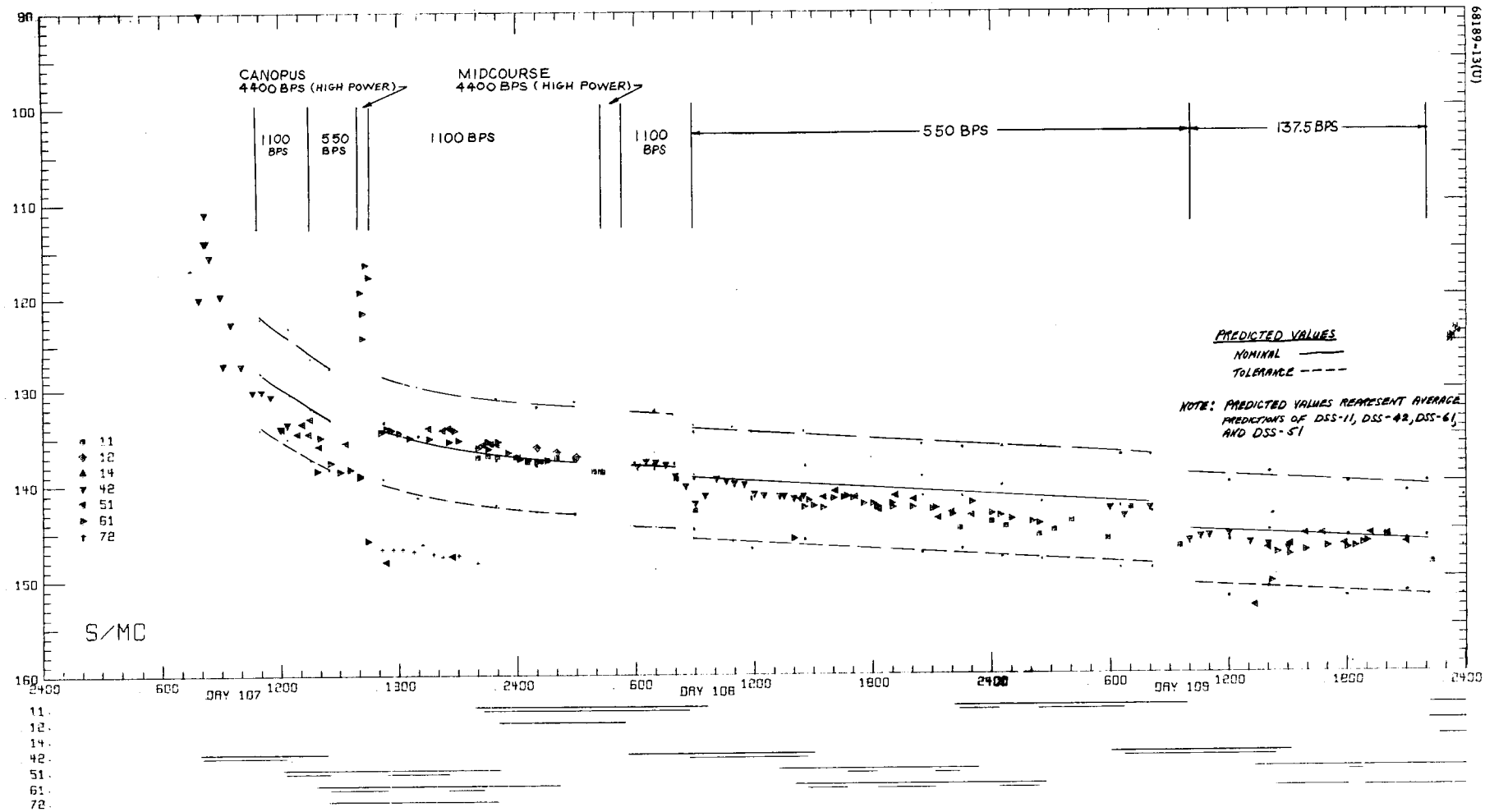

Figure 5.3-5. DSS Received Carrier Power

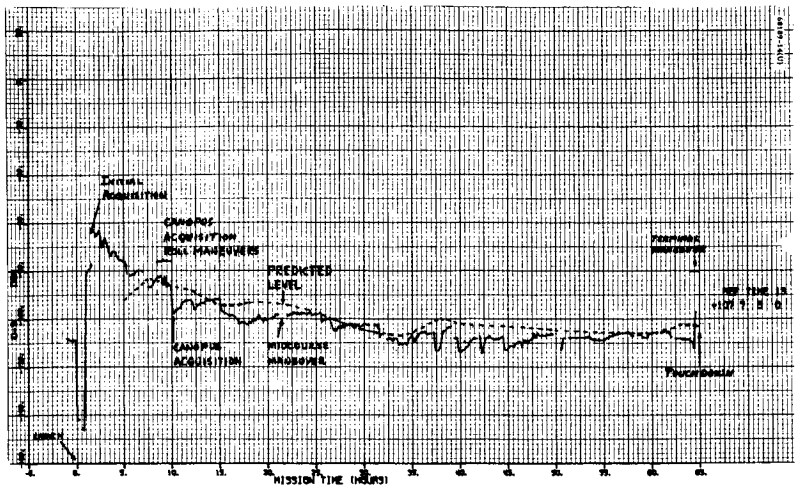

a) Receiver A

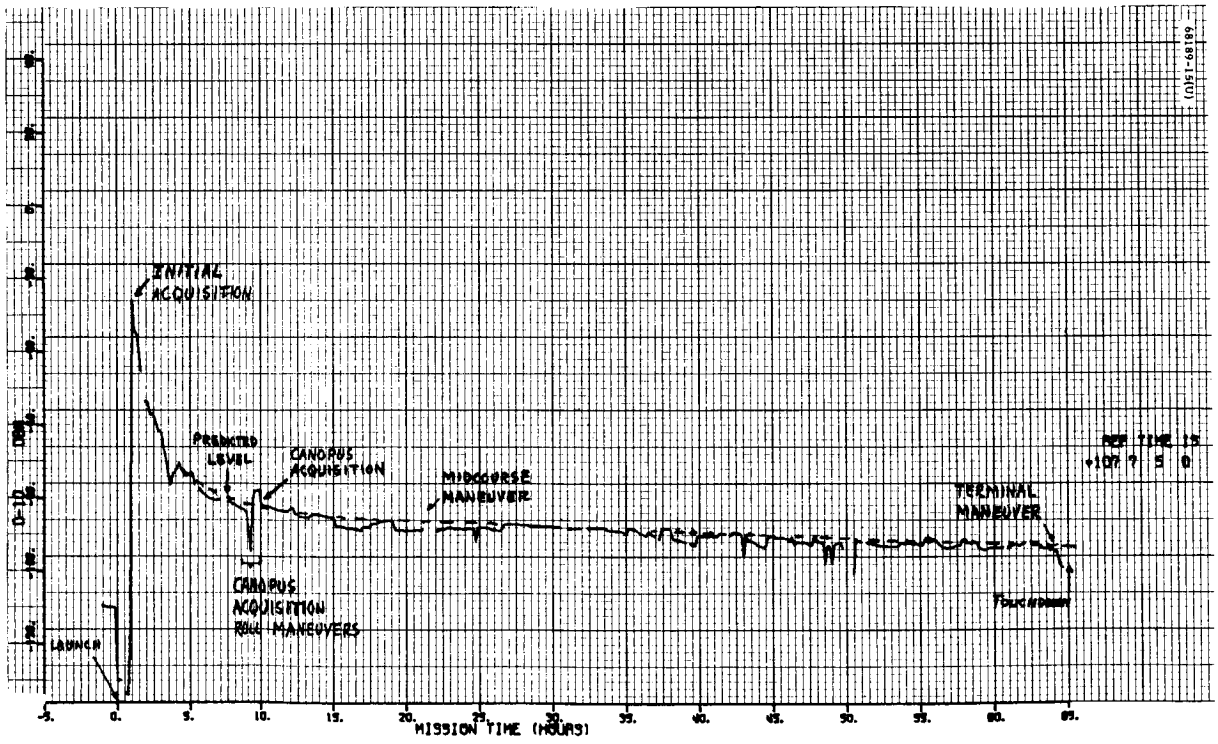

b) Receiver B

Figure 5.3-6. Automatic Gain Control Receivers

TABLE 5.3-7. ACQUISITION EVENTS

Event	GMT (Day 107), hr:min:sec	Comments
Transmitter B high power on	07:39:54.4	Spacecraft commanded to high power by Centaur.
DSS acquires spacecraft in one-way mode by SAA (acquisition aid) antenna	07:55:10	Accomplished 3 seconds later than predicted first visibility and 50 minutes and 9 seconds after launch.
DSS switch from SAA to SCM (85-foot dish) antenna	07:59:10	
DSS transmitter turned on	07:59:46	
Signal in passband of both spacecraft receivers	07:59:48	(From telemetry) Receiver B not phase locked. Receiver A pulling in (AFC capture mode).
Receiver A in AFC mode	08:00:02	(From telemetry)
Phase lock receiver B	08:00:07	DSS receiver dropped phase lock, indicating phase lock on receiver B.
DSS acquires spacecraft in two-way mode	08:00:30	DSS reacquired down link, indicating complete two-way acquisition 55 minutes and 29 seconds after launch. (DSS auto tracking on SCM.)
DSS confirms good two-way lock	08:01:30	
DSS turned on command modulation	08:03:13	
Transmitter B high power off	08:09:57	Spacecraft was in high power for 30 minutes and 3 seconds for initial acquisition phase (1-hour maximum allowed).

Referring to Figures 5.3-2 and 5.3-3, which show traces of the earth vector relative to omnidirectional antenna B down-link and omnidirectional antennas A and B up-link gain contours, it can be noted that changes in signal levels during the pre-Canopus acquisition phase and right at Canopus acquisition are in complete agreement with the antenna gain contour maps. The approximate antenna gains during the pre-Canopus phase are noted in Table 5.3-8.

Figures 5.3-5 and 5.3-6 indicate that, during the premidcourse and postmidcourse coast periods, received signal levels deviated from the predicted values in both the up and down links. During these two periods, eight three-axis gyro drift checks and four roll-axis-only drift checks were made. These checks accounted for earth vector variations not taken into consideration when generating the predictions. Figure 5.3-7 illustrates expanded antenna contour patterns for omnidirectional antenna B down link, omnidirectional antenna A up link, and omnidirectional antenna B up link, respectively, for the look angle region of pre- and postmidcourse coast phase operations. On each pattern is the average nominal trajectory trace for all stations assuming sun-Canopus lockon. Maximum deviations of +3 degrees in roll, -2 degrees in yaw, and +1-1/2 degrees in pitch from this nominal trace resulted from the performance of the gyro drift check. Even though a point-by-point evaluation of the received signal values versus the instantaneous gain values produced by the spacecraft drift does not correlate directly, the magnitude of the deviation in the signal level values seen in the data can certainly be attributed to antenna gain variations produced by the relatively small earth vector variations. The point is that even in the high gain regions, such as on omnidirectional antenna B, the antenna pattern characteristics are not smooth and that even minor variations in the earth vector can cause signal level variations. These variations are not completely predictable since minor spacecraft configuration changes can cause these pattern variations to shift slightly. However, as also seen from the data, the tolerances on the nominal signal level, which also includes antenna gain variations, quite conservatively bound those values seen in the mission data.

5.3.4.4 Mission Phase Three: Canopus Acquisition Maneuver

At approximately L+9 hours, the star acquisition maneuver was initiated. One roll about the Z-axis was required to make a star map and adequately identify Canopus. An additional 205 degrees of roll were required to finally acquire the star.

Real-time analysis indicated that the roll maneuver would take the earth vector through deep antenna nulls on both the up and down links of both omnidirectional antennas A and B. However, predicted signal level values during the maneuver, even considering worst-case tolerances, would not exceed the two-way tracking threshold. Also, the analysis indicated that no significant stars existed in the vicinity of possible data outages with the spacecraft transmitting via omnidirectional antenna B at a data rate of 4400 bits/sec.

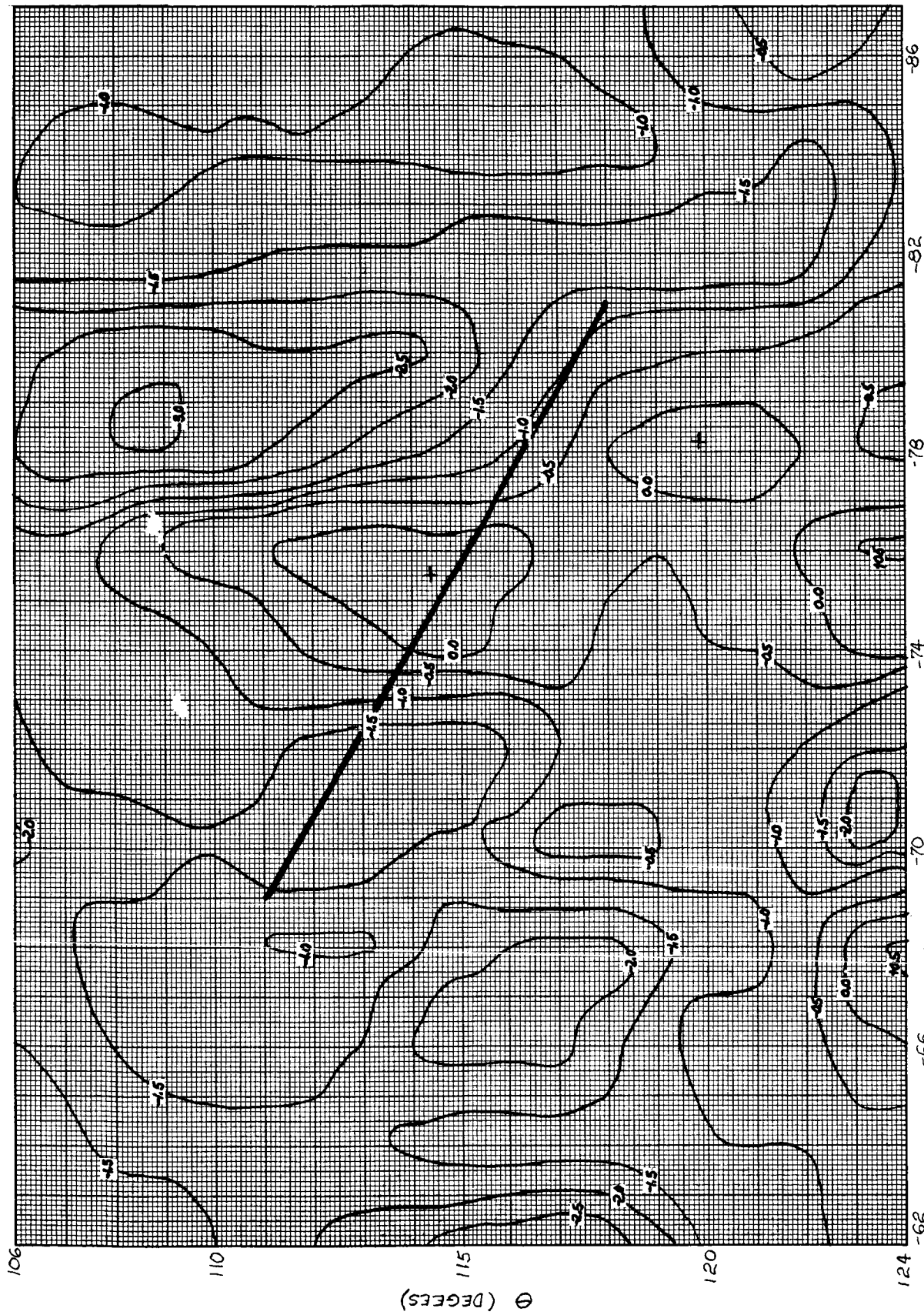

a) Omnidirectional Antenna B Down Link (2295 MHz)

Figure 5.3-7. Expanded Antenna Contour Patterns

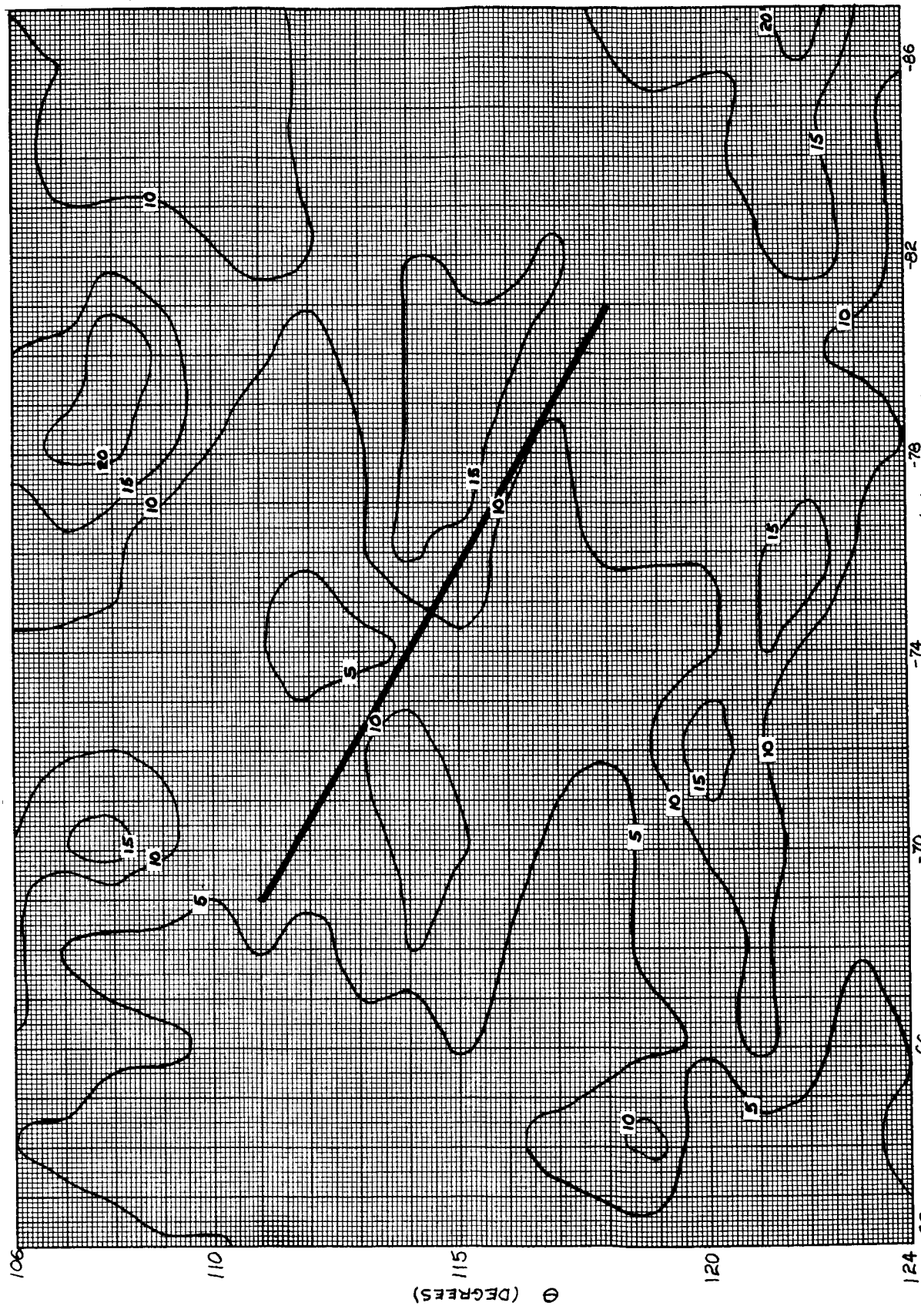

b) Omnidirectional Antenna A Up Link (2113 MHz)

Figure 5.3-7 (continued). Expanded Antenna Contour Patterns

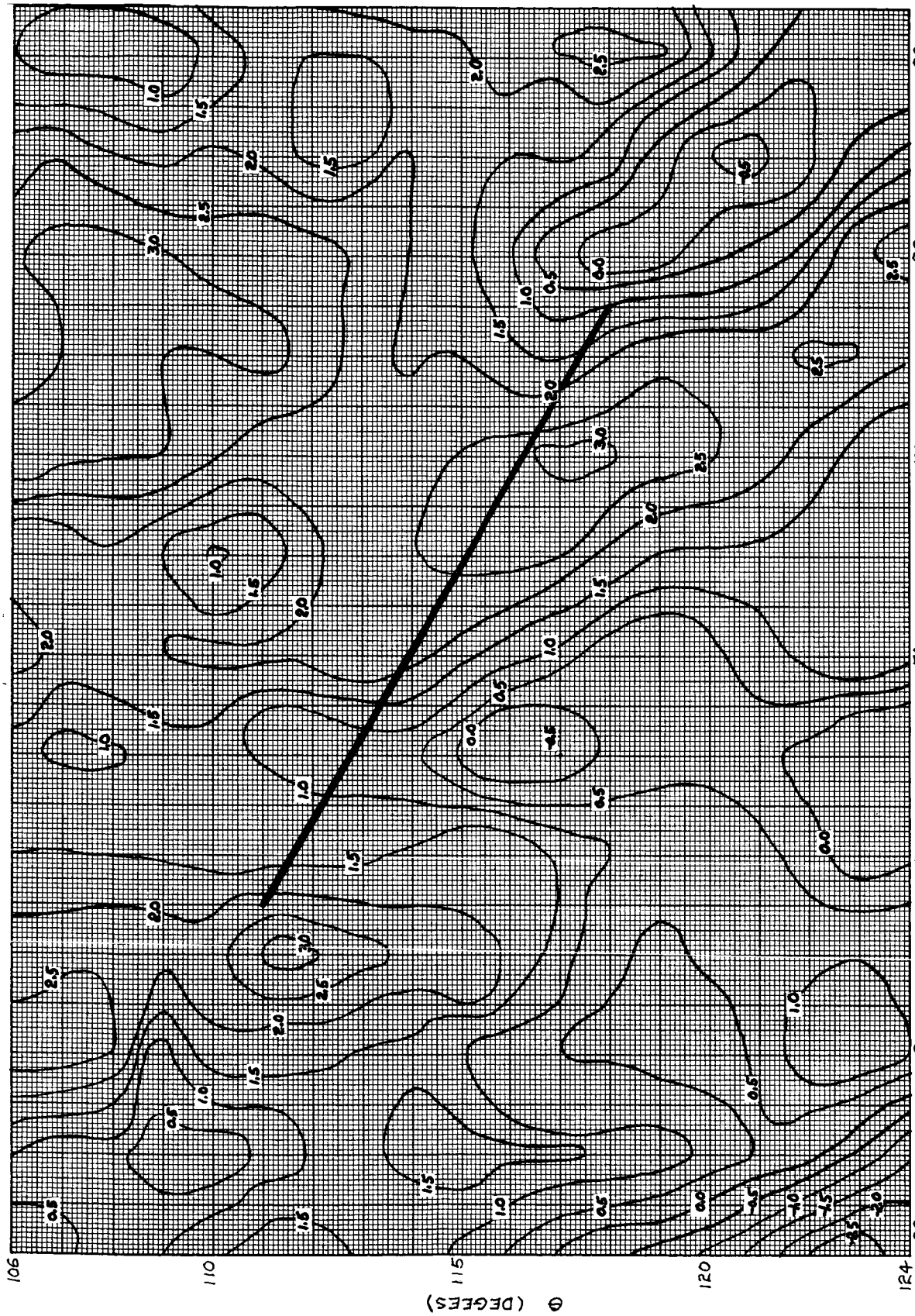

c) Omnidirectional Antenna B Down Link (2113 MHz)

Figure 5.3-7 (continued). Expanded Antenna Contour Patterns

TABLE 5.3-8. ANTENNA GAIN VARIATIONS PRE-CANOPUS

	Gain Variations (Coast), db		Pre-Canopus Gain, db		Gain at Canopus, db	
	Predicted	Actual	Predicted	Actual	Predicted	Actual
Omni B down link	-1.0 to -7.0	-3.0 to -8.0	-6.0	-4.5	-0.5	-0.5
Omni A up link	-2.0 to 0.0	-1.6 to 0.0	0.0	0.0	-5.0	-4.0
Omni B up link*	-4.0 to 0.0	-1.0 to 0.0	0.0	0.0	+2.0	+2.0

*Values include the -2.0 db bias in measured flight data which is discussed in the anomalies section.

At 16:02:25 GMT, transmitter B was commanded to high power. Transponder B was turned off at 16:05:52 GMT (one-way operation was selected in preference to two-way since two-way tracking was not required) and DSS 61 reacquired the spacecraft in the narrowband voltage controlled crystal oscillator mode. Star mapping was initiated at 16:09:12 GMT with the spacecraft transmitting data at 4400 bits/sec in mode 5. The 360-degree roll produced down link signal variations of approximately 30 db which agreed with the premaneuver predictions. Some parity errors were noted in the data, and minor difficulties were experienced in maintaining decommutator lock; however, no significant data outages occurred. Spacecraft received signal levels during the roll maneuver indicated deviations of approximately 20 and 18 db on receivers A and B, respectively. This again agreed with premaneuver predictions. Automatic Canopus lockon was accomplished at 16:27:51 GMT.

At 16:31:25 GMT, transponder B was turned on and two-way lock reestablished. Transmitter B high power was commanded off at 16:39:28 GMT, which resulted in 37 minutes and 3 seconds of high power operation for star acquisition. DSS 61 received signal level for low power operation was -133.3 dbm which was a 19.6-db decrease from high power operation. A 19.5-db increase in signal level was noted when going from low to high power operation prior to initiation of the star mapping sequence.

The spacecraft was 205 degrees in a positive roll sense from Canopus prior to the initiation of the Canopus acquisition/verification sequence. With this information and the antenna contour patterns, the variations in antenna gain seen in the data are compared to predicted variations and are illustrated in Figure 5.3-8 which compares omnidirectional antenna B down link, omnidirectional antenna A up link, and omnidirectional antenna B up link,

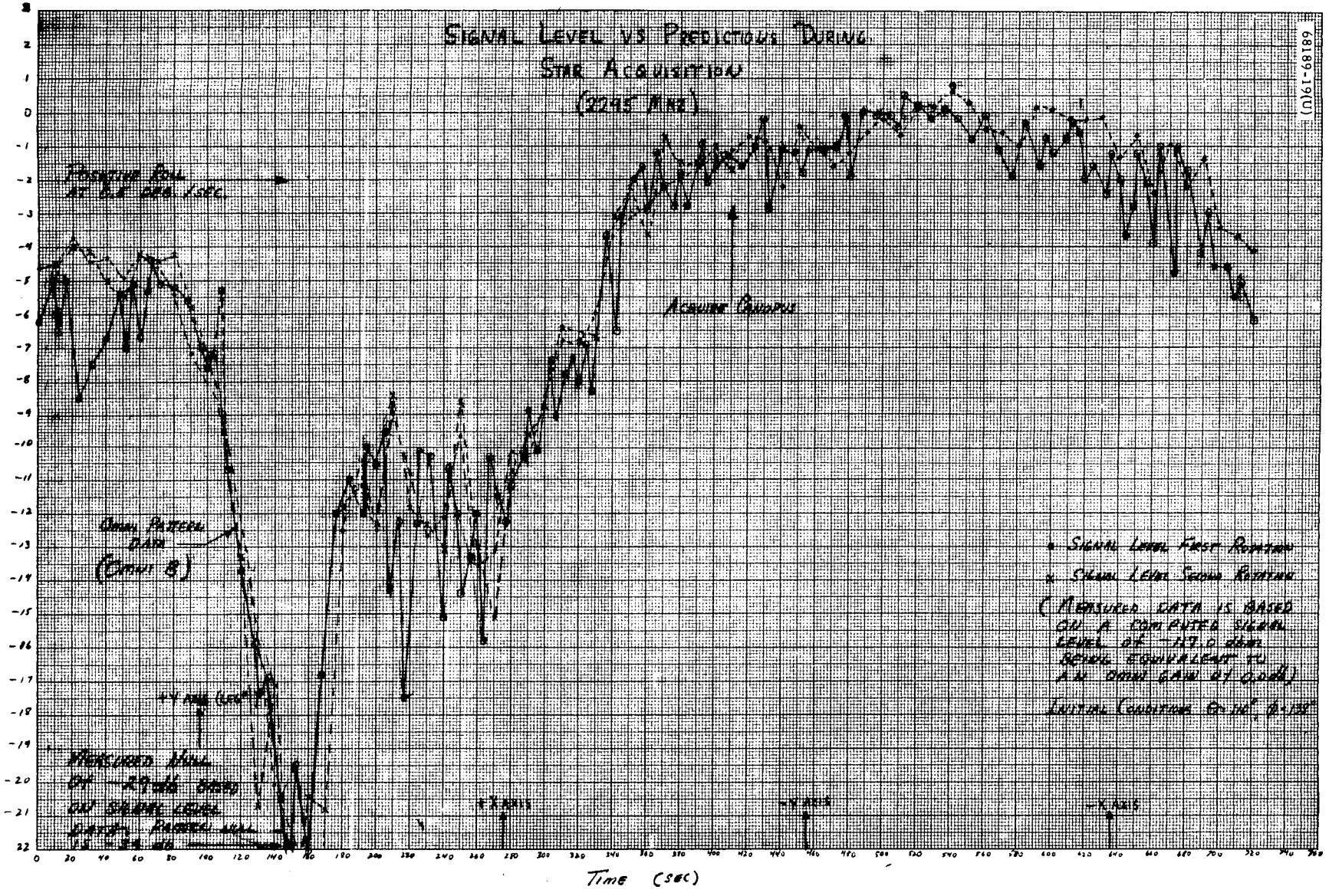

a) Omnidirectional Antenna B Down Link (2295 MHz)

Figure 5.3-8. Signal Level Versus Predictions During Star Acquisition

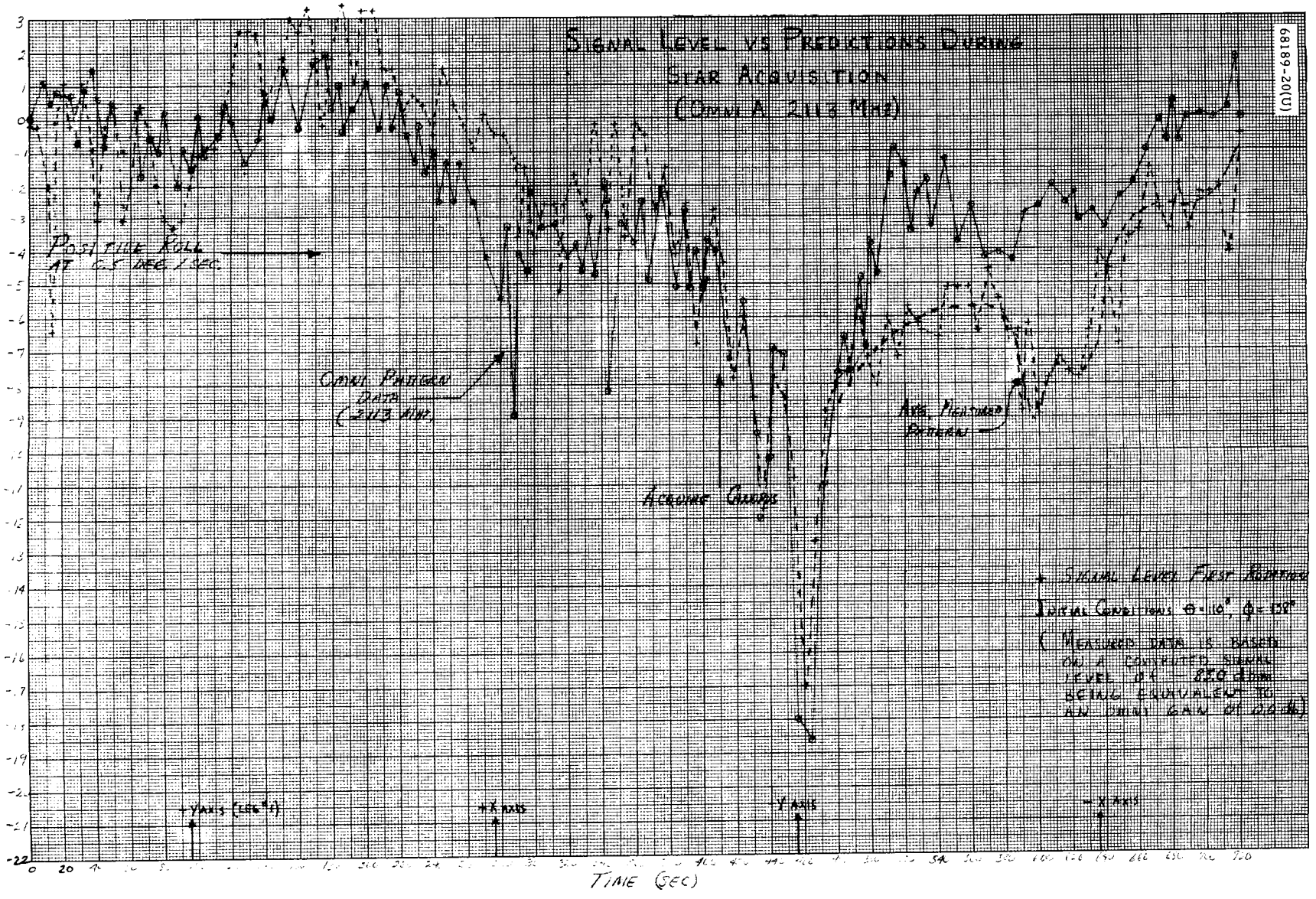

b) Omnidirectional Antenna A Up Link (2113 MHz)

Figure 5.3-8 (continued). Signal Level Versus Predictions During Star Acquisition

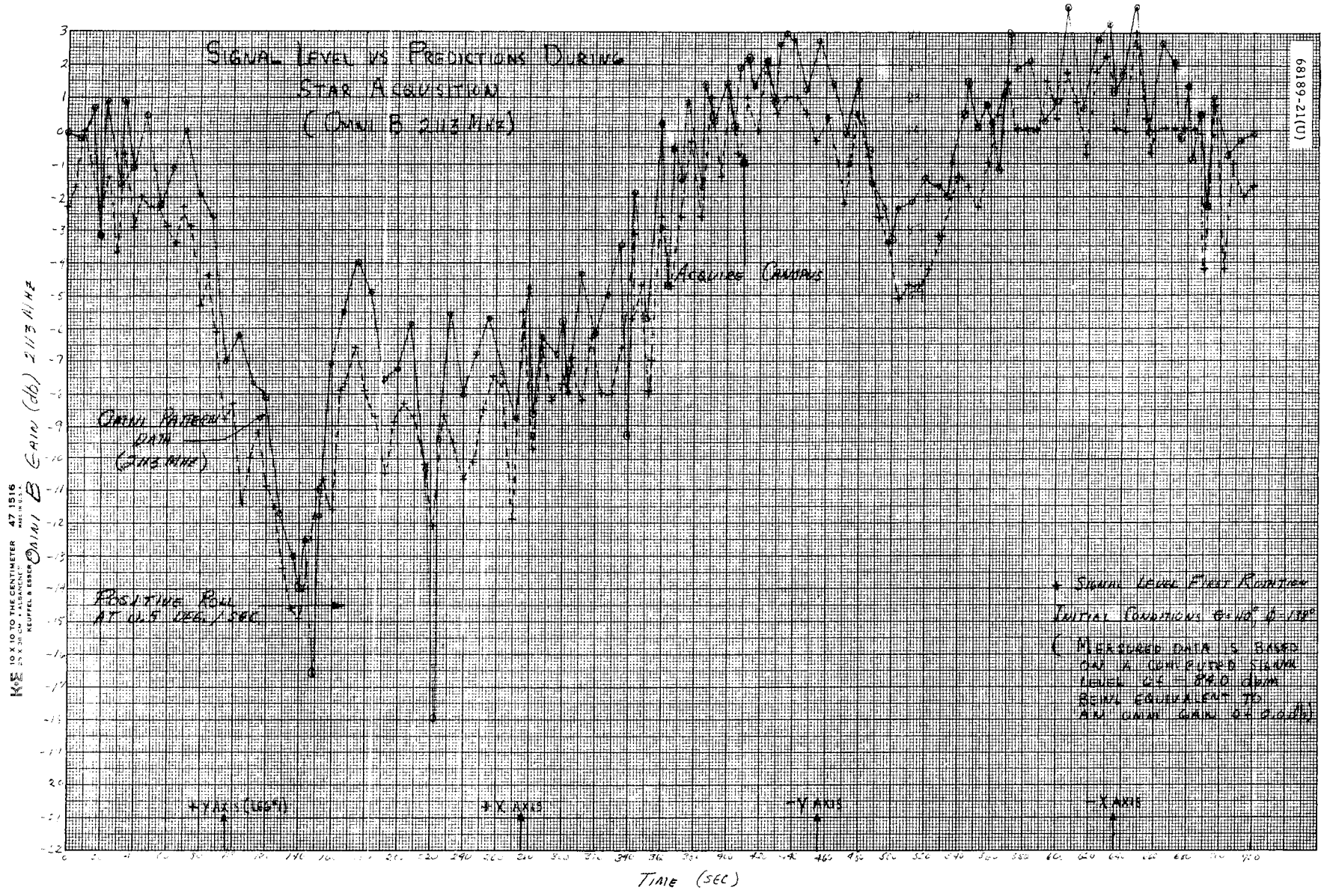

c) Omnidirectional Antenna B Up Link (2113 MHz)

Figure 5.3-8 (continued). Signal Level Versus Predictions During Star Acquisition

respectively. Both omnidirectional antenna B up and down link signal level variations agree well with antenna gain values. However, it was during this maneuver that the first evidence of the -2 db bias in receiver B performance was noted, and it is therefore necessary to adjust the actual mission antenna gain values on Figure 5.3-8c by +2.0 db to make the data consistent with that presented in other sections of this report. (For a discussion of the justification of such an adjustment, see the anomaly description in subsection 5.3.2.)

Relatively good agreement existed between omnidirectional antenna A up-link gain values and the actual signal level variations, except for those values in the region between the -Y axis and the -X axis. A deep null is indicated in mission data which cannot be explained from the analysis of antenna pattern data at points in the vicinity of this region. It has been noted in previous missions that the degree of correlation between antenna pattern data and mission data is not as good on omnidirectional antenna A as on omnidirectional antenna B. However, the presence of an unexplained null of this magnitude would indicate a condition not caused by normal configuration differences which result from assembly tolerances.

5.3.4.5 Mission Phase Four: Midcourse Maneuvers

The standard roll-pitch was selected from eight possibilities as the midcourse maneuver. Real-time analysis predicted the following variations in nominal omnidirectional antenna gain during the maneuver:

1) Omnidirectional antenna B down link: $-1.9 < G < +0.4$ db

2) Omnidirectional antenna A up link: $-18.3 < G < +1.17$ db

3) Omnidirectional antenna B up link: $-2.6 < G < +2.6$ db

Predicted minimum margins were 15.5 db for 4400 bits/sec telemetry, 7.7 db on receiver A, and 23.5 db on receiver B command links. Two-way (transponder) mode was recommended.

At 04:20:48 GMT, the spacecraft was commanded to high power and, at 04:21:31 GMT, the 4400 bits/sec data rate was selected. The ground received signal increased by 21.1 db when the spacecraft was commanded from low to high power, with DSS 11 reporting a received carrier power of -121.8 dbm prior to maneuvering. Maneuver initiation times were 04:46:54 GMT for the roll and 04:50:13 GMT for the pitch. The premidcourse maneuver ended at 04:51:31 GMT, with the DSS 11 received carrier power reading -120.2 dbm and having indicated approximately a 2.5-db variation during the maneuver as predicted.

Variations in omnidirectional antenna B down-link antenna gain seen in the data are compared to predicted variations and are illustrated in Figure 5.3-9a. The premidcourse maneuver was executed in mode 1; therefore, no spacecraft receiver signal values were available.

At 05:00:02 GMT, midcourse thrust was executed. DSS 11 received carrier power was steady with reported 0.3-db variations during the thrusting period.

At 05:01:16 GMT, mode 5 data were selected in preparation for the postmidcourse maneuver. Maneuver initiation times were 05:03:22 and 05:06:20 GMT for pitch and roll, respectively. The postmidcourse maneuver ended at 05:08:13 GMT with the DSS 11 received carrier power indications essentially retracing those seen during the premidcourse maneuver. Since the postmidcourse maneuver was executed in data mode 5, spacecraft received signal levels were available.

Variations in omnidirectional antenna A and B up-link antenna gains, as seen in the data, are compared to predicted variations and are illustrated in Figures 5.3-9b and 5.3-9c. The approximate -2 db bias in receiver B is again apparent in Figure 5.3-9c and, for data consistency, as was the case for the Canopus data, it is necessary to adjust the measured gain values on this figure by +2.0 db.

Canopus lockon was indicated at 05:08:04 GMT, and preparations were made to return the spacecraft to its cruise configuration. At the end of the midcourse sequence, the DSS 11 received carrier power (-121.2 dbm) indicated that a nominal positive 1100 bits/sec telemetry margin should exist with the spacecraft in low power. At 05:15:43 GMT, the 1100 bits/sec data rate was selected and, at 05:16:15 GMT, the spacecraft was returned to low power. The spacecraft operated in high power for 55 minutes and 28 seconds during the midcourse maneuver sequence.

The resulting -139.2 dbm received carrier level produced a -0.3 db telemetry margin for 1100 bits/sec data. Since the required bit error rate of 3×10^{-3} was not exceeded, the cruise data configuration remained at 1100 bits/sec.

5.3.4.6 Mission Phase Five: Terminal Maneuver

The yaw-pitch-roll optional maneuver was selected from eight possibilities as the terminal maneuver, and was optimum for the communications link. Real-time analysis predicted the following variations in nominal omnidirectional antenna gains during the maneuver:

1) Omnidirectional antenna B down link: $-1.2 < G < +1.8$ db

2) Omnidirectional antenna A up link: $-21.9 < G < +0.2$ db

3) Omnidirectional antenna B up link: $-4.9 < G < +2.2$ db

Predicted minimum margins were 8.4 db for 1100 bits/sec telemetry, -1.6 db on receiver A, and 15.4 db on receiver B command links. One-way mode was recommended even though adequate margins were available for the transponder operation. This recommendation was made since one-way configuration was required for the terminal descent sequence, and operationally, it was safer to establish before the terminal maneuver.

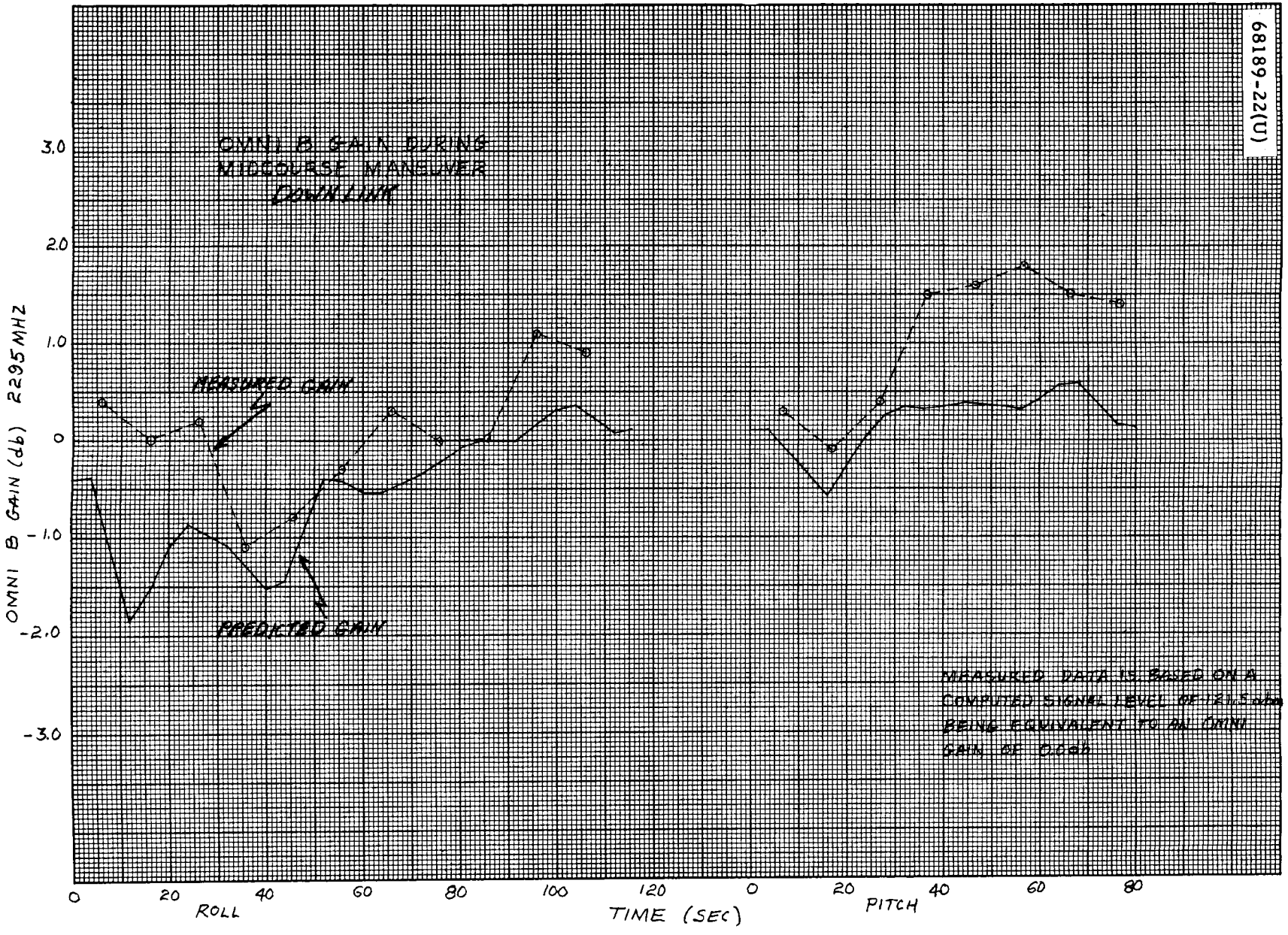

a) Omnidirectional Antenna B Down Link

Figure 5.3-9. Omnidirectional Antenna Gains During Midcourse Maneuver

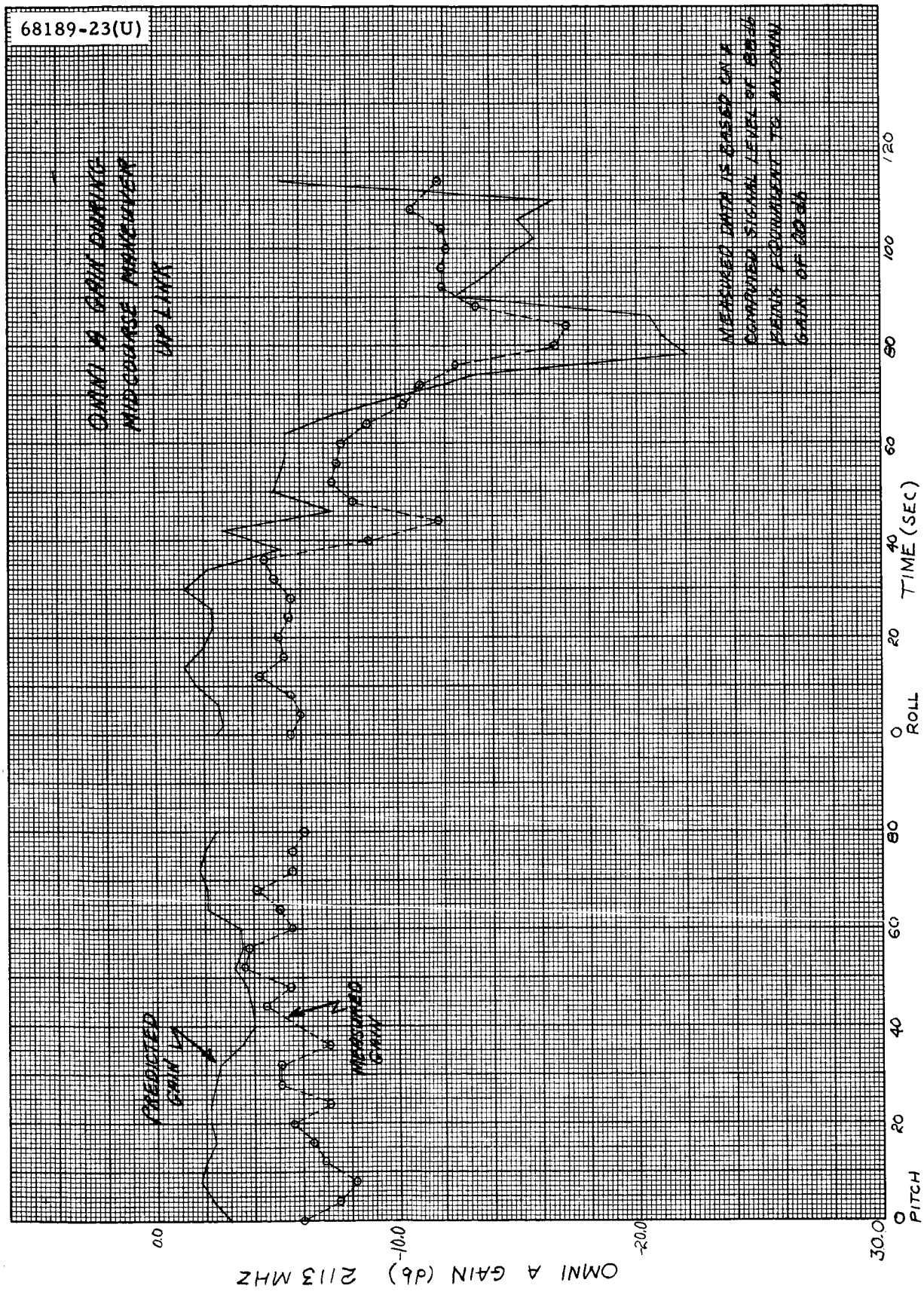

b) Omnidirectional Antenna A Up Link

Figure 5.3-9 (continued). Omnidirectional Antenna Gains During Midcourse Maneuver

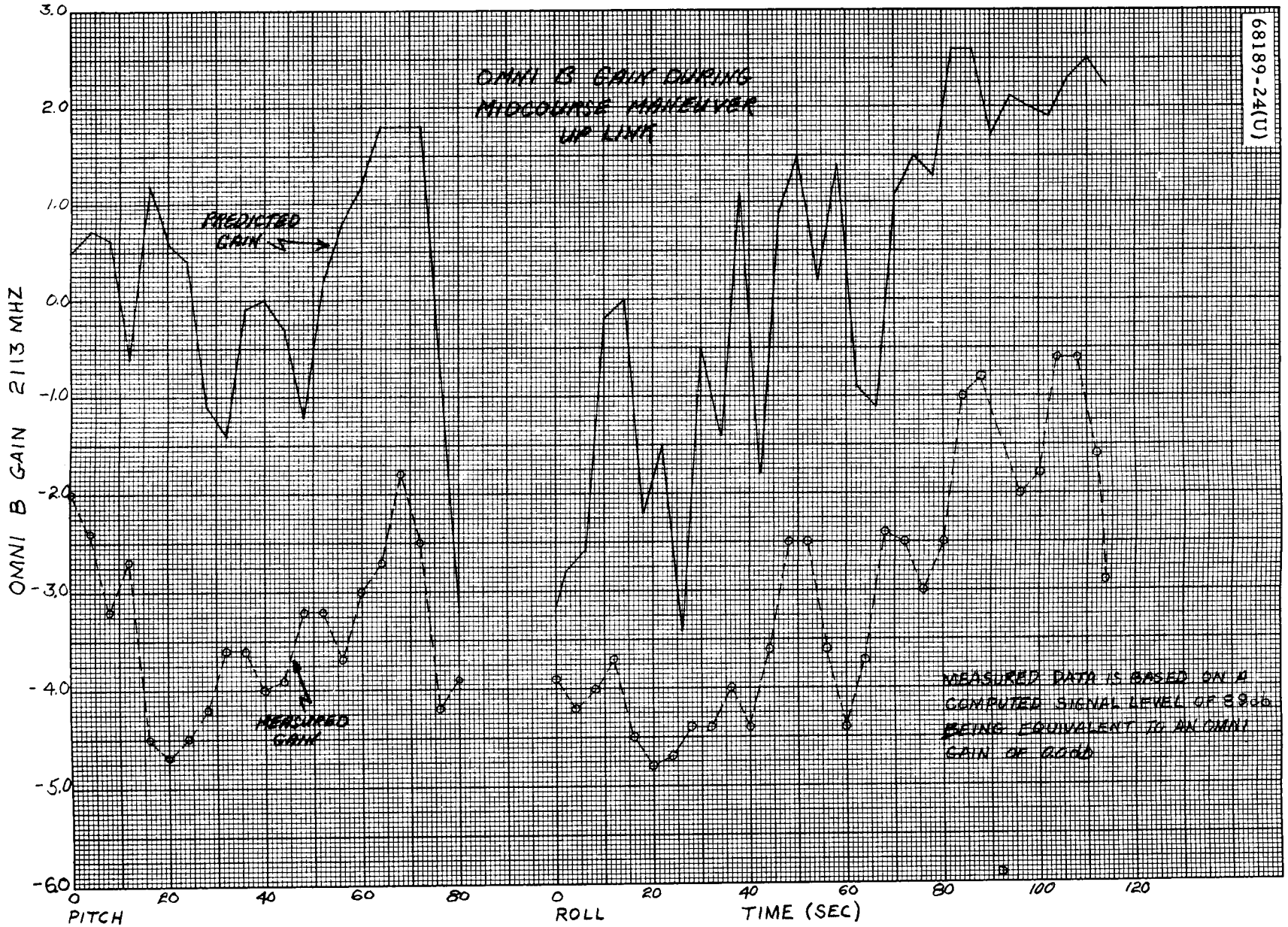

c) Omnidirectional Antenna B Up Link

Figure 5.3-9 (continued). Omnidirectional Antenna Gains During Midcourse Maneuver

The spacecraft was commanded to high power at 23:09:40 GMT, and 1100 bits/sec data were selected at 23:10:40 GMT. The resulting -125.0-dbm received signal level indicated an increase of 18.8 db over low power operation. Transponder B was turned off at 23:19:21 GMT, establishing the terminal sequence spacecraft configuration. Maneuver initiation times were 23:23:29 for yaw, 23:30:17 for pitch, and 23:34:35 for roll. The terminal maneuvers ended at approximately 23:36:40 GMT, with the DSS 11 received carrier power reading -124.0 dbm and having indicated approximately a 3-db variation during the maneuver, as predicted.

Up-link signal level variations observed in the telemetry data, as compared to predicted variations, are summarized as follows:

	Gain Variations, db	
	Actual	Predicted
Omnidirectional antenna A	26.8	22.0
Omnidirectional antenna B	6.2	7.0

5.3.4.7 Mission Phase Six: Descent and Touchdown

Preterminal maneuver analysis indicated that, during the descent phase, the strain gages would be turned on with the 1100 bits/sec PCM data if the DSS 11 received carrier power at the end of the terminal maneuver exceeded -127.2 dbm (level based on a BER of 1×10^{-2}). The actual DSS 11 received carrier of -124.0 dbm at the end of the terminal maneuver was 0.3 db lower than the predicted value, but well above the minimum established required level. At this point, it was predicted that 1100 bits/sec data, even under worst-case touchdown conditions, would be sustained at a BER less than 3×10^{-3}.

The signal level remained steady with approximately 2-db variations during retro firing and terminal descent. At 00:02:32 GMT (day 110), the touchdown strain gages were turned on by commanding on the spacecraft presumming amplifier. This was verified by a normal drop in DSS 11 received carrier power.

DSS 11 maintained phase lock throughout the descent and the touchdown phases which included the three touchdowns occurring from 00:04:18 to 00:04:54 GMT. Observation of the ground station dynamic phase error during the touchdown period indicates maximum peak-to-peak variations of less than 3 degrees in the 152 Hz threshold tracking loop bandwidth. Good 1100 bits/sec and strain gage data were reported up to and at touchdown. However, immediately after touchdown, spacecraft subsystems began reporting anomalous data. The nonstandard exercising of the RF subsystem that followed is described in Reference 1. It was determined from the investigation that the RF subsystem was performing normally and that the anomalous behavior of the data was a result of a signal processing failure.

5.3.4.8 Mission Phase Seven: Lunar

The data relative to the lunar phase consist of several disjointed topics. The topics applying to the RF subsystem will be summarized in the following text. Reference is made, where applicable, to the source of detailed discussions and analysis.

RF Assessment

Two spacecraft RF subsystem performance assessments were made during the first lunar day. These assessments essentially exercise the subsystem in all possible transmitting and command receiving configurations. Evaluation of the resulting data was somewhat limited since the spacecraft telemetry data were unreliable. However, it was clearly evident from the ground station performance during these assessments that all aspects of the subsystem were performing in a nominal manner.

TV Performance

The first 200-line TV picture was transmitted approximately 58 minutes after touchdown. Based on reported DSS signal levels, the computed signal-to-noise ratio for the first picture was 16.0 ±2 db.

The first 600-line TV picture was transmitted approximately 8.5 hours after touchdown, shortly after the planar array was aligned with the earth. Based on reported DSS signal levels, the computed signal-to-noise ratio for the first picture was 14.5 ±2.0 db.

In both cases, the signal-to-noise ratio was high enough to provide good quality detected video data which is apparent in the quality and resolution of the pictures.

Planar Array Gain/Temperature Sensitivity Experiment – Experiment 16

The planar array gain/temperature sensitivity experiment was performed to determine the planar array mainlobe characteristics as a function of temperature. The purpose of the experiment was to determine if the mainlobe gain pattern was significantly affected by temperature variations. These data, in turn, were to be considered when determining A/SPP repositioning requirements and to evaluate the antenna design.

Data were taken at planar array temperatures of 210° and 110°F on 27 April and 1 May, respectively. The data indicated that the gain sensitivity to temperature was negligible over the range of temperatures examined. Although somewhat speculative in light of basic data accuracy, it was concluded that a very minor perturbation occurred in which the mainlobe slightly elevated and the beam widened at the higher temperature. The basic data and plots of the relative mainlobe gain are available in Reference 4.

Telemetry Bit Error Rate Experiment – Experiment 17

The telemetry bit error rate experiment was performed 1) to gather data to be used for comparison of the different stations relative to telemetry bit error rate performance, 2) to evaluate actual bit error rate performance relative to specified requirements, and 3) to evaluate present prediction and analysis techniques. Although not the original intent, this experiment also provided data on the effect of intermodulation distortion relative to the 1100 bits/sec PCM and touchdown analog strain gage multiplex.

Data were taken at DSS 42 and 61 at 1100 and 550 bits/sec. In addition, data were taken at DSS 61 on the 1100 bits/sec channel with the touchdown strain gages multiplexed with the PCM data. The data taken accomplished the intent of the experiment with very satisfactory results. An apparent error in DSS 61 noise bandwidth data was noted, satisfactory performance relative to specifications was determined, the analytical model was verified to within measurement accuracy, and some degradation in the 1100 bits/sec channel was noted when strain gages were also on. The basic data and plots of the results are available in Reference 5.

5.3.4.9 Mission Data Plots

Subsystem telemetry signals are shown in Figures 5.3-10, 5.3-11, and 5.3-12. (Also see Figures 5.3-6 and 5.3-7 in the coast phase discussion for AGC signals.) All data indicated normal subsystem performance, and no unexplainable variations were noted. Plots of receiver B automatic frequency control and receiver A static phase error are omitted since, for the most part, the spacecraft configuration was such that these data points were essentially meaningless. A brief summary of each figure and the more significant events follows:

Receiver A Automatic Frequency Control (Figure 5.3-10) – Receiver A was in the automatic frequency control mode throughout transit. These data represent the DSS transmitter frequency offset from the automatic frequency control center frequency during the transit phase. A large error due to doppler shift rate is noted at acquisition. Steps in the data occurred at station transfer because the stations retuned their transmitters. Because of the high impedance of this signal, several predicted signal processing effects are apparent. Steps occurred in the data at high power turnon due to return line drop caused by the additional current in the ground return lines during high power operation. Spikes occurred during engineering interrogations of mode 4 due to step change in commutator unbalance current.

Receiver B Static Phase Error (Figure 5.3-11) – Receiver B was used for transponding through most of the mission. These data thus represent the DSS transmitter frequency offset from the receiver phase lock center frequency. Since these data are analogous to the automatic frequency control data discussed above, the comments apply equally well to these data. It should be noted, however, that this signal is not as sensitive to signal processing effects.

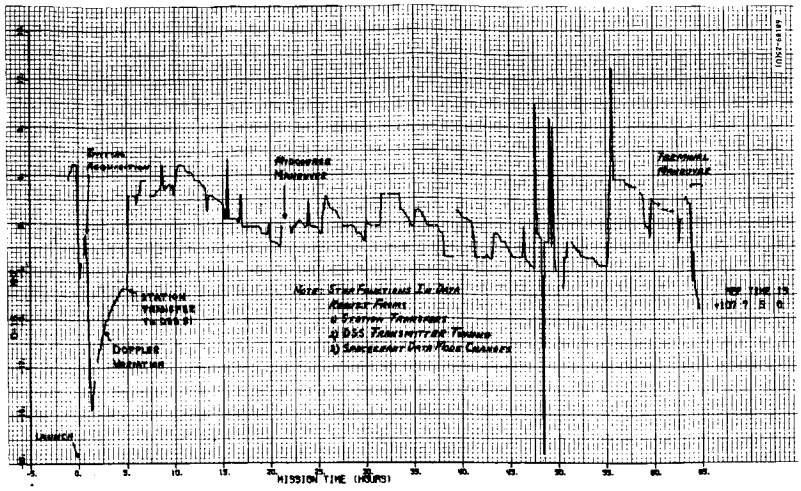

Figure 5.3-10. Receiver and Automatic Frequency Control

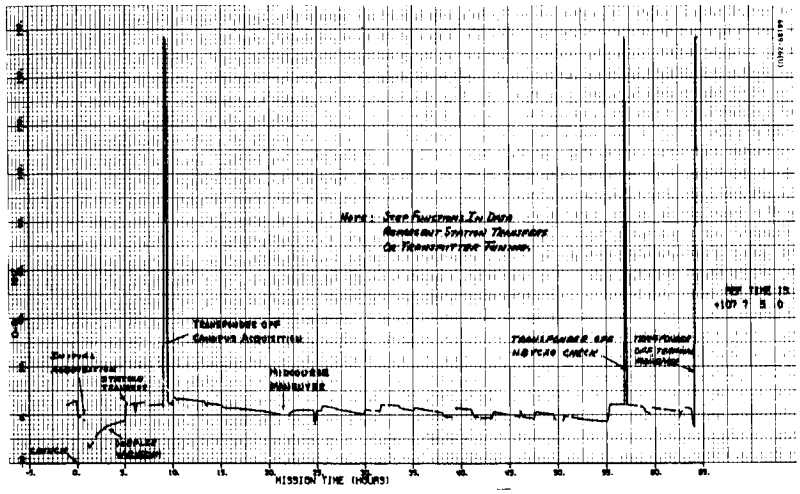

Figure 5.3-11. Static Phase Error B

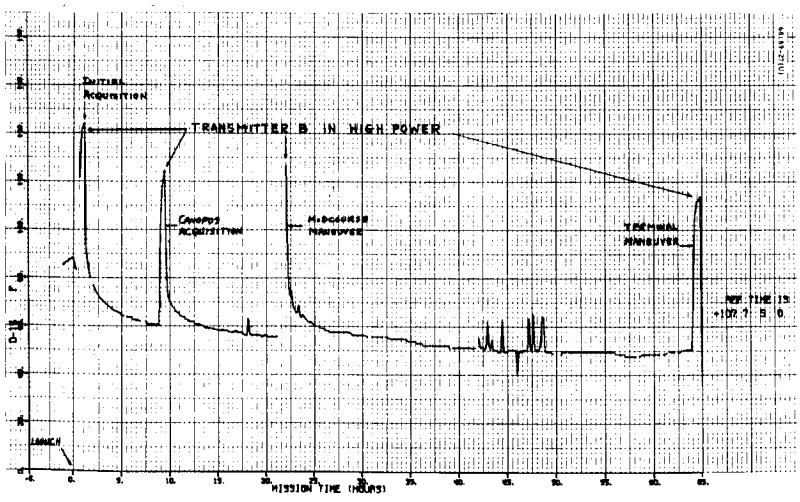

Figure 5.3-12. Transmitter B Temperature

Transmitter B Traveling-Wave Tube Temperature (Figure 5.3-12) — These data represent the temperature of the traveling-wave tube used for high power transmitter operation during transit.

5.3.5 REFERENCES

1) "Surveyor Mission C Space Flight Operations Report," Hughes Aircraft Company, SSD 74071, May 1967.

2) J.J. Dragovan, "Telemetry Calibration Data for SC-3, Revision C," Hughes Aircraft Company, IDC 2294.2/71.

3) J.J. Dragovan, "Command Receivers 231900-3 S/N 22 and S/N 23 Calibration (Signal Input Versus BCD Read) Space Environment," Hughes Aircraft Company, IDC 2294.2/69.

4) F.K. Rickman, "Results of Planar Array Gain/Temperature Sensitivity Experiment Performed on SC-3," Hughes Aircraft Company, IDC 2292/301.

5) F.K. Rickman, "Results of SC-3 Lunar Experiment on Telemetry Bit Error Rate Versus DSS Received Signal Levels," Hughes Aircraft Company, IDC 2292/313.

6) G.W. Garrison, "SC-3/DSS 71 Compatibility Test Quick Look Report," Jet Propulsion Laboratory, IOM 272-GG-67-258.

7) "Surveyor Mission C — Telecommunication Subsystem Prediction and Performance Summary Document," Hughes Aircraft Company, SSD 74021R, February 1967.

8) "Surveyor I Flight Performance Final Report," Volume 2, Hughes Aircraft Company, SSD 64241R, August 1966.

9) "Surveyor II Flight Performance Final Report," Hughes Aircraft Company, SSD 68189-2R, January 1967.

5.3.6 ACKNOWLEDGEMENTS

1) J.O. Votaw was the coordinator and author of this section.

2) Q.D. Howard and W. Mitchell for their assistance in reducing, formatting, and analyzing much of the data contained in this section.

3) The DSS tracking advisors at JPL for supplying ground station data.

4) The Space Performance/Analysis/Command Telecommunications Team, consisting of V.S. Amstadter, W. Mitchell, W.G. Moore, F.K. Rickman, and M.R. Weiner, for maintaining accurate mission records and logs.

5.4 SIGNAL PROCESSING

5.4.1 INTRODUCTION

The signal processing subsystem is composed of the following units:

1) Engineering signal processor (ESP)

2) Auxiliary engineering signal processor (AESP)

3) Central signal processor (CSP)

4) Signal processing auxiliary (SPA)

5) Low data rate auxiliary (LDRA)

These units contain two electronic commutators with a total of 6 operational modes, 2 analog-to-digital converters that have available 5 digital bit rates, 17 subcarrier oscillators for transmission of pulse coded modulation data and continuous real-time data, 9 summing amplifiers, and signal conditioning subsystem performed normally throughout the mission.

A summary of test and flight values for signal processing telemetry can be found in Table 5.4-1. Values for the Surveyor I and SC-2 flights have been included for comparison.

5.4.2 ANOMALIES

As mentioned in subsection 4.3.2, an anomaly occurred in the signal processing system coincident with the second touchdown. At that time the telemetry data became severely degraded. After initial linear sequences were completed and at various times during the first lunar day, special commutator assessments were made to provide a more accurate assessment of the telemetry subsystem. Analysis of the data from the commutator assessments indicated the following characteristics:

1) Digital words were not affected by the commutator anomaly.

2) The analog data were erroneous regardless of which A/D converter was being used.

TABLE 5.4-1. COMPARISON OF SIGNAL PROCESSING VALUES FROM TEST AND FLIGHT

Telemetry Signal	Surveyor III Retest Values, STV-C4	Surveyor III Flight Values, Day 107	SC-2 Flight Values	Surveyor I Flight Values
S-1* reference voltage, volts	4.86 to -4.9	4.86	4.9	4.88
S-2* reference return, volts	0	0	0.003	0.0024 to 0.0072
S-5* ESP commutator unbalance current, microamperes	-2.2 to -2.6	-2.1	-1.4	-3.1
S-7** AESP commutator unbalance current, microamperes	-1.0 to -1.2	-1.3	-1.7	-2.8

*Mode 4
**Mode 5

3) Analog data at the higher bit rates had a large number of erroneous readings containing consecutive ones and zeros (i.e., 511, 512, etc., BCD units).

4) The analog data showed a dependency on the value of the preceding word of any given measurement.

5) Analog data at 17.2 bps was within 10 to 20 percent of expected values, and the data from the AESP commutator were consistently lower than from the ESP commutator.

6) Data from the TV commutator was not affected by the anomaly.

Data characteristics noted above indicate that during operation of the commutators at the high bit rates, the voltage being sampled by the A/D converter is increasing or decreasing during each data word, thus setting erroneous digital states in the most significant bits. The reduced values of data at low bit rates indicated that loading of the commutators in the AESP and ESP was occurring. The most likely failure mode causing this type of indication is a short in one or more commutator switches in both the ESP and AESP. The result of these shorts is a complex resistor-capacitor (RC) load connected to the input to the A/D converter at low data rates. This RC load appears as a resistive load. The readouts at the higher bit rates are degraded because of the inability of measurements to reach a steady state during the sampling time. The effect is particularly severe if the

value of the preceding measurement differs considerably from the measurement being sampled. The readouts of measurements at the lower bit rates are degraded primarily by the resistive loading of the shorted commutator switches and their associated signal conditioning circuits.

The most likely cause of the resistive shorts in the commutator switches is a high voltage transient induced at the second touchdown. The existence of such a transient in the spacecraft electrical system seems to be confirmed by the other anomalies which occurred at the same time (i.e., RADVS high voltage off, inadvertent switching of the battery control logic, indexing of command decoders, and parity errors on telemetry channels). The transient may have been caused, either directly or indirectly, by high-voltage arcing in the RADVS power supply.

Several investigations of the signal processor failure were initiated soon after touchdown. The results of these investigations are presented in References 4 through 6. The primary objective of the analysis was to determine correction factors for the telemetry data so that it could be used during lunar operations. As cited in Reference 6, the majority of the data at the lower bit rates could be corrected by a simple resistive (voltage divider) model. These resistive loads were determined by comparing the data from EP-1, 29-volt nonessential voltage, before and after the anomaly. This resistance was determined for the ESP and AESP commutators and found to be 19,500 and 9850 ohms, respectively. Equations to correct the data at 17.2 bps for the data channels with an output impedance less than 5000 ohms were derived using these load resistances. These equations were then checked by correcting the data channel EP-30, boost regulator preregulated voltage, and 25 of the temperature channels. The data from EP-30 were within one BCD of the expected value, and the data from 21 of the ESP temperature channels were within ±3 BCD units of the corrected data from the corresponding channel from the AESP commutator. There appears to be an average offset of two BCD units between the commutators, but analysis of the voltage channels does not indicate which commutator is causing this offset. However, by using the correction factors developed, the 17.2-bps telemetry data collected during lunar operations could be used to control lunar operations and could also be used in analysis of spacecraft performance during these operations.

A secondary objective of the analysis was to determine which of the commutator switches had failed and to verify the failure mode. The approach taken in all three analyses was to construct an equivalent circuit or mathematical model of the failure mode. In two of the analyses, computer programs were used to fit the observed data to the models. In the third analysis (Reference 7), processing group tester (a rack of test equipment that integrates the entire signal processing system) was used to duplicate the observed Surveyor III telemetry data. Examination of the data collected at the high bit rates revealed that the capacitive load was large (10 microfarads or greater). This led to the conclusion that the shorted switches were associated with the flight control and radar signals having large capacitive loads. However, in attempting to further isolate the switches, the three reports come up with slightly different sets of switches that might have failed. The differences

arise because of the failure mode assumed in the analysis as well as the simplifications used in constructing the models. Refinements of the models which might further isolate the shorted switches are discussed in Reference 8. However, since the failure appears to be induced by the nonstandard operation of the spacecraft at landing, further isolation of the shorted switches may not be required, except for academic interest. The assumed models and results of analysis contained in the three reports are discussed briefly in the following paragraphs.

In the JPL report (Reference 8) it was assumed that a single channel failed in both the ESP and AESP. The analysis also eliminated all measurements that did not have a 10-microfarad capacitor in their interface. Based on these assumptions, it was concluded that the commutator switches that failed are used to commutate one of the following channels: FC-35, FC-39, FC-40, FC-43, R-2, R-3, R-4, or R-5.

The analysis which involved use of the group tester (Reference 7) also assumed that the failure involved switches in both the ESP and AESP associated with a given channel. However, it considered the case of multiple channel failure. Based on these assumptions, it was concluded that at least four commutator switches (two pairs) failed within the AESP and ESP. It was concluded that:

1) The switches associated with R-4 failed.

2) The switches associated with R-3 probably failed.

3) The switches associated with FC-32 and FC-39 may have failed, but further investigation would be required.

The analysis presented in Reference 6 did not limit itself to the case in which both the switches in the ESP and AESP associated with a given channel failed. A special computer program was also used to calculate the capacitive load required to produce the observed values for a chosen set of signals. The resulting capacitance was 13 microfarads for the ESP and 20 microfarads for the AESP. Since no single channel failure would produce such a large capacitance, it was concluded that more than one switch associated with each commutator had failed. In the AESP it was concluded that two of the following channels failed: R-2, R-3, R-4, or R-5. In the ESP it was concluded that the following signal pairs met the observed characteristics:

1) FC-15 and FC-35

2) FC-49, FC-50, or FC-51 and FC-39 and FC-40

3) FC-15 and FC-14 or FC-43

4) FC-41 and FC-12

Thus, some reasonable correlation with observed data characteristics has been achieved in the crude signal processing failure models generated to date.

5.4.3 SUMMARY

The signal processing subsystem performed properly throughout the flight until the second touchdown. At this time the telemetry became severely degraded. Subsequent investigation indicated that one or more commutator switches in both the ESP and AESP had shorted. Further analysis permitted corrections to selected data channels at low bit rate so that lunar operations were not impaired. The digital and TV telemetry data were not affected by the anomaly.

A thorough analysis of the touchdown strain gage multiplex was performed, particularly to measure the effects of intermodulation distortion. Computerized signal processing techniques were used, such as diversity combining and digital filtering.

5.4.4 SIGNAL PROCESSING ANALYSIS

5.4.4.1 Unbalance Current Corrections

In each telemetry commutator, transistor switches connect each analog output voltage (representing a spacecraft voltage, current, or temperature) with a common commutator line connected to the input of one of two analog-to-digital converters. A bootstrap unloader circuit is connected to this common line to reduce the stray capacitance, equalize the load impedance, and provide bias currents for the commutator and master switches. Since these bias currents are not exactly equal, a difference or unbalance current exists. The telemetry circuit being sampled must supply this current, causing an error in the measured voltage proportional to the output impedance of the circuit.

The unbalance current for a specific telemetry channel in each commutator (S-5 for ESP and S-7 for AESP) is measured in telemetry modes 2, 4, and 5. Figure 5.4-1 shows S-7 up to terminal descent. Although no plot of S-5 has been included, typical values have already been given in Table 5.4-1. The points at which vernier ignition during the midcourse maneuver and transfer to the auxiliary battery mode are noted in Figure 5.4-1.

5.4.4.2 Potentiometer Reference Voltage Corrections

The nominally 4.85 reference voltage is supplied by either the ESP or AESP units to the landing gear and solar panel position potentiometers, to the propulsion pressure transducers, and to the secondary sun sensors. This reference voltage, derived from the 29-volt nonessential bus, varies due to load and input supply voltage changes. The ESP voltage is telemetered in modes 2 and 4, and can be used to correct the affected signals whose calibrations are based on a reference voltage of exactly 4.85 volts. Since the AESP voltage is never telemetered, it must necessarily be obtained through computation.

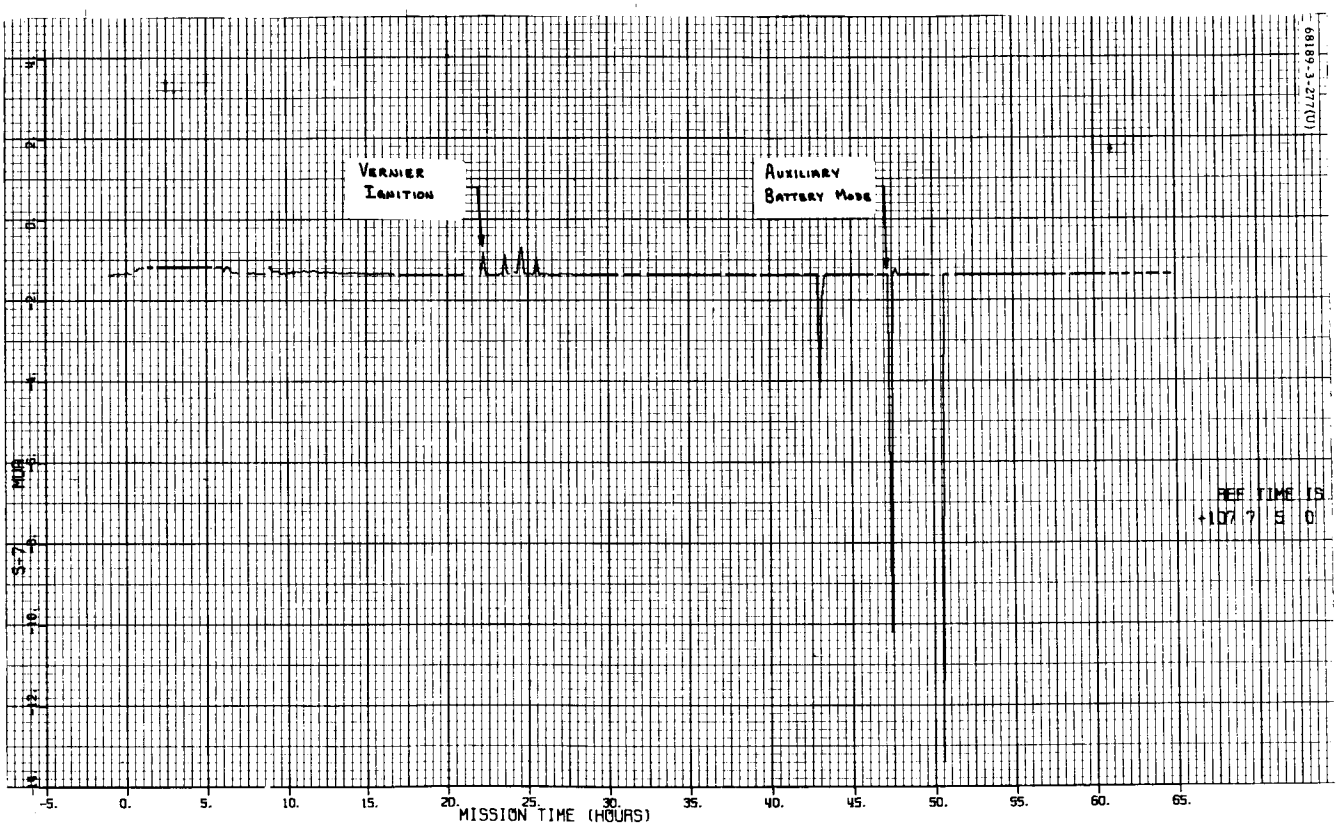

Figure 5.4-1. Commutator Unbalance Current (AESP)

The mechanism position signals do not normally change in flight after initial deployment, since they are mechanically held. Therefore, any apparent difference in a given signal reading from the ESP commutator to the AESP can be due only to a corresponding change in commutator-supplied reference voltage. Based on this assumption, Table 5.4-2 shows the calculation of the AESP reference voltage. At this point in the mission (L+8 hours), the AESP reference voltage was computed to be 1010 BCD (4.94 volts) which is the average of the three sensor calculations in Table 5.4-2.

TABLE 5.4-2. AESP REFERENCE VOLTAGE CALCULATION

GMT, day:hr:min	Mode	Signal	Telemetry Value, BCD	AESP Reference Voltage Calculation	AESP Reference Voltage
107:15:24	5	M3	608	NA	NA
		M4	380		
		M7	490		
107:15:28	4	M3	602	$\frac{X}{1000} = \frac{608}{602}$	1009.97
		M4	376	$\frac{X}{1000} = \frac{380}{376}$	1010.64
		M7	485	$\frac{X}{1000} = \frac{490}{485}$	1010.31
		S-1 reference voltage	1000		

5.4.4.3 Current Calibration Signals

Current measurements are accomplished by measuring the voltage drop across a low resistance shunt which is in series with the power line being monitored. This measurement is in the range of 0 to 100 millivolts. Since this voltage is not referenced to ground and is not scaled to the 0- to 5-volt telemetry input level range, it is necessary to amplify it with a differential amplifier. The nominal gain of this amplifier is 50, but its actual gain linearity and stability are not specified to a tight tolerance. To determine the current amplifier parameters and thereby increase the accuracy of current measurements, three calibration signals (with 0.2-percent stability) are amplified and telemetered in each commutator. These signals can thus be used by postmission processing for a continual in-flight calibration of the current amplifier.

The majority of the Surveyor III data was obtained in modes 5 and 6, and therefore only the AESP current calibration signals were investigated. Table 5.4-3 shows that these signals have increased by about 0.4 percent since being initially set at the unit flight acceptance test (FAT). It is also seen that the gain of the AESP current amplifier was reasonably constant over the mission.

TABLE 5.4-3. SUMMARY OF CURRENT CALIBRATION SIGNAL DATA IN AESP

Signal	Function, percent	Flight Data, percent	Remarks
EP-27	90	0.32	Coast phase 1
		0.42	Coast phase 2
EP-28	50	0.36	Coast phase 1
		0.47	Coast phase 2
EP-29	10	0.4	Coast phase 1
		0.5	Coast phase 2

This percentage change is not passed on to the current signal measurements, however, since the in-flight calibration process removes this effect completely.

The AESP midscale current calibration censor, EP-28, is shown in Figure 5.4-2 as a typical representative of the AESP calibration telemetry. It can be seen that the signal value is a function of bit rate. This effect was noted previously as occurring on SC-2. It was also noted that there is a slight decrease in the telemetry value when the AESP is commanded on. All of the AESP turnon points do not exhibit this effect due to frame editing of the data for plotting.

5.4.4.4 Touchdown Strain Gage Data

Magnetic tape data were obtained from two DSIF stations — via the 85-foot diameter antenna at the Pioneer site and the 210-foot diameter antenna at the Mars site. These two independent signal paths allow the technique of space diversity combining (References 1 and 2) to be used on the two sets of touchdown strain gage (TSG) data, resulting in a signal trace with improved signal-to-noise ratio (SNR).

In addition to diversity combining, low-pass filtering (by means of digital filtering on a computer) of 30 and 15 Hz (-3 db) bandwidth was

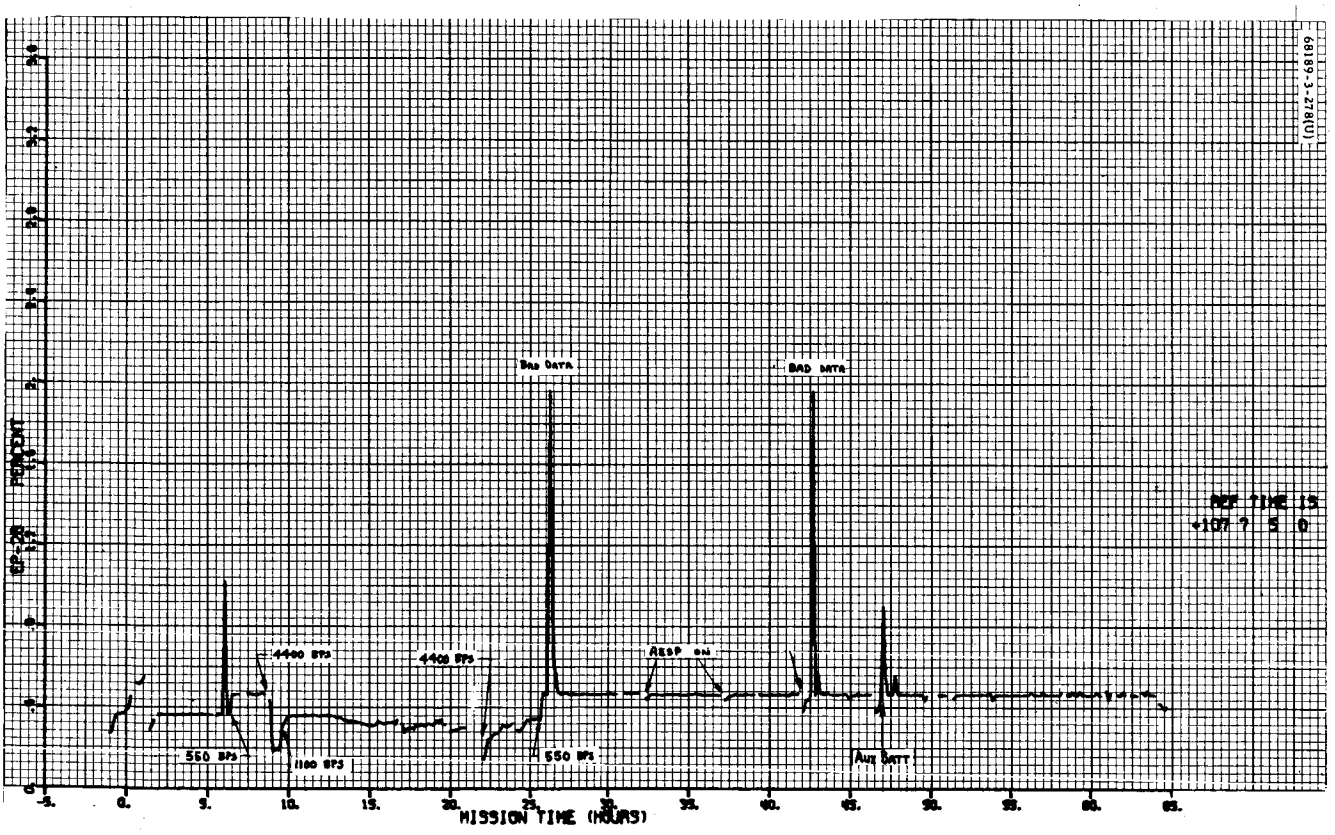

Figure 5.4-2. Midscale Current Calibration (AESP)

employed. The nominal channel postdetection filter bandwidth was approximately 56 Hz at the -3 db point (specified as 47 Hz, -0.5 db a sixth order Butterworth function).

The TSG multiplex exhibits intermodulation distortion (IMD), resulting in coherent noise in the channel outputs. In particular, TSG channel 2 exhibits the greatest IMD. Figure 5.4-3 shows the output of a computer simulation of the TSG multiplex, with no RF noise. To illustrate this IMD output noise phenomenon, it can be observed that the IMD-induced "noise" contaminating the output signal is composed mainly of an approximately 45.5-Hz component in this simulation. This frequency is within the -3 db postdetection bandwidth of this channel and would consequently appear in the output.

The significance of this noise is that diversity combining techniques will not be very effective, since the noise is coherent, and band stop or low-pass filtering will remove it. Use of a band stop filter is best, since less degradation of the signal waveform occurs than for low-pass filters.

Figures 5.4-4, 5.4-5, and 5.4-6 show the diversity combined strain gage waveforms, for the first landing, for TSG channels 1, 2, and 3, respectively. The postdetection bandwidths are the nominal ones ($\approx$56 Hz, -3 db).

Figures 5.4-7, 5.4-8, and 5.4-9 show these TSG channel outputs, diversity combined, for the second landing, in the same baseband. Note that TSG channel 2 signal was not properly read off the tape, but the noise trace is of significance for subsequent analysis. Figures 5.4-10, 5.4-11, and 5.4-12 show these channels under the same conditions for touchdown.

The signal-to-noise ratio listed on each plot is a mean power ratio of the signal from an assumed initial zero deflection point to an assumed final zero deflection point with respect to the noise defined over some interval prior to a touchdown. This analysis assumes that the noise variance is unchanged prior to and during the signal duration.

Figures 5.4-13, 5.4-14, and 5.4-15 show TSG channel output traces for landing 1 after operating on the diversity-combined waveforms in Figures 5.4-4, 5.4-5, and 5.4-6, with a sixth order Butterworth low-pass filter of 30-Hz (-3 db) bandwidth. Similarly, Figures 5.4-16, 5.4-17, and 5.4-18 show these channels, under identical conditions, for impact 2, and Figures 5.4-19, 5.4-20, and 5.4-21 give similar outputs for impact 3.

It will be observed from these heavily filtered plots that the noise level has dropped significantly. The predicted 45.5-Hz IMD noise on TSG channel 2 is attenuated by $\approx$21 db by the 30-Hz Butterworth filter. However, concurrently some signal degradation has occurred.

Figures 5.4-22, 5.4-23, and 5.4-24 show the TSG channel outputs, diversity combined, filtered by a sixth order Butterworth low-pass filter,

with a -3 db bandwidth of 15 Hz for landing 1. Similarly, Figures 5.4-25, 5.4-26, and 5.4-27 show these identically conditioned outputs for impact 2, and Figures 5.4-28, 5.4-29, and 5.4-30 provide the TSG data for the third impact.

5.4.4.5 1100 BPS Engineering Data Bit Error Rate

Due to the presence of IMD in the TSG multiplex when operating with 1100 bps engineering data subcarrier, the bit error rate (BER) of the engineering data channel is expected to increase (References 3 and 4). The carrier RF power levels during the descent phase were high, thus accounting for the absence of parity errors (assumed to be approximately equal to bit errors in this BER region). Therefore, no confirmation of the BER degradation due to IMD could be confirmed. Subsequent tests performed on Surveyor III (Reference 5) have confirmed this change in BER. Figures 5.4-31 and 5.4-32 give the received carrier level (AGC) and parity error rates during the mission. In the descent phase, prior to touchdown, the engineering data parity error rate was approximately zero due to the high subcarrier predetection SMR and relatively small number of bit samples.

5.4.5 REFERENCES

1. A.W. Dittmer, "The Use of Diversity Receiving Techniques to Enhance Surveyor SC-1 Strain Gage Signals," Hughes IDC 2292/188, 10 January 1967.

2. A.W. Dittmer, "Computer Analysis and Prediction of Surveyor Spacecraft (SC-1) Strain Gage Signals," Hughes IDC 2292/85.

3. R.J. Rechter, "Computer Analysis of SC-3 through SC-7 TSG Multiplex Intermodulation Distortion and Other Factors," Hughes IDC 2292/223, Rev. 1, March 1967.

4. M.Fashano and R.J. Rechter, "DTRB-21 Test Procedures, Results and Summary (TSG Multiplex)," Hughes IDC 2292/267, 5 May 1967.

5. F.K. Rickman, "Results of SC-3 Lunar Experiment in Telemetry BER DSS Received Signal Levels," Hughes IDC 2292/313, 16 June 1967.

6. J.P. Stringham, "Correction of SC-3 Commutator Data During Lunar Operation," Hughes IDC 2292.2/129, 26 June 1967.

7. W. Harold Lucey, "Post Touchdown Telemetry Data Failure on SC-3," Hughes IDC 2951/5, 23 June 1967.

8. D. Hersey and K. Kimball, "Investigation of the SC-3 Signal Processing Failure," JPL IM 273-B-848.

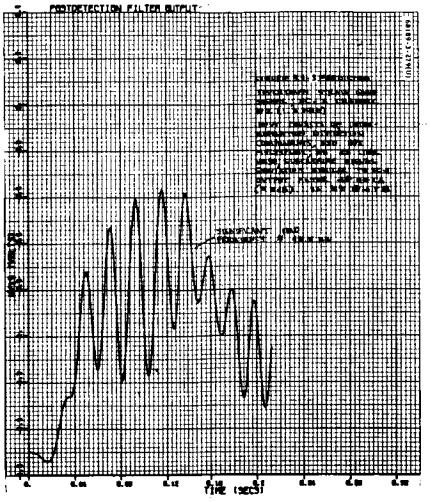

Figure 5.4-3. Predicted Touchdown Strain Gage Signal; Surveyor III Channel 2

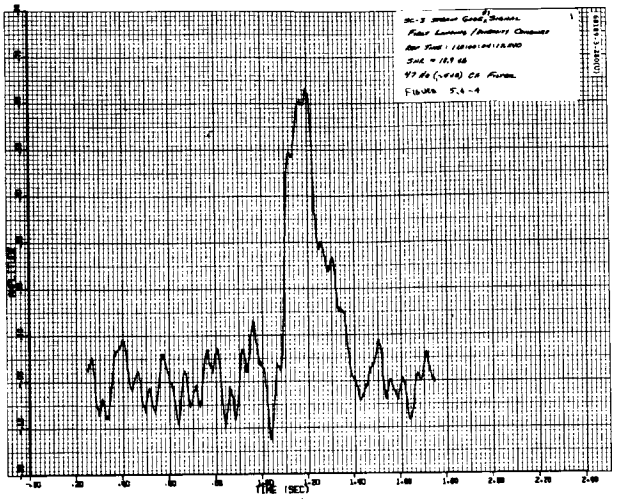

Figure 5.4-4. Surveyor III Strain Gage 1 Signal First Landing/Diversity Combined

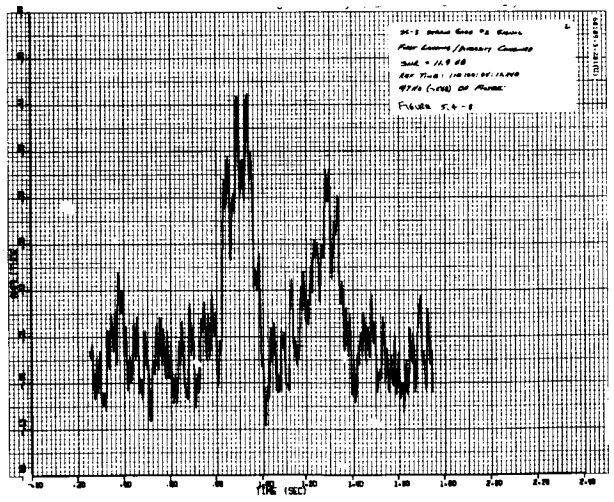

Figure 5.4-5. Surveyor III Strain Gage 2 Sigral First Landing/Diversity Combined

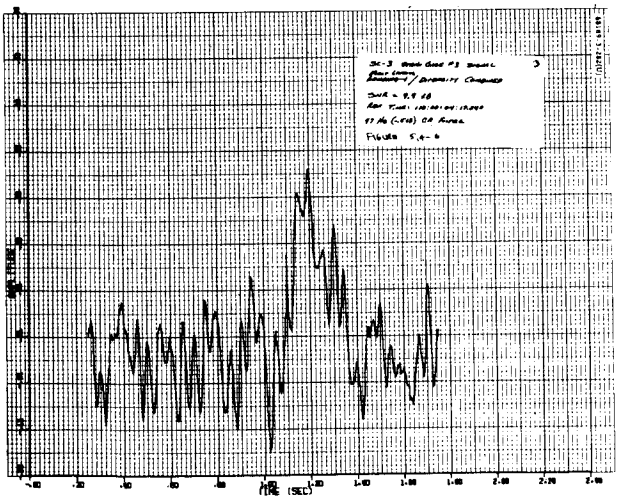

Figure 5.4-6. Surveyor III Strain Gage 3 Signal First Landing/Diversity Combined

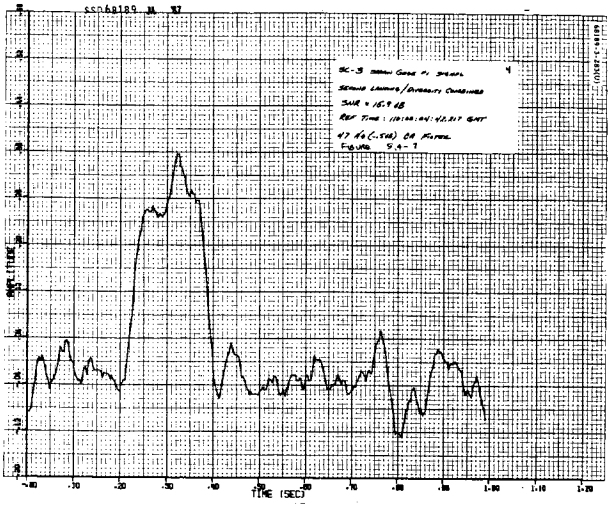

Figure 5.4-7. Surveyor III Strain Gage 1 Signal Second Landing/Diversity Combined

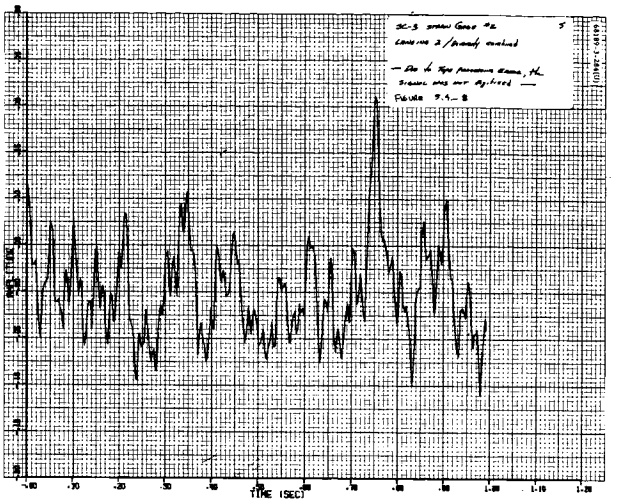

Figure 5.4-8. Surveyor III Strain Gage 2 Landing 2/Diversity Combined

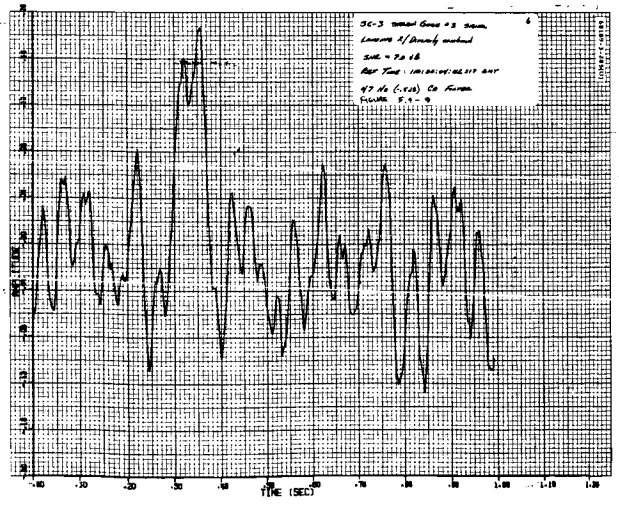

Figure 5.4-9. Surveyor III Strain Gage 3 Signal Landing 2/Diversity Combined

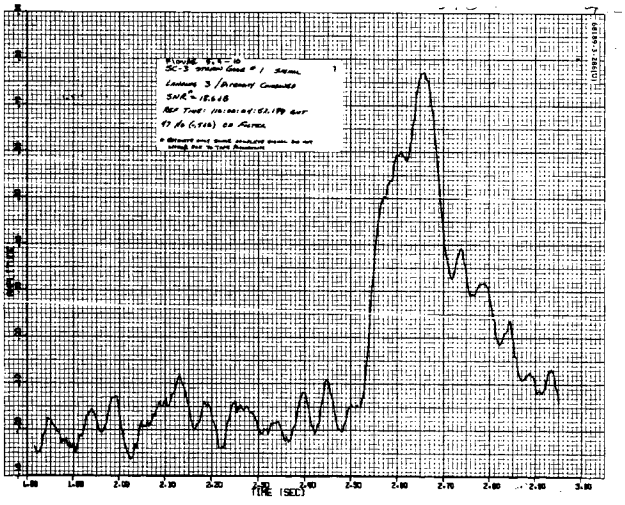

Figure 5.4-10. Surveyor III Strain Gage 1 Signal Landing 3/Diversity Combined

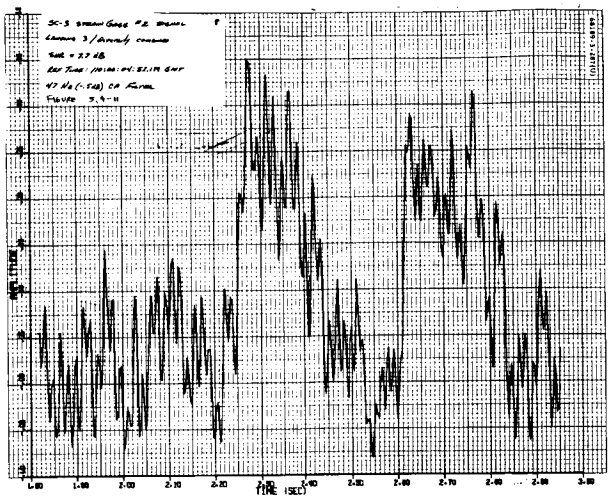

Figure 5.4-11. Surveyor III Strain Gage 2 Signal Landing 3/Diversity Combined

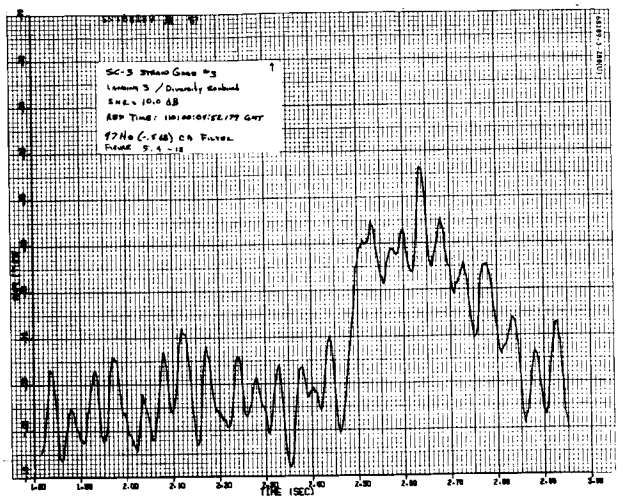

Figure 5.4-12. Surveyor III Strain Gage 3 Landing 3/Diversity Combined

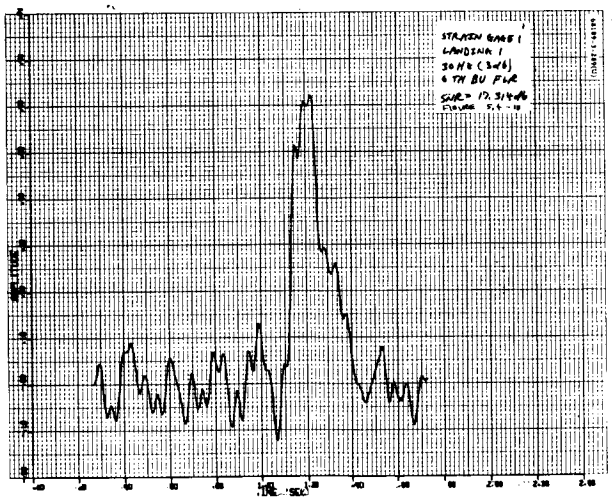

Figure 5.4-13. Strain Gage 1 Landing 1

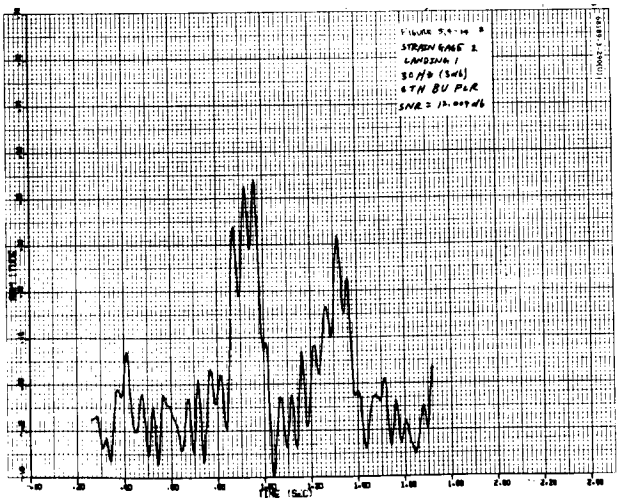

Figure 5.4-14. Strain Gage 2 Landing 1

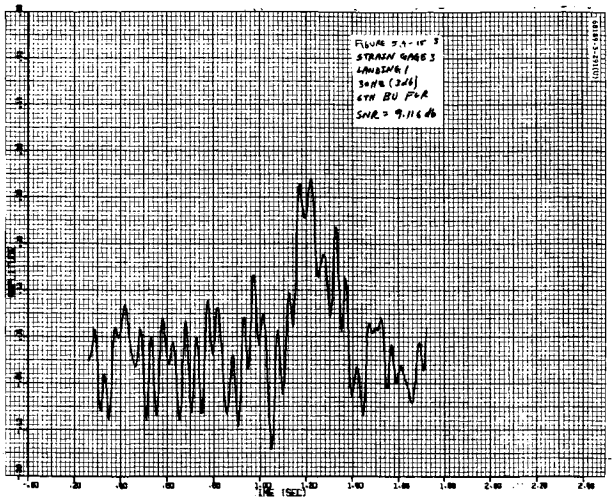

Figure 5.4-15. Strain Gage 3 Landing 1

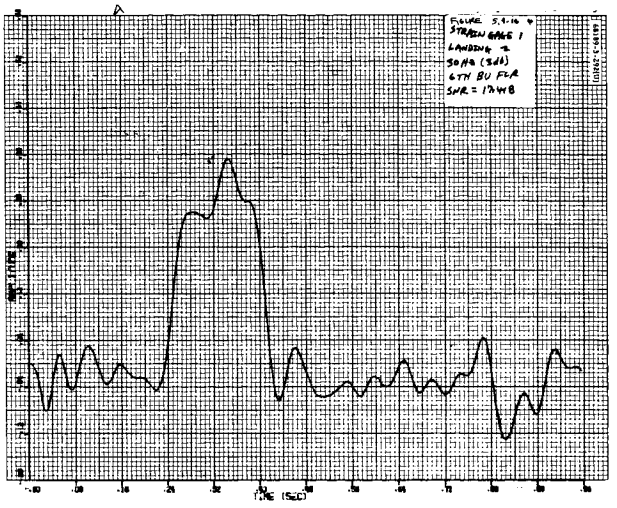

Figure 5.4-16. Strain Gage 1 Landing 2

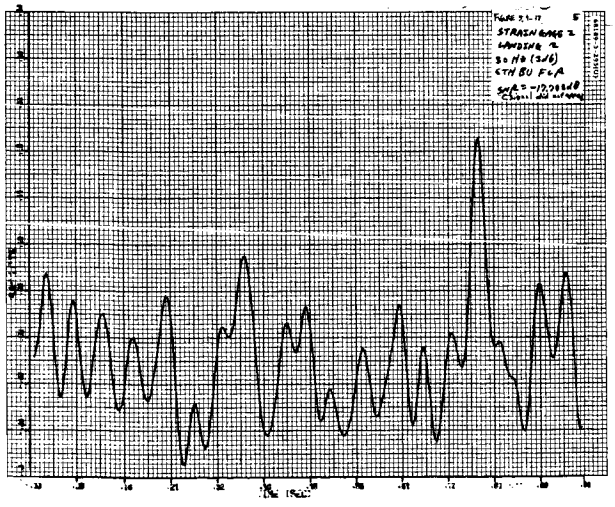

Figure 5.4-17. Strain Gage 2 Landing 2

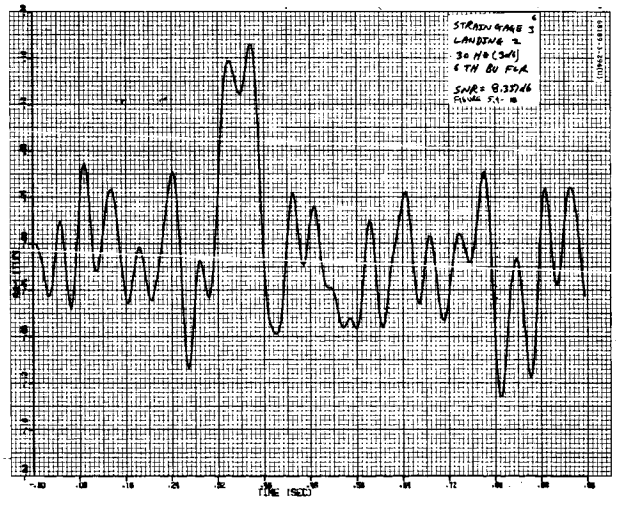

Figure 5.4-18. Strain Gage 3 Landing 2

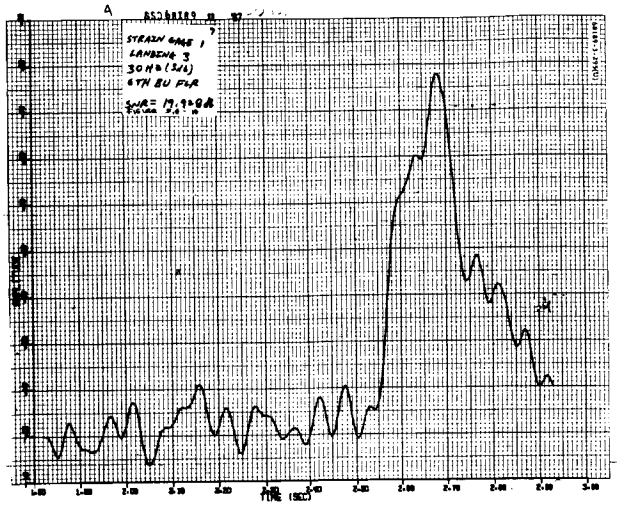

Figure 5.4-19. Strain Gage 1 Landing 3

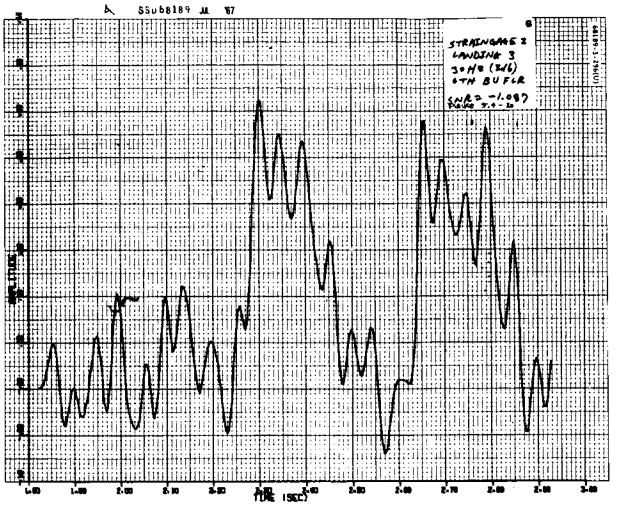

Figure 5.4-20. Strain Gage 2 Landing 3

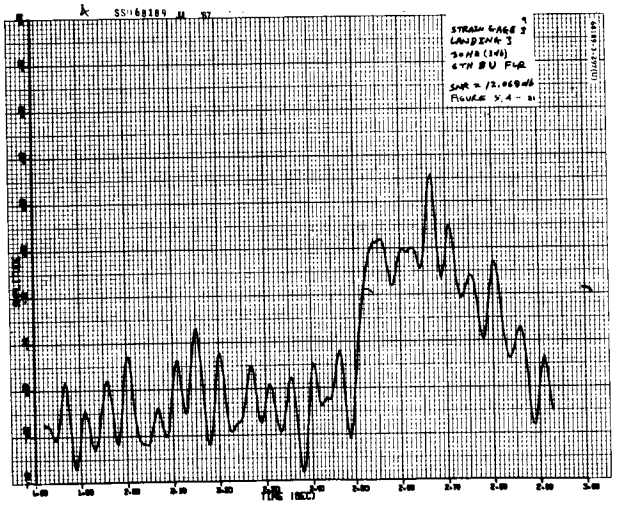

Figure 5.4-21. Strain Gage 3 Landing 3

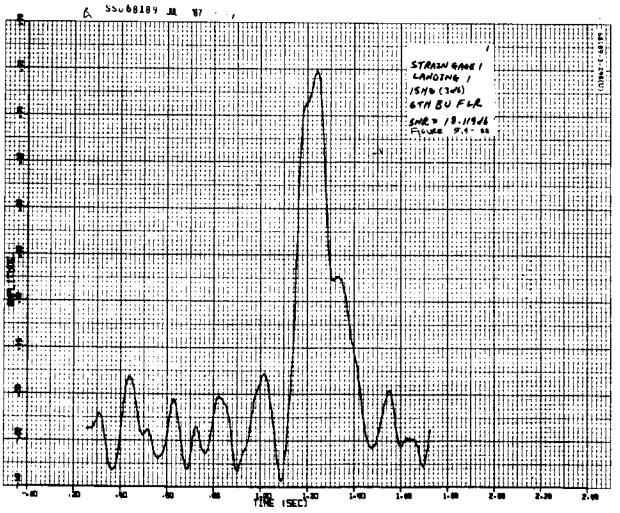

Figure 5.4-22. Strain Gage 1 Landing 1

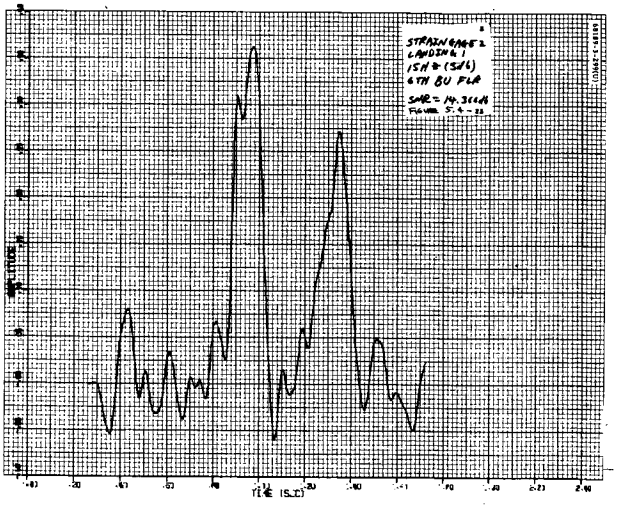

Figure 5.4-23. Strain Gage 2 Landing 1

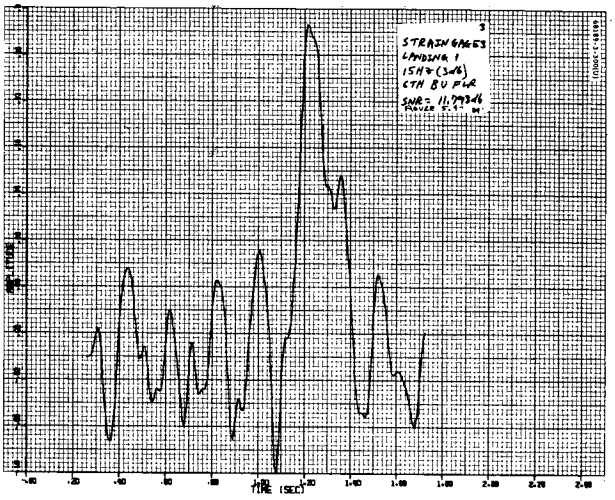

Figure 5.4-24. Strain Gage 3 Landing 1

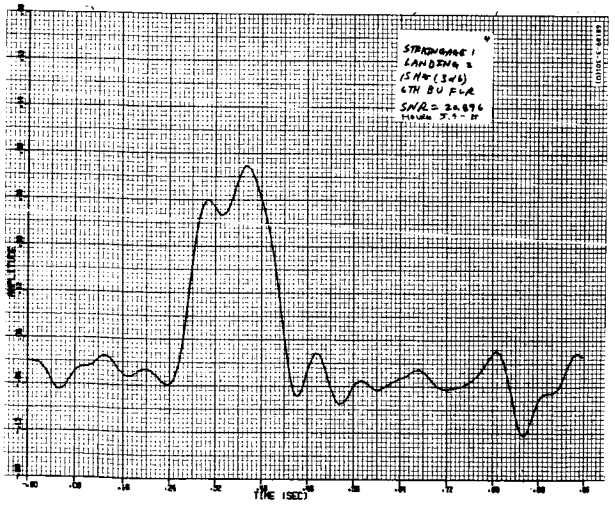

Figure 5.4-25. Strain Gage 1 Landing 2

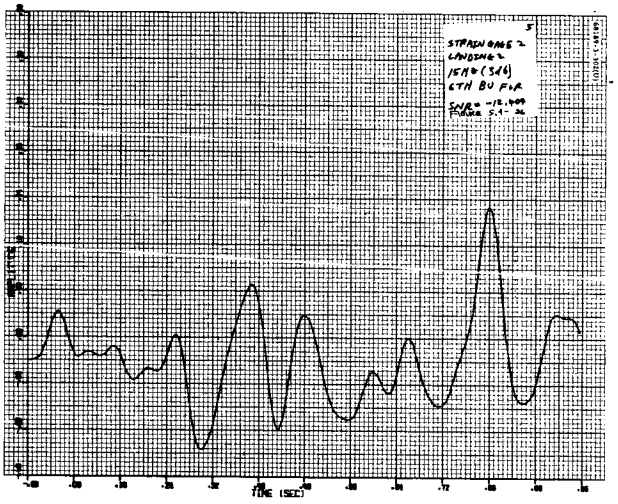

Figure 5.4-26. Strain Gage 2 Landing 2

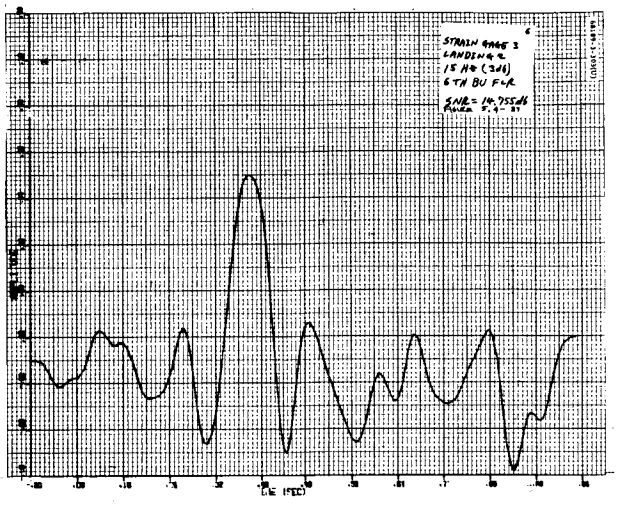

Figure 5.4-27. Strain Gage 3 Landing 2

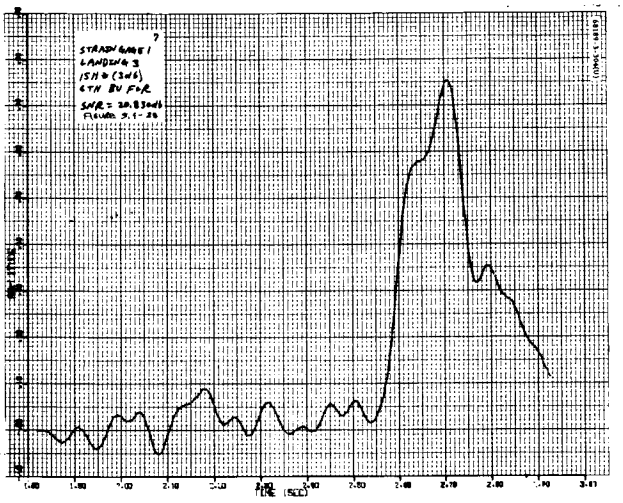

Figure 5.4-28. Strain Gage 1 Landing 3

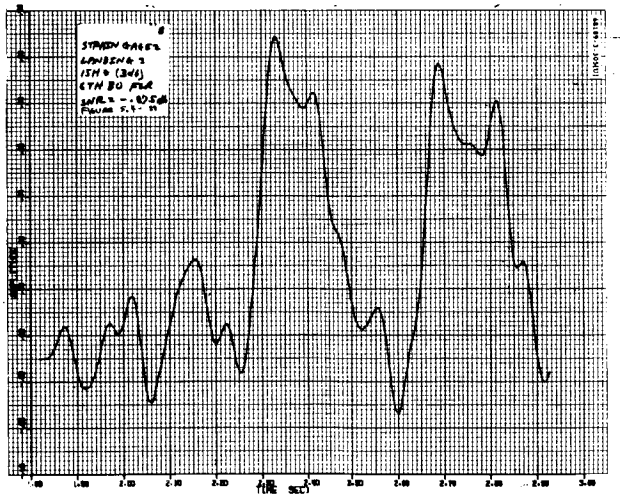

Figure 5.4-29. Strain Gage 2 Landing 3

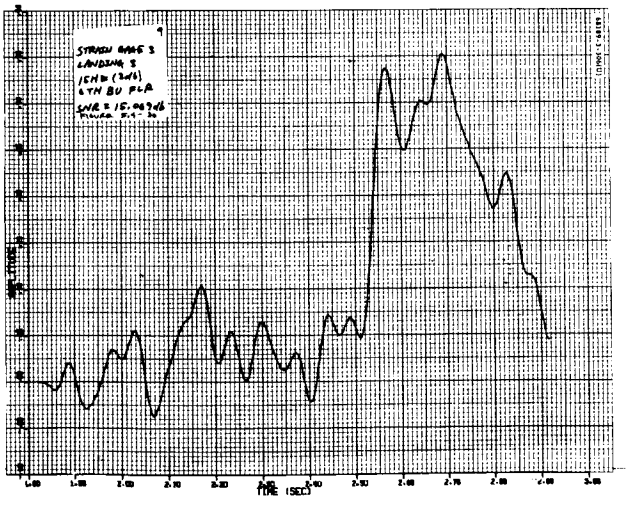

Figure 5.4-30. Strain Gage 3 Landing 3

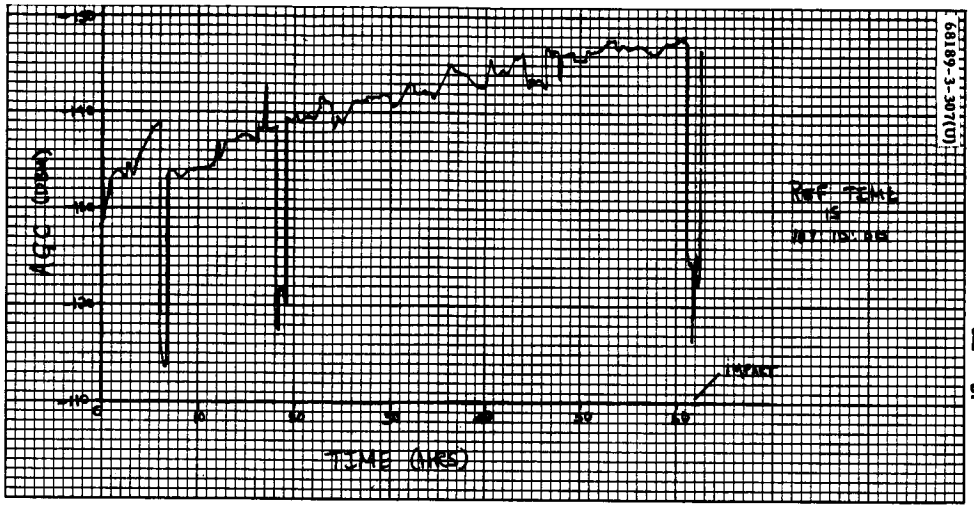

Figure 5.4-31. Surveyor III Received Carrier Signal Level

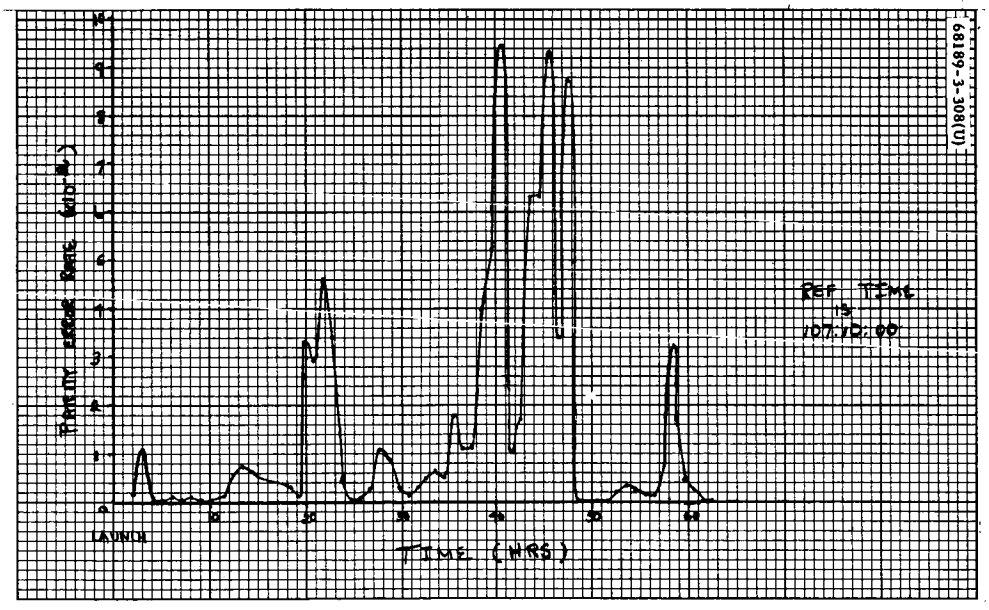

Figure 5.4-32. Surveyor III Parity Error Rate

5.4.6 ACKNOWLEDGEMENTS

The section was coordinated by R. J. Rechter. M. Fashano digitized touchdown strain gage magnetic tape, andhe and A. Dittmer performed the diversity combining. W. Mayfield developed the digital filtering routines for subsequent touchdown strain gage data filtering. B. McQuaid generated the computer simulation of the signal processing anomaly. G. Young and L. Bronstein organized the subsection describing the telemetry anomaly.

5.5 FLIGHT CONTROL

5.5.1 INTRODUCTION

The principal requirements of the Surveyor flight control system are attitude control, accurate angular maneuvers, precision velocity corrections, and a soft lunar landing. In order to accomplish these functions, the control system utilizes such hardware as gyros, gas jets, a solid fuel engine, liquid fuel engines, optical sensors, timing devices, radars, and acceleration sensing mechanisms.

5.5.1.1 Attitude Control

Attitude control is accomplished by two basic types of active control systems. During coast phase, a bang-bang type of attitude gas jet system is employed which utilizes artificial rate feedback for loop stabilization. During periods of potentially large moment disturbances, such as the main retro phase, the throttle-controlled vernier engine system is used. The error signals required for controlling the propulsion systems are derived from optical sensors or rate integrating gyros which are mounted on the spacecraft in such a way as to provide a three-axis control system. During coast phase, when the gas jet system is used, two modes of operation are available. One is the celestial referenced mode using the sun and Canopus, and the second is self-contained inertial referencing (gyros). The first mode is used to establish accurate spatial attitude, and the second mode is generally used when momentary inertial reference is desired; such an instance occurs during an attitude maneuver.

5.5.1.2 Angular Maneuvers

The rate integrating gyros are also used for accurate angular maneuvers, accomplished by precessing the gyros at precise rates for given time intervals and slaving the spacecraft to the gyros through the gas jet system.

5.5.1.3 Velocity Correction

A midcourse velocity correction capability is provided by a system consisting of three vernier engines, a precision timer, and an accurate acceleration sensing device. The difference between the commanded acceleration level and the output from an accelerometer provides the error signal that commands the vernier engines to the required thrust levels. The constant

acceleration and variable time concept used by the Surveyor flight control system provides the flexibility of choosing velocity corrections from 0 to 50 m/sec.

5.5.1.4 Soft Landing

Surveyor's soft landing capability is provided by a sophisticated technique utilizing radars to compute velocities and range. The range information is then used by an on-board computer to provide vertical velocity commands to the vernier engine system according to an approximate, constant acceleration, V^2/R function. The velocity information is used by the vernier engine attitude control loop to produce a near-gravity turn descent by aligning the spacecraft thrust axis to the true velocity vector. The velocity information is also used, along with velocity commands, to generate error signals for the velocity control loop.

To provide the required condition of low velocity for the soft landing phase, a large amount of approach velocity is removed by a solid fuel rocket engine during the initial portion of the terminal descent phase. Spacecraft attitude during this phase is inertially stabilized by the gyro vernier engine control system.

5.5.1.5 Mission Performance

During the Surveyor III mission, each of the above mentioned tasks was performed satisfactorily.

5.5.1.6 Analysis

Subsection 5.5.4 contains the analysis effort. The analysis items are categorized under major mission phases for easier identification and performance evaluation. A log of time and events is presented in Table 5.5-1, and a table of results (Table 5.5-2) is given in subsection 5.5.3.

5.5.2 ANOMALY DESCRIPTION

The flight control anomalies that occurred during the mission are described briefly below.

5.5.2.1 Prelaunch Roll Actuator Test

During the system readiness test which is part of the countdown procedure, an apparent movement of the roll actuator was detected following turn-on of flight control thrust phase power. In order to verify that the actuator was still pinned, position commands were provided to the actuator by precessing the roll gyro in both a positive and negative direction. The results of this special test were not consistent in that a significant movement of the actuator from the pinned position was noted in one direction, but not the other. The launch was then delayed until the same test could be run on the SC-5 spacecraft at El Segundo. The similarity of the SC-5 test results

TABLE 5.5-1. SURVEYOR III TIME AND EVENTS LOG

Event	Date, GMT	Mission Time	
		GMT, hr:min:sec	From Launch
Launch	17 April 1967	07:05:01	0
Injection		07:38:49	33M48S
Separation			
Electrical		07:34:54	29M53S
Mechanical		07:39:54	34M53S
Automatic sun acquisition			
Start		07:40:41	35M40S
Completed		07:47:58	42M57S
Automatic solar panel		07:49:54	44M53S
Deployment completed		07:49:54	44M53S
Canopus verification, started		16:09:13	9H9M11S
Canopus acquisition, completed		16:27:51	9H22M50S
Gyro drift check No. 1			
Start		17:29:17	10H24M16S
Stop		19:16:32	12H11M31S
Gyro drift check No. 2			
Start		19:23:34	12H18M33S
Stop		21:41:53	14H36M52S
Gyro drift check No. 3, roll only			
Start		23:11:19	16H06M18S
Stop	18 April 1967	02:11:00	19H05M59S
Premidcourse (+) roll, 56.7 degrees			
Start		04:46:51	21H41M50S
Stop		04:48:44	21H43M43S

Table 5.5-1 (continued)

Event	Date, GMT	Mission Time	
		GMT, hr:min:sec	From Launch
Premidcourse (-) pitch, 39.1 degrees			
Start		04:50:09	21H45M08S
Stop		04:51:28	21H46M27S
Midcourse thrust executed		05:00:02	21H55M01S
Sun reacquired		05:04:37	21H59M36S
Canopus reacquired		05:08:11	22H3M10S
Gyro drift check No. 4			
Start		07:35:58	24H30M57S
Stop		08:43:46	26H38M45S
Gyro drift check No. 5			
Pitch and yaw			
Start		17:31:26	34H26M25S
Stop		19:31:50	36H26M49S
Pitch and yaw			
Start		19:37:27	36H32M26S
Stop		20:22:35	37H17M34S
Gyro drift check No. 6			
Start		20:27:20	37H22M19S
Stop		22:50:05	39H45M04S
Gyro drift check No. 7, roll only			
Start		22:54:00	39H45M59S
Stop	19 April 1967	01:15:44	42H10M43S
Gyro drift check No. 8			
Start		01:23:36	42H18M35S
Stop		03:36:32	44H31M31S
Gyro drift check No. 9, roll only			
Start		03:57:26	44H52M25S
Stop		06:45:14	47H40M13S

Table 5.5-1 (continued)

Event	Date, GMT	Mission Time	
		GMT, hr:min:sec	From Launch
Gyro drift check No. 10			
Start		06:48:53	47H43M52S
Stop		09:09:21	50H04M20S
Gyro drift check No. 11 roll only			
Start		10:21:23	51H16M22S
Stop		12:41:24	53H36M23S
Gyro drift check No. 12			
Start		14:28:07	55H23M06S
Stop		16:55:53	57H50M52S
Gyro drift check No. 13, roll only			
Start		17:06:00	58H00M59S
Stop		20:50:51	61H45M50S
Preretro (-) yaw, 157.9 degrees			
Start		23:23:32	64H18M31S
Stop		23:28:48	64H23M47S
Preretro (-) pitch, 76.7 degrees			
Start		23:30:19	64H25M18S
Stop		23:32:53	64H27M52S
Preretro (-) roll, 63.9 degrees			
Start		23:34:38	64H29M37S
Stop		23:36:45	64H31M44S
AMR mark	20 April 1967	00:01:13	64H56M12S
Vernier ignition		00:01:18	64H56M17S
Retro eject		00:02:13	64H57M12S
1000-foot mark		00:03:53	64H58M52S
Touchdown			
No. 1		00:04:18	64H59M17S
No. 2		00:04:42	64H59M41S
No. 3		00:04:55	64H59M54S

TABLE 5.5-2. FLIGHT CONTROL RESULTS

	Controlling Specification	Specification Value	Results	Comments
Prelaunch				
Proper gyro temperature control			Roll 172.7°F Pitch 168.1°F Yaw 167.4°F	Time was 07:00 GMT
Verification of N_2 loading		4.6 pounds	4.6.3 pounds	
Centaur separation				
Time required to null rates to less than 0.1 deg/sec	224510E (3.3.3.3)	<0.1 deg/sec within 50 seconds	< 11 seconds	
Magnitude of angular rate at separation	224510E (3.3.2.1)	≤3.0 deg/sec	≈ 0 deg/sec	
Sun acquisition	224510E (3.4.1)	Minus roll maneuver until activation of acquisition sun sensor and then a plus yaw maneuver until primary sun sensor illumination		
Proper sun acquisition				
Roll			181 degrees of roll	
Yaw			38.1 degrees of yaw	
Total time			438.2 seconds	
N_2 gas used	Design	0.054 pound (average)	< 0.1 pound	Tank temperature may not have been at steady state.
Star acquisition	224510E (3.4.2)	Positive roll maneuver sufficient to produce an adequate star map for Canopus verification. Provide a lockon signal when Canopus appears in the sensor field of view		
Proper acquisition and verification of Canopus			Automatic lock-on	
Roll angle from beginning of maneuver to Canopus			205 degrees	
Stars identified			Procyon, Adhara, Altair, Canopus, Jupiter, earth, and moon	
Mean roll rate during star map phase	224510E (3.4.2.1.1)	0.5 deg/sec	0.5011 deg/sec	
Effective gain (relative to nominal Canopus) of Canopus sensor			1.03 - 1.22 x Canopus	
N_2 gas used	Design	0.048 pound (average)	0.01 pound	
Coast mode				
Sun and star tracking errors—tracking noise	224510E (4.3.1.1)	Roll axis shall be held to within 0.20 degree of sun-spacecraft line, plus a ±0.30 degree limit cycle		Sun and star error signal noise level were low enough to have no effect on the limit cycle performance.
Average error from sun line			0 (pitch) +0.02 (yaw)	
Average error from Canopus line of sight		Same magnitudes as above for Canopus-spacecraft line	-0.06 (roll)	
Limit cycle (gas jet system)				
Optical mode/inertial mode	224510E (4.3.1.1 and 4.3.1.2)	±0.30 degree		Values are that of the total deadband. Predicted values were:
Average amplitude — roll			0.55/0.46 (roll)	0.44/0.44
Average amplitude — pitch			0.51/0.48 (pitch)	0.44/0.44
Average amplitude — yaw			0.54/0.50 (yaw)	0.44/0.44
Average period			68.5 (optical) and 68.5 sec/pulse (inertial)[R]	80 (optical) and 117 sec/pulse (inertial)
Average N_2 usage	Design	0.0012 lb/hr (average)	0.0012 lb/hr	
Gyro drift	224510E (4.3.1.5)	<1 deg/hr		
Roll			Roll +1.12	
Pitch			Pitch +0.6	
Yaw			Yaw -0.8	
Gas jet thrust level	224510E (4.3.3.2)	>0.052 pound	0.066 pound (roll)	Design value is 0.057 pound
Premidcourse maneuvers				
Maneuver angles	224510E (4.3.2.1)	Rates shall be controlled to be 0.5 ± 0.0011 deg/sec		Assuming a precession level of 0.5000 deg/sec
Roll			+56.775 degrees	
Pitch			-39.215 degrees	
Precession command times	224510E (3.6.4.8)	0.2 second plus 0.02 percent of command interval magnitude		These times were obtained from the gyro error signal response profile
Roll			113.55 seconds	
Pitch			78.43 seconds	
Attitude maneuver accuracy (includes drift, initial attitude errors, and limit cycle)			0.18 degree (yaw) 0.04 degree (pitch)	Calculated using actual data of drift, attitude errors, and execution errors

Table 5.5-2 (continued)

	Controlling Specification	Specification Value	Results	Comments
Maximum acceleration error	224510E (3.6.3.2)	ΔV error < ±1.3 ft/sec		
Expected ΔV/tracking ΔV			4.19 m/sec 4.014 m/sec	
Shutdown impulse	224510E (4.2.2.7)	<5 lb-sec/engine Δ impulse < 0.66 lb/sec		Units are lb-sec
Engine 1			-0.31	
Engine 2			+0.42	
Engine 3			-0.11	
Preretro maneuvers				
Maneuver angles	224510E (4.3.2.1)	Rates shall be controlled to be 0.5±0.0011 deg/sec		Values only include execution error. The desired values were:
Yaw			-157.83 degrees	Yaw (-) 157.9 degrees
Pitch			- 76.7 degrees	Pitch (-) 76.7 degrees
Roll			- 83.95 degrees	Roll (-) 63.9 degrees
Precession command times	224510E (3.6.4.8)	0.2 second plus 0.02 percent of the command interval magnitude		The command values were:
Yaw			315.66 seconds	315.8 seconds
Pitch			153.4 seconds	153.4 seconds
Roll			127.9 seconds	127.9 seconds
Pointing accuracy (includes drift, initial attitude errors, and limit cycle)	224510E (3.9.3.2)	Within ± 1 degree	0.13 degree	
Gyro drift compensation values				
Roll			+1.1 deg/hr	
Pitch			+0.60 deg/hr	
Yaw			-0.80 deg/hr	
N_2 gas used	Design	0.18 pound	0.3 pound	
Terminal descent				
Approach angle of velocity vector to lunar vertical			0.1 degree	
AMR marking altitude	224510E (3.9.1.1)	Nominal slant range of 60 miles		
Main retro				
Burn time (from ignition to 3.5 g switch)	224510E (3.9.2.4)	Approximately 42 seconds	41.49 seconds	
Maximum retro thrust	224510E (4.2.1.3)	<10,000 pounds		Computed using retro accelerometer data
Peak attitude transient at vernier ignite – retro ignite				
Roll				
Pitch			-0.22 degree	
Yaw			-0.10 degree	
Main retro thrust vector to spacecraft center of gravity offset	224510E (4.1.3.3)	<0.18 inch	<0.04 inch	Exact values were limited by telemetry accuracy of the parameters
Thrust vector pointing accuracy during retro burn	224510E (3.9.3.2)	Within ±1 degree	0.35 degree	
Mean attitude error during burn				
Roll				
Pitch			≈0 degree	
Yaw			≈0 degree	
Roll actuator position				
Peak at retro ignition				
Mean value during burn				
Time between major events	224510E (3.9.2)			
AMR and vernier ignite		0 to 20 seconds	5.675 seconds	
Vernier ignite and retro ignite		1.1 ± 0.1 seconds	1.100 seconds	
Retro ignite and retro burnout		Approximately 42 seconds	41.49 seconds	
Retro burnout to retro eject		12.0 ± 0.1 seconds	12.000 seconds	
Retro eject to RADVS descent on		First possible attitude reference change: 2.15 ± 0.1 seconds	2.1 seconds	
Vernier engine startup		<10 lb-sec		
Total change in velocity during retro phase				

Table 5.5-2 (continued)

	Controlling Specification	Specification Value	Results	Comments
Retro burnout condition				
Altitude/slant range	224510E (3.9.4)	Depends on midcourse	36,158 feet (SR)	
Velocity	224510E (3.9.4)	Depends on midcourse	V_z = 462 ft/sec	V_x = -85.3 ft/sec and V_y = + 148 ft/sec
Angle between thrust vector and velocity vector				
Flight path angle (angle between velocity vector and local vertical)	224510E (3.9.4)	23 ± 16 degrees	21.1 degrees	
Time to cage the spacecraft Z-axis to velocity vector from the start of velocity controlled descent	224510E (3.10.2.1)	9 seconds maximum	< 5 seconds	
Descent segment intercept conditions				
Altitude			22,300 feet (SR)	
Velocity			495 ft/sec (V_z)	
Flight path angle				
Touchdown No. 1 conditions				
Vertical velocity	224510E (3.11.2.1)	<15 ft/sec	7-8 ft/sec	
Lateral velocity	224510E (3.11.2.2)	<5.0 ft/sec	≈ 0	
Approach angle	224510E (3.11.2.3)	<7 degrees	≈ 0	
Additional information				
Total nitrogen gas used	Design	0.64 ± 0.22 pound	0.94	See coast mode gas consumption
Gyro speeds	235159	Telemetry value = 50 cps for all three gyros		
Roll gyro			Roll = 50 cps (average)	
Pitch gyro			Pitch = 50 cps (average)	
Yaw gyro			Yaw = 50 cps (average)	
Gyro heater duty cycle				
Roll			Roll = 22 percent ON	
Pitch			Pitch = 40 percent ON	
Yaw			Yaw = 28 percent ON	

led to the conclusion that the roll actuator behavior was normal, and the countdown proceeded without any further delay. Subsequent laboratory testing and analysis revealed that the observed roll actuator motion resulted from internal movement of the position pickoff caused by structural compliance, rather than by any significant motion of the output shaft. These characteristics are normal when a change in the roll actuator position is commanded while in the pinned condition.

5.5.2.2 14-foot Mark Failure

The SC-3 terminal descent was normal until shortly after the 5-fps mode was reached. At this point, RADVS beam 3 broke lock, resulting in the loss of both reliable operate signals (RORA and RODVS). This caused the flight control system to switch to the minimum acceleration mode (0.9 g_m) approximately 4.5 seconds before the initial touchdown and prevented the

14-foot mark from being generated which, in turn, permitted the vernier engines to remain on until final touchdown. Evaluation of the available data revealed that the most probable cause of the break lock was a false sidelobe rejection of the main beam, as discussed in subsection 5.5.4.11. A hardware change was incorporated to inhibit the crosscoupled sidelobe logic circuit at the 1000-foot mark, preventing recurrence of the problem in future missions.

5.5.2.3 Midcourse Thrust Levels

During the midcourse velocity correction, a discrepancy existed between the thrust levels as indicated by the vernier engine commands and those indicated by the vernier engine strain gages. While the telemetered vernier engine command signals indicated that engine 1 was greater than engine 3 by approximately 4.0 pounds, the strain gage signals indicated that the engine 3 thrust was higher than engine 1 by approximately 3.0 pounds. The difference in thrust levels between engines 1 and 2 was approximately the same for both the telemetered strain gage and engine thrust command signals ($\approx$6.5 pounds). The anomaly is discussed in detail in subsections 4.3.1 and 5.6.4.3.

5.5.3 SUMMARY AND RECOMMENDATIONS

5.5.3.1 Summary

A summary of flight control system performance is presented in Table 5.5-2.

Anomalies

Loss of 14-foot Mark. The most probable cause of beam 3 break lock just prior to the first touchdown was a false sidelobe logic rejection of the main beam. To prevent loss of the 14-foot mark in future missions, the RADVS system was modified by providing a signal to inhibit the sidelobe rejection logic at the 1000-foot mark. The probability of either a sidelobe acquisition or loss of lock on a main beam below 1000 feet is small, and the sidelobe logic protection is needed primarily while the spacecraft is being aligned to the lunar vertical.

Midcourse Thrust Levels. The cause of the disparity in telemetered vernier engine thrust commands during the midcourse velocity correction is still under investigation. This anomaly in no way affected the successfully executed velocity correction. Since the anomaly is suspected to be a telemetry signal calibration problem, future calibrations of these signals will be obtained more accurately by combining the flight control electronics and vernier engine throttle valve during simulated fuel flow tests. Previous calibrations were accomplished separately on each of the units and combined mathematically for data evaluation.

Prelaunch Roll Actuator Behavior. It was determined that the indicated behavior of the telemetered roll actuator position signal during the systems readiness test was completely normal. The apparent motion of the actuator was actually internal movement of the position pickoff due to structural compliance of the parts under the torque commanded when thrust phase power was turned on with the actuator in its pinned position.

Spacecraft Separation From Centaur. Dissipation of spacecraft rotational rates after separation from Centaur was accomplished well within the 46-second period available prior to start of the sun acquisition roll maneuver. An apparent small disturbance impulse about the yaw axis at mechanical separation did not materially affect flight control system performance.

Canopus Acquisition. Canopus acquisition was accomplished for the first time using the automatic lockon signal. Four stars, including Canopus, were identified during the star map; Jupiter, earth, and the moon were also identified. A comparison of predicted star intensities and telemetered inflight intensities indicated that either the effective gain of the sensor was high by 16 to 28 percent or the predicted values were low by this amount. This in no way impaired the highly satisfactory operation of the sensor.

5.5.3.2 Recommendations

Recommendations to the flight control system are as follows:

Sidelobe Logic Rejection Telemetry Signal

Add a telemetry signal to monitor the sidelobe logic rejection circuit to indicate when a forced break of lock occurs. The addition of a gate circuit in the signal data converter and wiring changes to both the signal data converter and spacecraft wiring harness would permit monitoring of the three forced loss signals on a single telemetry channel.

Touchdown Switches

Investigate the use of touchdown switches to permit the vernier engines to burn down to the lunar surface.

Vernier Engine Thrust Commands

Calibrate the telemetered vernier engine thrust commands in conjunction with flow bench tests on the actual flight engines in order to provide a more realistic calibration. (See Section 5. 6. 4. 3.)

Canopus Sensor Sun Filter

Use the same sun filter (0. 8 x Canopus) for the SC-4 mission as was used for SC-3.

Gyro Error Signals

Supply pitch and yaw calibration data over the range of 0 to 5 telemetry volts to include the nonlinear regions at the end points. This will provide approximately ±12 degrees of pitch and yaw gyro error information versus the approximately ±6 degrees supplied previously.

5.5.4 SUBSYSTEM PERFORMANCE ANALYSIS

5.5.4.1 Prelaunch

Gyro Temperatures

The gyro temperatures at the turn-on of flight control 29-volt coast phase power and just prior to launch at 07:00 GMT are shown below in Table 5.5-3.

TABLE 5.5-3. PRELAUNCH GYRO TEMPERATURS (°F)

Gyros	Prelaunch	
	04:32 GMT	07:00 GMT
Roll	167.3	172.7
Pitch	155.1	168.1
Yaw	158.4	167.4

The roll and yaw gyro temperature controllers were cycling at launch, and cycling of the pitch gyro temperature controller occurred 9 minutes after launch.

Nitrogen Weight

The estimated on-board nitrogen weight at launch was 4.63 pounds based on a telemetered tank pressure of 4832 psi at a tank temperature of 84.8°F. This agreed closely with the best estimate of 4.6 pounds of nitrogen loaded. All subsequent nitrogen weight estimates were corrected for this 0.03-pound difference.

5.5.4.2 Launch Through Separation From Centaur

After extending its landing legs, Surveyor is separated from the Centaur booster. When the three legs-down signals and the separation signal have been generated, the programmer removes the logic signal which has been inhibiting operation of the gas jet amplifiers. At this same instant,

the magnitude register begins to count down 1024 counts for a 51-second interval; the start of sun acquisition is inhibited for this interval to give the cold gas attitude control system opportunity to rate stabilize the spacecraft. Table 5.5-1 presents these events in time reference.

Rate stabilization is accomplished by using the three-axis attitude control system to torque the spacecraft and drive the caged integrating rate gyros error signals to within the deadband of each gas jet amplifier. Thus, at the end of a nominal rate stabilization maneuver, the spacecraft has achieved a low angular velocity at a random orientation in inertial space. The system response is dependent upon the magnitude and direction of the initial velocity vector and the gas jet thrust levels, and is essentially dead-beat in nature.

Flight control system performance just after Centaur separation was evaluated for proper nulling of the separation rates, the time required to null rates to less than 0.1 deg/sec, the total angular excursion, and magnitude of angular rates due to separation. The events observed from launch through separation and sun acquisition are depicted in Figure 5.5-1.

Separation transients based on data received via the Space Flight Operations Facility are plotted in Figure 5.5-2. The pitch and roll transients appear normal and indicate that any separation-induced rates about these axes were essentially zero. While the yaw transient also indicates a very small separation-induced rate, it appears that there was an impulse disturbance about the yaw axis at mechanical separation. In order to better understand the nature of this disturbance, the initial conditions at separation were used as inputs to a three degree-of-freedom analog simulation. The results of the simulation for the case where no external forces are present at mechanical separation is shown in Figure 5.5-3a. The pitch and roll transients agree closely with the Space Flight Operations Facility data, while the yaw transient does not. A good match for the yaw transient was obtained by introducing a negative 5.25 ft-lb-sec disturbance about the yaw axis at mechanical separation (Figure 5.5-3b). The separation springs apparently were not the source of the disturbance since Centaur data (Reference 1) indicated that extension of the three separation springs was essentially simultaneous.

Consideration was given to the solar panel stepping as being the source of the disturbance, but a rough bounding calculation shows that the disturbance torque resulting from the stepping of the panel is well below that of the system's capability. This can be shown as follows:

Let

M = disturbance moment

I = solar panel inertia about spacecraft transverse axis = 1.15 slug-ft

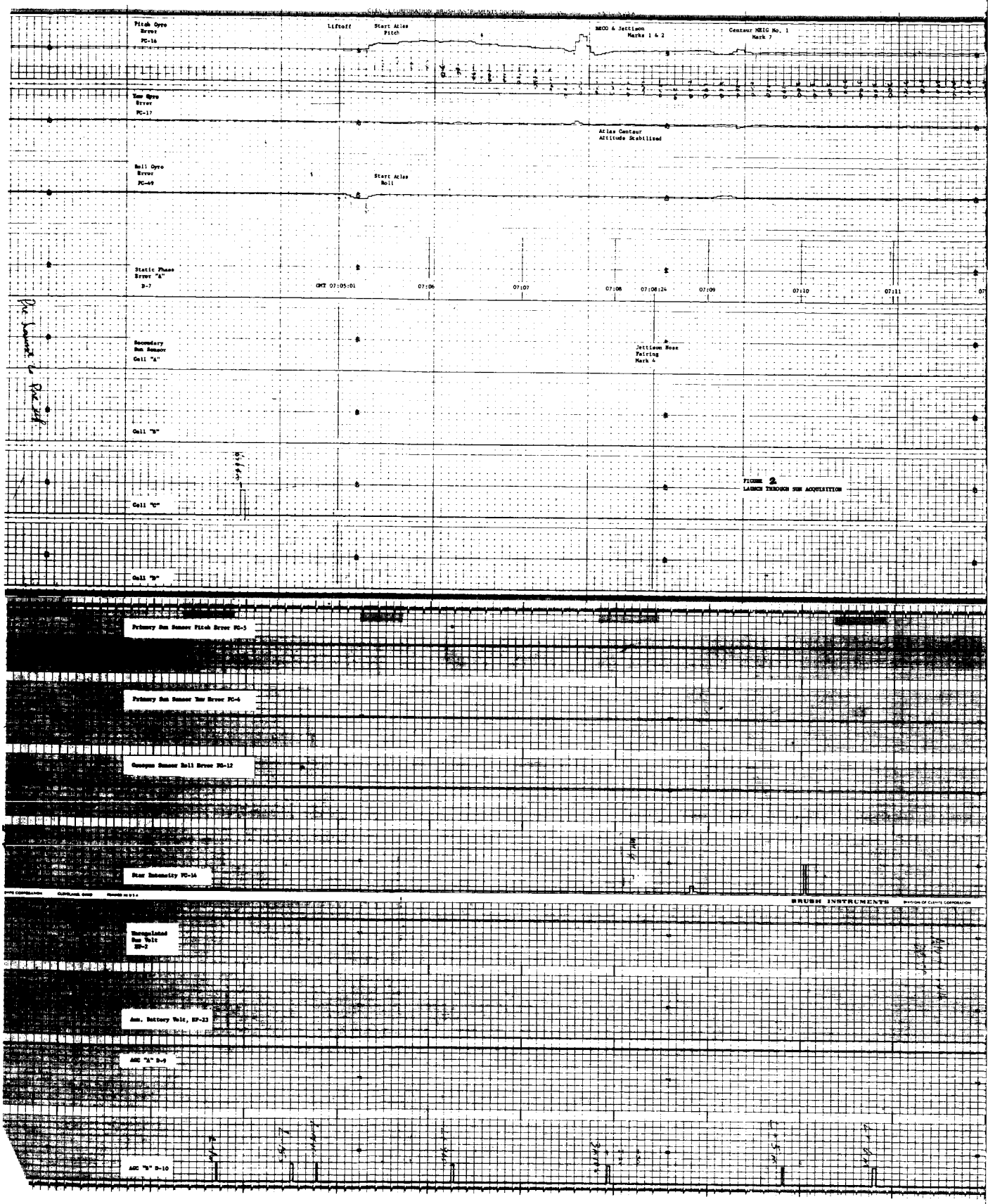

Figure 5.5-1. Launch Through Sun Acquisition

FOLDOUT FRAME 1

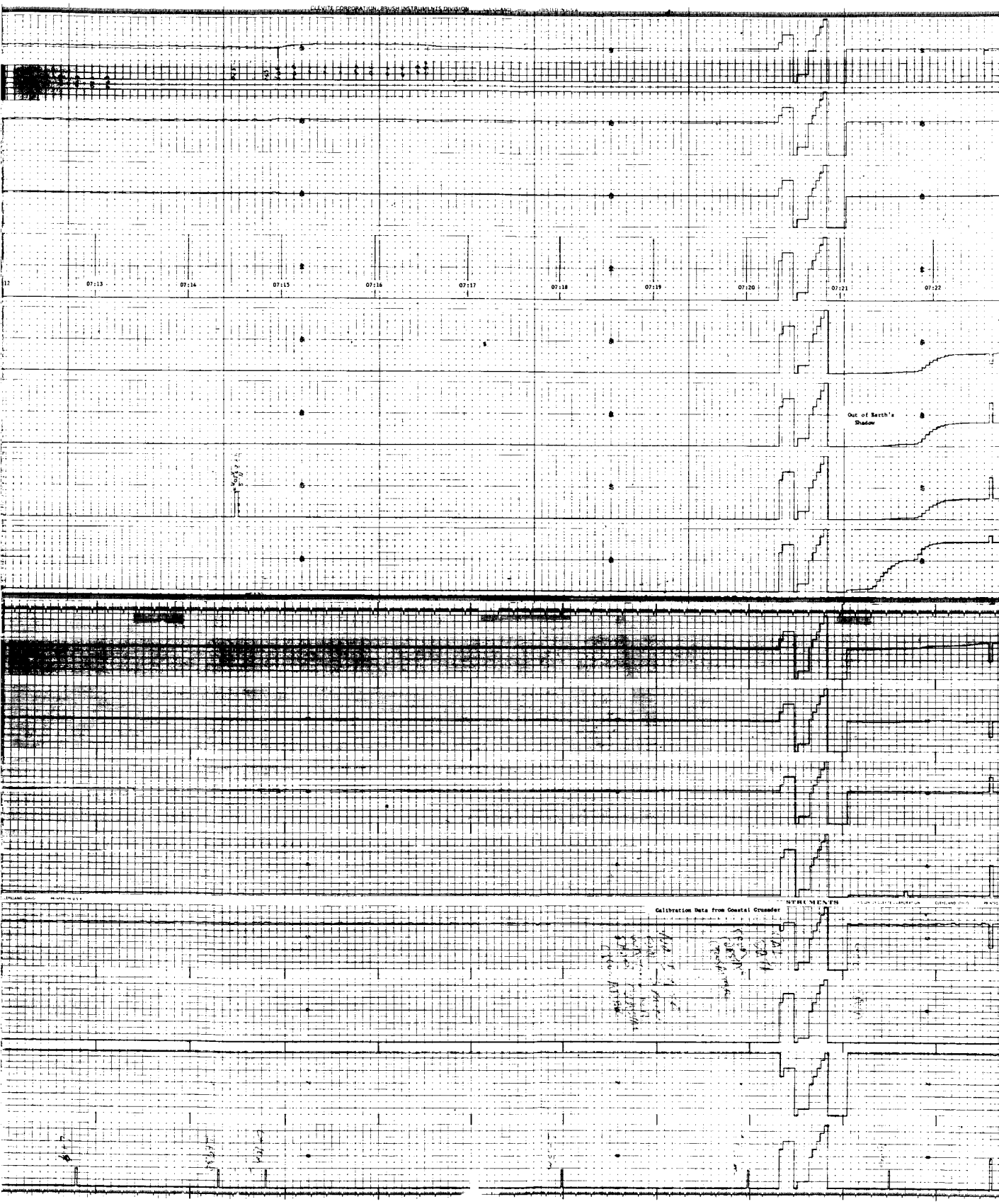

FOLDOUT FRAME 2

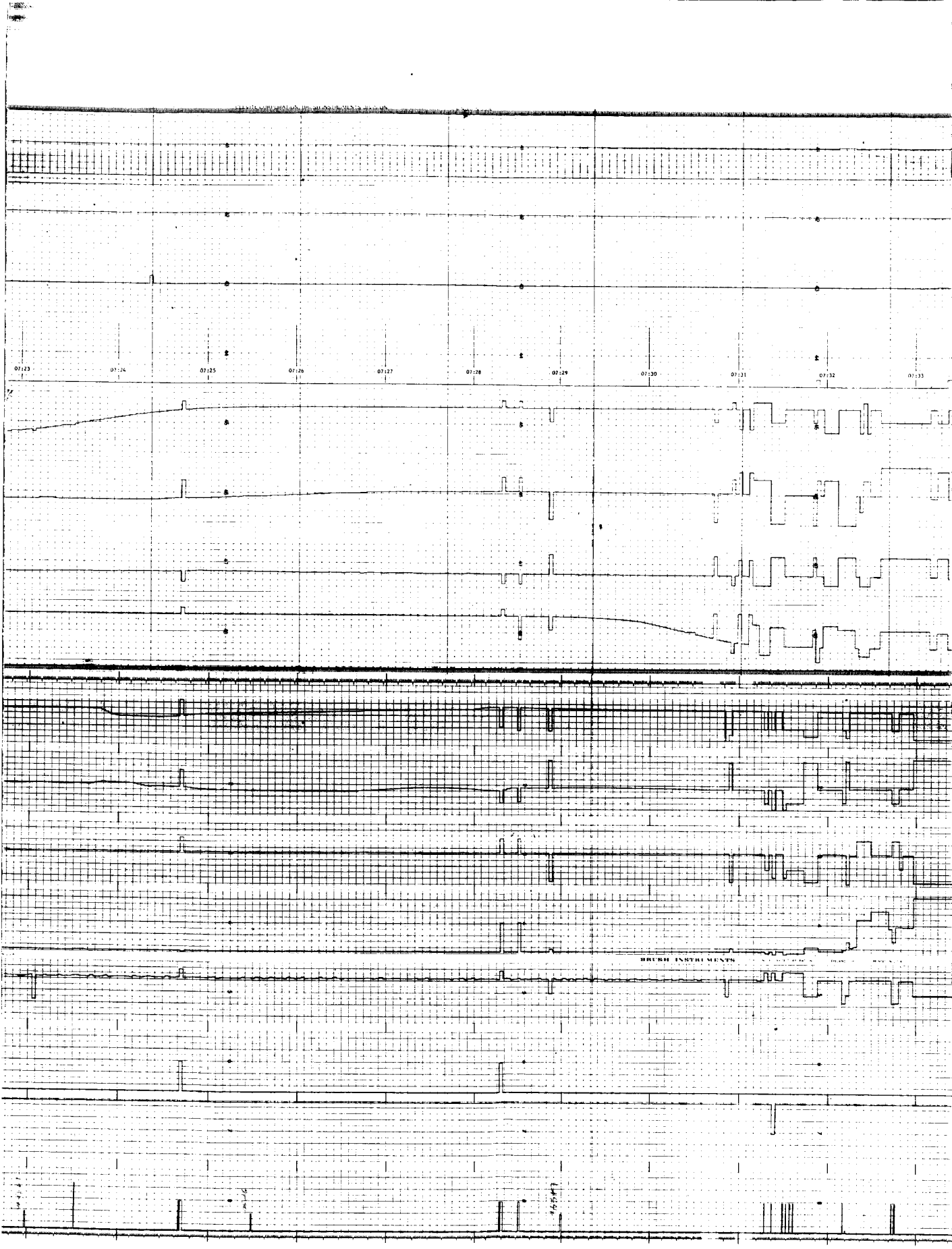

FOLDOUT FRAME 3

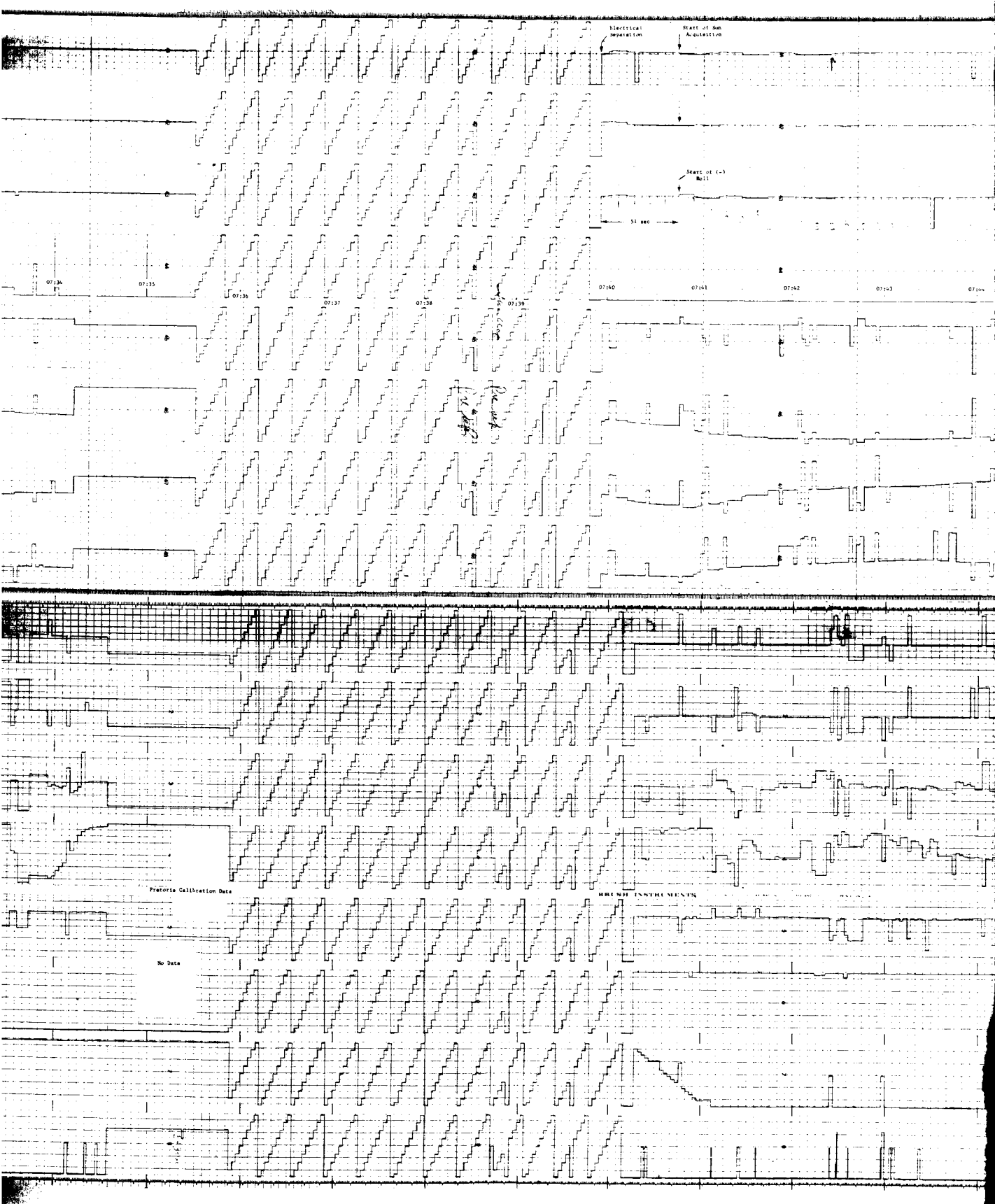

FOLDOUT FRAME 4

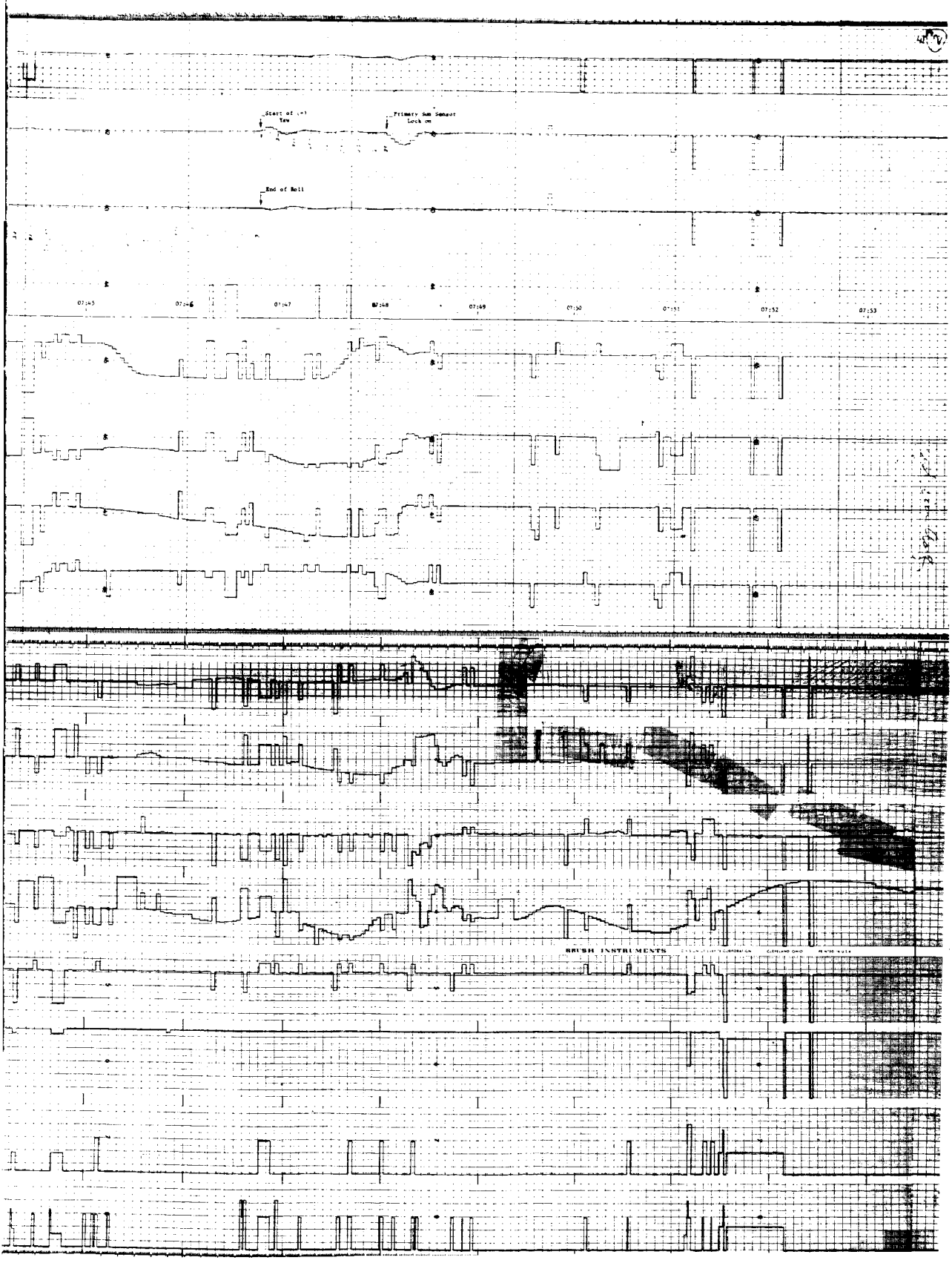

FOLDOUT FRAME 5

PRECEDING PAGE BLANK NOT FILMED.

REF. NO.: 2223/2752 Attachment 1

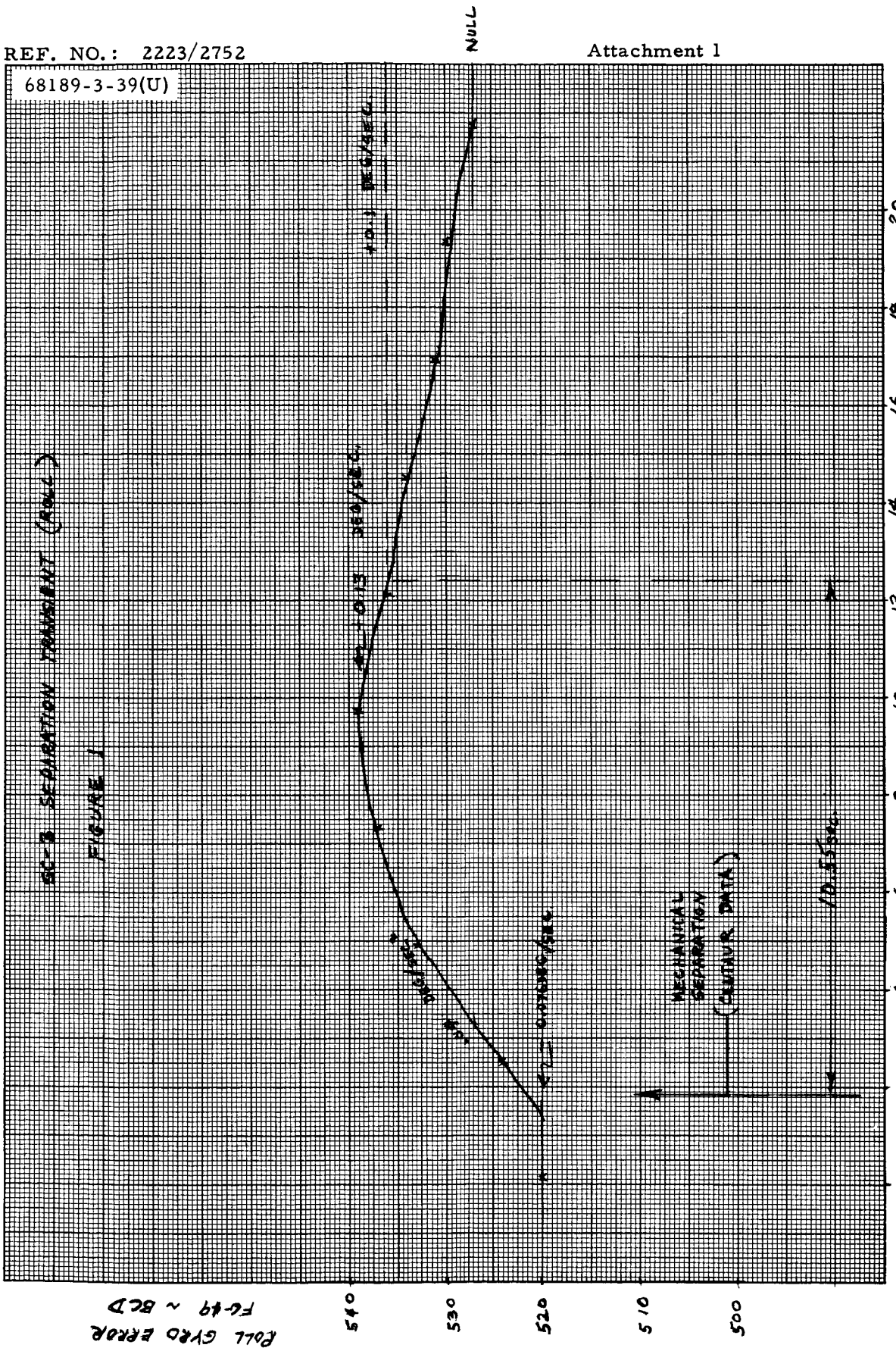

a) Roll

Figure 5.5-2. Separation Transient

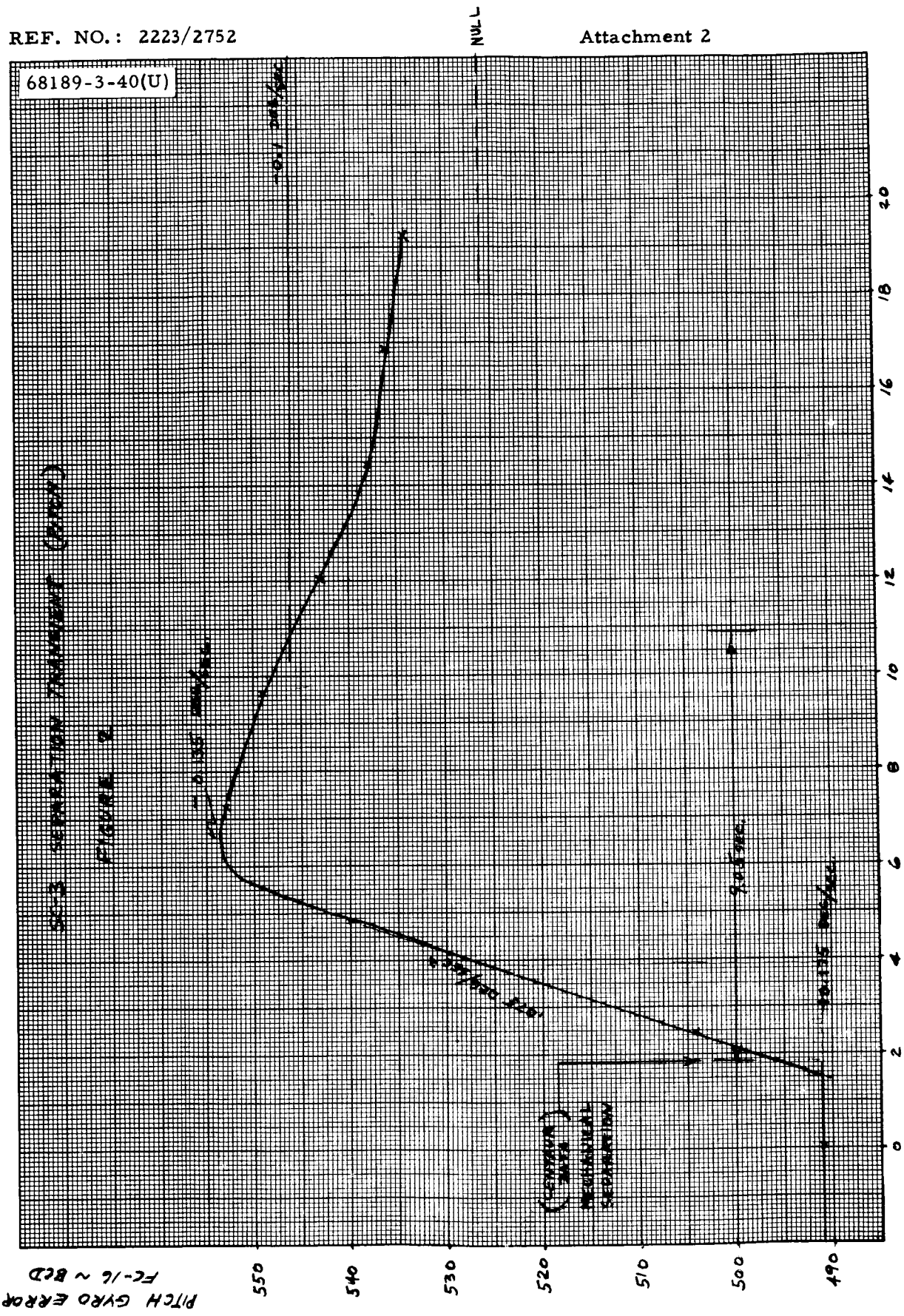

b) Pitch

Figure 5.5-2 (continued). Separation Transient

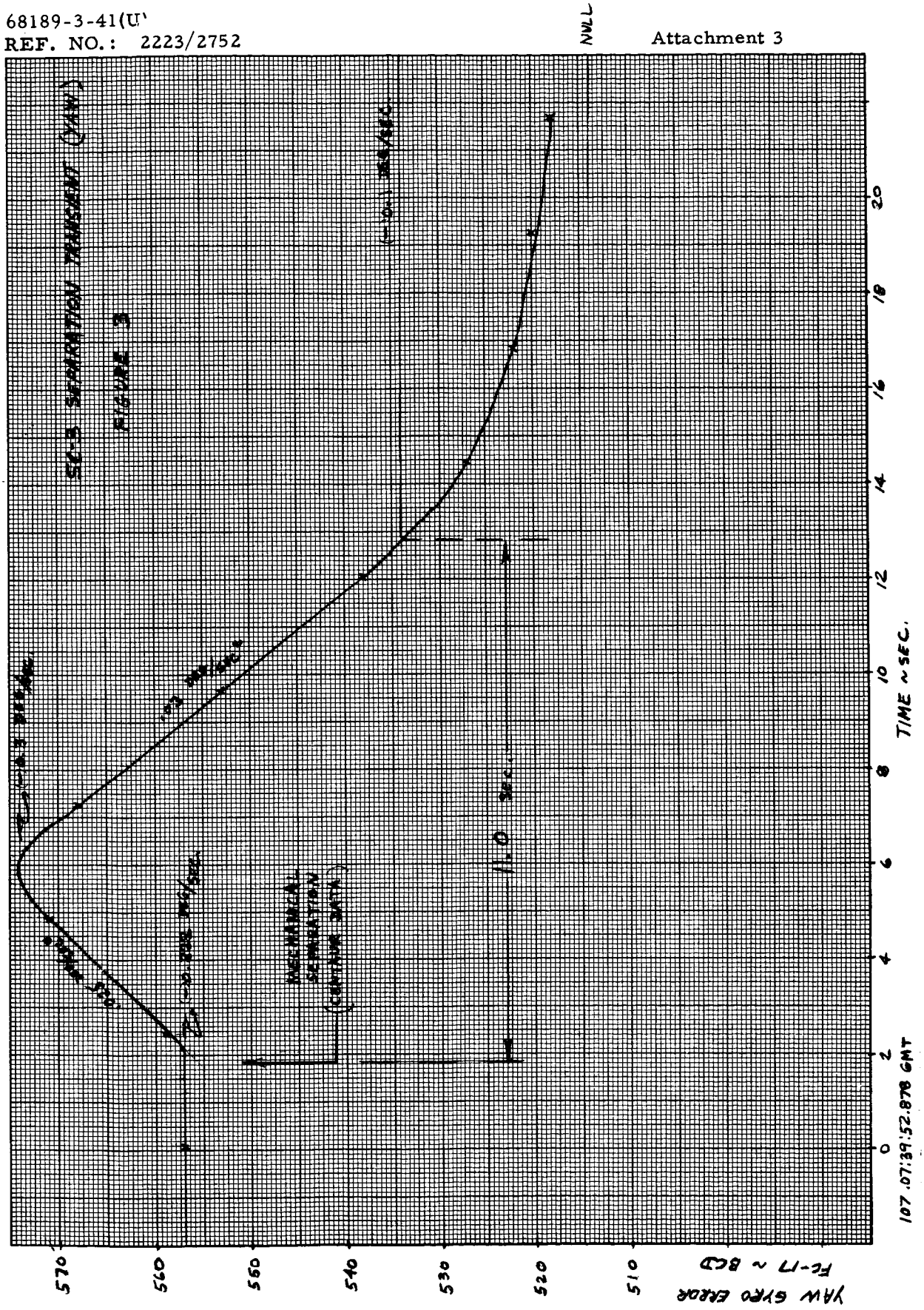

c) Yaw

Figure 5.5-2 (continued). Separation Transient

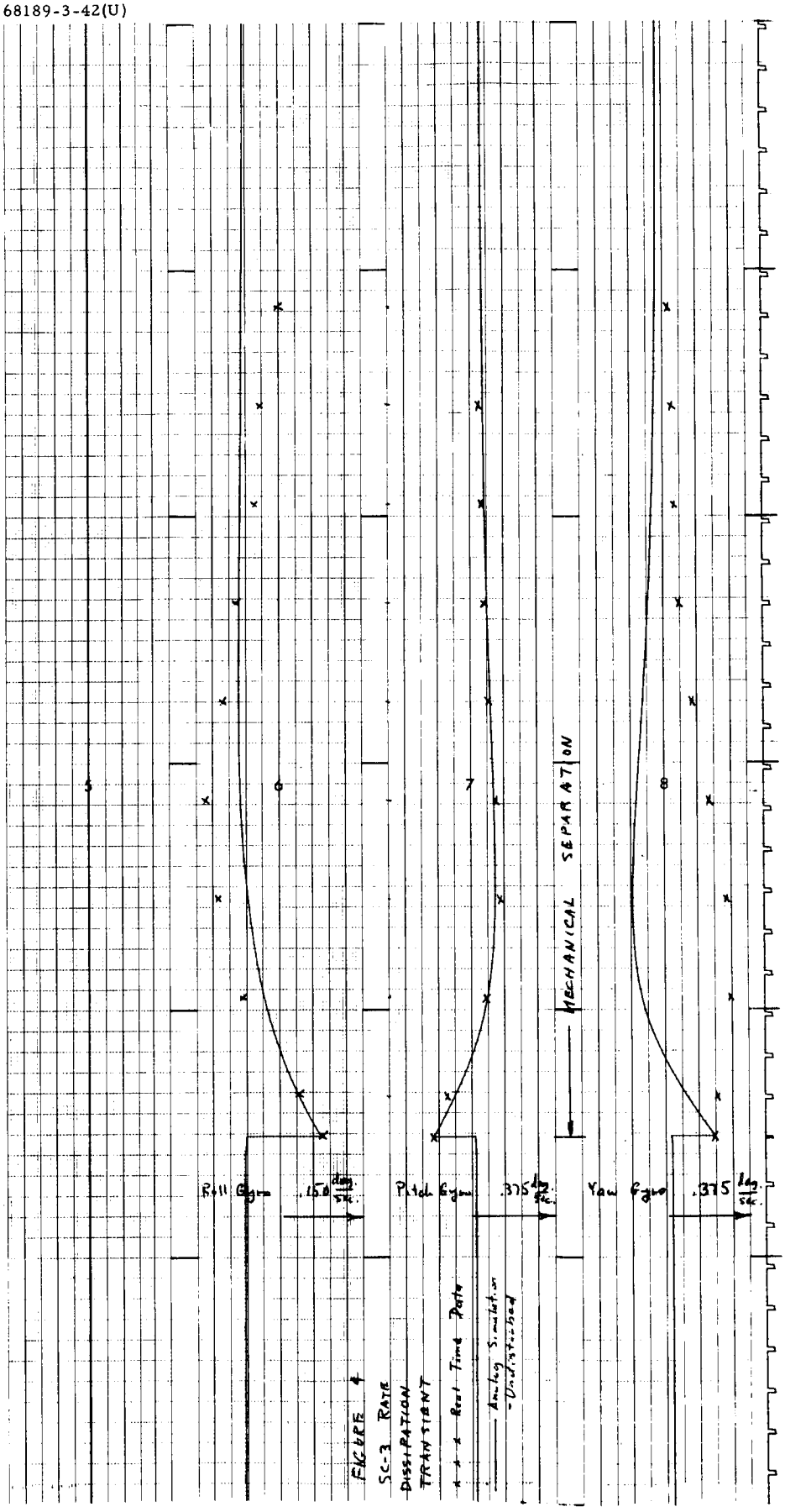

a) Without Induced Disturbance

Figure 5.5-3. Rate Dissipation Transient Simulation

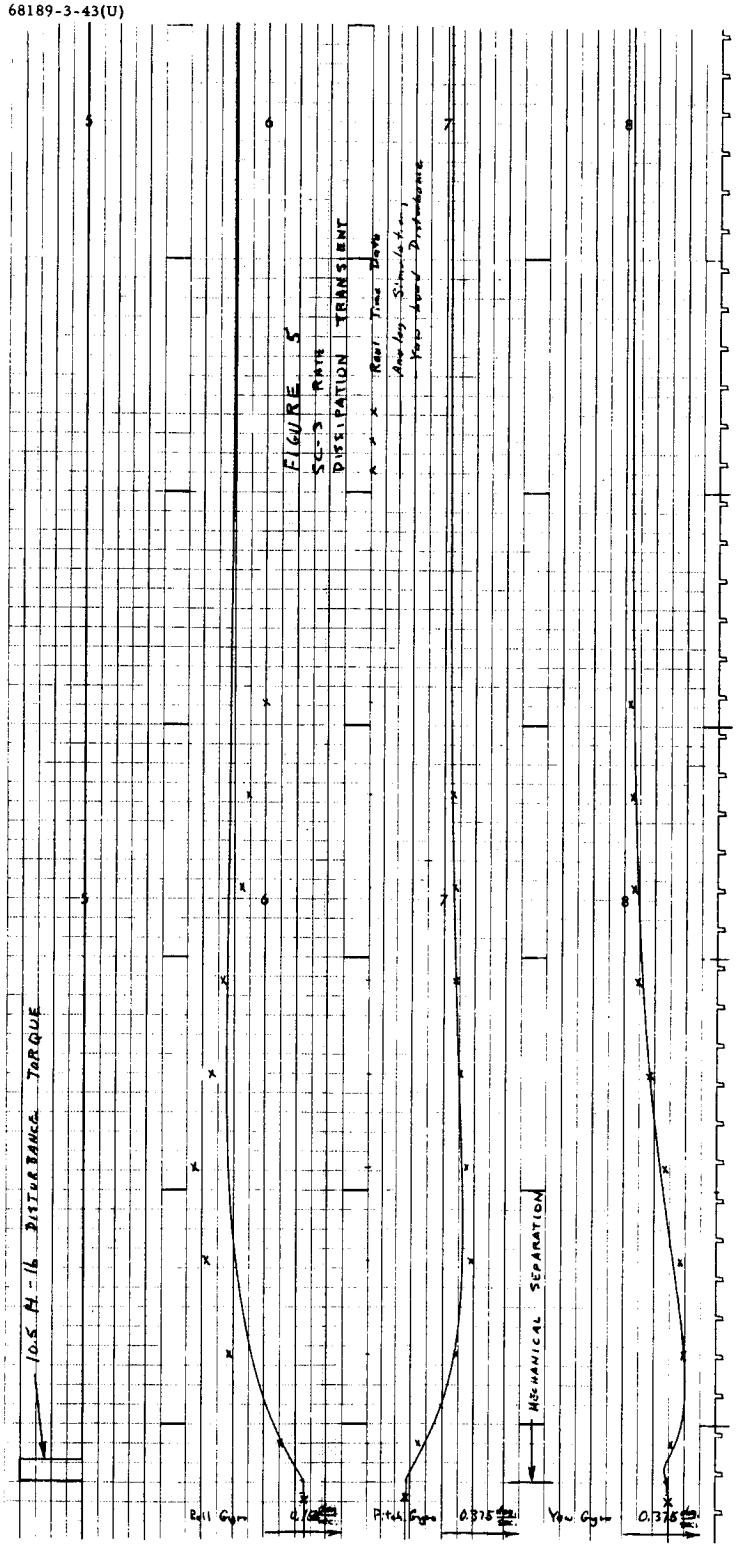

b) With Induced Disturbance

Figure 5.5-3 (continued). Rate Dissipation Transient Simulation

α = angular acceleration of solar panel

ω = angular rate of solar panel stopping

From the conservation of angular momentum

$$M = I\alpha = I\frac{d\omega}{dt}$$

The stepping frequency = 2 cps = F so that $\omega = 2\pi\rho = 12.56$ rad/sec. Assuming that the angular rate, (ω) may be expressed as the sum of an average rate plus a sinusoidal term, and assuming that the instantaneous angular rate never changes sign

$$\omega = \omega_{AV} + \omega_{AV} \sin wt$$

where ω_{AV} = average angular rate. Then

$$M_{max} = I\left(\frac{d\omega}{dt}\right)_{max}$$

$$= I\omega\ \omega_{AV}$$

$$= (1.15 \text{ slug-ft}^2)\ (12.56 \frac{\text{rad}}{\text{sec}})\ (0.25 \frac{\text{deg}}{\text{sec}})$$

$$= 6.32 \times 10^{-2} \text{ ft-lb}$$

This torque represents approximately one-tenth the acceleration capability of the spacecraft about the yaw axis. Thus, if this were the only disturbance at mechanical separation, the control system would have handled it readily and the transient response would have been that of Figure 5.5-3.

All three body rates were reduced to ≤0.1 deg/sec in less than 11 seconds. The total attitude change of the spacecraft from the time of mechanical separation until each body rate was less than 0.1 deg/sec is simply the time integral of the plots in Figure 5.5-2 over the applicable time range. Graphical integration provided the following results:

Roll: +0.90 degrees

Pitch: -0.50 degree

Yaw: -1.30 degrees

The nitrogen usage for rate dissipation is small. A typical rate dissipation transient will require the use of 0.040 pound of nitrogen. Because the measurement uncertainties are large compared to the usage, no quantitative measurement of nitrogen gas consumption during rate dissipation was attempted.

The nitrogen gas pressure telemetry has an estimated accuracy of 2.7 percent. For a full-scale pressure reading of 4960 psi, this represents a pressure uncertainty of (4960 psi) (0.027) = 134 psi.

The nitrogen gas temperature telemetry has an estimated accuracy of ±4°C. For a nominal pressure of 4600 psi and nominal temperature of 70°F, this represents a pressure uncertainty of (4°C) (9°F/6°C) (4600 psi/(460 + 70°F)) = 62.5 psi.

To regard these two pressure uncertainties as 3σ values of independent gaussian random errors results in a combined 3σ measurement error equivalent to $[(134)^2 + (62.5)^2]^{1/2}$ = 146 psi. To assume linearity of pressure with usage and a constant temperature means there is a static net nitrogen weight uncertainty of 146/4960 (4.5 pounds) = 0.13 pound.

5.5.4.3 Sun Acquisition

Fifty-one seconds after electrical separation, sun acquisition is initiated by a command from the flight control programmer which causes a vehicle roll maneuver of -0.5 deg/sec and continues until the sun comes into the acquisition sun sensor field of view which is aligned approximately to the spacecraft roll-pitch plane. When this occurs, the roll command is removed and a plus yaw maneuver is initiated to point the primary sun sensor line of sight toward the sun. When the sun falls into the primary sun sensor field of view, a lockon signal is generated. This signal switches vehicle attitude control to the primary sun sensor and also serves to indicate (via telemetry) the completion of sun acquisition.

The automatic sun acquisition mode was initiated at 07:40:40.685 GMT as indicated by the countdown of the programmer clock. The estimated magnitude of the roll maneuver based on a constant gyro precession rate of 0.5 deg/sec was 181 degrees, while the yaw maneuver was estimated to be 38.1 degrees based on real time flight data. The primary sun sensor lockon signal was generated at a primary sun sensor pitch error of approximately -1.5 degrees and a yaw error of -13.8 degrees which is within the expected lockon field of view range of the sensor. The sun acquisition phase is depicted in Figure 5.5-4.

Nitrogen Utilization

Following sun acquisition, the remaining nitrogen was estimated at 4.49 pounds, indicating that 0.11 pound was consumed during the separation rate dissipation and sun acquisition maneuvers. This is quite close to the expected nominal value of 0.094 pound.

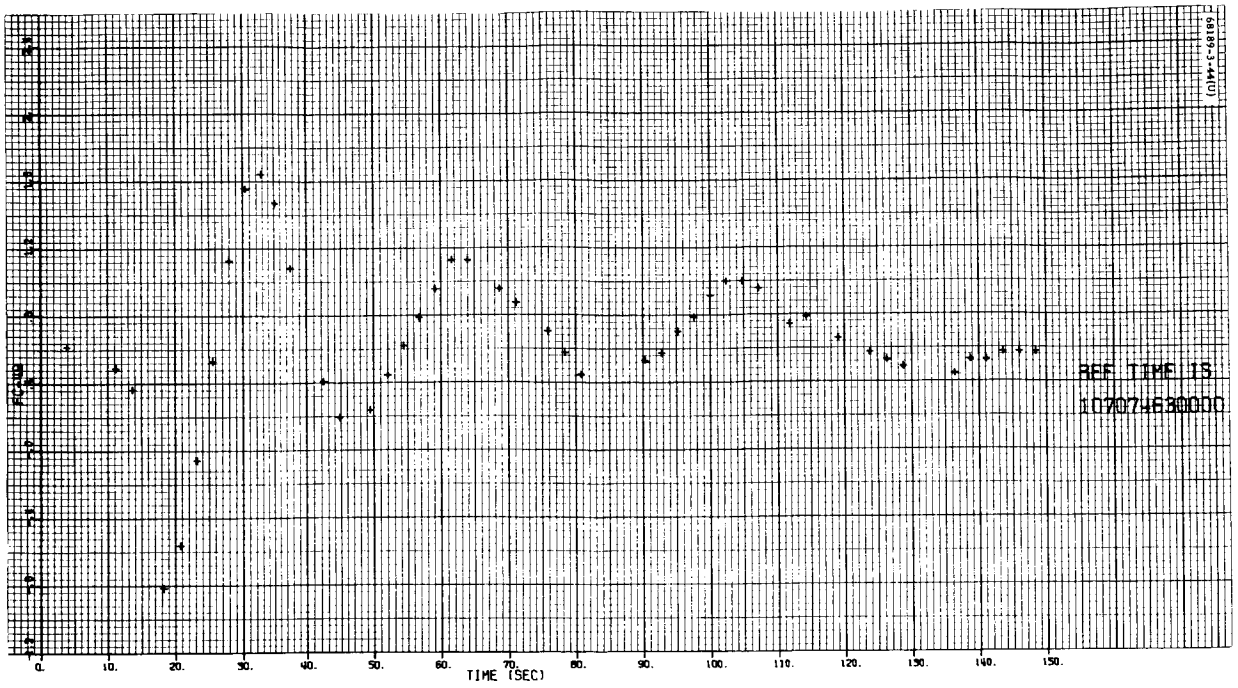

a) Roll Precession Command

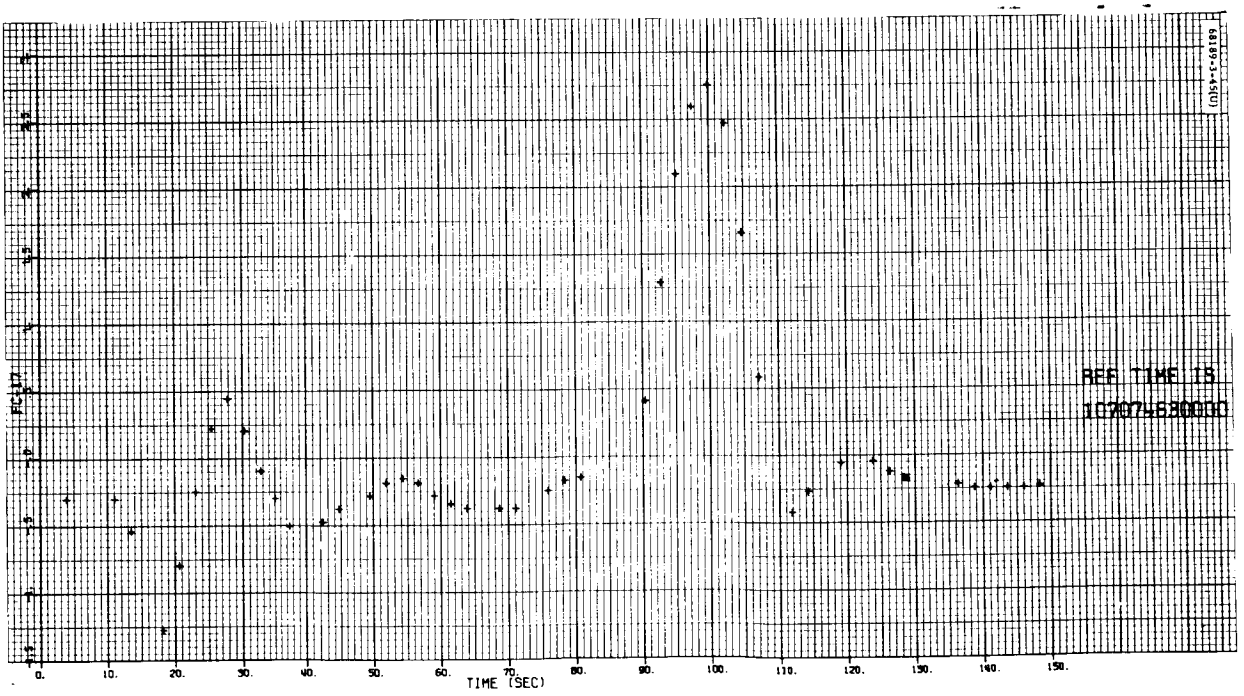

b) Yaw Gyro Error

Figure 5.5-4. Sun Acquisition Phase

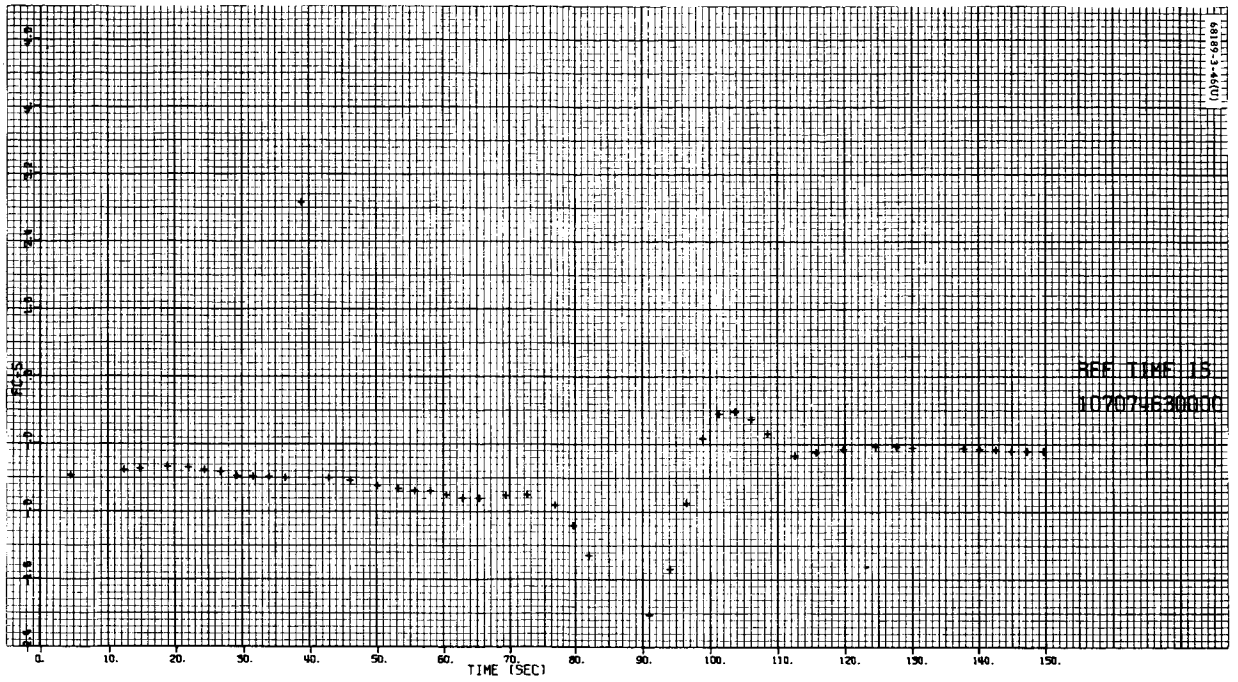

c) Primary Sun Sensor Pitch Error

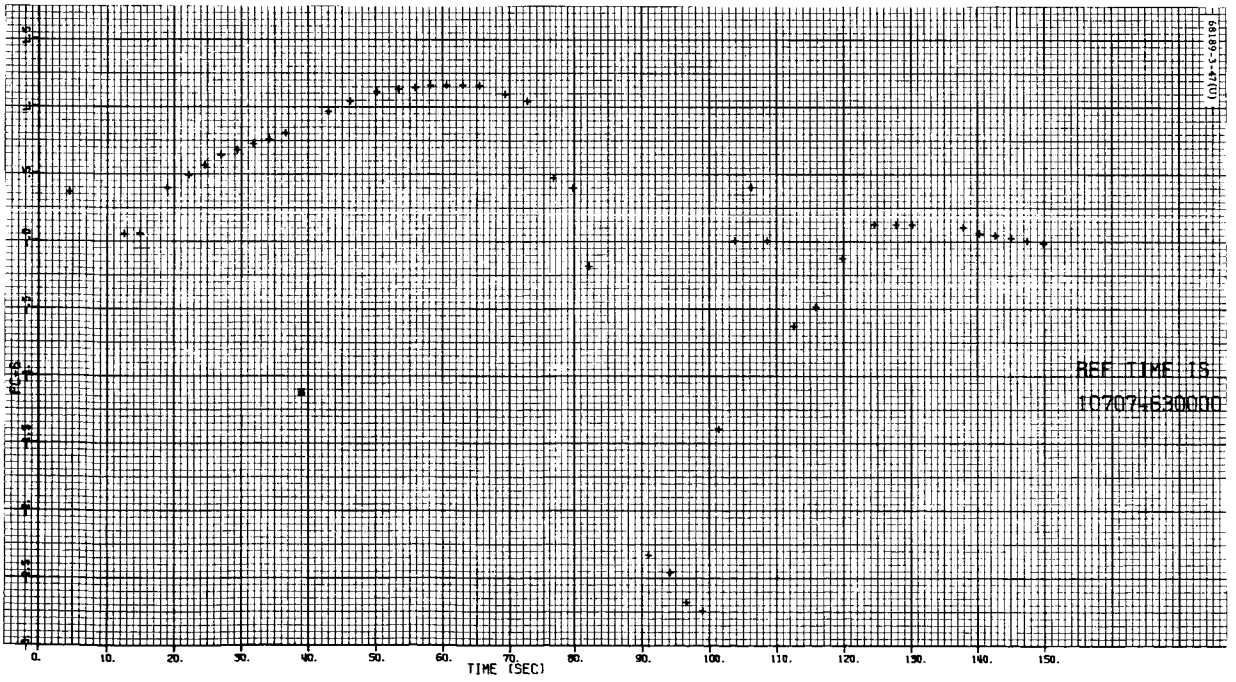

d) Primary Sun Sensor Yaw Error

Figure 5.5-4 (continued). Sun Acquisition Phase

5.5.4.4 Canopus (Star) Acquisition

As defined in Reference 2 (Specification 224510, Revision E) paragraph 3.4.2:

> ". . . the spacecraft is commanded to roll up to 720 degrees in one continuous roll. During this roll, the unthresholded star intensity signal, as well as the normal thresholded signal, is monitored. From these signals, a star map is made and Canopus identified. The capability for performing at least four of these verifications shall be provided. This verification shall be performed before the normal star acquisition mode is initiated. The star acquisition command starts a vehicle positive roll of 0.5 deg/sec until a star of the correct brightness falls into the sensor field of view. When this occurs, a lockon signal is generated which stops the 0.5 deg/sec roll rate and switches the vehicles roll control to the star sensor error signal."

During Mission C, the spacecraft was commanded to roll at +0.5 deg/sec at 107:16:09:12.2 GMT. Telemetered confirmation occurred at the received time of 107:16:09:12.7, corresponding to L+9:04:11.6. During the ensuing roll, a star map was generated by recording the analog signals star intensity (FC-14) (i.e., unthresholded star intensity) and star angle or roll error (FC-12) (i.e., thresholded star intensity) on a strip chart recorder. From this map, Canopus was positively identified (based on identifying the angular spacing of Canopus plus six other objects) during the first 360 degrees of roll. While the spacecraft was still rolling, it was decided to continue the roll and acquire Canopus when the star entered the field of view during the second revolution, i.e., beyond 360 degrees. It had been observed during the first roll revolution that the Canopus lockon signal was present when Canopus was in the field of view. Therefore, it was possible to effect the acquisition of Canopus by employing the single sun and star command. The spacecraft was commanded to the sun and star modes at 107:16:27:35.1, and telemetered confirmation occurred at the received time of 107:16:27:35.8. Canopus lockon, (FC-13) telemetry was received at 107:16:27:50.8, after which it required approximately 56 seconds for both the star intensity and roll error signals to stabilize to their deadband limits.

Star Map

At this point in time the spacecraft, moon, sun, and earth relationships in the ecliptic plane are as shown in Figure 5.5-5a. The center of the moon would pass approximately 4.0 degrees outside the field of view in a minus yaw direction, and the center of the earth would pass approximately 13.5 degrees outside the field of view in a minus yaw direction. As shown in Figure 5.5-5a, the spacecraft is behind the moon and earth and would therefore "see" less than a half-moon and a half-earth. Figure 5.5-5b depicts the relationship of the sensor field of view and the earth as the spacecraft's -X axis points toward the earth during spacecraft roll.

Since large area bright objects within approximately 35 degrees of the sensor's line of sight will reflect light into the sensor from baffles in the sensor's light shield, it was expected that some star intensity signal would result when the sensor was rolling past both the moon and the earth. In addition, 26 stars, plus the planet Jupiter, with intensities greater than 0.37×10^{-14} w/cm^2 come within the Canopus sensor's field of view during a complete roll revolution. However, based on laboratory measurements of star intensity signals versus star intensity on this particular sensor (S/N 12), it was predicted that only four to six stars, plus Jupiter, would be observed.

Figure 5.5-5c depicts the calculated angular (roll angle) spacing of the moon, earth, Jupiter, Canopus, and the other three stars actually observed looking towards the sun.

FC-12, FC-13, and FC-14 signals were sampled by telemetry once every 0.3 second, equivalent to +0.15 degree of roll at the mapping roll rate of +0.5 deg/sec.

Figure 5.5-6 depicts analog traces of primary sun sensor pitch angular error (FC-5), primary sun sensor yaw angular error (FC-6), roll precession command (i.e., roll gyro error (FC-49)), star angle, star intensity, digital word 1, digital word 2, and digital word 3 from the start of roll through Canopus acquisition. The traces of star angle and star intensity which comprise what is referred to as the "star map" indicate five clearly distinguishable star-type objects, plus a 23-degree-wide, low-intensity signal and a 44-degree-wide, high-intensity signal. The angular spacing of these signals was compared with the previously calculated object angles as shown in Figure 5.5-5c, thus permitting positive identification of Canopus, Jupiter, Procyon, Adhara, and Altair, plus the moon and earth.

Table 5.5-4 indicates the responses received versus predicted responses. Roll angle is measured to the nearest 0.15 degree based on peak star intensity amplitudes as digitally recorded at the Madrid (DSS-61) site.

Two objects appeared in the field of view during the first roll (at 68 and 172 degrees) but did not reappear during the second roll past the same angles. Both the star angle and star intensity telemetry signals for these objects looked like single point responses with brightness levels of approximately 75 percent Canopus. It is concluded that these objects were particles dislodged from the spacecraft at the start of the roll maneuver and were traveling outward from the spacecraft with a velocity component normal to the X-Y plane sufficient to carry them out of the sensor's field of view during the 12 minutes required to roll 360 degrees.

As noted in Table 5.5-4, the correlation between postflight and preflight calculated angles from Canopus of Jupiter, Procyon, Adhara, and Altair ranges from +0.1 to -1.3 degrees, with the larger differences occurring at the larger calculated roll angles. Since roll angles are calculated on the basis of a roll rate of exactly +0.5000 deg/sec, it appears that the spacecraft

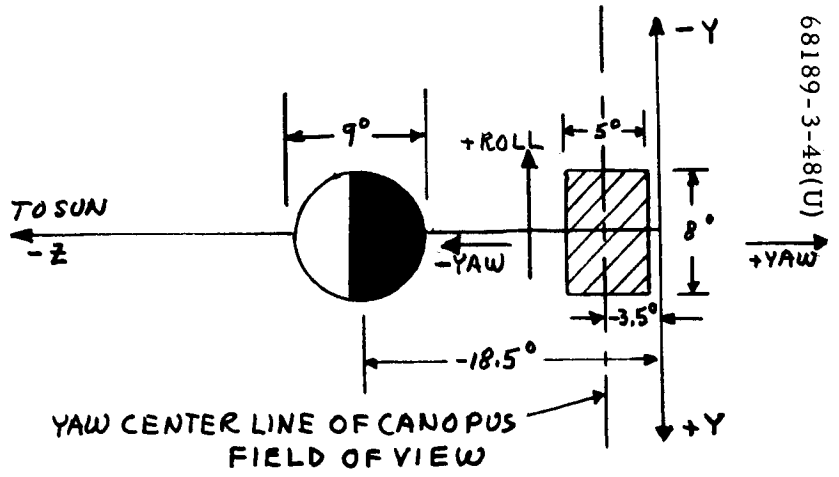

Figure 5.5-5a. Canopus Line-of-Sight Orientation to X-Y Plan

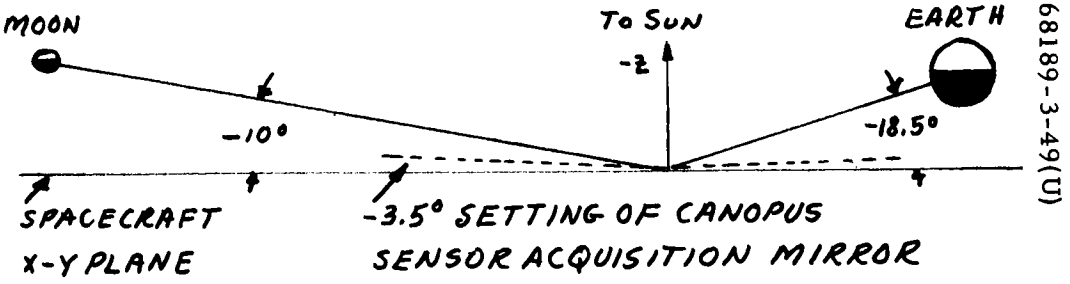

Figure 5.5-5b. Canopus Field of View Versus Earth Relative Position

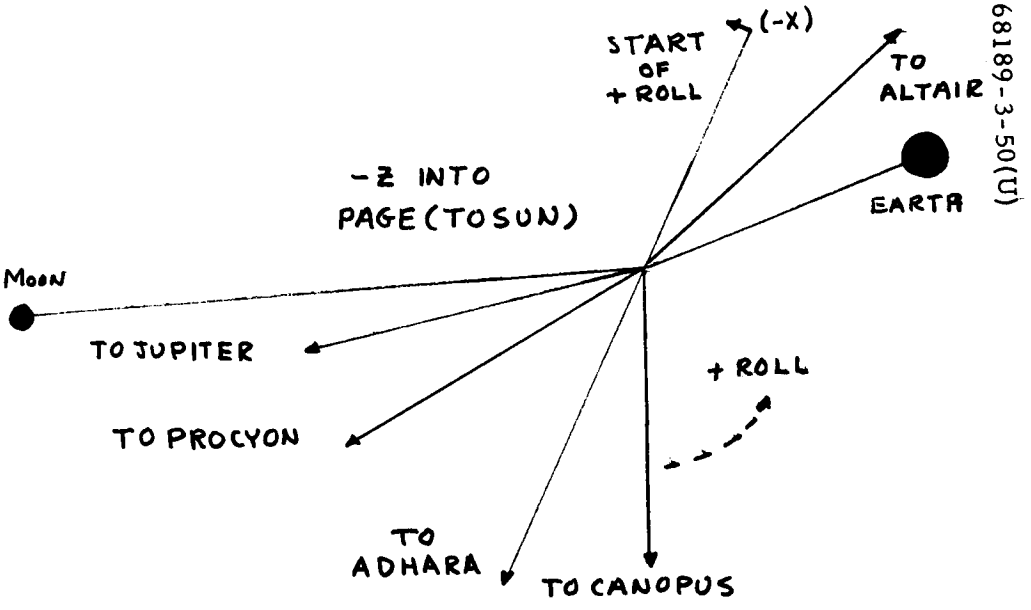

Figure 5.5-5c. Angular Spacing (in Roll) of Observed Objects

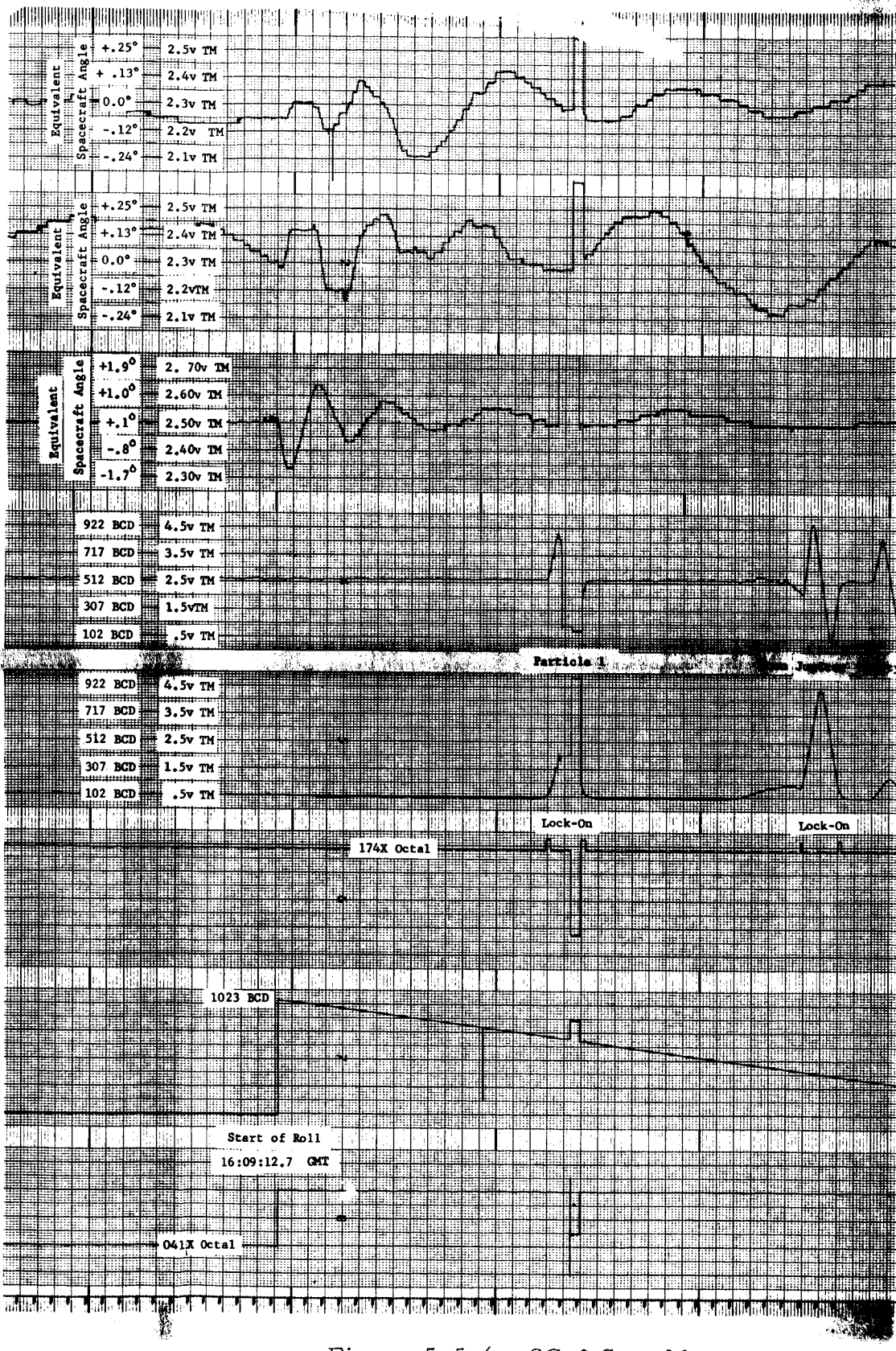

Figure 5.5-6. SC-3 Star Map

FOLDOUT FRAME 1

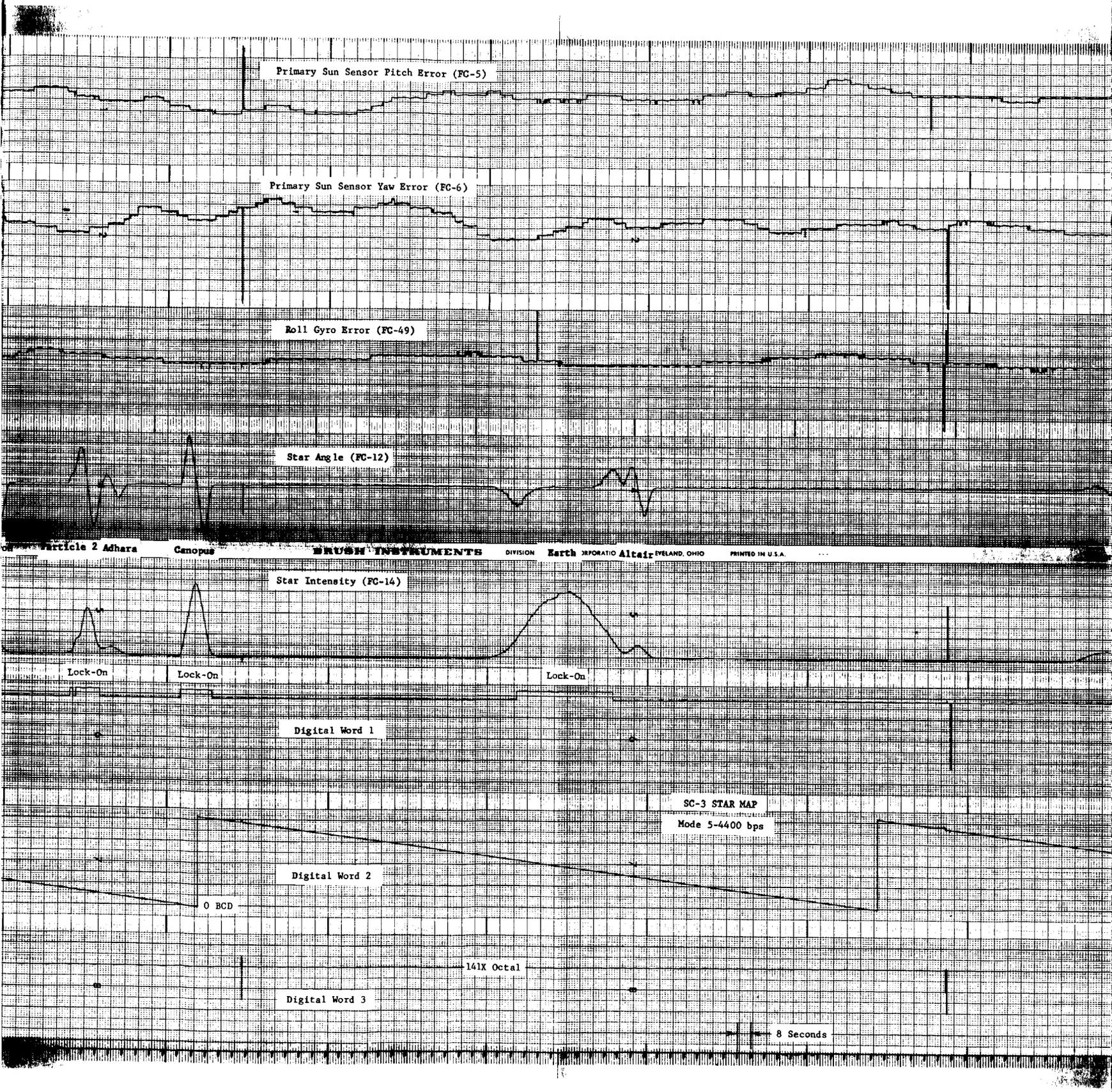

Particle 2 Adhara Canopus BRUSH INSTRUMENTS DIVISION Earth CORPORATIO Altair EVELAND, OHIO PRINTED IN U.S.A.

FOLDOUT FRAME 2

FOLDOUT FRAME

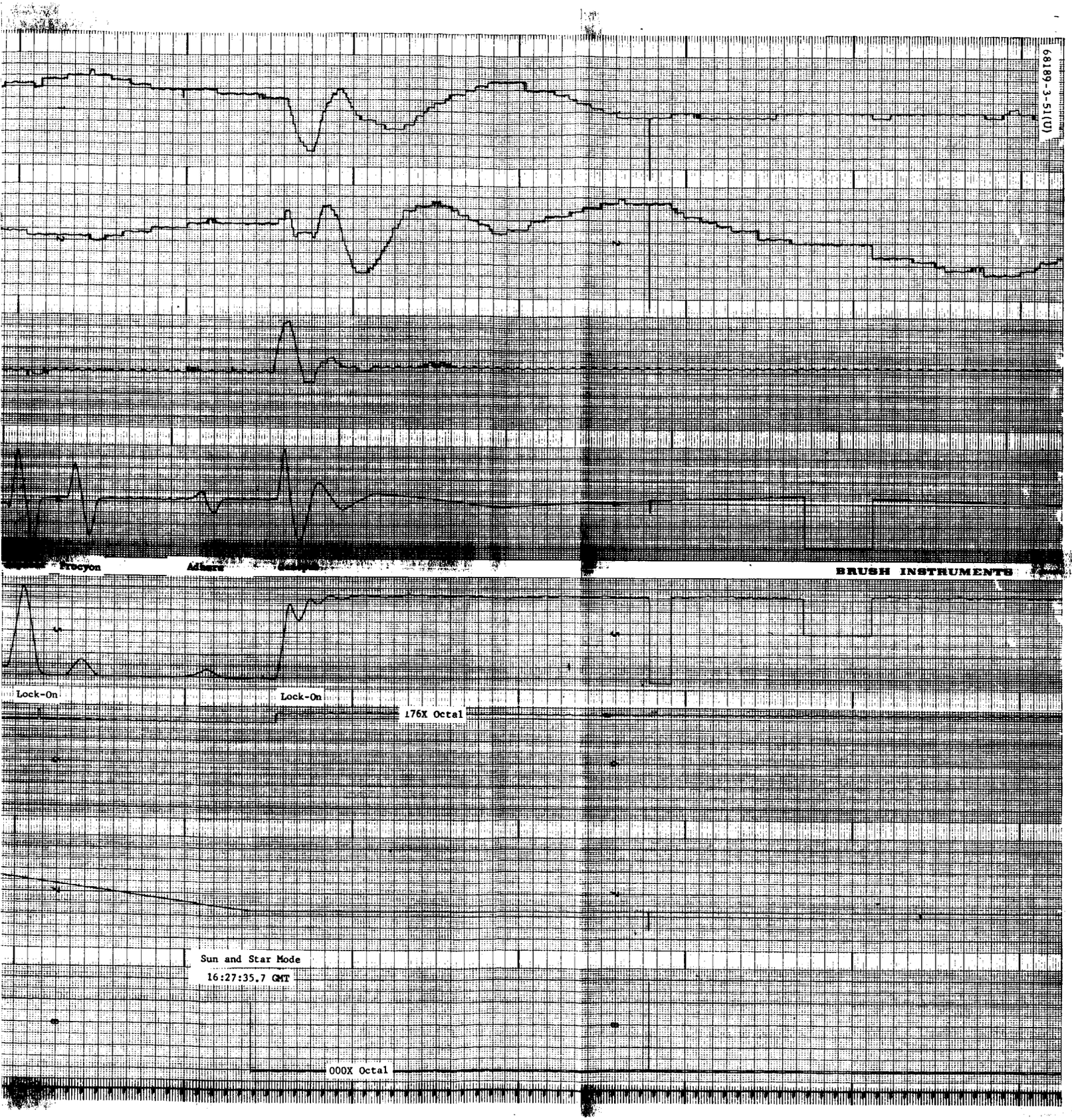

FOLDOUT FRAME 3

FOLDOUT FRAME 4

TABLE 5.5-4. STAR MAP RECEIVED VERSUS PREDICTED RESPONSES

GMT, hr:min:sec	Postflight Calculated Roll Angle, degrees = Δ time × 0.5 deg/sec	Object	Postflight Calculated Angle From Canopus, degrees	Preflight Calculated Angle From Canopus, degrees	Measured Peak Intensity During Roll, telemetry volts, FC-14	Predicted Peak Intensity During Roll, telemetry volts	Measured Peak Intensity at 0 Roll Rate, telemetry volts, FC-14	Predicted Peak Intensity at 0 Roll Rate, telemetry volts	Occurrence of Canopus Lockon, FC-13, Digital Word 1
16:09:12.7	0	(Start of roll)	-204.4	–	–	–	–	–	
16:13:13.9	120.6	Moon	-83.8	-86	0.957	–	–	–	No
16:13:28.3	127.8	Jupiter	-76.6	-76.7	4.414	4.62	–	–	Pulse when leaving field of view
16:14:01.2	144.2	Procyon	-60.2	-60.1	1.226	0.92	–	–	No
16:15:11.8	179.5	Adhara	-24.9	-24.6	0.830	0.63	–	–	No
16:16:01.6	204.4	Canopus	–	–	3.804	3.24	–	–	Yes
16:19:46.4	316.8	Earth	112.4	+111.5	3.530	–	–	–	Yes
16:20:27.2	337.2	Altair	132.8	+133.2	1.069	0.79	–	–	No
16:25:09.0	478.1	Moon	273.7	274	0.933	–	–	–	No
16:25:26.8	487.0	Jupiter	282.6	283.3	4.439	4.62	–	–	Pulse when leaving field of view
16:25:59.6	503.4	Procyon	299.0	299.9	1.211	0.92	–	–	No
16:27:09.7	538.5	Adhara	334.1	335.4	0.820	0.63	–	–	No
		Canopus	–	–	–	–	4.111	3.50	Yes
		No star	–	–	0.450	–	0.504	0.42	No

was rolling faster than +0.5000 deg/sec, which would result in shorter times between stars and, therefore, smaller calculated angles. The correlation on moon and earth angles ranges from +2.2 to -0.3 and, is attributed to the analyst's inability to accurately determine the exact center of broad, slowly varying signals.

The mean roll rate as determined from the incremental time when Jupiter was at the center of the field of view is 360/(16:25:26.8 - 16:13:28.3) = 360/11:58.5 = 0.5010 deg/sec. The mean roll rates, as determined from Procyon and Adhara incremental times of 11:58.4 and 11:57.9, are 0.5011 and 0.5015. Since Adhara is the weakest star observed, the incremental time between field of view crossings is less accurate. Therefore, less weighting is placed on the Adhara calculation of mean roll rate. The weighted mean roll rate of the spacecraft is therefore taken as 0.5011 deg/sec, which is 0.22 percent faster than 0.5 deg/sec. The error due to sampling time is 0.3/720 = 0.004 percent.

Using a roll rate of 0.5011 deg/sec to calculate postflight roll angles would result in the following:

Jupiter 128.1 and 488.1 degrees

Procyon 144.5 and 504.5 degrees

Adhara 179.9 and 539.7 degrees

The corresponding postflight calculated angles from Canopus would be as follows:

Jupiter -76.7 and 283.3 degrees

Procyon -60.3 and 299.7 degrees

Adhara -24.9 and 334.9 degrees

Correlation between postflight and preflight calculated angles from Canopus would be as follows:

Jupiter 0 and 0

Procyon -0.2 and -0.2

Adhara -0.3 and -0.5

Star Sensor Performance

The star sensor provides three outputs: star angle or roll error, Canopus lockon, and star intensity. A comparison of inflight and preflight measurements is used to determine how well the sensor performed in flight.

The star angle signal is designed to increase from a quiescent level, close to 512 BCD when no star is in the field of view, to a maximum, close to 1023 BCD, when Canopus is approximately +2 degrees from the X-Z plane. It returns to its quiescent level when Canopus is in the X-Z plane, then to a minimum, close to 0 BCD when Canopus is approximately -2 degrees from the X-Z plane, and finally decreases to its quiescent level as Canopus leaves the field of view.

The star intensity (FC-14) signal is designed to increase from a quiescent level when no star is in the field of view to a maximum when Canopus is in the X-Z plane. It then decreases to its quiescent level as Canopus leaves the field of view. No star and maximum intensity values are listed in Table 5.5-4.

Figure 5.5-6 depicts the star angle and star intensity signals for all stars observed during the star map. Figure 5.5-7 depicts an enlarged view of these signals during the time Canopus was in the field of view in the first revolution. From these figures, it can be seen that the star angle and star intensity signals perform as designed.

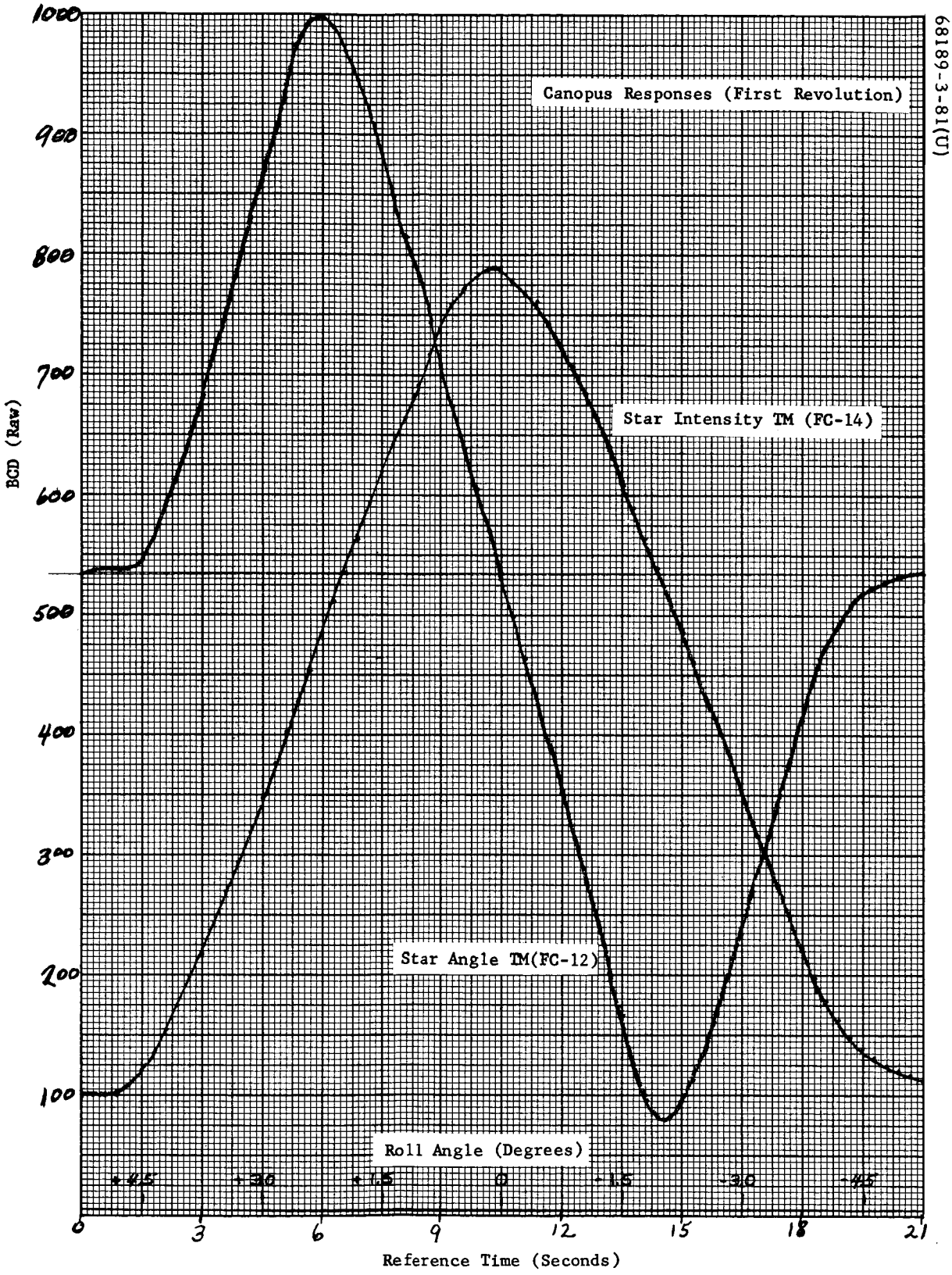

Figure 5.5-7. Canopus Responses (First Revolution)

Since the star intensity signal is a measure of the effective gain of the star sensor, the measurements as recorded in Table 5.5-4 are analyzed to determine effective gain. Star sensor gain is a function of the photomultiplier tube scale factor which is controlled by the intensity of the sunlight actually reaching the tubes through a sun filter in the sun channel optics. All preflight star sensor measurements are made with a unit sun intensity illuminating the sun channel. For flight, a flight filter is installed with a transmission factor that will admit more, equal, or less than a unit sun into the sensor. Mission A was flown with a sun filter calculated to increase the sensor gain so that Canopus would respond as 1.5 X Canopus. Analysis of inflight measurements indicated the effective gain was even greater than 1.5 X Canopus. Mission B was flown with a 1.17 X Canopus sun filter, and analysis of inflight measurements indicated the effective gain was still greater than 1.5 X Canopus, or 28 percent larger than expected.

Based on Missions A and B, it was decided to install a 0.8 X Canopus sun filter for Mission C which should result in an effective gain of 0.8 X 1.28, or 1.02 X Canopus. The actual observed peak intensity of Canopus, in a low roll rate condition after acquisition, is 4.111 volts compared to the preflight 1.0 X Canopus measurement of 3.50 volts (see Table 5.5-4). The 3.50-volt value is the weighted mean of nine intensity measurements ranging from 3.37 to 3.99 volts. Using these values, the effective gain of the sensor has a range of 1.22 to 1.03, with a weighted mean of 1.17 X Canopus versus a prediction of 1.02 X Canopus. The difference of 15 percent is attributed primarily to this amount of inaccuracy inherent in the preflight intensity measurements.

The third sensor output, Canopus lockon, is shown in Figure 5.5-6 as part of digital word 1 and is listed in Table 5.5-4. Since the Jupiter intensity signal sweeps through the Canopus lockon triggering levels of 0.67 and 1.5 X Canopus very rapidly as Jupiter enters and leaves the field of view, it is expected that a short lockon signal might appear, as it indeed did. Since the earth's intensity signal is between the lockon triggering levels, the lockon signal is present for an extended period. Based on these observations, it can be seen that the Canopus lockon signal performed as desired.

Canopus Acquisition Sequence

Since Canopus was identified during the first revolution and Canopus lockon was present when Canopus was in the field of view, it was decided to send the sun and star command after the earth had sufficiently cleared the field of view. The automatic acquisition sequence could then occur.

Figure 5.5-8 depicts the response of the star intensity, star angle, and roll error, signals after Canopus lockon has put the spacecraft in a closed-loop roll error controlled mode. When lockon occurs, the spacecraft is rolling at +0.5 deg/sec, and the roll error signal is increasing to a maximum which commands the spacecraft to roll positive to obtain a nulled roll error signal. Thus, the positive command causes the plus roll rate to increase until the roll error signal crosses its null position into the lower

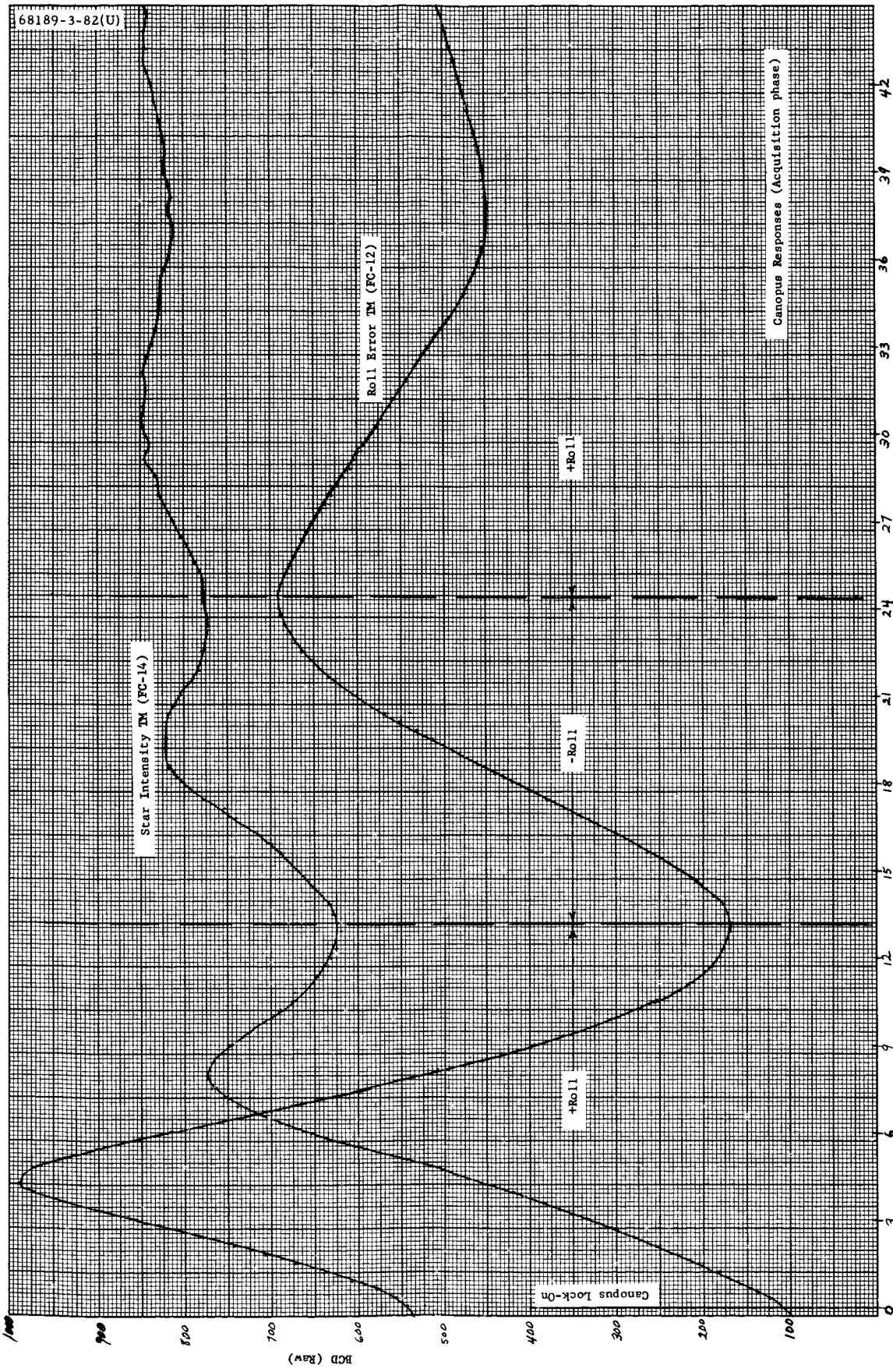

Figure 5.5-8. Canopus Responses (Acquisition Phase)

area, at which time it commands the spacecraft to roll negative. This negative roll command slows the roll rate to zero and reverses the roll direction such that the roll error again crosses its null position into the upper area which commands the spacecraft to roll positive. After several such cycles, the spacecraft settles down to a slow roll oscillation which causes the roll error signal to oscillate above and below its null position. This oscillation is bounded, and the bounds are referred to as the roll optical limit cycle.

As noted in Figure 5.5-8, the star intensity peak value increases as the roll rate decreases. This is the normal response of a signal having a time constant in the vicinity of 1 second.

Conclusions

The Canopus sensor performed as designed without malfunction. The star intensity signal, with Canopus in the field of view, was higher than the nominal predicted, but within the accuracy of the preflight measurements. The automatic star acquisition capability was successfully utilized.

5.5.4.5 Coast Phase Attitude Control

Limit Cycle Performance

The gas jet attitude control system is designed to cause the spacecraft to limit cycle about all three axes in the process of maintaining optical or inertial references during the nonacceleration portions of the mission.

Pulsing Rate

Based on analyses of 19.7 hours of data, the mean time between gas jet pulses for both the optical and inertial mode limit cycle performance was 68.5 sec/pulse. The predicted performance (Reference 3) with low optical sensor noise was 117 sec/pulse. The difference can be accounted for in part by the following:

1) The prediction was based on a gas jet thrust level of 0.057 pound. Gas jet thrust for full-flow conditions was determined to be 0.066 pound. This would lower the prediction by (0.066 - 0.057/ 0.066) 100 percent = 13.7 percent.

2) The average pulsed thrust was greater than the thrust under full-flow conditions. This is caused by pressure buildup in the fuel lines between the regulator and the gas jets. As the regulator leaks, a pressure buildup occurs whose effect is to increase thrust when a jet fires. The nominal pressure is 42 psi and, depending upon the time history of gas jet firings, it could rise as high as 50 psi. This further lowers the predicted mean time between gas jet pulses by somewhere between zero and ((50 - 42)/ 50) 100 percent = 16 percent.

3) The minimum gas jet impulse bit was originally assumed to be nominally 30 milliseconds, which is the gas jet amplifier minimum impulse. In fact, the gas jet minimum on-time is approximately 44 milliseconds, as shown below.

This effective increase in the minimum impulse bit would lower the predicted mean time between gas jet pulses by (44 milliseconds - 30 milliseconds/ 44 milliseconds)(100 percent) = 35 percent.

Double Pulsing

Double pulsing accounted for approximately 16 percent of the gas jet firings and occurred almost entirely in the roll channel. It is thought that the increased thrust and increased pulse bit discussed above are the reasons a double-pulse mode is created. That it is able to be sustained for several cycles in the roll channel is probably characteristic of the symmetry of the roll limit cycle, i.e., an existing limit cycle period and waveform about the roll axis tends to perpetuate itself.

Soft-limit Cycle Operation

Because of its symmetrical configuration, the spacecraft is not readily susceptible to space environment disturbance torques and was predicted to have a hard-limit cycle. Surveyor III exhibited a few instances of soft-limit cycle operation, mainly about the roll axis. This phenomena is most likely caused by gas jet leakage and exhibits itself in the roll channel because it is the roll limit cycle which has (on the average) the longest time between gas jet pulses.

It is of interest to compare the angular velocity change caused by a gas jet pulse with the initial angular velocity which will cause the vehicle to just barely reach the opposite side of its deadband when opposed by a leakage disturbance torque:

$$\Delta\omega p \text{ (single pulse)} = \frac{(6.6 \times 10^{-2} \text{ pound})(6.47 \text{ feet})(44 \times 10^{-3} \text{ second})(57.3 \frac{\text{deg}}{\text{rad}})}{2.24 \times 10^{2} \text{ slug-ft}^2}$$

$$= 4.81 \times 10^{-3} \frac{\text{deg}}{\text{sec}}$$

$$\Delta\omega_L \text{ (from leakage disturbance torque)} = \alpha t_1 \qquad (1)$$

where

α = acceleration (caused by leakage).

t_1 = elapsed time until $\omega = 0$.

$$\text{Deadspace} = D = \Delta\omega t_1 - \frac{1}{2}\alpha t_1^2 \qquad (2)$$

Solving for t_1 from Equation 1 and substituting in Equation 2 gives

$$\Delta\omega_L = [2\,\alpha\,D]^{1/2}$$

The maximum allowable gas jet leakage is 20 cc/hr, which corresponds to a thrust of 1.04×10^{-6} pound.

So

$$\Delta\omega_L = [(2)\,(\alpha)\,(0.5 \text{ degree})]^{1/2}$$

$$= \left[(2)\left(\frac{T_L\, r}{I_z}\right)(0.5 \text{ degree})\right]^{1/2}$$

$$= \left[(2)\,\frac{(1.04 \times 10^{-6} \text{ pound})\,(6.47 \text{ feet})}{224 \text{ slug-ft}^2}\,(0.5 \text{ degree})\right]^{1/2}$$

$$= 1.31 \times 10^{-3} \text{ deg/sec}$$

Regarding $\omega_p = 4.81 \times 10^{-3}$ deg/sec as the maximum angular velocity with which a limit cycle boundary may be left and assuming that the probability distribution of all such velocities is uniform, a roll gas jet leakage (within specification) could result in soft-limit cycles as much as $((1.31 \times 10^{-3})/(4.81 \times 10^{-3}))\,(100 \text{ percent}) = 27$ percent of the time.

It was concluded that:

1) 68.5 sec/pulse is a typical limit cycle pulsing rate. Similar performance is anticipated on all future missions.

2) Double-pulsing and soft-limit cycles are probable occurrences considering actual hardware characteristics.

Gas Jet Thrust Level

Reference 4 developed the following expression for the gas jet thrust level:

$$\text{thrust} = T = \frac{I_z \dot{\varphi}_c}{T t_p}$$

where

I_z = roll inertia - 224 slug-ft^2

$\dot{\varphi}_c$ = commanded precession rate = 0.5 deg/sec

R = gas jet moment arm = 6.47 feet

t_p = thrusting time of the gas jet from initiation of precession command to point at which $\dot{\varphi}_{gyro} = 0$

This equation, a coast phase analog simulation, and SC-3 test data were used to determine the thrust level. A quasi-independent check of this number was performed by matching mission data to a roll transient simulated on the analog mechanization.

The above equation has an uncertainty associated with the thrusting time (t_p). The gas jet does not operate continuously from initiation of the precession command signal until the error signal peaks ($\dot{\varphi}_{gyro} = 0$) for the following reasons:

1) The gas jet will not be turned on until the error signal exceeds the deadspace.

2) The derived-rate network around each amplifier develops a feedback signal whose polarity is such as to turn off the gas jet amplifier and whose effect is to cause the amplifier to pulse on and off.

3) There is an electronic saturation between the gyro and gas jet amplifier which limits the error signal into the gas jet amplifier.

Section 1.14 of Reference 5 records the following data with respect to the roll inertial channel:

Total dead space = 0.44 degree (+0.22 degree)

K_e (derived-rate gain) = 9.1

These parameters, the predicted electronic saturation level, and thrust (0.066 pound) were incorporated into the simulation described in Reference 6. The response of this simulation to a 0.5 deg/sec precession command is shown in Figure 5.5-9.

The time from command initiation until $\dot{\varphi}_{gyro} = 0$ on this mechanization was 5.89 seconds. The No. 1 gas jet amplifier is off 1.32 seconds of this time (see Figure 5.5-9). So t_p = 5.89 seconds - 1.32 seconds = 4.57 seconds.

68189-3-83(U)

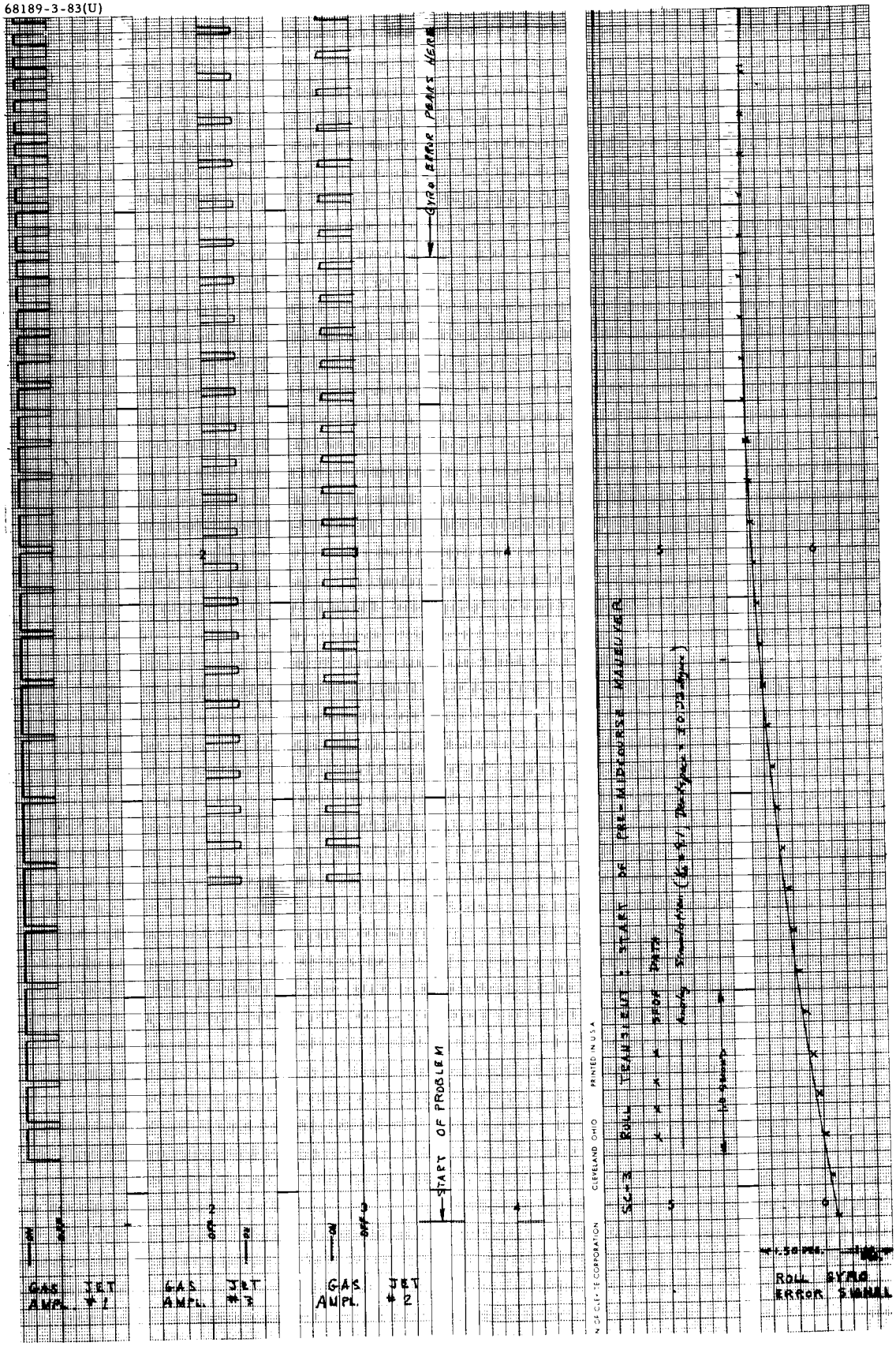

Figure 5.5-9. Gas Jet Thrust Level Determination of firing time

$$\text{thrust} = \frac{I_z \dot{\varphi}_c}{R t_p} = \frac{(224 \text{ slug-ft}^2)(0.5 \text{ deg/sec})}{(6.47 \text{ feet})(4.57 \text{ second})} = 0.066 \text{ pound}$$

The thrust level in the analog mechanization was actually iterated several times until the flightdata werematched and the thrust equation was satisfied. A cross-plot of flight data on the analog trace is also shown in Figure 5.5-9.

The results of the SC-3 gas jet thrust level investigation can be summarized as follows: The thrust for the gas jet pair No. 2 on SC-3 was 0.066 pound for full-flow conditions. The ±4 percent error associated with this thrust measurement scheme in Reference 4 is valid.

Section 13 of Reference 5 shows that the thrust levels for all six jets during test were within 3.5 percent of each other. On this basis, it can be assumed that the nominal thrust level for the six gas jets was 0.066 pound.

It is recommended that the above gas jet thrust level be modified when investigating limit cycle performance to account for the difference in regulator performance between full-flow and pulsed operation.

Nitrogen Consumption

Nitrogen consumption for the period from launch to preretro maneuvers was 0.80 pound. This number compares favorably with predicted usage when measurement uncertainties and postgyro drift lockon transients are taken into account. Mission nitrogen usage was obtained from pressure and temperature information telemetered on flight control signals FC-4 and FC-48.

The predicted nitrogen usage for each maneuver was determined from the simulation defined in Reference 7; a detailed breakdown of the predicted impulse and weight expenditures is documented in Reference 8.

For the number and sequence of Mission C maneuvers, Attachment 1 of Reference 8 yields the following nominal impulse consumption budget:

	lb-sec
Vernier phase of midcourse maneuver	2.00
Limit cycle operation	4.50
Sun acquisition	3.25
Inertial roll maneuvers (2)	3.00
Star verification	1.50
Star acquisition	1.40
Inertial pitch manuevers (2)	5.00
Rate dissipation	2.75
Postmidcourse rate dissipation	1.00
Total =	27.80

Assuming an average I_{sp} of 60 seconds yields a nominal nitrogen usage prior to the preretro maneuvers of approximately 0.46 pound. Reference 8 also predicts a 3 σ usage uncertainty of 0.22 pound for this particular mission profile.

Two items were not considered in formulating the fuel consumption prediction: postgyro drift check lockon transients and increased limit cycle fuel consumption. The increased limit cycle fuel consumption is a direct result of increased limit cycle thrust and increased minimum gas jet pulse width, as discussed previously, and is barely significant as far as fuel consumption weight is concerned. The increase amounts to approximately 0.013 pound. The gyro drift lockon transients are much more significant. Surveyor III had 13 gyro drift checks — 8 three-axis checks and 5 roll-axis-only drift checks. Using the final angular attitude positions of each drift check as initial conditions to the simulation documented in Reference 7 yields the following:

1) The average impulse expenditure for one of the post-three-axis drift transients was 0.70 lb-sec.

2) The average impulse expenditure for one of the post-roll-axis-only drift transients was 0.55 lb-sec.

So there is an increase in the nitrogen consumption prediction of

$$0.013 \text{ pound} + \frac{5(0.55)\text{ lb-sec} + 8(0.90)\text{ lb-sec}}{60 \text{ seconds}} = 0.179 \text{ pound} \cong 0.18 \text{ pound}$$

The net prediction would be

$$(0.46 + 0.18) \pm 0.22 = 0.64 \text{ pound} \pm 0.22 \text{ pound}$$

The static measurement uncertainty of nitrogen weight of 0.13 pound (discussed in subsection 5.5.4.2) should also be considered.

It was concluded that the measured nitrogen usage of 0.80 pound is within anticipated limits and that postgyro drift lockon transients should be considered in the fuel budget for future flights.

5.5.4.6 Premidcourse Attitude Maneuvers

In order to orient the spacecraft thrust axis properly prior to vernier engine ignition, a positive roll maneuver of 56.7 degrees and a negative pitch maneuver of 39.1 degrees were commanded. Although these were the values entered into the magnitude register, the desired maneuvers per the midcourse and terminal guidance system calculations were 56.7438 degree of roll and 39.1251 degree of pitch.

Several variables affect the accuracy of an angular maneuver: precession rate accuracy, precession command time, gyro drift, and initial attitude errors due to biases and limit cycle. When several maneuvers are performed

with large time intervals between them, attitude errors due to gyro drift must be included. A list of all parameters affecting the midcourse attitude maneuver accuracy is presented in Table 5.5-5 along with their allowable 3σ values and actual performance values wherever possible.

Determination of Precession Times

The register was loaded with 284 bits for roll and 196 bits for pitch. For a clock rate of 2.5 cps, the respective times are 113.4 and 78.2 seconds with a maximum error of 0.20 second ± 0.02 percent.

The telemetered gyro error signal data were used in determining the actual precession time. The sampling rate during the maneuvers was 20 times/sec, giving a resolution of 0.05 second. The results are as follows (Figure 5.5-10):

T = 113.55 seconds, or 56.775 degree of roll

T = 78.43 seconds, or 39.215 degree of pitch

Precession Rates. The accuracy of the precession rates imposed by the "Surveyor System Functional Requirements Specification" is 0.5000 ± 0.0011 deg/sec. The precession rate obtained during the star mapping phase indicated that the positive precession rate was 0.5011 deg/sec.

Attitude Maneuver Error

Reference 9 develops two orthogonal equations that specify the spacecraft thrust axis pointing error during midcourse thrusting. The equations were derived for the roll-pitch rotation sequence which applies here.

Neglecting error sources that are present only after engine ignition results in the following equations:

$$\text{Error about pitch axis} = \theta_{R_E} + \theta_{A_E} \cos \varphi - \psi_{A_E} \sin \varphi$$

$$\text{Error about yaw axis} = (\varphi_{A_E} + \varphi_{E_E}) \sin \theta - \psi_{A_E} \cos \theta \cos \varphi$$

$$- \theta_{A_E} \sin \varphi \cos \theta$$

where

$(\varphi, \theta, \psi)_{A_E}$ = spacecraft inertial reference alignment errors

$(\theta, \varphi)_{R_E}$ = rotation errors

TABLE 5.5-5. PREMIDCOURSE ATTITUDE ERROR SUMMARY

Parameter	3σ Requirement	Reference Number	Measured Value	Comments
Primary sun sensor null with respect to FCSG roll axis	0.2 degree	2 (paragraph 4.3.1.1)	Pitch = +0.013 degree Yaw = +0.13 degree	
Canopus sensor null with respect to FCSG roll/pitch plane	0.2 degree	2 (paragraph 4.3.1.2)	+0.05 degree	
Pitch/yaw limit cycle	0.3 degree	2 (paragraph 4.3.1.1)	+0.08 degree	Based on sun sensor error signals at start of pitch
Roll limit cycle	0.3 degree	2 (paragraph 4.3.1.2)	-0.306 degree	Based on Canopus error signal at start of roll
Gyro torquer scale factor	0.15 percent	12 (paragraph 3.2.5.1.3)	0.2 percent	
Precession current source accuracy	0.13 percent			
Precession current source drift	0.1 percent			
Timing source accuracy	0.2 second ± 0.02 percent		Roll = +0.075 degree Pitch = +0.116 degree	Based on timing errors determined in subsection 5.5.4.6
Gyro alignment to FCSG roll axis	0.14 degree	12 (paragraph 3.2.5.1.4)	Pitch = +0.017 degree Yaw = +0.067 degree	
FCSG/spacecraft roll axis alignment	0.1 degree	2 (paragraph 4.1.3.7.1)		
Gyro non-g sensitive drift	1.0 deg/hr	2 (paragraph 4.3.1.5)	Roll = +0.24 degree Yaw = (-)0.2 degree Pitch = +0.09 degree	Based on measured +1.1 deg/hr in roll for 13 minutes and 12 seconds, -1.2 deg/hr in yaw for 9 minutes and 54 seconds, and +0.6 deg/hr in pitch
Total attitude error prior to ignition			0.184 degree with 0.1-degree uncertainty	

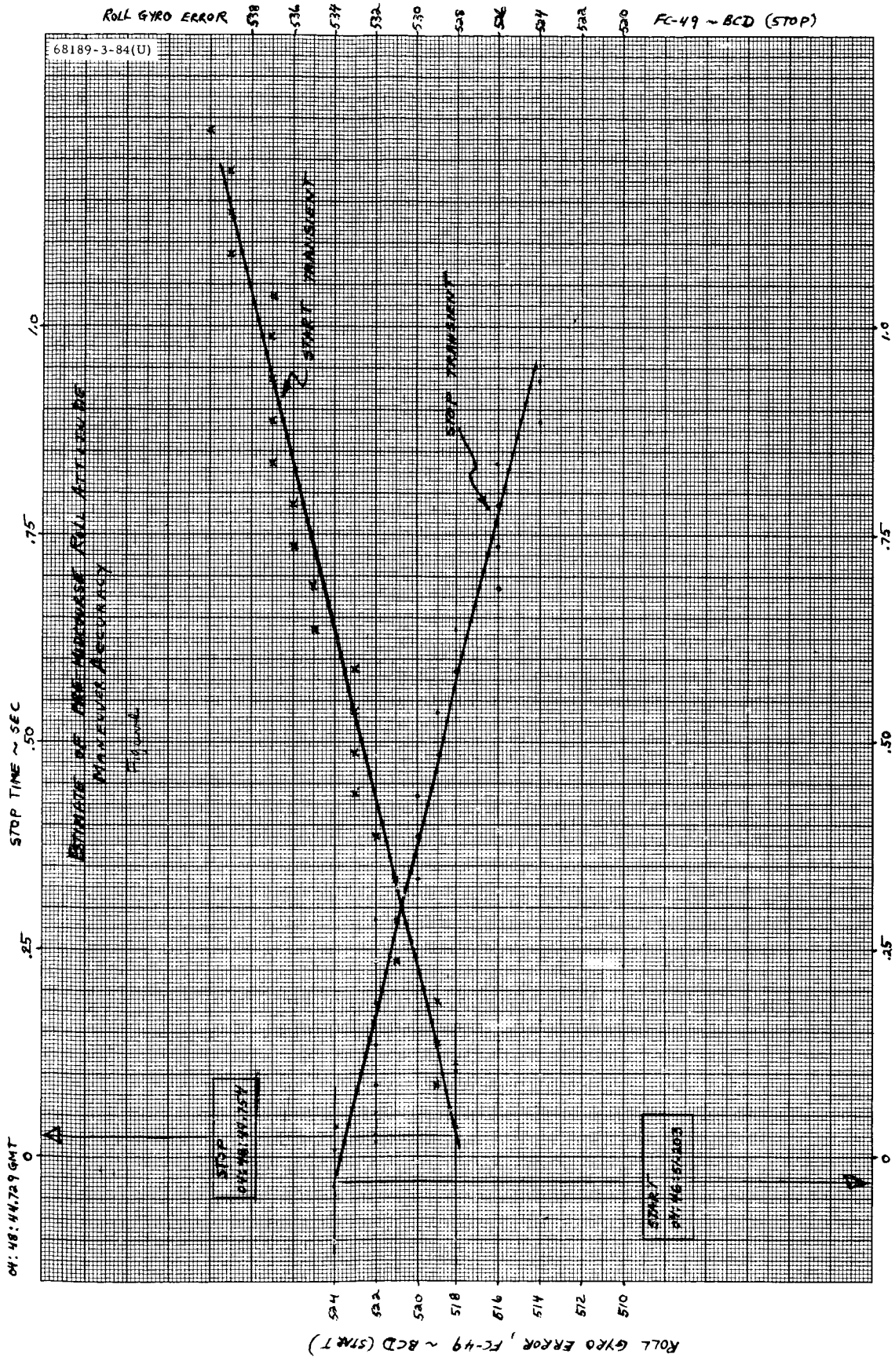

a) Roll

Figure 5.5-10. Gyro Error

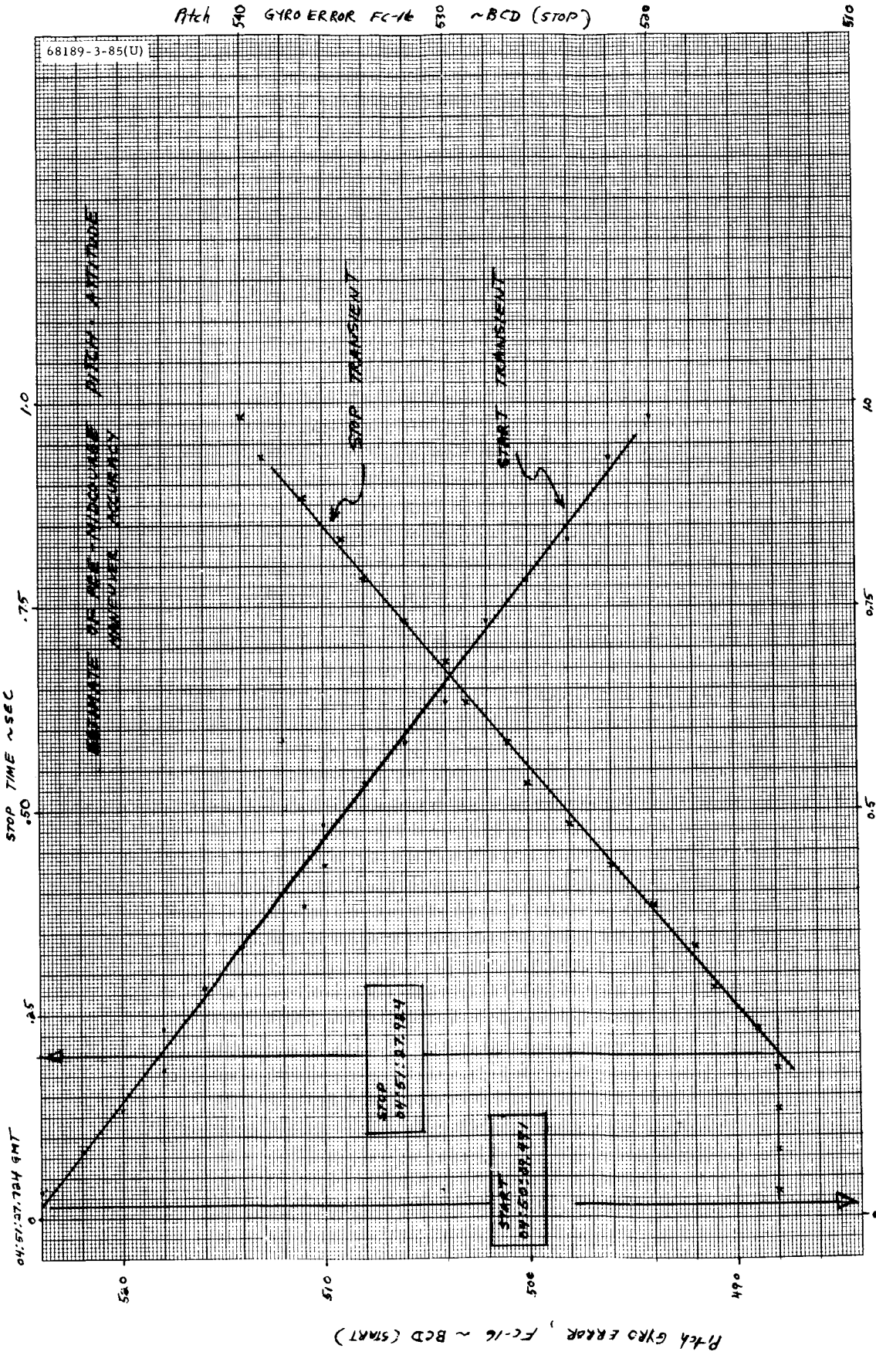

b) Pitch

Figure 5.5-10 (continued). Gyro Error

Use of $\varphi = 56.7$ degrees, $\theta = -39.1$ degrees, and the errors listed in the summary chart results in an 0.18-degree attitude error about the negative yaw axis and an 0.04-degree error about the negative pitch axis. The resultant pointing error has a 99-percent circular probable uncertainty of 0.10 degree.

5.5.4.7 Postmidcourse Attitude Maneuvers

The postmidcourse attitude maneuvers are used to realign the spacecraft to the celestial reference after performing a midcourse velocity correction. To accomplish this, two reacquisition schemes are available. One method is to perform the premidcourse attitude maneuvers in reverse, and the other is to perform another automatic sun acquisition sequence. The first method is more desirable since real-time monitoring of optical sensor signals provides a good indication of premidcourse maneuver accuracy and attitude control during the thrust period. If reacquisition of the sun and Canopus is not achieved to within a fair degree of accuracy, one or more of the following conditions must have existed:

1) Nonsymmetrical precession commands
2) Spacecraft attitude change occurred between maneuver periods
3) Premidcourse maneuvers were not accurate
4) Postmidcourse maneuvers were not accurate
5) Vernier engine shutoff transients excessive

The first method was chosen for the Surveyor III mission, and the celestial reference was successfully reacquired.

Determination of Precession Times

For the postmidcourse attitude maneuvers, the magnitude register was loaded with 196 bits for pitch and 284 bits for roll. This corresponds to 78.2 and 113.4 seconds, respectively.

The precession times, using gyro error signal data, were found to be as follows:

T = 78.3 seconds (pitch)

T = 113.64 seconds (roll)

The postmidcourse maneuvers were performed using the coast mode commutator at 4400 bits/sec, thereby increasing the data granularity to 0.3 second from the 0.05 second obtained for the premidcourse attitude maneuvers which were performed using the mode 1 commutator at 4400 bps.

5.5.4.8 Midcourse Velocity Correction

The midcourse velocity correction was successfully executed starting at 05:00:03.433 GMT on 18 April. From orbit determination, the actual

magnitude of the velocity change was estimated to be 4.0139 m/sec compared to the commanded value of 4.19 m/sec. This constitutes a ΔV execution error of 0.176 m/sec. Also from orbit determination, the midcourse thrust vector pointing error was within the accuracy of two-way doppler tracking system and estimated to be <0.2 degree. Using prelaunch alignment information and inflight data, the preignition pointing error was calculated to be 0.184 degree in subsection 5.5.4.6.

Midcourse Engine Ignition Characteristics

The SC-3 midcourse velocity correction was characterized by a smooth vernier ignition followed by a nominal, uneventful thrusting phase (Figure 5.5-11). Peak pitch and yaw gyro errors during thrusting were 0.30 degree or less during the ignition transient and less than 0.25 degree thereafter until engine cutoff. A summary of the midcourse pitch and yaw gyro errors is given in Table 5.5-6.

TABLE 5.5-6. MIDCOURSE IGNITION TRANSIENT CONTROL SUMMARY

Gyro error telemetry resolution = 0.016 degree

Initial (preignition) gyro errors, degrees:	
Pitch	= +0.05
Yaw	= -0.25
Peak angular overshoot, degrees:	
Pitch	= -0.125
Yaw	= +0.3
Peak angular rates, deg/sec:	
Pitch	= -0.3
Yaw	= +0.55
RSS total	= 0.625
Vernier engine startup time = <0.15 second	

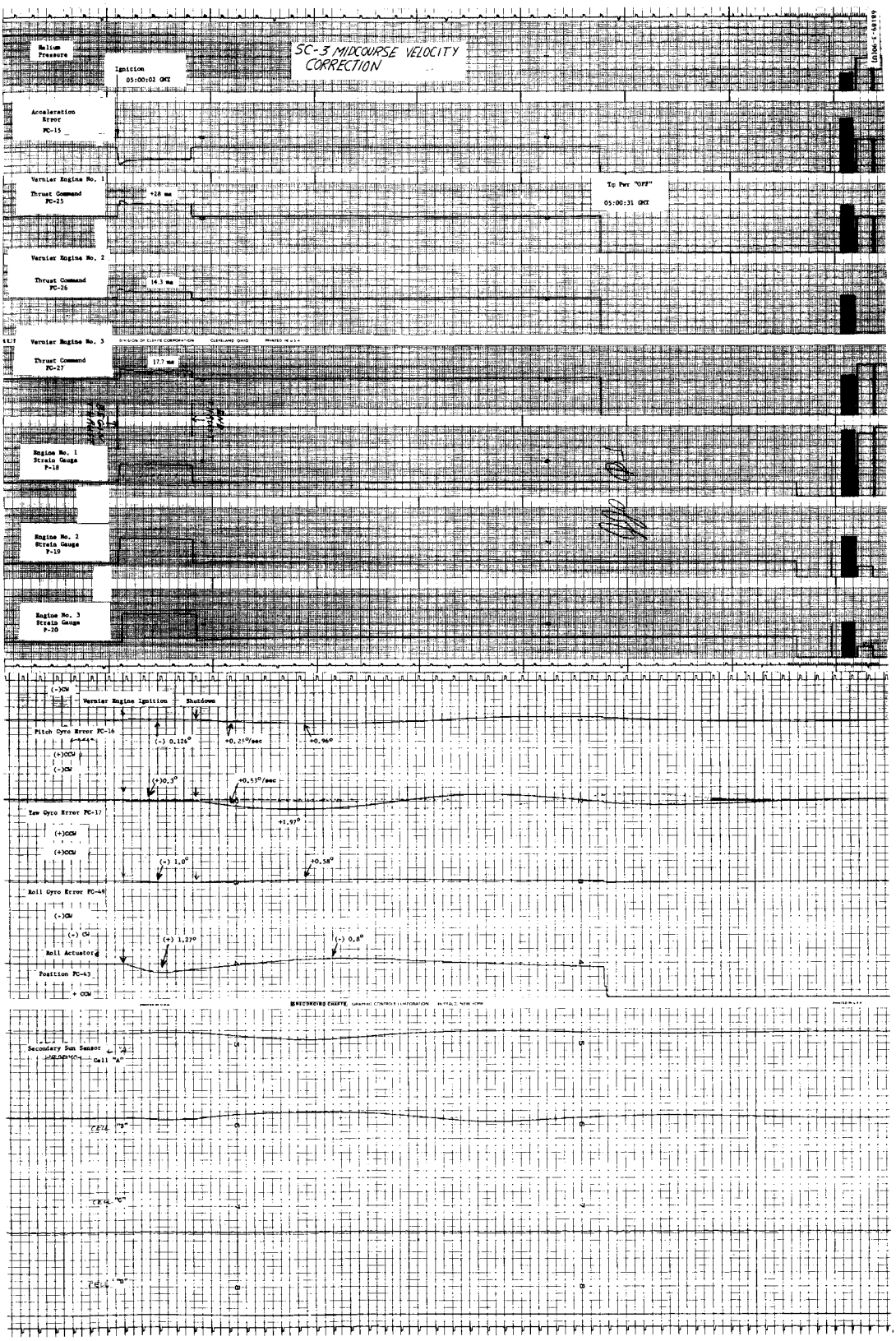

Figure 5.5-11. Midcourse Correction Velocity

Prior to vernier ignition, pitch and yaw gyro errors were maintained within the inertial deadband of ±0.22 degree by the gas jet system. At the instant of ignition, these errors were +0.05 and -0.25 degree for pitch and yaw, respectively. The subsequent transient at ignition was reduced to zero in approximately 2 seconds. The yaw error transient overshoot was +0.05 degree, while the pitch error overshoot was -0.066 degree. The transient behavior of both errors was dominated by the 1.0-second time constant of the attitude control loops.

Peak angular rates of (approximately) -0.3 deg/sec in pitch and +0.55 deg/sec in yaw occurred at vernier ignition. The startup impulse dispersions (deviations from average startup impulse) of the three engines are calculated by the procedure outlined in Reference 10 to be approximately as follows:

Leg 1: +0.073 lb-sec

Leg 2: +0.355 lb-sec

Leg 3: -0.428 lb-sec

These figures imply a maximum startup impulse variation (between legs 2 and 3) of 0.78 lb-sec. However, at engine ignition, the control system null reference changes from that which existed for the gas jet attitude control system to that which exists for the vernier engine attitude control system. This change in reference produces a significant portion of the gyro motion at ignition and tends to mask any effects due to uneven engine startup.

Based on the acceleration error telemetry signal (FC-15) (Figure 5.5-12), it was concluded that all three engines were producing controlled thrust within about 0.150 second of the ignition command signal. Therefore, acceleration signal amplifier saturation, which requires a startup delay of 0.26 second, did not occur, and no ΔV error information was lost.

Midcourse Engine Shutdown Dispersions

A summary of the peak spacecraft angles and angular rates and computed vernier engine shutdown impulse dispersions are given in Table 5.5-7.

It should be noted that peak gyro angles were less than 2 degrees and well within the required travel range of ±10 degrees. Inertial reference was therefore retained, and reacquisition of the sun and Canopus was accomplished via the reverse maneuver sequence.

Vernier engine shutdown impulse dispersions (relative to mean impulse of the three engines), calculated from pitch and yaw angular rate data as per the procedure outlined in the "Midcourse Engine Startup Characteristics," were well within the specification limit of ±0.63 lb-sec (Reference 11).

Midcourse Velocity Determination

The general concept of midcourse correction capability employed by Surveyor is to apply a constant acceleration for a finite period of time. Thus,

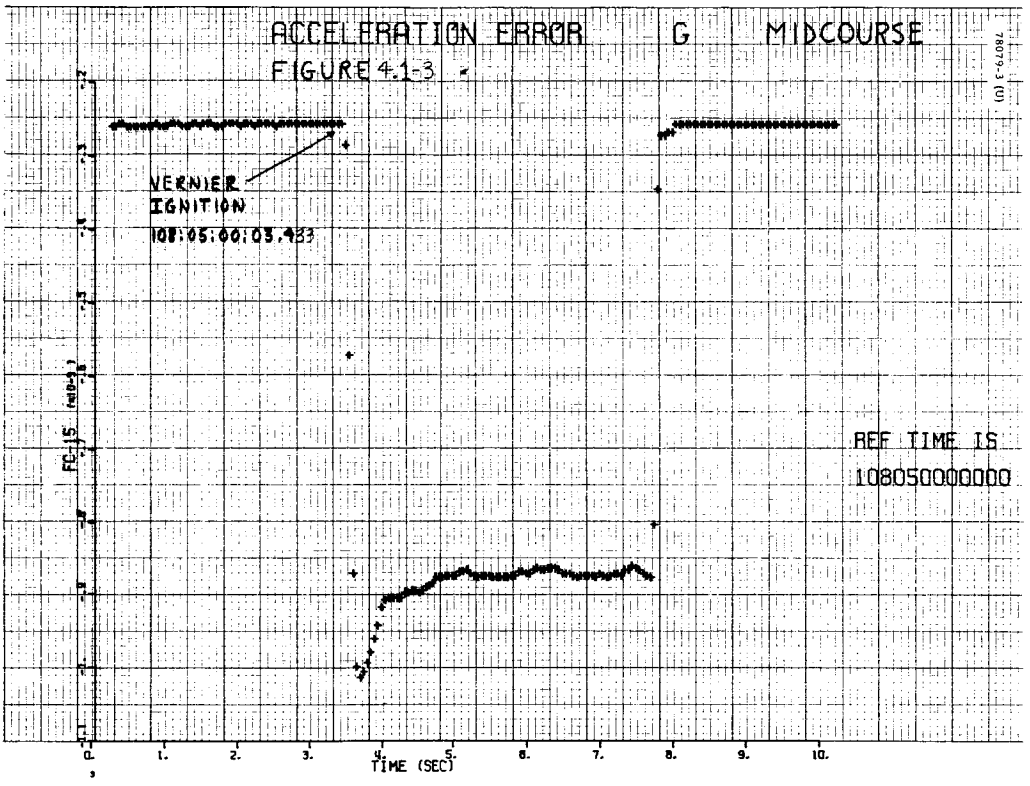

Figure 5.5-12. Acceleration Error

TABLE 5.5-7. MIDCOURSE SHUTDOWN SUMMARY

Peak angular errors, degrees:

Pitch	= +0.96
Yaw	= +1.97
Roll	= +0.58
Roll act	= -0.8

Peak angular rates, deg/sec:

Pitch	= +0.25
Yaw	= +0.53
RSS total	= 0.58

Vernier shutdown impulse dispersions, lb-sec:

Leg	SC-3 (Computed)
1	-0.31
2	+0.42
3	-0.11

in theory, once the magnitude of the velocity correction is known, the exact duration of the constant acceleration phase can be determined. In practice, this approach is slightly altered to account for such error sources as engine ignition transients, shutdown impulse, and hysteresis. Thus, the actual command time ΔT is slightly higher.

The desired values used during flight were as follows:

1) Desired ΔV = 4.19 m/sec (13.74 fps)
2) Desired ΔT = 4.278 seconds

Duration of Burn Time. The acceleration error signal data was used in an attempt to determine the actual burn time. The results (Figure 5.5-13) indicated that the burn time was 4.245 seconds for a timing error of 0.03 second. (The magnitude register was loaded with 86 counts — ΔT = 4.275 seconds).

Estimate of ΔV. Assuming that acceleration command remained at the design value of 3.23 ft/sec^2, the actual acceleration level was determined by subtracting the acceleration error value (ϵ_A = 0.008 ft/sec^2) from the

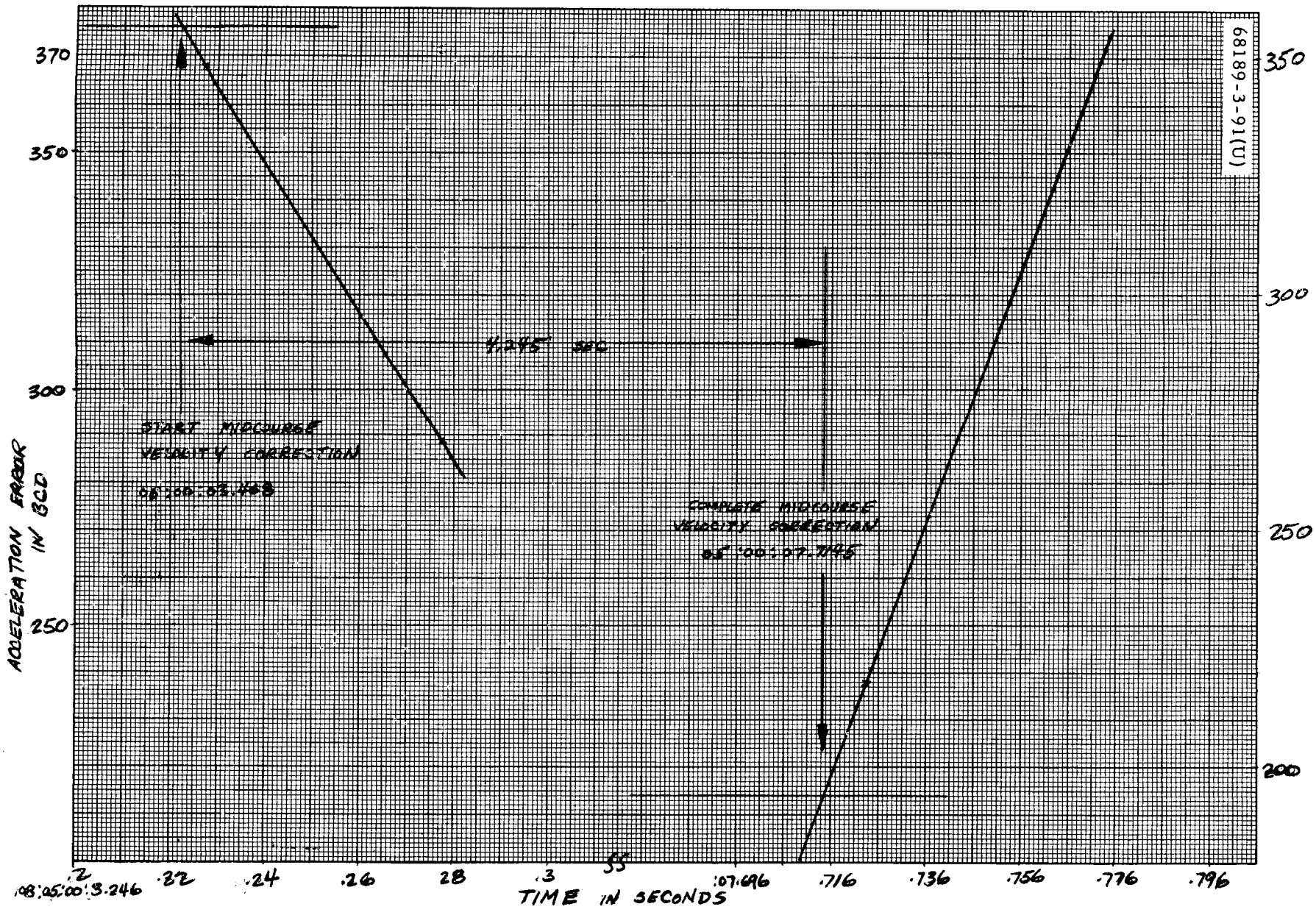

Figure 5.5-13. Midcourse Velocity Correction
Timing accuracy using acceleration error (FC-15)

design value. The acceleration error signal remained essentially constant during the burn period. Therefore, the actual acceleration level was 3.223 ft/sec^2, and the midcourse ΔV was 3.223 × 4.245 = 13.67 fps. From orbit determination, it was concluded that the actual midcourse ΔV was 4.0739 m/sec (13.36 fps). The ΔV value obtained from the acceleration command data is within 3.0 percent of the actual.

A list of parameters affecting the accuracy of the velocity correction is presented in Table 5.5-8 along with the values of maximum allowable errors. Actual performance values were used wherever possible.

TABLE 5.5-8. SC-3 MIDCOURSE VELOCITY CORRECTION ACCURACY

Item	Parameter	Requirement 3σ or Limit	FPS	Specification	Performance Value, ft/sec	Comments
1	Errors proportional to maneuvers magnitude					Much of the error was anticipated and was included in the calculation of the desired burn time
	Accelerometer accuracy	1.1 percent	0.15	234632C		
	Reference signal	0.5 percent	0.068	234600E		
	Flight control electronics null	0.15 percent	0.02	234600E		
	Thrust bias variation	0.09 percent	0.01	287105		The difference between the actual value of ΔV and the desired value is -0.38 fps
	Control channel gain variation	0.07 percent	0.009	234600E	0.17	
	Accelerometer misalignment	0.06 percent	0.008	234600E		This value is more meaningful than the 0.19 fps given as performance value
	Total proportional errors (RSS)	1.22 percent	0.17			
2	Errors independent of maneuver magnitude					
	Shutdown impulse dispersion	±0.63 lb-sec	0.016	287015	-0.012	
	Hysteresis limit cycle	3 milliamperes	0.035	287105	0.035	
	Ignition transient	–	0.47	–	0	
	Timing granularity	0.05 second	0.16	224510D 3.6.3.2	-0.07	
	Total independent errors (RSS)		0.497		0.08	
3	Total magnitude errors (RSS)		0.525		0.19	

Telemetered Thrust Levels

During the midcourse velocity correction, the telemetered vernier engine 1 thrust command level was greater than the engine 2 level by approximately 14 milliamperes (Figures 5.5-14a and b). This difference, which is equivalent to around 7 pounds of thrust, corresponds to a cg offset of approximately 1 inch. Although the absolute values of thrust, as indicated by the strain gages, did not agree with the vernier engine command values as shown by a comparison of Figures 5.5-14 and 5.5-15, the difference in thrust levels between engines 1 and 2 was approximately the same as that indicated by the engine commands.

Since this was the first spacecraft to employ the redesigned thrust command telemetry circuit, the expected accuracy of the circuit was reviewed (Reference 11) to confirm that this was not the cause of the discrepancy. Results indicated a worst-case variation of ±4 percent on the thrust command telemetry signals at a temperature of 90°F, which was the temperature indicated by FC-45 during the midcourse velocity correction.

The large difference in the engine thrust command level apparently was not due to telemetry circuit errors since the thrust levels were in close agreement immediately before and after the midcourse velocity correction and during terminal descent. A discussion of updated calibration techniques for thrust telemetry is given in Sections 5.6.4.3 and 4.3.1.

5.5.4.9 Preretro Maneuvers

Before retro ignition, it is required that the spacecraft thrust axis (roll axis) be aligned to the translational velocity vector of the spacecraft as part of the gravity turn terminal descent phase guidance. The alignment is performed by means of two sequential rotations about the spacecraft body (gyro) axes. A third roll rotation may be required to align the high-gain planar array with the spacecraft-earth line to secure a favorable omnidirectional antenna pattern or to satisfy a RADVS sidelobe constraint (Reference 15).

These maneuvers are accomplished by using the cold gas attitude control system, with the body-fixed integrating rate gyros as inertial references. To accomplish a rotation, the appropriate gyro torquer winding is driven by a constant current source for a precise length of time; the spacecraft is slaved to this changing reference at a constant rate of 0.5 deg/sec.

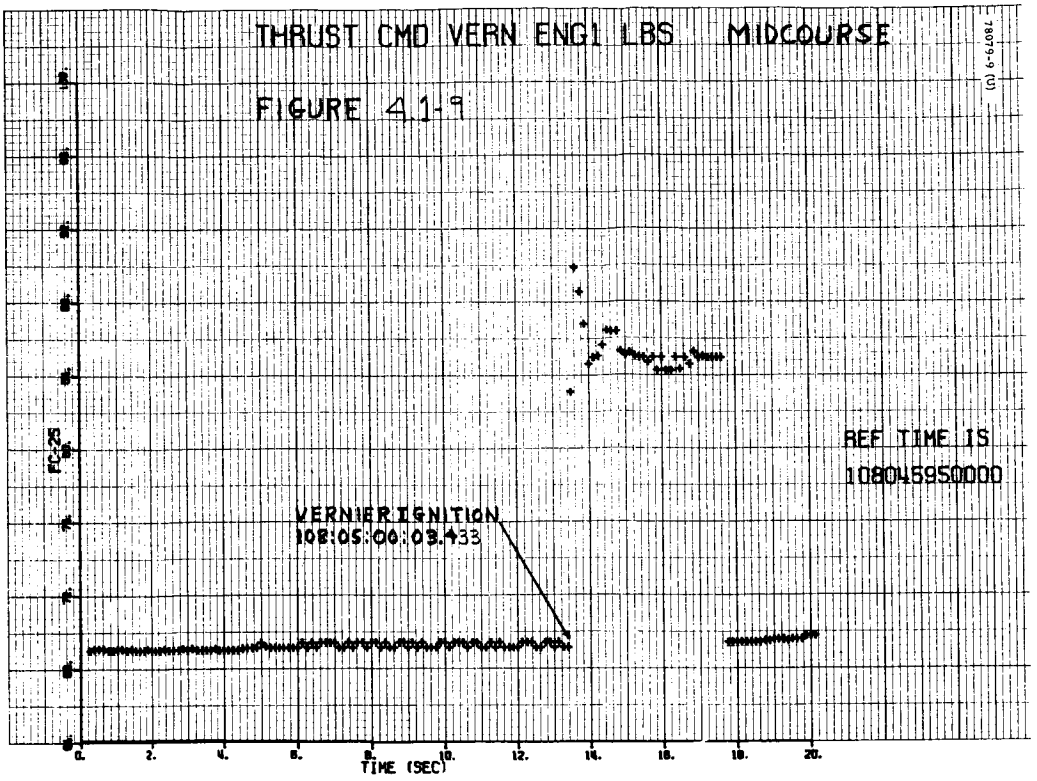

a) Engine 1

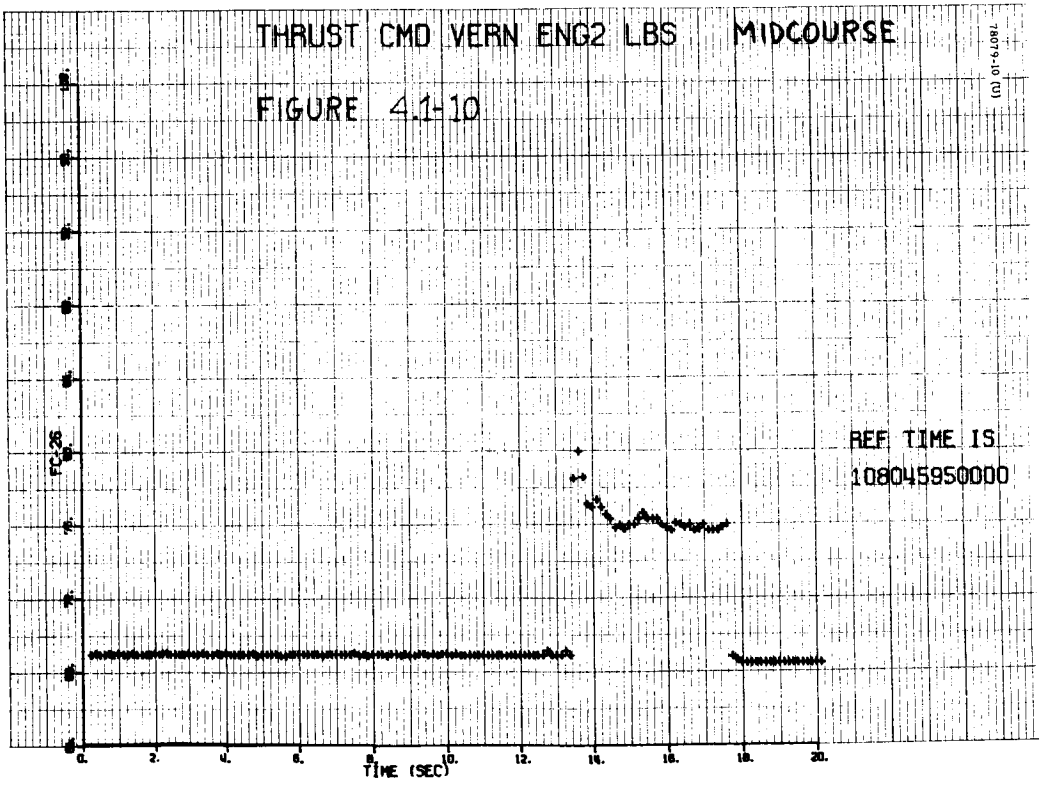

b) Engine 2

Figure 5.5-14. Vernier Engine Thrust Commands

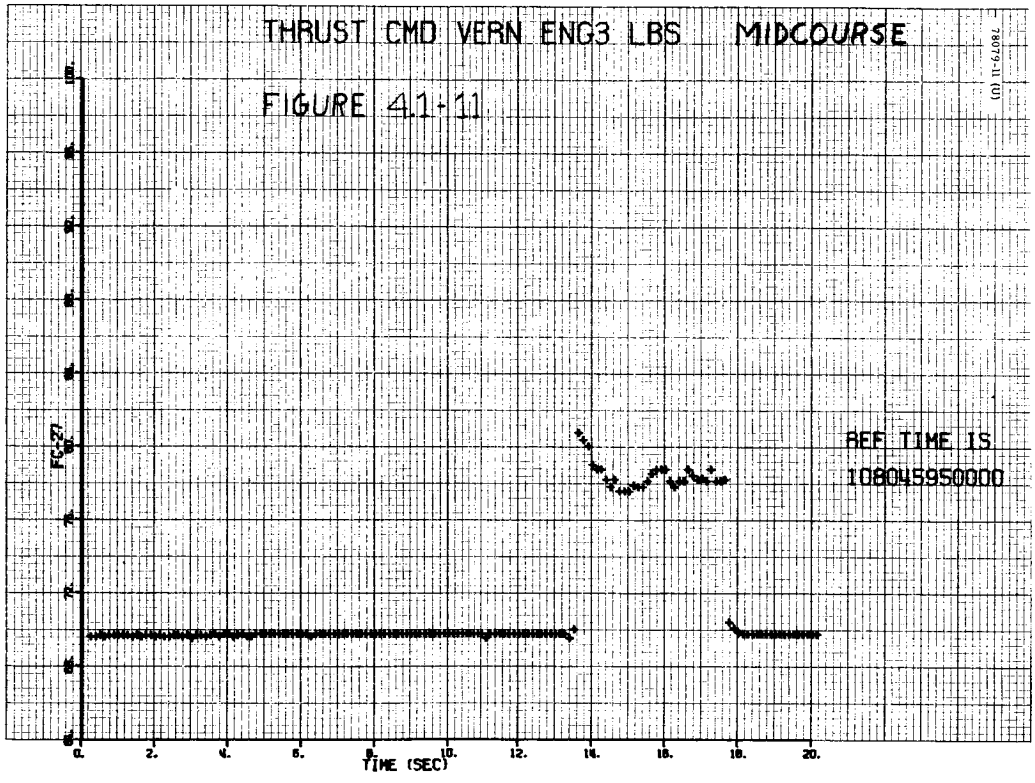

b) Engine 3

Figure 5.5-14 (continued). Vernier Engine Thrust Commands

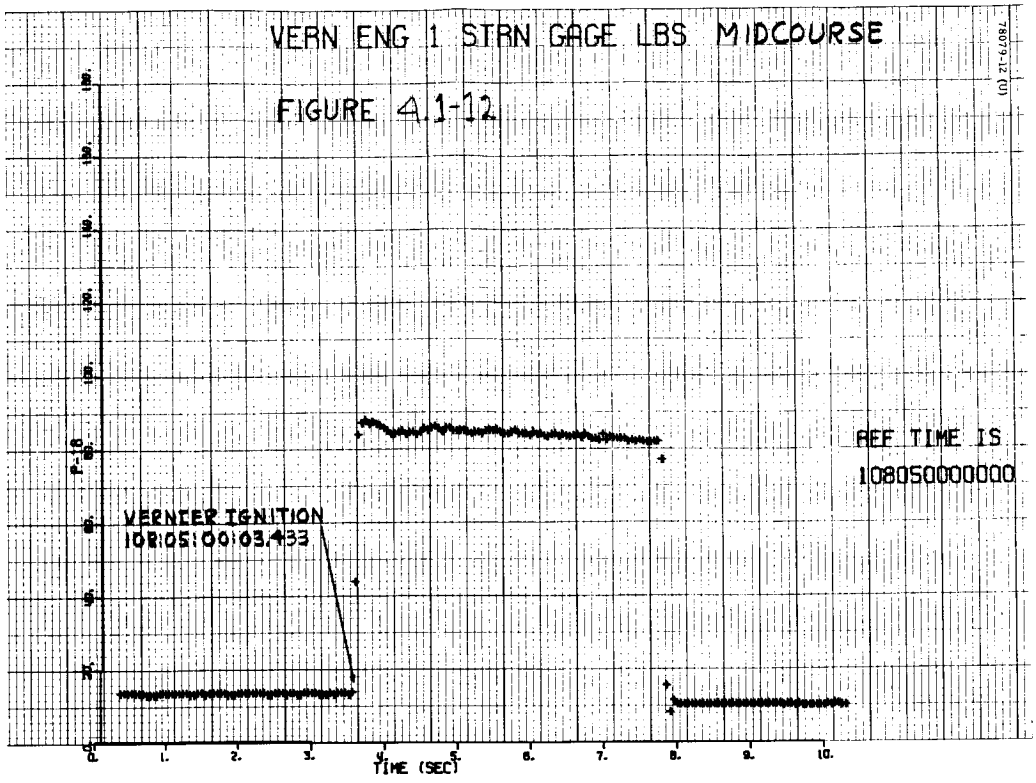

a) Engine 1

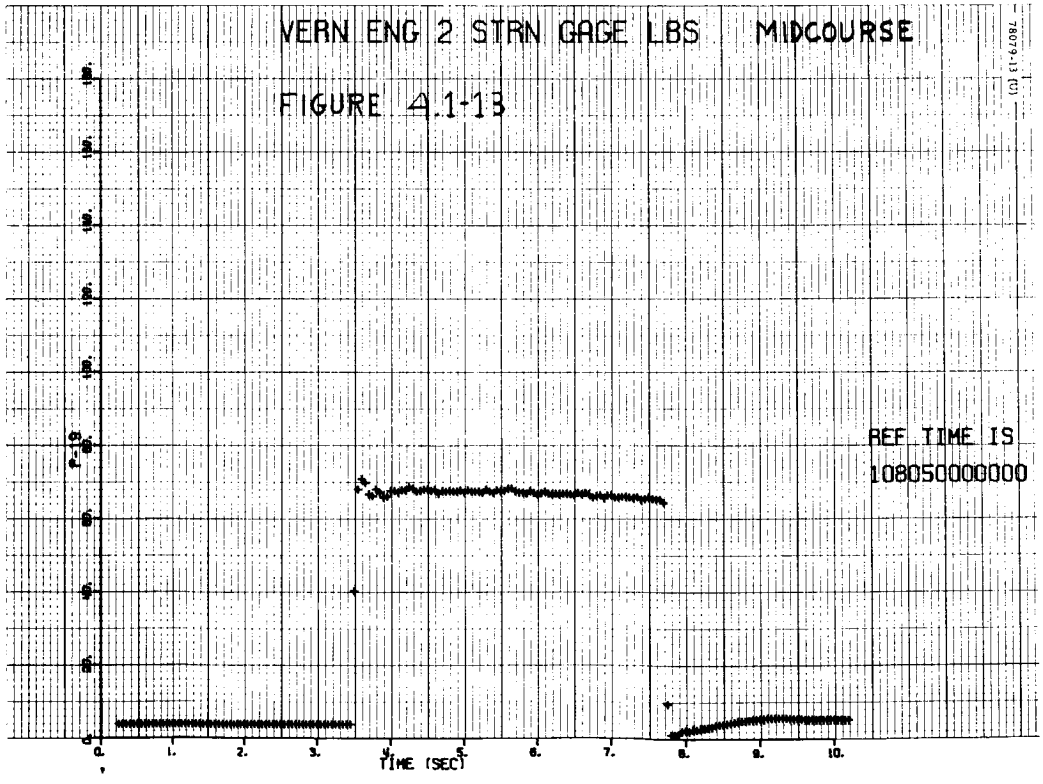

b) Engine 2

Figure 5.5-15. Vernier Engine Strain Gages

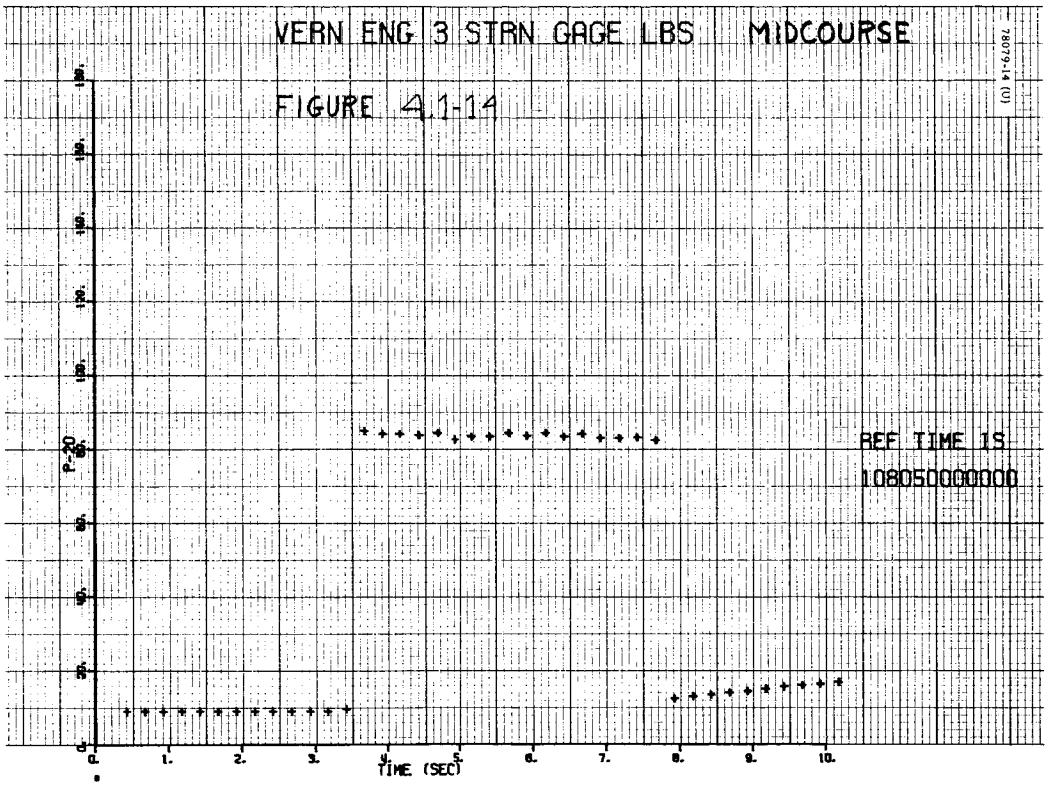

c) Engine 3

Figure 5.5-15 (continued). Vernier Engine Strain Gages

The major events and times associated with the preretro maneuvers are given in Table 5.5-9.

The preretro maneuvers were analyzed in terms of the following:

1) The gyro precession times were determined from gyro error signals and precession logic signals and compared to commanded times.

2) Using these attitude errors and the initial sun and Canopus error signals, the terminal pointing accuracy was determined.

The first attitude maneuver (yaw) was initiated 37 minutes and 47 seconds before retro ignition. Normally, the time constraint on break of optical lock is 33 minutes based on an allowable 1 deg/hr gyro drift contribution to the pointing error (Reference 2). Since the attitude maneuver magnitudes were compensated for in flight measurements of gyro drift, the earlier maneuver time was acceptable.

TABLE 5.5-9. MAJOR EVENTS AND TIMES (DAY 109) FOR PRERETRO MANEUVERS

Event	Command	GMT, hr:min:sec	
Begin yaw	0713	23:23:32.085	
End yaw		23:28:47.745	Determined from Space Flight Operations Facility data
Begin pitch	0712	23:30:19.441	
End pitch		23:32:52.816	
Begin roll	0711	23:34:37.672	
End roll		23:36:45.548	
Retro ignition		00:01:19.13 (day 110)	

Gyro Precession Times

The attitude maneuvers entered into the flight control programmer magnitude register are as follows:

Maneuvers, minus	Degrees	Bits
Yaw	157.9	790
Pitch	76.7	384
Roll	63.9	320

Table 5.5-10 presents the estimated gyro precession times.

TABLE 5.5-10. ESTIMATED GYRO PRECESSION TIMES

Attitude Maneuver	Commanded Time, seconds	Observed Time, seconds	ΔT, seconds	Rotation Error, degrees
Yaw	315.8	315.66	-0.14	$\Delta\psi$ = -0.07
Pitch	153.4	153.4	0	$\Delta\theta$ = 0
Roll	127.8	127.9	+0.10	$\Delta\varphi$ = +0.05

Since the gyro error signals are only sampled once every 1.2 seconds (coast mode at 1100 bits/sec) during the preretro maneuvers, it was assumed that the shapes of roll and pitch gyro transients were the same as those observed during the premidcourse attitude maneuvers when the gyro error signals were sampled once every 0.05 second. The precession times were then estimated graphically based upon the intersection points of the start and stop transients with the steady-state gyro error values (Figure 5.5-16).

Gyro Drift Compensation

Eight three-axis gyro drift checks were made during the mission, two of them prior to the midcourse velocity correction. Five roll-axis-only drift checks were also made. A summary of gyro drift measurements is presented in Table 5.5-11. Two techniques were used to measure the drift rates. The first was based on average slopes of the optical error signals obtained from analog Brush recorder and Milgo plots. In the second technique, iterated calculations were made as described in Reference 16. A sample of the analog recorder drift data is shown in Figure 5.5-17.

The preterminal attitude maneuvers were compensated for by the following gyro drift rates:

Roll = +1.1 deg/hr
Pitch = +0.6 deg/hr
Yaw = -0.8 deg/hr

The roll and pitch gyro drift values selected for preterminal maneuver compensation were based essentially upon an average of all measurements made during the mission. Since the yaw gyro exhibited a definite trend toward a lower drift value, the later yaw gyro drift measurements were weighted more heavily in determining the final value used for yaw maneuver compensation. The gyro drift measurements are depicted versus mission time in Figure 5.5-18. The fixed drift history for each such gyro is shown in Figure 5.5-19. While the roll and pitch gyros tend to indicate a trend toward an increase in positive drift rate as experienced during the mission, no such trend is evident for the yaw gyro.

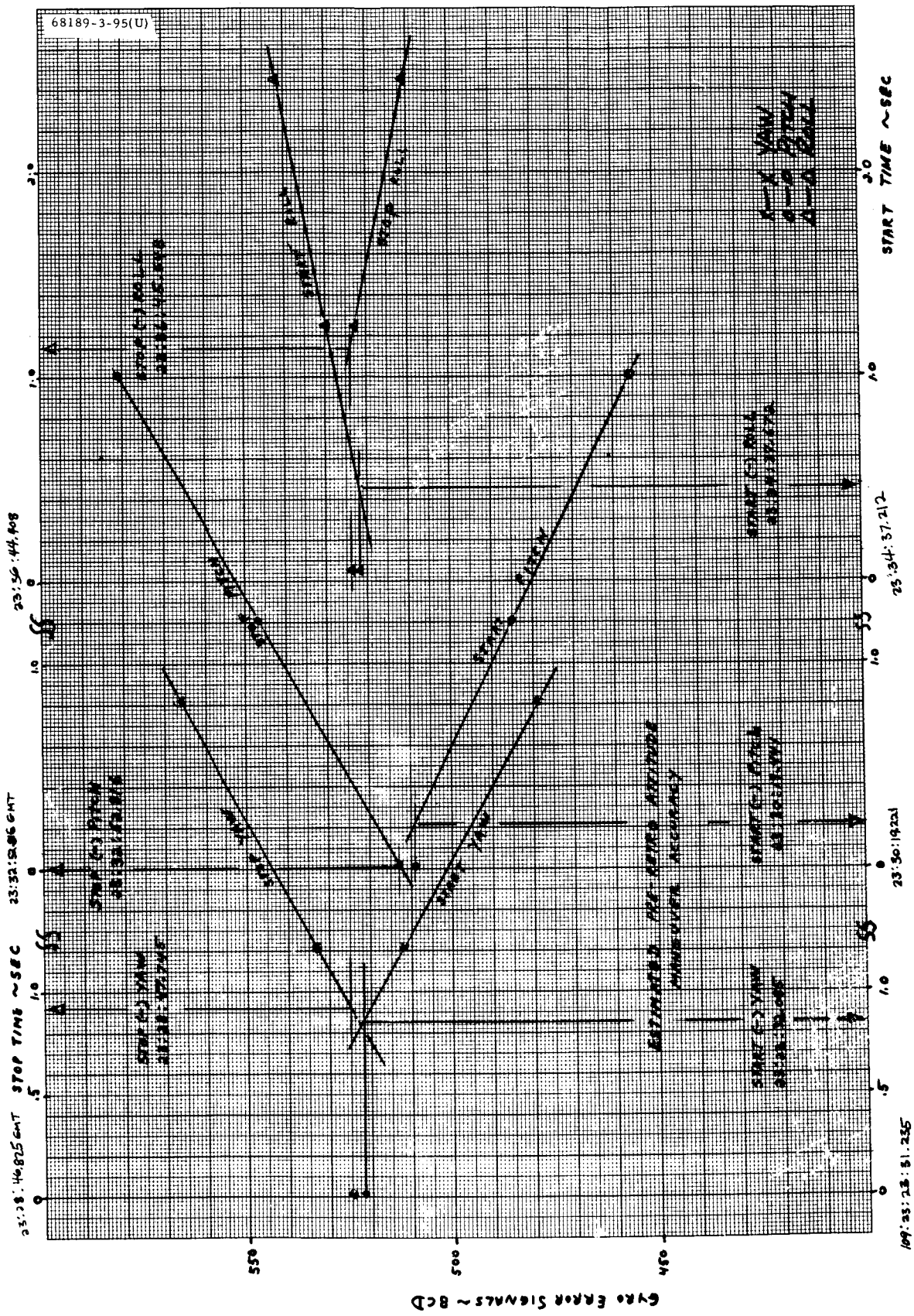

Figure 5.5-16. Gyro Error Signals

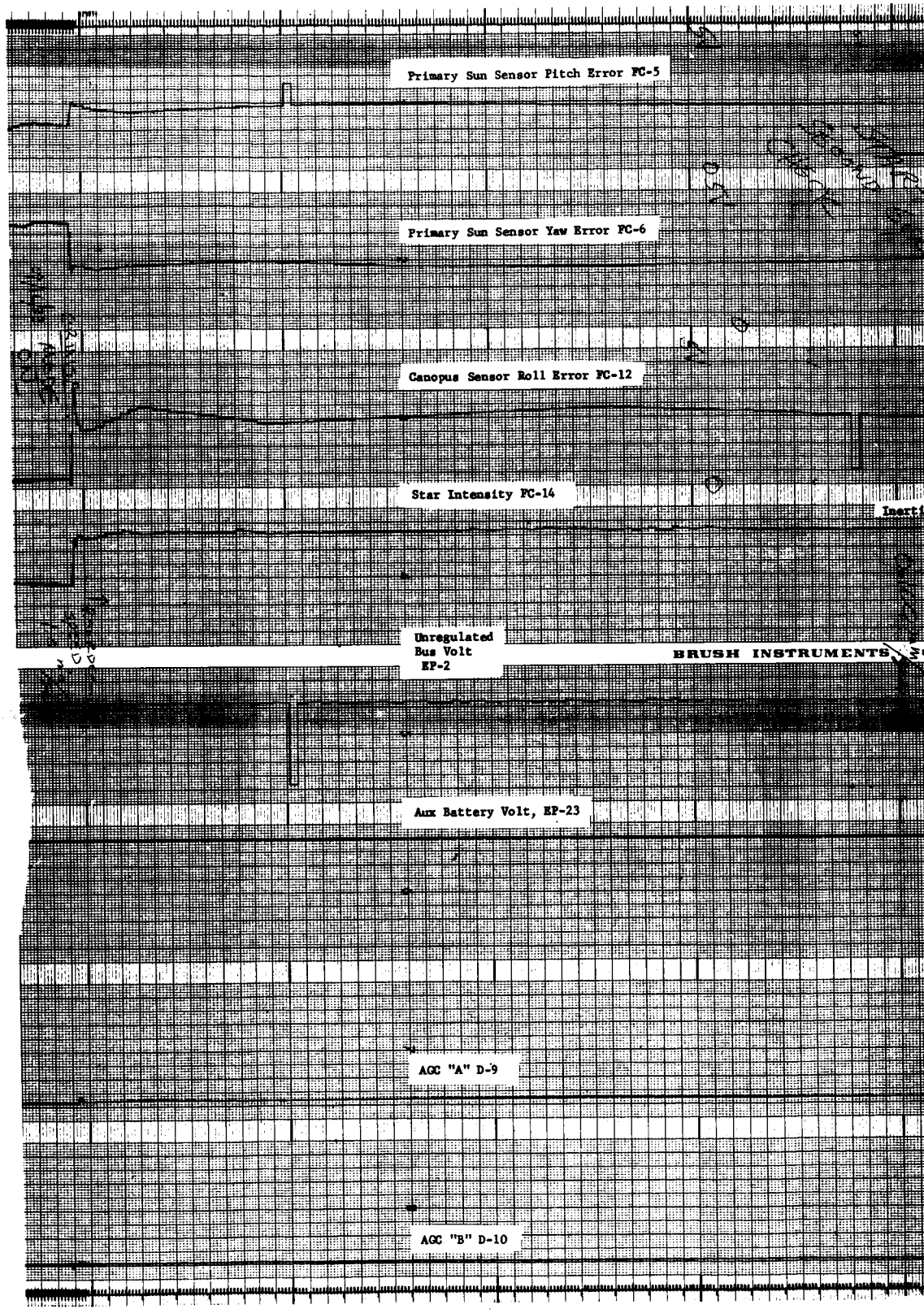

Figure 5.5-17. Gyro Drift Check No. 2

FOLDOUT FRAME 1

SC-3 GYRO DRIFT CHECK #2
Figure-8

FOLDOUT FRAME 2

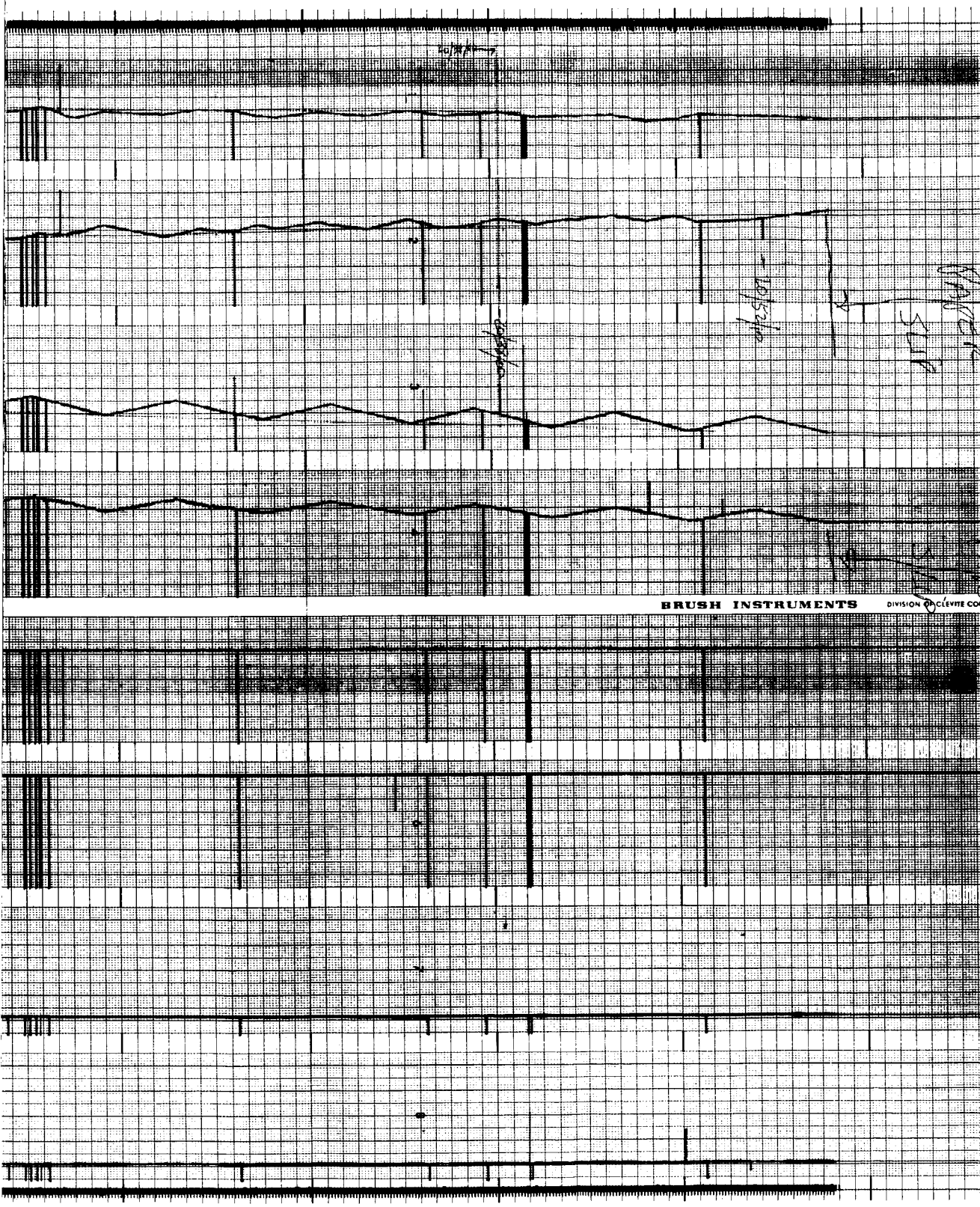

FOLDOUT FRAME 3

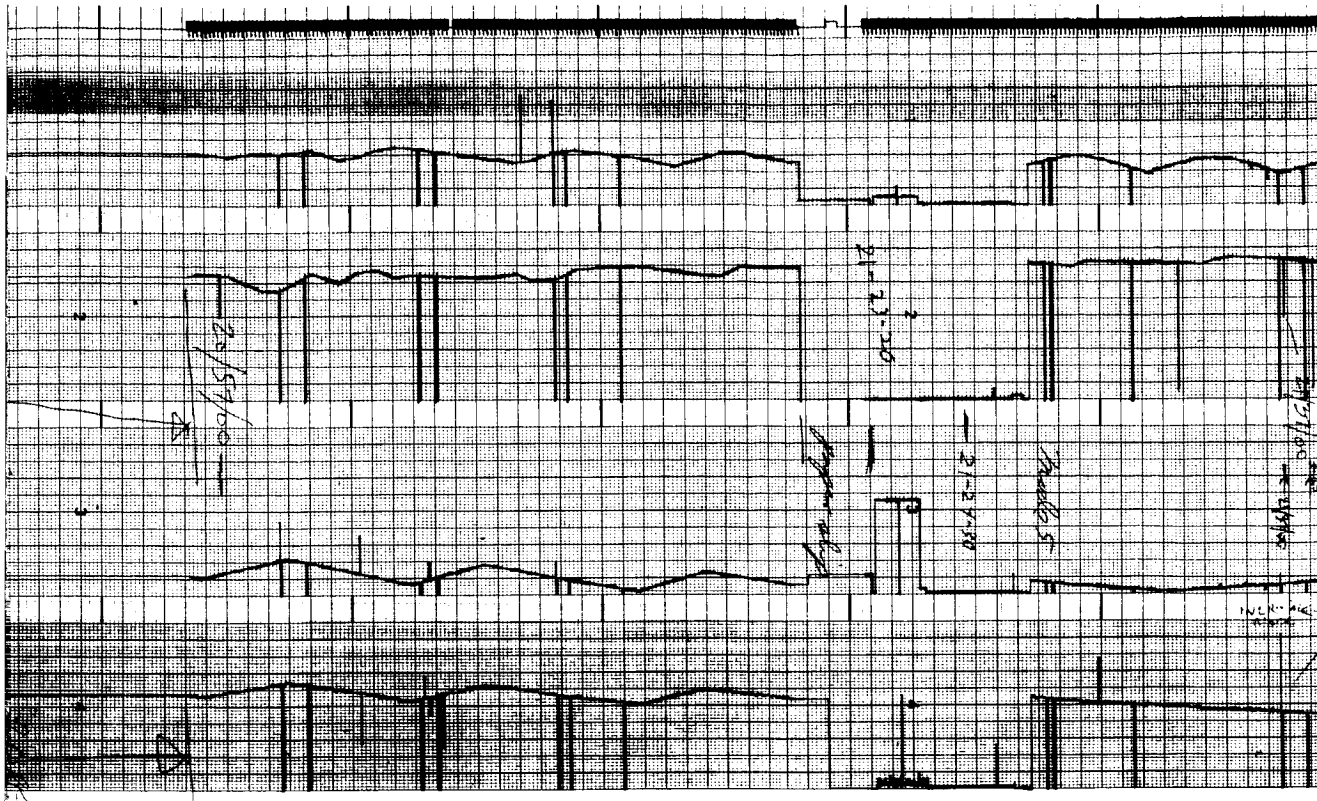

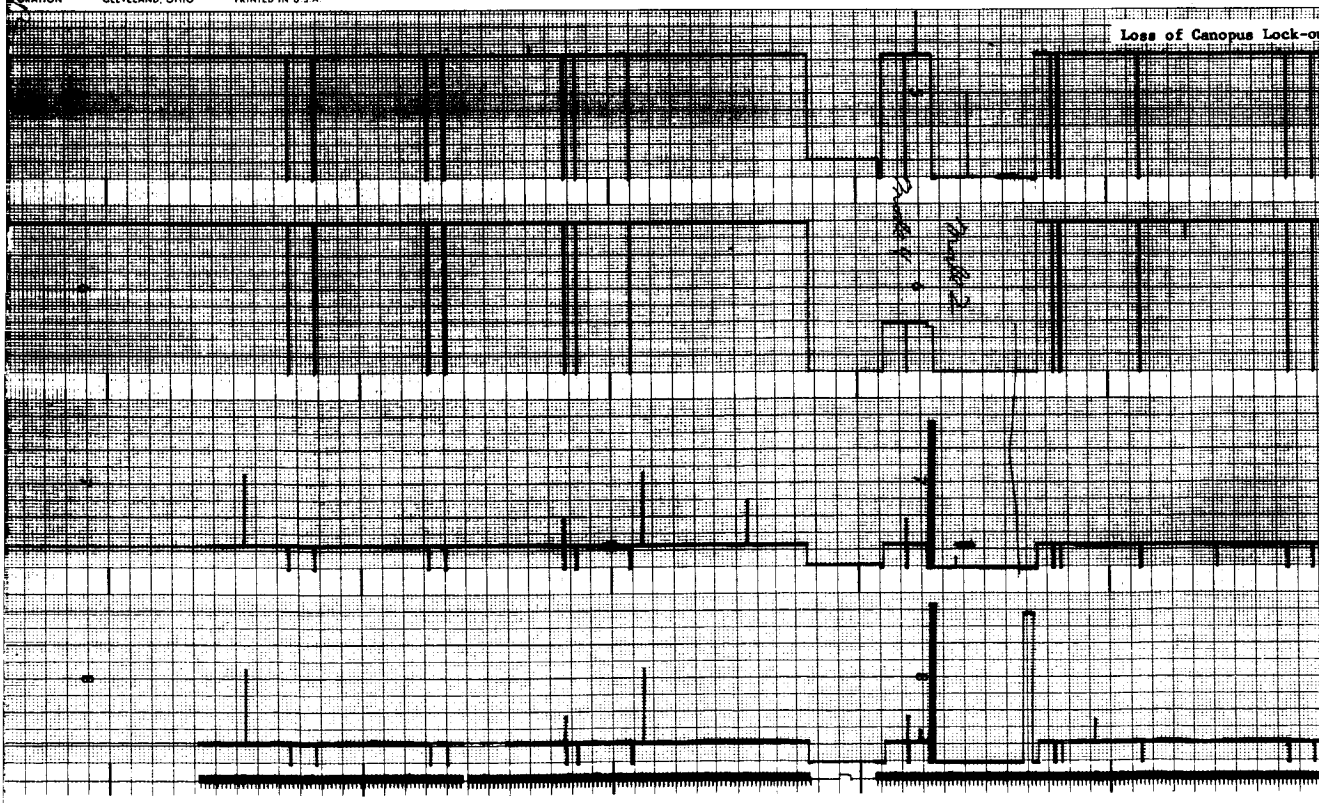

FOLDOUT FRAME 4

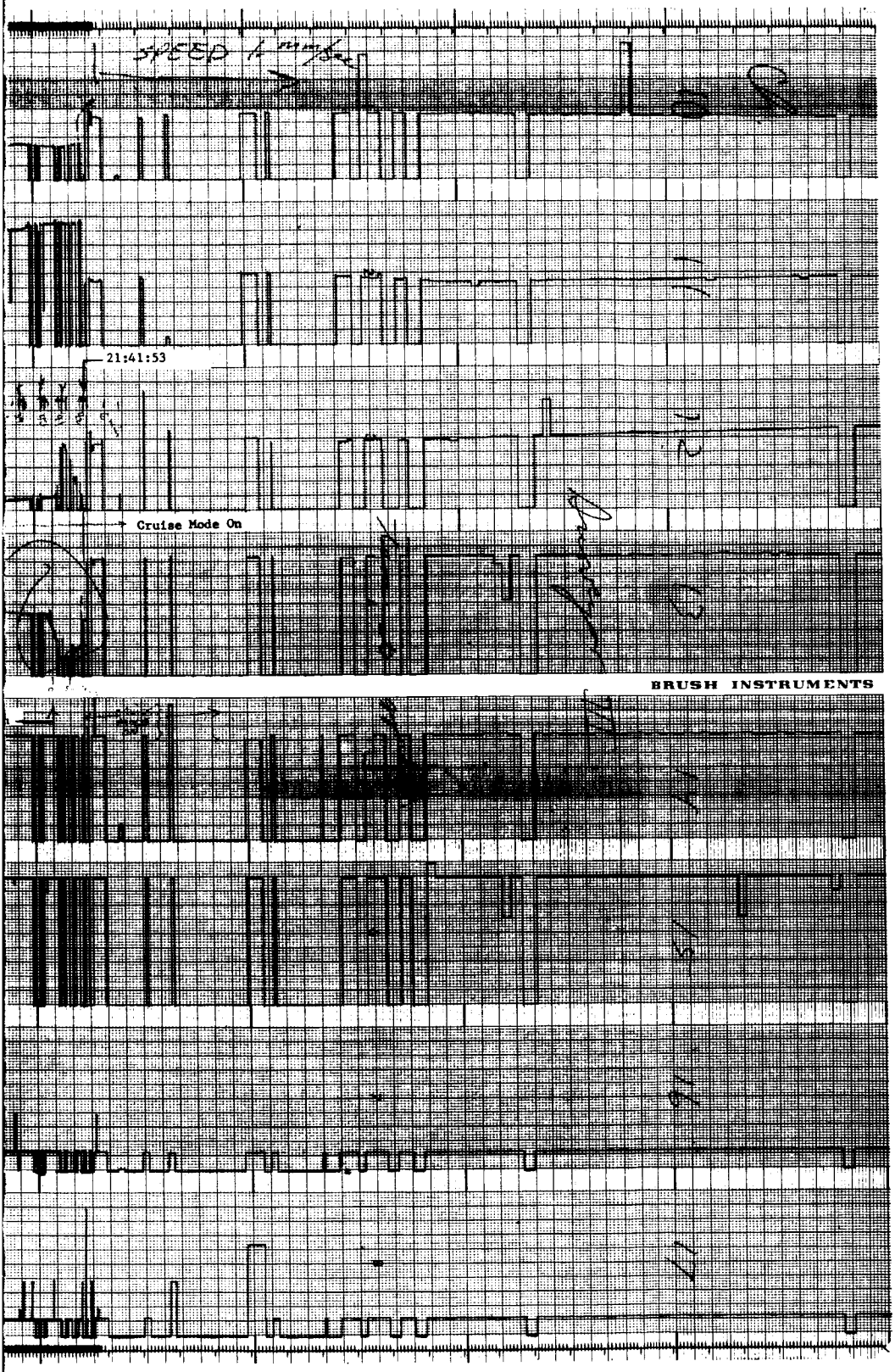

FOLDOUT FRAME 5

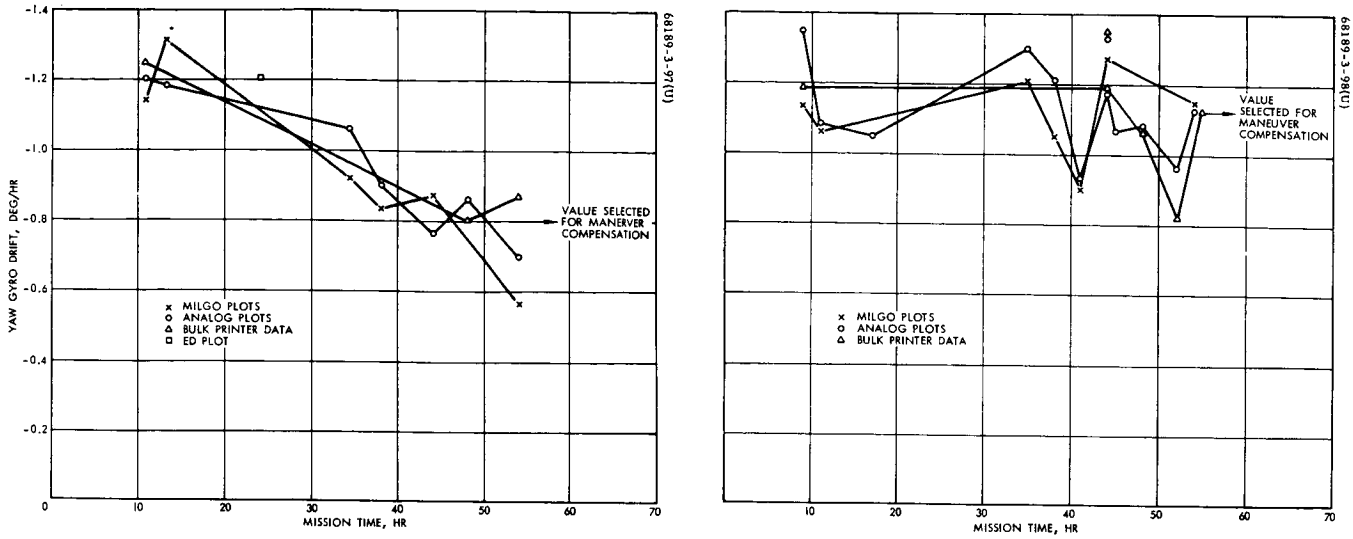

a) Yaw

b) Roll

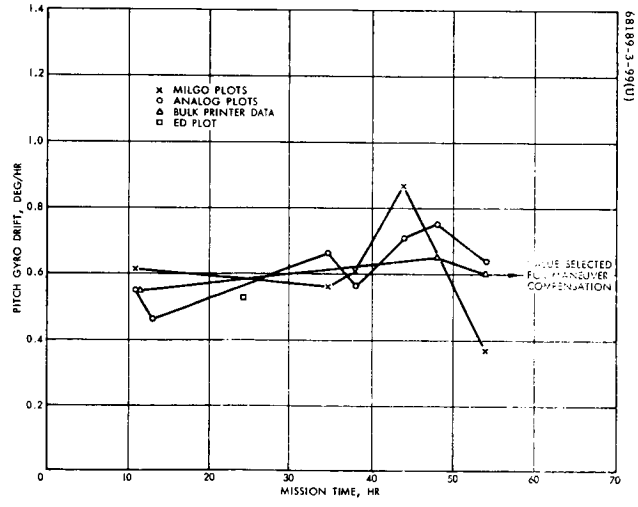

c) Pitch

Figure 5.5-18. Gyro Drift Measurements Versus Mission Time

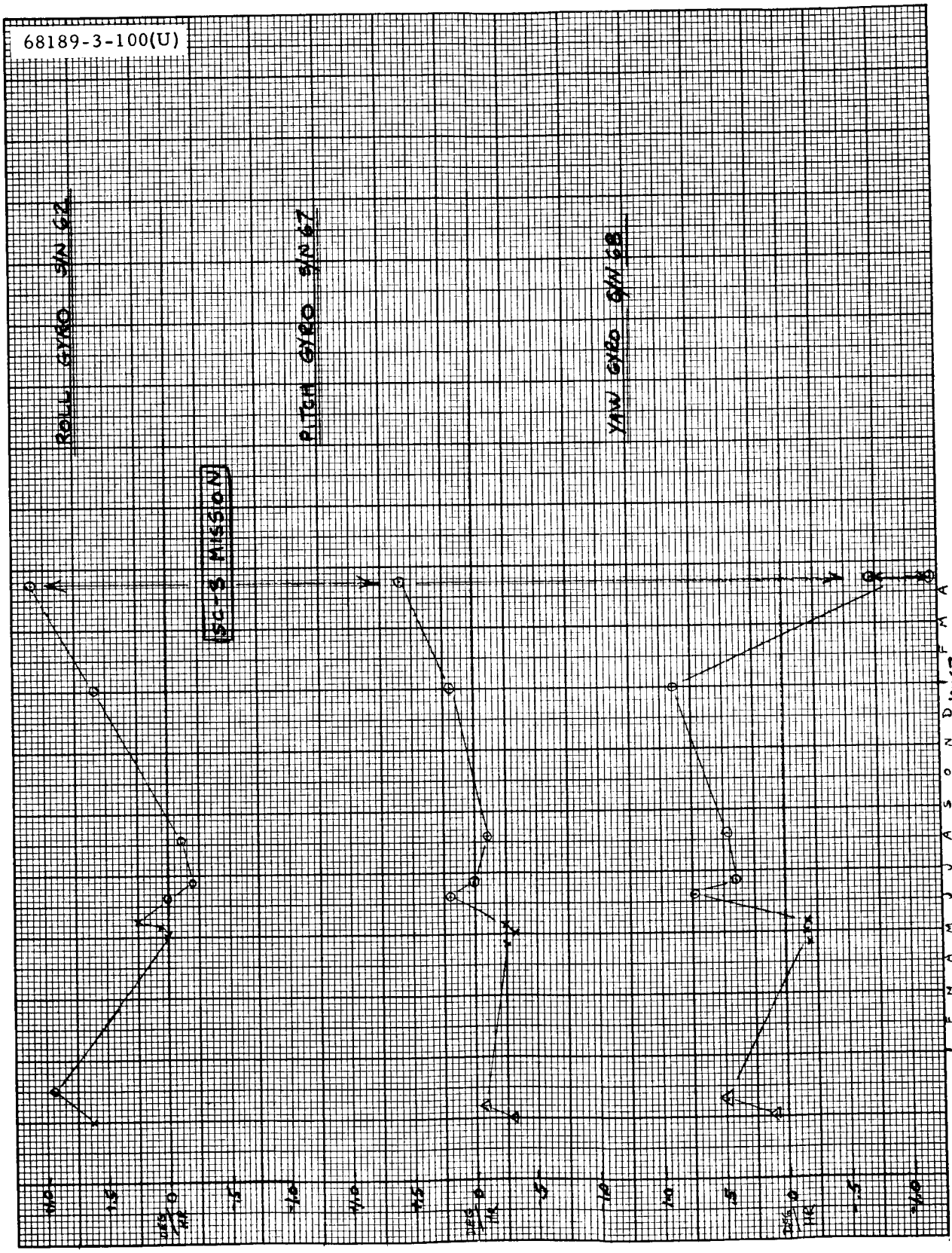

Figure 5.5-19. History of Gyro Fixed Drift

This page intentionally left blank

TABLE 5.5-11. GYRO DRIFT SUMMARY

GMT, day:hr:min:sec	Roll			Pitch			Yaw		
	Milgo	Analog	Bulk	Milgo	Analog	Bulk	Milgo	Analog	Bulk
107:17:29:17 to 107:19:16:32	1.13	1.35	1.19	0.61	0.55	0.55	-1.14	-1.20	-1.25
107:19:23:34 to 107:21:41:53	1.06	1.08			0.46		-1.31	-1.18	
107:23:11:19 to (roll only) 107:02:11:00		1.05							
Drift check 108:07:36:xx to 108:09:43:xx				ED plot	0.53		ED plot	-1.2	
108:17:31:25 to (sun mode) 108:19:31:38	1.21	1.3		0.57	0.67		-0.92	-1.07	
108:20:27:19 to 108:22:50:03	1.05	1.21		0.61	0.56		-0.83	-0.9	
108:22:55:08 to 108:01:15:42	0.903	0.93							
108:01:23:34 to 108:03:36:35	1.28	1.33 1.17	1.19 1.35	0.87	0.71		0.87	-0.77	
Roll only 109:03:57:30 to 109:06:45:13		1.07							
109:06:48 to 109:09:09		1.08	1.07		0.75	0.65		-0.86	-0.8
Roll only 109:10:12:22 to 109:12:41:23		0.96	0.825						
109:14:28:06 to 109:16:55:52	1.15	1.13	1.13	+0.37	0.64	0.60	-0.56	-0.70	-0.88

Preretro Pointing Error Determination

A digital computer program was developed to determine the retro pointing error. The method was essentially that used for the midcourse pointing error determination as described in the "Surveyor I Flight Performance Final Report," Volume II (SSD 68222R).

The initial attitude errors at initiation of the terminal attitude maneuver were as follows:

Pitch = -0.023 degree
Yaw = +0.175 degree
Roll = -0.200 degree

Because of data uncertainties and electrical null shifts with battery voltage, these values have a ±0.04-degree uncertainty associated with them. These values were obtained from the plots of the primary sun sensor and Canopus sensor error signals (Figures 5.5-20 and 5.5-21).

The following gyro drift rates were determined approximately 6-1/2 hours prior to the start of the terminal attitude maneuver, and were used in the computation of a drift-compensated maneuver. It should be noted that had the gyro drift compensation been perfect no pointing error would have resulted from this source; however, the drift rates had to be used in the simulation of the pointing direction since the terminal attitude maneuver actually used was biased to compensate for these drift rates which are as follows:

Pitch = +0.6 deg/hr
Yaw = -0.8 deg/hr
Roll = +1.1 deg/hr

The desired terminal attitude maneuver was as follows:

Yaw = -157.90 degree
Pitch = - 76.78 degree
Roll = - 63.92 degree

From telemetry data the actual maneuver was as follows:

Yaw = -157.83 degree
Pitch = - 76.70 degree
Roll = - 63.95 degree

Assuming the validity of the determination of the actual maneuver and initial attitude errors listed above, the computer simulation gives a resultant

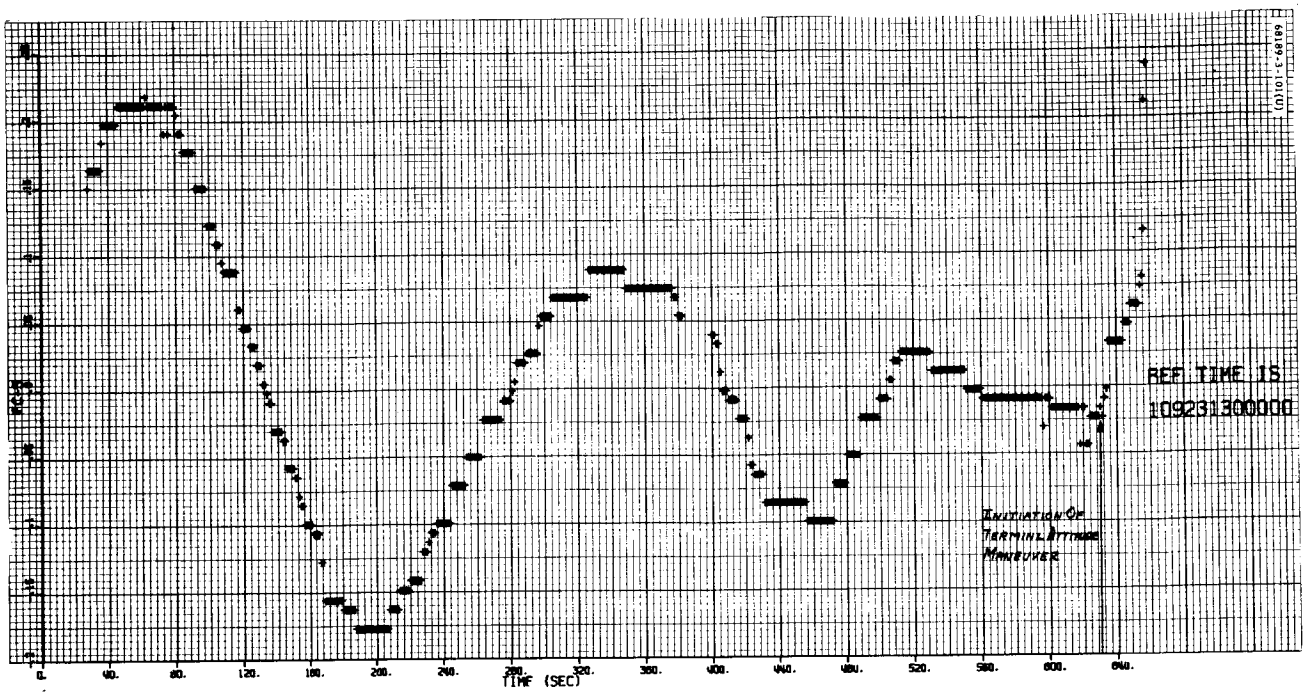

a) Pitch

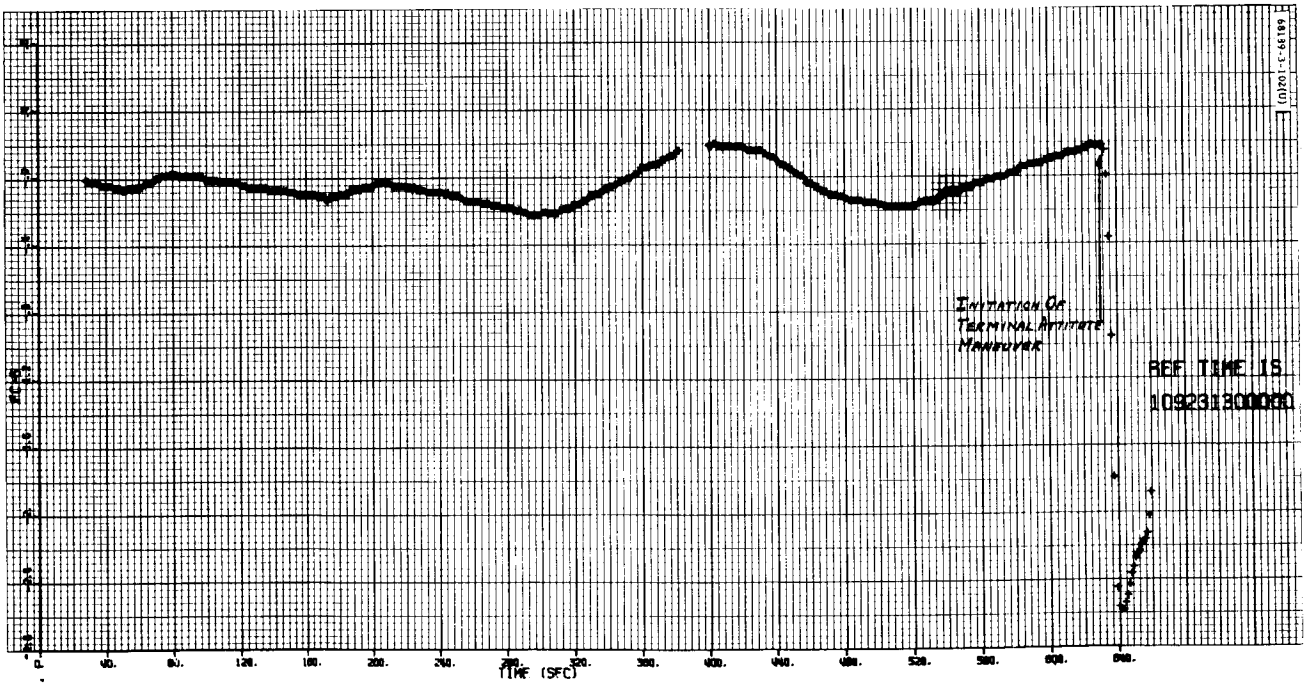

b) Yaw

Figure 5.5-20. Primary Sun Sensor Error Signals

pointing error magnitude of ≅0. 13 degree in a direction defined in Figure 5. 5-22. The magnitude of the pointing error, as determined from burnout conditions, was ≅0. 35 degree in a direction defined in Figure 5. 5-22. It would appear that there are essentially two reasons why the two independent determinations of the pointing error do not agree more closely: 1) the indeterminacy in obtaining more precise values of initial attitude errors, gyro drift rates, and actual maneuver negotiated; and, 2) error sources not considered. As an example of 1), a simulation was run with a change in drift rates to:

Pitch = +0. 63 deg/hr (a change of +0. 03)

Yaw = -0. 70 deg/hr (a change of +0. 10)

Roll = +1. 13 deg/hr (a change of +0. 03)

The resultant pointing direction as projected in the nominal spacecraft XY plane changed by ≅25 degrees. This is to be expected since the nominal and actual pointing directions were very nearly parallel.

Other error sources not considered were as follows:

1) Alignment of main retro thrust axis with respect to the sensor group roll axis

2) Tracking error

3) Control system stiffness

4) Inadequate compensation of g force loading on the sensor group

Due to the indeterminacy of the values of error sources considered in the simulation and to the error sources not considered at all, this technique can give only gross indications of the pointing error. Better results would be obtained only if a more detailed simulation model were used in conjunction with more precise values of the errors.

5. 5. 4. 10 Main Retro Phase

Main retro phase began at 110:00:01:12. 82 GMT with the indication of altitude marking radar mark and successfully ended at 00:02:12. 52 of the same day with the verification of retro eject. At the start of the RADVS-controlled descent phase, the longitudinal velocity was reduced to approximately 462 fps with a slant range of 36, 158 feet. The predicted values for burnout conditions were 445 fps at an altitude of 34, 734 feet.

During this phase, the function of the flight control system is to maintain the attitude of the spacecraft inertially fixed and to provide and execute a fixed sequence of commands to establish the necessary initial conditions for the vernier descent phase. The following analysis reveals that these functions were performed satisfactorily.

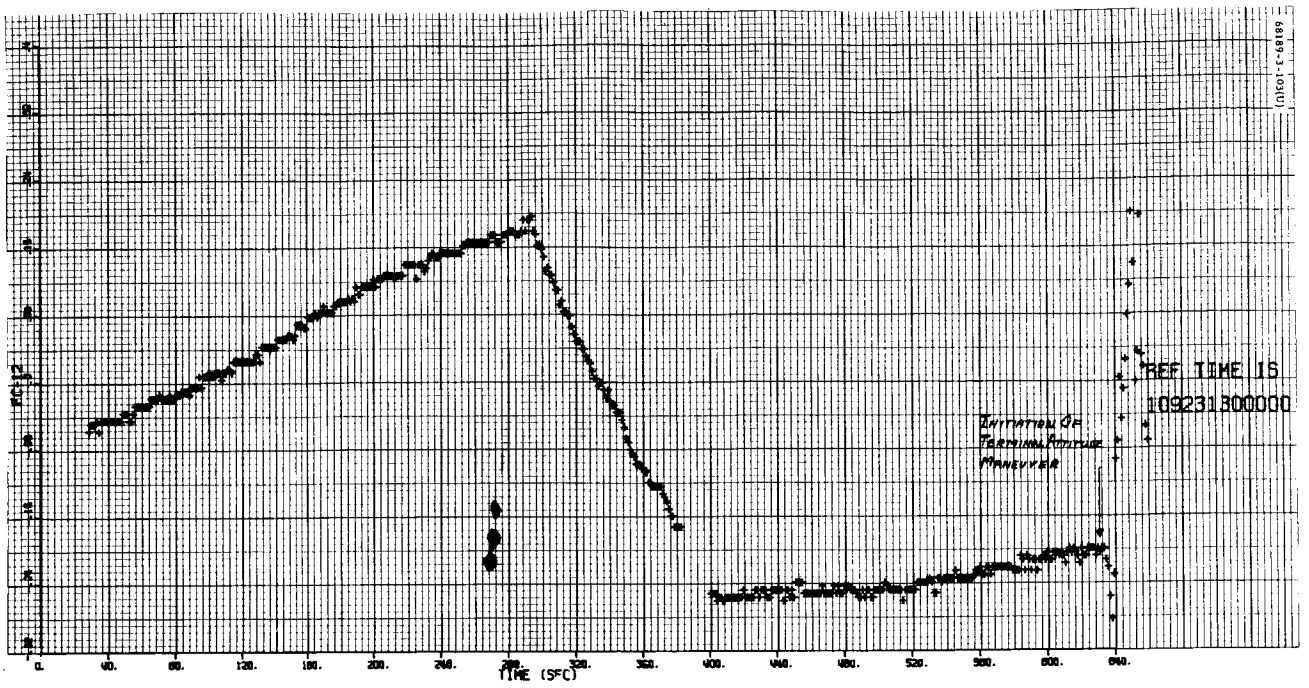

Figure 5.5-21. Canopus Sensor Error Signals

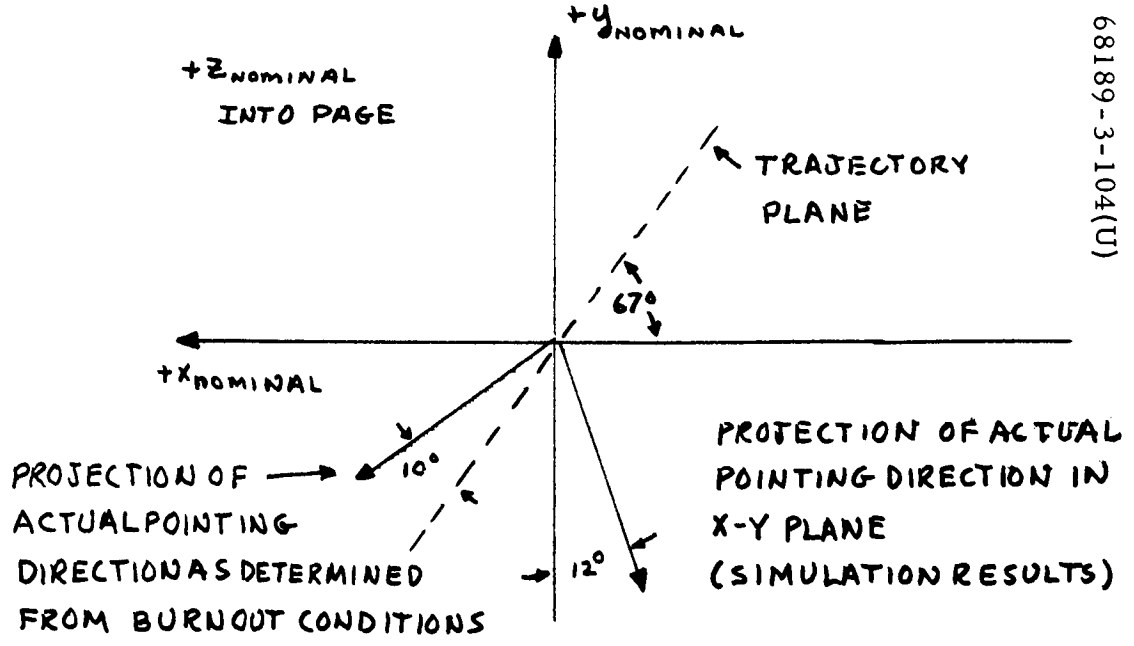

Figure 5.5-22. Resultant Pointing Error Direction

A list of retro phase events and their corresponding time of occurrence is given in Table 5.5-12 along with expected time intervals. These results confirm the performance of the magnitude register and programmer.

TABLE 5.5-12. TIME AND EVENTS LOG, RETRO PHASE

Main Retro Phase Event	Time of Occurrence, Day 110 GMT, hr:min:sec	Time Between Events, seconds	Expected Time Intervals, seconds
Altitude marking radar signal (FC-64)	00:01:12.82		
Vernier ignition (FC-28)	00:01:17.91	5.07	5.075
Retro ignition (FC-29)	00:01:19.01	1.100	1.1
RADVS on	00:01:19.88	0.87	0.55
Retro burnout (FC-30) 3.5 g switch	00:02:00.49	40.61	41.5 (retro burn)
Retro eject (FC-31)	00:02:12.49	12.0	12.0
Start RADVS-controlled descent (FC-42)	00:02:14.62	2.13	2.15

The following data confirm that the altitude marking radar mark occurred prior to emergency altitude marking radar:

	DSS Time
Altitude marking radar mark (FC-64)	00:01:12..830 ± 0.041
Emergency altitude marking radar	00:01:14.41 ± 0.15

The transmission time for emergency altitude marking radar command was obtained from Reference 16.

Ignition of the vernier engines during the main retro phase was executed smoothly, with impulse dispersions between engines well within the specification values. Again, the change in gyro angles due to a shift in reference

null at engine ignition limits the accuracy of the startup impulse dispersion calculations.

Retro Phase Attitude Control

During the main retro phase, extending from vernier ignition through case separation, spacecraft attitude motion was small in all three axes (Figure 5.5-23). Peak pitch and yaw inertial attitude motion, as read directly from gyro error telemetry data (FC-16 and FC-17), occurred at vernier ignition and amounted to +0.1 degree in yaw and -0.22 degree in pitch. Following ignition, static attitude error was virtually zero in both pitch and yaw axes. Roll inertial attitude error was less than 0.90 degree throughout the main retro phase (less than 1.0 degree is required).

Since all gyro error signals were maintained to within ±1.0 degree (during retro burn), each gyro was exercised less than 10 percent of the available travel range of more than ±10 degrees. A summary of pitch and yaw inertial attitude angles produced at various points in the retro phase is given in Table 5.5-13. No attitude disturbance was noted at retro eject, indicating a clean case separation.

TABLE 5.5-13. RETRO PHASE ATTITUDE CONTROL SUMMARY

Peak attitude motion, degrees

Event	Pitch	Yaw
Vernier ignition	-0.22	+0.1
Retro ignition	+0.06	-0.06
Retro burnout	-0.08	0
Retro eject	-0.08	0

Pitch and yaw control moments generated by the vernier engines were estimated by means of the following equations:

$$L_x = -2.969\ T_1 + 0.5723\ T_2 + 2.397\ T_3$$

$$L_y = -1.053\ T_1 + 3.098\ T_2 - 2.045\ T_3$$

where L_x and L_y are pitch and yaw control torques (ft-lb), respectively, and T_1, T_2, and T_3 are thrusts (pounds) generated by engines 1, 2, and 3,

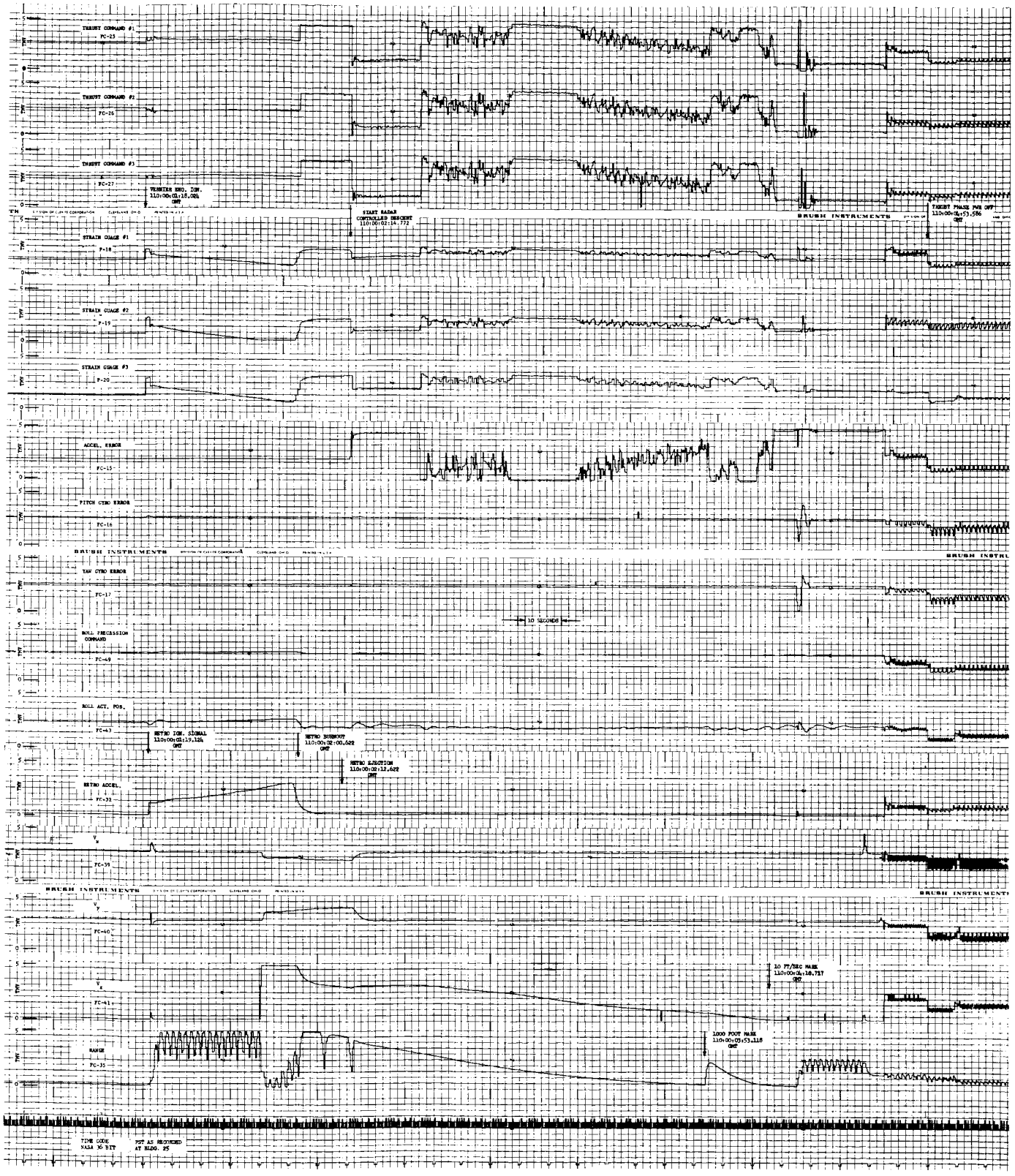

Figure 5.5-23. SC-3 Terminal Descent

respectively. Values for T_1, T_2, and T_3 were estimated from the thrust command telemetry signals (FC-25, FC-26, and FC-27) (Figure 5.5-24). As indicated by the telemetry data, very little throttling of the engines occurred during the retro period. Shortly after retro ignition, differential throttling equivalent to approximately 32.0 ft-lb of control torque were produced. At all other times during the retro burn period, there was essentially no differential engine throttling.

The maximum thrust vector to center of gravity offset can be estimated using this maximum control torque magnitude of 32 ft-lb. Assuming a 9550-pound retro thrust, the offset was estimated as

$$\text{Maximum center of gravity offset} = \frac{32.0 \text{ ft-lb}}{9550 \text{ pounds}} \times \frac{12 \text{ inch}}{\text{feet}}$$

$$= 0.04 \text{ inch}$$

This compares to the required value of 0.18 inch (Reference 15).

The maximum attitude error produced by the retro disturbance torques was also determined from the maximum torque magnitude of 32 ft-lb. Since the static gain (stiffness) of the pitch and yaw attitude control loops is

$$\text{static gain} = 1200 \text{ ft-lb/deg}$$

the maximum static attitude error is estimated to be

$$\text{maximum static error} = \frac{32}{1200} = 0.027 \text{ degree}$$

which is less than the allowable value of 0.12 degree.

5.5.4.11 Terminal Descent Phase

The RADVS-controlled terminal descent phase began at 110:00:02:14.62 GMT with initiation of the minimum acceleration (4.85 ft/sec^2) mode and a spacecraft attitude maneuver to null lateral velocities and align the thrust axis with the total velocity vector. The initial conditions at this time included a vertical velocity of 462 fps and a slant range of 36,158 feet. The lateral velocities (V_x = -85.3 fps, V_y = +148 fps) were nulled within 5 seconds (9 seconds allowed) and remained essentially at zero to first touchdown. It was estimated that the spacecraft roll axis was maneuvered through a total angle of 21 degrees.

Intercept of the descent line segments occurred at approximately a vertical velocity of 495 fps and a slant range of 22,300 feet. The descent segment tracking performance of the flight control system (Figure 5.5-25) was normal until loss of reliable radar operation (loss of lock on beam 3) occurred approximately 30 feet above the lunar surface. This caused the

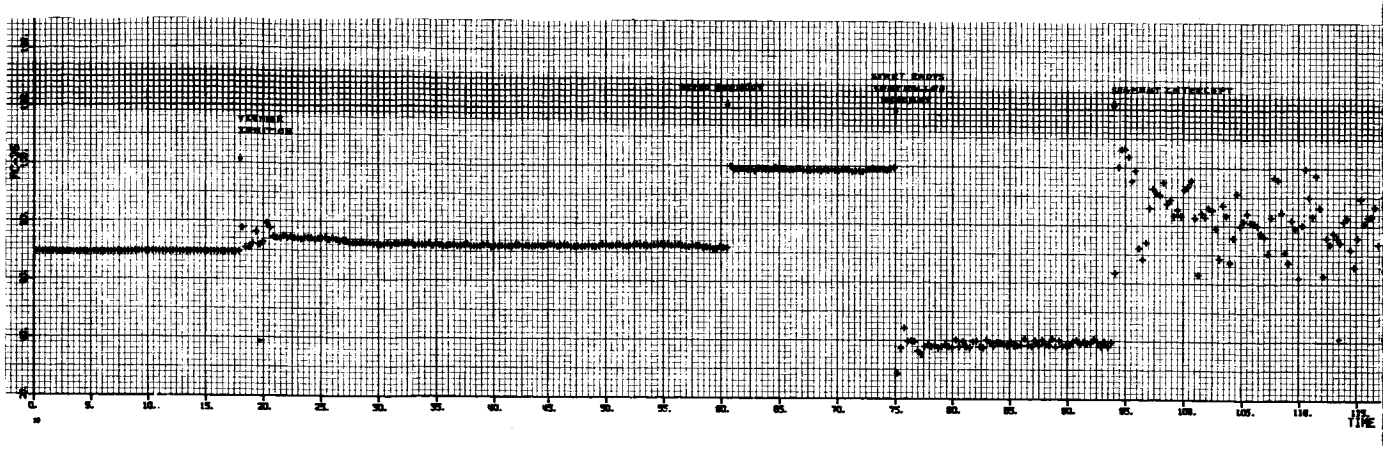

a)

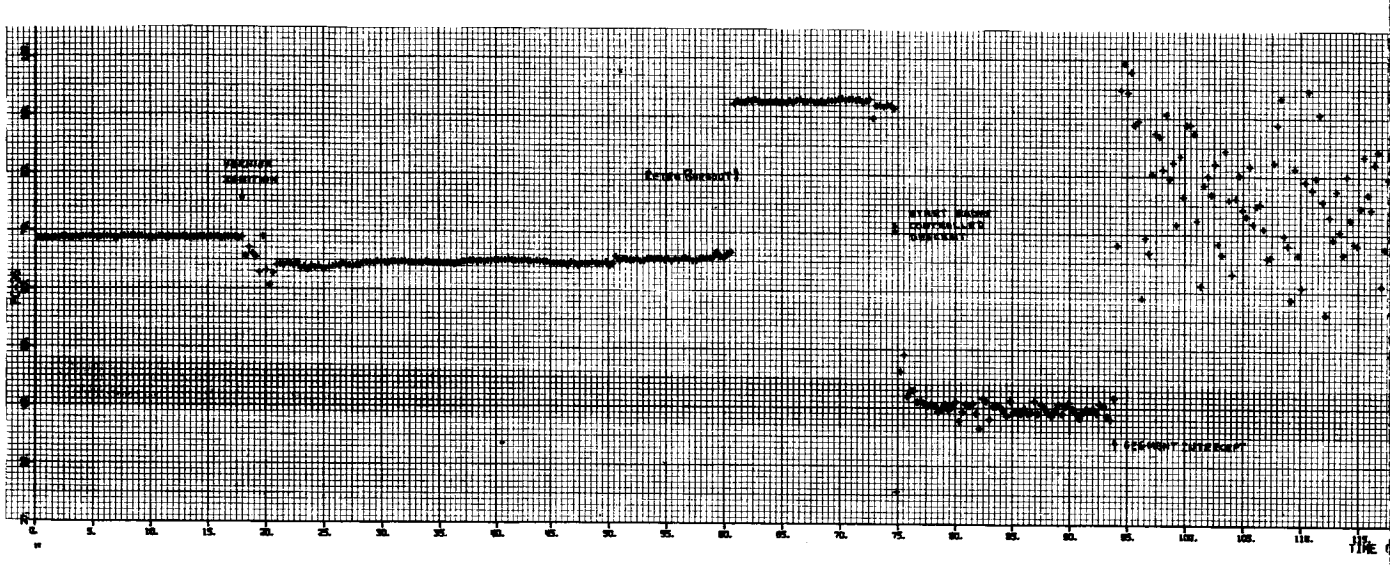

b)

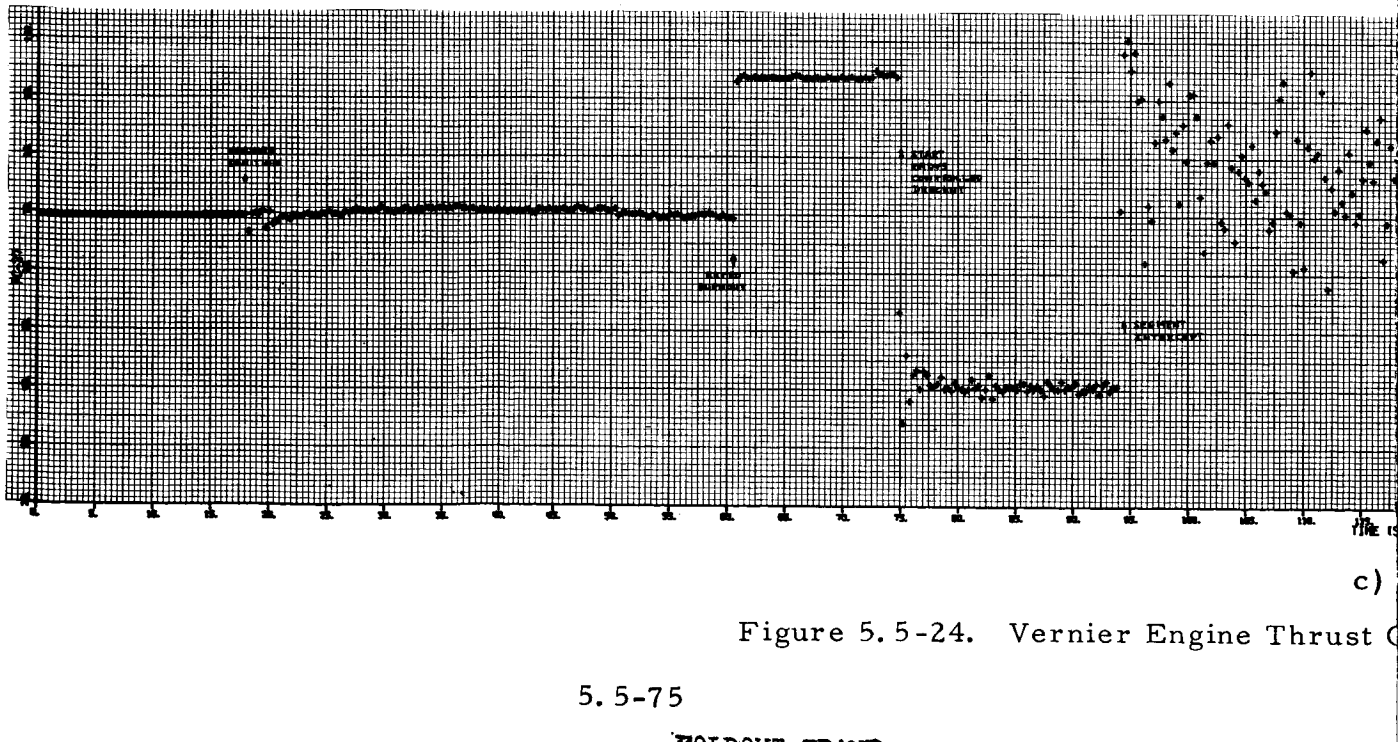

c)

Figure 5.5-24. Vernier Engine Thrust C

FOLDOUT FRAME

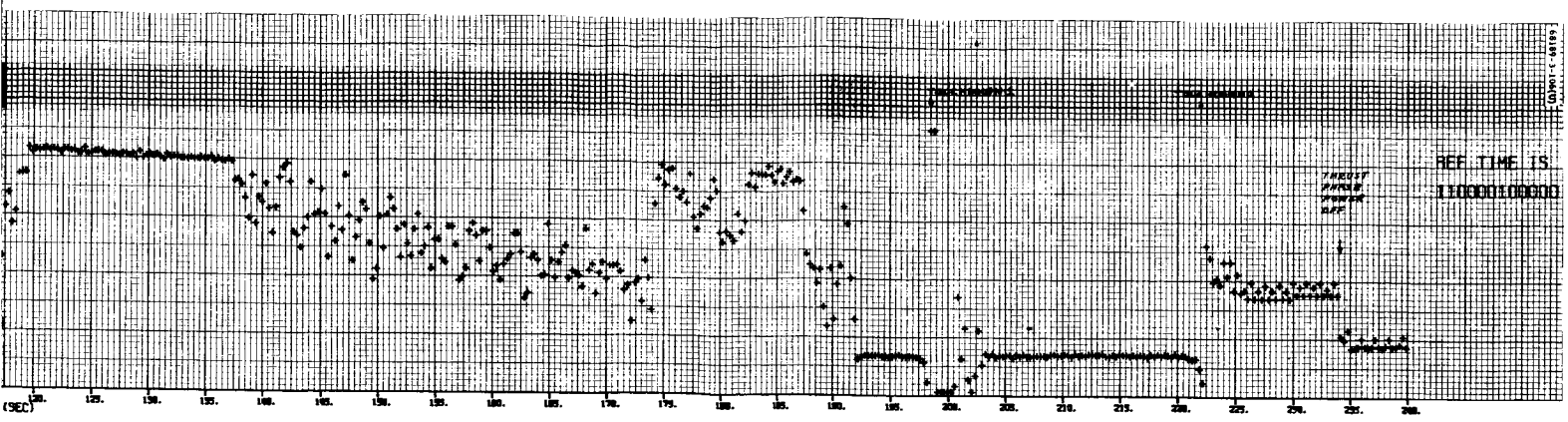

Engine 1

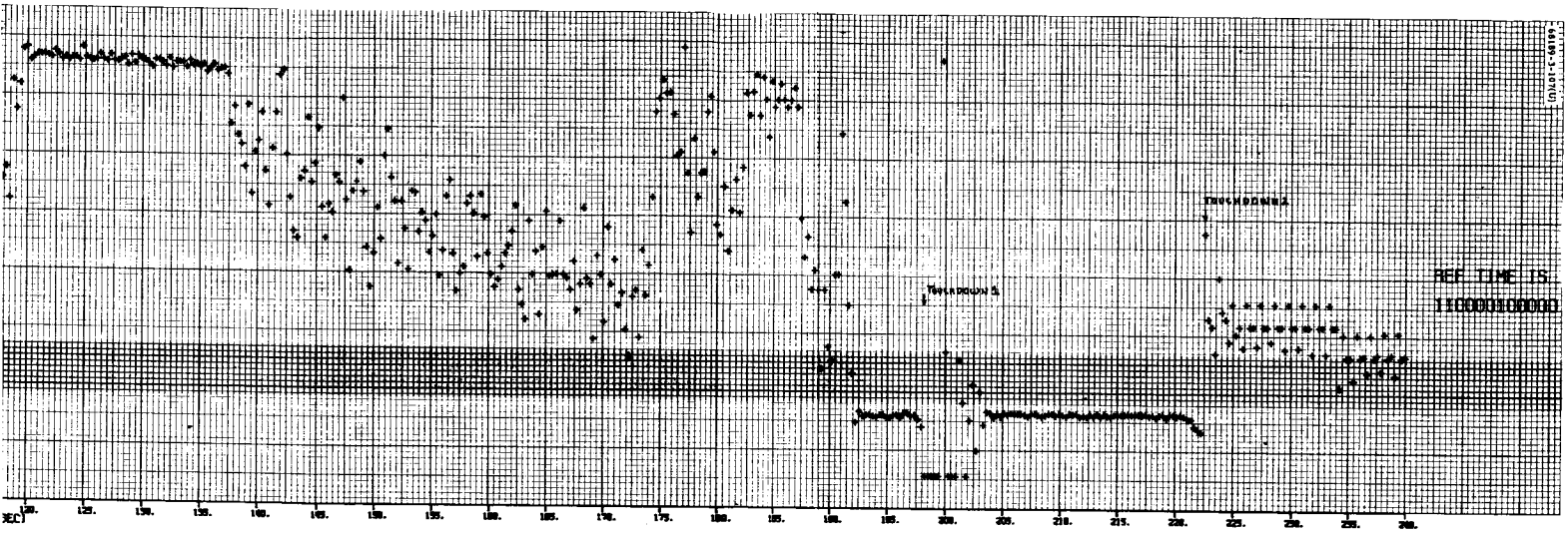

Engine 2

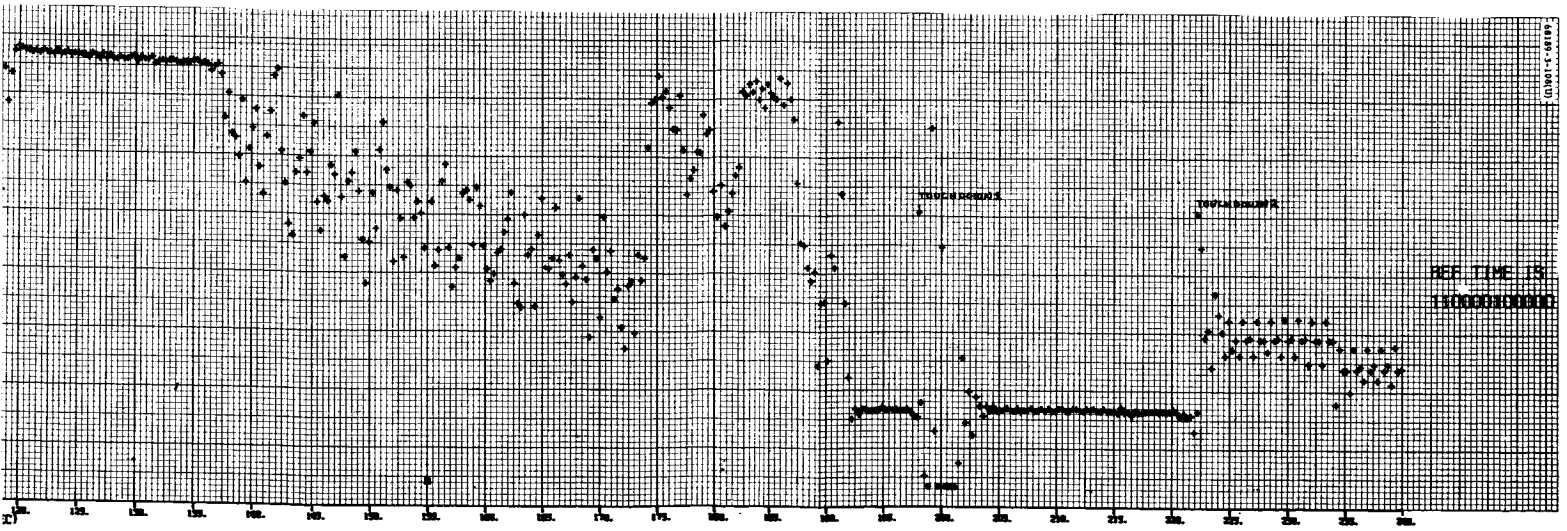

Engine 3

ommands During Retro Phase Attitude Control

FOLDOUT FRAME

5-5-76

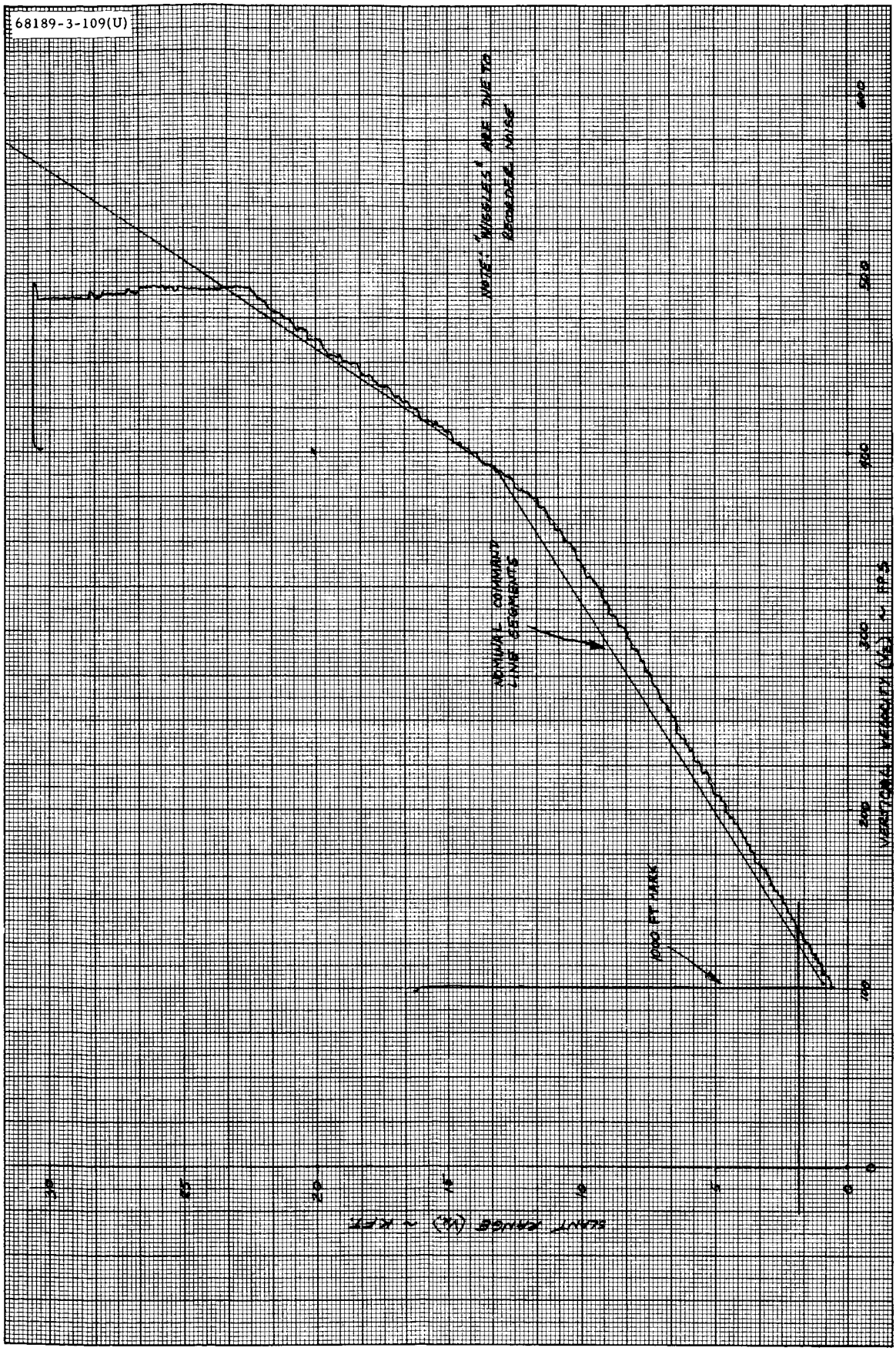

a) Above 1000 Feet

Figure 5.5-25. Range Versus V_z

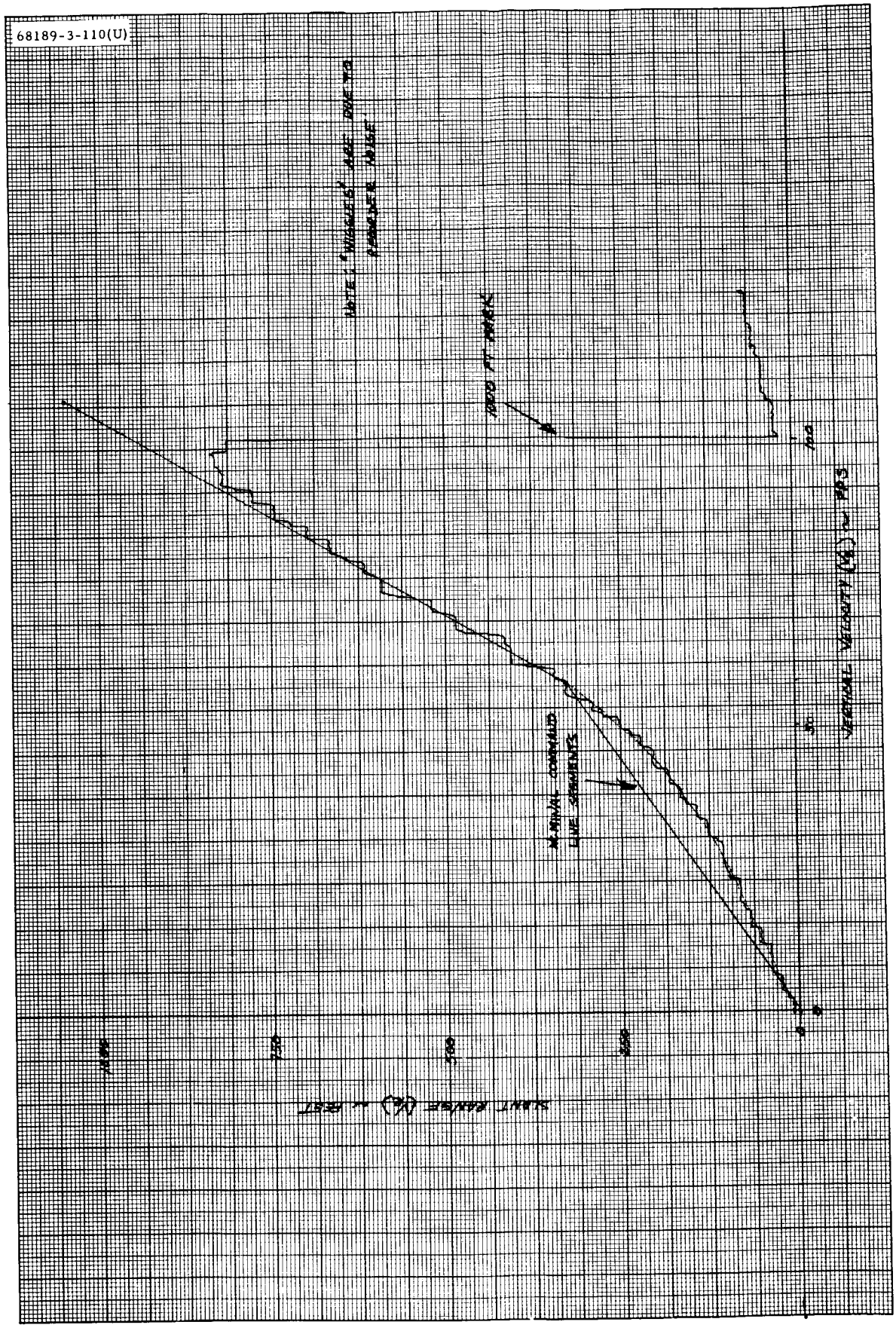

b) Below 1000 Feet

Figure 5.5-25 (continued). Range Versus V_z

flight control system to revert to the minimum acceleration (0.9 g_m) mode from the normal 5-fps mode; the 14-foot mark was therefore not generated and the vernier engines continued to burn to touchdown. The spacecraft acceleration was 0.1 g_m for approximately 4.5 seconds, thereby producing a vertical velocity of between 7 and 8 fps at touchdown. The resulting attitude error due to landing on a slope caused an increase in the vernier engines thrust which combined with the rebound action of the legs to make the spacecraft rise from the surface. The spacecraft attitude was immediately stabilized, and the vernier engines throttled down to maintain the commanded 0.9-g_m level. Approximately 24 seconds after the first touchdown, the spacecraft landed again and the hopping sequence was repeated. Approximately 1.0 second before the third touchdown (12.5 seconds after the second), DSS-11 commanded the vernier engines off. Analog telemetry data became erroneous at the second touchdown.

A list of pertinent terminal descent events and times of occurrence are presented in Table 5.5-14.

Vernier Descent Attitude Control

Spacecraft attitude motions determined from gyro error telemetry signals (FC-16, -17, and -49) were maintained to less than ±1.0 degree in each axis during the vernier descent phase.

Following generation of the RODVS signal and the delayed burnout signal, the spacecraft initiated an attitude maneuver to align the thrust axis with the total velocity vector. Initial velocity conditions preceding the maneuver were as follows (taken from RADVS telemetry data, FC-39, FC-40, and FC-41) (see Figures 5.5-26, 5.5-27, and 5.5-28).

Premaneuver velocity conditions 02:14.64 GMT were as follows:

V_x = -85.3 fps

V_y = +148 fps

V_z = +462 fps

The alignment maneuver was completed in less than 5 seconds (9 seconds allowed), after which time V_x and V_y were held at zero and V_z became equal to the total velocity of 490 fps. The attitude maneuver magnitudes were computed as follows:

$$\text{Pitch maneuver: } \Delta\theta_x = \tan^{-1}\frac{V_y}{V_x} = 10.4 \text{ degrees}$$

$$\text{Yaw maneuver: } \Delta\theta_y = \tan^{-1}\frac{V_x}{V_z} = 18.4 \text{ degrees}$$

The spacecraft Z-axis was therefore maneuvered through 21.1 degrees.

TABLE 5.5-14. TERMINAL DESCENT PHASE LOG OF EVENTS, DAY 110

Event	GMT, min:sec
RORA off	02:13.49
Start of RADVS-controlled descent (minimum acceleration)	14.64
RORA on	15.89
Segment intercept	33.99
1000-foot mark	03:53.02
10-fps mark	04:10.62
RORA and RODVS off	13.49
5 fps (minimum acceleration mode)	13.80
Touchdown 1 (all beams unlock and switch to gain 3)	18.05
Touchdown 2 (analog data bad)	42.03
Thrust phase power off	53.59
Touchdown 3	54.42
RADVS off	10:35.90
Flight control power off	10:40.02

Measurable gyro gimbal errors (equivalent to spacecraft lateral velocity errors for pitch and yaw prior to the 10-fps mark) occurred during certain portions of the vernier descent phase (Table 5.5-15).

Radar Performance

The following is excerpted from Reference 17 which presents an extensive discussion of the most probable cause of loss of the 14-foot mark during the final stages of the SC-3 terminal descent. The cause is attributed to the sidelobe logic rejection of the main beam.

To demonstrate how the sidelobe logic could have caused the break lock, the cross-coupled sidelobe logic and the pertinent characteristics of RADVS performance during the period of break lock will be described. The logic is such that it determines the validity of a particular signal to which it is locked by comparing it with the adjacent beam on a doppler frequency and amplitude basis. (On SC-4 and subsequent systems, this logic exists between each pair of beams. On SC-3, it only exists between beams 2 and 3.) The criteria for the signal to be classified as a sidelobe are as follows:

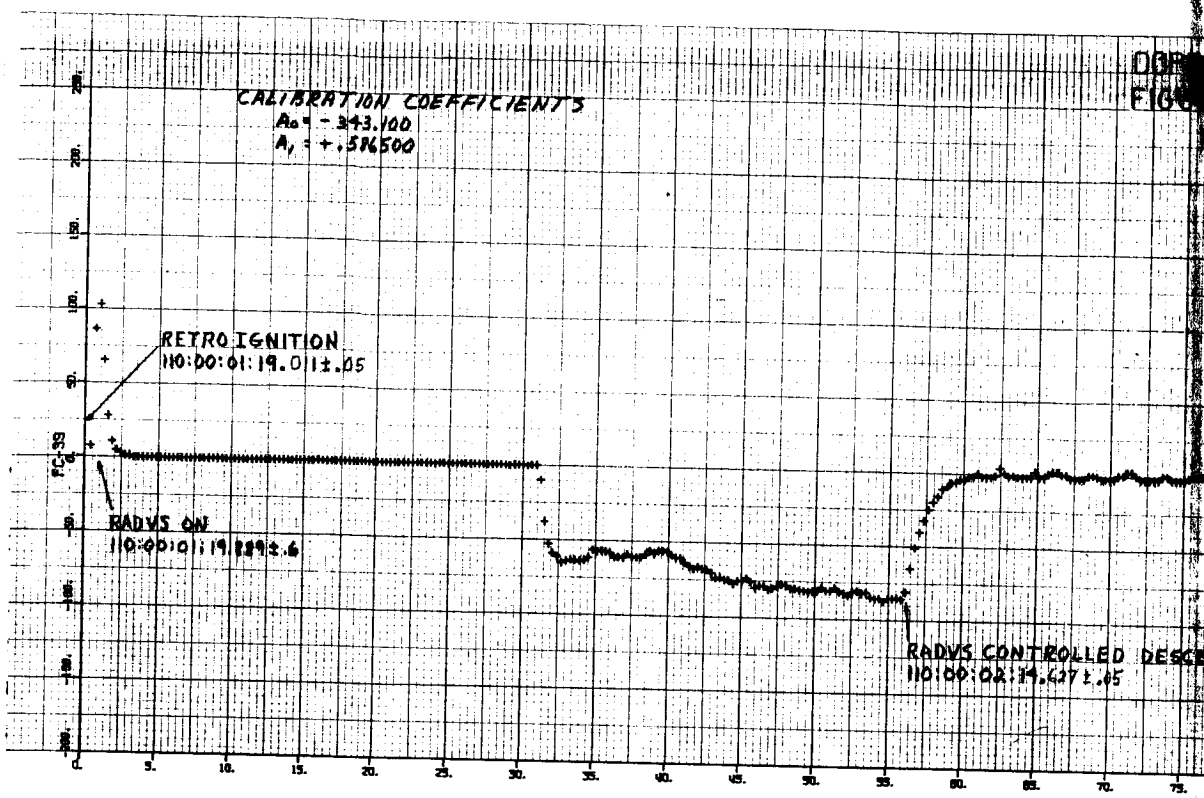

Figure 5.5-26. Doppler Velocity, V_x

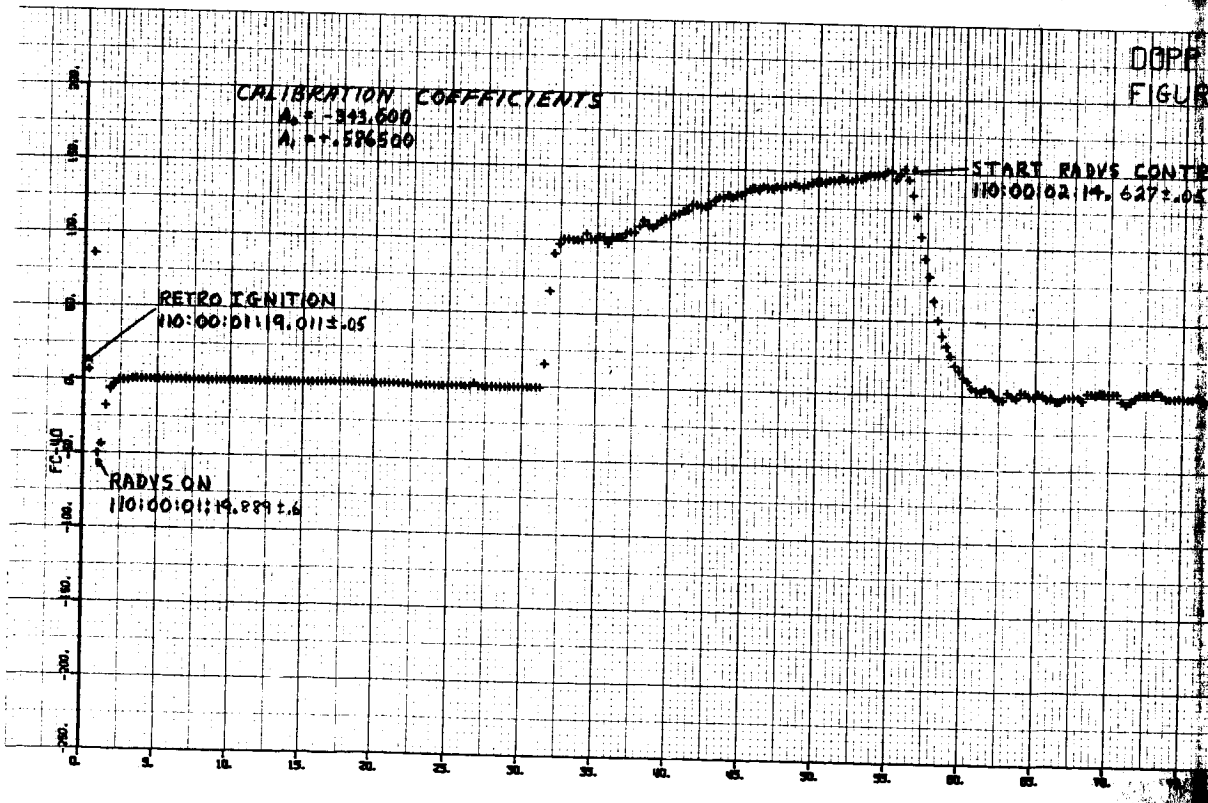

Figure 5.5-27. Doppler Velocity, V_y

FOLDOUT FRAME

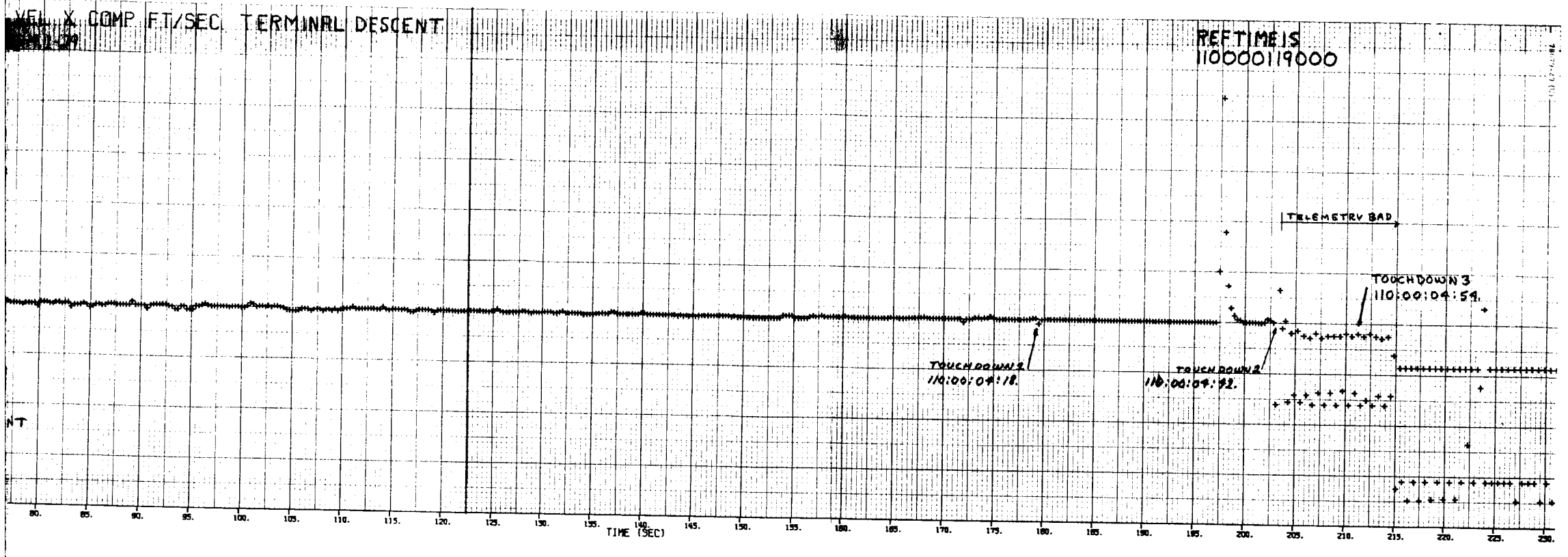

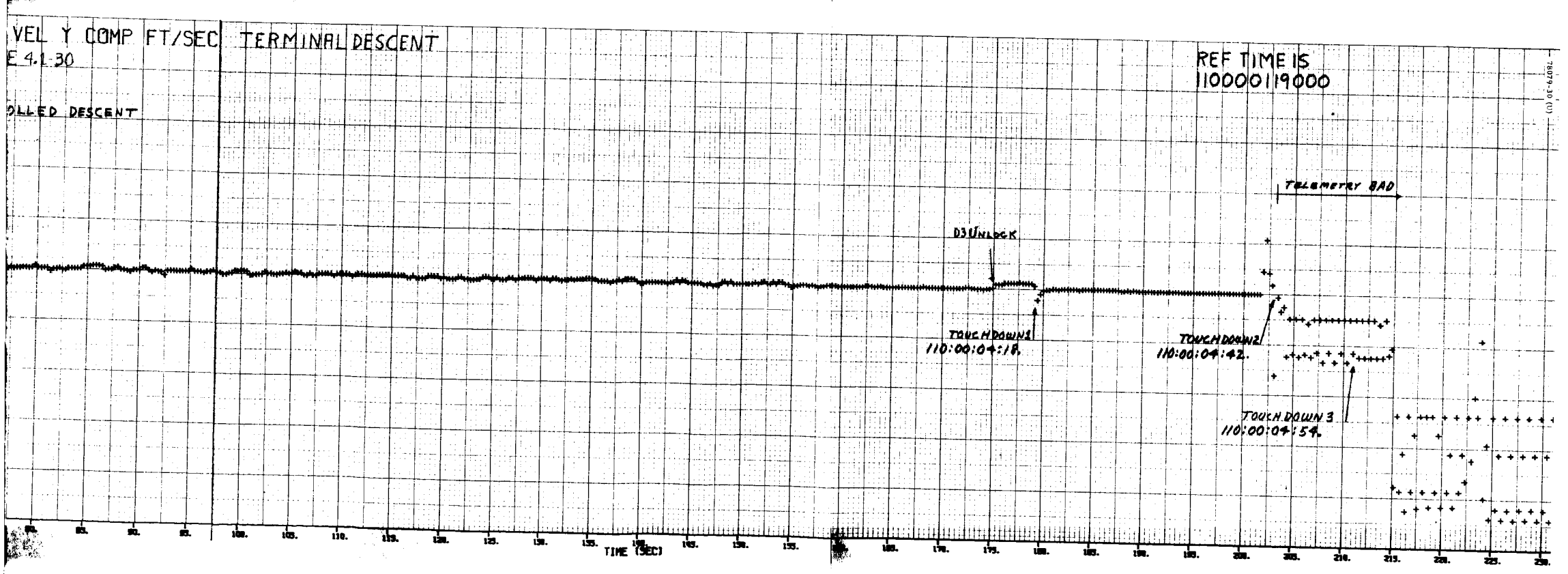

FOLDOUT FRAME

FOLDOUT FRAME

5-5-82

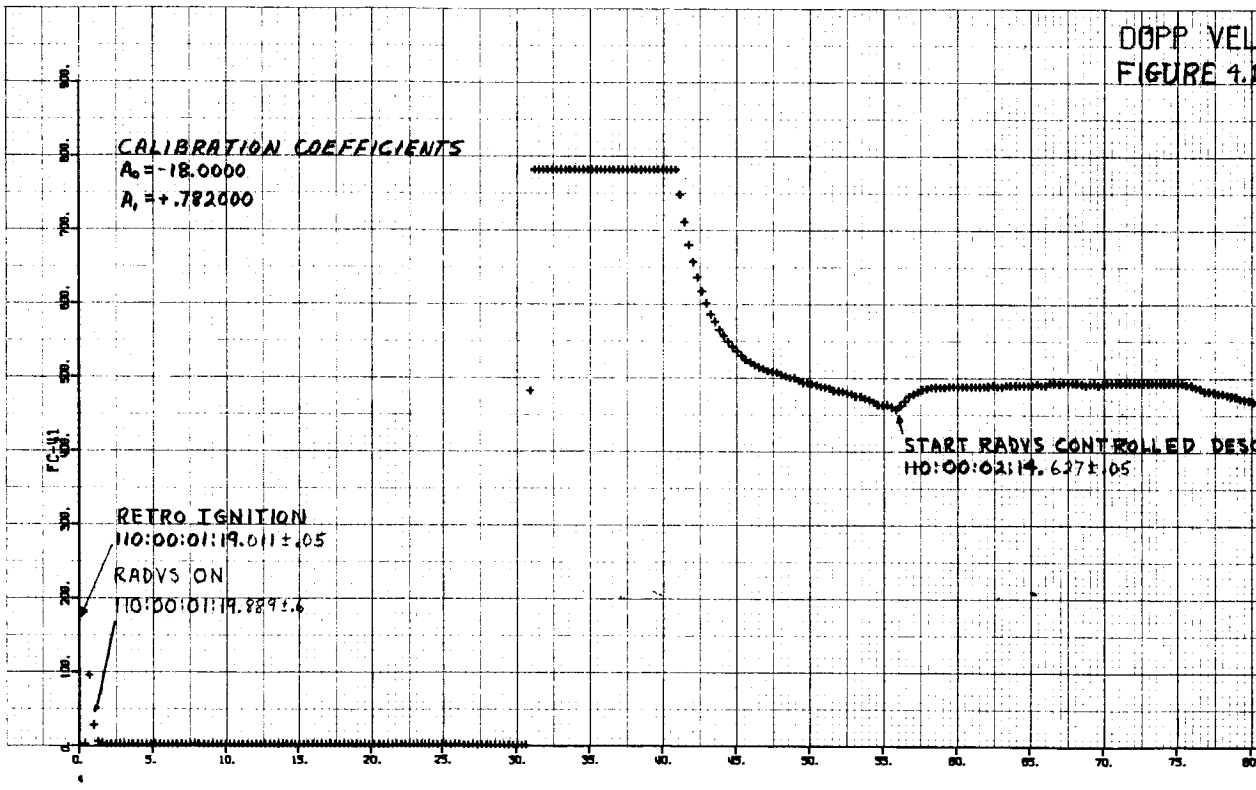

Figure 5.5-28. Doppler Velocity, V_Z

FOLDOUT FRAME

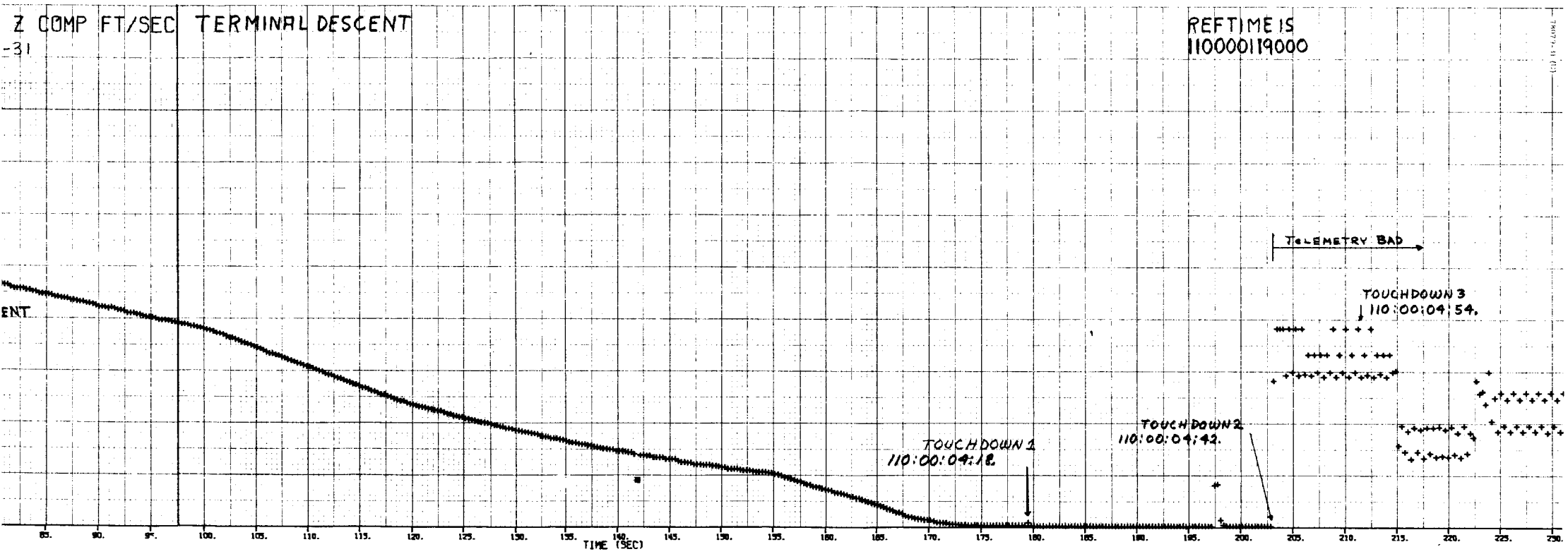

FOLDOUT FRAME

FOLDOUT FRAME

5.5-84

TABLE 5.5-15. PEAK GYRO GIMBAL ERRORS, DEGREES

Phase of Descent	Pitch	Yaw	Roll	Roll Actuator
Start of alignment to velocity vector	-0.31	-0.30	+0.1	-0.1
Segment intercept	-0.15	0	-0.82	+1.16
R < 1000 feet	<0.4	<0.2	<0.9	<1.1
Touchdown 1	6.0	>6.0*	+0.17	-0.54

*Telemetry saturated.

Sidelobe criteria

1) The two trackers must be locked.

2) The frequency difference between the two returns must be less than 1200 Hz (SC-3 only).

3) The amplitude difference must be at least 25 db. (On SC-4 and subsequent spacecraft, this delta varies with the beam combination.)

4) On SC-3, the gain states must be different. (The SC-4 logic functions in equal gain states as well so that this criteria vanishes.)

During the final seconds of the SC-3 mission and just prior to the loss of lock on beam 3, both beam 2 and 3 indicated lock. This satisfies criteria 1. The spacecraft was erected to the lunar vertical and its descent was vertical so that the doppler frequencies on beam 2 and 3 should have been well within the required 1200 Hz of one another, thereby satisfying criteria 2. Immediately prior to the break lock, beam 3 was in gain state 3 (90 db) and beam 2 was in gain state 2 (65 db), which satisfies criteria 4. This leaves only criteria 3 to be satisfied.

With beam 3 in the 90-db gain state, an additional amplifier rolloff of about 12 db/octave is now in the beam 3 signal path. Beam 2 does not have this additional rolloff to account for so that the amplitude criteria at low frequencies (~5 fps) is reduced to an actual difference of some 5 db instead of the 25 db stated (this being due to the difference in preamp rolloffs). The lunar reflectivity signals for the various beams indicate wide variations at this time so that a difference of 5 db for 0.4 second is quite reasonable, either due to a signal fade in beam 3 or an increase in return to beam 2, or a combination. The main beam area of illumination for any one beam at 40 feet is approximately 3 or 4 feet in diameter, so that small surface irregularities would be noticed in beam return. Also, even in a vertical descent,

the beams transverse the terrain since they are tilted to the spacecraft axis. Thus, it is concluded that criteria 3 may easily have been satisfied also.

It is seen, therefore, that all conditions were satisfied, or at least could have been, making the break lock occur normally and not as a result of some component failure or other system malfunction. The margin against a break lock caused by the signal dropping below threshold is in the order of 49 db, making this an extremely low probability of occurrence. All data analyzed to date tend to reenforce this supposition and none yet negates the theory.

A further reenforcement of the supposition of crosscoupled sidelobe rejection causing the break lock may be found in considering the geometry of the approach. Beam 4 essentially was illuminating an area directly below the spacecraft from at least 1000 feet to the first touchdown. This circle of illumination would be approximately 88 feet in diameter. For a vertical descent, the area illuminated by all beams from about 90 feet altitude until touchdown would lie within the original 88-foot circle (Figure 5.5-29). If the lunar surface characteristics were responsible for the low signal return (and apparent scintillation) of beam 4, then the variations in apparent signal strength as observed in the other beams from 90 feet down could be a result of these same characteristics.

Logic Modification

A simple fix has been developed for the problem cited. Since the probability of either a sidelobe acquisition or a mainbeam break lock below 1000 feet attitude is extremely remote, it is planned to lock out the sidelobe logic with the 1000-foot mark. The sidelobe logic protection is really only needed until the vehicle is erected to the lunar vertical. From this point on in the trajectory, as a sidelobe is received by an antenna, the mainlobe is superimposed and much stronger, so that no deleterious effects are experienced. In short-term mainlobe dropouts, even if the sidelobe is acquired briefly, relock to the mainlobe will occur as soon as it reappears. This means that any time after about 10 to 30 seconds of steering the sidelobe logic is no longer needed. The first available signal that could be used to disable the logic is the 1000-foot mark signal generated within the signal data converter.

The exact mechanization chosen for this modification was largely dictated by packaging considerations. There are obviously many ways to disable the logic and, consequently, the one easiest to implement in hardware already built was chosen. Figure 5.5-30 shows how the disable function has been added. Once the 1000-foot mark is generated, the disable input to the inhibit gate is a logical "0," causing the frequency comparison input to the crosscoupled sidelobe logic and gate to be a "0," thereby negating the logic.

Circuit and Mechanical Design

This change consists of adding another input to each of three gates in the A14 frequency detector submodule. The inputs are generated by a transistor switch circuit which is controlled by the 1000-foot mark signal (Figure 5.5-31).

Analysis of the 1000-foot mark circuit loading indicates adequate margin with the added switch. Protection of the circuit from telemetry commutator noise is provided by a 100K resistor to -29 volts dc in the flight control sensor group. The transistor selected is rated at approximately 10 milliamperes. The load on the transistor will be less than 2 milliamperes.

Failure of the added circuit would result in a loss of all or part of the inhibit function at 1000 feet, but would not affect the operation of either the 1000-foot mark or the logic circuitry.

Physically, this modification consists of a new submodule which is bonded to the logic motherboard assembly. Wire leads from the new submodule pick up the desired circuit connections:

1) Gate inputs on the A14 submodule.

2) +25 volts dc and ground from the motherboard interconnections.

3) The 1000-foot mark from pin 5 of the logic motherboard. (By fortunate coincidence, this signal was on this pin, although not used in this motherboard subassembly.)

At the lead terminations, connection is made with existing circuitry by wrapping the lead around an existing component lead protrusion and resoldering both to the existing etched circuit pad. The wires are dressed and hysol coated for mechanical attachment to the subassembly. (This technique has been proven in use on other modifications and etch circuit repairs within units.)

Crosscoupled Sidelobe Logic Telemetry Signal

Because of the complexity of this logic (some 700 to 850 components), it would be extremely desirable to add a telemetry signal to give an indication of a forced break lock. Two spare channels are available in word 12, mode 6. A circuit addition of a gate in the signal data converter and wiring changes to both the signal data converter and spacecraft harness would allow the monitoring of the three forced loss signals on a single telemetry channel. This would be satisfactory, since other data, such as tracker lock signals, would identify the channel that forced it into search. The feasibility and advisability of making this change will be further pursued with the hope of incorporating it into later spacecraft.

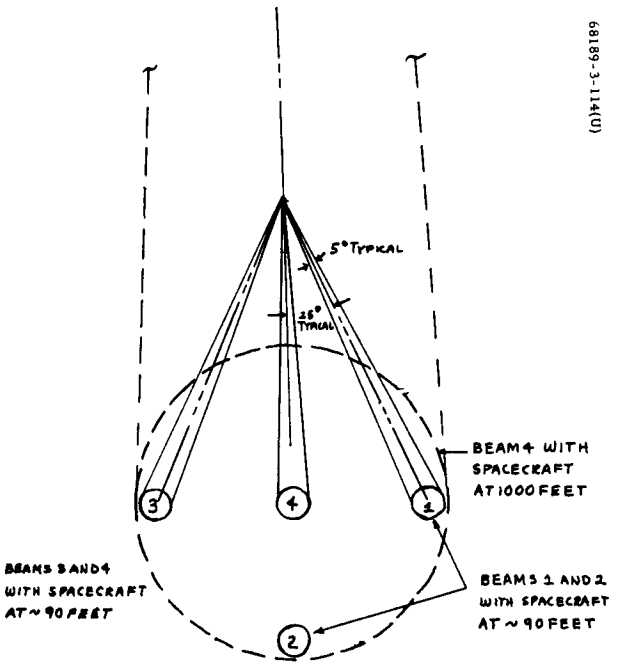

Figure 5.5-29. RADVS Illumination Patterns at 1000- and 90-foot Altitudes

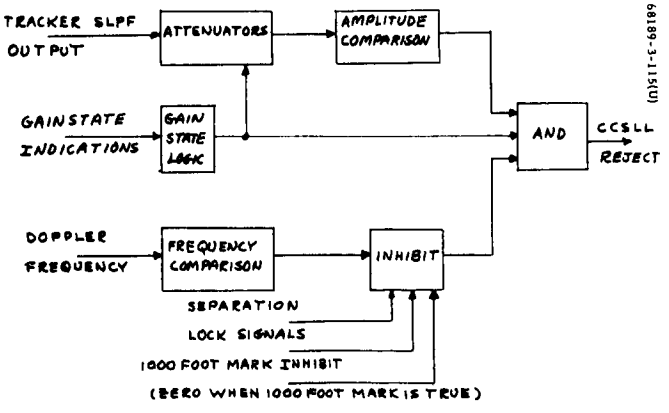

Figure 5.5-30. Crosscoupled Sidelobe Logic Block Diagram

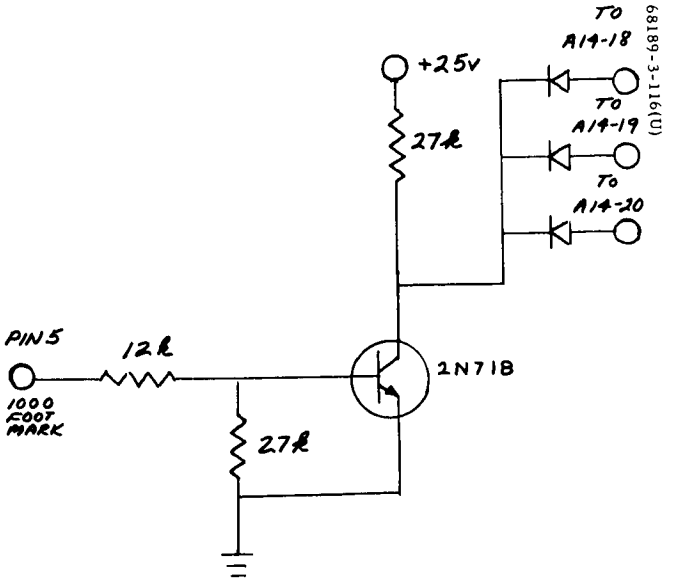

Figure 5.5-31. Crosscoupled Sidelobe Logic Inhibit

5.5.4.12 Nitrogen Gas Consumption Summary

The estimated nitrogen gas consumption for the Surveyor III mission is shown in Table 5.5-15. It was assumed that exactly 4.6 pounds of nitrogen was loaded prior to launch. Since the prelaunch estimate of nitrogen weight using telemetered data indicated that 4.63 pounds were on board, all subsequent estimates were corrected by 0.03 pound. The actual and expected values compare favorably up to the point after midcourse.

TABLE 5.5-15. SC-3 NITROGEN GAS CONSUMPTION

GMT	Telemetry		Nitrogen Remaining, pounds	
	FC-4, psi	FC-48, °F	Actual	Expected (nominal)
107:07:31 Prelaunch	4815	83	4.6 (4.63)*	4.6
107:08:27 After sun acquisition	4689	85.7	4.49 (4.52)	4.5
108:05:48 After midcourse	3598	37.2	4.1 (4.13)	4.2
109:13:44	3495	50.4	3.87 (3.9)	—
109:23:23			3.8	—
109:23:47 (After term maneuvers)			3.66**	—

*Before 0.03-pound correction.

**Based on estimated consumption for maneuvers as follows:

Yaw	0.034 pound
Pitch	0.068 pound
Roll	0.041 pound

It was estimated that this mission used about 0.94 pound of nitrogen up to the time of retro ignition. This compares with 0.68 pound for the Surveyor I mission. The difference, 0.26 pound, is relatively unimportant to the mission, but can be reconciled by considering the number and types of maneuvers accomplished by Surveyor III (in comparison with the Surveyor I. For midcourse and preretro maneuvers, the Surveyor III mission included three pitch, two roll, and one yaw gyro precessions. Surveyor I accomplished four roll and two yaw precessions. The difference in fuel consumption (for typical maneuvers) between the two missions is

$$3\,(0.068) + 2\,(0.041) + (0.034) - 4\,(0.041) - 2\,(0.034) \cong 0.09 \text{ pound}$$

Also, it is noted that the Surveyor III mission had seven more gyro drift checks than did Surveyor I. The additional lockon transients (each gyro drift check terminates with one) account for all the remaining 0.17-pound difference in nitrogen utilization as discussed in subsection 5.5.4.5.

5.5.5 REFERENCES

1. "AC-12 Post Flight Data Review," GDA Report.

2. "Functional Requirements," Hughes Specification 224510.

3. R. H. Bernard, "Limit Cycle Behavior of the Surveyor Gas Jet Attitude Control System With Simulated Canopus Sensor Noise," Hughes Aircraft Company IDC 2223/772, 15 February 1965.

4. K. Kobayashi, "A Method for Determining Gas Jet Thrust Level – Post Mission Analysis," Hughes Aircraft Company IDC 2253.4/25, 1 March 1966.

5. G. L. Puckett, "SC-3 Flight Control Data Package," Volume II, 10 April 1967.

6. R. H. Bernard, "Restoration and Updating of Surveyor Coast Phase Analog Computer Mechanization," Hughes Aircraft Company IDC 2223/77, 29 July 1964.

7. R. H. Bernard, "Surveyor Sun Acquisition With the A.S.S. Oriented to Include the Roll and Pitch Uses," Hughes Aircraft Company IDC 2223/540, 14 December 1964.

8. R. H. Bernard, "Revised Gas Jet Fuel Consumption for 66-hour Mission," Hughes Aircraft Company IDC 2223/843, 19 February 1965.

9. E. I. Axelband, "Analysis of Inertial Pointing Accuracy of Surveyor Midcourse Thrust Vector," Hughes Aircraft Company IDC 2242/2706, 17 June 1963.

10. H. D. Marbach, "Angular Rates at Midcourse Shutdown," Hughes Aircraft Company IDC 2223/731, 3 February 1963.

11. "Interface Document, Surveyor Vernier Propulsion Thrust Chamber Assembly," Hughes Specification 287015.

12. "Spacecraft Flight Control Subsystem," Revision E, Hughes Specification 234600.

13. R. P. Crook, "FCEU Thrust Command T. M. Circuit-Accuracy," Hughes Aircraft Company IDC 2223/2850, 11 May 1967.

14. "Standard Transit Sequence of Spacecraft Operations," Hughes Specification 224550.

15. O. N. Hertzmann, "SC-3 RADVS Performance Evaluation," Hughes Aircraft Company IDC 2223/2891, 8 May 1967.

5.5.6 ACKNOWLEDGEMENTS

J. Angerman, Technical Coordinator

O. N. Hertzmann

B. N. Smith

L. R. Stumpf

R. H. Bernard

P. L. Welton

M. R. Buehner

T. L. Parker

5.6 VERNIER ENGINE SUBSYSTEM

5.6.1 INTRODUCTION

5.6.1.1 System Description

The Surveyor vernier propulsion system (VPS) is a bipropellant, variable thrust, liquid rocket system utilizing an oxidizer composed of 90 percent nitrogen tetroxide and 10 percent nitric oxide (Mon 10) and a fuel composed of 72 percent monomethyl hydrazine and 28 percent water (Figure 5.6-1). The VPS consists of three regeneratively-cooled thrust chambers (TCAs) with radiation-cooled expansion cones. Each TCA has a variable thrust range from 30 to 104 pounds vacuum thrust.

Propellant is supplied to the TCAs from six tanks employing positive expulsion bladders. One fuel tank and one oxidizer tank supply each TCA and are located adjacent to the TCA near each of the three spacecraft landing legs.

Propellant expulsion is accomplished by pressurizing the propellant tanks on the gas side of the bladders with helium gas. The helium is stored under high pressure in a spherical pressure vessel. The helium tank, together with the pressure regulator, dual check and relief valves, and servicing connections, is mounted outboard of the spaceframe between landing legs 2 and 3.

Thermal control of the VPS is both active and passive. Electric heaters are installed on two oxidizer tanks, one fuel tank, and all propellant feedlines to the TCAs. Passive thermal control consists of the application of black and white paint and vapor-deposited aluminum to selected portions of the VPS, together with super insulation applied to the propellant tanks. The feedlines are wrapped with aluminum foil to deter heat loss.

5.6.1.2 System Purpose

The VPS has three main functions during the mission:

1) Midcourse velocity correction and attitude control

2) Attitude control during retro phase

3) Attitude control and velocity correction during the final descent maneuver

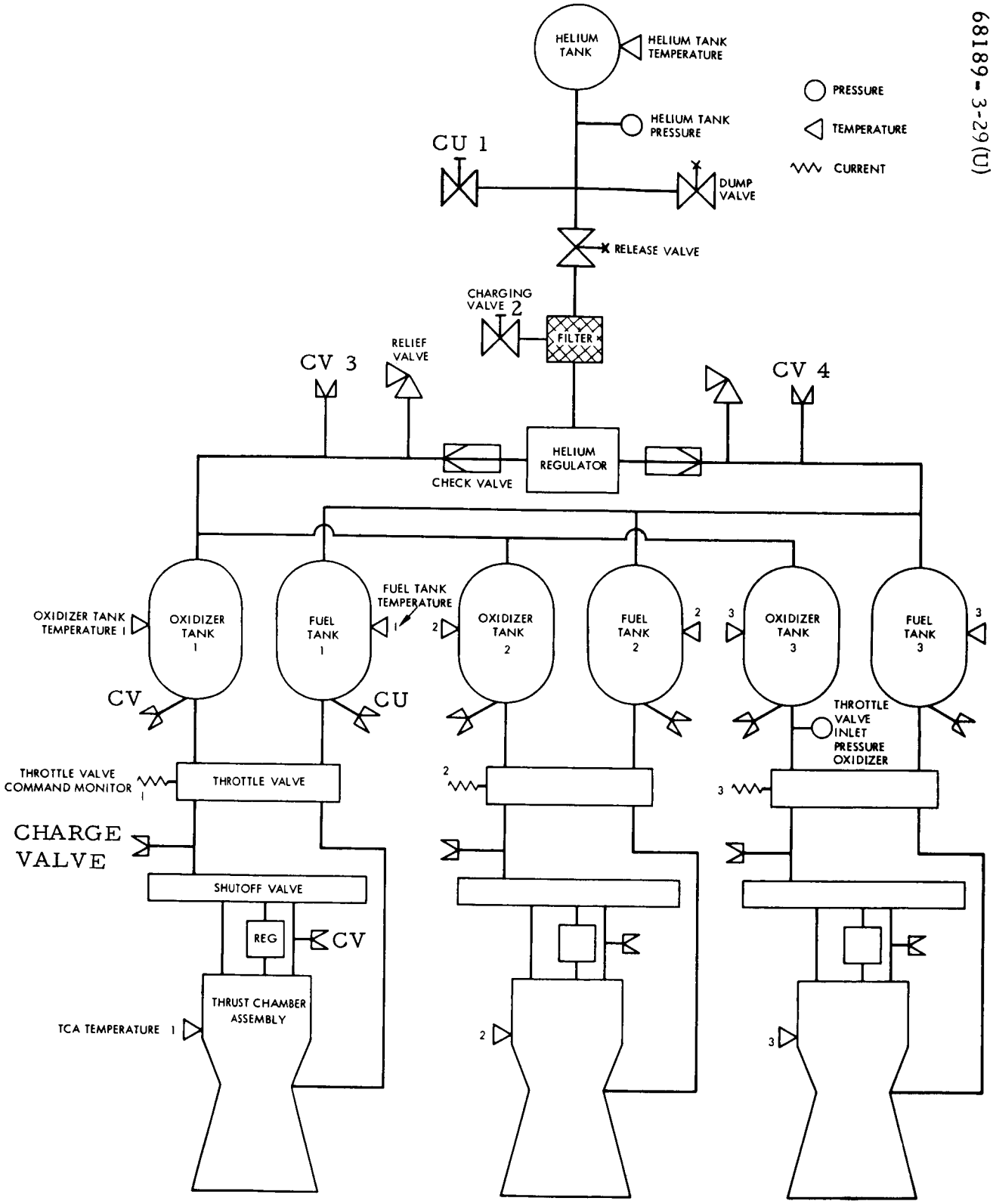

Figure 5.6-1. Vernier Propulsion System Schematic

The midcourse velocity correction may be required to correct initial launching and injection errors. The VPS provides velocity corrections up to 50 m/sec with sufficient propellant remaining to successfully land the spacecraft on the moon. The required correction is transmitted to the spacecraft in the form of a desired burn time at a constant acceleration of 0.1 g, which results in a thrust level of approximately 75 pounds for each TCA. In addition to providing the required velocity change, the VPS also provides spacecraft attitude control during the maneuver.

Attitude control during firing of the spacecraft retro motor is provided by the VPS. The VPS is ignited approximately 1.1 seconds prior to retro ignition. Attitude control by the VPS is biased around a total vernier thrust level of either 150 or 200 pounds, depending on predictions of spacecraft attitude and velocity at retro burnout. The desired vernier thrust level is transmitted to the spacecraft several minutes prior to initiation of the retro maneuver sequence. Following retro burnout, the vernier thrust level is increased to 280 pounds total thrust to further slow the spacecraft to allow the ejected retro motor case to fall clear.

Following retro motor ejection, the VPS is throttled to approximately 110 pounds total thrust under radar control. When the spacecraft intersects the first descent segment, the VPS, operating in the closed-loop mode with the radar system, acquires the predetermined altitude-velocity profile and keeps the spacecraft on the profile. Each succeeding segment of the profile is acquired in a similar manner. At an altitude of 14 feet, the VPS is shut down, and the spacecraft free falls to the lunar surface.

5.6.2 ANOMALIES

Two apparent anomalies were evident during the earth/lunar transit:

1) Unequal vernier engine thrust indications during the midcourse maneuver

2) Vernier engines were not commanded to shut off prior to lunar touchdown

Neither of these anomalies prevented completion of the mission. The first anomaly has been attributed to telemetry system calibration inaccuracies (Reference 1); the second was the result of a radar failure to generate a 14-foot mark. Postlanding system behavior was similar to SC-1.

5.6.3 SUMMARY AND RECOMMENDATIONS

The vernier engine system performed in an essentially nominal manner, meeting or exceeding all its transit and landing requirements. There were no verified anomalies or unexpected failures in any part of the vernier engines, fuel storage and distribution, or fuel pressurization equipment.

The following recommendations are made:

1) Flight control system modification to assure generation of 14-foot mark (vernier engine shutdown signal).

2) Thrust command channel calibration using latest solvent flow data as discussed in subsection 5. 6. 4. 3.

Table 5. 6-1 lists the time of occurrence of the major events concerning or influencing the vernier engine system. A summary of the vernier engine system performance parameters, as determined from postflight analysis, is given in Table 5. 6-2 along with the predicted values.

TABLE 5. 6-1. SC-3 PROPULSION EVENTS

Event	GMT, day:hr:min:sec	Mission Time, hr:min:sec	Command
Pressurize propellant tanks	108:04:55:21	L+21:50:20	0605
Engine ignition – midcourse	108:05:00:02	L+21:55:01	0721
Engine shutdown – midcourse	108:05:00:06	L+21:55:05	–
Engine ignition – terminal descent	110:00:01:18	L+64:56:17	–
Engine shutdown – postlanding	110:00:04:51	L+64:59:50	0730
Helium dump	114:20:35:37	TD+116:30:43	0610

5. 6. 4 SUBSYSTEM PERFORMANCE ANALYSIS

5. 6. 4. 1 Prelaunch

Final propulsion preparations for the SC-3 launch were begun on 25 March when propellant loading of the vernier system was initiated. The desired and actual loadings are given in Table 5. 6-3 and show that the spacecraft was loaded within the specified tolerance in Reference 2.

The helium tank was charged on 9 April to a pressure of 5241 psig at 73°F. Prelaunch telemetry readings of the tank temperature and pressure

TABLE 5. 6-2. MISSION PARAMETERS – PREDICTED AND ACTUAL

	Predicted	Actual
VPS midcourse thrust, pounds	228. 1	227. 6***
Midcourse shutdown impulse dispersion, lb-sec		
Leg 1	+0. 64*	-0. 342**
Leg 2	-0. 36*	-0. 446**
Leg 3	-0. 28*	-0. 124**
VPS retro phase thrust, pounds	200	199
VPS retro eject thrust, pounds	282	278***

*From TCA flight acceptance test.
**Reference 6.
***Reference 1.

TABLE 5. 6-3. ACTUAL VERSUS PREDICTED SC-3 PROPELLANT LOADING

	Predicted at 105°F, pounds		Predicted at 70°F, pounds		Actual at 70°F, pounds	
	Oxidizer	Fuel	Oxidizer	Fuel	Oxidizer	Fuel
Total loaded gross	110. 35	75. 75	113. 90	77. 22	116. 25	76. 96
3σ loading tolerance	0. 75	0. 75	0. 75	0. 75	0. 75	0. 75
Offload	0	0	3. 55	1. 47	6. 32	1. 56
Total loaded net	109. 60	75. 00	109. 60	75. 00	109. 16	74. 65
Unusable at 0°F	1. 29	0. 86	1. 29	0. 86	1. 29	0. 86
Total usable	108. 31	74. 14	108. 31	74. 14	107. 87	73. 79

were taken over a 6-day period. These data indicate a helium leakage rate of 13.5 std cc/hour, well within the limit of 237 std/cc hour called out in Reference 3.

The spacecraft was initially thermally conditioned to 75°F. Two and one-half hours prior to launch, the shroud temperature was increased to 85°F. Table 5.6-4 compares the predicted propulsion temperatures with the actual stabilized values at launch. Temperature differences are due to thermal gradients within the shroud. All temperatures were within tolerances, and all propulsion parameters appeared normal at launch.

5.6.4.2 Coast I (L+46M to L+21H)

The initial postinjection spacecraft interrogation indicated that all propulsion parameters were normal. Indication of heater operation on the leg 2 propellant line was noted at L+14H8M. Subsequently, it remained between 19 and 22 degrees, except when the engines were operating.

Helium pressure increased from 5222 psia at 70.1°F at L-2H27M to 5278 psia at 71.0°F at L+20H16M. Leakage calculations over this period are not meaningful since the helium is not in thermal equilibrium with the tankage; however, these data indicate no significant leakage.

The temperature fluctuations of vernier engine 2 observed throughout the mission were a result of frequent gyro drift checks which moved engine 2 into the shade. Its temperature rose again to the predicted level of about 75°F when the spacecraft was returned to the normal coast attitude.

5.6.4.3 Midcourse Operations (L+21H to L+23H)

Propulsion system status just prior to the midcourse correction was nominal. All temperatures were within the predictability range of the thermal analysis (Table 5.6-4).

The helium release squib was actuated at L+21H50M, and the propellant tank pressure increased from 252 to 762 psia (corrected for mode) within 2.27 seconds (Figure 5.6-2). It remained at this pressure until engine ignition at midcourse. The observed helium tank pressure drop was 220 psi.

Ignition of all three engines was smooth and well controlled. Midcourse thrust level totaled 227.6 pounds (Reference 1), corresponding closely to the desired spacecraft acceleration of 0.10 g.

The TCAs produced controlled thrust 0.30 second after ignition.

Peak gyro angles at shutdown were less than 0.126 degree. The shutdown impulse dispersions are shown in Table 5.6-2.

Helium pressure at vernier ignition was 5058 psia (Figure 5.6-3); helium pressure at cutoff was 4956 psia. The computed pressure drop was 91 psia compared to the 102 psia drop noted.

Propellant consumption during midcourse is shown in Table 5.6-5.

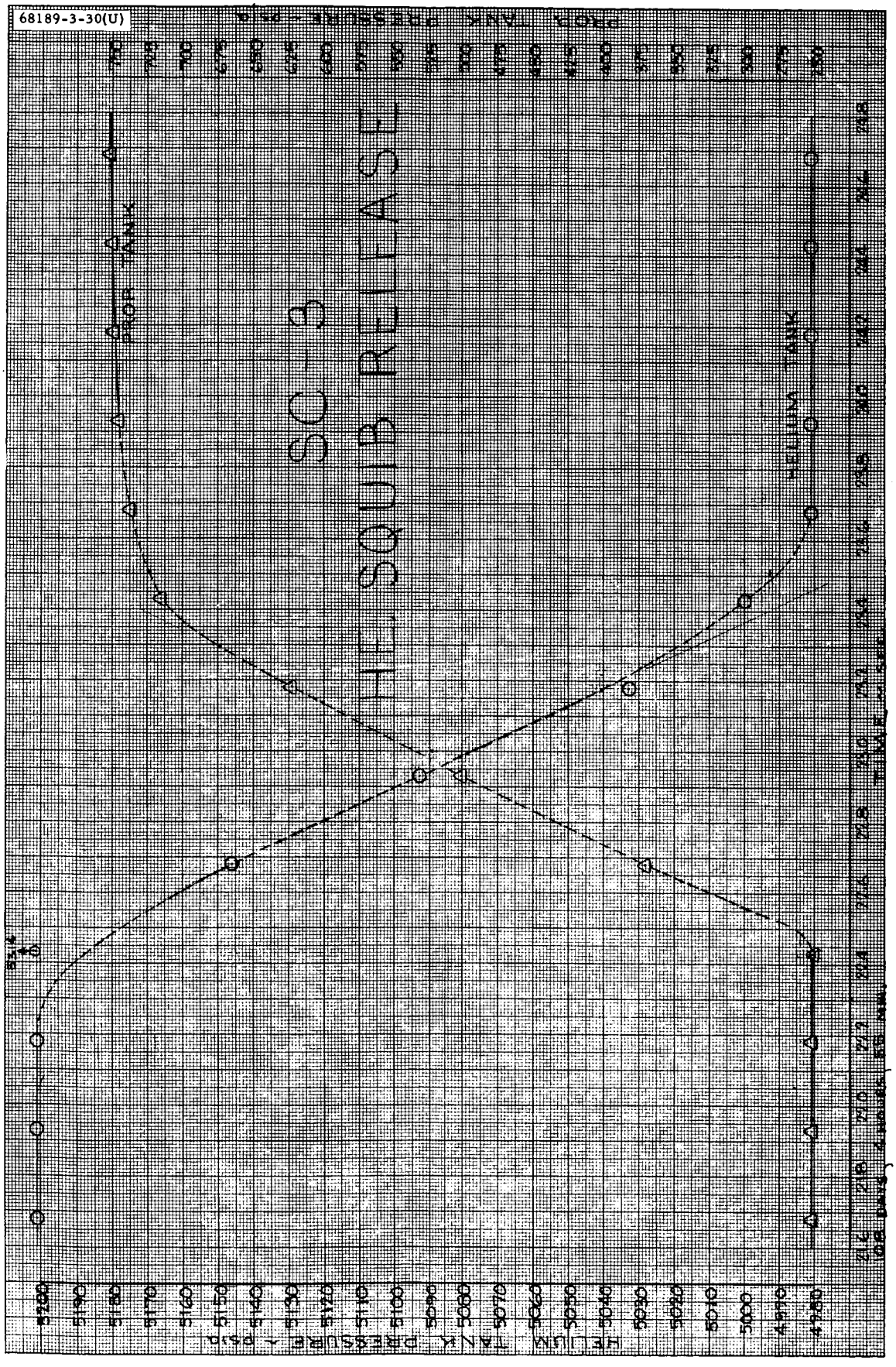

Figure 5.6-2. Helium Squib Release

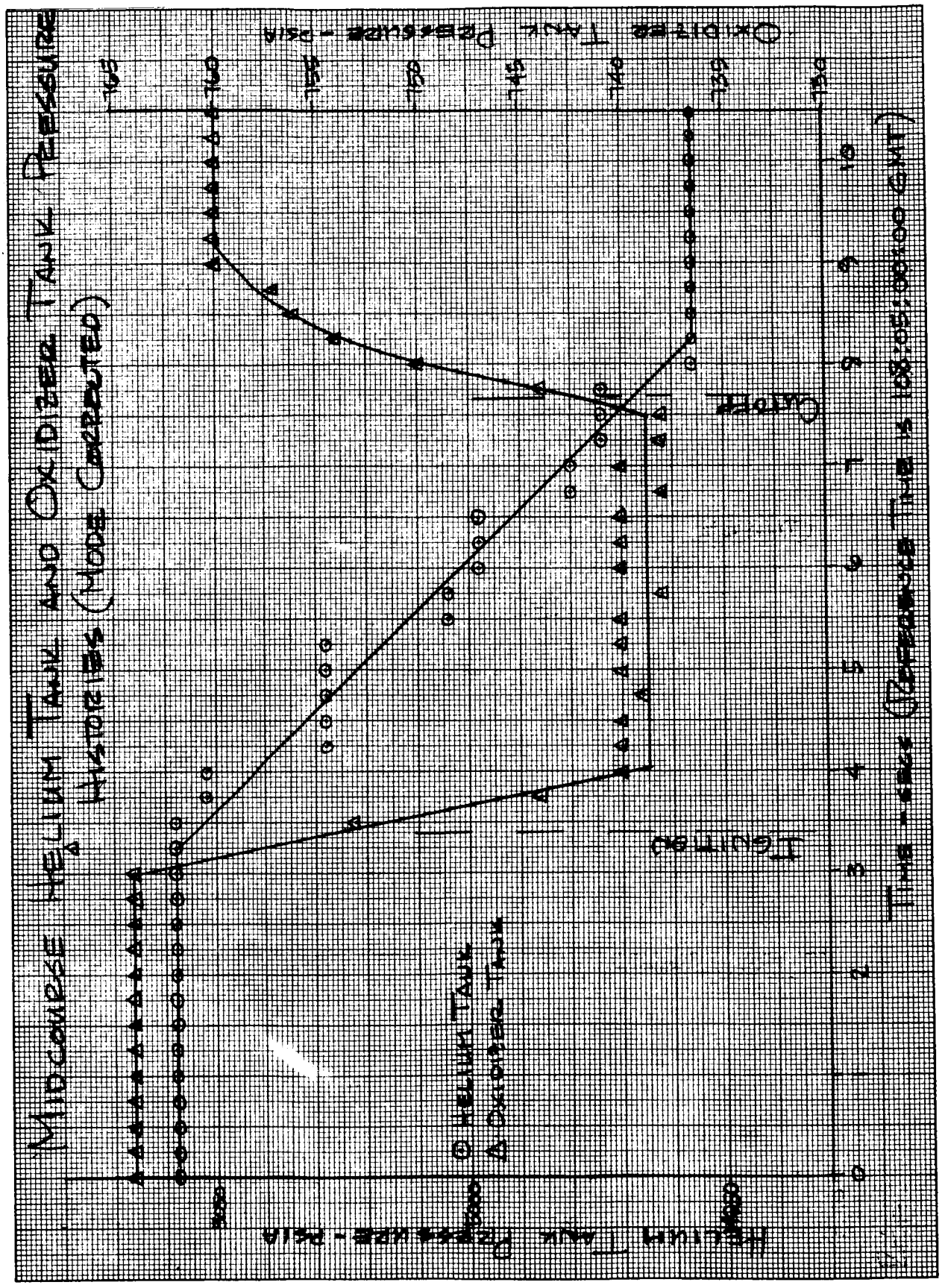

Figure 5.6-3. Midcourse Helium Tank and Oxidizer Tank Pressure Histories (Mode Corrected)

TABLE 5. 6-4. ACTUAL VERSUS PREDICTED TEMPERATURES (°F)

Temperature Sensor	Launch		Midcourse		Terminal Descent	
	Actual	Predicted	Actual	Predicted	Actual	Predicted
P4, leg 2 line	85	85	19	18-28	25	18-28
P5, leg 2 fuel tank	71	75	46	49	33	19
P6, leg 3 oxygen tank	76	79	48	42	30	17
P7, leg 1 TCA	83	80	56	60	62	60
P8, leg 1 line	85	85	31. 0	18-28	30	18-28
P9, leg 3 line	85	85	20	18-28	20	18-28
P10, leg 2 TCA	85	80	77	84	80	84
P11, leg 3 TCA	84	80	66	66	69	66
P13, leg 1 fuel tank	76	76	60	62	55	50
P14, leg 3 fuel tank	76	76	57	60	52	43
P15, leg 1 oxygen tank	75	75	50	51	41	34
P16, leg 2 oxygen tank	74	78	35	40	15	15
P17, helium tank	82	81	72	75	74	75

TABLE 5. 6-5. PROPELLANT AND HELIUM USAGE

Event	Helium, psi		Propellant, pounds		
				Actual	
	Predicted	Actual	Predicted	From Helium Usage	From Thrust Command
Squib release	178	220	0	0	0
Midcourse	91	102	3. 5	4. 1	3. 6
Terminal descent					
Touchdown 1	2500	2592	134. 1	137. 7	146. 3
Touchdown 2	0	120	0	9. 8	
Touchdown 3	0	63*	0	5. 2	4. 8*
Total, all events	2769	3097	137. 6	156. 8	154. 7

Notes:

1) Loaded propellant = 181. 7 pounds
2) Residual propellant = 27. 0 pounds
3) Loaded helium = 5222 psia
4) Residual helium at third touchdown = 2167 psia*

*Extrapolated from touchdown 2 to touchdown 3.

Temperature stratification in the propellant tanks was noted during midcourse as was the case in previous missions. The temperature increase results from the flow of warmer layers of propellant past the sensor location. However, the temperature gradient is largely negated at midcourse so that subsequent temperature readings more accurately reflect bulk propellant temperatures. The rate of temperature decrease is correspondingly reduced during coast phase II. This behavior was not accounted for in the temperature predictions but will be incorporated for future flights.

Postmidcourse analysis (Reference 4) indicated there was a possible imbalance in the vernier engine thrust levels even though all indications were that the spacecraft was stable during the thrust period and that the velocity correction was as predicted. The investigation revealed the following:

Telemetered thrust command data were corrected for the following error sources:

1) Zero thrust BCD level change between that used in calibration of the telemetry channel and that observed during the mission.

2) Differences between the thrust versus delta-milliampere curve used to derive the telemetry channel calibration and that inferred from the last solvent flow check done on the engines at Eastern Test Range (ETR).

These corrections (Reference 1) to the midcourse data brought the individual engine thrust levels to within 4. 2 pounds of those predicted and the total thrust to within 0. 8 pound of that predicted. The accuracy of the corrected thrust levels was estimated at ±3. 12 pounds. The same magnitude of differences was found when these corrections were applied to the retroeject phase of terminal descent. Consequently, it was concluded that these differences were not the result of either a spacecraft center of mass change or a change in vernier performance, but were due to thrust command channel calibration inaccuracies. Table 5. 6-6 is a summary of spacecraft thrust command data and corrections applied for midcourse (Reference 1).

To improve thrust command channel calibrations on future spacecraft, the following calibration procedures will be implemented:

1) Obtain copy of the lastETR prespacecraft installation thrust chamber assembly flow check and plot delta-milliamperes versus total weight flow.

2) Take TCA log book "hot fire" static delta-milliampere values and corresponding I_{sp} and convert ETR data to thrust versus delta-milliampere.

3) In conjunction with flight control sensor group (FCSG) flight acceptance test data, generate thrust versus telemetry voltage.

4) Compute calibration coefficients based on the data obtained in (3) above.

TABLE 5. 6-6. MIDCOURSE THRUST COMMAND DATA AND CORRECTIONS APPLIED

Parameters	Engine			Total
	1	2	3	
Telemetered thrust* commands with FC-77 correction applied, lb_f	82. 493	74. 147	76. 508	233. 1
Thrust commands corrected for offset from channel calibration level, lb_f	81. 258	73. 007	74. 902	229. 2
Correction for ETR flow check (20 delta-millamperes), lb_f	-2. 5	-0. 5	+1. 4	
Corrected thrust, lb_f	78. 758	72. 507	76. 302	227. 6
Thrust predicted from space-craft aligned center of mass location and accelerometer setting, lb_f	75. 1	76. 7	76. 6	228. 4
Difference between corrected and predicted thrust levels, lb_f	+3. 7	-4. 2	-0. 3	-0. 8

*The telemetry data present the average of eight consecutive samples for each engine. Each engine was averaged over the same time period.

5. 6. 4. 4 Coast II (L+23H to L+64H30M)

Following the midcourse firing and reacquisition of sun and Canopus, the propulsion system temperature began to follow the predicted profiles within the accuracies discussed. After the midcourse correction, the regulator locked up at 764 psia and maintained this value until initiation of terminal descent. As before, this is negligible, i. e. , undetectable, helium leakage during this period.

The oxidizer line 3 temperature remained several degrees above the thermostatic control point until 45 hours into the mission. At this time, heater cycling started and continued throughout the remainder of the mission.

5.6.4.5 Terminal Descent

Prior to retro ignition, all propulsion temperatures were normal. Maximum deviation from the predicted nominal was 14°F for the fuel tank 2 sensor (Table 5.6-3).

Vernier ignition was indicated at L+64H56M7S and appeared smooth.

Steady-state thrust during retro burning was approximately 199 pounds (based on corrected thrust command data), which compares well with the required level of 200 pounds. The corresponding retro eject thrust levels are 278 pounds experienced versus 282 pounds required.

Thrust levels varied between 28 and 104 pounds during radar-controlled descent. The radar system failed to generate the 14-foot mark. This signal normally shuts off the vernier engines which continued to operate through touchdown. Minimum thrust level was commanded to maintain the desired 0.9 lunar g. With the spacecraft in a near weightless state, it hit on a sloping lunar surface and, due to the landing dynamics, bounced some 38 feet vertically and 20 feet horizontally. This sequence was repeated once more to a height of 11 feet with a horizontal movement of 8 feet. The third hop was smaller; and, at approximately 3 feet above the lunar surface, a control center command to shut off the engines was received, allowing the spacecraft to drop to the lunar surface.

Pressurization system history is shown in Figures 5.6-4 and 5.6-5. Propellant and helium usage are presented in Table 5.6-5. Helium usage from vernier engine ignition to the first touchdown was 2592 psi versus 2380 psi predicted. The difference is due, in part, to the extended burn period when the engines did not shut down at the 14-foot altitude.

5.6.4.6 Lunar Period (Touchdown to End of First Lunar Day)

Final touchdown occurred at approximately L+65H.

After resolution of the post-touchdown data anomaly, all propulsion parameters appeared normal, i.e., similar to those experienced on SC-1.

At lunar touchdown, the helium tank pressure and temperature were 2215 psia and 60°F, respectively. The oxidizer 3 tank pressure and temperature were 738 psia and 32°F, respectively. The helium pressure was not vented until the desirability of additional lunar translation could be determined. The helium pressure slowly increased to 2735 psia as the temperature rose to 136°F. A solar eclipse occurred during the fifth earth day of lunar operations. During the eclipse, the helium tank temperature fell to 10°F. Shortly after the eclipse, the helium tank was depressurized since no lunar TCA firings were to be attempted. A profile of the helium tank pressure is given in Figure 5.6-6.

The oxidizer relief valve vented helium from the propellant tanks approximately 14 times during the lunar day (Figure 5.6-7). The nominal crack pressure was 808 psia, and the nominal reseat pressure was 793 psia. The maximum crack pressure was 830 psia, after which the oxidizer pressure slowly dropped and leveled off at 712 psia.

5.6.5 REFERENCES

1) J. F. Stocky to A. Briglio Jr., "Vernier Engine Thrust Command Data During the SC-3 Mission," JPL Memo SP/SA 123, 19 June 1967.

2) R. Laird to Distribution, "A21 and A21A/114 Vernier Propulsion Systems Propellant Inventory," Hughes Aircraft Company, IDC 2227.1/1110, 29 September 1966.

3) G. F. Pasley to Distribution, "Revised Helium Leakage Rates for the Surveyor Vernier System," Hughes Aircraft Company, IDC 2227.1/1331, 31 March 1966.

4) "Surveyor Mission C Space Flight Operations Report," SSD 74071, May 1967.

5) "SC-3 Flight Performance Report (Preliminary)," SSD 78079, May 1967.

6) H. A. Langer to P. E. Sterba, "SC-3 Engine Shutdown Impulse Dispersion," Hughes Aircraft Company, IDC 2292/304, 13 June 1967.

7) T. B. Shoebotham to N. C. Smith, "Thrust Command Calibration Coefficients for SC-4, 5, 6, and 7," Hughes Aircraft Company IDC 2227.2/1198, 12 June 1967.

5.6.6 ACKNOWLEDGEMENTS

The following people aided in the preparation of this report:

G. F. Pasley, Coordinator

T. B. Shoebotham

J. P. Amelsberg

J. F. Stocky (JPL)

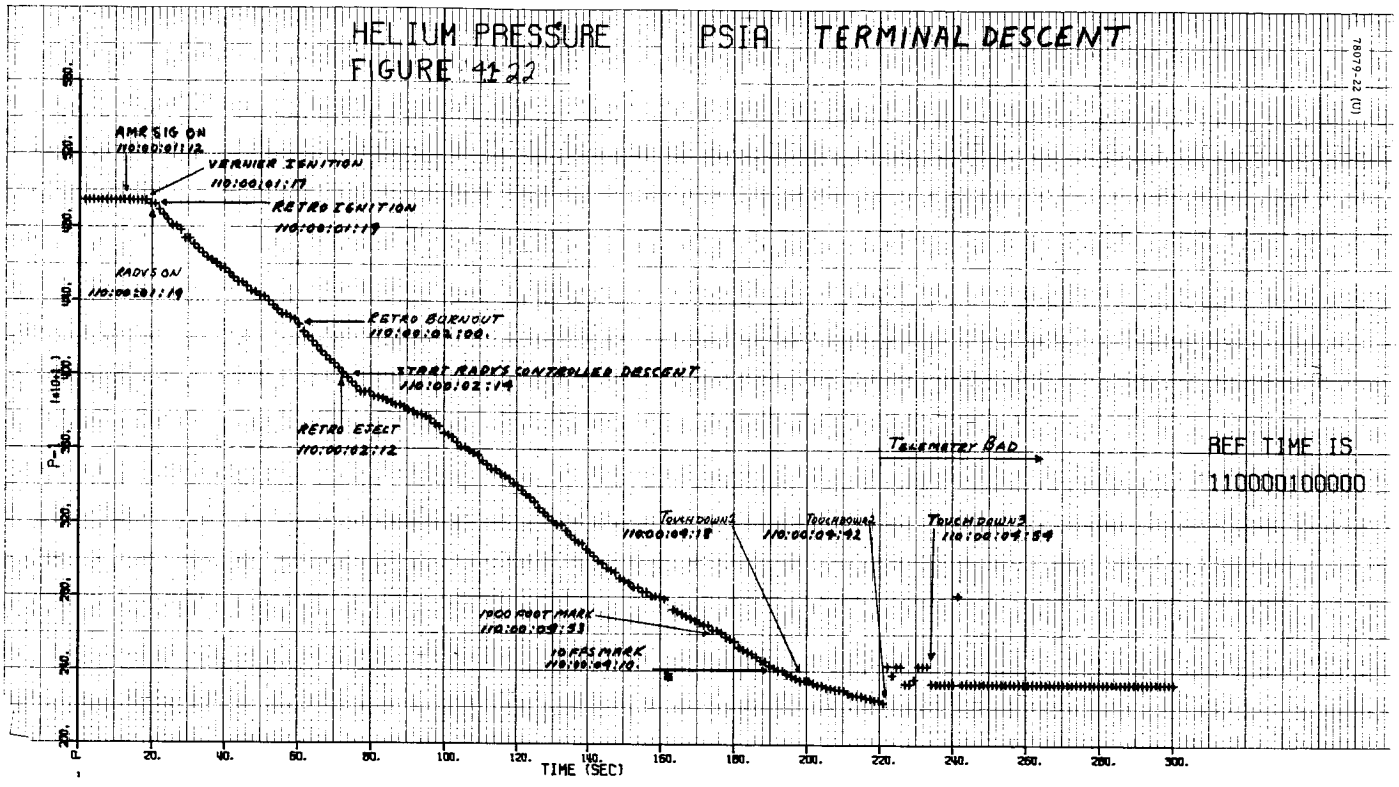

Figure 5.6-4. Helium Tank Pressure

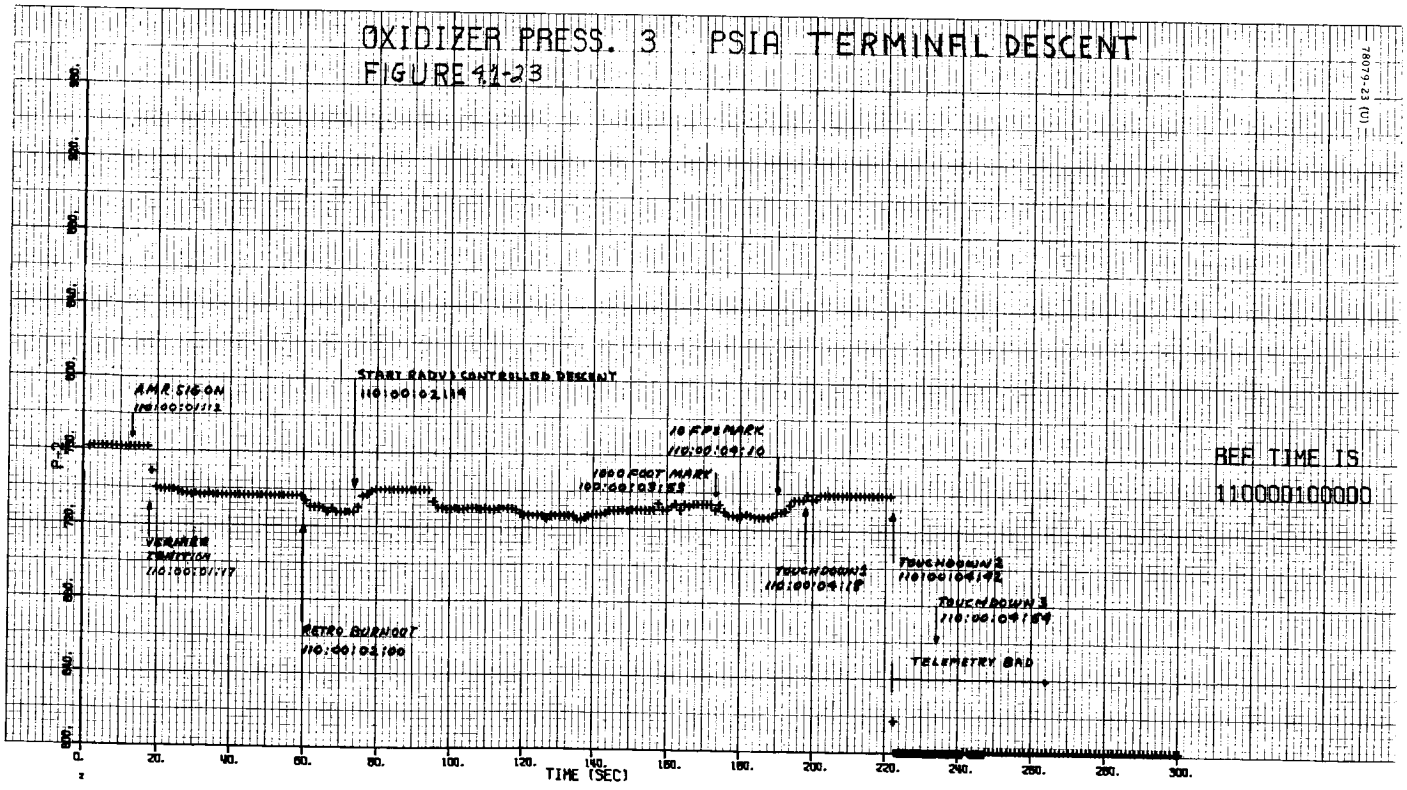

Figure 5.6-5. Oxidizer 3 Tank Pressure

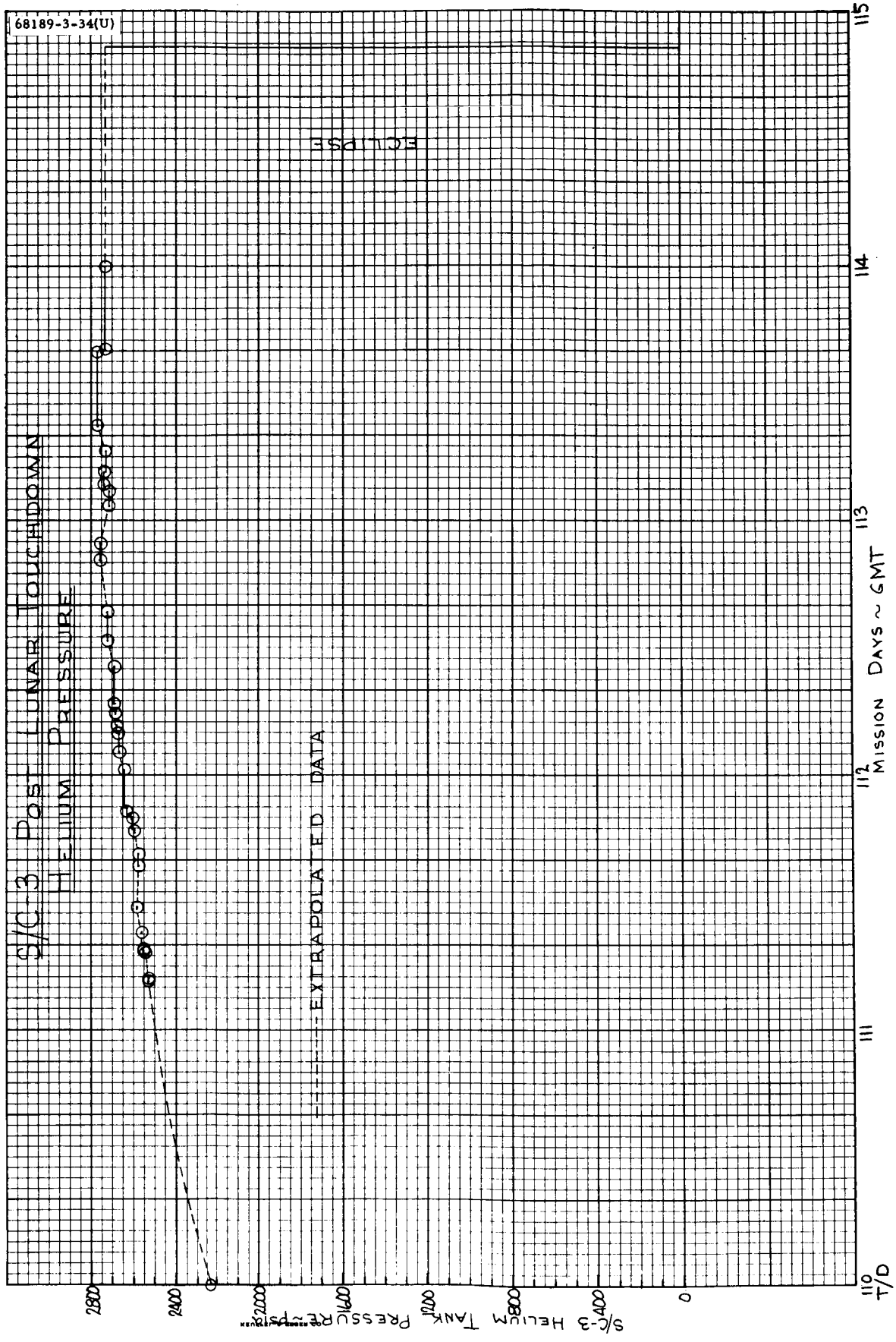

Figure 5.6-6. Postlunar Touchdown Helium Tank Pressure

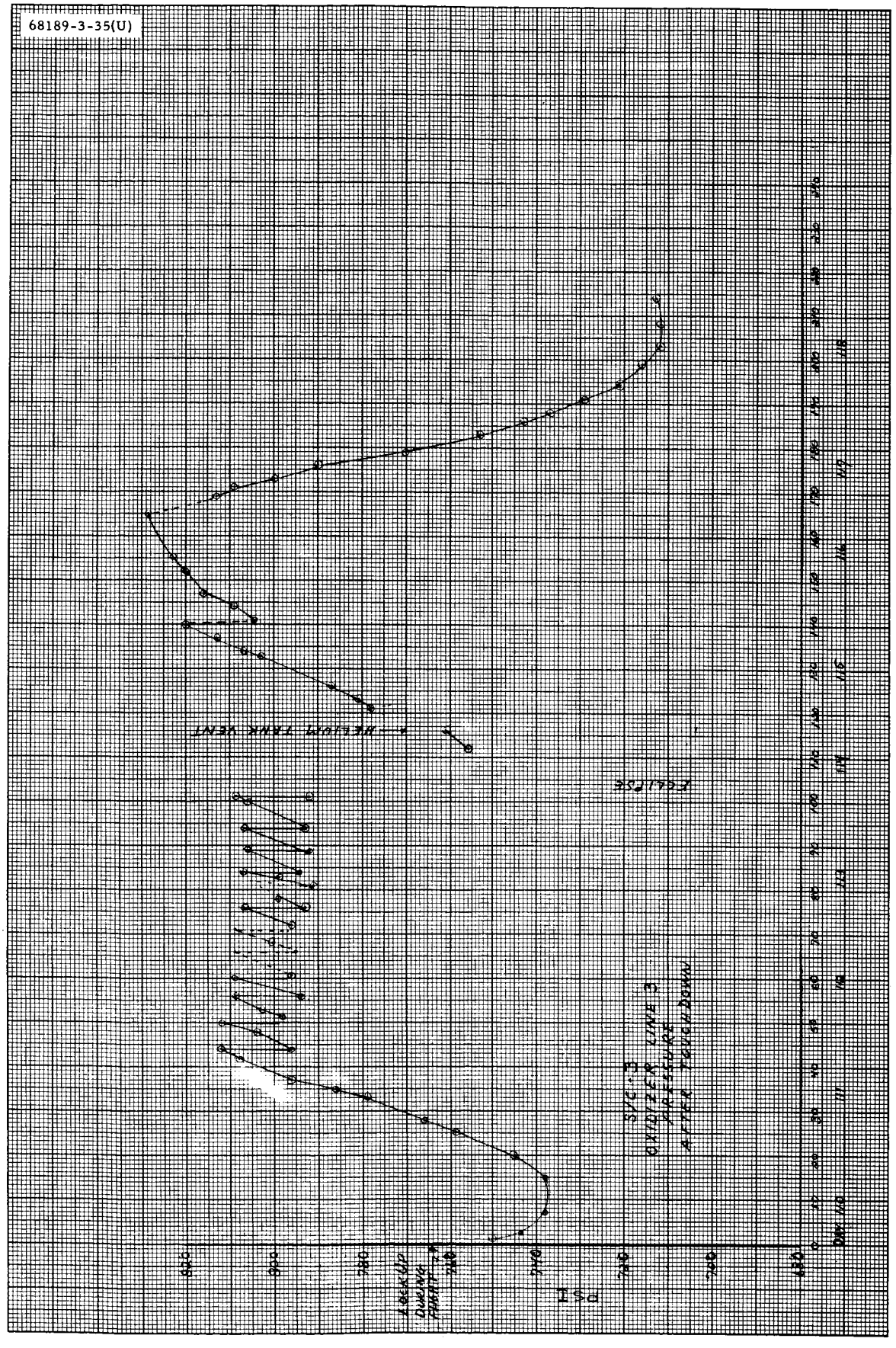

Figure 5.6-7. Postlunar Touchdown Oxidizer Line 3 Pressure

5.7 PROPULSION – MAIN RETRO

5.7.1 INTRODUCTION

The main retro-rocket, which performs the major portion of spacecraft deceleration during terminal descent, is a spherical solid propellant unit with a partially submerged nozzle.

The unit is attached at three points to the spacecraft near the landing leg hinges, with explosive nut disconnects for postfiring ejection. Friction clips around the main retro-rocket engine nozzle flange provide attachment points for the altitude marking radar. The igniter gas pressure ejects the altitude marking radar when the retro firing sequence is initiated. The main retro-rocket engine ignition squibs and retro release explosive nuts operate from a pulsed, 19-ampere, constant-current source. Commands are initiated by the flight control system.

The nozzle is partially submerged to minimize overall length. It has a graphite throat insert backed up by laminates of carbon cloth phenolic with a fiberglass exit cone lined with bulk carbon phenolic. The case is of high strength steel and is insulated with asbestos and inorganic fiber filled buna-N rubber to maintain the case at a low temperature level during burning.

The main retro-rocket engine with propellant weighs approximately 1445 pounds. The engine utilizes an aluminum, ammonium perchlorate, polyhydrocarbon, case-bonded, composite-type propellant, and conventional grain geometry. The engine thrust may vary between 8000 to 10,000 pounds over a temperature range of 50° to 70°F.

Two thermal sensors are installed on the main retro-rocket engine case for telemetering engine temperature during transit. One thermal sensor is installed for monitoring the nozzle temperature during transit.

The main retro-rocket engine employs a safe and arm device that has dual firing and single bridgewire squibs for the engine igniter. In addition, provisions for local and remote safe and actuation and remote indication of inadvertent firing of the squibs are included. Both mechanical and electrical isolation exists between squib initiator and pyrogen igniter in the safe condition.

5.7.2 ANOMALIES

No anomalies were noted in the main retro subsystem.

5.7.3 SUMMARY AND RECOMMENDATIONS

The SC-3 main retro-rocket engine operated well within all required tolerances. No changes to the SC-4 retro-rocket engine or to the engine performance prediction models are recommended. Table 5.7-1 presents a summary of main retro performance parameters.

TABLE 5.7-1. SUMMARY OF MAIN RETRO PERFORMANCE PARAMETERS

Parameter	Predicted Main Retro Value	Required Main Retro Value and Tolerance	Actual Value	Uncertainty
Bulk temperature, °F	55	±15	52	±5
T3500, seconds	41.09	±0.4	41.02	±0.1
Maximum thrust, pounds	9600	<10,000	9550	±100
Total impulse, lb-sec	376755	±3600	376039	±1800
Specific impulse, seconds	289.5	±3	288.9	±1.5
Center of gravity excursion, inch	—	<0.030		
Thrust vector excursion			0.024*	±0.005
Displacement, inch	—	<0.040		
Angular, degree	—	<0.2		
Roll torque, in-lb	—	<80	12*	±6

*Total value from all sources.

5.7.4 SUBSYSTEM PERFORMANCE ANALYSIS

Table 5.7-2 gives the major events and times associated with the firing of the retro engine.

TABLE 5.7-2. MAJOR EVENTS AND TIMES FOR RETRO OPERATION, DAY 110

Event	GMT, min:sec	Maximum Error, second
Vernier ignition	01:17.915	±0.025
Retro ignition	01:19.011	±0.05
3500-pound thrust level	02:00.089	+0.05, -0.06
"Actual" 3.5 g	02:00.319	+0.05, -0.06
3.5 g switch	02:00.528	±0.05
Retro ejection signal	02:12.527	±0.05

Items constituting the analysis effort are as follows:

1) Reconstruction of thrust versus time curve from accelerometer and doppler data (Figure 5.7-1)

2) Calculation of engine specific impulse

3) Determination of thrust vector excursions and roll moments generated by the retro engine

4) Determination of T3500

5.7.4.1 Thrust Versus Time

The technique used in the reconstruction of the thrust versus time trace from both accelerometer and doppler data is discussed in Reference 1, subsection 5.15.6.2. This reconstructed trace varies from the predicted trace, as shown in Figure 5.7-1. The maximum difference is 5 percent, and it occurs 2 seconds after ignition. This, however, is in an area of higher error for the accelerometer data, since the spacecraft passes through a period of rapid change in acceleration to a fairly steady acceleration.

Figure 5.7-1. Main Retro Engine Thrust Versus Time

5.7.4.2 Specific Impulse

The main retro-rocket engine specific impulse was obtained by correcting the predicted nominal specific impulse used in the preflight descent trajectory computer program by the change in velocity measured during retro burning on SC-3. The difference between the actual and predicted change in velocities, 8422 and 8438 fps, respectively, amounts to 0.19 percent low versus the 1 percent allowed. This approach is conservative from the retro-rocket engine point of view since the velocity difference is actually due to a number of sources in addition to the main retro-rocket engine. Some of these other sources are as follows:

1) Uncertainty in vernier engine specific impulse

2) Uncertainty in vernier engine thrust level

3) Uncertainty in vernier engine weight versus time

4) Uncertainty in retro-rocket engine specific impulse versus time

5) Uncertainty in retro-rocket engine weight versus time

6) Uncertainty in doppler data

5.7.4.3 Retro Disturbance Torques

1) Retro ignition produced a short duration disturbance torque of approximately 20 ft-lb.

2) Following retro ignition, all three vernier engines settled near their midthrust condition and remained very steady throughout retro burning. This indicates that the retro engine did not experience any measurable thrust vector excursion or lateral cg shift during operation.

3) The maximum required corrective roll torque produced by the vernier engine after accounting for bracket bending was 1 ft-lb. Assuming all this torque was produced by the main retro engine, the engine roll torque is still well below the 7 ft-lb maximum moment allocated to the retro engine.

4) During retro engine ejection from the spacecraft, a 15 ft-lb disturbance torque was easily corrected by the vernier engines.

5.7.4.4 T3500

The T3500 (time from ignition to the time when thrust decays to 3500 pounds) prediction was excellent. The total error of 0.17 percent is well within the 1 percent tolerance for the prediction. This total error is the result of the actual engine temperature gradient uncertainty, the error in

calculating the bulk temperature corresponding to that gradient, telemetry error, and prediction error.

5.7.5 REFERENCES

1) "Surveyor I Flight Performance Final Report," Volume III, Hughes Aircraft Company, SSD 68189R, October 1966.

2) "Surveyor Spacecraft A21 Model Description," Hughes Aircraft Company, Document No. 224847B, 1 March 1965.

3) "Surveyor Main Retro Engine A22-8 Support Documentation," Thiokol Chemical Corporation.

4) "Surveyor Flight Performance Report (Preliminary)," Hughes Aircraft Company, SSD 78079, May 1967.

5.7.6 ACKNOWLEDGEMENTS

The following people contributed to the main retro analysis:

L. M. Spicer, coordinator

E. W. White (System Analysis)

L. H. Davids (System Analysis)

J. H. Green (System Analysis)

5.8 ALTITUDE MARKING RADAR

5.8.1 INTRODUCTION

The Surveyor altitude marking radar (AMR) is a small, conventional, pulsed, X-band, fixed dual range gate, marking radar designed and supplied by Hughes Aircraft Company. The purpose of the AMR is to provide, with high accuracy and reliability, a positive indication that slant range from the Surveyor spacecraft to the lunar surface has decreased through a preset value, nominally 60 statute miles for the A-21 series of engineering models. This signal starts an on-board timer, whose runout time is set by ground command earlier in flight, to initiate vernier and main retro engine ignition. Since the AMR is installed in the exhaust cone of the main retro engine, and has served its purpose in providing ignition timing, it is forcibly jettisoned from the spacecraft when that engine is ignited.

The AMR is a conventional noncoherent radar, employing a pulsed magnetron, single antenna, duplexed mixer, crystal-controlled solid-state local oscillator, wide-band IF amplifier, noncoherent detector, and video processing circuitry. Dynamic range is extended by AGC of the IF amplifier; AGC voltage is telemetered, and provides an indication of received signal power. The video circuitry is of special design to mark at a preset range with high accuracy and reliability. Two fixed, adjacent range gates continuously examine the video signal. Their outputs are continuously summed and differenced. When the sum exceeds a fixed threshold and the difference simultaneously crosses zero with positive slope, the mark signal is generated. Sum threshold is set for an extremely low probability of marking on noise (false mark) throughout the operating time, while video integration plus a very substantial radar gain margin ensure a high probability of successful marking.

Two separate ground commands, whose timing is controlled, are required to fully activate the AMR. The first signal, called simply AMR on, commands on the primary power to the AMR, which includes all internal power except high voltage to the transmitter. The video signal is inhibited from reaching the marking circuits until the second command, thus eliminating any residual probability of false marking on noise during this warm-up interval. The second signal, called AMR enable, commands on the transmitter high voltage and also removes the video inhibit. This enabling function is timed, not only for favorable thermal conditions at the expected marking time, but also for the purpose of precluding premature marking on

second-round echoes at much longer ranges. In a lunar mission, flight path analysis and command (FPAC) supplies marking time prediction based on trajectory data. The prescribed times for spacecraft analysis and command (SPAC) transmission of these two commands are on at 280 ± 10 seconds, and enable at 100 ± 10 seconds, before predicted marks.

For proper analysis, complete trajectory information is required. While either known or assumed for preflight predictions, it must be known or derived for post-flight evaluation. Spacecraft attitude and velocity data are supplied by FPAC from tracking and trajectory computations. Residual range uncertainty, however, exceeds that of the AMR itself, which is assumed to have marked with mean value and dispersion predicted by radar analysis prior to each mission. In conjunction with approach velocity and attitude conditions from FPAC, the trajectory can then be extrapolated backward with high accuracy by a special two-body program. This program derives all of the significant AMR parameters throughout the nominally 100-second interval from enable to mark, and calculates correction factors to be applied to observed telemetry data before comparison with predicted received signal power.

5.8.2 ANOMALIES

There were no anomalies in the operation of the AMR during the Surveyor III mission.

5.8.3 SUMMARY AND RECOMMENDATIONS

The Surveyor III AMR functioned normally. The true altitude mark was generated at the expected time and initiated the automatic terminal descent sequence as planned. Routine emergency mark backup command transmission was received after the on-board mark had been generated. AGC indicated signal strength within 2 to 3 db of predicted value throughout the operating time (Figure 5.8-1); while a little weaker than expected, these values are within normal tolerances and may actually indicate weaker than nominal terrain. The late gate signal was normal, confirming the presence of RF return signal and detected video within the gate at the proper time relative to the mark.

As described below, significant pulse-stretching of the return signal occurs, and also varies widely during the AGC observation interval. Calibration has shown the AGC to be only roughly proportional to pulse energy. While wholly satisfactory for functional operation, the nonlinearity involved requires separate treatment of peak power and of stretched pulse length for proper AGC interpretation. For this reason, additional pre-flight calibration at longer pulse lengths, already predicted for SC-4 and SC-5, has been recommended for all remaining missions.

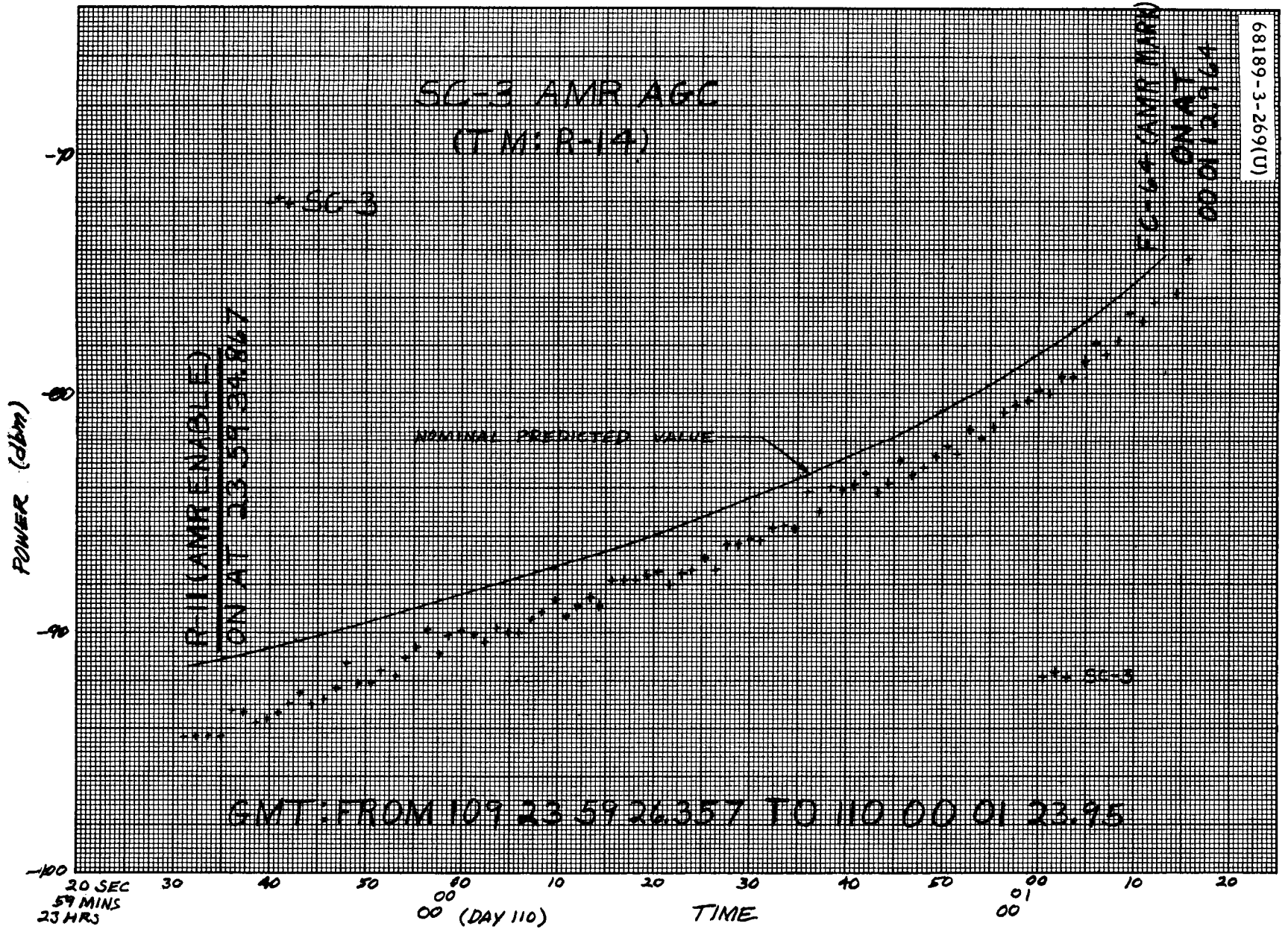

Figure 5.8-1. Surveyor III AMR Automatic Gain Control

Continued use of the AMR on future spacecraft is required for reliable terminal descent initiation. The backup command may be retained for residual reliability as long as its timing continues to be tightly controlled.

5.8.4 AMR SUBSYSTEM PERFORMANCE ANALYSIS

5.8.4.1 Event Times

From the table of Surveyor III events associated with radar operation (Section 5.9), the following AMR events are repeated in Table 5.8-1. The times listed are GMT when recorded at DSIF-11.

TABLE 5.8-1. AMR EVENT TIMES

Channel	Name	GMT at DSIF-11 Day:Hr:Min:Sec
R-1	AMR on	109:23:56:34.895 ± 0.6
R-11	AMR enable	109:23:59:34.890 ± 0.6
FC-64	AMR mark	110:00:01:12.821 ± 0.05
FC-28	Vernier ignition	110:00:01:17.922 ± 0.05
FC-29	Retro ignition	110:00:01:19.023 ± 0.05

The warm-up time (on to enable) was 180.0 ± 1.2 seconds, well within the nominal 180 ± 10 seconds. The enabled time was 97.9 ± 0.65 seconds, also within the nominal 100 ± 10 seconds.

AMR mark time can be refined to 110:00:01:12.830 ± 0.041 from readings of the magnitude register.

5.8.4.2 Late Gate Signal

Concerning the trajectory reconstruction for AGC evaluation, the total stretched pulse length as received was about 14.7 microseconds and the effective closing rate was 8588.9 fps, both at the time of mark. The corresponding video pulse closing rate was therefore about 17.5 microseconds per second. The video late gate measured before launch was 19.6 microseconds (20 ± 1, required). It should therefore have produced output within 3 db of peak for (14.7 + 19.6)/17.5 = 1.96 seconds, ensuring that one of the samples at 1.2-second (mode 6) intervals of telemetry channel

R-29 should be close to peak amplitude. In Surveyor III, this sample occurred at 00:01:12.6, or within 0.2 second of the mark, with one partial amplitude sample on each side, as is proper. This confirms presence of proper radar return at the mark. Figure 5.8-2 shows this channel for Surveyor III. (All AMR channels go full scale at engine ignition.)

5.8.4.3 AMR AGC Post-Mission Evaluation

Because of the significant distance traveled during the nominal 100 seconds from enable to mark, it was desired to evaluate accurately the parameters involved during this time interval as a function of the mission variables.

Trajectory constants are found from "initial" conditions at mark, supplied by FPAC. All quantities are then evaluated analytically without approximation at each of a number of trajectory points determined by stepping speed in arbitrary increments. Negative increments of speed produce a backward extrapolation from mark to enable. The only approximation used is for the time interval between trajectory points, which assumes linearized distance and velocity between points. Adequate time accuracy results with the steps used.

Of particular interest are the AMR slant range (Figure 5.8-3), the incidence angle at the surface, and the accompanying received pulse stretching effect. The latter is seen to vary quite significantly, because of slant range variation. The incidence angle is remarkably constant, despite variation of both flight path and attitude angles relative to local vertical, primarily because of the constant inertial attitude assumption.

Surveyor III conditions at mark have been obtained from FPAC as follows:

$V1 = 8,588.9$ fps

$C1 = 22.77$ degrees

$M1 = 23.36$ degrees

$R1 = 60.0$ miles

Figure 5.8-4 illustrates the geometry, where

B = selenocentric polar radius

G = selenocentric polar angle

V = speed

C = flight path angle (with local vertical at present position)

K = lunar radius (assumed spherical)

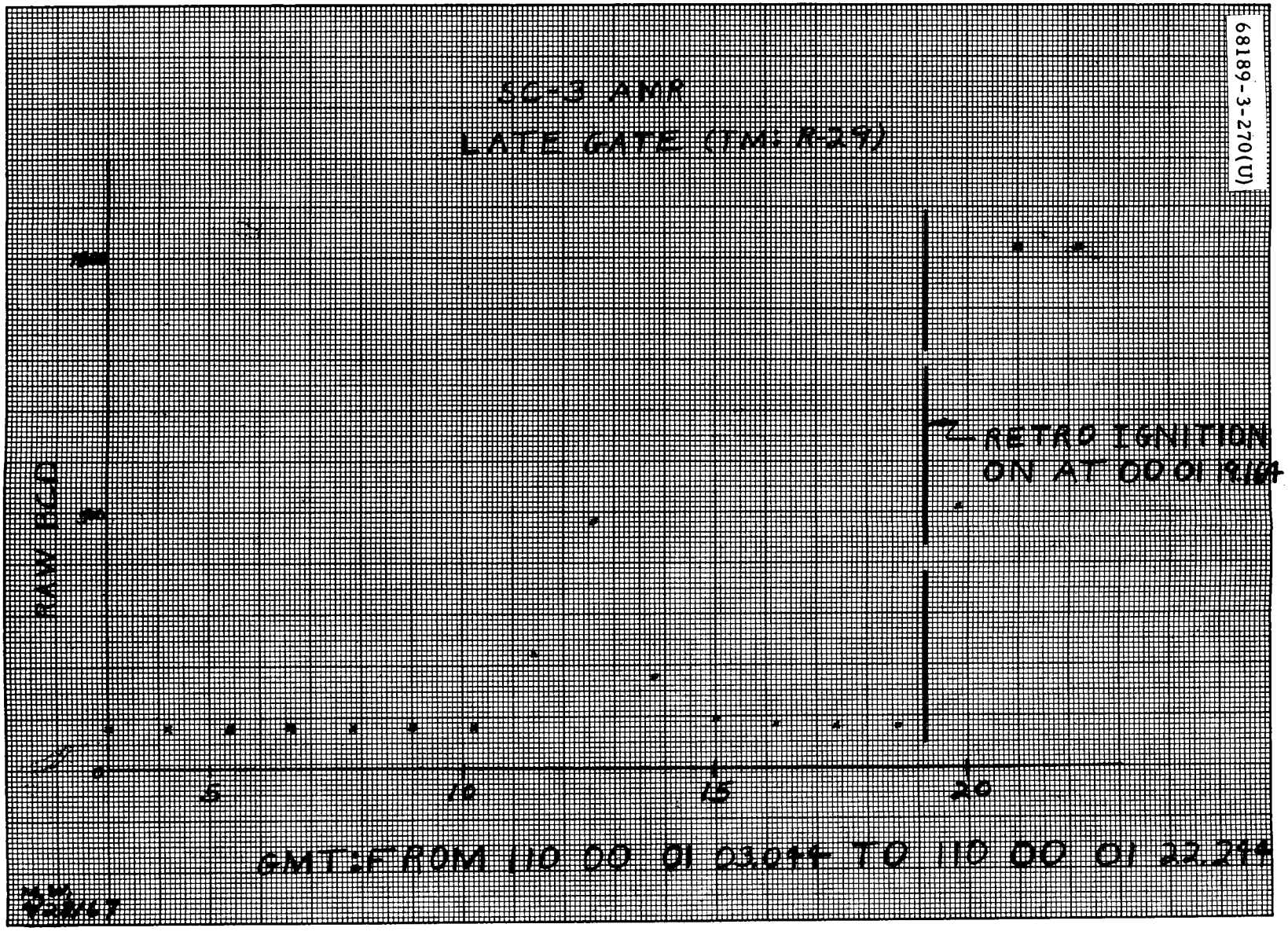

Figure 5.8-2. Surveyor III AMR Late Gate (TM:R-29)

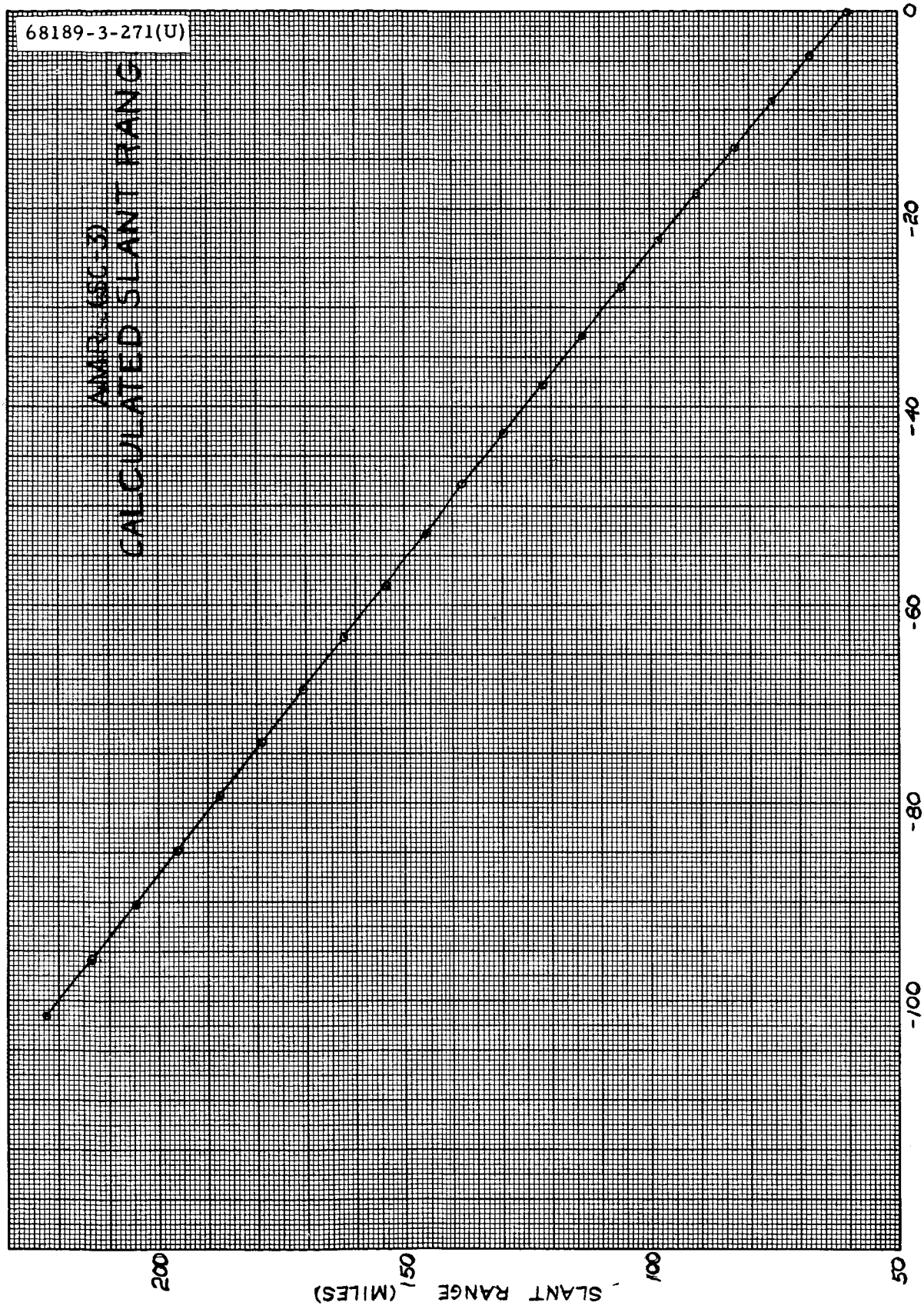

Figure 5.8-3. Surveyor III AMR Calculated Slant Range

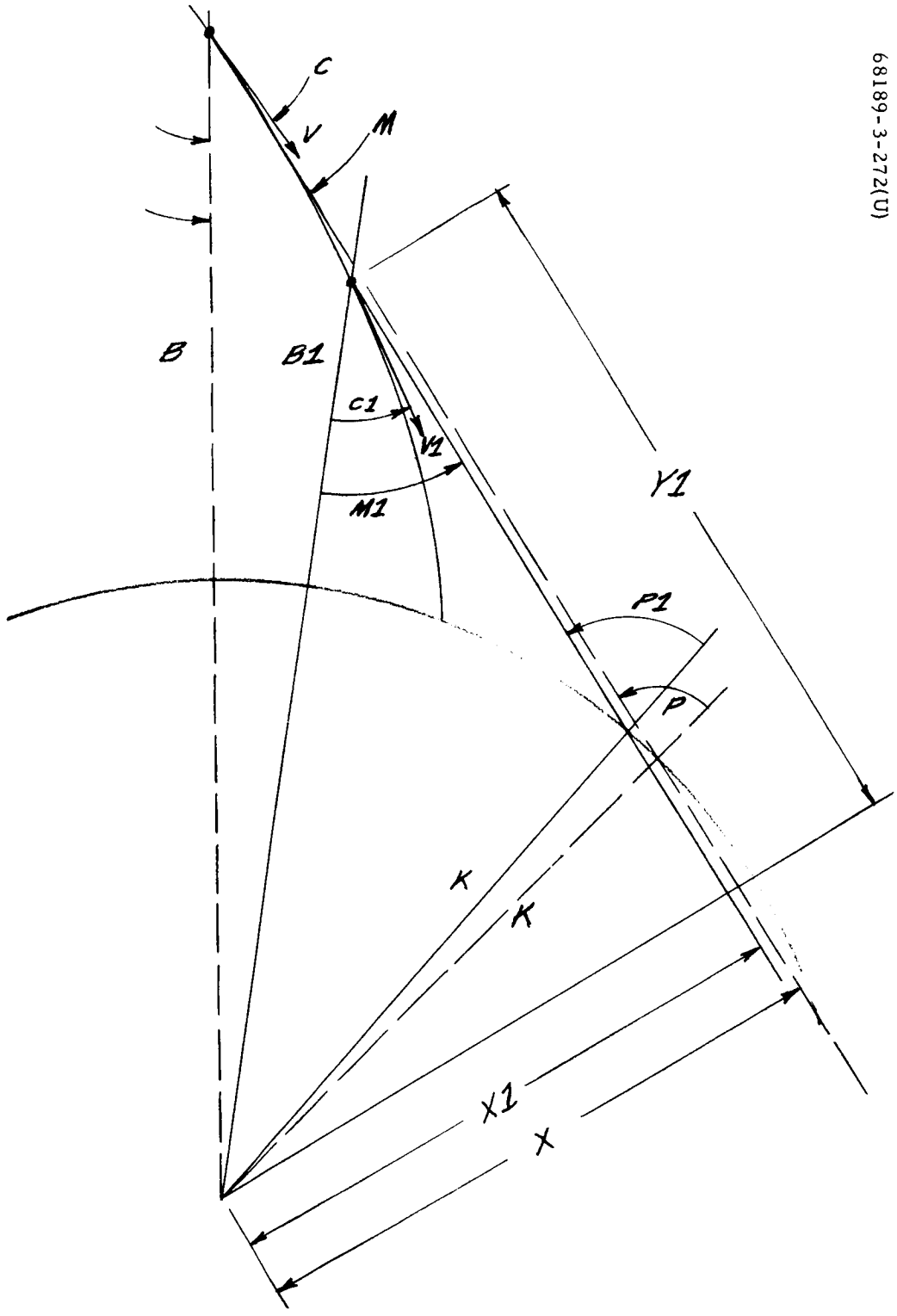

Figure 5.8-4. Lunar Approach Geometry

K3 = lunar gravity at its mean surface

E = conic eccentricity

L = semilatus rectum

A = semimajor axis

M = attitude angle (with local vertical at present position)

R1 = 60.0 miles is the expected marking range (Reference 1) which also shows the total 3σ RSS marking error at 25 degrees to be 0.345 mile. At V-1, this is a time error of 0.212 second (3σ). By coast phase orbit determination, the a priori mark time uncertainty has been reported as 0.8 second (1σ almost 12 times larger). Hence, while orbit determination provides excellent velocity data, integration into position is less accurate, and the predicted AMR mark range is the best estimate available.

Surveyor III was analyzed at both the 3.6 degrees maximum beamwidth, and the 3.25 degrees typical value (Reference 2). The associated pulse stretching change is equivalent to about 0.3 db in AGC calibration interpretation.

The peak instantaneous received power is

$$Pr(max) = \frac{P_t \lambda^2 G^2 L_F}{(4\pi)^3 R^4} \sigma(\theta) A_\rho$$

where

P_t = transmitted power (peak)

λ = wavelength

G = peak gain (one-way)

R = slant range along beam axis

L_F = loss factor (drifts)

θ = incidence angle

$\sigma(\theta)$ = effective radar cross section per unit projected area

A_ρ = projected area

Now $A\rho = (B, R)\ (c\gamma/2 \cot \theta)$ for beamwidth limiting in azimuth and pulse limiting in elevation, and

$$\sigma(\theta) = \eta(K/\alpha^3)\ F(\theta)$$

$$F(\theta) = \alpha^3/(\sin \theta + \alpha \cos \theta)^3$$

is the Muhleman model, in which the AMR values are

$$\alpha = 0.36$$

$$K/\alpha^3 = +\ 10.70 \text{ db}$$

and the best current $\eta = 0.065$ is now being used in place of the former 0.075 value.

Letting $P_{av} = P_t\ \tau\ f_r$

where

P_{av} = avenge transmitted power

τ = transmitted pulse length

f_r = repetition rate

(since P_{av} is measured in testing) produces the equivalent expression

$$Pr(max) = \left(\frac{c^3}{128\ \pi^3}\right)\left(\frac{P_{av} G^2 L_F}{f^2 f_r R^3}\right)\ (\beta_1 \cot \theta)\sigma(\theta)$$

where

$c = 9.8362 \times 10^8$ ft/sec

$c = f\lambda$

$f = 9.300 \times 10^9$

$\pi^3 = 31.0062$

$$\frac{c^3}{128\,\pi^3} = 1.62901 \times 10^{12} \text{ (for R in miles)}$$

β_1 = equivalent beamwidth

= 0.7 × one-way total beamwidth at half power

This is very nearly the peak value of the received power as the pulse traverses the illuminated patch of terrain.

When $c\tau/2 \cot \theta \geq \beta_1 R$, then beamwidth is limiting in both directions, $A_\rho \rightarrow (\beta_1 R)^2$, and $Pr \propto R^{-2}$. For R = 60 miles, β_1 = 3.25 degrees, τ = 3.2 μsec, this crossover occurs at θ = 7.14 degrees incidence. Some pulse stretching still occurs, however. Figure 5.8-5 shows calculated received power.

It is significant, therefore, that received pulse length varies appreciably during the enable-to-mark interval (Figure 5.8-6) and that proper AGC interpretation prior to mark requires knowledge of AGC calibration at pulse lengths longer than the 3 μsec, 10 μsec, and 30 μsec standard values for AGC calibration (Figure 5.8-7).

By special request before the Surveyor III flight, the following typical variation of peak input versus pulse length required for constant AGC voltage, with db referred to the 10 μsec level (Figure 5.8-8) was supplied:

τ (μsec):	3	5	7.5	10	15	20	25	30	35
db:	+7.5	+4	+2.7	0.0	- 2.0	- 3.2	- 3.8	- 4.2	- 4.7

These values, though only representative, are used for Surveyor III post-mission evaluation.

It is important for future post-mission analyses that adequate AGC calibration data for each spacecraft be obtained before launch.

5.8.4.4 DB Budget

The Surveyor III AMR db budget, revised for a postflight incidence angle of 24.62 degrees, is

P_t (aver)	+ 33.62 dbm
G^2	+ 69.0 db
B_1	- 13.57 db
σ (0 degree)	- 1.17 db

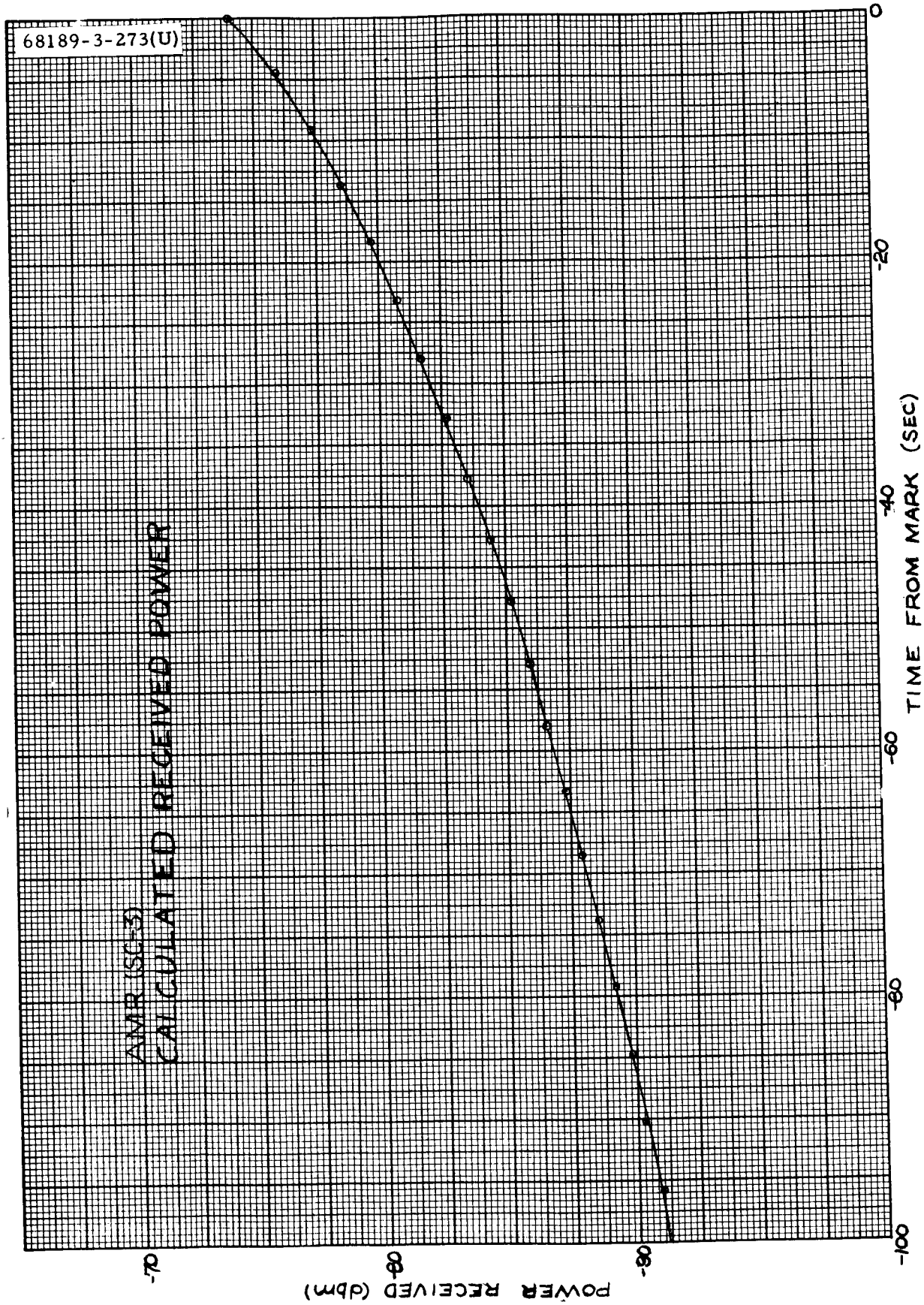

Figure 5.8-5. Surveyor III AMR Calculated Received Power

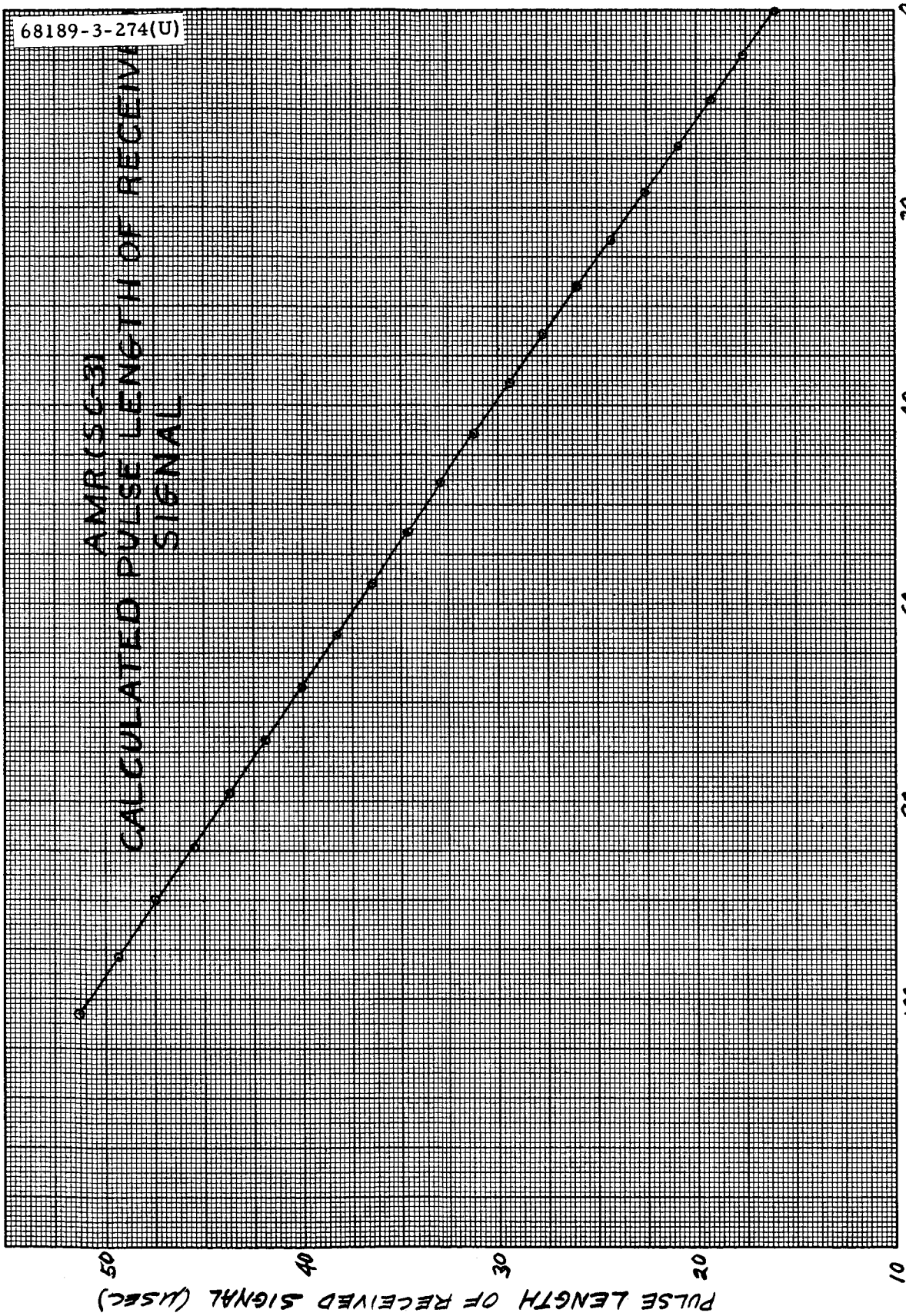

Figure 5.8-6. Surveyor III AMR Calculated Pulse Length of Received Signal

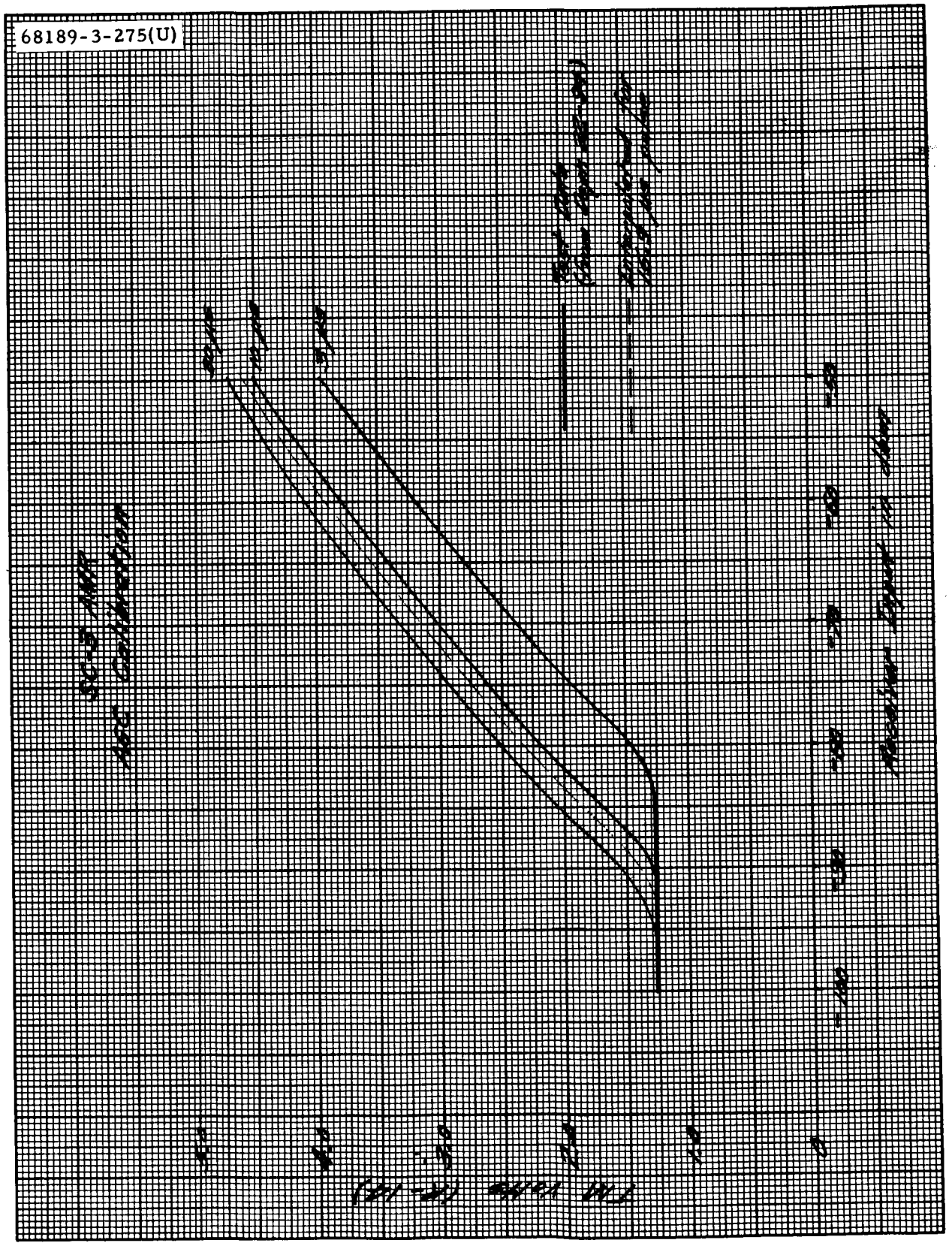

Figure 5.8-7. Surveyor III AMR Automatic Gain Control Calibration

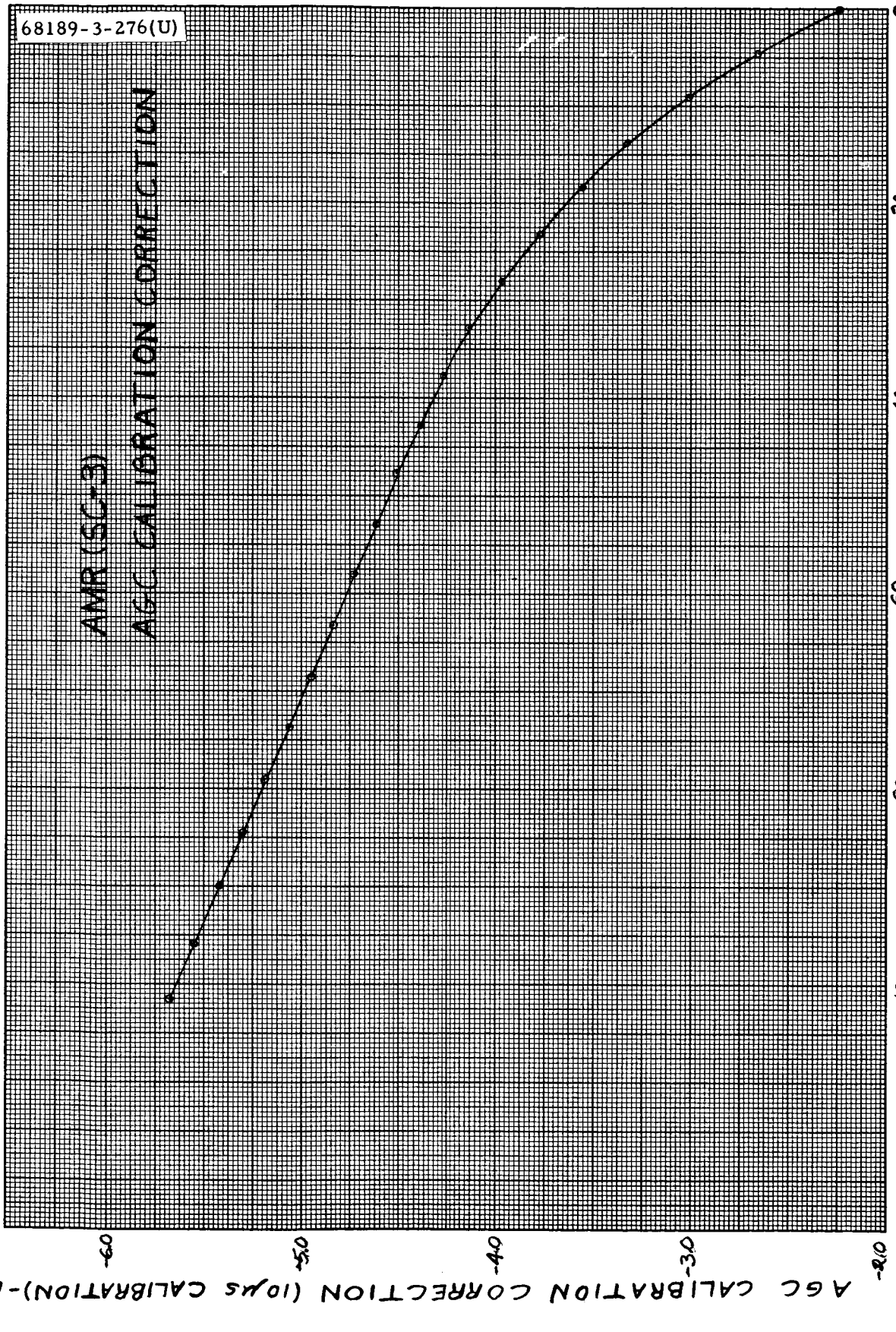

Figure 5.8-8. Surveyor III AMR Automatic Gain Control Calibration Correction

R^{-3}	- 53.34 db
f^{-2}	-199.37 db
f_r^{-1}	- 25.54 db
$\left(\frac{1}{2}\right)\left(\frac{c}{4\pi}\right)^3$	+122.12 db
cotan 24.62 degrees	+ 3.38 db
F (24.62 degrees)	- 9.48 db
Pr (peak)	- 74.35 dbm
P_{min} (14.7 μsec)	- 98.9 dbm (nominal)
P_{min} (3.0 μsec)	- 92.0 dbm (nominal)
P_{min} (3.0 μsec)	- 95.2 dbm (measured)
P_{min} (14.7 μsec)	-102.1 dbm (predicted)
DB margin	+ 27.7 db

5.8.5 REFERENCES

1. R.A. Dibos, "SC-3 AMR (S/N-15) Predictions," Hughes IDC 2253.4/79, 10 April 1967.

2. S. Thaler, "The AMR — Predicted Performance," Hughes IDC 2729.1/11, 29 March 1965.

DOCUMENTATION

I. Holtzman, "AMR Marking Range Bias as Function of Angle of Incidence," Hughes IDC 2253.3/294, 13 May 1965.

R.A. Dibos, "Post-Mission Analyses Involving Radar Data," (unpublished, 188 pp.), 25 March 1966.

"Radar Studies of the Moon," Lincoln Laboratory, Quarterly Report No. 2, 15 May 1966, p. 11.

R.A. Dibos, "Radar Performance Evaluation," SC-1 Symposium (NASA at JPL), September 1966.

R.A. Dibos, "Preliminary Study of AMR at Large Angles," (unpublished IDC), 4 November 1966.

"Decibel Allocation and Margin Summary," Hughes Aircraft Company, SSD 4021R-2, 28 November 1966.

J.R. Hanley, "SC-3 AMR Calibration Data," Hughes IDC 2294.5/37, 5 January 1967.

W.T. Black, "SC-3 AMR Subsystem Anomalies at ETR (PVT-3)," Hughes IDC 2294.5/63, 28 February 1967.

W.T. Black, "SC-3 AMR Marking Accuracy Performance," Hughes IDC 2294.5/65, 3 March 1967.

W.T. Black, "TSS 3.7.48 Range Delay Timing and Mark Accuracy Retest ---," ETR 3.4.118, 20 March 1967.

R.A. Dibos, "AMR Test Data Required for Analyses," Hughes IDC 2253.4/71, 20 March 1967.

R.A. Dibos, "Special Retest of SC-3 AMR," Hughes IDC 2253.4/72, 20 March 1967.

K.L. Arends, "AMR S/N 15 (SC-3) Test Data," Hughes IDC 2294.5/81, 10 April 1967.

K.L. Arends, "TSS 3.7.63 – AMR Marking Accuracy Retest," Hughes IDC 2294.5/82, 10 April 1967.

R.A. Dibos, "SC-3 Radar Prediction and Analysis Material," Hughes IDC 2253.4/81, 20 April 1967.

"SC-3 Flight Performance Report (Preliminary)," Hughes Aircraft Company, SSD 78079, May 1967.

R.A. Dibos, "TM Mode 6 Data Relating to Radar Performance," Hughes IDC 2253.4/84, 15 June 1967.

R.A. Dibos, "SC-3 Digital Signals Relating to Radar Performance," Hughes IDC 2253.4/85, 15 June 1967.

R.A. Dibos, "AMR AGC Post-Mission Evaluation," Hughes IDC 2253.4/88, 27 June 1967.

5.8.6 ACKNOWLEDGEMENTS

Calibration data were supplied by K.L. Arends, W.T. Black, J.R. Hanley, and by Division 27.

AGC and late gate data processing were performed and graphed by M.R. Weiner and Q.D. Howard. The latter also confirmed digital word event times. G.A. Young assisted in magnitude register timing interpretation.

This section was technically coordinated and authored by R.A. Dibos.

5.9 RADVS PERFORMANCE

5 9.1 INTRODUCTION

The radar altimeter and doppler velocity sensor (RADVS) is a coherent CW microwave radar designed and supplied by Ryan Electronics, San Diego. Its primary function is to measure velocity and slant range relative to the lunar surface during the terminal descent of the Surveyor spacecraft. These quantities are measured directly in spacecraft coordinates, allowing direct utilization by the spacecraft flight control system for both attitude steering and deceleration thrust control.

The doppler velocity sensor (DVS) portion of the system is essentially a three-beam coherent CW autodyne doppler radar. A single klystron (two-cavity type) provides undeviated output at a nominal frequency of 13, 300 MHz. Its output is divided equally among the transmitting horns for beams 1, 2, and 3. Each beam has a separate receiving horn, with adequate RF isolation against direct leakage, and a separate and independent receiver utilizing a small sample of the transmitted signal as local-oscillator (bias). Associated with each receiver is a separate and independent frequency tracker, capable of acquiring and tracking the doppler signal corresponding to that component of velocity associated with the spacecraft orientation of that particular beam. The spacecraft beam orientations are such that the nominal velocity components V_i (i = 1, 2, 3) along the axes of these three beams are determined by the spacecraft coordinate components of velocity according to the matrix multiplication

$$\begin{pmatrix} V_1 \\ V_2 \\ V_3 \end{pmatrix} = \begin{pmatrix} +A & +A & +B \\ -A & +A & +B \\ -A & -A & +B \end{pmatrix} \begin{pmatrix} V_x \\ V_y \\ V_z \end{pmatrix}$$

where

$$A = \sin 45 \sin 25 \text{ degrees} = 0.29884$$

$$B = \cos 25 \text{ degrees} = 0.90631$$

and the spacecraft coordinates are a Cartesian right-hand triad with + Z along the roll axis in the normally descending direction.

The frequency outputs of these three frequency trackers are properly scaled and summed in three converters whose outputs are analog voltages representing the spacecraft velocity components:

$$V_x = \frac{V_1 - V_2}{2A} \; ; \; V_y = \frac{V_2 - V_3}{2A} \; ; \; V_z = \frac{V_1 + V_3}{2B}$$

The radar altimeter (RA) portion of the system is basically a single-beam coherent FM-CW microwave radar altimeter. Beam 4, fixed along the spacecraft +Z axis, also contains separate transmit and receive horns, a fourth receiver, and a fourth frequency tracker The same kind of transmitter-derived local-oscillator (bias) signal configuration is used, but the RA uses a reflex klystron whose frequency is sawtooth deviated in standard FM-altimeter fashion. The operating portion of the sawtooth has a negative slope (with time) to avoid any range-velocity ambiguities. The beam 4 receiver and frequency tracker therefore operate at a frequency which is the sum of scaled slant range and scaled doppler velocity inevitably appearing along that beam. The RA converter corrects the frequency output of the beam 4 tracker by a properly scaled term (V_Z compensation), obtained from the DVS V_Z converter, to provide an analog output voltage proportional to R_Z, the slant range along the +Z axis of the spacecraft. [Nominal RA operating frequency is 12,900 MHz Deviation is nominally 40 MHz at 8,000 MHz/second below 1000 feet, and 4 MHz at 800 MHz/second above 1000 feet.]

Each receiver is actually two parallel receiving channels, each with separate microwave mixers and audio preamplifiers. Microwave mixer, signal and bias inputs are phased so that the parallel audio channels are essentially in phase quadrature, with equal amplitudes, for all normal doppler signals. Each frequency tracker uses these quadrature audio signals to single-sideband modulate an internal reference signal held at 600 kHz, thus reproducing doppler frequencies unambiguously at tracker IF, and preserving the sense of the velocities. (In a more general application, this would permit measuring negative and positive beam velocities unambiguously. In Surveyor, it serves primarily to reject negative velocities including the unwanted radar return from the main retro engine after separation from the spacecraft.) Each frequency tracking loop is closed by a voltage-controlled oscillator (VCO), the frequency of which is controlled by a discriminator-integrator combination, whose output is a direct measure of the frequency being tracked.

To preserve the high degree of both amplitude and phase balance between the parallel, quadrature channels of each receiver, over the full dynamic range of signals and over the region of operating temperatures, the preamplifier gains are switched in discrete steps by wide-band (at audio) gain-switching threshold circuits. AGC is not used. A set of discrete outputs is provided and telemetered to indicate the gain state of each receiver, as follows:

	Gain state 1	Gain state 2
High-gain (DVS, 90 db; RA, 80 db)	Off	Off

Mid-gain (DVS, 65 db; RA, 60 db)	Off	On
Low-gain (DVS and RA, 40 db)	On	On

Other discrete outputs are provided and telemetered. A set of tracker-lock signals indicates the search or track status of each of the four frequency trackers. A reliable operation – RA (RORA) discrete is on when and only when beams 1, 3, 4 are locked, thus providing reliable range. Both reliable operation – DVS (RODVS) and CRO-DVS discretes are provided according to a rather involved logic described in Appendix C.* From the analog range output, the RADVS itself derives and supplies two discrete range mark signals – one at 1000 feet (to change flight control loop parameters) and the other at 12 feet (to cut off vernier engines). The latter is termed the 14-foot mark for RADVS purposes, but is referred to the RADVS antenna boresight, which itself is 24 inches above the legs-extended position of the landing pads on the spacecraft structure (whose position at vernier engine cutoff, in turn, has been used in landing stability analyses).

The RADVS hardware is packaged in five units, each of which is a control item in Hughes spacecraft configuration control. Since certain telemetry signals (temperatures) are identified with these units, their basic composition is indicated below:

A/VS antenna – Beams 1 and 4 antenna, mixer, and preamplifier components

DVS antenna – Beams 2 and 3 antenna, mixer, and preamplifier components

KPSM (klystron, power supply, modulator) – all components implied, for both DVS and RA

SDC (signal data converter) – all frequency trackers and data converters

Waveguide assembly

5 9.2 ANOMALIES

During the Surveyor III mission, the RADVS equipment appeared to function as designed. The terminal descent was nominal until approximately 6 seconds before touchdown, at which time beam 3 of the RADVS lost lock and did not reacquire. This resulted in the vernier engines continuing to burn through touchdown instead of being shut off by the RADVS at 14 feet. All

*Appendices are included at the end of Section 5.9.

subsequent anomalies were a direct result of this loss of lock. This loss of lock and subsequent RADVS anomalies are described herein.

5.9.2.1 Beam 3 Loss of Lock Anomaly

All three RADVS DVS beams locked on as soon as their acquisition conditions were met (while the retro was still burning) and tracked without interruption until beam 3 lost lock after the 10-fps mark and before the 14-foot mark. While not absolutely conclusive, there is strong evidence to indicate this was a forced break lock caused by a false sidelobe rejection of the main beam.

To prevent the possibility of one of the beams locking into a sidelobe return from one of the other beams, crosscoupled sidelobe (CCSL) rejection logic between beams 2 and 3, as well as tight roll attitude control, was incorporated in the Surveyor III RADVS and descent design. This crosscoupled sidelobe problem is described in more detail in Appendix A.

This logic will cause a tracker to reject a signal and return to a search mode when all of the following conditions exist for the two beams being compared (beams 2 and 3 in Surveyor III):

1) The trackers being compared must be locked up.

2) Received frequencies must be within 1200 Hz of each other.

3) Preamplifier gain states must be unequal.

4) Amplitude differences between the two beams must be at least 25 db after rolloff.

During the final seconds of the Surveyor III mission just prior to the loss of lock, the gain states were changing rapidly on all three beams. Immediately prior to the break lock, beam 3 was in gain state 3 (90 db) and beam 2 was in gain state 2 (65 db), a condition which satisfies criterion 4. Since the spacecraft was erected to the lunar vertical at the time, the frequency requirement (2) was clearly satisfied. Since the first criterion was obviously satisfied, this left only the amplitude comparison check to be fulfilled to send beam 3 into search. Since beam 3 was in the high gain state, an additional preamplifier rolloff comes into play, reducing the amplitude comparison delta to about 5 db at 5 fps instead of 25 db. This condition was never seriously considered earlier since there exists an 18-db margin against getting into the 90-db gain state at this point in the mission.

Return signal scintillation is clearly present as indicated by the several gain state switches. It is apparent then that a signal unbalance of as long as 0.4 second of the order of 5 db is quite conceivable in this environment. The averaging effect is gone at low altitudes where the beam angle subtends a circular area 3 to 4 feet in diameter. It should also be pointed out that it is the difference in amplitude that is sensed, so that a fade deep enough to cause

gain state 3 on beam 3 (which occurred) would also satisfy the unbalance condition, as long as beam 2 had faded at least 5 db less. It is seen, therefore, that all conditions were satisfied, or at least could have been, making the break lock occur normally and not as a result of some component failure or other system malfunction. All data analyzed to date tend to reinforce this supposition and none yet negate the theory.

Once the reject command is generated, the channel having a false lockon will go into search and presumably acquire the mainlobe next. If, however, the spacecraft velocity is low (10 fps or less), it is virtually impossible for the radar to reacquire. This is due to the preamplifier rolloff (6 or 12 db per octave depending on gain state) and to the tracker lower sweep limit of 800 Hz, which demands a tremendously large signal to acquire at these low doppler frequencies (2.3 volts at 100 cps compared with 0.006 volt at 500 cps). This rolloff is not necessarily a design weakness, per se, and is included in the system to reduce the analog noise at the lower altitudes and velocities where signal return certainly should be no problem.

Other possible causes of the break lock which were considered and discounted are:

1) Received signal strength in beam 3 falling below its tracking threshold due to low lunar reflectivity

2) Component failure in the KPSM or SDC

3) Spacecraft transmitter interference

4) Too low vertical velocity

Examination of the RADVS reflectivity signals showed essentially normal signal strength on all beams down to approximately 60 feet or just a few seconds before the break lock. All four beams were in gain state 3 (90 db) at least once during the final seconds of the descent, a decidedly abnormal situation and one not observed on Surveyor I. Preflight analysis predicted an 18-db margin against a DVS beam ever getting into the high gain state in the critical region that occurs at first contact with 5-fps vertical velocity and a 47-db margin against falling below threshold. Postflight analysis of received signal strength (subsection 5.9.4.9) indicates that while the lunar reflectivity was low enough to cause operation in gain state 3 in all beams, the probability of its falling or scintillating down another 30 db is extremely low.

Since all beams appear down in received signal strength, a transmitter problem was postulated. But since the altimeter, as well as the doppler system, appeared affected, this would require a degradation of both klystrons or the power supply. The normal characteristic for a fading klystron is a sudden and large dropoff both in output and input power. These characteristics do not appear in the data. Also, a high-voltage malfunction

would have affected altimeter deviation, but this appeared normal. A tracker failure could explain the break lock, but then it again is unlikely that all low returns can be explained in this manner. Because of the apparent requirement for multiple component failures to match the data, it is concluded that this is not the most probable cause and that the system was electrically functioning properly at the time of break lock.

Spacecraft transmitter interference was considered briefly since it was a problem noted in the solar thermal vacuum (STV) chamber. It was considered a possible cause since the spacecraft landed in a crater, making spurious returns conceivable. No rationale could be developed to prove this, and the idea was discarded in favor of more promising possibilities.

While an approach velocity on the order of 1 fps could result in a break lock of these signal strengths due to the low frequency rolloff, both telemetry data (subsection 5.9.4.8) and trajectory considerations (5.12.4.9) show that V_z was close to nominal at the break-lock condition.

In summary, it is apparent that with a high probability the break lock was caused by:

1) The reflected signal strength fading enough to put beam 3 receiver in gain state 3.

2) The reflectivity characteristics being such that beam 2 received at least 5 db more signal (or faded 5 db less) than beam 3 and was in gain state 2.

3) This combination of events then causing the beam 3 tracker to break lock and return to search via the CCSLL.

5.9.2.2 KPSM Cycling Anomaly

At the first touchdown, the RADVS KPSM recycled, meaning a return to initial warmup conditions with high voltage off until restoration after a normal internal time-in (about 18 seconds in Surveyor III). This was confirmed by a drop in prime current drain from full-load to warmup load current at first touchdown, followed 18 seconds later by return to full load current, and by sweeping of the altimeter during the 18-second off period. At the second touchdown, the KPSM again cycled off and back on another 18 seconds later. This cycling appeared to repeat several times in the subsequent 2 minutes, until the KPSM finally went off and stayed off, indicating continued arcing and recycling of the high voltage until final failure of the KPSM.

Although a prime bus voltage transient or electrostatic discharge to the lunar surface are potential causes for this anomaly, the most likely cause is a high-voltage arcover in a glow discharge made possible by the plume from the still burning vernier engines. Analysis has shown (Appendices B and C) that with all three engines burning to touchdown, the lunar surface can reflect enough vernier exhaust products into the area of the KPSM to make likely high-voltage arcing.

5.9.2.3 RADVS Range After Touchdown Anomaly

During the hop after the first touchdown and following the KPSM recycle, the altimeter relocked for a few seconds just before the second touchdown. This in itself would have been normal, but the analog range value of about 400 feet is far too large to be valid at that time This must be considered as a third RADVS anomaly. It can only be postulated that one or more of several hardware mechanisms (possibly the result of the KPSM arcing) must have caused this malfunction.

5.9.2.4 RADVS Turnoff Anomaly

RADVS off command is reported as having been sent at about 110:00:10:30. It must be noted that the spacecraft indication of RADVS on (R-28) remained on for at least 10 seconds thereafter, until the apparent failure of digital word 9 starting with the frame whose start time was 110:00:10:40.072 at DSIF-11. This and subsequent available frames had every bit on in digital word 9.

5.9.3 SUMMARY AND RECOMMENDATIONS

The Surveyor III RADVS performance was essentially nominal in all aspects from initial turnon to the loss of lock of beam 3 just prior to touchdown. The event times for those functions of concern to the RADVS are shown in Table 5.9-1. Significant performance parameters were as summarized in Table 5.9-2. A copy of the real-time range versus velocity plot made from raw telemetry in the space flight operations facility (SFOF) is shown in Figure 5.9-1 and the real-time analog traces of pertinent telemetry channels are shown in Figure 5.9-2.

In summary, the following performance items should be noted:

1) Very minor perturbations of RADVS analog signals at the time of RADVS power on (essentially at retro ignition) appear to be simply a telemetry signature analogous to that associated (prior to SC-5) with telemetry transients at AMR on.

2) Telemetry conditioning smoothing of the altimeter sweep function during KPSM cycle appears adequate to explain the compressed limits of the FC-35 analog range sweep pattern. (This applies not only to the low-deviation sweep during normal time-in during retro, but also to the high-deviation sweep during KPSM recycle after first touchdown.)

3) Acquisition of lunar reflected signals by all four RADVS beams again (as in Surveyor I) appeared to occur at the earliest opportunities, i.e., as soon as each beam's signal frequency decreased to its tracker's upper sweep limit. Altimeter acquisition occurs predictably later in time than for DVS beams, according to trajectory and RADVS parameters. Signal margins

TABLE 5.9-1. SURVEYOR III RADVS EVENTS

Channel	Name	On/Off	GMT at DSS 11, min:sec
FC-62	Retro sequence mode	On	55:13.771 ± 0.6*
R-1	AMR on	On	56:34.895 ± 0.6
FC-66	Thrust phase power	On	57:35.490 ± 0.6
R-11	AMR enable	On	59:34.890 ± 0.6
FC-64	AMR mark	On	01:12.821 ± 0.05
FC-28	Vernier ignition	On	01:17.922 ± 0.05
FC-29	Retro ignition (also FC-64 Off)	On	01:19.023 ± 0.05
EP-33	RADVS pyro switch	On	01:19.687 ± 0.6
R-28	RADVS on (Z23)	On	01:19.885 ± 0.6
FC-63	Inertia switch	On	02:00.183 ± 0.6
FC-30	Retro burnout	On	02:00.523 ± 0.05
FC-31	Retro eject	On	02:12.523 ± 0.05
V-4	Retro not ejected	Off	02:13.282 ± 0.6
FC-42	Start RADVS descent (also FC-62 Off)	On	02:14.624 ± 0.05
FC-37	1000-foot mark	On	03:53.021 ± 0.05
FC-36	10-fps mark	On	04:10.622 ± 0.05
Postfirst Touchdown Signals			
FC-36	10-fps mark	Off	04:36.521 ± 0.05
		On	04:37.921 ± 0.05
		Off	04:42.420 ± 0.05
EP-32	High current mode off	On	04:42.477 ± 0.6
FC-36	10-fps mark	On	04:43.820 ± 0.05
EP-31	Auxiliary battery mode	On	04:46.076 ± 0.6
FC-36	10-fps mark	Off	04:53.920 ± 0.05
FC-66	Thrust phase power	Off	04:53.475 ± 0.6
FC-38	14-foot mark	On	05:03.021 ± 0.05
Digital word 9 (all 10 bits on)			10:40.072 ± 0.6
End of data, frame starting (still on were R-1, R-11, R-28)			10:49.445

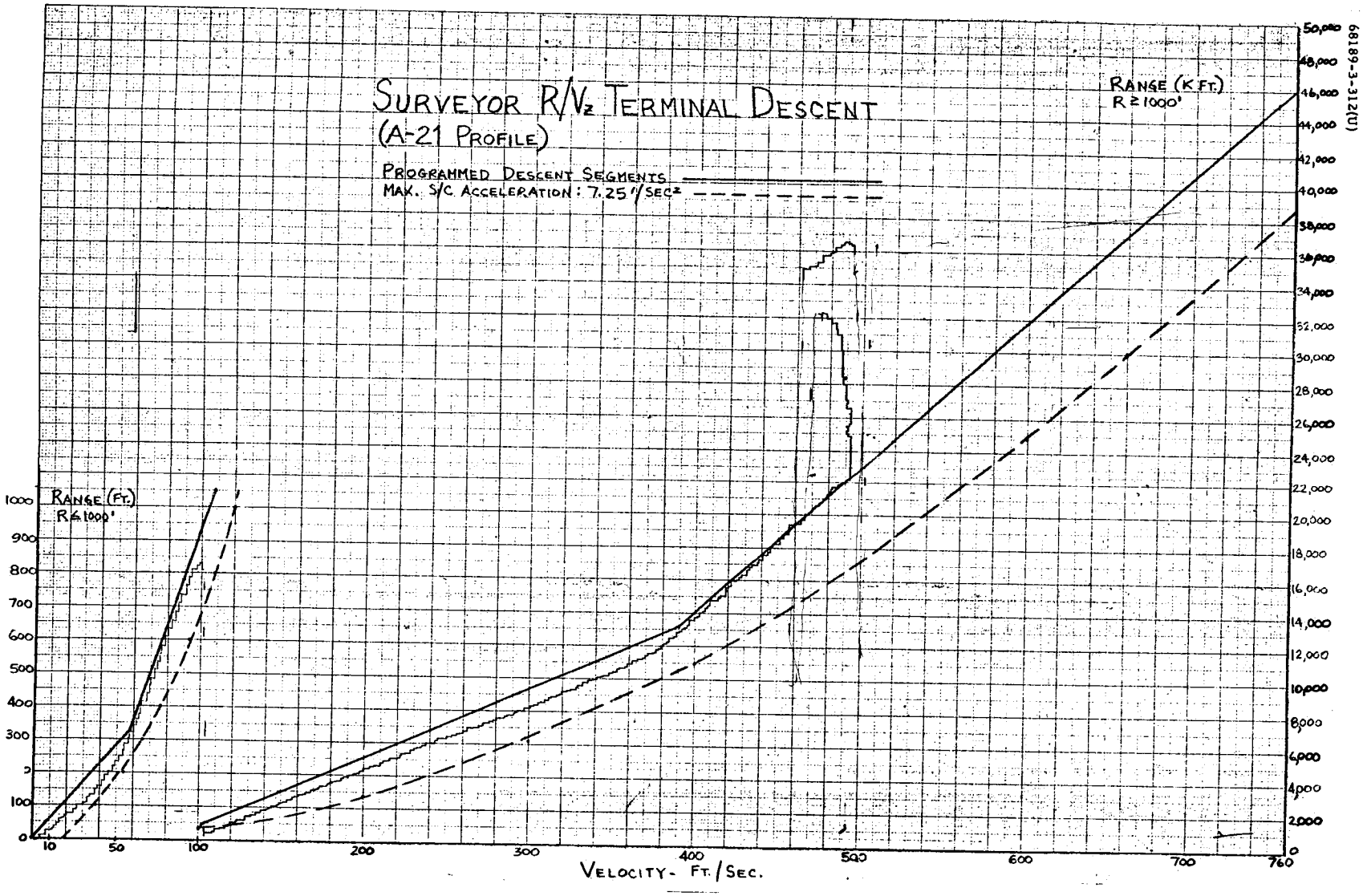

Figure 5.9-1. R/V_Z Terminal Descent

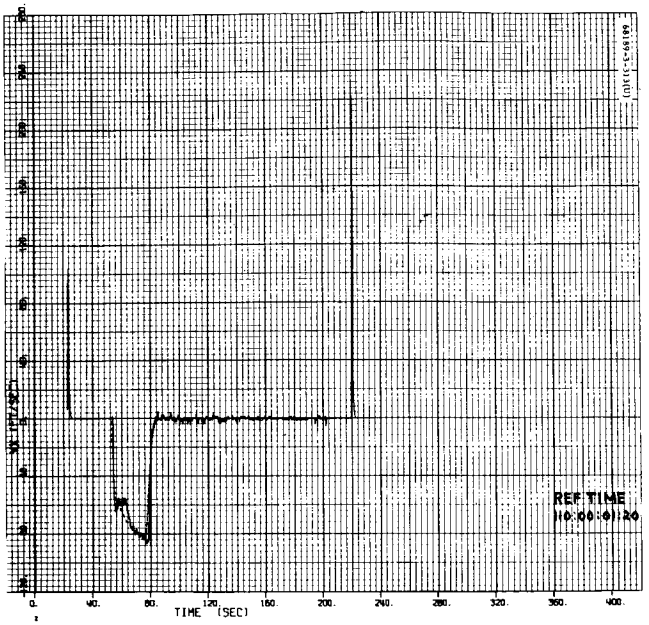

a) V_x Versus Time

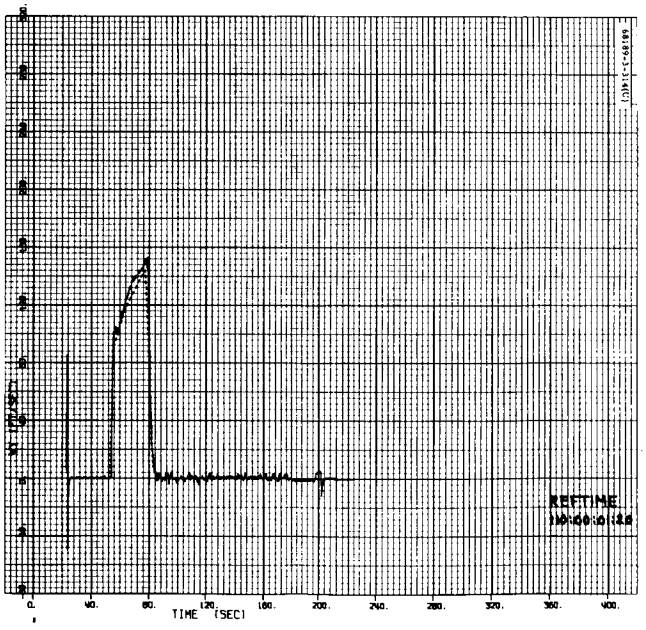

b) V_y Versus Time

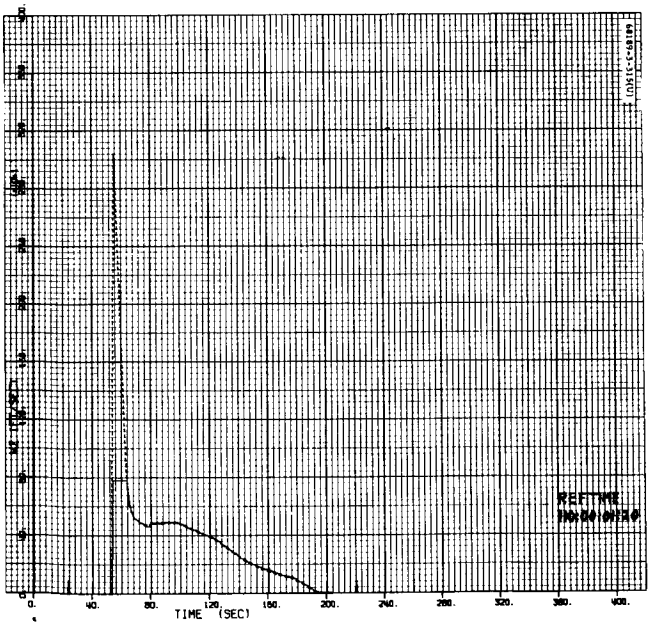

c) V_z Versus Time

Figure 5.9-2. Doppler Velocities

TABLE 5.9-2. RADVS PERFORMANCE PARAMETERS SUMMARY

Initial acquisition	Nominal on all beams
Dropouts near burnout	None on DVS beams Two on RA, with gain switches
Steering after burnout	Normal
Descent to segments	Normal
Segment acquisition	Normal
Descent profile	Normal to below 10 fps
Switch to attitude hold	Normal at 10 fps
Altimeter to touchdown	Normal
DVS to touchdown	Beam 3 dropout, probably by CCSLL
Failure to reacquire	Normal at that time
Velocity accuracy, including telemetry error	Well within radar requirements alone
Range accuracy, including telemetry error	About at specification limit on radar alone
Noise and ripple	Comparable to noise models and to Surveyor I

at acquisition, as indicated by telemetry reflectivity signals, were close to predicted nominal values, except that the altimeter return appeared consistently weak by some 5 to 8 db throughout the descent.

4) Depression of the altimeter sweep pattern at time of DVS acquisition is normal because of heavy V_Z-compensation within the altimeter converter at first appearance of (telemetry-saturated) V_Z. Also normal is a more gradual rise of the altimeter sweep as V_Z decreases (still during retro) prior to altimeter acquisition. Altimeter sweep disappears at altimeter acquisition, and reported telemetry range is initially telemetry saturated.

5) In Surveyor III there were two altimeter dropouts – one just after retro case separation, and the other about 8 seconds prior to that. Each was for a minimum relock interval of one sweep period. Each was associated with a gain switch from gain state 3 to 2, and a return to gain state 3 with relock. Lunar signal was inadequate for tracker lock in gain state 2, and dropout was normal for a gain state 2 switch. Cause of the gain switch was no doubt the retro case itself after separation; cause of the earlier gain switch and dropout can only be postulated as a retro plume effect, perhaps a chunk of liner expelled in the erratic thrust tail-off region. (Gain-switching is on a wide-band basis, as opposed to tracker acquisition and tracking.)

6) There was no interruption of any DVS beam from first acquisition to the anomaly at about 30 feet. While the Surveyor I retro case appeared to interrupt beam 3, the Surveyor III retro case appeared to interrupt beam 4, indicating more nominal separation dynamics. These mainbeam interruptions had no effects on either of the Surveyor I or III descents.

7) An apparent glitch in V_z about 12 seconds before the 1000-foot mark was only one bad data word in FC-41 with parity error. PREPRO was modified to ignore bad data.

8) Similar glitches in processed analog data a few seconds after the 1000-foot mark was only one bad data word with parity error in FC-77. PREPRO now ignores these and substitutes the last valid value.

9) The anomalous unlock of beam 3 and subsequent events are covered in subsection 5.9.2 "Anomalies," and in subsection 5.9.4 "Performance Analysis."

As a result of the Surveyor III anomaly and related factors in the RADVS development, the following recommendations have been implemented in SC-4 and up:

1) Engineering change proposal (ECP-23) has been added to provide complete rejection of any and all crosscoupled sidelobes in all gain state combinations, at any approach angle, at any roll angle, and at any burnout velocity where system capability otherwise exists. This replaces the old logic which afforded quite limited protection.

2) CCSL rejection logic (ECP-23) will be disabled by the 1000-foot mark, to prevent recurrence of the Surveyor III anomaly.

3) CRO steering will not be disabled until the 1000-foot mark.

For future postmission analyses, the procedures utilized in this report will be available in almost fully automated forms. The only exception is the

significant process of trajectory reconstruction by iteration of the 6DOF program to match all aspects of the telemetry data. This process, performed by the Guidance and Trajectory Department powered flight section is a major step in spacecraft performance evaluation. Inclusion of radar modeling not only allows radar telemetry data to aid in this reconstruction, but also produces predicted nominal values for all RADVS quantities for the reconstructed trajectory. Once this is achieved completely automated facilities are then available for outputting and/or machine plotting of both nominal and telemetry values for each of a wide variety of RADVS signals.

Recommended machine plots for future postmission analyses include:

1) 6DOF nominal values versus PREPRO-processed (FC-77 corrected and telemetry coefficient converted) flight values of V_X versus FC-39, V_Y versus FC-40, V_Z versus FC-41, and R_Z versus FC-35. (Time and scaling features are available.)

2) 6DOF nominal values versus PREPRO-processed (FC-77 and conversion) flight values of POWREC versus reflectivity corrected for rolloff, for each beam separately, showing total power at receiving feedhorns before rolloff.

3) 6DOF nominal values versus PREPRO-processed (FC-77 and conversion) flight values of EQDBMA versus reflectivity signal without rolloff correction, for each beam separately, showing apparent power after first rolloff, valid for gain state 2 and 1. EQDBMB is correct 6DOF for gain state 3, but will differ insignificantly from EQDBMA at the high frequencies normally seen when gain state 3 exists early in the descent.

4) Beam incidence angle and nominal REFLECT signals from 6DOF, for each beam separately, the latter being the total $\sigma(\theta)$ cross section per unit projected area in db.

5) 6DOF EQDBMB signals showing apparent signal strengths after first and second rolloffs, for each beam. These are exact for gain state 3 comparison with PREPRO-processed telemetry without rolloff correction when in gain state 3. They are also the correct values in all gain states for the signals seen by the gain-switching threshold circuits, for direct comparison with preflight measured gain-switching levels.

Hand work should still be employed to properly handle special situations where tracker unlocks cause artificial data and/or corrections. (PREPRO is being modified to use zero rolloff correction when a tracker is unlocked.)

5.9.4 RADVS PERFORMANCE ANALYSIS

5.9.4.1 RADVS Turnon

RADVS turnon occurred properly at retro ignition as indicated by altimeter search sweep on the range signal telemetry output. Subsequent time-in of the high voltage occurred approximately 19 seconds after turnon as indicated by the change in current on the radar squib current telemetry channel, EP17.

5.9.4.2 Velocity Acquisition Conditions

All three beams of the velocity sensor acquired and commenced tracking as soon as the signal came within the acquisition sweep frequency limits. The conditions at initial acquisition for each beam were as given below.

Beam	Slant Range Along Beam, kft	Velocity Along Beam, fps	Beam Incidence Angle, degrees	Doppler Frequency, kHz	Maximum Search Frequency, kHz
1	69.0	3160	26.7	85.5	≈85
2	62.4	3190	9.1	86.3	≈85
3	76.7	2934	40.0	79.3	≈85

The spacecraft conditions at the time of RODVS (all three DVS beams locked and computing V_x, V_y, and V_z) were as follows:

V_x	≈	-51.8 fps
V_y	≈	+86.8 fps
V_z	≈	+3230 fps
Range	≈	63.9 kft
Attitude		23.73 degrees
Altitude		58.5 kft

5.9.4.3 Range Acquisition Conditions

From telemetry and terminal descent 6DOF reconstruction, the conditions at range tracker lockon are estimated as follows:

V_x	≈	-73.2 fps
V_y	≈	+120.1 fps

V_z	$\approx$	+632 fps
Range	$\approx$	43.7 kft
Attitude	$\approx$	23.80 degrees
Altitude	$\approx$	40.0 kft

5.9.4.4 Operation During Retro Burn and Retro Separation

All three velocity sensor beams acquired during retro burning and tracked properly throughout the remainder of the retro burn phase and retro separation without any glitch or loss of lock. There is no evidence of any anomalous effects of retro plume or vibration on the RADVS performance, which confirms the Surveyor I performance.

The altimeter beam (beam 4) acquired during the retro thrust tailoff period approximately 10 seconds prior to retro case separation. Approximately 6 seconds before and 2 seconds after case separation, beam 4 lost lock and immediately acquired on the subsequent search sweep. This second loss of lock was almost assuredly caused by the ejected retro case passing through the beam. The cause for the first loss of lock, however, is not definitely known. As seen in subsection 5.9.4.9, the signal strength is well above threshold at this time. One possible cause is interference from the plume or some ejecta, such as case insulation, from the retro during its tailoff condition.

5.9.4.5 Telemetry Correction Factors

Table 5.9-3 shows the preflight test data on analog velocity and range values and compares them with the nominal linear response. Bias values appeared randomly distributed, as expected in test results, within test and system performance specifications. There is no apparent systematic departure from nominal linearity. Preflight coefficients using A_o and A_1 terms only are shown in Table 5.9-4 where the A_o terms represent the expected FC-77 effect when not corrected before coefficients. Table 5.9-5 shows postflight coefficients used in programs which automatically make FC-77 corrections to raw data before conversion to engineering units.

The entire trajectory reconstruction effort used these last values in iterating the 6DOF program against PREPRO telemetry data. This iteration includes the recognition and separation of system bias errors, telemetry bias errors, system scale factor errors, and telemetry scale factor errors. Starting with SC-4, the telemetry handbook coefficients for FC-35, -39, -40, and -41 will be second order rather than fifth order, and in general can be used directly in the future.

TABLE 5.9-3. SURVEYOR III RADVS TELEMETRY CALIBRATION

Feet per Second	Nominal, bcd	FC-39 (V_x)		FC-40 (V_y)	
		Measured, bcd	Bias, bcd	Measured, bcd	Bias, bcd
-300	000	064	64	066	66
-200	170.5	231	60.5	244	73.5
-50	426.25	493 494	66.75 67.75	498	71.75
0	511.5	579 582 582 582 583	67.5 70.5 70.5 70.5 71.5	582 583 583 584 583	70.5 71.5 71.5 72.5 71.5
+50	596.75	670	73.25	669 670	72.25 73.25
+200	852.5	922	69.5	933	80.5
+300	1023	1023	—	1023	—
Sum Bias			752.25		794.75
Binary coded data			68.386		72.250
Volts dc			0.334		0.353
Feet per second			40.11		42.37

Table 5.9-3 (continued)

FC-41 (V_z)				FC-35 (R_z)			
Feet per Second	Nominal, bcd	Measured, bcd	Bias, bcd	Feet	Nominal, bcd	Measured, bcd	Bias, bcd
9.8	12.53	035	22.47	40,000	1023	1023	–
38	48.59	073	24.41	36,530	934.25	961	26.75
54.5	69.69	093	23.31	14,000	358.05	382 383	23.95 24.95
67	85.68	111	25.32			381	22.95
100	127.87	153 153	25.13 25.13	2,000	51.15	076	24.85
325	415.59	438	22.41	1,710	43.73	067	23.27
560	716.10	740	23.90	902	461.37	488	26.63
700	895.12	917 919 919	21.88 23.88 23.88	300 240	153.45 122.76	177 145	23.55 22.24
				10	5.12	026	20.88
Sum Bias			261.72				240.02
Binary coded data			23.793				24.002
Volts dc			0.116				0.117
Feet per second			18.606				
Feet (R > 1 kft)							938.50
Feet (R < 1 kft)							46.924

TABLE 5.9-4. SURVEYOR III RADVS PREFLIGHT TELEMETRY CALIBRATION (A_o, A_1)

FC-35 (R_z)

A_o = -938.5 ft (R > 1000 feet)

A_1 = +39.10 ft/bcd (R > 1000 feet)

A_o = -46.92 ft (R < 1000 feet)

A_1 = +1.955 ft/bcd (R < 1000 feet)

$A_2 = A_3 = A_4 = A_5 = 0$

FC-39 (V_x)

A_o = -340.11 fps

A_1 = +0.5865 fps/bcd

$A_2 = A_3 = A_4 = A_5 = 0$

FC-40 (V_y)

A_o = -342.37 fps

A_1 = +0.5865 fps/bcd

$A_2 = A_3 = A_4 = A_5 = 0$

FC-41 (V_z)

A_o = -18.61 fps

A_1 = +0.7820 fps/bcd

$A_2 = A_3 = A_4 = A_5 = 0$

TABLE 5.9-5. SURVEYOR III RADVS POSTFLIGHT TELEMETRY CALIBRATION USING FC-77 CORRECTION

All $A_2 = A_3 = A_4 = A_5 = 0$

FC-35 (R_z)

> 1000 ft $A_o = 0.0$

$A_1 = +39.10 \times [(FC-35) - (FC-77)]$

< 1000 ft $A_o = 0.0$

$A_1 = +1.955 \times [(FC-35) - (FC-77)]$

FC-39 (V_x)

$A_o = -329.6$ fps

$A_1 = +0.5865\ [(FC-39) - (FC-77)]$

FC-40 (V_y)

$A_o = -330.1$ fps

$A_1 = +0.5865\ [(FC-40) - (FC-77)]$

FC-41 (V_z)

$A_o = 0.0$

$A_1 = +0.7820\ [(FC-41) - (FC-77)]$

(For all four: for first word only in each frame, substract FC-77 value in previous frame; for second, third, and fourth words, subtract FC-77 value in same frame.)

5.9.4.6 Noise on Analog Outputs

Visual examination of Surveyor III analog telemetry data showed that the amount on analog noise on V_x, V_y, V_z and R was similar to that on Surveyor I. Thus, because of the large amount of hand calculations required, and because digital programs for this analysis are not yet complete, a detailed noise evaluation was not made. Program capability for deriving and plotting automatically the differences between 6DOF and telemetry data, in addition to direct comparison plots, is being explored for subsequent postmission analyses.

5.9.4.7 Reconstructed Trajectory

As described in subsection 5.12, "Terminal Descent Analysis," the descent trajectory from retro ignition to touchdown is reconstructed by use of a 6-degree-of-freedom digital computer program (6DOF) and iterating on this program to produce a best fit to the actual flight telemetry data. The method and accuracy of this approach is discussed in subsection 5.12.4.9. Shown in the following figures and described briefly below are the results of this trajectory reconstruction.

Figure 5.9-2 and 5.9-3 show the nominal values of V_x, V_y, V_z and R_s from the best fit 6DOF program compared to the corrected telemetry values. Figures 5.9-4a and -4b are similar R_s versus V_z plots. In these figures the dotted line marks the computed values and the solid line the telemetry values.

Figures 5.9-5 through 5.9-7 are plots of computed radar parameters using the reconstructed trajectory. Figure 5.9-5 shows the incidence angle, θ, relative to local lunar vertical and the Muhleman factor $F(\theta)$ (see subsection 5.9.4.10) for each beam. (Effective cross sections are 1.72 db lower.) Figure 5.9-6 shows the computed values of received signal strength in each receiver prior to any rolloff. Figure 5.9-7 shows the apparent signal power in each receiver after the first rolloff. As can be seen, all beams were well above threshold at first acquisition.

Figure 5.9-8 shows the computed values of received signal power after the first rolloff (at 65-db tap) and after both rolloffs (at gain switching threshold circuit) as a function of range. Also noted on these curves are the gain-switching thresholds.

5.9.4.8 Touchdown Conditions from RADVS Telemetry

Due to the nonstanding landing conditions (vernier engines on and RADVS beam 3 searching) the radar telemetered velocities cannot be used directly to obtain a measure of the touchdown velocities. However, they can be manipulated as shown below to obtain bounds on these velocities.

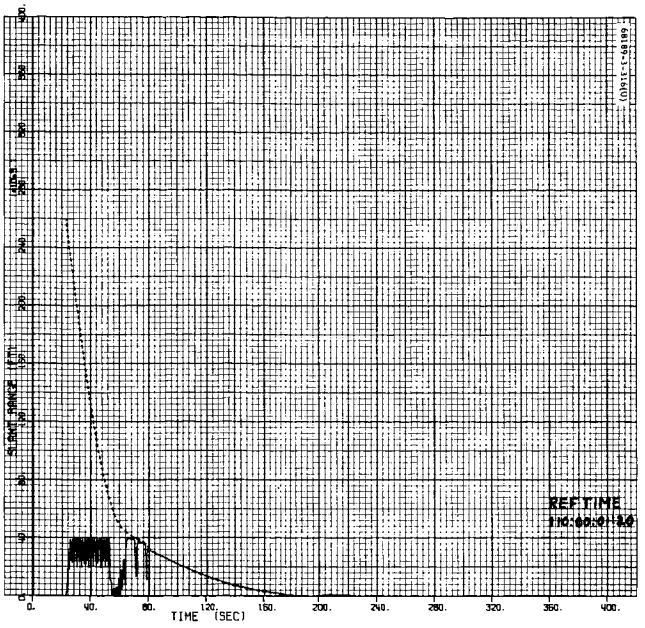

Figure 5.9-3. Slant Range Versus Time

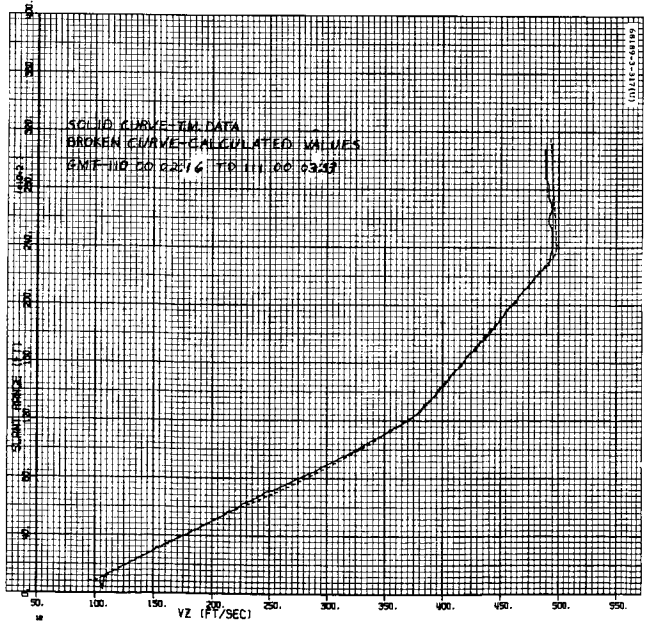

a) > 1000 Feet

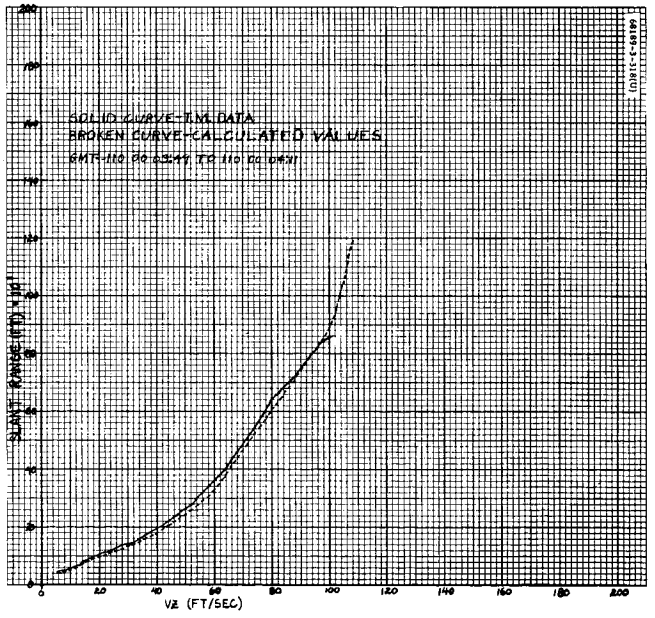

b) < 1000 Feet

Figure 5.9-4. Slant Range Versus V_z

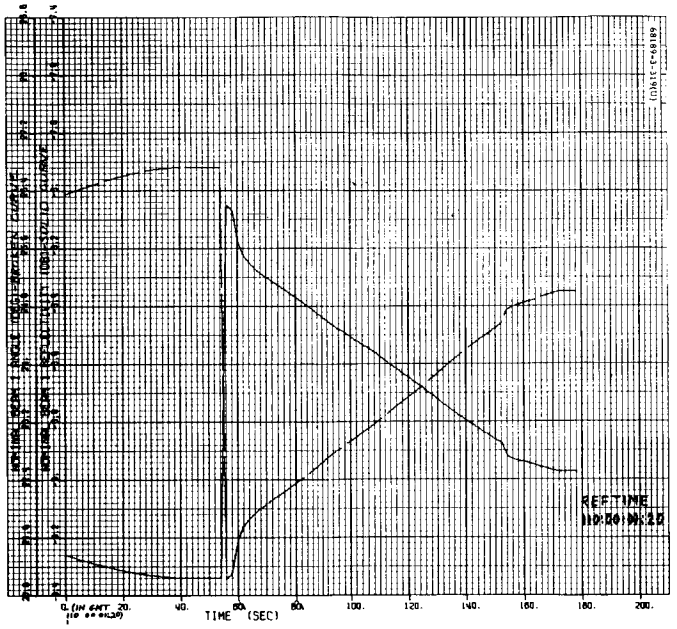

a) Beam 1

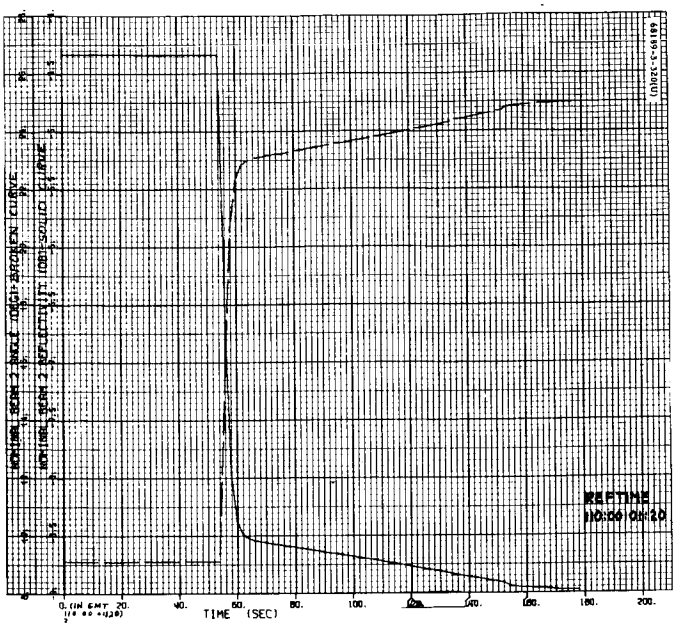

b) Beam 2

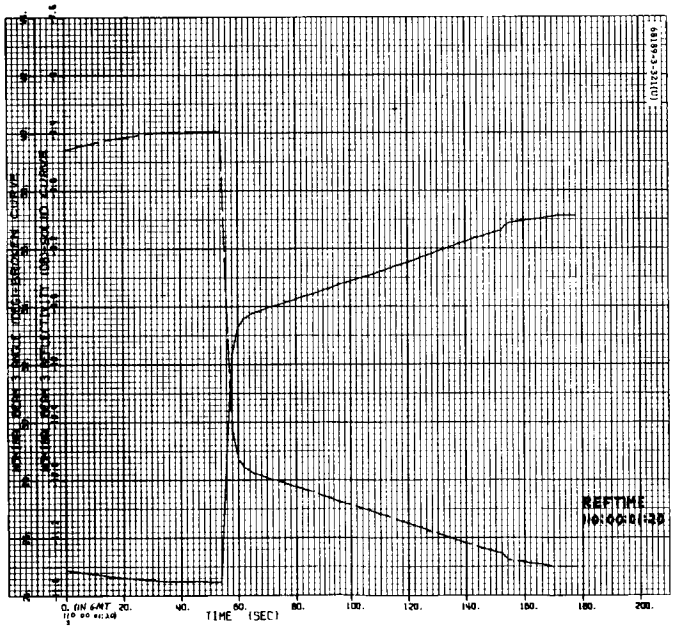

c) Beam 3

d) Beam 4

Figure 5.9-5. Beam Angle and Reflectivity Versus Time

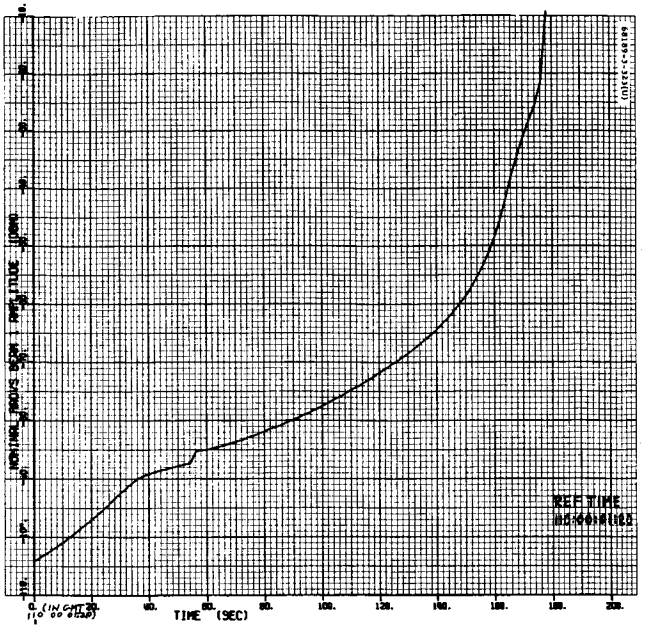

a) Beam 1

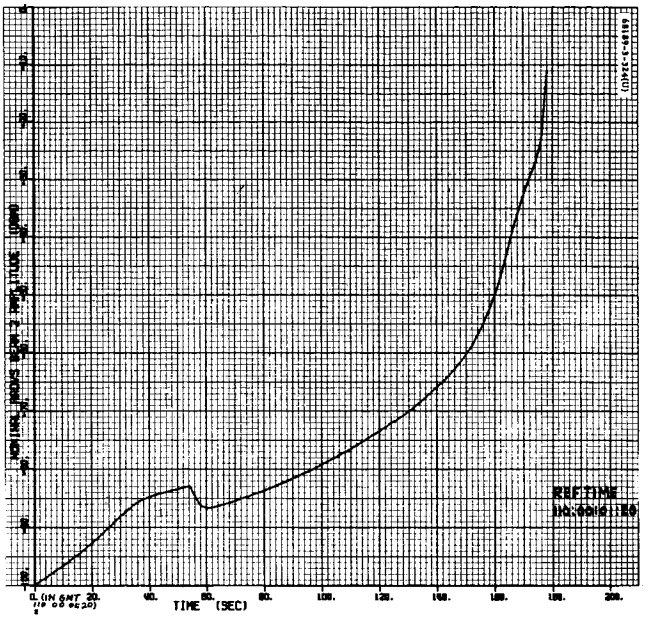

b) Beam 2

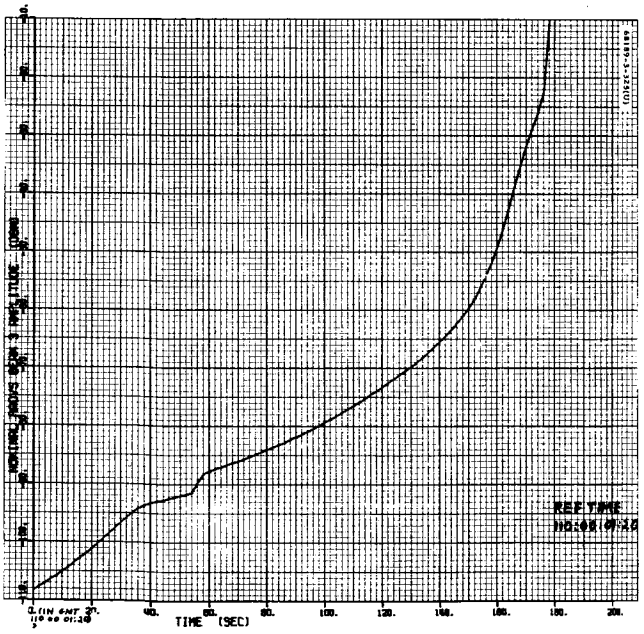

c) Beam 3

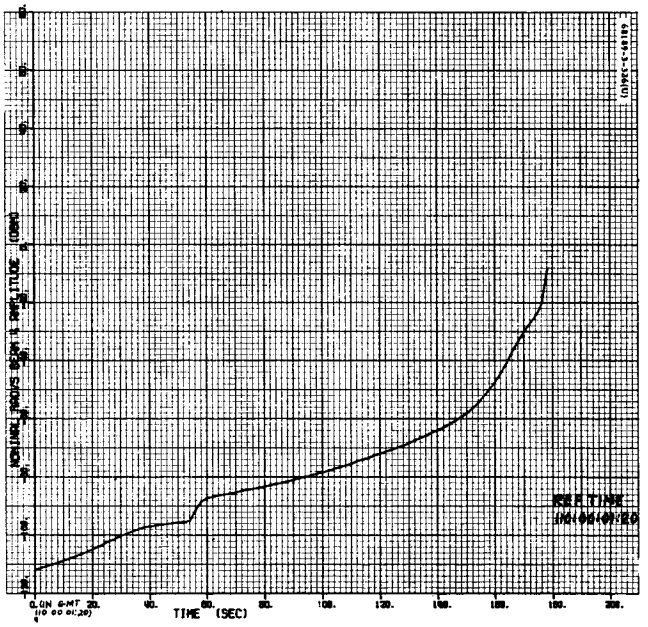

d) Beam 4

Figure 5.9-6. Beam Amplitude Versus Time

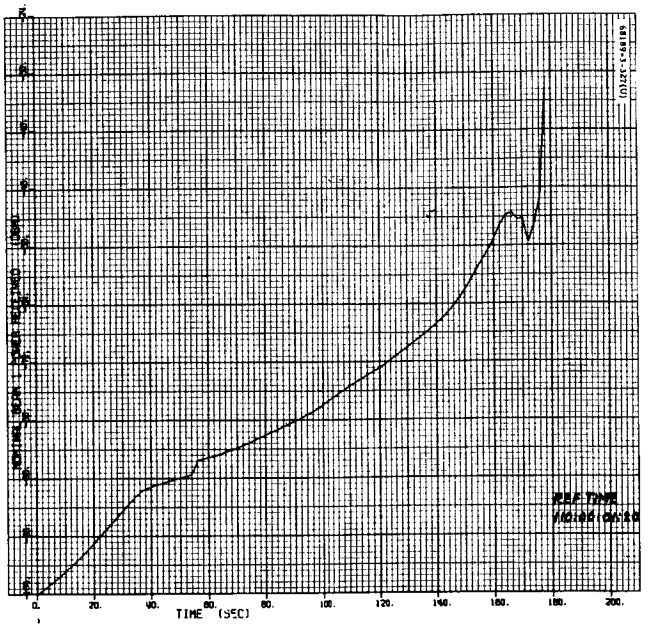

a) Beam 1

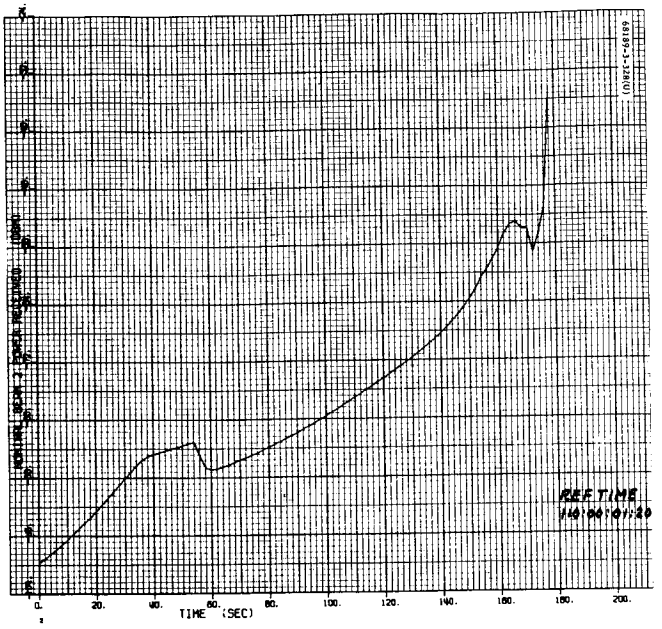

b) Beam 2

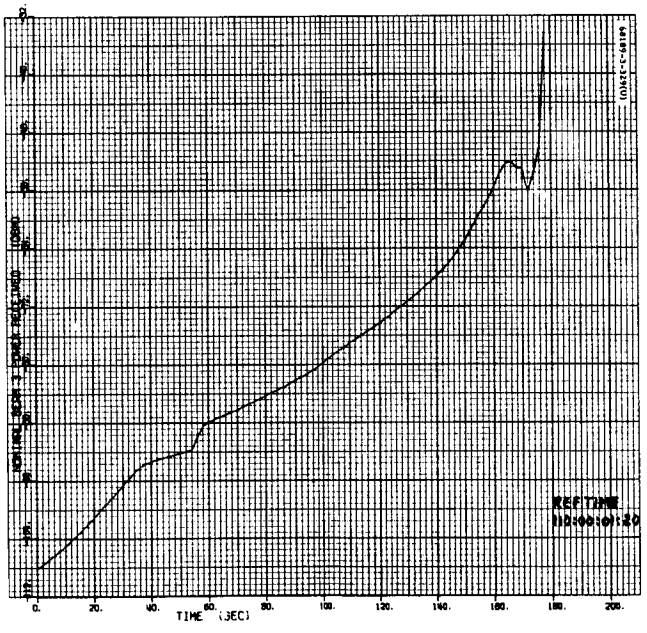

c) Beam 3

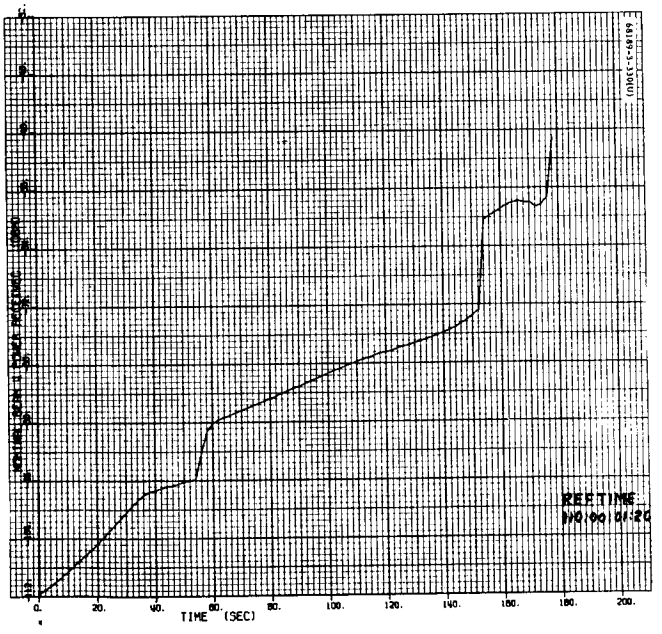

d) Beam 4

Figure 5.9-7. Beam Power Received Versus Time

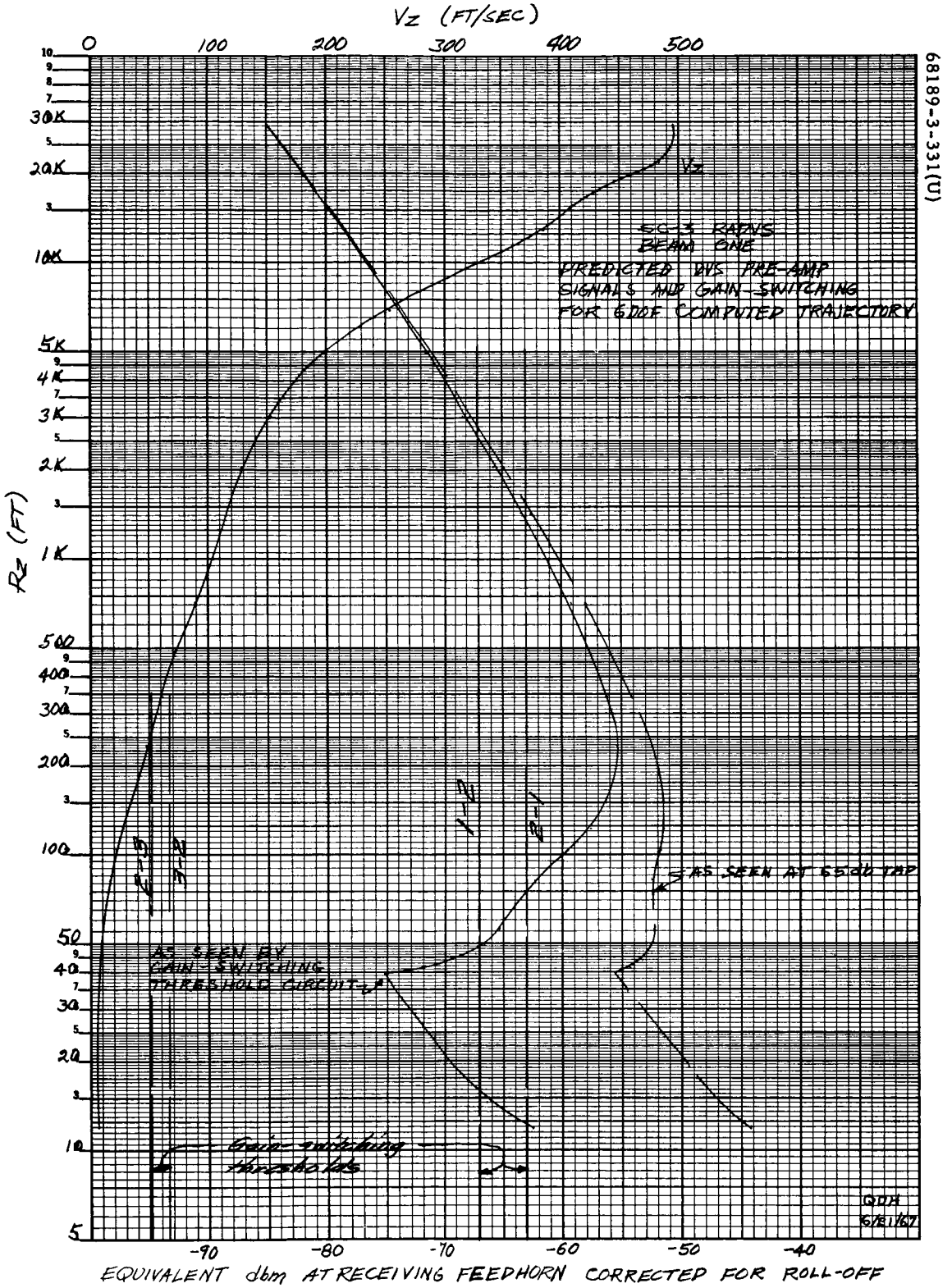

a) Beam 1

Figure 5.9-8. Beam Predicted DVS Preamplifier Signals and Gain Switching

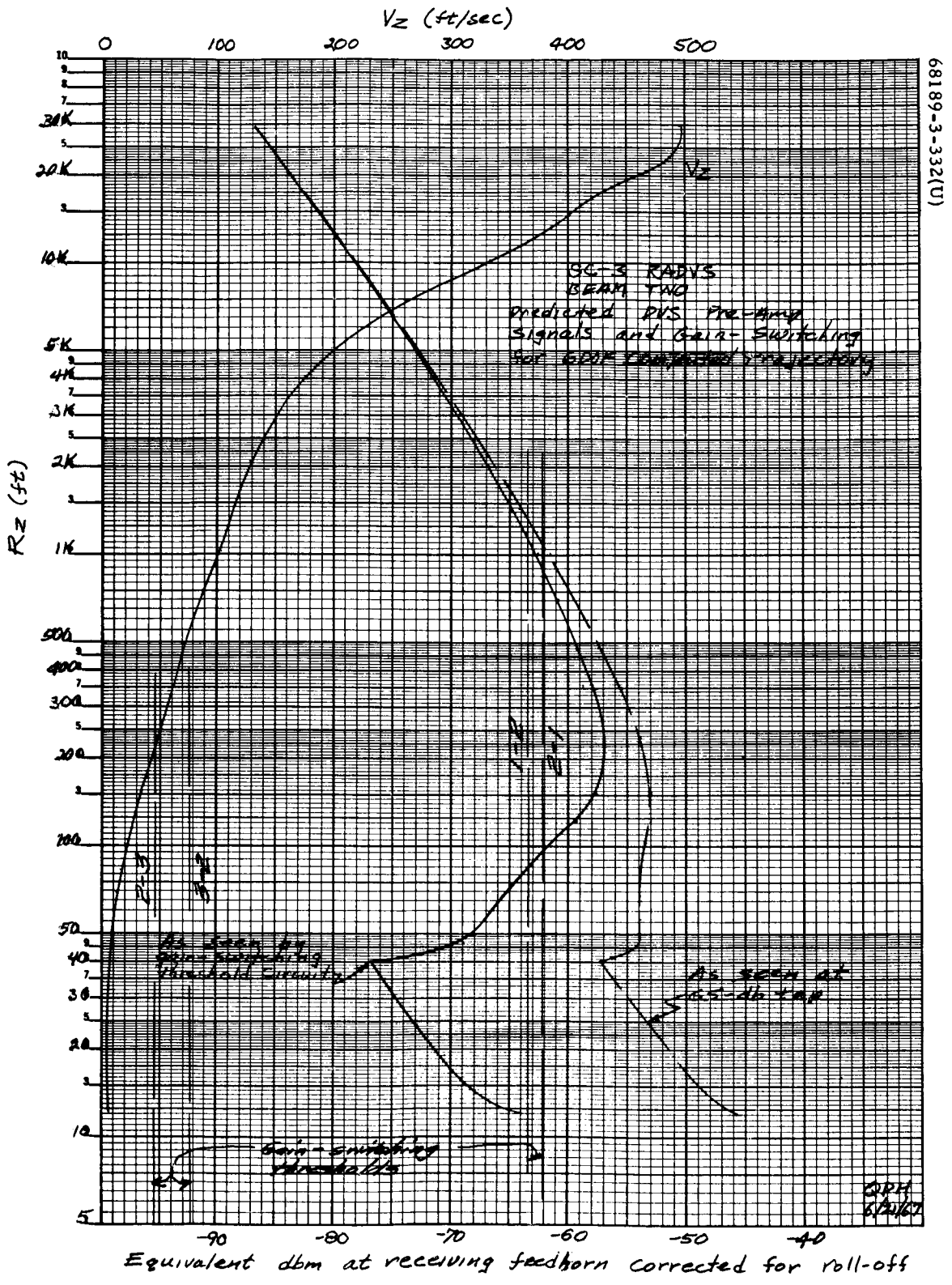

b) Beam 2

Figure 5.9-8 (continued). Beam Predicted DVS Preamplifier Signals and Gain Switching

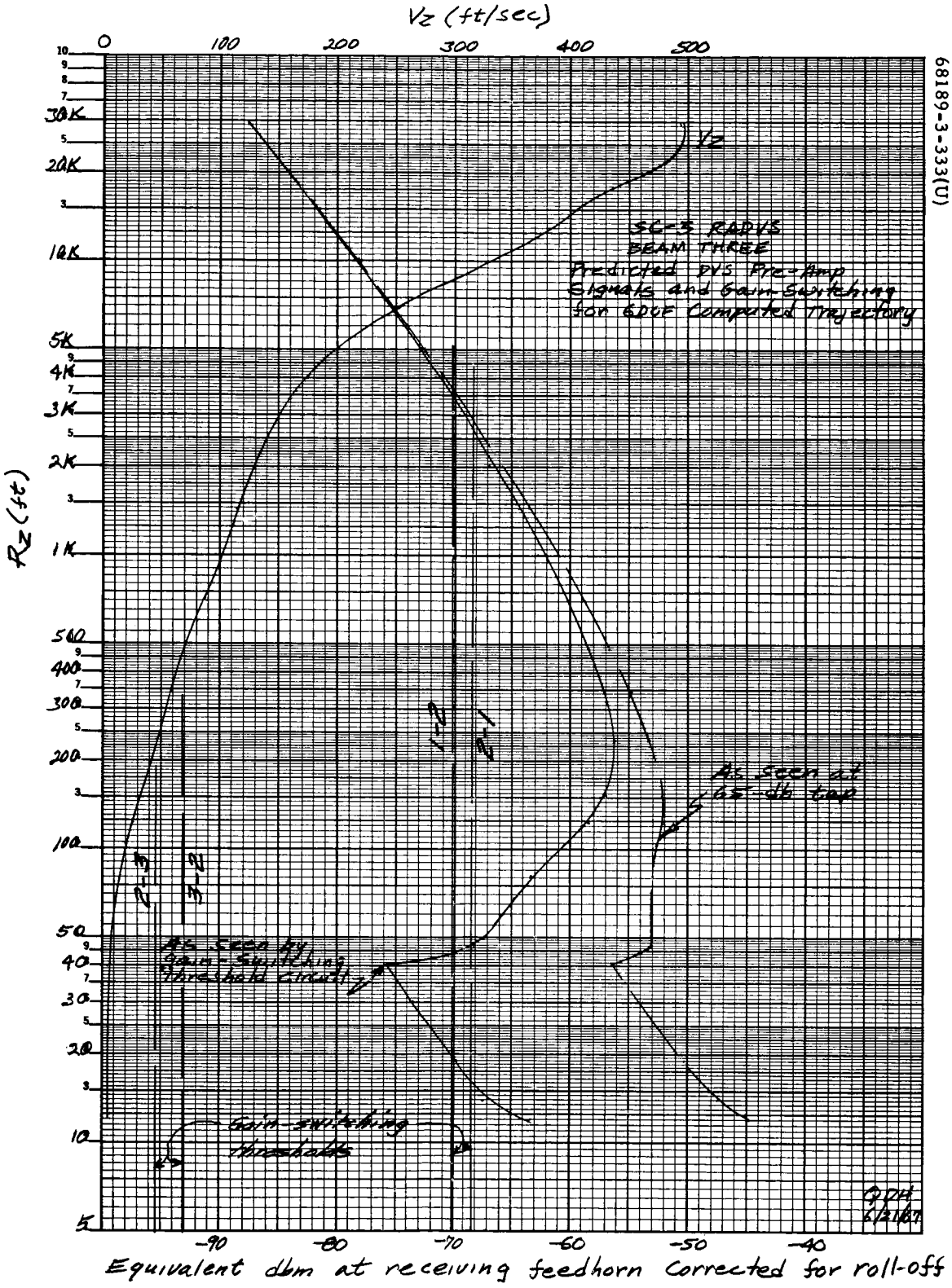

c) Beam 3

Figure 5.9-8 (continued). Beam Predicted DVS Preamplifier Signals and Gain Switching

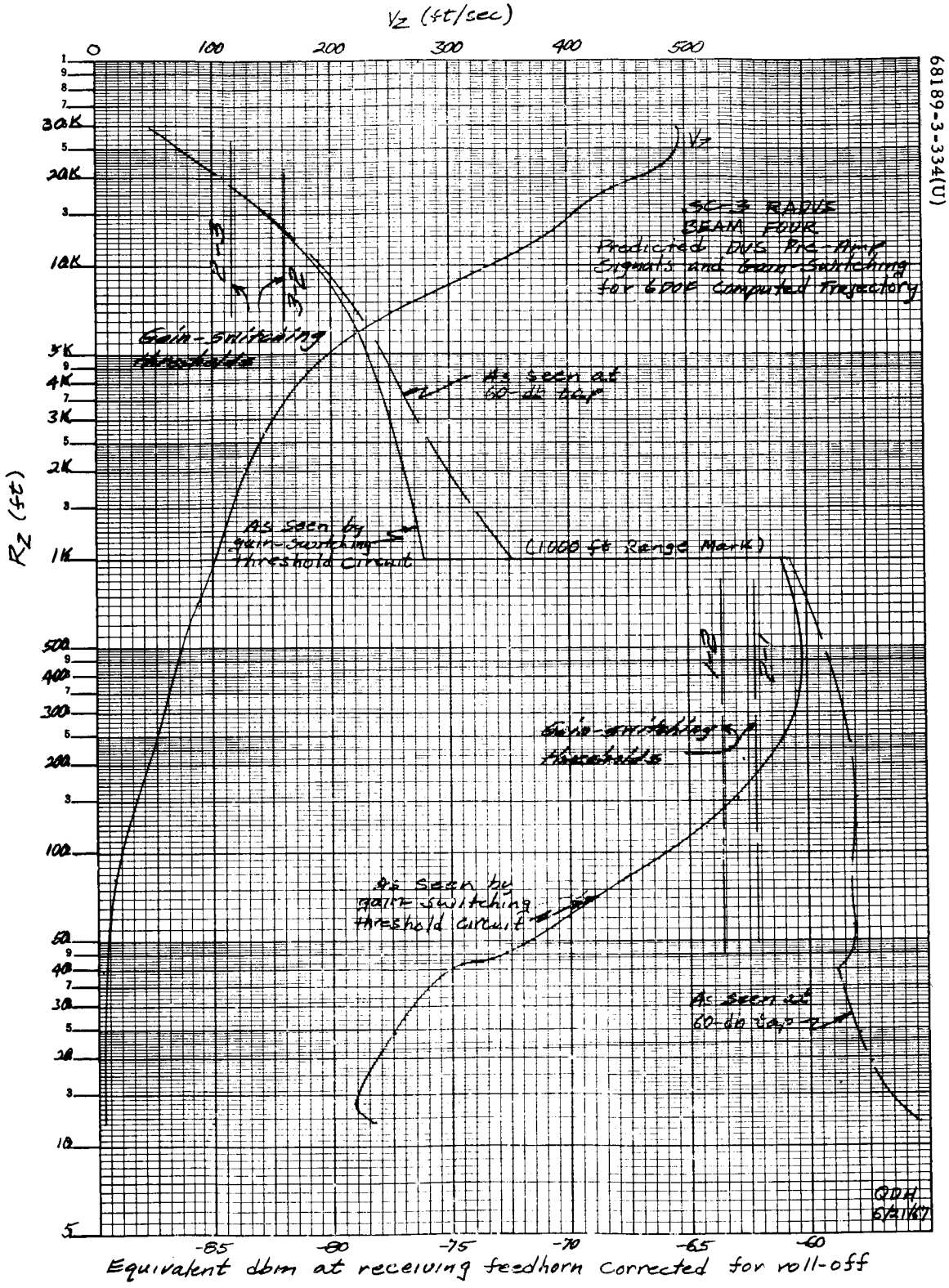

d) Beam 4

Figure 5.9-8 (continued). Beam Predicted DVS Preamplifier Signals and Gain Switching

From the general equations

$$\tilde{V}_x = \frac{\tilde{V}_1 - \tilde{V}_2}{0.59768}$$

$$\tilde{V}_y = \frac{\tilde{V}_2 - \tilde{V}_3}{0.59768}$$

$$\tilde{V}_z = \frac{\tilde{V}_1 + \tilde{V}_3}{1.81262}$$

in the introduction (where tildes denote indicated values), from the fact that 1) an operative tracker reports a doppler frequency with a discriminator offset bias of 40 Hz equivalent to 1.47907 fps in DVS trackers, 2) that velocity arithmetic converters apply a corrective bias to each tracker's input whether that tracker is locked or not, and 3) that a tracker output is zero doppler (600-kHz reference) without bias when unlocked, it is seen that a lateral velocity (V_x or V_y) converter has a bias of 2.4747 fps with one tracker unlocked, and zero bias with both trackers locked or with both trackers unlocked. The sign of the bias is that of the beam velocity term, in the above equations, for the unlocked tracker. In the V_z converter, the bias is zero with both trackers locked, +0.81598 fps with one unlocked, and +1.63196 fps with both unlocked.

In Surveyor III, from the beam 3 unlock to first touchdown, therefore:

$$\tilde{V}_x = V_x = \frac{V_1 - V_2}{0.598} \approx 0$$

$$\tilde{V}_y = \frac{V_2 - 1.48}{0.598}$$

$$\tilde{V}_z = \frac{V_1 + 1.48}{1.813}$$

and the beam velocities V_1 and V_2 were:

$$V_1 = 1.813\ \tilde{V}_z - 1.48$$

$$V_2 = 0.598\ \tilde{V}_y + 1.48$$

then

$$V_1 \approx 0.906\ V_z \approx V_2$$

Application to Surveyor III data shows that V_z was indeed between 4 and 5 fps. Considerable algebraic manipulation, including true FC-77 as an unknown, has been unable to refine this value because of quantization uncertainties.

5.9.4.9 Radar Reflectivity Analysis

RADVS gain-switching events and reflectivity signal amplitudes for the Muhleman reflectivity model were derived, described, and presented in a succession of radar description and Surveyor I prediction packages over a year ago, and were presented again in the Surveyor I postmission report. The unusual difference in frequency responses seen by the signal circuits and by the gain-switching threshold circuits was treated in detail, with predictions of higher than necessary gain states at very low altitude, starting about 10 seconds before touchdown. This response was confirmed in the Surveyor I mission performance and again in Surveyor III. However, in Surveyor III the effect became aggrevated due to a generally lower reflectivity which caused the beam 3 mainlobe to be rejected by the CCSLL just prior to touchdown.

Premission predictions for each individual beam were again made for Surveyor III using actual Surveyor III system test data and nominal descent trajectories. Because of a number of design tolerances, however, actual flights may differ from these nominal values by amounts which, while well within such tolerances, still have a significant effect on the geometric dependencies of the radar signals. Not just for radar purposes, but for the larger analyses of the entire terminal descent of each mission, an appreciable effort is devoted to a complete and accurate nine-dimensional trajectory versus real-time reconstruction. While this process is hampered by lack of direct data on spacecraft attitude once steering has started, it is possible to converge on an accurate and unique solution in which attitude is implicit by iteration of a precise spacecraft simulation against every significant telemetry channel, as described in the terminal descent discussion. Radar data aid in this reconstruction, and in return, the simulation provides expected or predicted reflectivity signal strengths throughout the descent. This process was almost trivial in the almost exactly nominal Surveyor I, but has proved its utility in matching the roughly 1 σ Surveyor III. Utilization of this process for reflectivity analysis has become largely automated for Surveyor III, though some handwork has been done, and should be fully automated for SC-4 and subsequent postmission analyses.

The results were presented in subsection 5.9.4.7 and the received signal strength versus time plots are represented here in Figure 5.9-9 along with the actual telemetered received signal strength data for comparison. Also shown on these plots are the gain states for each receiver throughout the descent phase.

All three DVS beams averaged about 2 to 3 db lower than nominal, with scintillation of about ±1 to ±2 db. The altimeter beam averaged about 5 to 8 db (varying with time) lower than nominal, with apparent scintillation of about ±2 to ±4 db (also increasing with time). The DVS values are within hardware tolerances including calibration errors. The altimeter values are within Ryan Electronics estimated accuracy of ±8 db, allowing scintillation in addition. The altimeter may be subject to second-harmonic effects.

It should be noted that the reflectivity signal voltage is not always a true indicator of received signal strength when the preamplifier is switching between two gain states. This is quite evident on all beams in the regions where the transition from gain state 2 to 1, for example, occurs over an interval in which switching is temporarily frequent and even rapid – sometimes more rapid than the gain state signal sampling. For this reason, not all gain state signal indications can be taken at face value, particularly since the switching time constant can be appreciably less than the state signal sampling interval.

Reflectivity signal voltage is an unambiguous value, but its dbm interpretation may be either ambiguous or completely obscure. For this reason, special symbols are employed in Figures 5.9-9 through 5.9-12. Where there is no apparent ambiguity or inconsistency with state indications, three symbols are used, namely

Δ	0	X
GS3	GS2	GS1

Where the indicated state is probably correct but an alternative interpretation is possible, the probable value is shown by one of the above, and the alternative value by a box (■). The converse of this, one of the above and a box-stroke (◤ or ◥) implies that the state has probably changed since last sampling, and a literal reading of data appears wrong. Two boxes imply uncertainty as to true value, which is probably somewhere in between.

5.9.4.10 Reflectivity Model

The lunar radar reflectivity model used by Hughes and approved by JPL for design and evaluation of both Surveyor radars was developed by D.O. Muhleman, then of JPL and now at Cornell. Dr. Muhleman is still active on the Surveyor scientific evaluation team's Electrical Working Group.

It is not proposed to enter the realm of esthetic dissatisfaction with Muhleman's model, now popular in several notable scientific circles. The admittedly quasi-specular assumptions are not debated pro or con, but Hughes does not share the concern it has heard expressed on two specific counts. One is an objection to a nonvanishing probability of infinite slopes. This seems not only logical on a centimeter scale, but actually confirmed

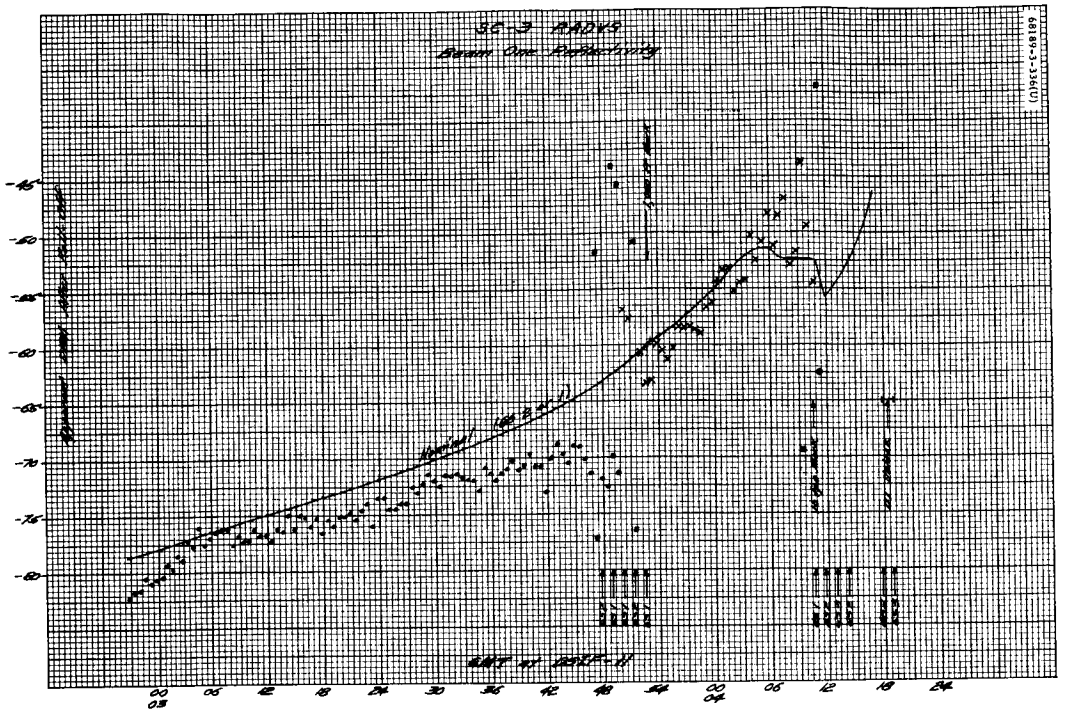

a) GMT: Day 110, 3 to 4 Minutes

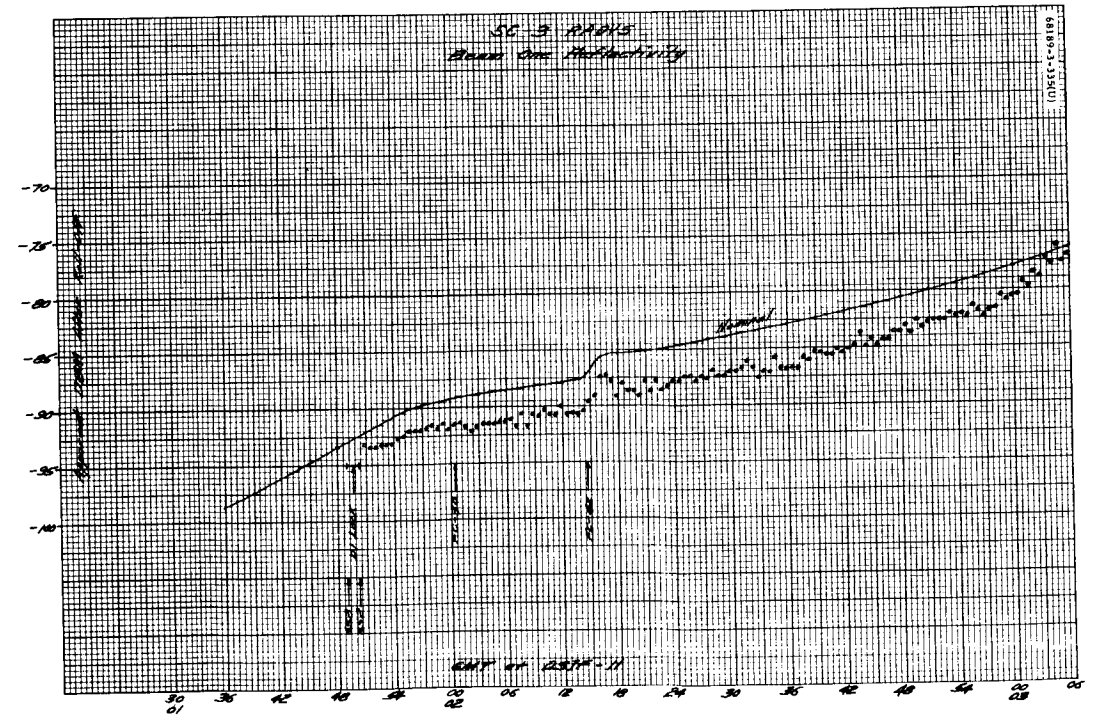

b) GMT: Day 110, 1 to 3 Minutes

Figure 5.9-9. RADVS Beam 1 Reflectivity

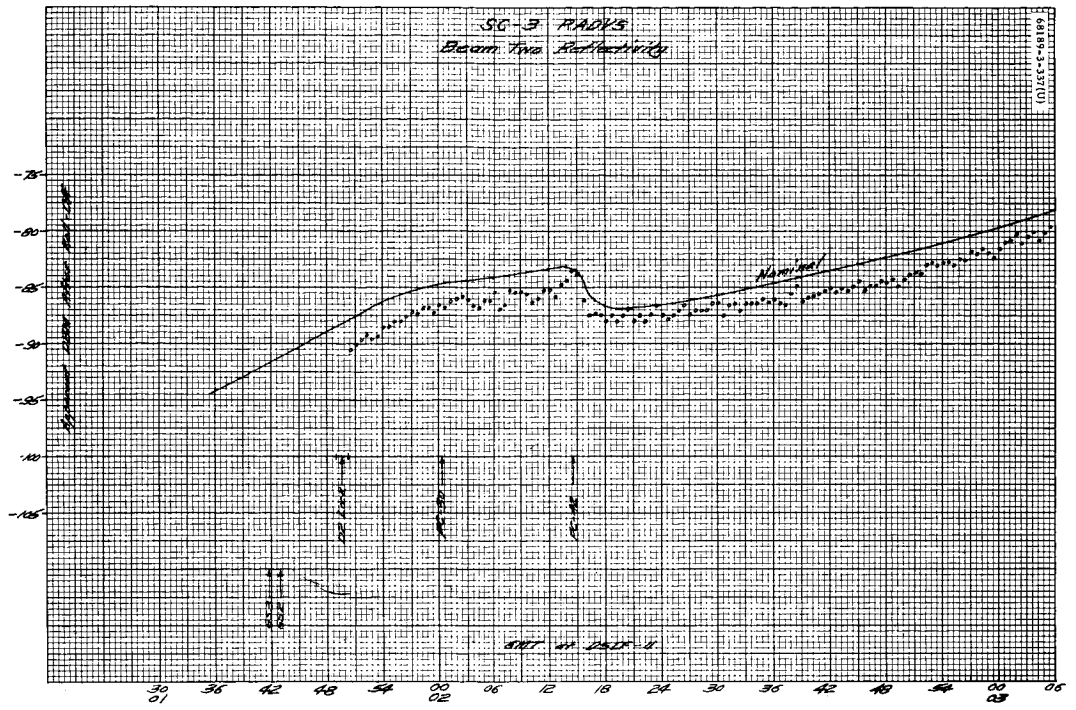

a) GMT: Day 110, 1 to 3 Minutes

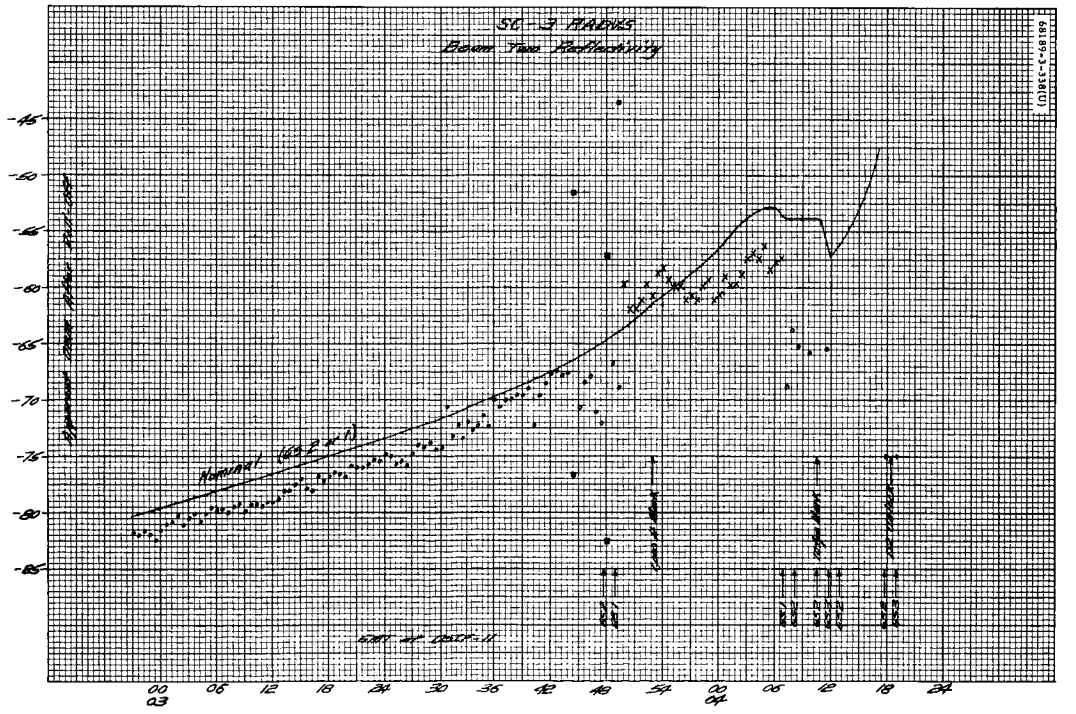

b) GMT: Day 110, 3 to 4 Minutes

Figure 5.9-10. RADVS Beam 2 Reflectivity

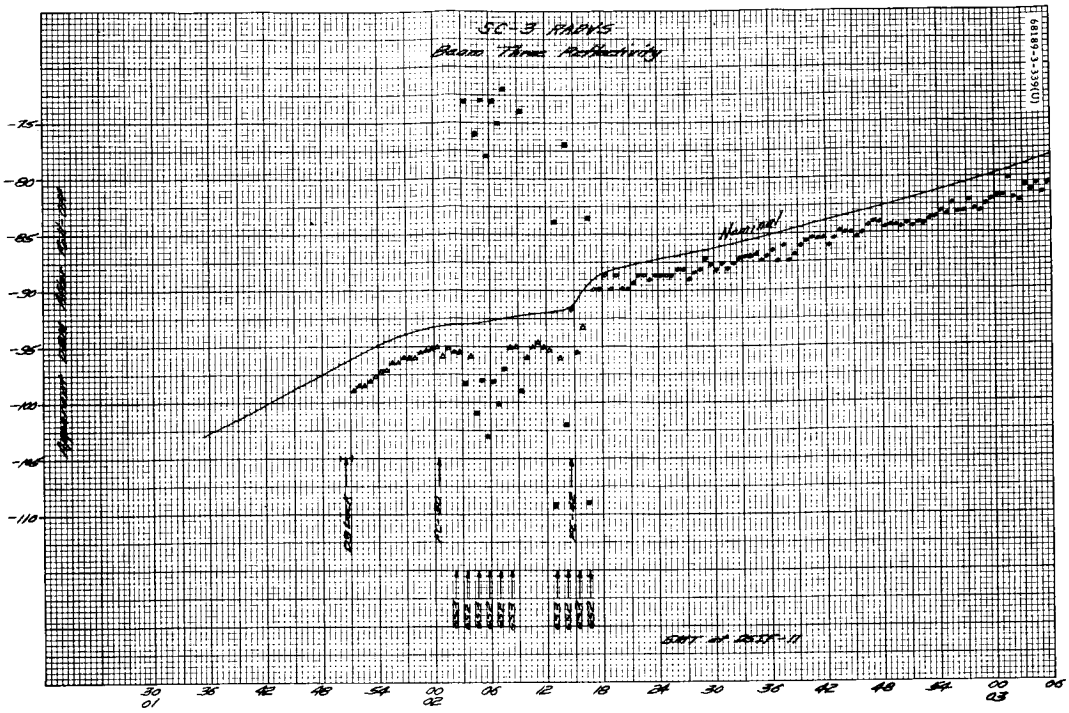

a) GMT: Day 110, 1 to 3 Minutes

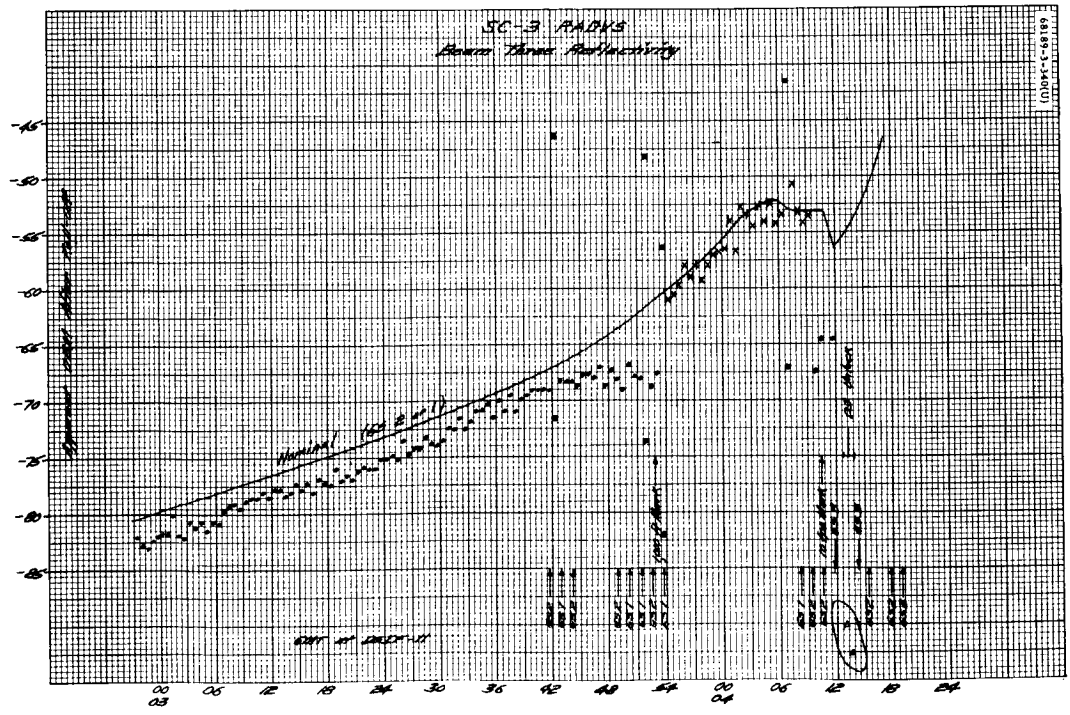

b) GMT: Day 110, 3 to 4 Minutes

Figure 5.9-11. RADVS Beam 3 Reflectivity

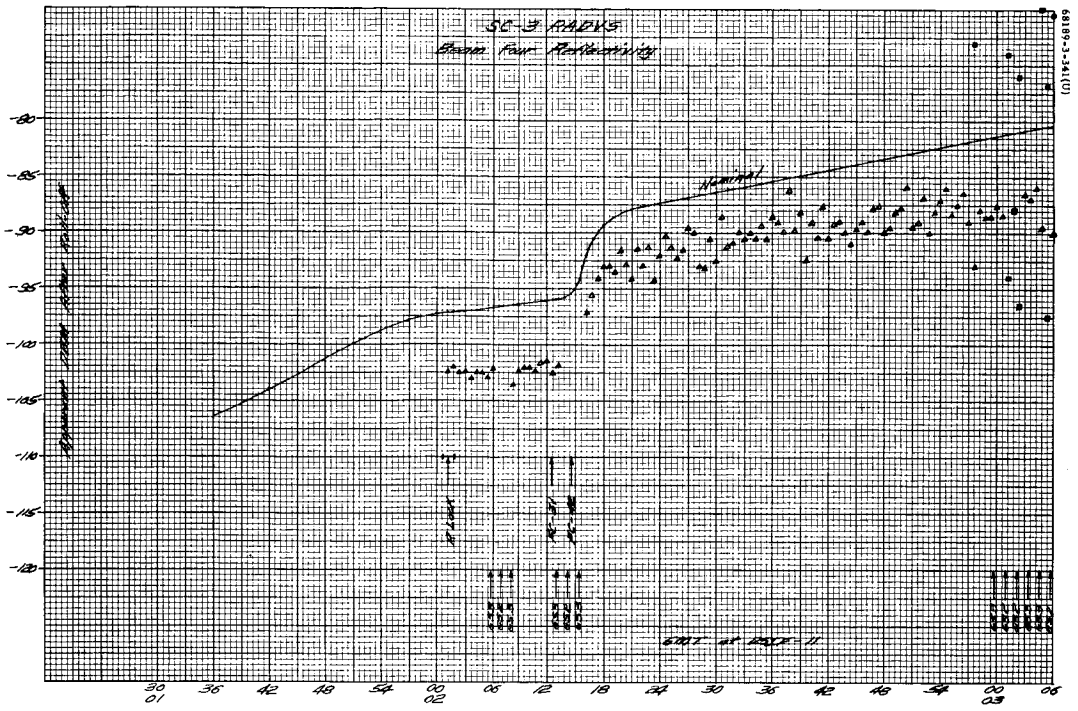

a) GMT: Day 110, 1 to 3 Minutes

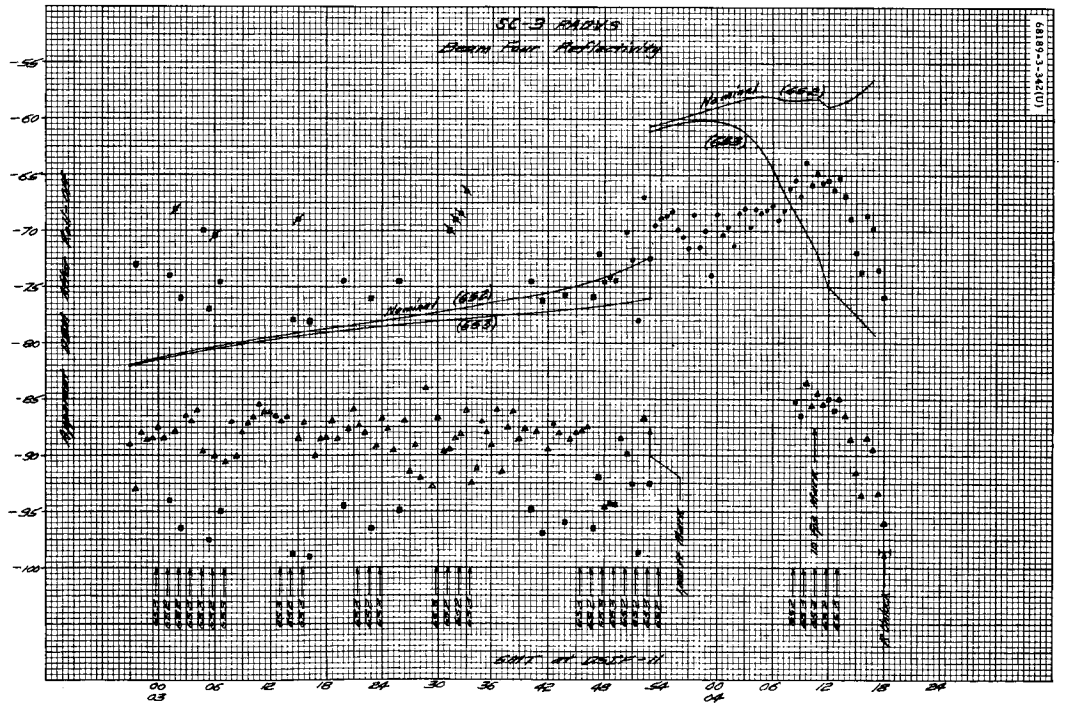

b) GMT: Day 110, 3 to 4 Minutes

Figure 5.9-12. RADVS Beam 4 Reflectivity

by Surveyor photographs demonstrating not only vertical but even reversed slopes on a 2.25-cm baseline; the very dependence of the rate of decay of such probability upon wavelength seems at least qualitatively obvious. The other is the extreme limit of the model in the other direction, that of a vanishing mean-slope parameter producing an impulse reply (for a transmitted impulse) from the subobservation point. The data quoted by other sources only confirm this tendency, in Hughes' view, at longer and longer wavelengths. The most strenuous objection is that the model is empirical. Even if the logical formulation and the mathematical rigor of the subsequent derivation are to be ignored, the very admission of its empirical fit only enhances its applicability to engineering purposes, however utilitarian. In studies not yet published, Hughes has computer processed the model against every available set of reliable earth-based data, and has found the fit to be excellent.

With the simple and admittedly approximate expedient of a small time scale shift in lieu of precise convolution with pulse length, a simultaneous best fit of this shift and the wavelength parameter has confirmed that a single analytic expression is available from subearth point to limb, including all the fine structure in the immediate vicinity of the former, to the accuracy of the test data itself. The preference for at least three separate piece-wise models, admitted to be not yet understood in basis, and each itself empirically adjusted, is itself not understood. The final objection of annular-ring averaging is not unique to the Muhleman model. Local, high-resolution departure from any hemispheric average should hardly be surprising; it must, and has been, anticipated and provided for to the same reasonable degree that should be required of any such model.

Muhleman's derivation permitted rigorous treatment of density functions for orientation of normals to ray-optics surface facets, without their size being specified or even appearing in the derivation. For earth observations, this was no conceptual obstacle, but its validity for high resolution at close ranges was really unknown prior to Surveyor I. It is gratifying that, despite consistently increased scintillation at near-vertical incidence (apparently a coherent interference phenomenon when phase variation across the illuminated patch is slow, rather than rapid as at larger incidence angles), the nominal coefficient, high resolution applicability, and the angular dependence function were confirmed by Surveyor I for its incidence angles, confirmed again by Surveyor III at similar angles, and confirmed also at additional incidence angles peculiar to Surveyor III.

Based on Lincoln Laboratory reports of total lunar hemisphere effective radar cross section, using earth-based radars calibrated with a 1-square-meter effective area conducting sphere in earth orbit, this factor has been revised downward from the former estimate of 0.075 (-11.25 db) to 0.065 (-11.87 db). This is, of course, a dimensionless coefficient — the ratio of actual radar cross section to that of a lossless and isotropic sphere of lunar radius, where the latter is simply the area of the projected lunar disc. The capability to operate at 6 db (required), 10 db (desired), below nominal reflectivity has been a functional requirement

for Surveyor radars. This requirement is being retained as insurance against terrain variation effects.

The angular dependence derived by Muhleman is:

$$F(\theta) = \alpha^3/(\sin\theta + \alpha\cos\theta)^3$$

where θ is the angle of incidence (off local lunar vertical) and α is a wavelength dependent mean-slope parameter. Subjecting this function to a hemispheric integral normalization condition requires that it be multiplied by a factor (K/α^3). Pertinent values are:

AMR:	$\lambda = 3.2$ cm	$\alpha = 0.36$	$K/\alpha^3 = +10.70$ db
RADVS:	$\lambda = 2.3$ cm	$\alpha = 0.39$	$K/\alpha^3 = +10.15$ db

The total factor

$$\sigma(\theta) = \eta\,(K/\alpha^3)\,F(\theta)$$

$$= \eta\,K/(\sin\theta + \alpha\cos\theta)^3$$

is essentially the power reflection coefficient of the lunar surface relative to a lossless and isotropic sphere. It is also the effective radar cross section per unit projected area, a dimensionless ratio. It is not the surface backscatter function, which is cosine θ times this factor or the effective radar cross section per unit surface area (σ_o).

Introduction of this factor into the range equation produces

$$\frac{dPr}{d\Omega} = \frac{P_t\,\lambda^2\,G^2\,g^2\,\sigma(\theta)}{(4\pi)^3\,r^4}$$

as the backscattered power density per unit solid angle subtended at the antenna of a monostatic, single beam lunar radar, where the one-way antenna power pattern has a peak gain G relative to isotropic and an angular dependence g normalized to unity maximum.

Integration over the azimuth angle only produces the inverse-range-cubed variation of instantaneous peak power received from a pulsed radar with pulse length short compared with elevation pulse stretching as described in subsection 5.8, "Altitude Marking Radar."

Integration over both azimuth and elevation of the CW power received by a Gaussian pencil beam produces

$$P_r\,(CW) = \frac{P_t\,\lambda^2\,(G/2)\,\sigma(\theta)}{(4\pi R)^2}$$

where R = slant range along the direction of peak gain G. The factor 1/2 in (G/2) is the approximate result of double integration of the three simultaneously varying factors of slant range, incidence angle variation of $F(\theta)$, and the pattern factor g to each incremental element of area. By an analytic first-order error analysis, this factor of 1/2 is exact, for a Gaussian pencil beam, within less than 0.10 db for incidence angles beyond 10 degrees. Right on the vertical, however, because of the essentially exponential nature of $F(\theta)$ at small angles, analytic double integration produces a received power 0.78 db less than indicated by the above range equation with the factor 1/2 and at $\theta = 0$ degree. This beamwidth-limited integration for CW is analogous to convolution of the sharp exponential with pulse length when considering pulsed return from the immediate vicinity of the sub-observation point, and has a similar suppressing effect.

The design features of both radars, all pertinent background material for performance analysis and evaluation, detailed description of postmission data forms and procedures for their evaluation (plus specific Surveyor I test data affecting the interpretation) were detailed in a package entitled "Post-Mission Analyses Involving Radar Data" (3-25-66) requested by the Surveyor scientific evaluation team. Predicted preamplifier signal strength and gain-switching behavior of test model T-2 (5-20-66), a similar treatment of flight model A-21 (5-30-66), and a complete Surveyor I prediction package (5-31-66) were also prepared. Though unpublished by Hughes, all these documents were widely distributed in reproduced handwritten form not only to all concerned Hughes personnel but also to other members of both the spacecraft analysis team (SCAT) (the Surveyor I equivalent of TFAG for Surveyor III) and the scientific electrical group prior to Mission A. Selected portions of this material, including that describing and illustrating the normal but peculiar behavior of gain-switching and preamplifier outputs at low altitudes — notably the cusp in apparent signal strength upon reaching 5 fps, so significant in Surveyor III — plus numerous specific Surveyor III items shown in the documentation, were also distributed prior to Mission C.

While all Surveyor III beams averaged somewhat weaker than nominal compared with Surveyor I data, these values are still within hardware tolerances including calibration errors (except for the altimeter), and even the altimeter (allowing for scintillation) is within Ryan's estimated absolute accuracy of ±8 db. There is not yet any systematic variation indicative of improper $F(\theta)$ mean-slope dependence, and the original model has been confirmed moderately well over more incidence angles — out to 40 degrees,

in fact. The ability to operate within 6 db (required) or 10 (desired) of nominal is still a functional requirement.

5.9.5 RADVS DOCUMENTATION

R.A. Dibos, RADVS Design Review Material, 22 July 1965.

R.A. Dibos, "Behavior of Telemetered Range Near 1000-ft Scale Factor Charge," Hughes IDC 2253.1/523, 27 December 1965.

R.A. Dibos, "Post-Mission Analyses Involving Radar Data," 25 March 1966.

Lincoln Laboratory, "Radar Studies of the Moon," Quarterly Report No. 2, 15 May 1966.

R.A. Dibos, "Nominal Descent RADVS Signals and Gain-Switching," 20 May 1966.

R.A. Dibos, "A-21 RADVS – Predicted Minimum Margin Performance," 30 May 1966.

R.A. Dibos, "SC-1 RADVS – Real Time Predictions," 31 May 1966.

R.A. Dibos, "RADVS Cross-Coupled Sidelobe Study," 9 September 1966.

R.A. Dibos, "Radar Performance Evaluation," SC-1 Symposium (NASA at JPL), September 1966.

R.A. Dibos, "Graph of A-21 Cut-Off/Touchdown Conditions," Hughes IDC 2292/119, 4 November 1966.

R.A. Dibos, "RADVS Preamplifier Roll-Off Characteristics," 15 November 1966.

"Decibel Allocation and Margin Summary," SSD 4021 R-2, 28 November 1966.

R.A. Dibos and F.K. Rickman, "Recommended SC-3 Attitude at Retro Burnout," Hughes IDC 2292/193, 15 February 1967.

R.A. Dibos, "RADVS Lateral Velocity Saturation," Hughes IDC 2253.4/67, 9 March 1967.

R.A. Dibos, "Extended RADVS Equations for Six-Degree Digital Program," Hughes IDC 2253.4/69, 15 March 1967.

W.T. Black, "SC-3 RADVS Analog Output Calibration Data," Hughes IDC 2294.5/77, 30 March 1967.

R. A. Dibos, "SC-3 RADVS Reflectivity Predictions," Hughes IDC 2253.4/80, 12 April 1967.

E. White, "Timetic Method for Determining Surveyor System Errors," Hughes IDC 2293/105, 14 April 1967.

R. A. Dibos, "SC-3 Radar Prediction and Analysis Material," Hughes IDC 2253.4/81, 20 April 1967.

A. N. Hertzmann, "SC-3 RADVS Performance Evaluation," Hughes IDC 2223/2891, 8 May 1967.

J. W. Tully, Jr., "KPSM Power Interruption Effect Profile," Ryan IDC, 15 May 1967.

N. C. Smith, "SC-3 Telemetry Calibration Handbook Final Post Flight Update," Hughes IDC 2294.8/101, 17 May 1967.

"SC-3 Flight Performance Report (Preliminary)," SSD 78079, May 1967.

K. L. Arends, "RADVS Dropout Sensitivity at Low Altitudes and Velocities," Hughes IDC 2294.5/89, 22 May 1967.

R. A. Dibos, "SC-3 RADVS Reflectivity Signal Telemetry Calibration," Hughes IDC 2253.4/82, 22 May 1967.

N. C. Smith, "Use of Lower Order Polynomial Equations in Telemetry Handbook," (SC-4 and up), Hughes IDC 2294.8/104, 22 May 1967.

J. M. Hansen, "SC-3 Plasma and Sparking," Hughes IDC 2294.1/129, 31 May 1967.

B. O. Steenson, "Probability of Fade of a Narrowband Gaussian Process," Hughes IDC 2253.4/83, 1 June 1967.

R. A. Dibos, "TM Mode 6 Data Relating to Radar Performance," Hughes IDC 2253.4/84, 15 June 1967.

R. A. Dibos, "SC-3 Digital Signals Relating to Radar Performance," Hughes IDC 2253.4/85, 15 June 1967.

J. F. Cashen, S. J. Klapman, A. W. Rogers, and J. G. Seubold, "SC-3 KPSM Failure," Hughes IDC 2245.10/59, 15 June 1967.

J. G. Seubold, "Heat Transfer to Lower Surfaces of the Surveyor with Engines Burning Near the Surface," Hughes IDC 2245.10/60, 22 June 1967.

S. J. Klapman and J. F. Cashen, "The Possibility of SC-3 Sparking to the Lunar Surface," Hughes IDC 2245.10/62, 26 June 1967.

B. O. Steenson, "RADVS Range Sweep Search Function After TM Smoothing," Hughes IDC 2253.4/89, 7 July 1967.

N. C. Smith, "SC-3 Telemetry Calibration Handbook Post Landing Supplement," Hughes IDC 2294.8/124, 25 June 1967.

R. A. Dibos, "Preliminary Report on RADVS CCSL Antenna Patterns," Hughes IDC 2292/175, 27 January 1967.

5.9.6 ACKNOWLEDGEMENTS

Technical coordinator and author: R. A. Dibos.

All DSIF-11 taped data were processed to engineering units and supplied in both raw form and engineering units by S. Volansky and W. McIntyre.

PREPRO programming and processing were performed by D. C. Passey and Nancy Krupa. 6DOF programming and processing were performed by E. R. Kopitzke.

Terminal descent trajectory reconstruction (see Section 5.12) was performed by V. Marclia, E. White, E. R. Kopitzke, T. L. Parker, and D. C. Passey, under supervision of L. H. Davids.

Discrete events data were checked by Q. D. Howard. Reflectivity data were checked by Q. D. Howard and M. R. Weiner. Graphical plots were coordinated by M. R. Weiner.

TFAG evaluation was by O. N. Hertzmann and A. L. Neil, supported by K. L. Arends, W. T. Black, G. R. Dreher, R. B. Harper, and M. E. Megowen. Supporting analyses at Hughes were by J. F. Cashen, J. M. Hansen, S. J. Klapman, A. W. Rogers, and J. G. Seubold. Supporting analyses at Ryan were by S. Hatchett and J. W. Tully, Jr. Failure Review was supervised by G. W. Kerster and K. C. Beall, and was chaired by J. D. Cloud.

Telemetry conditioning smoothing of the altimeter sweep function, plus the analysis of joint probability of depth and duration of Rayleigh fades, were analyzed by B. O. Steenson.

APPENDIX A

TO SECTION 5.9

CROSSCOUPLED SIDELOBES

There was no acquisition of any crosscoupled sidelobe (CCSL) in the Surveyor III descent. As in any mission, the consequences of acquisition of any of the six CCSLs inherent in each RADVS would have produced the associated combination of false steering and/or false profile sensing. The resulting probability of a successful descent by the flight control system under such RADVS conditions is unknown, but probably very low indeed; in the most probable circumstance, the false lateral velocities induced by wrong direction of thrust would result in excessive spacecraft angles at touchdown, making a soft stable landing unlikely.

The probability of a CCSL acquisition by the RADVS was analyzed and reported extensively. The report itself is too voluminous for complete reproduction in every reference to this material. Salient among its conclusions, however, are the following paraphrases:

1) A tracker whose mainbeam lock is broken, as by passage of the main retro case, will invariably acquire a CCSL — whether lower or higher in frequency than the mainbeam — if that CCSL is above tracker threshold for the gain state involved.

2) Without rejection logic, the only way to prevent CCSL acquisition and continued tracking is to prevent CCSL and mainlobe amplitudes from both being within the dynamic range of the same gain state for a given beam. Probability distributions of mainlobe and CCSL amplitudes, with due regard to gain state, were derived as functions of burnout dispersions as related to approach geometry.

3) It is possible, within limits, to control any selected CCSL-mainbeam amplitude relationship at burnout through control of spacecraft roll attitude. By so doing, CCSL acquisition cannot be prevented during a mainbeam dropout, but the CCSL can be forced out of threshold with the return of the mainbeam. Without such geometric control of amplitude, CCSL tracking would continue even after return of the mainbeam in hardware not protected by CCSL rejection logic.

4) There are six such CCSL-mainbeam combinations to be considered simultaneously. Two of these six are related to the old

form of CCSL rejection logic, which operated only in unequal gain states. Thus, in Surveyor III, there were four to be considered in all gain-state combinations and two in equal gain-state situations. These were all analyzed extensively in later documentation for Surveyor III specifically, as reported herein.

5) The probability of CCSL acquisition without rejection logic and without roll attitude constraint is a function of approach angle, roll angle, burnout velocity, the specific CCSL levels, the specific acquisition thresholds, and of the specific gain-switching levels all involved in flight of a specific set of equipment in a specific mission. These probabilities have been extensively evaluated for Surveyor III purposes as discussed below, assuming the opportunity for such acquisition.

6) Opportunities for such acquisition were also discussed at length. There are at least three types, the third being most significant. First, such acquisition could occur at initial lockon, which normally occurs at the upper sweep limit during main retro burning; an undesirable roll angle is all that is required to meet amplitude requirements. An inverted frequency relationship is also required, resulting from dispersed burnout velocities at flight path angles higher than nominal with nontrivial probabilities. Second, such acquisition could occur at burnout if initial lock had been to a spurious frequency induced during retro, a period in which the RADVS is not used in the flight control implementation. Prior to Surveyor I, this interval was a large uncertainty in RADVS operation; both Surveyors I and III have demonstrated normal DVS wide-band operation, however. Third, interruption of a DVS beam by the separating case of the expended main retro engine can break normal lock on a mainbeam, precisely the DVS beam interruption postulated in item 1 above. This did happen to beam 3 in Surveyor I; it also happened to beam 4, unrelated to CCSL, in Surveyor III.

7) Modeling of the relative dynamics of retro case separation is quite simple in concept. The axial components are straightforward to analyze within the uncertainties of engineering data on the specific characteristics of residual thrust many seconds after nominal burnout. Complete lack of any engineering data on the random, off-nominal, lateral components makes the parametric values involved in relative dynamics analysis completely speculative and conjectural. Pressure to assign a palliative but meaningless specific quantitative measure has been stoutly resisted.

8) The probability of CCSL acquisition without rejection logic and without roll attitude constraint becomes virtually the probability of retro case interruption of that DVS beam most vulnerable to CCSL acquisition in any specific geometry. This probability has

been variously estimated, not evaluated, as from 10 percent to 30 percent, subject to the above comments, and has repeatedly been so reported in documentation and numerous JPL-Hughes conferences extending back to mid-1966.

9) The ability to achieve a satisfactorily complete and adequate roll angle constraint solution is partly fortuitous, varying primarily with the approach angle dictated by the launch window, landing site combination for each mission, and by the specific hardware parameters involved. Adopted to meet Surveyor III requirements, this potential solution was far too tenuous to be a permanent solution for all subsequent missions.

10) The addition of complete three-beam, all gain-state CCSL rejection logic was recommended by the 9 October 1966 study, and has since been justified by the exhaustive antenna measurement effort which confirmed and established CCSL levels capable of acquisition if unprotected in every remaining spacecraft.

The Surveyor III spacecraft roll attitude was carefully controlled to minimize CCSL acquisition possibilities, evaluated by 90 graphs of all significant geometric combinations using over 240 Monte Carlo cases (of 500 cycles each), carefully verified by exhaustive measurement of the Surveyor III antennas in January 1967, and fully evaluated with additional probabilistic treatment of all significant parameters before the mission (15 February 1967). This Surveyor III roll angle constraint precaution would have been effective with over 96 percent probability, even if any DVS beam had been interrupted by passage of the main retro case after separation. Since no DVS beam was interrupted in Surveyor III (until much later in the descent), these analyses were neither confirmed nor refuted by the mission. Their value, however, remains that of a successful mission in that part of the descent.

As a result of the low-altitude dropout of beam 3 in Surveyor III (every available indication being that of a force-loss signal from the old CCSL rejection logic under the special circumstances discussed elsewhere), a simple but significant hardware modification to disable ECP-23 with the 1000-foot mark signal was recommended, and has since been implemented, for SC-4 and up. As contrasted with the narrow-band, low-frequency, high-resolution situation at the Surveyor III beam 3 loss, the types and degrees of phenomena involved at 1000 feet and above should render any similar rejection extremely unlikely in future spacecraft. At 1000 feet, the beam dimension is almost 100 feet (not 3 feet), the doppler frequency is about 2.83 kHz (not 0.12 kHz), the doppler bandwidth is almost 100 Hz (not 5 Hz), and the probability of more than a few (not two or perhaps three) significant reflectors in a single illuminated patch becomes quite high.

APPENDIX B

TO SECTION 5.9

SURVEYOR III PLASMA AND SPARKING ANALYSIS*

SUMMARY

It is improbable that a static discharge to the lunar surface occurred on the Surveyor III touchdown.

A gaseous electrical discharge originating in the KPSM is likely. It is possible that the electrical discharge terminated on the KPSM temperature sensor, thus causing the failure of the analog telemetry.

STATIC DISCHARGE

The static charging-discharging effects of the vernier and retro plumes were calculated previously (Reference 1). There does not appear to be any reason to change the conclusions. Static charge buildup is impossible because of conductivity and/or collection of ions from the plume.

GAS FLOW

The live touchdown introduces one new circumstance: reflection from the lunar surface onto the spacecraft of a large amount of the vernier engine plumes.

The case of one jet impinging normally on a nearby flat surface has been analyzed many times. The result is a flow outward away from the axis, near the surface, under a shock wave of considerable diameter roughly parallel to the surface. In this case, little gas is returned to the neighborhood of the source.

The use of more than one jet in close proximity to the surface introduces a new effect (Reference 2). Where the surface flows of the jets come together, if the overhead pressure of the direct jet impingement is less than the pressure of the merging surface flows, the flows erupt from the surface

*Synopsis from J. M. Hansen, Hughes IDC 2294.1/129, 31 May 1967.

approximately normal to the surface. A large amount of gas is returned to the neighborhood between the sources.

A calculation for multiple jets was made (Reference 3) for a spacecraft elevation as low as 9 feet, for which no reverse flow was found. However, the greatest elevation for a reverse flow was not determined. At touchdown, the vernier engines are only about 14 inches from the terrain. The half distance between two engines is about 33 inches (66 inches apart) and to the axis of the spacecraft is 37 inches. The midpoint between two engines, at the lunar terrain, is beyond the M = infinity jet boundary. (For vernier engine plume, see Figure 1 of Reference 1.) Reverse flow must have occurred at touchdown, and probably for a few feet above (before and after touchdown).

The flow and duration merit some speculation. At the first touchdown, the landing and takeoff speeds were about 7 and 6 ft/sec (Reference 4). If the backflow begins at an elevation of a few feet, the duration is about 1 or 2 seconds. At touchdown on a sloping surface, the total thrust of the vernier engines will rise (Reference 5) from 108 to approximately 260 pounds (from 36 pounds each engine to 120 pounds for two engines and 24 pounds for one engine) as the spacecraft tries to maintain a vertical attitude. As the spacecraft tilts, other thrust combinations will occur. The total duration of the high thrusts of Surveyor III must have been about 1 second, and have occurred within an elevation of about 3 feet.

GAS DENSITY

The density of the gas impinging on the spacecraft can be approximated in several ways. The ambient density at 13 feet elevation was previously calculated (Reference 1) at about 1×10^{-6} atmospheres, based on the assumption that the low thrust (equals spacecraft lunar weight) exhaust impinged upon the lunar terrain and departed equally in all directions. Now the distance is less, and the assumption of splashing in all directions is partly true. The area of a hemisphere of 13 feet radius is 1000 square feet. The area of the spacecraft is about 30 square feet.

About 1/6 to 1/4 of the 360 degrees about each engine is covered by the spacecraft, so about this fraction of the exhaust (at most) will flow under the spacecraft and backflow. The density of the expanding gas will be nonuniform, and the flow will be deflected by the spacecraft components, but the average will be about $(1/5) \times 1000\ ft^2/30\ ft^2 = 7$, or about 7 times that computed previously, or about 7×10^{-6} atmosphere for low thrust, and 16×10^{-6} atmosphere for high thrust. When corrected for molecular weights (24 for vernier engine exhaust, 29 for air), this is 0.5 or $1.1 \times 10^{-6}\ lb/ft^3$.

The density can be approached more directly from the thrust and velocity. The thrust (108 pounds, low, 3 engines) is velocity (10,000 fps) times rate of mass burned. This gives 0.35 lb/sec. Take 1/5 (1/4 to 1/6) of this to go under the spacecraft and be spread over its area of 30 square feet. Then the density = $0.23 \times 10^{-6}\ lb/ft^3$ for low thrust, or

0.55×10^{-6} lb/ft^3 for high thrust on two engines. These are probably the more accurate average density numbers. They differ by only a factor of 1/2 from the previous estimate.

GAS PRESSURE

Where a flow impinges on a box, a shock wave will form. The stagnation pressure will be density $\times$ (velocity)^2. Using the density found above, and a velocity of 10,000 fps, the pressure is found as 0.7 or 1.7 lb/ft^2, or 0.25 or 0.61 mm Hg, for low thrust or for two-engines-high thrust.

The pressure can be approached in another, more elemetary way. Some of the plume is reflected back onto the spacecraft. The thrust of the vernier engines is due to the momentum change imparted to the engine exhaust gases. Part of these are deflected by the lunar surface and then by each other onto the spacecraft, where their direction is again deflected horizontally by the bottoms of the boxes. The force on the box bottoms is the rate of momentum deflection. For a low engine thrust of 108 pounds, for 1/5 of this flowing under the spacecraft and erupting without thermal loss, and for 1/2 of this striking the spacecraft because of voids in the spacecraft structure, and for a spacecraft area of 30 square feet, one half of which is void, the pressure = force/area = 108 lb $\times$ 1/5 $\times$ 1/2(30 ft^2 $\times$ 1/2) = 0.72 lb/ft^2 for low thrust, or 1.7 lb/ft^2 for two-engines-high thrust. (This computation differs from the previous one in not using the Newtonian pressure formula density x (velocity)^2.) The results here are the same as for the previous computation.

The stagnation pressure of the reverse flow against the boxes is taken to be about 0.25 or 0.6 mm Hg average. The flame is nonuniform. The stagnation pressure is probably two or three times this where the eruption is greatest, and will change rapidly and greatly with location, being high where exposed to oncoming flow, and low where shadowed. Probably the reverse flow is greater between the engines than near an engine. An ambient pressure has little significance. The 90-percent relaxation time for the density outside the boxes will be about 2 or 3 milliseconds.

PASCHEN'S LAW

The breakdown voltage for a gas is a function of the product of gas density and path length between the discharge electrodes. A plot of the function for some gases is shown in Reference 6. The voltage is a minimum of about 400 volts at a value of about 4, of the product of the pressure in mm Hg and the distance in mm. For higher voltages, the product (for limiting conditions of breakdown) is less and more. For 2100 volts, the product required is as low as about 1 mm-mm Hg.

The path taken by a gaseous electrical discharge is hard to predict. Depending on pressure (density), the discharge may prefer or require a long path. For a pressure of 1/10 mm, the least distance required by 2100 volts

would be about 1/0.1 = 10 mm = 0.4 inch. The longest path is beyond the scale of Reference 6, and would be several inches. For lower pressure, the minimum and maximum distances would be increased. For a distance of 4 inches = 100 mm, the minimum pressure required by 2100 volts would be about 1/100 mm = 10 microns.

HARDWARE

The high voltage is located in the klystron power supply module (KPSM). The high voltages in this box are -2150, -800, -500, +500. The box is approximately cubical, with an edge of 4 or 5 inches. It is well packed with mostly wired components. The box interior is loosely divided into compartments by partitions. The cable entrance is at one corner, also containing a temperature sensor, which is the only telemetry lead to this box. In the middle compartment on the same box-face is the high-voltage transformer. In the other corner compartment on the same box face are several high-voltage components. Direct communication (holes) between the sensor-containing compartment and the middle compartment mentioned is not evident. However, there appears to be an opening between the two corner compartments by means of the space within a double-walled partition. The high-voltage transformer extends into this space. The exact degree of access from this space to the temperature-sensor compartment is not clear, but appears to be the nearest proximity of high voltage to the sensor. This double-walled space also communicates with the outside at the top of the box by means of a row of slots in the box top cover. The cable connection is at the top. The klystron compartments also communicate with the double-walled space by means of roughly formed corners.

Access of the reverse flow of gas to the box is most likely by means of the microwave plumbing flanges. This is spaced a small distance from the matching box walls, and the overlap faces the oncoming gas stream. The KPSM box is tilted so that the microwave attachment face is conveniently accessible to the back flowing gas. The flow on the microwave face may be assisted by the spillage from the bottom of the nearby compartment A and the radar antenna. The back flow would be greatest in the region midway between two vernier engines, and compartment A and the radar antenna occupy such a position.

The high-voltage circuits are coated with a conformal coating that is brushed on, and is so thin that it is sometimes invisible. It seems unlikely to prevent sparking.

BOX PRESSURE

The pressure computed exceeds the amount required for sparking. It appears that sparking is probable, but favorable conditions (high thrust, favorable impingement) may be necessary to cause it.

The KPSM box has an entrance slot where reflected vernier gases would impinge. This slot is between the top cover and the corner pieces carrying the waveguide (see Figure B-1). The thickness of the slot is 0.040 ± 0.003 inch. The distance that the gases must pass in the slot is 5/8 inch, except for the bottom front 2 inches and about one half of the bottom side 3 inches, where the overlap of the covers is about one third of 5/8 inch = 0.2 inch.

The top cover's top has a series of holes in the form of slits, having a total area of about 1.7 in^2 = 11 cm^2.

It is likely that most of the gas entering would come into the box through the bottom slots in the face of the box because of the impingement of the gases against this face and edge, although some may come also through the 3-inch slots that face each other on the face of the box and on the sides.

The gas would probably leave the box by way of the slit-shaped holes in the top of the top cover. The gases would be moving rapidly up the sides of the box and away from the top. It is unlikely that the flow would make any pressure at the top surface where the holes are. The rapid flow would be like a diffusion type of vacuum pump, entraining any gas molecules that should wander into the stream. There probably was a good vacuum at the top of the box over the holes.

The flow into the box can be estimated from the slot dimensions and stagnation pressure. The slot on the lower front 2 inches (two slots, total 4 inches) is 0.040-inch thick and about 0.20-inch high. The flow through the slot may be restrained by three things — energy, viscosity, and/or molecular flow. The energy available to accelerate a mass of the gas is pressure times volume. A simple calculation indicates that at the low density here, the stagnation pressure can accelerate the gas to a speed much higher than viscosity would permit with this same pressure and the dimensions of the slot. Flow is therefore restrained by viscosity, or by molecular considerations, depending on mean free path and dimensions.

The mean free path in air is 5 cm at 1 micron pressure (and normal temperature). Flow is viscous (Reference 8) when the aperture dimension is 100 times the mean free path, about equally viscous and molecular flow when the ratio is 10, and molecular flow when the ratio is 1. For the case in hand, take the stagnation pressure as 250 microns (low thrust) and 600 microns (high thrust). Probably the gas that enters the slot has flowed along the face of the box and cooled considerably.

A simple calculation of specific heats and conductivities (Reference 9) and of flow velocity indicates that the gas will be cooled near to the wall temperature in a small fraction of time necessary for it to flow through the slot. Take, then, the average pressure of 125 microns and of 300 microns, and normal temperature, to compute density and mean free path. This gives for the mean free path 5 cm/125 = 0.4 mm and 5 cm/300 = 0.17 mm. The slot thickness is 1 mm. The flow through the slot is molecular to mixed. The flow into the box will be computed as viscous, for the high-pressure

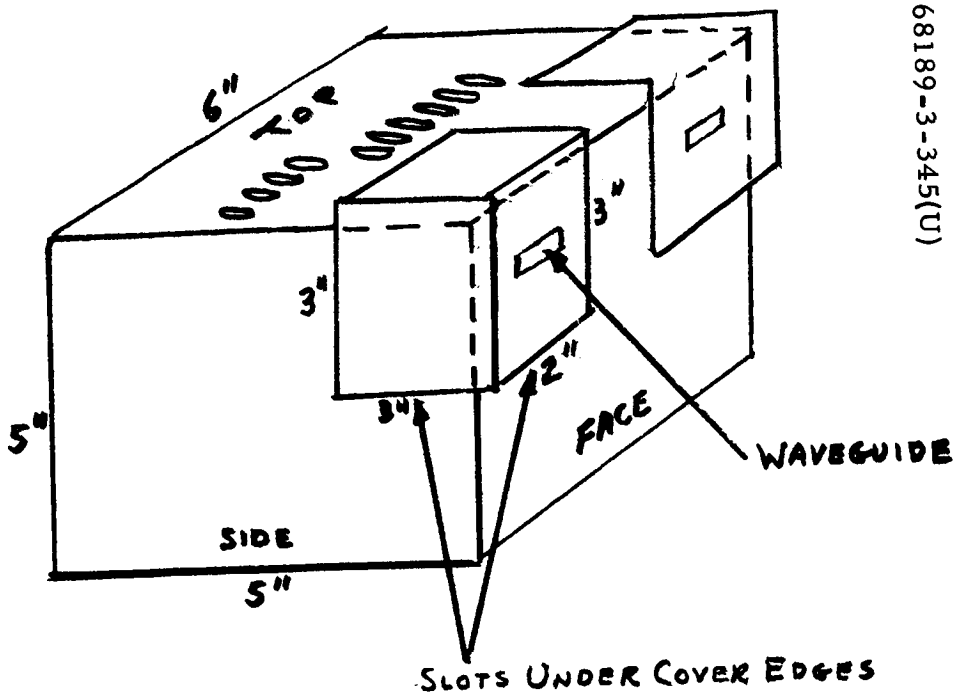

68189-3-345(U)

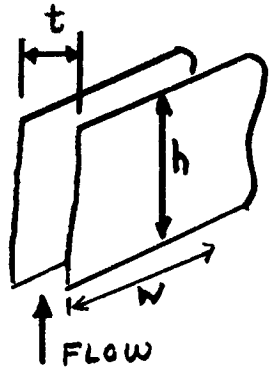

68189-3-346(U)

Figure B-2. Slot Dimensions

case. For lower pressures, the flow is nearly proportional to pressure simply because the gas density is proportional to pressure and, in molecular flow, it is every molecule for itself. For high pressure, the flow (molecules per second) would become proportional to the square of the pressure, because the speed and the density are both proportional to pressure, the viscosity being independent of density (pressure).

For the slot formed by the overlap (Figure B-2), a double integration gives for the flow

$$F = \frac{P\ W\ t^3}{12\ h\ n}$$

where

F = flow through slot, volume/time

P = pressure difference at inlet and outlet

t = thickness of slot

h = length of passage through slot

n = viscosity of gas

Take

$$n = 18 \times 10^{-6}\ \frac{\text{newton-sec}}{m^2} = 2.6 \times 10^{-9}\ \frac{\text{lb-sec}}{in^2}\ \text{(air)}$$

$$P = 600\ \text{microns} = 0.012\ \text{lb/in}^2$$

t = 0.04 inch

h = 0.20 inch

W = 4 inch (bottom edge of both covers)

Then

$$F = 492\ \text{in}^3/\text{sec} = 8100\ \text{cm}^3/\text{sec}$$

This is the flow into the box through the two slots at the bottom of the klystron covers. It will be taken to have an average pressure (density) of one half of 600 microns, because the exit pressure (in the box) is only a small fraction of the entrance pressure, as will be shown.

The gas in the box will escape through the holes in the top of the top cover. Their combined area is 1.7 in^2 = 11 cm^2, and equals the area of a circle of 1.9-cm radius. The box overall dimension is about 5 by 5 by 6 inches = 150 in^3 = 2.5 liters. These figures are approximately those found in a table in Reference 8, page 97, listing molecular flow for some typical laboratory cases. The last row refers to an exit hole of radius 2 cm and length 1 cm. The slots in the box top have about this ratio of half-width to metal thickness, although this ratio is not critical. The rate of flow of air into a vacuum is given as 1.2 x 10^5 cm^3/sec. The time required for a 1-liter volume, not receiving any air, to lose 90 percent of its contents through the hole, is given as 0.020 second.

For equilibrium, the number of molecules entering and leaving must be equal. For constant temperature, this requires the product of pressure and volume flow rate to be the same in as out. For

P in = 300 microns

F in = 8100 cm^3/sec

F out = 1.2 x 10^5 cm^3/sec

the pressure at the orifice inside the box is found to be 20 microns. The 2.4-liter box (if empty of components) would have a 90-percent relaxation time of 0.05 second.

The pressure found has assumed that outside the bottom slots is the high-thrust average stagnation pressure, has neglected other slots formed by the klystron covers, and has assumed an empty box. Probably the other slots under the covers receive more gas than they lose, especially the vertical slots on the face and the bottom slots on the sides. The pressure of 600 microns was averaged over all of the spacecraft bottom. The actual pressure will be nonuniform and will be both higher and lower than this in various places.

The partition and components in the box make the pressure nonuniform inside the box. The pressure would be considerably higher in the klystron compartments than elsewhere. If the connections of the klystron compartment to the double-wall partition space are as open as the top cover slots, the pressure in the klystron compartment will be doubled to 40 microns. If one fifth is open, then the pressure would approach 100 microns, being restrained by leakage at the other slots and reduction of the pressure difference at the input slots.

The effect of the contents on the relaxation time is hard to estimate, but this time is so short that the box pressure must be sensibly in equilibrium, except during a very rapid shift of the gas stream.

The pressure computed (20 microns, average in box, and average pressure of high thrust) exceeds the amount required for sparking according

to Paschen's law (10 microns). The computation is approximate. Gas densities in the box will be nonuniform, and flow against the spacecraft will be nonuniform. It appears that sparking is probable, but favorable conditions (high thrust, high flow onto box) may be necessary to cause it.

EFFECTS

It is likely that the reverse flow of the vernier engines at and near touchdown impinged on the KPSM box (and other boxes) and entered the box chiefly through the downward-facing overlap of the microwave plumbing flange. The stagnation pressure here may have been about the average value of 0.25 to 0.6 mm Hg for low or for high thrust. The gas pressure in the box would rise until the flow outward equaled the flow inward. This would be a fraction of the pressure against the overlap, perhaps as much as a quarter of a tenth in the more accessible spaces in the box. The pressure in some parts of the box may have risen to as much as 1/10 mm. The 2100 volts would spark at a pressure of 1/100 mm for a distance of 4 inches, and at less pressure at greater distances. There is an overlap of required and likely pressure of about 10/1.

The shutdown of the radar occurred at touchdown (Reference 7). This suggests that the box may have been slow to fill, or that the highest gas density available was needed for breakdown, requiring both the nearest lunar proximity and the extra boost of the high vernier engine thrust (Reference 5). Perhaps the stagnation pressure taken against the overlap is excessive. It is the maximum of the average over the spacecraft. Local areas will be higher or lower. The fraction to be taken for the pressure inside the box is unknown. The leaks out of the box slots in the top cover are greater than the leaks into the box, but there are partitions in the box.

The shutdowns (Reference 7) continued for 18 seconds, which is approximately the normal recycle time (20 seconds) for the high-voltage power supply. This hints that the breakdown was of this supply. The first touchdown did not damage the telemetry circuit; this fault appeared coincidental with the second touchdown. The third touchdown occurred before completion of the recycle from the second touchdown, so we cannot infer anything from the lack of reverse flow (vernier engines commanded off, spacecraft dropped) at the third touchdown.

The next shutdown was considerably later (about 70 seconds after recovery). Subsequent recycles were abortive; the circuit would not stay on in the absence of backflow. Evidently some insulation had been damaged in the sparking, and it completely disintegrated during the 70 seconds.

It appears likely that sparking of the high voltage did occur. That it involved the telemetry line may have resulted from the protrusion of the high-voltage transformer behind the partition on which it is fastened, near to the temperature sensor, depending on certain box details. It may be possible, but is unlikely, that the discharge terminated outside the box, the ambient ionization being considerable.

Possible treatments would include closing (caulking?) the cracks, or potting or covering the high-voltage circuitry.

CONDUCTIVITY

The reverse flow gas has appreciable conductivity. The resistivity was computed (Reference 1) at 6.7×10^4 ohm-cm. This is independent of gas density, but the number given may be low (conductivity estimated high) because of recombination of ions, which was neglected in the computation. Probably the resistivity does not exceed ten times the number given.

This conductivity will tend to connect together any accessible circuits, as at uncovered cable ends, or depending on details of gas flow, to extend the spark from the KPSM box out through the holes in the box.

HEATING

Heating effects of a multiple jet reverse flow have not been computed. The duration was short (a few seconds), but thin things such as cable wrappings may have been damaged.

REFERENCES

1. J. M. Hansen, "Rocket Charging in Vacuum," Hughes IDC 2258.4/141, 7 December 1965.
2. J. M. Hansen, "Surveyor Landing Exhaust Flow," Hughes IDC 2258.4/65, 27 August 1965.
3. R. H. Edwards, "Multiple Jet Interaction," Hughes IDC 2241.13/27, 5 October 1965.
4. "Lunar Landmarks," Vol. III, No. 5, 24 April 1967.
5. J. M. Hansen, "Premature Touchdown Detection for Surveyor," Hughes IDC 2253.1/655, 24 May 1966.
6. American Institute of Physics Handbook, 1963.
7. G. Kerster, "SC-3 Signal Processing Anomaly at Touchdown," Hughes IDC 2294.1/105, 4 May 1967.
8. Dushman and Lafferty, Scientific Foundations of Vacuum Technique, Wiley, 1962.
9. Thermodynamics, Sears, Addison-Sesley, 1959, pages 248, 266, 268.

APPENDIX C

TO SECTION 5. 9

SURVEYOR III KPSM ARCING ANALYSIS*

SUMMARY

In the normal descent of Surveyor onto the surface of the moon, the vernier engines are shut down at an altitude of 14 feet. When Surveyor III descended and the vernier engines were still operating, the KPSM shut down very near to or on the surface. It is conjectured that the exhaust gases from the engines strike the lunar surface and a fraction rebounds to impinge on the landing vehicle, creating a gas pressure about the high-voltage supply. At a critical condition given by experimental Paschen curves of striking voltage versus the product of pressure and electrode separation, the gas breaks down.

The contention in this memo is that even though the gas may be passing an increased current, it does not necessarily mean that the system will stop operating. Only when the gas demands a current which the system is not capable of supplying will it cease operating. This memo therefore seeks to determine the gas pressure surrounding the landing vehicle versus altitude, and the current that this gas will support, and thereby determine a critical altitude above which there cannot be shutdown of the system. The conclusion of this memo is that at an altitude above 10 feet it is impossible for the KPSM to become inoperable because of glow discharge. With a reasonable fractional ionization of between 10^{-4} and 10^{-5}, we conclude that the system would break down at 3 ± 2 feet. The inaccuracies arise from the very complicated fluid flow pattern which gives us the pressure of the gas at the vehicle versus altitude and the uncertainty in the fractional ionization of this gas.

GASDYNAMIC CALCULATIONS

Accurate prediction of the gas pressure in the vicinity of Surveyor is extremely difficult. The analysis described here is very crude, but is believed to account for all important physical phenomena. It should give at least some indication of the pressure as a function of altitude. The present calculations were carried out for the condition of all three verniers at full thrust, and other engine conditions as given in the following listing:

---

*Synopsis from J. F. Cashen, S. J. Klapman, A. W. Rogers, and J. G. Sevbold, Hughes IDC 2245. 10/59, 15 June 1967.

$d_e = 5.09$ inches

$\theta_n = 0$ degree

$$\varepsilon = \frac{A_e}{A^*} = 86.9$$

$$R = 1545 \left(\frac{32.2}{22.8}\right) = 2180 \ \frac{ft^2}{sec^2 \ ^\circ R}$$

$M_e = 5.20$

$T_e = 1510^\circ R$

$T_c = 5000^\circ R$

$\rho_e = 7.84 \times 10^{-6}$ slugs/ft^3

$p_e = 0.179$ psi

$p_c = 250$ psi

$$m_e = 0.30 \ \frac{lb_m}{sec} \text{ (per engine)}$$

Thrust = 104 pounds (per engine)

$\gamma = 1.31$ (free plume)

$\gamma = 1.26$ (for impinging flow). This is an effective specific heat ratio.

To determine a bounding value for the pressure at zero altitude, two separate calculations were made. In the first, the stagnation pressure under the vehicle was taken to result from normal shock impingement of the exhaust at the nozzle exit conditions, with no further losses. This produces an extremely high stagnation pressure – 5.5 psi (284 mm) at 250 psi (17 atmospheres) chamber pressure. If it is then supposed that, at zero altitude, 1/6 of the engine mass flow is caught under the vehicle, and must flow back up through the vehicle, we can determine the conditions at the vehicle. The resulting Mach number is quite high, and the stagnation pressure on the vehicle (after a normal shock) will be only a small fraction of the 5.5 psi (284 mm) at the surface – M = 7 and $p_{stag} = 0.020$ psi (1.0 mm) for the present calculation. For the second calculation, the Mach number was taken to be unity at the vehicle. With a chamber temperature of 5000° R, the velocity and density can then be calculated. The resulting stagnation pressure under the vehicle is 0.0108 psi (0.56 mm). This was assumed to be the actual stagnation pressure under the vehicle at zero altitude. Losses from secondary shocks, mixing, and boundary layer were assumed to reduce the stagnation pressure by a factor of 0.0108/5.5 = 0.00196.

We now consider what is the change in pressure as the altitude is increased, assuming constant thrust. Clearly the mass flow through the vehicle goes down as the altitude increases, if only because the available escape area for the flow increases. A second, more important factor is the reduction in stagnation pressure as a result of the increasing jet impingement Mach number. In the present calculation, this second effect was found to dominate, so that the flow rate through the vehicle decreases with increasing altitude faster than would be found by considering the area alone.

The stagnation pressure under the vehicle was taken to be proportional to the total pressure ratio across a normal shock at the Mach number on the jet centerline at an axial station equal to the altitude of the nozzle above the lunar surface. The ratios are scaled to a zero-altitude pressure of 0.0108 psi, as described in the preceding paragraphs. The Mach number at the vehicle was taken to be unity, and the total temperature conserved at 5000° R. Although we know the boundary layer on the lunar surface will reduce this temperature, the tools for calculating this effect are not yet available. This should not affect the pressure predictions to the order of the present calculations, as the assumed high secondary pressure loss includes the heat transfer in a gross manner, and the total pressure is proportional to the square root of total temperature by the method used here.

The predicted pressure as a function of altitude is shown in Figure C-1. At low altitude the Mach number on the axis is not completely representative of the losses, and the dashed line indicates what might be expected to happen. At an altitude of 8 or 9 feet, the multiple plumes intersect and no longer allow backflow up the axis of the vehicle. This effect, described earlier by Edwards (Reference 4), drastically reduces the backflow to the vehicle above this altitude. It is indicated by the dotted line in Figure C-1. The present analysis is consistent with the work of Edwards, but the two cannot be readily combined to give a complete analysis for all altitudes. One of the conclusions of the present work is that above the altitude determined by Edwards, the reverse flow to the vehicle is small, but even below this altitude the reverse flow is not necessarily sufficient to cause breakdown.

Landing on a surface of moderate slant (say less than 20 degrees) should not greatly affect the results presented here. A surface with rocks a few inches in diameter or larger might be a serious problem. Such irregularities can reflect large flows back onto the vehicle, but no quantitative estimates are being made at this time.

The plot of pressure may also be taken as indicative of the dust raised. Thus, keeping the engines on until touchdown raises an order of magnitude more dust than cutting them off just a few feet up. Edwards' analysis indicates that above an altitude of 8 to 9 feet, all the dust should be blown sideways rather than up onto the vehicle. One aspect of the dust problem that has not been considered heretofore is the effect of engine transients. This problem appears if the engines are firing close to the surface on a descent, with the thrust level changing for attitude control, and on a hopping mission where the engines are restarted.

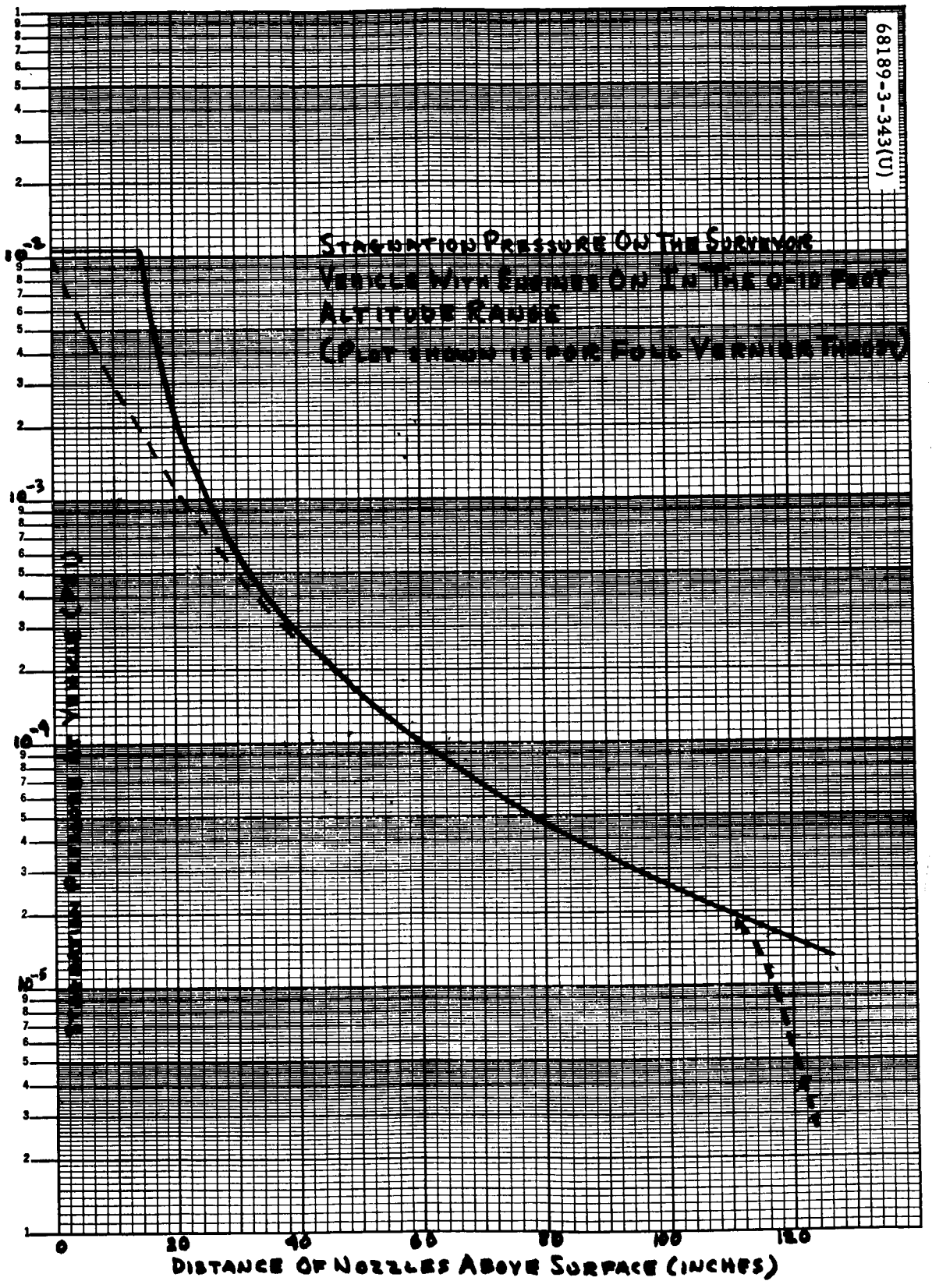

Figure C-1. Stagnation Pressure on Surveyor Vehicle With Engines On in 0-to-10-Foot Altitude Range

The accuracy of the pressure versus altitude curve is certainly questionable, and there is no way of determining how bad it is. The two distinct methods for calculating total pressure on the vehicle at zero altitude gave results different by only a factor of three, so we have some confidence in this end. On the high altitude end, the work of Edwards tells us to expect a sudden pressure drop at a vehicle altitude of 8 to 9 feet. Thus the lack of accuracy is a handicap only if the engines are to be fired between 0 and 8 to 9 feet, at the same time that components adversely affected by the impingement are operating and/or exposed and needed later.

SPARK BREAKDOWN

The mechanisms of dc spark breakdown are complex and in some cases not well understood. Only approximate theories have been developed. Part of the complexity lies with the sensitivity breakdown as to geometry and electrode surface condition and chemistry. Since it is not known where breakdown might have occurred in the KPSM, the following analysis is only a rough indicator of the phenomena.

The KPSM unit houses electronics for the RADVS radar. It has dc (and ac) voltages ranging up to a 2150-volt peak. During the first two of the three Surveyor III touchdowns, the inverter supplying the high voltage disabled itself. This disabling was most probably caused by a current overload. Ryan concurred with this diagnosis and suggested that a four or five times overload on the 2150-volt circuit would have been sufficient to disable the inverter. The normal load on the circuit is 55 milliamperes.

Examination of possible breakdown points was made on a sample KPSM. G. Dreher was most helpful in this respect. In making an assessment of possible breakdown locations, it was necessary to assume that the 2150-volt circuit was the only one experiencing breakdown shorting. It is possible that a lower voltage circuit (e. g. , 500 volts) broke down in Surveyor III, but the probability is just that the higher voltage broke down.

The 2150-volt circuit supplies high voltage to the high-power klystron (doppler). The actual connection of high voltage to the tube is within a semi-sealed container and could not be examined. However, there were several other points where the voltage is exposed by a bare* terminal. The typical diameter dimension of the terminal exposures appears to be about 1/8 inch.

Since the case and chassis are both at positive ground, they act as the anode electrode to the terminal exposure cathode. Typical maximum clear-path distances measured between the high-voltage terminals and the case or chassis were on the order of 3/4 inch. Figure C-2 shows a cold cathode discharge tube model based on the measurements.

---

*Actually, the terminals are coated with a 0. 002-inch coating of conformal plastic sealer. The effectiveness of this coating as a deterrent to corona and/or breakdown is not known. Therefore, it must be assumed in this analysis that its effect is negligible.

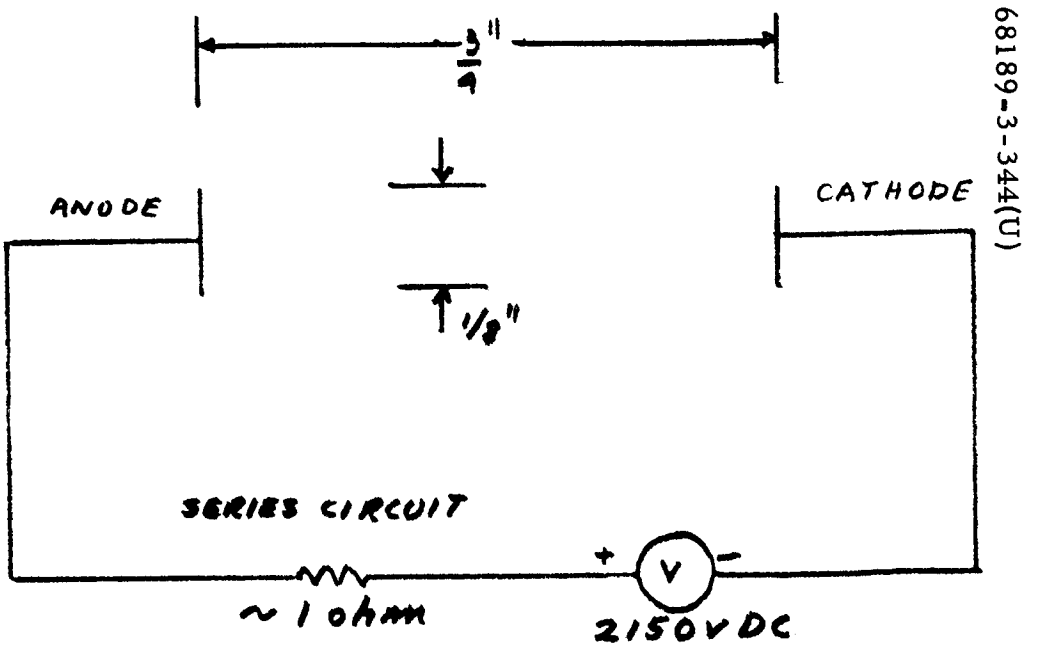

Figure C-2. Discharge Tube Model

Paschen's law is often used as a guide in determining conditions for dc breakdown. It is empirically derived based on measurements on discharge tubes similar to that shown in Figure C-2. The law states that

$$V_B = f(pD)$$

for a given gas and set of electrodes. V_B is the voltage at breakdown, p is the pressure, and D the distance between the electrodes. The functional relationship of pD to V_B is very complicated and most often expressed in terms of the experimental parameters referred to as the ionization per volt and second Townsend coefficient, η and γ. The breakdown is then established by

$$\gamma e^{\eta V_B} = 1$$

It should be understood that many factors can alter the prediction ability of this law. In particular, when γ shows significant dependence on p or D separately or when surface ionization on the electrodes commences to make a large contribution to the breakdown (Reference 1).

To calculate V_B, assume that the vernier engine's exhaust vapor is N_2. It is really a mixture of N_2, CO, CO_2, H_2O, and H_2, but mixture effects on Paschen's law are not well known. For N_2, experimental values of η/p and γ/p are given as functions of E/p in References 2 and 3. The electric field, E, is assumed to be 2150 volts across 19 mm or 1070 volts/cm. The pressure, p, is left as a parameter as follows:

p, Torr	$\left(\frac{E/p, \text{ V}}{\text{cm Torr}}\right)$	γ	$\left(\frac{\eta, \text{ ion pairs}}{\text{volt}}\right)$	V_B, volts
10^{-3}	10^6	>0.05	>4 x 10^{-5}	<7.5 x 10^4
10^{-2}	10^5	>0.05	4 x 10^{-4}	~7.5 x 10^4
10^{-1}	10^4	>0.05	3 x 10^{-3}	~9 x 10^2
1	10^3	0.04	1.2 x 10^{-2}	5 x 10^2
10	10^2	0.1	1.3 x 10^{-2}	6 x 10^2

Paschen's law has a minimum V_B. This minimum occurred for the above data at P = 3.5 x 10^{-1} Torr. The voltage at this point is 275 volts. The above list indicates the breakdown is likely to occur for 2150 volts at a pressure above 10^{-2} Torr, but below 10^{-1} Torr; interpolation gives pD = 1 Torr-mm for V_B = 2150 volts.

A Townsend (or corona) discharge can exist at pressures below that required for breakdown. This is a self-maintaining, low-current discharge which is not unstable (e. g. , does not avalanche). Brown (Reference 2) gives an equation for calculating the maximum current possible before instability sets in. The equation is

$$I_{max} = \frac{2A \epsilon_o v^+}{\eta D^2}$$

where

A = electrode area

ϵ_o = permittivity of free space

v^+ = ion drift velocity

I_{max} varies with pressure due to v^+ and η dependence on p. The peak of I_{max} with pressure for the model appears to be at 10^{-3} Torr. The I_{max} at this pressure is only 1 milliampere. It is clearly a negligible amount and it can be concluded that the power supply overload could not have occurred from corona but only from actual breakdown.

A calculation has been made to determine those pressures under which the gas, with the parameter being fractional ionization (F), can support the overload current of 200 milliamperes. The breakdown condition given by the Paschen curve, namely pD = 1 Torr-mm for V = 2150 volts, has been used. The breakdown is as follows:

F	p, Torr	p, psi
1	5.2×10^{-7}	10^{-8}
10^{-3}	5.2×10^{-4}	10^{-5}
10^{-4}	5.2×10^{-3}	10^{-4}
10^{-5}	5.2×10^{-2}	10^{-3}

It is unreasonable to expect 100 percent ionization, but if this is so, then above 10 feet it is impossible to have breakdown (see Figure C-1). A reasonable fractional ionization might be between 10^{-4} and 10^{-5}, so it would appear that breakdown of the system would occur at 3 ± 2 feet. If the fractional ionization is 10^{-6}, Figure C-1 indicates that breakdown occurs at zero altitude.

REFERENCES

1. J. R. Acton, J. D. Swift, Cold Cathode Discharge Tube, Academic Press, 1963.

2. Sanborn C. Brown, Basic Data of Plasma Physics, John Wiley & Sons, 1959.

3. A. von Engel, Ionized Gases, Oxford Press, 1965.

4. R. H. Edwards, "Multiple Jet Interaction," Hughes IDC 2241. 13/27, October 1965.

5.10 STRUCTURES PERFORMANCE

5.10.1 INTRODUCTION

Structures post-mission analysis is confined to launch and touchdown phases of the mission and is concerned with structural loads, landing gear performance, and landing dynamics. Because of the nonstandard landing of Surveyor III, some elements of flight control data have been incorporated here to achieve a more complete analysis of the landing.

During the launch phase, vehicle acceleration levels were monitored and vehicle separation and extension of the landing gear verified. During touchdown, shock absorber strain gages indicated the landing gear load time histories and enabled a prompt but approximate assessment of landing conditions, such as impact velocity and vehicle incidence relative to lunar surface. Before and after landing, leg deflections were monitored to establish that the operating characteristics of the shock absorbers had not been impaired during the mission.

Post-mission analysis consists of analyzing accelerometer data, leg deflection potentiometer data, and shock absorber strain gage data. A mathematical model was used to simulate Surveyor III landing conditions and enabled close reproduction of rigid body and structural acceleration levels. The analytical results obtained from the mathematical model, combined with other data, can facilitate evaluation of lunar surface mechanical properties.

5.10.2 ANOMALY DESCRIPTION

No anomalies were noted in the structures subsystems during flight and the multiple touchdown.

5.10.3 SUMMARY

Surveyor III landing legs deployed in a normal fashion during the launch phase and operated normally during and after the landing events. No indication of shock absorber pressure loss was observed.

The structural loads experienced by Surveyor III during the launch and landing phases were low relative to design levels.

During landing, three separate landing events took place on the inside slope of a crater. In each event, leg 2 was pointing essentially uphill and the vehicle horizontal velocity was essentially downhill. The vehicle roll axis in the inertial reference condition was inclined to the lunar vertical by approximately 0.5 degree in the downhill direction. This orientation contributed to the increase in lateral velocity which occurred throughout the touchdown sequence. Touchdown phase information is summarized in Table 5.10-1.

TABLE 5.10-1. TOUCHDOWN EVENTS SUMMARY

Parameters	Landing Event			Between Events 1 and 2	Between Events 2 and 3**
	1	2	3*		
Vertical impact velocity, fps	6	4.5	5		
Horizontal impact velocity, fps	0.5	2.5	3		
Site slope, degrees	12	12.5	12		
Surface friction coefficient	0.4	0.4	0.4		
Elapsed time, seconds				24	12.4
Bounce height, feet				38	13
Horizontal distance, feet				50	35

*Prior to event 3, the vernier engines were cut off when the vehicle was approximately 1.0 foot above the surface.

**Observed surface penetrations for events 2 and 3 were in the region of 1 to 2 inches. Soft surface touchdown simulations have implied a surface static bearing strength of 5 to 7 psi. These results correlate with those obtained from Surveyor I postmission analysis.

5.10.4 PERFORMANCE ANALYSIS

5.10.4.1 Launch Phase

Structural Response Loads

During liftoff and for the initial 5 minutes of powered flight, 2 channels (interrange instrumentation group channels 14 and 17) of spacecraft accelerometer data were recorded in real time on a direct write oscillograph. Telemetry channel 14 transmitted a commutated signal of accelerometer CY 54 0 (column base leg 3, Z direction), CY 77 0 (GDC transducer on Centaur adapter) and CY 78 0 (flight control sensor group Z direction). Accelerometer CY 53 0 (column base at leg 2) was disconnected prior to launch and, therefore, did not appear on the channel 14 signal. Channel 17 transmitted the continuous signal of accelerometer CY 52 0 which was located at the column base of leg 1.

A review of the real-time test data verified that all spacecraft accelerometers operated normally. The vibration levels at launch and magnitude and duration of in-flight shock transients were observed to be similar to values experienced during the flight of Surveyor I and II.

Table 5.10-2 is a summary of the vibration environment experienced by accelerometer CY 52 0 (the only continuous signal).

Leg Extension and Vehicle Separation

Due to a temporary loss of data shortly after launch, landing gear extension and vehicle separation were not verified in real time. These events were first confirmed when data returned at 07:39:55 GMT of day 108.

Leg Deflections

The landing gear position potentiometers were first monitored at 08:20:16 GMT of day 108 and were as follows:

Leg 1: V-5 = -0.1 degree

Leg 2: V-6 = 0.2 degree

Leg 3: V-7 = 0.7 degree

With the landing gear extended, the nominal value for these signals is 0.0 degree with an allowable variation of ±5 percent, or ±1.2 degrees. A check of these signals just before touchdown phase at 23:15:52 GMT of day 110 showed them to be:

Leg 1: V-5 = -0.2 degree

Leg 2: V-6 = 0.0 degree

Leg 3: V-7 = 0.4 degree

TABLE 5.10-2. VIBRATION DATA FOR CY 52 0 DURING LAUNCH OF SURVEYOR III

Flight Event	Result
Liftoff	T_o - 0.2 second, 3.3 g 0 to peak (single spike)
	T_o 0.8 g retromotor simulator (estimated value)
	T_o + 4 seconds, 0.4 g retromotor simulator (estimated value)
	T_o + 8 seconds, 0.1 g retromotor simulator (estimated value)
Atlas booster engine cutoff	1.75 g 0 to peak
	(1-cycle pulse, 0.8-second duration)
Insulation panel jettison transient	10 g 0 to peak decayed to 0 g in 0.08 second
Boost engine jettison	15 or more extremely sharp peaks*
	>6 g with 3 peaks >10 g (no oscillatory decay)
Nose fairing jettison	6-cycle oscillation. Maximum level 1.0 g 0 to peak. Approximate frequency 18 cps.
Atlas sustainer engine cutoff Atlas Vernier Company	Single pulse less than 0.5 g 0 to peak
Atlas/Centaur separation	High frequency transient >10 g 0 to peak, decayed to 0 g in 0.15 second

*These transients are probably the result of telemetry dropout. Similar spikes occur on channel 14 during switching when signals were not being monitored.

These slight changes are acceptable because of the 0.7-degree mechanical backlash in the landing gear.

5.10.4.2 Touchdown

During the descent of Surveyor III, the 14-foot mark was not generated and consequently the vernier engines were not automatically shut off. The spacecraft continued its descent with the verniers thrusting at 0.9 lunar g. As the spacecraft settled onto the sloping surface, the attitude control system,

in trying to keep the spacecraft Z-axis vertical, caused the thrust on engines 1 and 3 (the downhill engines) to increase, thereby causing the spacecraft to rise back off the lunar surface aided by the rebounding of the landing gear. On becoming horizontal again, the engines throttled back down to 0.9 lunar g, and the spacecraft vertical rise slowed to a stop. It then accelerated back toward the lunar surface with an acceleration of 0.1 lunar g (0.53 ft/sec^2). It contacted the lunar surface again 24 seconds after the touchdown, and the above hopping procedure repeated. Just prior to the third touchdown (12.4 seconds after the second), the engines were commanded off via a ground command, and the spacecraft remained on the surface at the third touchdown.

Figure 5.10-1 shows the shock absorber strain gage outputs for the three contacts, and Figures 5.10-2 shows each individual landing on an expanded time scale. Table 5.10 -3 presents the shock absorber maximum forces for the three touchdowns and the impact times for each footpad. During each of the landing events, footpad 2 struck the surface ahead of the other two footpads. Generally, the load levels experienced during landing event 1 were slightly higher than those of landing 2, but slightly less than those of landing event 3. Following the last landing, the magnitude of the forces in the shock absorbers is consistent with the value required to support the static weight of the spacecraft with no vernier engines firing. These data preclude the possibility of a fourth landing event. The load histories of landing event 3 correspond to those recorded during the landing of Surveyor I, i.e., a primary impact followed by a small bounce of the vehicle and then a secondary impact with oscillating loads of low level. The final small bounce of Surveyor III during the third landing was probably about 2 inches high. The first touchdown occurred at approximately 00:04:18 GMT of day 110, the second 24 seconds after the first, and the third 12.4 seconds after the second.

Landing Dynamics

Simulation of Surveyor III landing dynamics has been achieved using a three-dimensional mathematical model which incorporates a flight control system. Simulations have considered recorded time histories of shock absorber strain gages, flight control gyro errors, and vernier engine thrust commands together with pertinent information obtained from post-landing TV coverage. One objective of the analysis has been to produce a set of strain gage time histories for each landing event which result from impact velocities entirely consistent with the simulated trajectories flown by the mathematical model between each landing event. This would result in a consistent simulation of the entire landing phase. A high degree of success has been attained in this endeavor.

Positive correlation between simulated and flight strain gage data was obtained by considering horizontal touchdown velocities of 0.5, 2.5, and 3.0 fps, respectively, for landing events 1, 2, and 3. (The 0.5 fps for event 1 is well within the flight control 3σ lateral velocity capability of 1.5 fps. The 3 fps for event 3 is consistent with TV observations of the distance between footpad 2 imprints and the time, from strain gage data, between the occurrence of the imprints.) However, with the vehicle horizontal at the time of

68189-3-117(U)

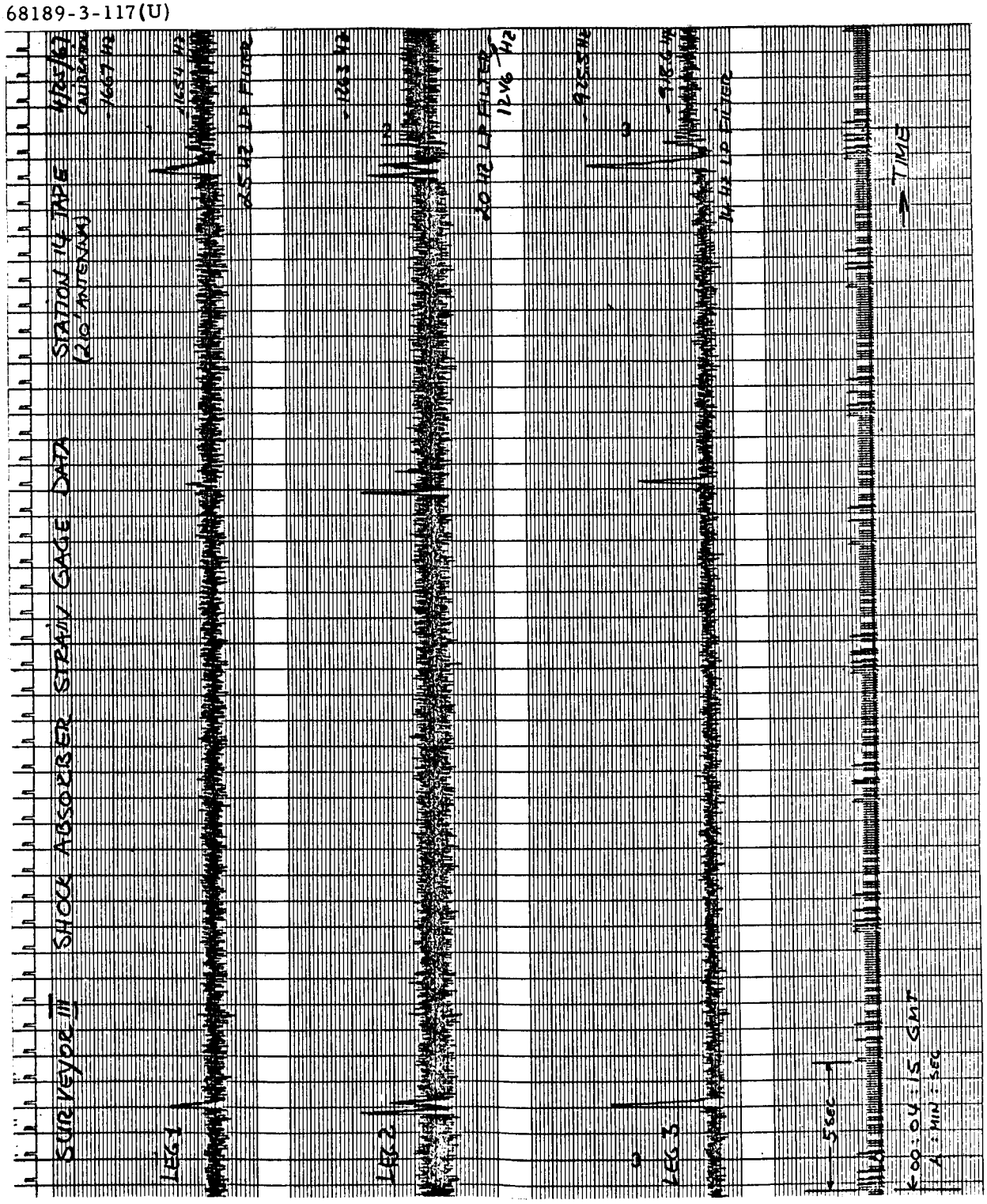

Figure 5.10-1 Surveyor III Shock Absorber Strain Gage Data

68189-3-118(U)

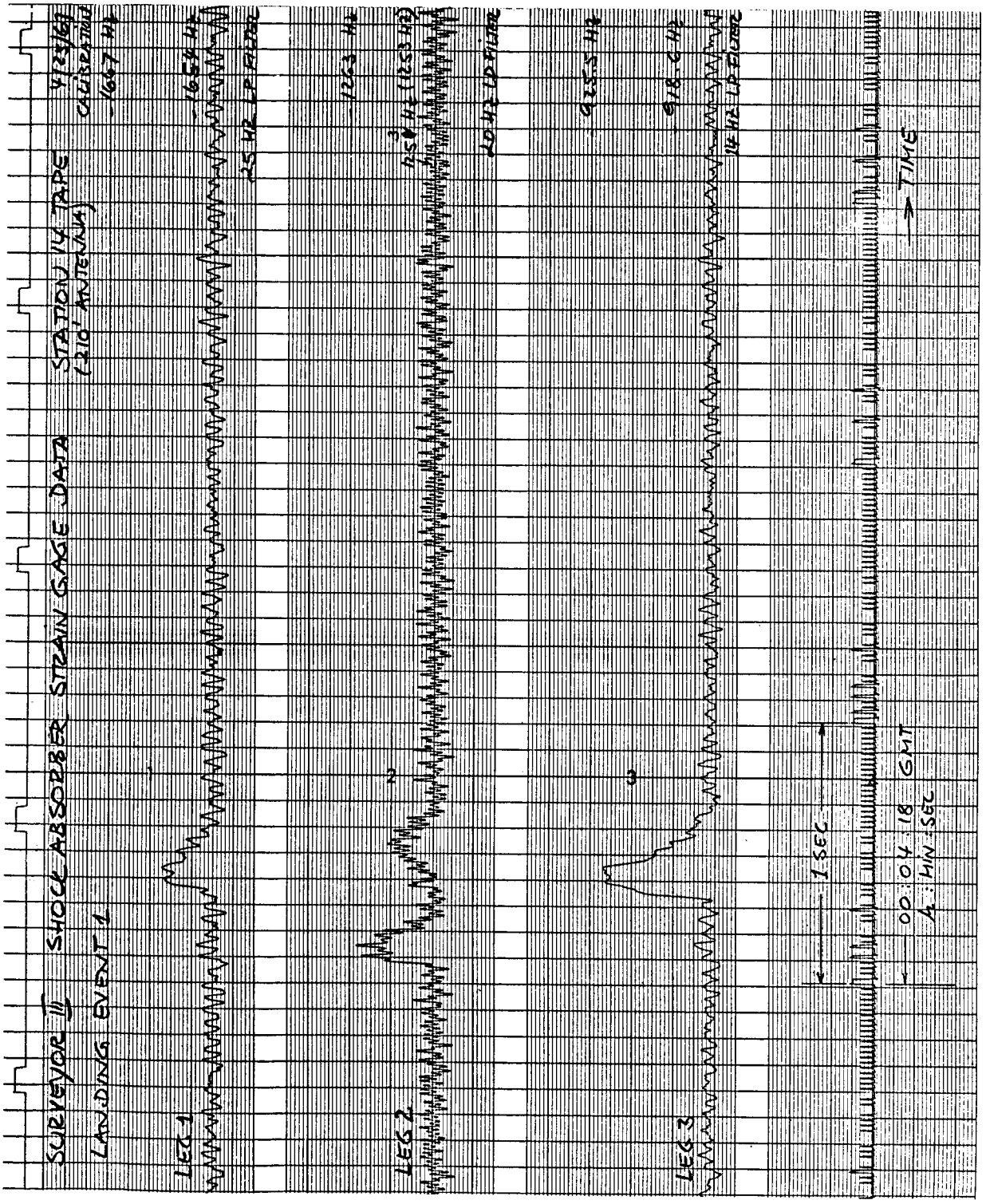

a) Landing Event 1

Figure 5.10-2. Surveyor III Shock Absorber Strain Gage Data

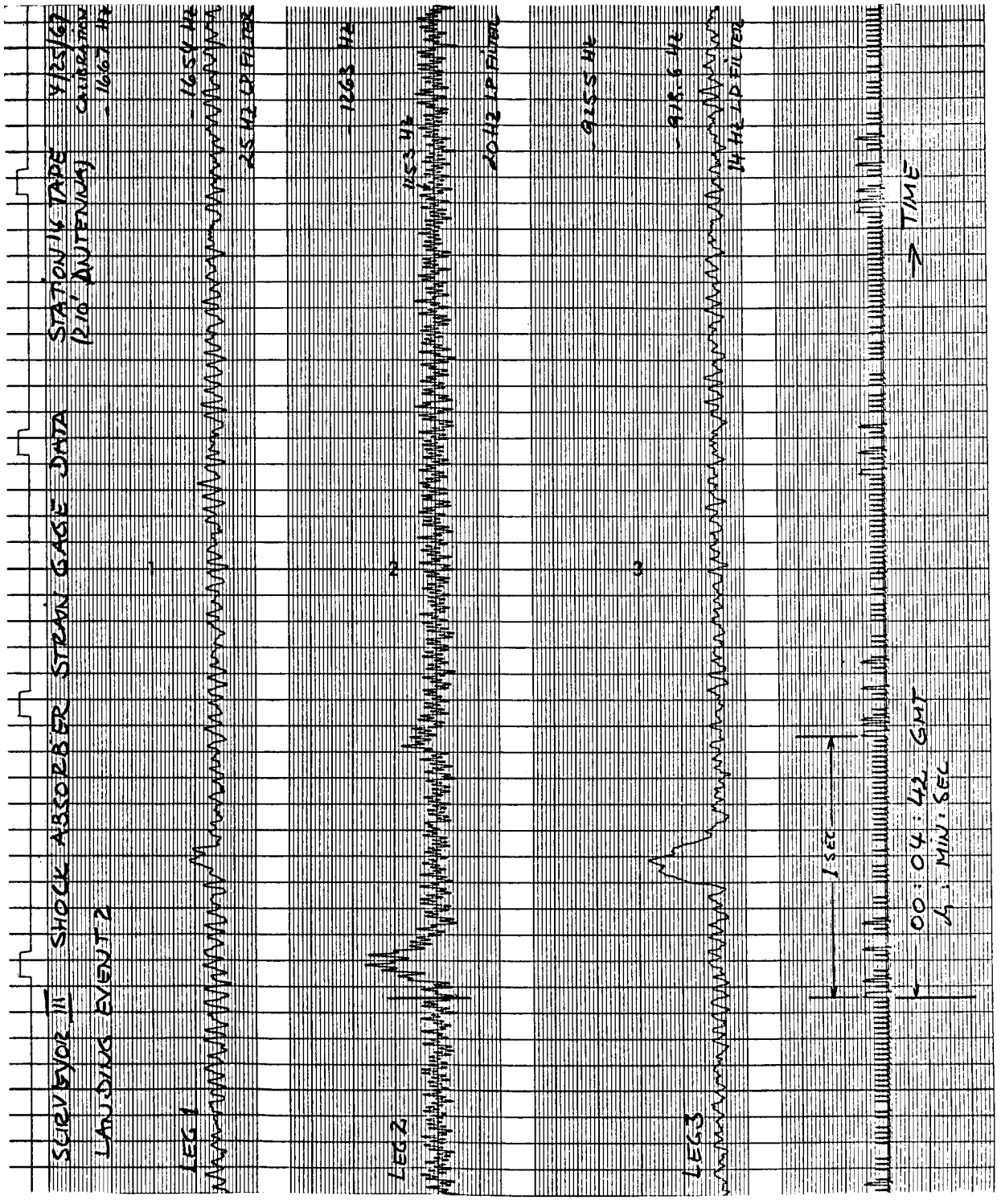

b) Landing Event 2

Figure 5.10-2 (continued). Surveyor III Shock Absorber Strain Gage Data

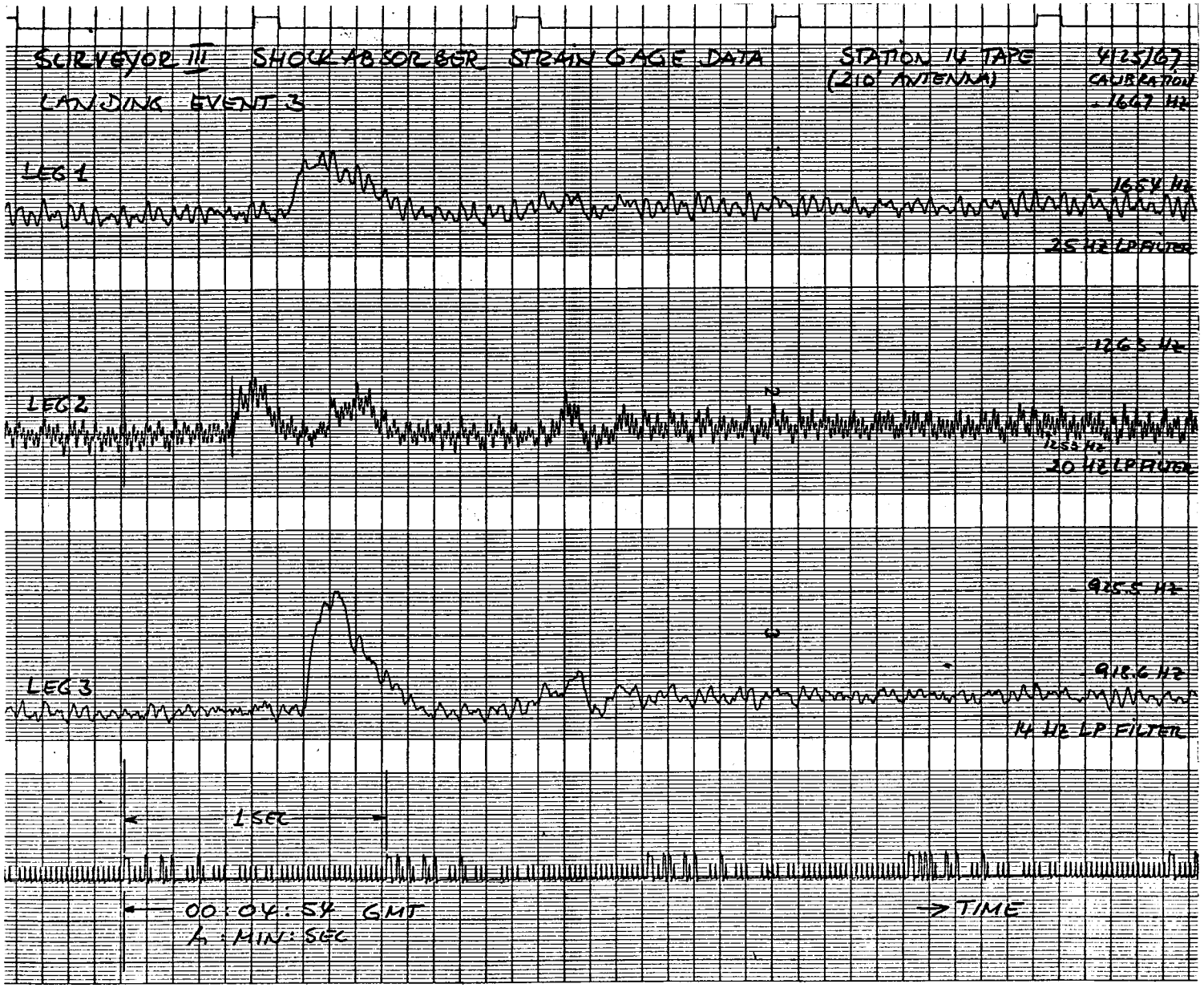

c) Landing Event 3

Figure 5.10-2 (continued). Surveyor III Shock Absorber Strain Gage Data

TABLE 5.10-3. SURVEYOR III SHOCK ABSORBER PEAK FORCES

	Event 1		Event 2		Event 3	
Leg	Peak Force, pounds	Time,* Min-Sec-MSC	Peak Force, pounds	Time,* Min-Sec-MSC	Peak Force, pounds	Time,* Min-Sec-MSC
1	700	04:18:360	290	04:42:510	930	04:54:660
2	690	04:18:060	660	04:42:070	610	04:54:410
3	910	04:18:330	560	04:42:440	980	04:54:710

*Time of initial contact

Calibration factors

Leg 1	70 lb/div
Leg 2	51 lb/div
Leg 3	37 lb/div

touchdown, it is not possible to produce a consistent set of impact velocities, as shown by the results of Table 5.10-4. The increases in horizontal velocity achieved during events 1 and 2 are due to horizontal components of vernier thrusts during tilting of the vehicle down the lunar slope. It can be seen that the touchdown reactions alone do not fully account for the increase in lateral velocity between events 1 and 3. Because of this it was considered probable that the roll axis of Surveyor III was not aligned perfectly with the lunar vertical during its inertial hold. By holding the vehicle with a tilt in the downhill direction (Figure 5.10-3), the vehicle would pick up additional lateral velocity during its flight between landings. Using a tilt of one-half degree in the computer program gave lateral velocities for the following events very close to those which produced the best matchings with flight strain gage histories. These velocities are also shown in Table 5.10-4.

The best comparisons of strain gage time histories achieved for each landing event are shown in Figure 5.10-4. Smoothed curves of the flight data are subject to errors as high as 20 percent due to signal noise level. During landing event 1, time histories of vehicle pitch and yaw gyro errors and vernier engine thrust commands were obtained. These are compared with analytical simulations in Figures 5.10-5 and 5.10-6 which are achieved from the same touchdown conditions as in Figure 5.10-4.

Using data from the best computer simulation of landing events 1 and 2, the vernier engine thrusts were plotted together with the heights above the ground of the vernier engine nozzles. This assumes a planar surface. The results are shown in Figure 5.10-7. In the case of engine 3 during landing event 2, proximity to the surface has been established by TV data to be approximately 3 inches less than indicated in Figure 5.10-7b because of surface irregularities. Probably, during that event, this discrepancy is representative of the uncertainty in proximity to engines 1 and 2.

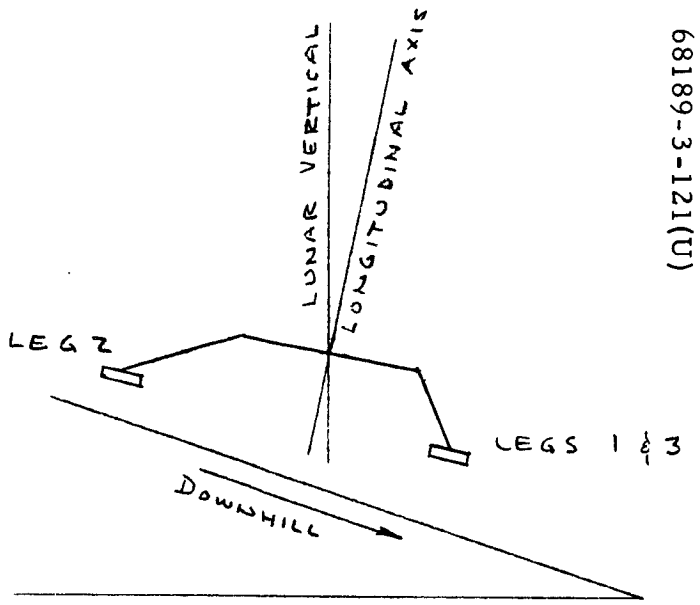

68189-3-121(U)

Figure 5.10-3. Estimated Spacecraft Inertial Orientation

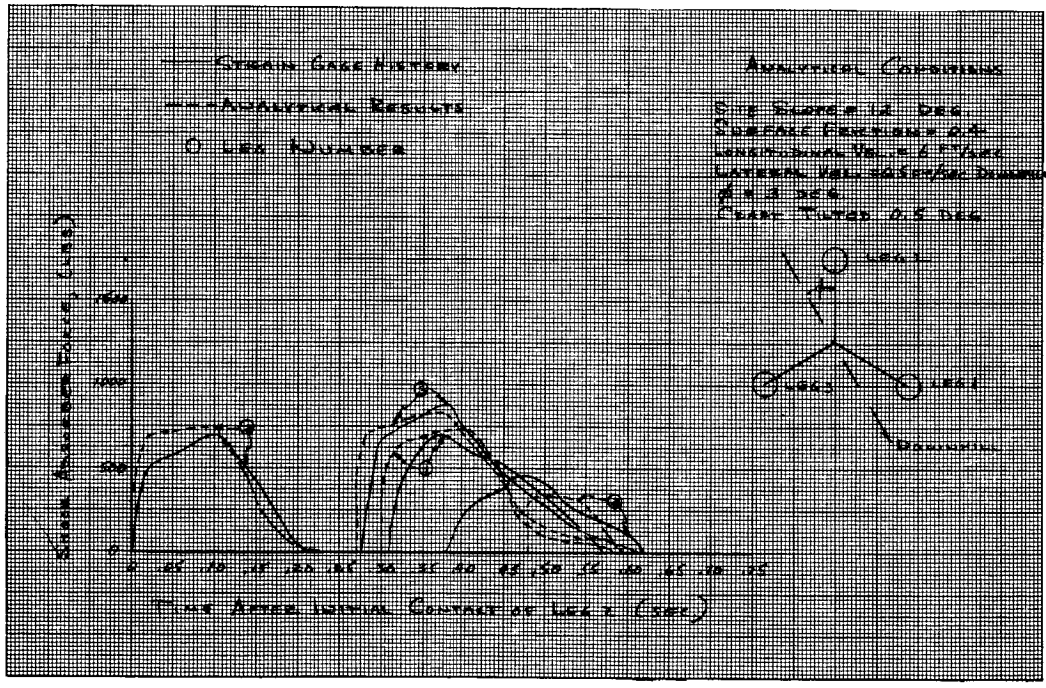

68189-3-122(U)

a) Event 1

Figure 5.10-4. Comparison of Strain Gage Histories and Analytical Results for Surveyor III Shock Absorbers

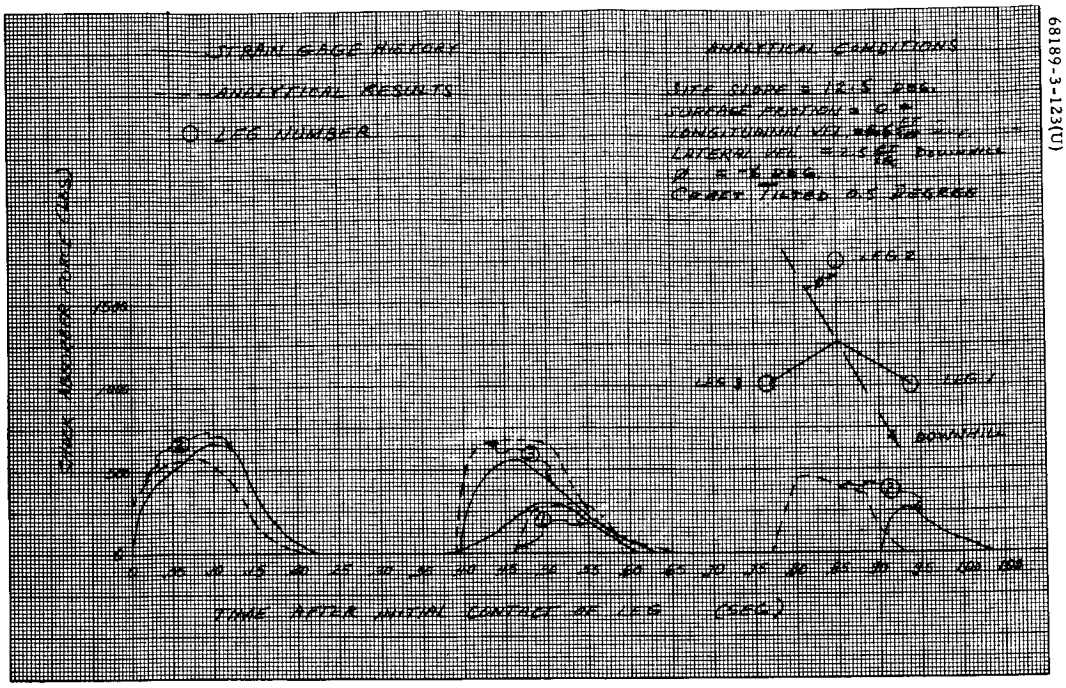

b) Event 2

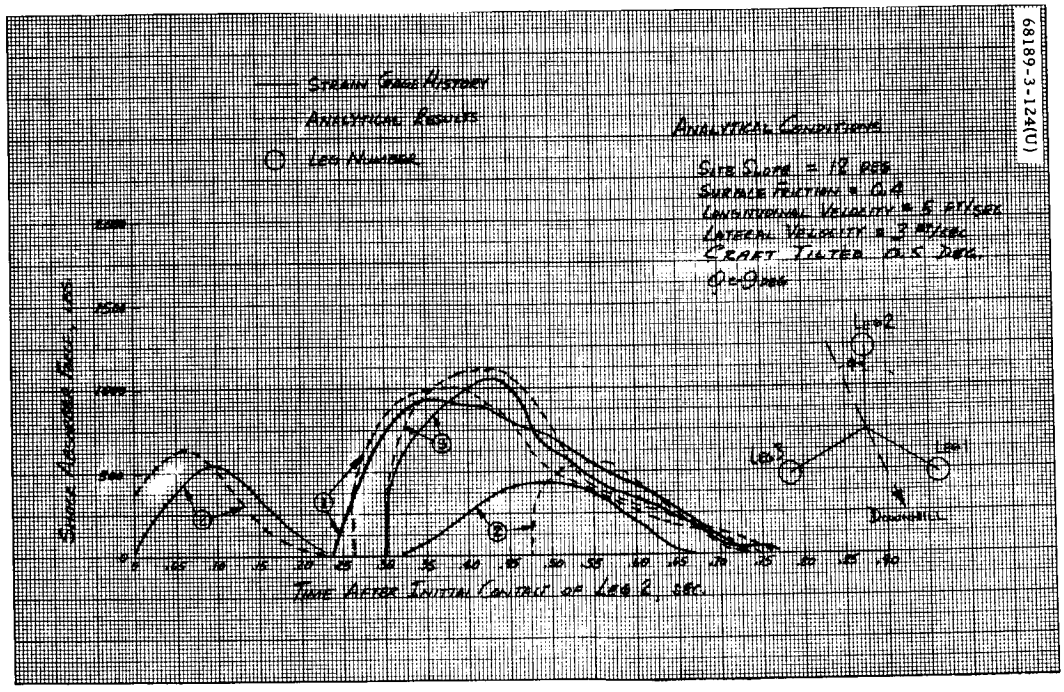

c) Event 3

Figure 5.10-4 (continued) Comparison of Strain Gage Histories and Analytical Results for Surveyor III Shock Absorbers

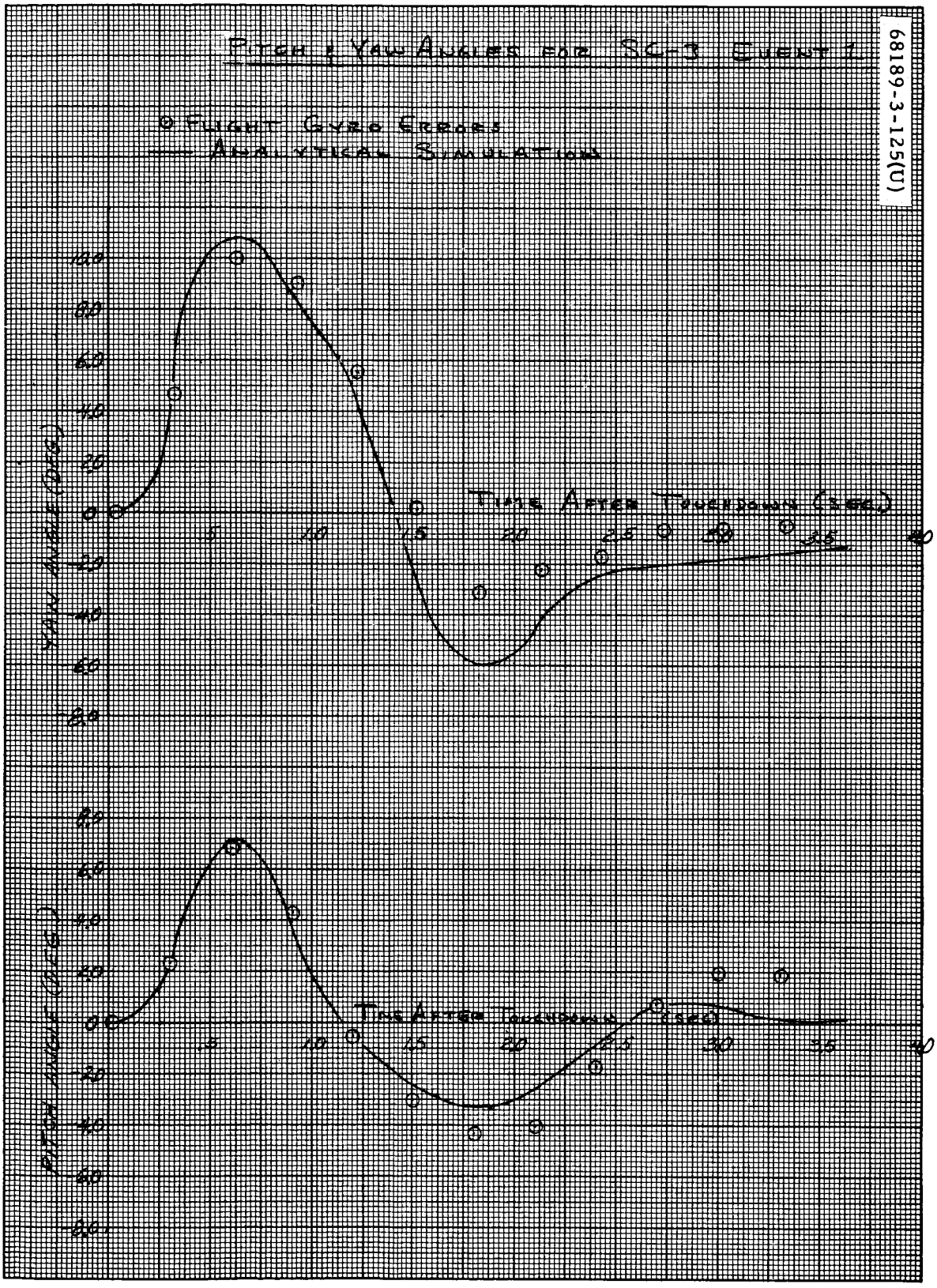

Figure 5.10-5. Pitch and Yaw Angles for Surveyor III Event 1

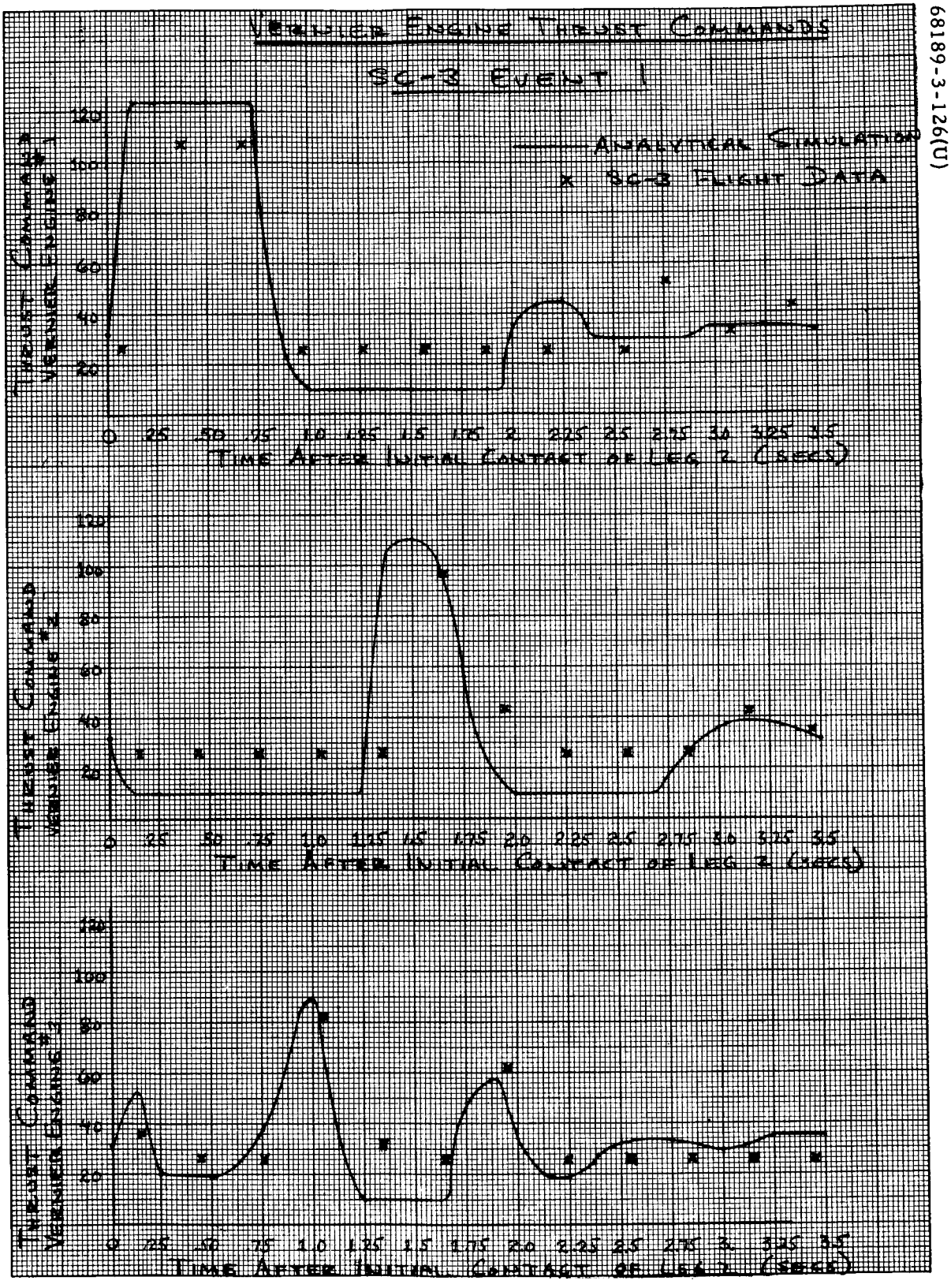

Figure 5.10-6. Surveyor III Event 1 Vernier Engine Thrust Commands

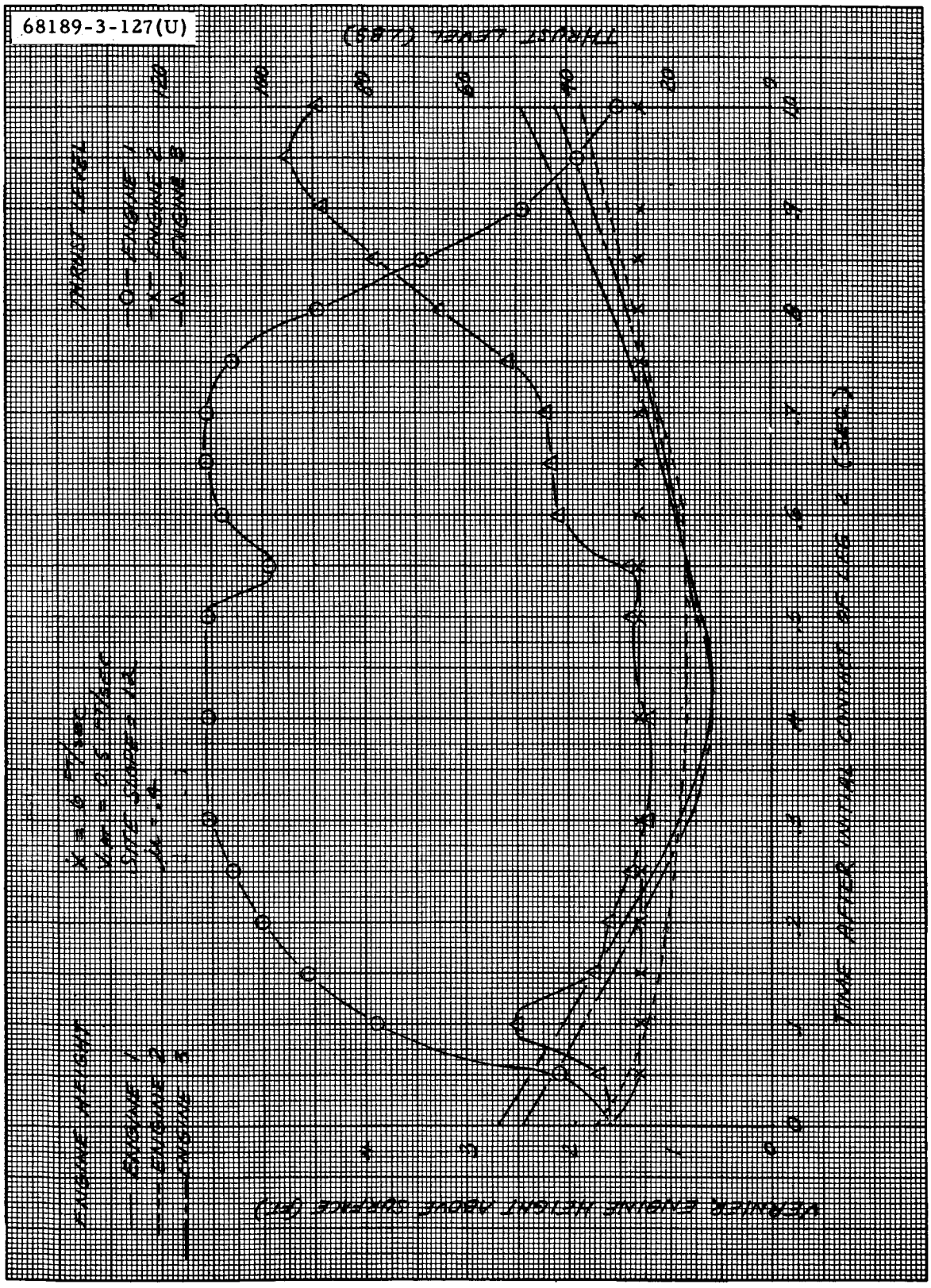

a) Event 1

Figure 5.10-7. Engine Heights Above Surface and Thrust Levels

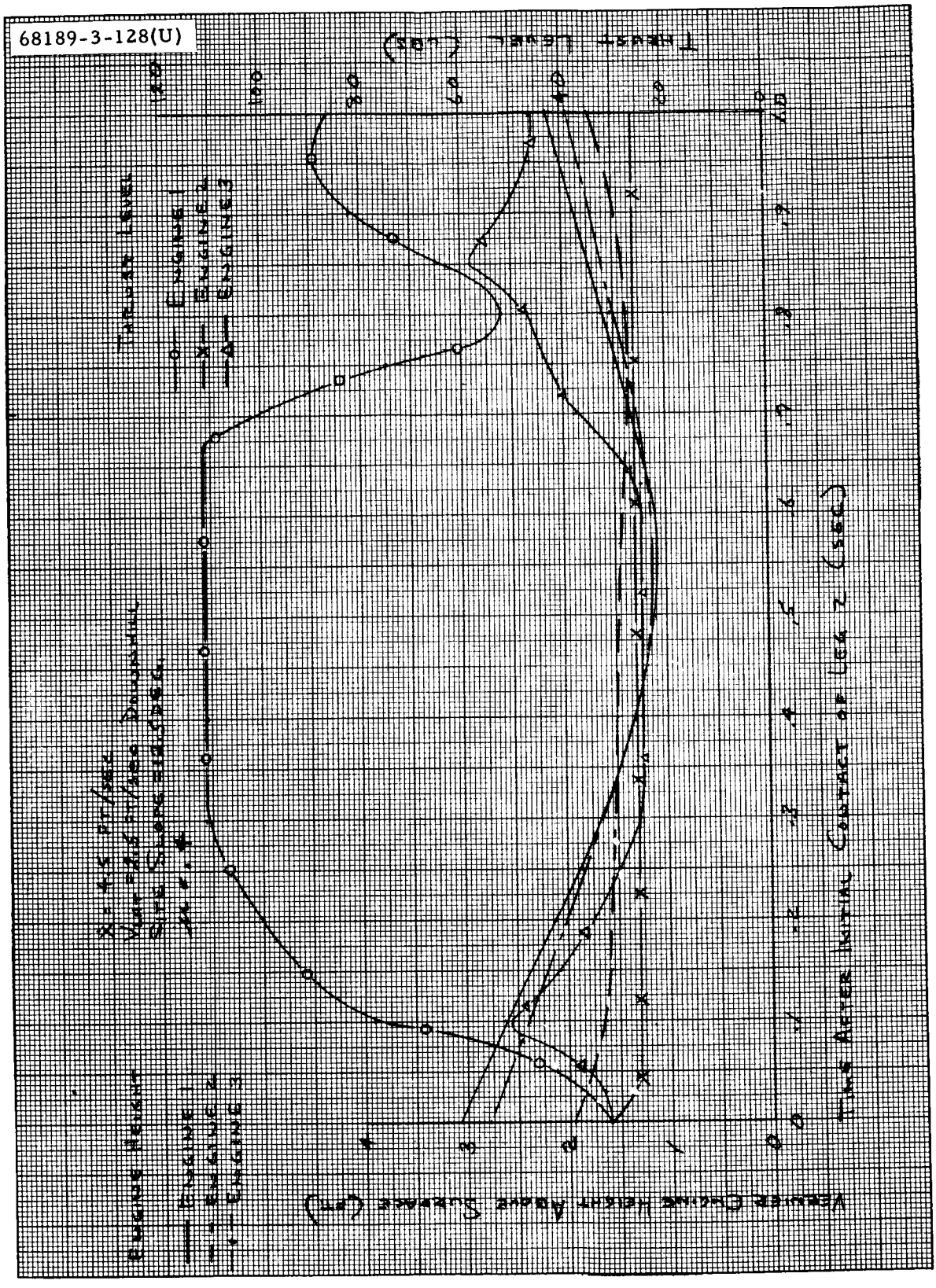

b) Event 2

Figure 5.10-7 (continued). Engine Heights Above Surface and Thrust Levels

TABLE 5.10-5. COMPARISON OF FLIGHT AND SIMULATED DATA

Parameter	Event 1 to Event 2		Event 2 to Event 3	
	Simulation	Flight Data	Simulation	Flight Data
Elapsed time	18.5	24	14.5	12.4
Downhill distance traveled, feet	38.0 (in 18.5 seconds)		41.4 (in 14.5 seconds)	
	50.8 (in 24 seconds)		35.6 (in 12.4 seconds)	36*
Height of bounce, feet	21.4	38**	13.1	13**
Lateral velocity achieved, fps	2.26		2.9	3*
Longitudinal velocity achieved, fps	4.46		5.0	

*Obtained by analysis of TV pictures.

**Obtained by simple considerations of elapsed time and a 0.1-lunar gravity field. Probably more accurate than simulated data.

information was obtained to determine that the leg deflections were not excessive. It was therefore considered there was no necessity to lock the landing gear at that time.

The landing gear position potentiometers were monitored during the first part of the first lunar day to detect any changes that might indicate shock absorber leakage. During this time, a lunar eclipse occurred, resulting in a rapid temperature drop on the shock absorbers. The leg position readings underwent only minor random fluctuations and no trends were detected that would indicate a faulty shock absorber. A summary of leg angle readings is presented in Table 5.10-6.

TABLE 5.10-4. LATERAL VELOCITY SIMULATION

V_L* Prior to Event 1	Resulting V_L Prior to Event 2	V_L Prior to Event 2	Resulting V_L Prior to Event 3
Roll Axis Parallel to Lunar Vertical			
0.5	1.6	2.0	2.3
1.0	1.9	2.5	2.6
1.5	1.9	3.0	2.9
Vehicle Pitched Downhill 1/2 Degree			
0.5	2.3	2.5	2.9

*V_L = lateral velocity, fps.

Simulation of the trajectories between events 1 and 2 and 2 and 3 produced good correlation between impact velocities and those required for strain gage correlation, as previously explained. However, the time durations of the trajectories did not correlate well with observations. Results are shown in Table 5.10-5. Differences could be due to slight discrepancies between the actual and simulated control systems, or to integration errors accumulating over the long integrating period. The results for the flight from events 2 and 3 were arrived at assuming the vernier engines cut off when the spacecraft was 1.0 foot above the lunar surface. This results in a longitudinal impact velocity, for event 3, of 5 fps and thus corresponds with the conditions used to generate Figure 5.10-4c.

Structural Response Loads

The longitudinal velocities during the landing events of Surveyor III touchdown were from the above analysis, 6, 4.5, and 5 fps. These compare with a Surveyor I impact velocity of approximately 11.5 fps. Structural loads calculated to occur during the Surveyor I landing were less than 20 percent of the design load levels. It is considered that Surveyor III structural load levels were even less than those of Surveyor I and that a detailed analysis was therefore unwarranted.

Leg Deflections

The presence of poor analog data just after the landing prevented accurate determination of the landing gear positions. However, sufficient

TABLE 5.10-6. LANDING GEAR DEFLECTION ANGLES (DEGREES)

Day	Leg		
	1	2	3
111	1.1	1.5	1.5
112	1.0	1.4	1.5
115	1.0	1.4	1.6
117	1.0	1.4	1.6
121	0.8	0.8	1.4

5.10.5 ACKNOWLEDGEMENTS

The total analysis effort of the section was coordinated by R. H. Jones. Analysis of the boost phase data was performed by L. W. Gammell and B. T. Stafford. Comparisons between flight data and analytical simulation of the landing were achieved by C. D. Conaway, aided by J. D. Hinchey and D. R. Williamson. Successful incorporation of the flight control system into the landing dynamics computer program was due to the efforts of Margaret Dove, J. D. Hinchey, W. G. O'Brien, W. B. Silber, and P. L. Welton.

5.11 MECHANISMS SUBSYSTEM

5.11.1 INTRODUCTION

This section deals with the mechanical performance of the spacecraft landing legs, omnidirectional antennas, and antenna and solar panel positioner (ASPP). For purposes of this report, these mechanisms are collectively defined as the mechanisms subsystem.

Items constituting the main headings for this analysis effort include:

1) Landing gear deployment – When each landing gear is fully deployed, it opens an electrical switch on the telescoping strut. The actuation of these switches indicates that the landing gear is deployed, and is required for initiation of automatic sun acquisition at separation from Centaur. The telemetry designations for these functions are V-1, V-2, and V-3 for each landing leg, respectively.

2) Omnidirectional antenna deployment – When each omnidirectional antenna is fully deployed, it opens an electrical switch to produce a change of state for telemetry purposes only. The telemetry designation for omni antenna A is M-1, for omni antenna B, M-2.

3) ASPP automatic solar panel deployment and lunar operations – The ASPP function after separation is to deploy the solar panel surface perpendicular to the roll axis to achieve maximum receipt of solar energy during transit. After landing on the moon, the ASPP is commanded from earth to orientate the solar panel surface perpendicular to the sun rays, and the planar antenna beam toward the earth.

The ASPP has four rotation axes which are moved in steps upon command from earth. The axes are polar, solar, elevation, and roll. The polar axis rotates 1/16 degree per command, the other axes rotate 1/8 degree per command. Figure 5.11-1 illustrates the ASPP with the polarity of rotation for each axis. The telemetry designation for the ASPP axis positions are:

Solar panel	M-3
Polar axis	M-4

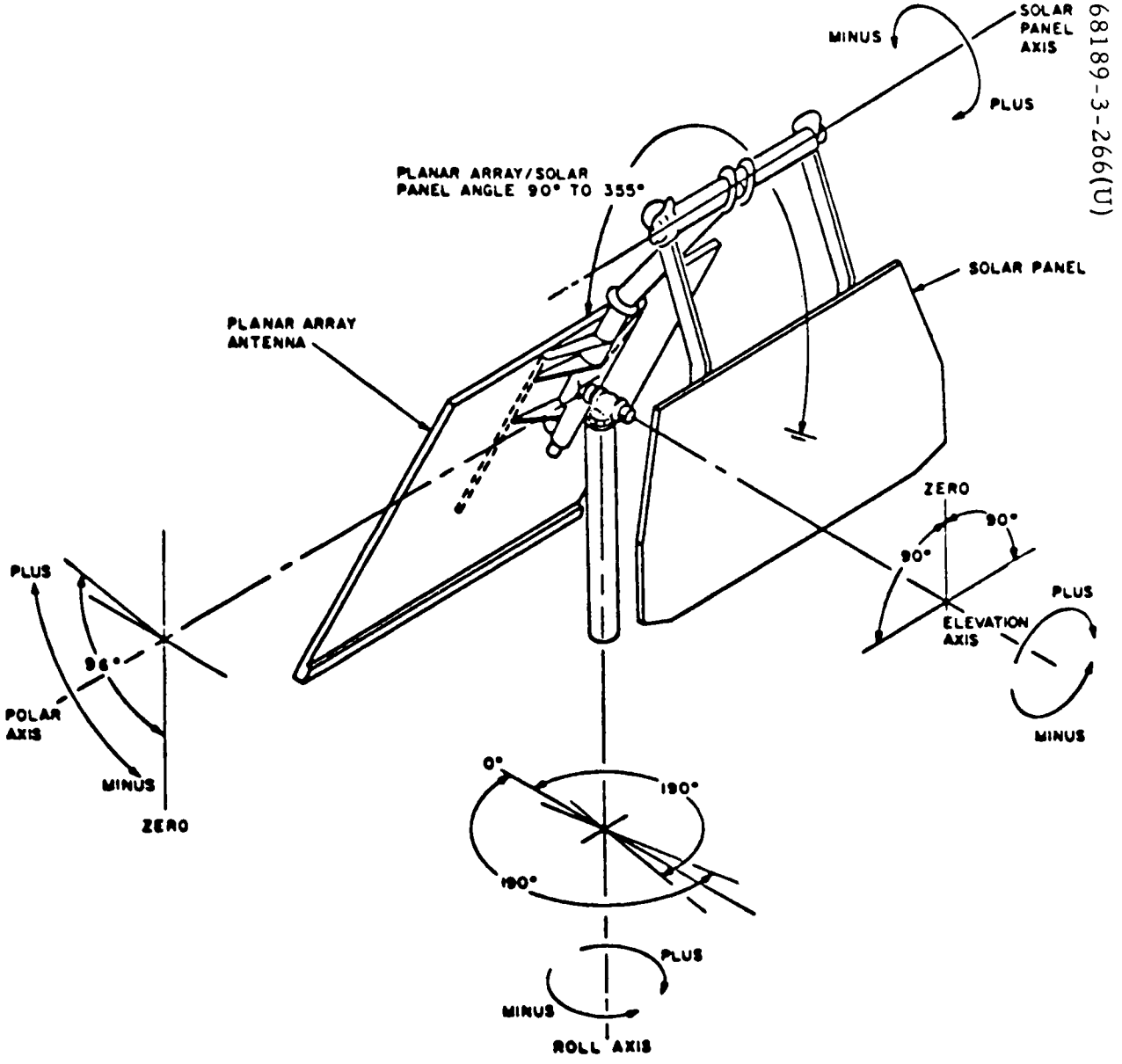

68189-3-266(U)

Figure 5.11-1. Antenna and Solar Panel Positioner

Elevation axis	M-6
Roll axis	M-7

5.11.2 ANOMALIES DESCRIPTION

There were no anomalies in the mechanisms subsystem. The data telemetered during the transit phase indicated that all parameters were as expected and that all functions were performed properly. Lunar operation of the ASPP was verified first by establishing the spacecraft attitude through ASPP and TV surveys. These were accomplished by using step counts rather than telemetry data, since engineering data became unreliable after the second touchdown. Once the attitude of the spacecraft was established by these surveys, and after a period of time, predetermined step commands were sent to reposition the solar panel and planar array to point toward the sun and earth, respectively. The results of this positioning method indicated the stepping efficiency was well within the specified response.

5.11.3 SUMMARY AND RECOMMENDATIONS

It may be concluded that all mechanisms functions were performed properly and at the correct times. Some uncertainties in trajectory times do cause some functions to appear to be reversed in order of occurrence. For example, the solar panel unlocked signal which most closely matches the actual vehicle separation, appeared to occur prior to the Centaur command for that function. However, the tolerance placed upon the accuracy of the M-14 on signal due to the sampling times will place the solar panel unlock time after actual vehicle separation.

The performance of the ASPP was normal during the automatic deployment sequence and lunar operations. The ASPP was operated by step count while on the moon and, with the TV system, was used to determine spacecraft attitude. Analysis of the ASPP stepping efficiencies indicates all axes responded 100 percent to commands.

5.11.4 SUBSYSTEM PERFORMANCE ANALYSIS

Table 5.11-1 shows the occurrence of major events for the mechanisms subsystem. The times for Centaur commands were obtained from GDA data from Centaur telemetry.

Table 5.11-2 presents a summary of the subsystem parameters reduced from telemetry data. The expected values were obtained from flight acceptance, type approval, and solar thermal vacuum testing, and from specified design performance values.

TABLE 5.11-1. OCCURRENCE OF MAJOR EVENTS

Day 107, 1967

Event	Expected Time of Occurrence, GMT ‡ hr:min:sec	Actual Time of Occurrence, GMT hr:min:sec
Launch	—	07:05:01.059
Centaur extend landing gear command	07:39:08.86	07:39:12.889
	Before	
Landing legs extended V-1, V-2 and V-3 "On"	07:39:15.1	07:39:13.377 ±1.2
Centaur extend omnidirectional antennas command	07:39:19.24*	07:39:22.889
	Before	
Omnidirectional antennas extended M-1 and M-2 "On"	07:39:25.3	07:39:25.056 ±1.2
Centaur command for spacecraft electrical separation	07:39:45.22*	07:39:49.06**
Spacecraft electrical separation, M-9 "On"		07:39:50.258 to -2.40 seconds
Centaur command for spacecraft vehicle separation	07:39:50.86*	07:39:54.46**
ASPP solar panel unlocked, M-14 "On"		07:39:53.846 to ±1.188 seconds
ASPP solar panel locked in transit position, M-11 "On"		07:45:51.456 to ±1.2
ASPP roll axis locked in transit position, M-13 "On"		07:50:05.238 to -2.4

‡ Expected times are based on Centaur actual times, nominal landing gear type approval test deployment times, and nominal omni antenna flight acceptance test deployment times.

* GDC predicted times.

** Times are based on trajectory information.

TABLE 5.11-2. PERFORMANCE PARAMETERS SUMMARY*

Parameter	Expected Value, Nominal	Measured Value
Time from Centaur extend landing gear command to legs extended indications (V-1, V-2, and V-3 on)	< 2.3 seconds	0.5 ± 1.2
Time from Centaur extend omnidirectional antenna command to omnidirectional antennas extended (M-1 and M-2 on)	< 2.4 seconds	2.1 ± 1.2
Solar axis deployment time (A/SPP solar panel auto-deployment)	357 seconds	357 seconds
Roll axis deployment time (A/SPP solar panel auto-deployment)	254 seconds	254 seconds
Total ASPP solar panel auto-deployment time	611 seconds	611 seconds
Solar axis launch position	355 degrees	355.5 degrees
Polar axis launch position	0 degree	0.3 degree
Elevation axis launch position	0 degree	-0.9 degree
Roll axis launch position	-59.9 degrees	-60.5 degrees
Solar axis transit position	270 degrees	270.7 degrees
Roll axis transit position	0 degree	0.1 degree
Solar axis stepping efficiency (lunar)	> 97 percent	Calculations indicate a probable 100-percent response for all axes
Polar axis stepping efficiency (lunar)	> 97 percent	
Elevation axis stepping efficiency (lunar)	> 97 percent	
Roll axis stepping efficiency (lunar)	> 97 percent	

*Expected times are based on nominal landing gear TAT deployment times, and nominal omnidirectional antenna FAT deployment times.

5.11.4.1 Landing Gear Deployment

Table 5.11-2 shows the nominal expected deployment time for the landing gear to be about 2.3 seconds. Flight data show the deployment time to be 0.5 ± 1.2 seconds, which is slightly below the expected value. However, it is assumed the landing gear deployed normally; any small variation lies with the data time uncertainties during this period.

5.11.4.2 Omnidirectional Antenna Deployment

The nominal expected omnidirectional antenna deployment time is 2.4 seconds. The mission deployment time was 2.1 ± 1.2 seconds, which indicates probable nominal deployment performance. Data show that both omni antennas were deployed at the same time.

5.11.4.3 ASPP Performance

Automatic Solar Panel Deployment

Automatic solar panel deployment begins upon closure of the 22-volt switch in the separation sensing and arming device at vehicle separation. The solar panel launch lock is unlocked and the solar panel is stepped from 355 to 270 degrees where it is relocked. At this point the roll axis is stepped from -59.9 to 0 degrees and relocked. Both positions are locked until after touchdown.

Table 5.11-3 compares the switch closure times and solar panel deployment times for Surveyor III solar thermal vacuum (STV) Phase A and Surveyor III mission. Deployment time comparison is also shown in Table 5.11-2. The two deployment times are nominally the same, indicating normal functional performance. The nominal deployment time based on 2 steps/second from multivibrator is 9 minutes, 40 seconds. The stepping commands are not counted during auto-deployment. The maximum deployment time is 12 minutes. The Surveyor III mission solar panel deployment time was 10 minutes, 12 seconds. Comparing the mission deployment time to that in STV-φA, the agreement is better than 99 percent, even considering worst case of data time uncertainties. Since the response in STV was 99.5 percent for the solar drive and 99.3 percent for the roll drive, the mission deployment time is within the requirement of 97-percent stepping efficiency. This assumes the multivibrator pulse rate is constant for both cases.

Figure 5.11-2 is a graph of the ASPP roll and solar axis positions during the automatic solar panel deployment. It is to be noted that the slopes of both curves is the same, indicating the same stepping response during auto-deployment.

Table 5.11-4 shows the positions of the ASPP axis before and after the automatic solar panel deployment. These all fall within the required limits when corrections are applied to the telemetry data.

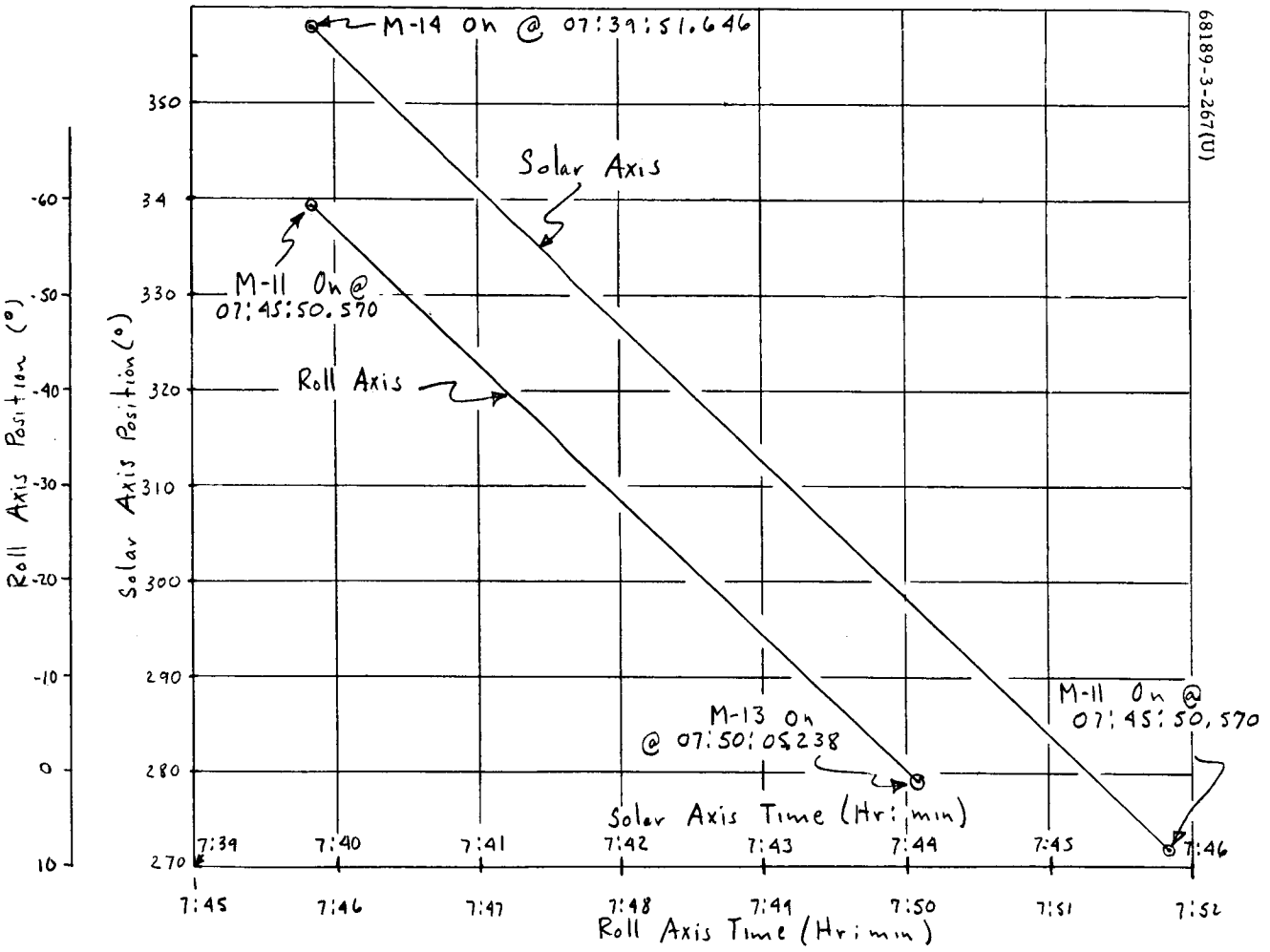

Figure 5.11-2. Roll Axis and Solar Axis Positions Through Autodeployment

TABLE 5.11-3. SURVEYOR III MISSION AND STV-φA SWITCH CLOSURE TIMES

	SC-3 Mission	STV-φA
M-14 on (solar panel unlock)	07:39:54, GMT	09:24:03, PDT
M-11 on (solar panel relock)	07:45:51, GMT	09:30:00, PDT
M-13 on (roll axis relock)	07:50:05, GMT	09:34:14 $^{+0}_{-9}$ seconds, PDT
Solar axis stepping time (M-14 – M-11)	5 minutes 57 seconds	5 minutes 57 seconds
Roll axis stepping time (M-11 – M-13)	4 minutes 14 seconds	4 minutes 14 seconds
Total deployment time (M-14 – M-13)	10 minutes 11 seconds	10 minutes 11 seconds

Post Landing Performance

Because of the anomaly that occurred in the spacecraft telemetry at touchdown, all ASPP operations were performed by maintaining an accurate step count for all gimbal axes. Table 5.11-6 presents the complete record of stepping commands during lunar operations. It also includes a statement of the functions being performed during each block of stepping. Figure 5.11-3 presents this in graphical form, along with the ASPP temperatures.

Table 5.11-5 provides the number and direction of step commands sent for each ASPP gimbal axis.

Drive Stepping Response. Although a telemetry correction for the 17.2-bps data was supplied near the end of the lunar day, confidence levels were not established for this correction which would permit an accurate assessment of stepping response. Nevertheless, agreement of less than 1 degree was generally observed between step count and corrected telemetry values, even at the end of the lunar day in which 19,491 commands were transmitted. A qualitative estimate of ASPP drive stepping response can be obtained, however, from ASPP performance during the latter days of lunar operations. Once the spacecraft attitude on the lunar surface was established from the ASPP sun and earth sighting, the gimbal angle settings required to track the sun and earth throughout the remainder of the lunar day were obtained from available computer programs. Stepping the antenna to these predicted earth locations provided sufficient accuracy so that fine positionings or additional steps were not required.

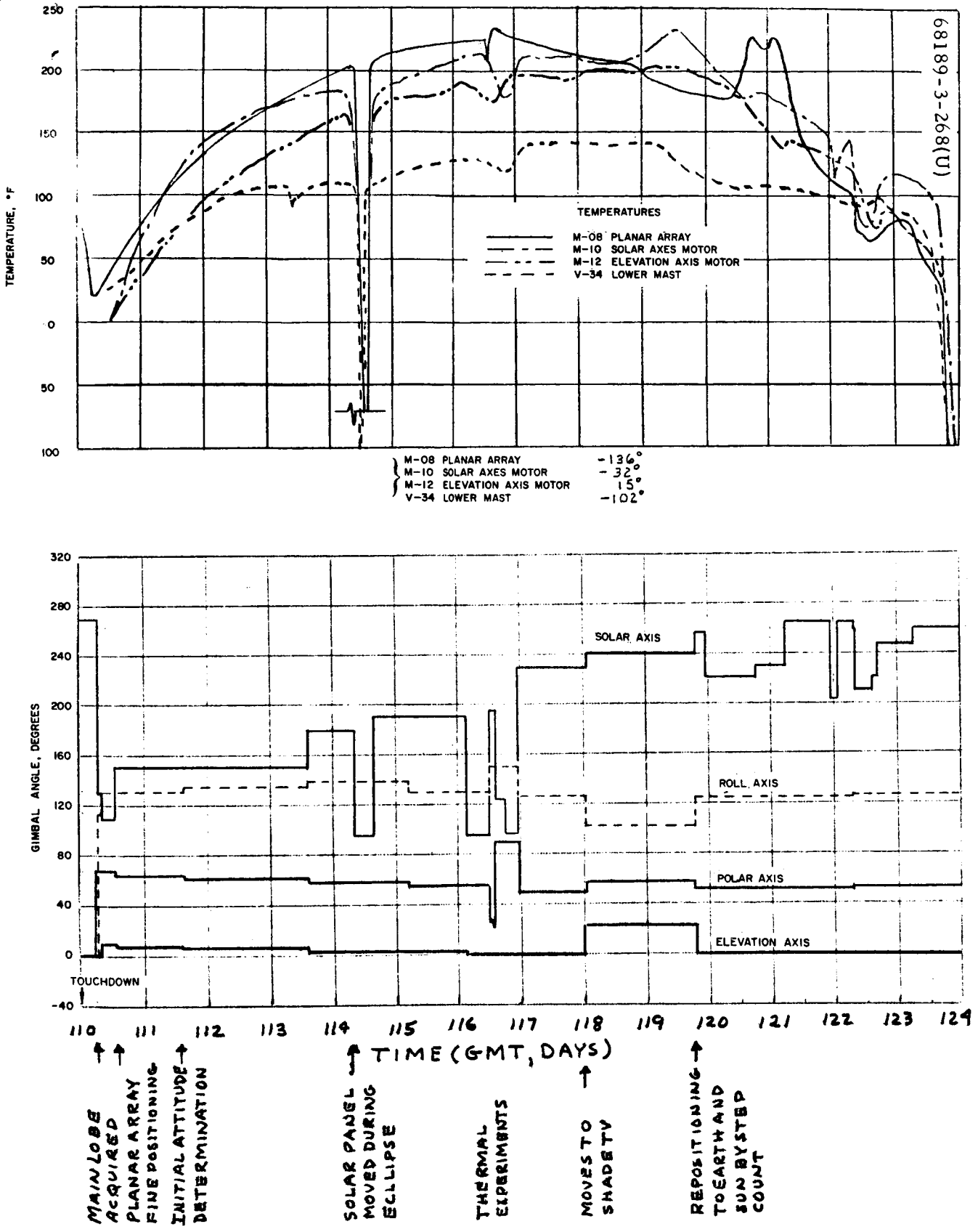

Figure 5.11-3. A/SPP Gimbal Angles and Temperatures Versus Time First lunar day

TABLE 5.11-4. ASPP AXIS POSITIONS FOR PRELAUNCH AND POST-AUTO-DEPLOYMENT CONDITIONS

	Prelaunch*				Post-auto-deployment, Transit**			
	Raw Data		Corrected Data		Raw Data		Corrected Data	
	BCD	Indicated angle, degrees	BCD	Angle, degrees	BCD	Indicated angle, degrees	BCD	Angle, degrees
M-03 solar axis	850	357.7	843	355.47	608	272.1	606	270.7
M-04 polar axis	379	0.82	376	0.30	380	0.93	378	0.45
M-06 elevation axis	488	0.69	484	-0.88	487	0.38	485	-0.89
M-07 roll axis	324	-59.09	320	-60.48	490	0.92	488	0.13
S-01 reference voltage	1001	–	–	–	996	–	–	–
S-02 reference return	0	–	–	–	0	–	–	–
S-05 commutator unbalance current	128	–	–	–	139	–	–	–

*Prelaunch data time 106:20:19:36.534.

**Post-auto-deployment data time 107:21:53:29.339.

TABLE 5.11-5. POSTLANDING ASPP STEPPING COMMANDS SUMMARY

Axis	Solar		Polar		Elevation		Roll	
Direction	Plus	Minus	Plus	Minus	Plus	Minus	Plus	Minus
Command	0401	0402	0403	0404	0407	0410	0405	0406
Total	4757	4835	3232	2359	715	727	1935	931
Total plus and minus	9592		5591		1442		2866	
Grand total	19,491							

5.11.5 ACKNOWLEDGEMENTS

F. D. McLaughlin, Technical Coordinator.

R. L. Lackman

TABLE 5.11-6. ASPP STEPPING COMMAND LOG

Execution Time Day:Hr:Min:Sec	Command	Quantity	Function
110:06:32:29	0402	120	Postlanded stepping began with the nominal block of continuous stepping that points the panels in the general vicinity of the earth and the sun.
110:06:34:12	0403	120	
110:06:35:40	0405	120	
110:06:36:59	0402	120	
110:06:38:25	0403	120	
110:06:39:47	0405	120	
110:06:41:02	0402	120	
110:06:42:20	0403	120	
110:06:43:36	0405	120	
110:06:47:06	0402	120	
110:06:48:23	0403	120	
110:06:49:37	0405	120	
110:06:50:51	0402	120	Steps are in small blocks because of drive temperature constraints on duty cycle and on time.
110:06:52:04	0403	120	
110:06:53:17	0405	120	
110:06:54:30	0402	120	
110:06:55:44	0403	120	
110:06:56:59	0405	120	
110:06:58:13	0402	120	
110:06:59:28	0403	120	
110:07:00:41	0405	120	
110:07:01:54	0402	120	
110:07:03:07	0403	120	
110:07:04:23	0405	120	
110:07:07:46	0402	120	
110:07:09:02	0403	120	
110:07:10:25	0405	94	
110:07:12:45	0402	120	
110:07:14:08	0403	120	
110:07:18:13	0402	36	
110:07:27:03	0403	64	An antenna lobe is discovered and centered.
110:07:28:19	0407	84	
110:07:37:34	0410	12	
110:07:40:43	0403	29	
110:07:43:26	0404	68	
110:07:55:08	0403	120	A second lobe is detected which indicates mainlobe location.
110:07:59:24	0403	120	
110:08:06:47	0404	120	
110:08:11:38	0404	120	The mainlobe is acquired.
110:08:15:30	0404	120	
110:14:13:03	0410	18	Planar array fine positioning.
110:14:19:26	0407	9	
110:14:22:28	0404	40	
110:14:30:17	0410	9	Lead the earth.

Table 5.11-6 (continued)

Execution Time Day:Hr:Min:Sec	Command	Quantity	Function
111:12:28:20	0405	11	
111:12:39:15	0401	168	
111:13:07:42	0402	50	
111:13:30:36	0401	6	
111:13:33:58	0405	14	
111:13:47:27	0406	4	The sun is accurately
111:13:49:56	0401	2	acquired for attitude
111:13:51:43	0402	4	determination.
111:13:56:56	0401	160	Lead the sun.
111:14:07:59	0410	18	The earth is accurately
111:14:14:41	0407	8	acquired for attitude
111:14:16:09	0404	36	determination.
111:14:24:47	0404	8	Lead the earth.
111:14:25:47	0410	8	
112:22:07:32	0406	48	Initiate bit error rate test.
112:23:01:24	0405	48	Test cancelled.
113:11:49:03	0401	40	Three sun and earth fine
113:11:50:14	0407	36	positionings are per-
113:11:51:19	0404	20	formed for attitude
113:11:52:34	0406	40	determination.
113:11:55:53	0401	40	
113:12:02:31	0402	16	
113:12:09:12	0406	22	
113:12:28:11	0405	10	
113:12:29:49	0402	10	
113:12:34:28	0401	20	
113:12:48:15	0406	12	
113:12:51:43	0405	4	
113:12:53:47	0406	24	
113:13:00:23	0405	12	
113:13:02:13	0404	40	
113:13:09:44	0403	48	
113:13:13:46	0410	40	
113:13:15:33	0405	60	
113:13:19:49	0404	16	
113:13:21:43	0405	4	
113:13:23:09	0406	28	
113:13:33:28	0404	8	
113:13:34:53	0405	12	
113:13:37:09	0404	16	
113:13:41:28	0403	32	
113:13:47:12	0405	24	
113:13:49:33	0406	40	
113:13:52:57	0404	32	

Table 5.11-6 (continued)

Execution Time Day:Hr:Min:Sec	Command	Quantity	Function
113:13:55:52	0405	16	
113:13:56:51	0404	24	
113:13:59:33	0403	56	
113:14:17:40	0410	40	
113:14:19:52	0405	40	
113:14:22:18	0410	40	
113:14:24:00	0405	56	
113:14:26:27	0410	40	
113:14:28:20	0405	56	
113:14:39:12	0406	16	
113:14:41:29	0403	32	
113:14:46:08	0404	48	
113:14:54:09	0405	88	
113:14:59:46	0406	16	
113:15:00:56	0403	24	
113:15:04:36	0407	40	
113:15:06:13	0406	40	
113:15:07:43	0407	40	
113:15:09:02	0406	88	
113:15:15:14	0405	24	
113:15:16:34	0406	8	
113:15:18:36	0404	64	
113:15:24:25	0406	8	
113:15:32:58	0401	160	
114:07:15:33	0402	240	Solar panel faced away from sun during the solar eclipse.
114:08:35:57	0402	442	
114:15:13:19	0401	768	
115:04:57:08	0406	64	Planar array repositioning.
	0404	40	
116:04:00:00	0410	8	Begin thermal experiment.
116:04:05:00	0402	760	
116:12:19:00	0405	60	
116:12:19:53	0404	60	
116:12:20:39	0401	60	
116:12:21:27	0405	60	
116:12:22:13	0404	60	
116:12:23:06	0401	60	
116:12:25:06	0405	21	
116:12:27:07	0404	60	
116:12:27:45	0401	60	
116:12:34:51	0404	60	
116:12:35:35	0401	60	
116:12:36:47	0404	60	
116:12:37:27	0401	60	

Table 5.11-6 (continued)

Execution Time Day:Hr:Min:Sec	Command	Quantity	Function
116:12:38:57	0404	44	
116:12:41:21	0401	508	
116:12:55:08	0403	32	
116:13:30:01	0403	16	Shadowing of compartment for thermal experiment.
116:14:00:01	0402	60	
116:14:00:38	0403	60	
116:14:01:15	0402	60	
116:14:02:25	0403	60	
116:14:03:27	0402	60	
116:14:04:33	0403	60	
116:14:05:34	0402	60	
116:14:06:12	0403	60	
116:14:06:43	0402	60	
116:14:07:29	0403	60	
116:14:08:21	0402	60	
116:14:08:57	0403	60	
116:14:09:58	0402	60	
116:14:10:34	0403	60	
116:14:11:35	0402	60	
116:14:12:13	0403	60	
116:14:13:14	0402	60	
116:14:13:50	0403	60	
116:14:14:52	0402	24	
116:14:15:10	0403	60	
116:14:16:41	0402	24	
116:14:20:04	0403	230	
116:14:25:17	0401	31	
116:15:00:08	0401	15	
	0402		
116:16:00:01	0402	28	
116:16:30:01	0401	5	
116:17:00:01	0401	3	
116:17:30:04	0401	7	
116:18:00:01	0402	254	
116:22:50:11	0404	65	Reposition to standard tracking configuration.
116:22:51:36	0406	60	
116:22:52:34	0401	60	
116:22:53:22	0404	55	
116:22:54:07	0406	60	
116:22:54:52	0401	60	
116:22:55:42	0404	60	
116:22:56:49	0406	60	
116:22:57:34	0401	60	
116:23:01:57	0404	60	

Table 5.11-6 (continued)

Execution Time Day:Hr:Min:Sec	Command	Quantity	Function
116:23:03:45	0401	60	
116:23:04:56	0404	60	
116:23:05:48	0401	60	
116:23:07:00	0404	60	
116:23:07:51	0401	60	
116:23:09:03	0404	60	
116:23:09:53	0401	60	
116:23:11:04	0404	60	
116:23:11:56	0401	60	
116:23:13:08	0404	60	
116:23:14:00	0401	60	
116:23:15:38	0404	52	
116:23:16:28	0401	480	
116:23:29:33	0406	4	
116:23:30:52	0401	60	
117:15:30:21	0410	16	Planar array gain
117:15:31:59	0407	64	experiment.
117:15:41:35	0410	32	
117:15:43:51	0403	16	
117:15:45:07	0404	36	
117:15:51:15	0403	16	
117:16:10:25	0403	96	
117:16:16:57	0404	96	
117:16:22:16	0407	6	
117:16:22:27	0405	5	
117:16:22:55	0407	6	
117:16:23:07	0405	5	
117:16:23:31	0407	6	
117:16:23:42	0405	5	
117:16:24:12	0407	6	
117:16:24:23	0405	5	
117:16:24:55	0407	6	
117:16:25:05	0405	5	
117:16:25:35	0407	6	
117:16:25:46	0405	5	
117:16:27:16	0410	36	
117:16:28:34	0406	30	
117:17:06:36	0404	32	Bit error rate test.
117:17:07:52	0410	32	
117:17:09:06	0404	32	
117:17:10:12	0410	26	
117:17:19:01	0404	8	
117:17:33:46	0403	10	
117:17:41:21	0404	17	
117:17:50:11	0410	6	

Table 5.11-6 (continued)

Execution Time Day:Hr:Min:Sec	Command	Quantity	Function
117:19:12:46	0404	12	
117:19:30:40	0403	23	
117:19:33:15	0407	7	
117:19:37:57	0410	12	
117:19:45:44	0403	8	
117:19:56:35	0407	13	
117:20:00:56	0410	10	
117:20:10:17	0403	3	
117:20:12:09	0407	33	
117:20:12:57	0403	30	
117:20:18:04	0407	33	
117:20:19:47	0403	27	
117:21:37:57	0401	40	
117:21:39:17	0404	6	
117:21:40:36	0410	16	
117:21:43:04	0406	8	
117:21:44:15	0401	40	
117:23:07:46	0406	40	Nonstandard ASPP
117:23:08:25	0407	40	positioning to shade
117:23:08:58	0403	40	thermal compartments
117:23:09:31	0406	40	and TV camera.
117:23:10:04	0407	40	
117:23:10:37	0403	40	
117:23:11:11	0406	40	
117:23:11:44	0407	40	
117:23:12:22	0403	16	
117:23:13:38	0406	40	
117:23:14:11	0407	40	
117:23:15:39	0406	40	
117:23:17:30	0403	16	
117:23:21:04	0407	28	
117:23:26:10	0410	8	
117:23:26:59	0404	8	
119:18:53:38	0410	40	Reposition the ASPP to
119:18:54:15	0405	40	lead the sun and track the
119:18:54:51	0401	32	earth in a normal
119:18:55:50	0410	40	configuration.
119:18:56:35	0405	40	
119:18:57:08	0404	40	
119:18:57:43	0401	32	
119:18:58:59	0410	40	
119:18:59:33	0405	40	
119:19:00:07	0401	32	
119:19:03:55	0410	40	

Table 5.11-6 (continued)

Execution Time Day:Hr:Min:Sec	Command	Quantity	Function
119:19:04:30	0405	40	
119:19:05:05	0404	40	
119:19:05:38	0401	32	
119:19:06:46	0410	20	
119:19:07:07	0405	32	
119:21:27:23	0402	280	Decrease charge rate and shade TV.
120:18:18:25	0401	40	Reposition solar panel.
121:06:08:01	0401	320	Reposition solar panel.
121:22:55:30	0402	480	Unshade the TV solar panel.
122:02:17:28	0401	480	Retrun solar panel to sun.
122:03:58:45	0410	24	Planar array gain test
122:04:02:09	0407	44	second phase.
122:04:09:39	0410	20	
122:04:12:28	0403	32	
122:04:14:49	0404	88	
122:04:22:03	0403	128	
122:04:46:53	0404	96	
122:04:51:54	0407	6	
122:04:52:05	0405	5	
122:04:52:31	0407	6	
122:04:52:41	0405	5	
122:04:53:08	0407	6	
122:04:53:17	0405	5	
122:04:53:44	0407	6	
122:04:53:54	0405	5	
122:04:54:26	0407	6	
122:04:54:35	0405	5	
122:04:55:08	0407	6	
122:04:55:17	0405	5	
122:04:58:30	0410	36	
122:04:59:40	0406	30	
122:06:00:25	0403	128	Bit error rate test.
122:07:16:37	0407	40	
122:07:45:19	0410	40	
122:07:47:31	0404	88	
122:08:05:16	0405	9	
122:08:07:20	0406	1	
122:08:08:46	0402	46	
122:09:02:15	0402	400	Reposition solar panel.
122:15:19:38	0401	96	Reposition solar panel.
122:17:35:02	0401	288	Reposition solar panel.
123:10:08:47	0401	12	Reposition solar panel.

5.12. TERMINAL DESCENT TRAJECTORY PERFORMANCE

5.12.1 INTRODUCTION

The terminal descent and landing phase begins with the transition from coast mode II to the terminal descent phase. Terminal descent itself starts with the preretro attitude maneuvers. These maneuvers reposition the attitude of the spacecraft from the sun-star reference so that the expected direction of the retro thrust vector will be aligned with respect to the velocity vector. This alignment achieves the desired retro burnout conditions. Following completion of the attitude maneuvers, the altitude marking radar (AMR) is activated. The AMR is preset to generate a mark signal when the range to the lunar surface is 60 miles. A backup mark signal, delayed a short interval after the time the AMR mark should occur, is transmitted to the spacecraft to initiate the automatic sequence in the event the AMR mark is not generated. The desired delay between the altitude mark and retro ignition is stored in the flight control programmer by ground command. Vernier engine ignition is automatically initiated 1.1 seconds prior to retro ignition.

During the retro phase, spacecraft attitude is maintained in the inertial direction established at the end of the preretro maneuvers by the vernier attitude control system, and the total vernier thrust is maintained at midthrust. As the mass of the vehicle decreases due to expenditure of retro and vernier propellant, the spacecraft thrust to mass ratio (T/M) increases from approximately 4 g_e (g_e = 32.2 ft/sec^2) at ignition to 10 g preceding burnout. Prior to burnout, the inhibit is removed from the acceleration switch output, and the doppler radar and altimeter (RADVS) is activated.

As the thrust decays during retro burnout, the acceleration switch signals when the T/M level has dropped to 3.5 g_e. At this time, the vernier engine thrust command is automatically changed to high thrust, and a counter in the flight control programmer is initiated. After 12.0 seconds following the receipt of the burnout signal, the explosive bolts attaching the retro to the spacecraft are activated, allowing the retro case to separate from the spacecraft. Following a programmed delay of 2.15 seconds after separation begins, the vernier thrust command is changed from the open-loop mode to a closed-loop acceleration control mode. Nominal acceleration commanded at this point is 4.85 ft/sec^2.

When reliable radar operation occurs, attitude control of the vehicle is switched from inertial to radar control, and the spacecraft maneuvers to align the vernier thrust axis to the velocity vector. When the combined range and velocity, as measured by the radar, indicates that the spacecraft has descended to the programmed range/velocity descent profile, the total vernier engine thrust is controlled to achieve a trajectory along this profile. When a velocity of 10 fps is reached, attitude control of the spacecraft is switched to inertial reference, and thrust control is servoed to maintain descent velocity at 5 fps. At 14 feet above the surface, the radar generates a signal commanding vernier engine cutoff, and the vehicle free falls to the lunar surface. The touchdown impact is absorbed by the spacecraft landing system, completing the terminal descent phase.

The spacecraft performance was close to nominal for the entire terminal descent period. The spacecraft successfully landed in a small lunar crater with a downward lunar slope of approximately 12 degrees. All events occurred as per spacecraft design; however, failure of the 14-foot mark to occur resulted in continued vernier engine thrusting to touchdown. Since the engines were still on and the spacecraft landed on an inclined surface, the resulting up vernier engine throttling to correct the induced attitude error and landing gear rebound produced multiple touchdowns until the engines were manually commanded off.

There was an apparent drop lock of the radar altimeter beam just prior to and immediately following the RADVS-controlled terminal descent steering phase. This resulted in loss of reliable operation of the radar altimeter (RORA); however, the loss of RORA at this point had no effect on the steering phase since the spacecraft would be in the minimum acceleration control mode.

A summary of the terminal descent performance and the major time events are presented in this section followed by a discussion of the spacecraft terminal descent performance, as reconstructed by calibrated telemetry data and analytic reconstruction techniques.

5.12.2 ANOMALY DESCRIPTION

An anomaly during the terminal descent phase is defined as any deviation from the expected mission or system performance during this phase of the mission.

The doppler velocity beam 3 dropped lock approximately 2.8 seconds after the 10-fps mark. This resulted in loss of RORA and RODVS, placing the spacecraft attitude control loop in inertial hold and the thrust acceleration control loop in a minimum acceleration mode. Since the beam lost lock at a low velocity, it became virtually impossible to reacquire lock. This anomaly, plus the three spacecraft legs not touching down simultaneously, resulted in multiple soft touchdowns until the engines were manually commanded off. Further detail of this RADVS anomaly is given in Sections 5.5

and 5.9. Still being investigated is an apparent discrepancy in the telemetered slant range during the minimum acceleration of the powered descent phase. The vernier engine midcourse thrust anomaly is discussed in Sections 4.3.1 and 5.6.4.3.

5.12.3 SUMMARY AND RECOMMENDATIONS

Table 5.12-1 lists the significant terminal descent events and the most accurate determination of each event's time of occurrence. The DSS time is either plus or minus the one-way transit time delay (approximately 1.215 seconds), depending on whether the event is a command or a telemetered spacecraft action.

The significant terminal descent performance parameters are summarized in Table 5.12-2, along with the predicted values. From this table, it can be seen that Surveyor III performed as well as can be expected, except for the failure of the vernier engines to cut off before touchdown. The cause and the corrective action to be taken to prevent recurrence of this problem has been investigated and are discussed further in Section 5.9.

5.12.4 PERFORMANCE ANALYSIS

5.12.4.1 Introduction

Surveyor III's terminal performance has been investigated and analyzed by comparing processed telemetry data by the PREPRO program (described in subsection 5.12.4.2) with a precision six-degree-of-freedom (6DOF) digital simulation. Various nominal predicted preflight parameters within the 6DOF are adjusted so as to coincide discrete time events with discrete telemetry time events. These events provide the 6DOF program with significant data points for constructing a best-fit trajectory. Table 5.12-7 shows the discrete time events determined from telemetry data and compared with the best match reconstruction by the 6DOF program.

The one-way doppler data, as received from the spacecraft by the tracking station, is utilized to determine the retro thrust-time curve, retro specific impulse, total ΔV during the retro and vernier phases, and reconstruction of the multiple touchdowns due to the drop lock of radar beam 3 near touchdown.

Total vernier propellant consumption is determined by utilization of vernier engine flight acceptance data of mixture ratio and I_{sp} as a function of thrust for the midcourse, main retro, and vernier phases. The spacecraft and retro case landing location are determined by utilization of the 6DOF program. The computed spacecraft location can be compared with the Lunar Orbiter IV high resolution photographs of the general landing area.

Since Surveyor III performed close to nominal, the trajectory reconstruction scheme utilized depends on establishing a good reference point. The slant range, V_x, V_y, and V_z data are of prime importance in reconstructing the terminal phase. Based on postmission RADVS assessment,

TABLE 5.12-1. BEST ESTIMATE TIMES FOR SC-3 TERMINAL DESCENT

Event	GMT, Day 110 Hour 00	
	At DSS 11 Min:Sec	At Spacecraft Min:Sec
AMR mark	01:12.829 ± 0.05	01:11.606 ± 0.05
AMR backup command sent	01:11.000 ± 0	01:12.215 ± 0
Vernier engine ignition	01:17.922 ± 0.05	01:16.707 ± 0.05
Retro engine ignition	01:19.023 ± 0.05	01:17.808 ± 0.05
3.5 g point	02:00.322 ± 0.05	01:59.107 ± 0.05
3.5 g switch actuation	02:00.492 ± 0.025	01:59.277 ± 0.025
Retro ejected signal	02:12.492 ± 0.025	02:11.277 ± 0.025
Loss of RORA	02:13.368 ± 0.6	02:12.153 ± 0.6
Start RADVS-controlled descent	02:14.642 ± 0.025	02:13.427 ± 0.6
Return of RORA	02:15.786 ± 0.6	02:14.571 ± 0.6
First segment acquisition	02:33.816 ± 0.11	02:32.601 ± 0.11
Segment 1	02:58.415 ± 0.11	02:57.200 ± 0.11
1000-foot mark	03:53.023 ± 0.05	03:51.798 ± 0.05
End segment 2	03:53.093 ± 0.03	03:51.878 ± 0.03
End segment 3	04:01.713 ± 0.11	04:00.498 ± 0.11
10-fps mark	04:10.623 ± 0.05	04:09.398 ± 0.05
Drop lock beam 3	04:13.275 ± 0.6	04:12.060 ± 0.6
Loss of RODVS	04:13.382 ± 0.6	04:12.167 ± 0.6
Loss of RORA	04:13.387 ± 0.6	04:12.172 ± 0.6
14-foot mark	None	None
Touchdown 1	04:18.050 ± 0.11	04:16.835 ± 0.11
Touchdown 2	04:42.030 ± 0.11	04:40.815 ± 0.11
Touchdown 3	04:54.420 ± 0.11	04:53.205 ± 0.11

TABLE 5.12-2. SUMMARY OF TERMINAL DESCENT PERFORMANCE PARAMETERS

Parameter	Predicted Value	Best Estimate Value
Retro phase initial conditions		
Time, day:hr:min:sec	110:00:01:17.81	110:00:01:17.922
Attitude, degrees	22.94	22.94
Slant range, feet	273,170	271,334
Velocity, fps	8617.5	8617.5
Retro burnout conditions		
Slant range, feet	34,734	36,158
Longitudinal velocity, fps	445.2	462.36
Lateral velocity, fps	116.6	171
Attitude, degrees	23.8	23.8
Flight path angle, degrees	9.15	3.8
Misalignment angle during retro		
In-plane, degrees	0	0.34
Out of plane, degrees	0	0.02
1000-foot mark conditions		
Slant range, feet	1010.4	998.92
Velocity, fps	106.45	103.27
Attitude, degrees	1.09	0.51
10-fps mark conditions		
Slant range, feet	43	46
Velocity, fps	8.6	8.6
Attitude, degrees	0.01	0.025
Engine cutoff conditions		
Slant range, feet	13	–
Velocity, fps	5	–
Attitude, degrees	0.01	–
Vernier propellant used*	137.65	140.06

*Predicted based on engine cutoff at 13-feet slant range. Best estimate value is total to first touchdown.

the calibrated V_x, V_y, and V_z at start of the vernier phase (synonomous to start of RADVS-controlled descent or retro burnout) was selected as the reference point. The corrected telemetry data of the burnout velocities are as follows:

$$V_{BO_x} = -85.3 \text{ fps}$$

$$V_{BO_y} = 148 \text{ fps}$$

$$V_{BO_z} = 462 \text{ fps}$$

5.12.4.2 Digital Computer Programs Utilized

PREPRO

PREPRO is a preprocessing program utilized to reduce the telemetry data from raw BCD counts into appropriate engineering units. The Surveyor III preflight calibration coefficients are utilized for the conversion of the telemetry signals, except for the SR, V_x, V_y, and V_z coefficients which are determined from postmission RADVS and telemetry channel assessment. Prior to conversion to engineering units, the FC-77 correction is made to the appropriate signals. The engineering data, significant to terminal descent reconstruction, are then interpolated into preselected equal time interval steps. PREPRO then outputs two tapes: tape No. 1 of the interpolated engineering data, and tape No. 2 of the signals in proper engineering units as telemetered.

POSTPR

POSTPR provides machine plots (CALCOMP) of input data tapes. The program has been modified to accept both PREPRO tape No. 1 and 6DOF data tape. This provides the capability of superimposing 6DOF and PREPRO parameters on the same plot.

6DOF

6DOF is a precision six-degree-of-freedom digital program that simulates RADVS and flight control system and rigid body dynamics, including weight and moment of inertia changes. Preflight assessment of Surveyor III parameters is input into the program. By matching significant time events with telemetry discrete times, a fairly accurate reconstruction of the terminal phase trajectory can be established by the 6DOF program in the absence of gross system and/or telemetry errors in V_x, V_y, and V_z at the start of the vernier phase. In the SC-3 mission, the error sources are apparently small as indicated by the near perfect matching of pertinent telemetry data and discrete time events with the 6DOF reconstruction.

DOPP

DOPP reconstructs the main retro thrust-time curve from the spacecraft transmitter's one-way doppler data. This reconstruction technique is especially accurate since the frequency of the transmitter is very stable. Various error sources can exist in the doppler data, such as temperature sensitivity drift; however, they have been accounted for in the final reconstruction. The program was also utilized for determining vernier phase ΔV, maximum and minimum thrust acceleration, and reconstruction of the multiple touchdowns.

TD1

TD1 is utilized for determining propellant consumption and breakdown of the propellant into fuel and oxidizer in all six propellant tanks. This program models the spacecraft to the extent necessary for accurate propellant consumption determination. Both mixture ratio and specific impulse as a function of thrust are included for each Surveyor III engine from flight acceptance test data.

5.12.4.3 Velocity Change due to Thrusting During Retro Phase and Determination of Ignition Conditions

Ignition velocity V_o, flight path angle γ, and roll angle φ serve as initialization parameters and are determined from tracking data. The 3σ uncertainty in free flight velocities is <0.5 fps. Since ignition altitude has a calculated 3σ inaccuracy of 1820 feet due to marking range errors (with a V = 8500 fps), the equivalent ignition velocity uncertainty due to this error source is

$$\Delta V = gt = 5 \times \frac{1820}{8500} = 1.1 \text{ fps}$$

Hence, the total uncertainty in ignition velocity is 1.2 fps when these two independent error sources are combined. The direction of $\underline{V}_o$ at ignition has an uncertainty of <0.07 degree. Therefore, the best estimate ignition conditions are

$$V_o = 8617.5 \pm 1.2 \text{ fps}$$

$$\gamma_o = -67.06 \pm 0.07 \text{ degree}$$

Gravity-induced Component of Velocity

During the retro phase (from vernier ignition to start of RADVS-controlled descent), gravity contributes to the spacecraft velocity by an amount $\int \underline{g}\, dt$. Lunar gravity varies in magnitude from 4.9 ft/sec^2 (at

vernier ignition) to 5.28 ft/sec^2 (at the start of RADVS). In addition, $\underline{g}$ varies in direction since the spacecraft has horizontal motion. The change in direction of $\underline{g}$ over the retro phase is about

$$\int_o^t \sin^{-1}\left[\frac{V \sin \psi \, dt}{R_\ell}\right] = 0.88 \text{ degree}$$

where

t = retro time

ψ = velocity vector incident angle

V = spacecraft velocity

R_ℓ = moon centered radial distance

Since the vehicle spends more time at lower altitudes than at higher ones, the average value of g for the retro phase will be closer to 5.28 ft/sec^2. The average value of g over the retro phase was 5.16 ft/sec^2. The time duration of the retro phase is 56.7 seconds (see Table 5.12-1). Actual numerical integration of $\int g \, dt$ gives gt = 293.2 ±1 fps.

Thrust-induced Velocity Change

The two methods used to calculate velocity change during the retro phase due to the thrusting of the engines are as follows:

1) $\underline{\Delta V}$ from vector addition — The vector equation (Figure 5.12-1a) $\underline{V}_{B/O} = \underline{V}_o + \underline{g}t + \underline{\Delta V}$ can be solved to find $\underline{\Delta V}$. $\underline{V}_o$ and $\underline{g}t$ are available as discussed above; the spacecraft axis components of $\underline{V}_{B/O}$ (the burnout velocity; the velocity at start of RADVS) are available from telemetry. The axial velocity V_z is known to an estimated accuracy of better than 1 percent at a given time based on correlation of simulated versus actual discrete time events such as segment intercept and 10-fps mark. V_x and V_y at burnout have calculated uncertainties of 1.6 and 2.0 fps, respectively, based on 3σ telemetry and sensor errors. At burnout, the velocity components are:

$$V_{B/O_x} = -85.3 \pm 1.6 \text{ fps}$$

$$V_{B/O_y} = 148 \pm 2 \text{ fps}$$

$$V_{B/O_z} = 462 \pm 4.6 \text{ fps}$$

This method will yield ΔV to an accuracy of 4.7 fps. δ_I, the in-plane angle (Figure 5.12-1b) between $\underline{V}_o$ and z, defined as positive when z is "above $\underline{V}_o$" as shown, is known to be within ±0.04 degree based on the uncertainties in V_{B/O_y} which is primarily in-plane. δ_o, the out-of-plane angle between these two directions, is known to be within ±0.02 degree based on V_{B/O_x} uncertainties; δ_o is positive when z has a component out of the paper. This method yields:

$\Delta V = 8415 \pm 4.8$ fps

$\delta_I = 0.354 \pm 0.04$ degree

$\delta_o = 0.066 \pm 0.02$ degree

2) $\underline{\Delta V}$ from doppler data (Figure 5.12-2) shows the radial velocity change during retro phase versus time. The curve is from doppler data which has been corrected for temperature-dependent frequency drift of the transmitter aboard the spacecraft. This curve includes the gt velocity due to lunar gravity.

ΔV is found by dividing the radial velocity change over the retro phase, 6081 fps, by the cosine of the angle ζ between the tracking station-spacecraft line and the thrust axis, and then adding the gravity-induced velocity component in the thrust direction, gt cos ξ as shown in Figure 5.12-1c. ζ and ξ are not coplanar since the Z-axis does not lie in the plane of the spacecraft station and moon center. A correction must be made for the earth's rotation, which accounts for part of the doppler velocity seen by the tracking station as follows:

$$V_{ROT} = 2.2 \pm 0.1 \text{ fps}$$

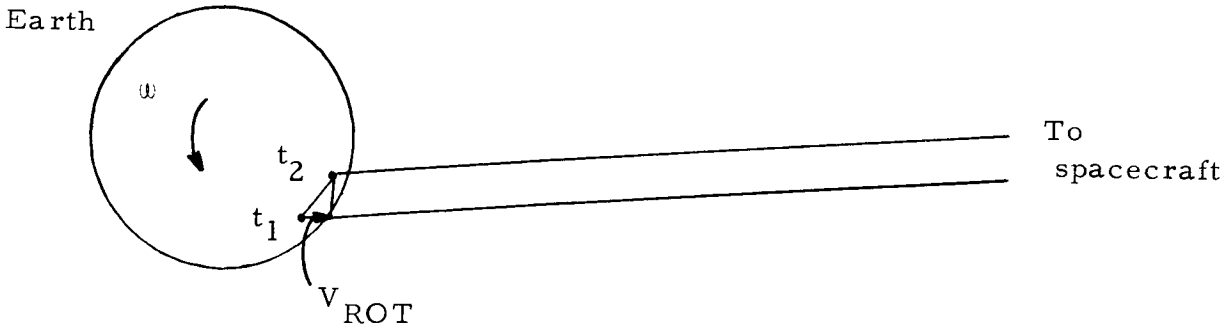

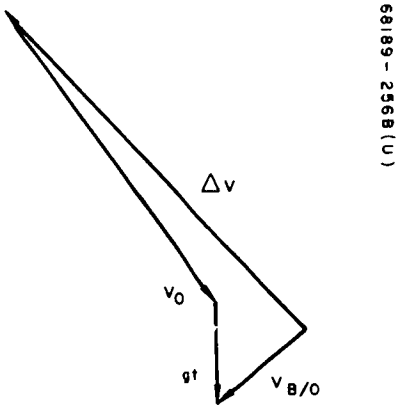

a) Vector Diagram

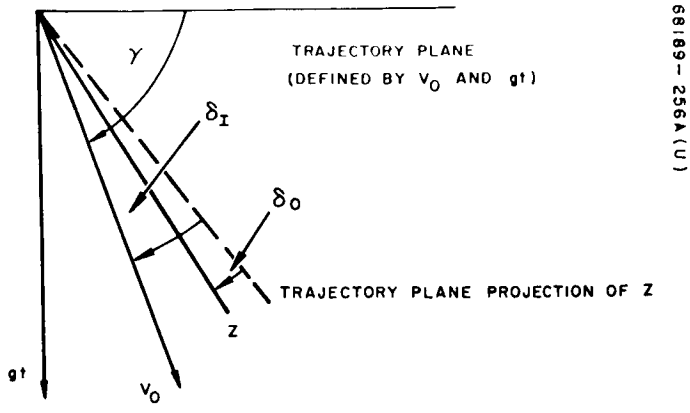

b) Trajectory Plane

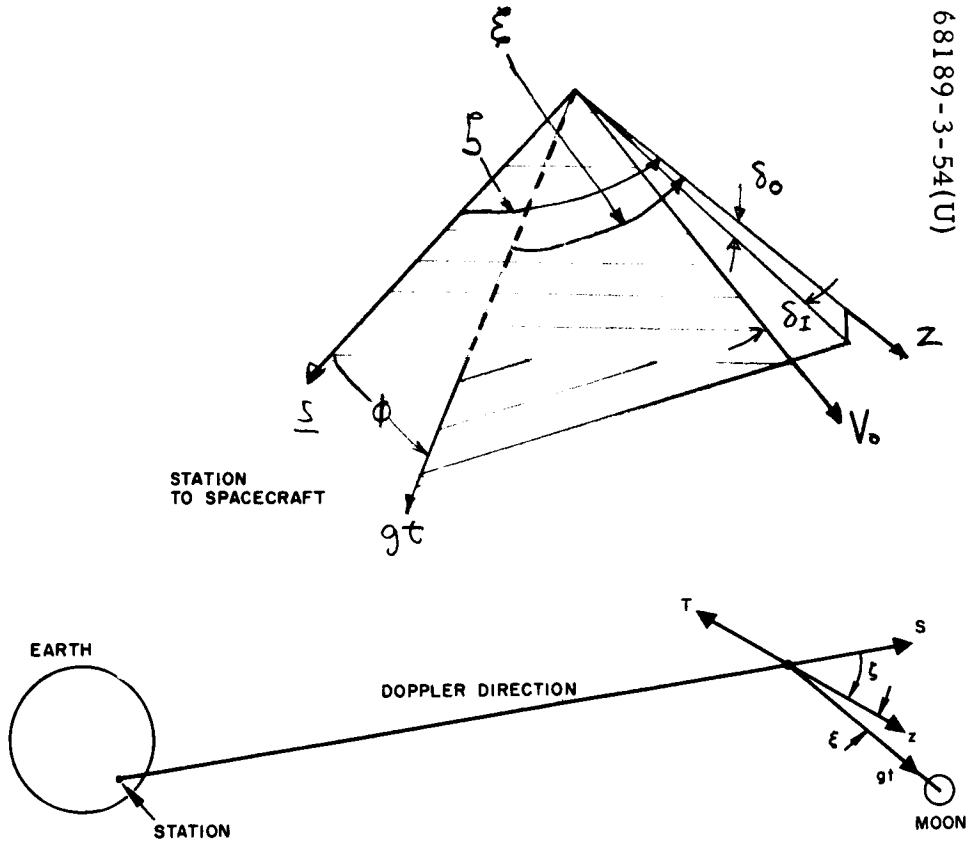

c) Doppler Geometry

Figure 5.12-1. Spacecraft Velocity During Retro Phase

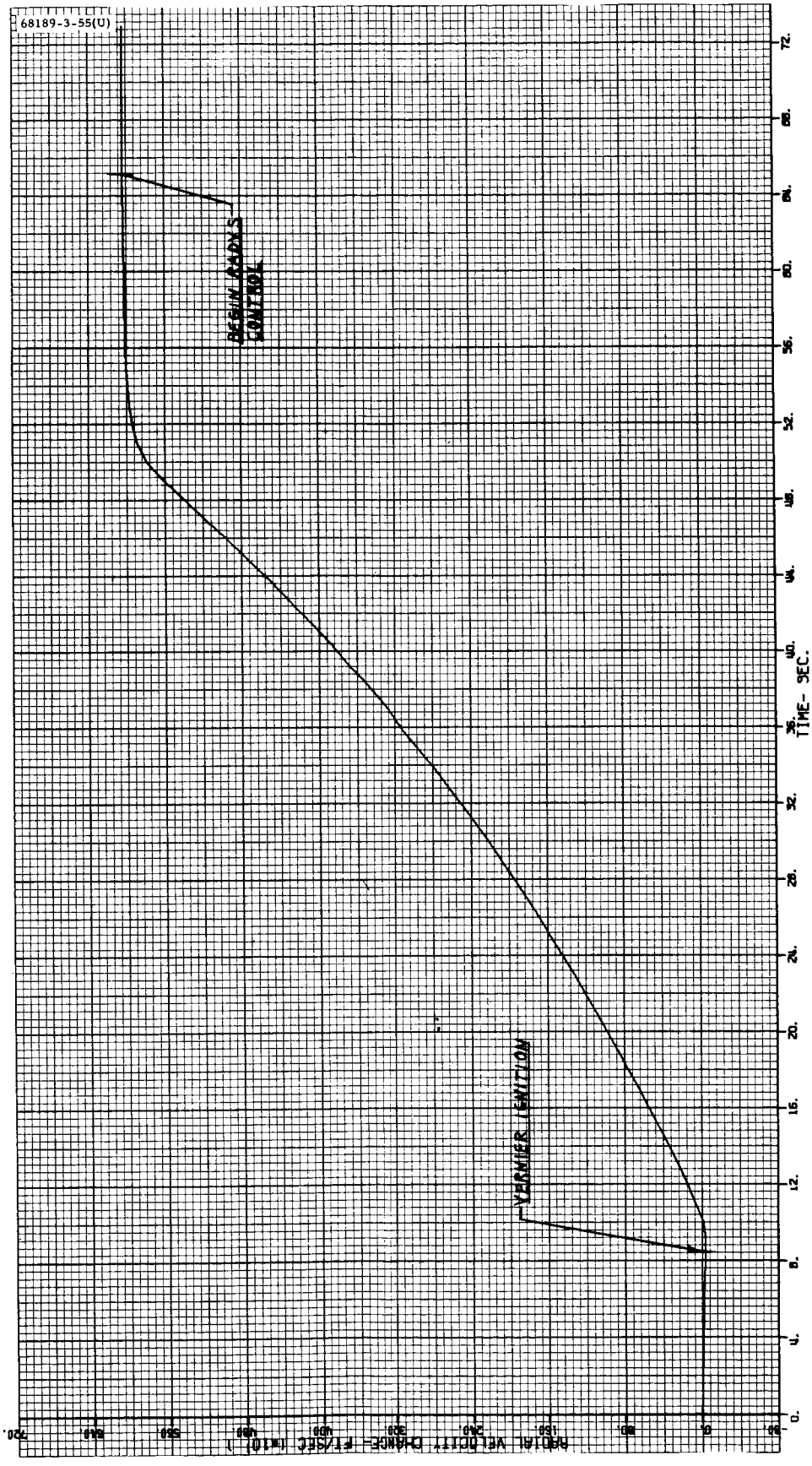

Figure 5.12-2. Spacecraft Radial Velocity Changes Relative to Earth Reference time, GMT-110:00:01:09.5

If ΔV_{DOPP} is the velocity change seen by the tracking station

$$\Delta V_{DOPP} = \Delta V \cos \zeta - gt \cos \varphi - V_{ROT}$$

or

$$\Delta V = \frac{\Delta V_{DOPP}}{\cos \zeta} + gt \frac{\cos \varphi}{\cos \zeta} + \frac{V_{ROT}}{\cos \zeta}$$

Values of the various angles in degrees shown in Figure 5.12-1c are as follows:

$\delta_I = 0.354$

$\delta_o = 0.066$

$\xi = 23.19$

$\zeta = 40.91$

$\varphi = 19.08$

Hence

$$\Delta V = \frac{6086}{\cos 40.91} + 293.2 \frac{\cos 19.08}{\cos 40.91} + \frac{2.2}{\cos 40.91} = 8422$$

So, from doppler data, $\Delta V = 8422 \pm 8.8$ fps.

The inaccuracy is due primarily to errors in the angles ζ and φ; the former is known to be ± 0.08 degree from tracking data combined with in- and out-of-plane attitude error calculations, and the latter to be ± 0.12 degree from known lateral translation of the spacecraft during descent.

Comparison of ΔVs and Retro Performance Implications

It is interesting to note that not only do the absolute magnitudes of ΔV check surprisingly well, but, out of necessity, so does the inertial thrusting direction as computed from burnout conditions. The doppler data is inherently one-dimensional and, to be useful in computing the retro thrust ΔV, the angular information supplied by the vector addition method of computing ΔV must be accurate. Thus, due to the geometric relation of the earth vector and trajectory plane, an uncertainty of 0.1 degree in the out-of-plane angle (δ_o) would cause a 7.0 fps variation in the total ΔV as computed by doppler. Since the two ΔVs check within 7 fps, this would give added confidence in the thrusting direction computed from the telemetered and corrected burnout conditions.

Assuming a nominally performing main retro and vernier system, the main retro phase ΔV should have been 8438.4 fps as compared to 8418.5 fps actual (average of the two methods). Of the nominal 8438.4 fps total ΔV, the vernier system contributed approximately 317 fps. If the vernier system is considered to have performed nominally, then the percentage loss in retro total impulse (δ Timp/Timp) is

$$\frac{\delta \text{ Timp}}{\text{Timp}} = \frac{\delta \Delta V}{\Delta V \text{ retro}} \times 100 \text{ percent}$$

$$= \frac{8418.5 - 8438.4}{8438.5 - 317} \times 100 \text{ percent}$$

$$= 0.24 \text{ percent}$$

The above percent loss in total impulse results in a retro specific impulse of 288.6 seconds as compared to the nominal predicted value of 289.3 seconds. The uncertainty based on the more accurate method of computing ΔV (vector addition) is ± 0.05 percent assuming a nominal inerts weight loss.

5.12.4.4 Main Retro Thrust Versus Time Curve

Two independent methods used to calculate the retro's thrust versus time curve are as follows:

1) Thrust/time from retro accelerometer data – Before being used to calculate a thrust curve, the raw accelerometer data are given the following three corrections:

   a) Biases are removed by comparing telemetered values with known values of acceleration which occur at times such as those prior to vernier ignition (zero g), after retro separation $\approx$(0.9 g), etc.

   b) A scale factor error is removed. This is done by integrating the unbiased accelerometer data over time and comparing the resulting integral with the retro phase ΔVs found by the other two methods of computing ΔV described above. The scale factor is then the integral divided by the mean of the other two ΔVs. The unbiased acceleration divided by this scale factor is then assumed free of bias and scale factor errors.

   c) A hysteresis error is removed by actually determining two biases: one for the rising part of the acceleration curve, and the other for the falling part.

The bias on each part of the curve can be removed to an accuracy of 0.1 g_{earth}, and the accuracy of the scale factor is 0.1 percent.

The corrected acceleration is then used in the equation

$$T(t) = \frac{a(t)}{g_o}\left[W_o - \int_o^t \frac{T(t)}{I_{sp}}\,dt\right]$$

which is integrated numerically to obtain total thrust (W_o is weight at retro ignition). Vernier thrust is then subtracted out to obtain the retro thrust.

I_{sp} for this calculation is found from the relation below where W_L is the weight lost from retro ignition to burnout.

$$I_{sp} = \frac{\Delta V}{g_o \ell n \frac{W_o}{W_o - W_L}}$$

Figure 5.12-3 shows the SC-3 thrust-time curve as determined from accelerometer data, with the nominal predicted plot, raw accelerometer, and corrected accelerometer curves also shown.

2) Thrust/time from doppler data — Figure 5.12-4 shows the main retro thrust curve as constructed from doppler counts received at Goldstone; the nominal predicted curve is also plotted. To construct the curve, a retro phase simulation trajectory program using a nominal thrust curve calculates nominal radial velocities relative to the tracking station and converts these to doppler counts that the station would receive from a stable spacecraft transmitter on a nominal trajectory.

The nominal thrust curve is then perturbed until the doppler data from the perturbed curve are arbitrarily close to the doppler data actually received. For each point considered on the thrust curve, a difference between actual and perturbed counts over a 1-second interval of two counts (i.e., about 0.4 fps) is considered close enough. In addition, the sum of such differences is constrained to be within 20 counts (4.3 fps).

Radial velocity divided by the cosine of the angle between the tracking station and the thrust direction (40.91 ±0.08 degree) gives total velocity. When gt cos ξ is added, the remaining velocity differences are entirely due to thrusting and give the thrust acceleration. Multiplication by the mass then gives the thrust level.

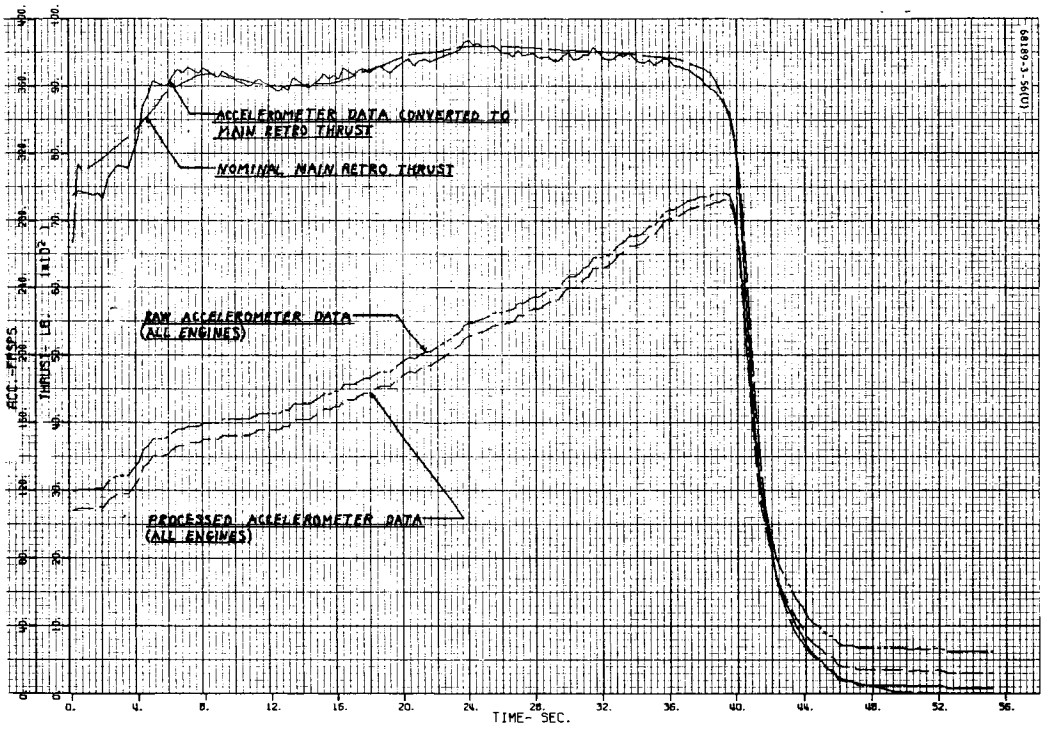

Figure 5.12-3. Retro Phase Thrust and Acceleration Versus Time

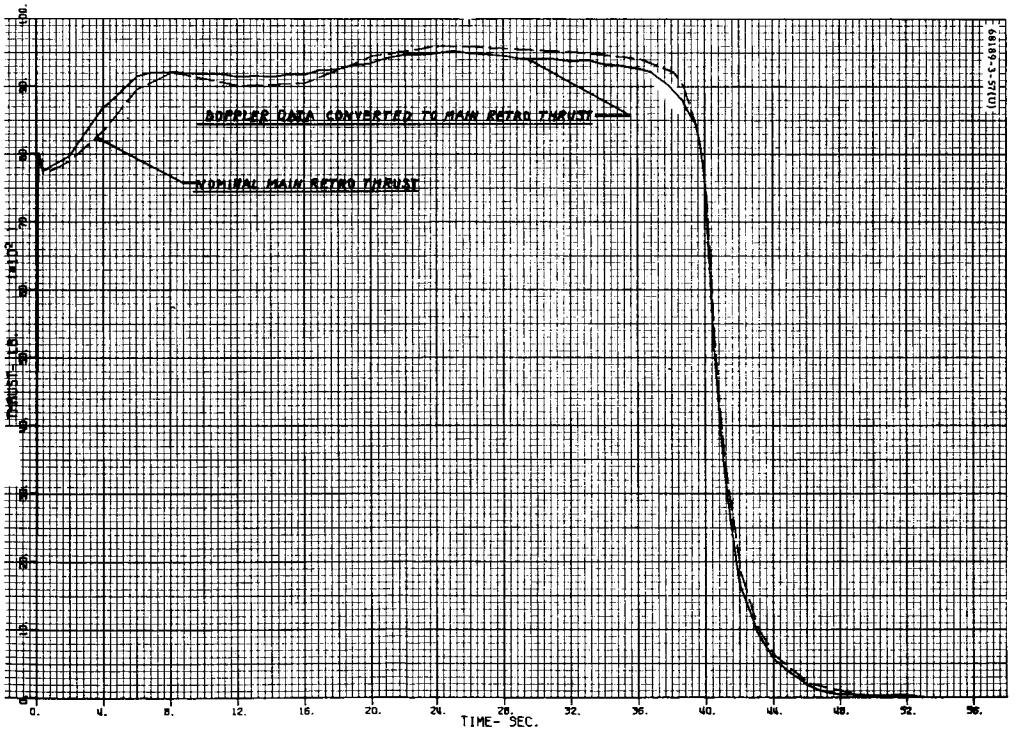

Figure 5.12-4. Main Retro Thrust Versus Time (Doppler)

Misalignment between V_o and z is accounted for, as is the loss of inert mass (14.20 lb_m). Since the data used were taken at 1-second intervals, the accuracy of the thrust curve during the transient phases at ignition and tailoff is somewhat questionable.

Comparison of Two Methods for Retro Thrust/Time Curve

Comparing the doppler curve against the accelerometer curve, it is obvious that the former is much smoother. With the exception of the first few seconds along the accelerometer curve, both have the same general shape. Both show slightly higher thrusts than nominal during the first 18 or so seconds of burn and slightly lower than nominal thrusts during the remainder of the burn. The maximum thrust difference between the nominal and doppler curves is about 250 pounds and occurs in the first few seconds of burn. Generally, the difference is less than 100 pounds, which is about the same as the difference between the accelerometer and nominal curve. Nominal peak thrust is 9600 pounds, while doppler peak thrust is about 9520 pounds. Both occur at the same time point. Accelerometer peak thrust of 9680 pounds, also occurring at the same time point, is most likely too high since it occurs at the top of a "bump" probably caused by accelerometer striction.

The extremely low initial thrust indicated by the accelerometer curve is most likely caused by striction error. The doppler curve, which shows higher than nominal thrusts in this region, is the more accurate of the two methods.

Burn times match well among the nominal predicted curve and both computed curves. The nominal time between retro ignition and the 3500-pound thrust point is 41.09 seconds. The corresponding time is 41.02 seconds from doppler and 41.01 from the accelerometer curve. Both times have an estimated accuracy of ±0.05 second.

5.12.4.5 Vernier Phase ΔV From Doppler Data

Figures 5.12-5a and b show the spacecraft velocity changes during the vernier phase of descent. These velocity changes are obtained by correcting the radial doppler velocity as seen by the earth tracking station for the angle difference between the doppler direction and spacecraft velocity. As seen in Figure 5.12-5a, the spacecraft velocity change between the beginning of RADVS-controlled descent and touchdown is 495 fps, which agrees well with the telemetry velocity of 492 fps at the beginning of this period. Segment acquisition points can easily be spotted from this plot. However, since doppler data are available at only 1-second intervals, these points are only accurate to ±0.5 second in time. All segment acquisition points from doppler data match the corresponding times determined from telemetry within the time tolerances specified above. Figure 5.12-5a can also be used to determine A_{max} (spacecraft saturation acceleration). The doppler velocity slope remains a constant 7.23 ft/sec^2 for about 19 seconds after the second segment has been acquired, which means that the spacecraft acceleration is saturated during this period. When added to 5.31 ft/sec^2 (the value of gravity at this point), 12.54 ft/sec^2 is obtained, which agrees well with the nominal preflight value of 12.50 ft/sec^2. Figure 5.12-5b shows the minimum acceleration phase of the vernier descent (beginning of RADVS-controlled descent to first segment acquisition). The slope of the doppler velocity plot is -0.40 ft/sec^2 which, when added to the lunar gravity of 5.28 ft/sec^2 at this point, gives $A_{min} = 4.88$ ft/sec^2, as compared to the nominal preflight value of 4.90 ft/sec^2.

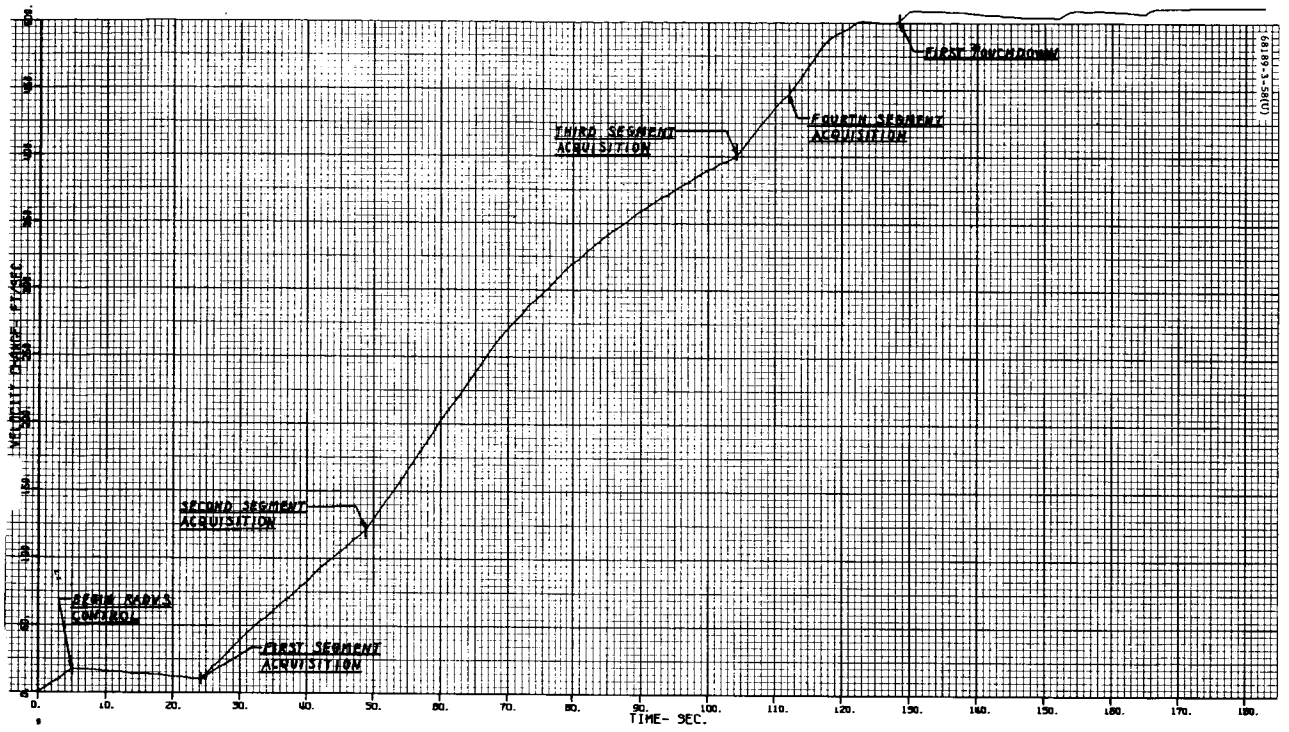

a) Vernier Phase Velocity Change Versus Time (Doppler)

Start of RADVS-controlled descent to touchdown

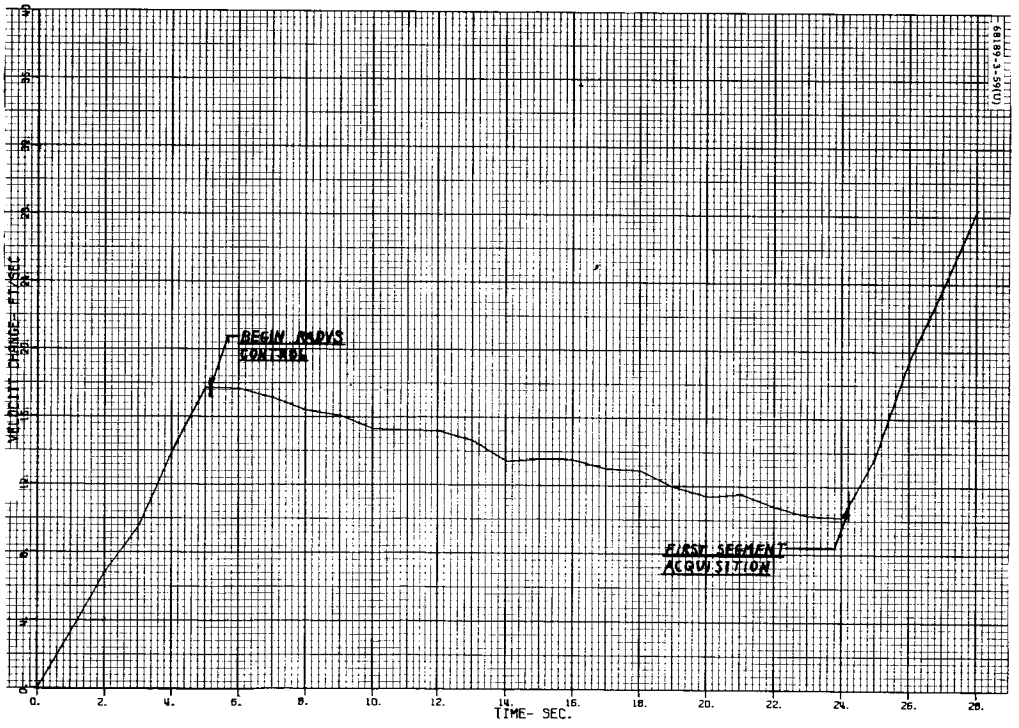

b) Minimum Acceleration Phase Velocity Change Versus Time

Start of RADVS-controlled descent to first segment acquisition

Figure 5.12-5. Spacecraft Velocity Changes During Vernier Descent

Reference time, GMT-110:00:02:09.5

5.12.4.6 Touchdown Phase from Doppler Data

The major anomaly during the SC-3 flight occurred just prior to touchdown. When the spacecraft reached an altitude of approximately 30 feet with a vertical velocity of approximately 4 to 5 fps, the RADVS beam 3 dropped lock. This occurred just after the 10-fps mark, at which time the spacecraft commands a constant 5-fps velocity. Since it is virtually impossible for the RADVS system to relock at velocities this low, the spacecraft then switched to the inertial mode of operation, falling with its engines thrusting at about 0.9 lunar g (4.88 ft/sec^2 nominally). The spacecraft remained in inertial hold and rebounded off the lunar surface three times, as indicated by strain gage data before, coming to rest. The vernier engines were cut off at 110:00:04:53:907 GMT just prior to the last bounce. Strain gage and gyro error signal data showed that the spacecraft landed on a slight slope. Strain gage data show that the spacecraft footpads did not touch down simultaneously for any of the three bounces, indicating that touchdown occurred on a slope. This caused some spacecraft rotation as evidenced by the telemetered gyro error signals. When the spacecraft flight control sensed this attitude error, it throttled the engines to correct for it. The increased engine thrusts, resulting in a thrust acceleration greater than 1 lunar g, caused the spacecraft to rise again after each touchdown.

Telemetered velocity and slant range are not available during the multiple touchdown phases due to the loss of RORA and RODVS. However, the doppler velocity changes, as measured by the earth tracking station (Figure 5.12-6), clearly shows each touchdown. The spacecraft velocity in this figure has been referenced to the moon's surface with downward velocities being positive. This figure, which begins a few seconds before the loss of RORA and RODVS, shows that the spacecraft lost lock at a velocity of 4 or 5 fps, switched to inertial attitude hold, and had a thrust acceleration of 0.9 lunar g until hitting the lunar surface at about 6 fps. The spacecraft then rebounded with an upward velocity of about 3 or 4 fps, still in inertial hold. The spacecraft hit for the second time at about 4 fps and rebounded at about a velocity of 1.5 fps. The third touchdown occurred at about 1.5 fps, resulting in a slight rebound. Since the engines were manually commanded off slightly before the third touchdown, the rebound was small. The spacecraft was airborne for approximately 24 seconds following the first rebound, 12.4 seconds following the second, and 1 second following the third. Touchdown times shown in Figure 5.12-6 were determined from strain gage data and show good correlation with the doppler data.

There appears to be a discrepancy in the doppler data after the spacecraft has come to rest since a final upward velocity of 2 fps is indicated. This is most likely caused by a slight shift in the spacecraft transmitter frequency at the time that the vernier engines were cut off, resulting in an erroneous velocity change. The transmitter had a varying drift rate for about 1 minute after the spacecraft came to rest. It then settled down to the same constant temperature drift rate which was observed before the retro engine was ignited. It thus seems reasonable that a slight frequency shift could have been introduced by shutting down thrust phase power.

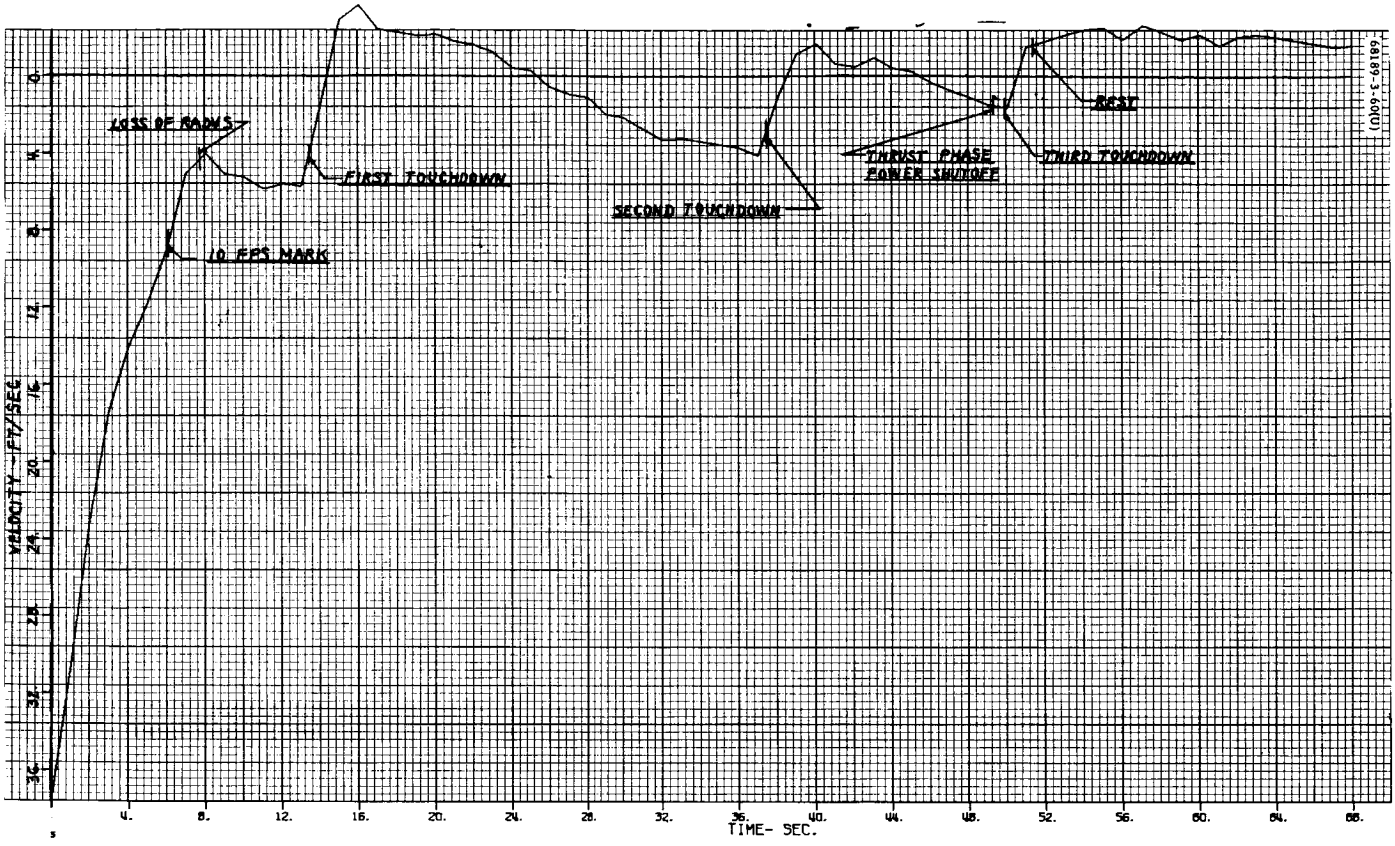

Figure 5.12-6. Spacecraft Velocity Multiple Touchdown Phase Versus Time (Doppler)

Reference time, GMT-110:00:04:04.5

Because of the velocity shift mentioned above, the points of zero velocity relative to the lunar surface could not be determined by looking at the doppler data after the spacecraft came to rest. The shift was determined instead by comparing doppler velocities to RADVS velocities before RORA and RODVS were lost.

Since the spacecraft hit on a slope, some lateral velocity was undoubtedly introduced. Doppler can sense only a small component of this lateral velocity as it can only sense velocity changes along a radial line from the earth tracking station to the spacecraft. Since the lunar vertical is about 18 degrees from this radial line, only a small component of this lateral velocity is seen by doppler. Thus, doppler velocities may be somewhat inaccurate during the later bounces where the spacecraft may have achieved a sizable lateral velocity.

5.12.4.7 Vernier Propellant Consumption

Table 5.12-3 presents a tabulation of the propellant consumption (only to first spacecraft touchdown) from individual tanks based on vernier engine acceptance test performance data of both specific impulse and mixture ratio. The use of in-flight propellant temperature data variations (on the order of 30° F variations) was neglected since it has a negligible effect on total consumption (less than 0.2 pound total). The total propellant consumption is broken down into three phases (midcourse, main retro, and vernier phases) and finally arrives at the propellant margin at the end of the first touchdown. A later discussion outlines the total propellant consumed during the multiple touchdown phases.

Midcourse

The predicted landing location for the midcourse maneuver of 4.19 m/sec and the postflight determination of the landing location as indicated in subsection 5.12.4.8 are within 2 to 3 kilometers. As a result of the apparent near-perfect landing with respect to the predicted site, an error in the midcourse maneuver is apparently negligible. The total propellant consumption is approximately 0.08 pound less than the operations prediction since the prediction is based on an approximate solution of the conversion of ΔV to pounds of propellant.

Main Retro Phase

The main retro phase propellant consumption computations are inherently the most inaccurate because of the open-loop nature of the thrust commands. While at midcourse, the change in spacecraft velocity is a very accurate measure of engine impulse; during the retro phase, the main retro engine overshadows any expected variation in vernier performance.

An attempt was made to determine the actual thrust levels during retro burn and during retro separation, since the telemetered values disagreed with premission computations of the vernier thrust levels of

TABLE 5.12-3. VERNIER PROPELLANT USAGE (POUNDS)

Engine Tanks	Engine 1		Engine 2		Engine 3		Totals Calculated						Preterminal Mission Predictions, Oxidizer Plus Fuel
	Oxidizer Tank	Fuel Tank	Oxidizer Tank	Fuel Tank	Oxidizer Tank	Fuel Tank	Engine 1	Engine 2	Engine 3	Oxidizer	Fuel	Oxidizer Plus Fuel	
1) Midcourse	0.69	0.46	0.70	0.47	0.71	0.47	1.15	1.17	1.18	2.10	1.40	3.50	3.58
2) Main retro	8.73	5.78	8.94	5.90	8.98	5.86	14.51	14.84	14.84	26.65	17.54	44.19	43.83
3) Vernier phases	17.95	11.99	18.41	12.29	18.51	12.22	22.94	30.70	30.73	54.87	36.50	91.37	90.30
4) Total used	27.27	18.23	28.05	18.66	28.20	18.55	45.60	46.71	46.75	83.62	55.44	140.06	137.71
5) Average mixture ratio							1.502	1.504	1.521			1.509	
6) Total loaded	36.34	24.92	36.43	24.87	36.40	24.84	61.26	61.30	61.24	109.17	74.65	183.82	
7) Trapped (lines and expulsion efficiency	0.43	0.28	0.43	0.28	0.43	0.28	0.71	0.71	0.71	1.29	0.84	2.13	
8) Usable loaded (item 6 minus item 7)	35.91	24.64	36.00	24.59	35.97	24.56	60.55	60.59	60.52	107.88	73.81	181.69	181.7
9) Usable loaded less total used	8.64	6.41	7.95	5.93	7.77	6.01	14.95	13.88	13.77	24.26	18.37	41.63	
10) Propellant remaining after one tank runs dry, assuming propellant is consumed at mid-course thrust levels	0.87	1.33	0.19	0.73	0	0.97	2.20	0.92	0.97	1.06	3.03	4.09	
11) Nominal propellant margin — nominally usable propellant in excess of nominal consumption (item 9 minus item 10)	7.77	5.08	7.76	5.20	7.77	5.04	12.75	12.96	12.80	23.20	15.34	37.54	33.69*

*Includes a median shift allowance of 5.5 pounds for uneven propellant consumption.

196.9 during retro burn and 276.4 during retro separation. However, the attempt showed no correlation between premission computations, in-flight calibration consideration of telemetry data, and the actual telemetered data. The following discussion clarifies the reason for the lack of confidence in the thrust command telemetry data.

After case separation and during the minimum acceleration phase, the spacecraft center of gravity is determined from preflight determinations. Table 5.12-4 shows: 1) the expected vernier engine thrust from preflight knowledge of the spacecraft center of gravity and the differential thrust values between engines, 2) actual telemetered data as shown in Figure 5.12-7, and 3) in-flight calibration of telemetry data. As can be seen from the table, there is no correlation between the differential thrust values either in magnitude or cyclic order.

Even though the thrust commands are now telemetered from the differential current commands to the engines instead of voltage and are not temperature sensitive as was the case for Surveyor I, the telemetry data of vernier engine thrust is still suspect. The telemetry calibration is based on preflight test acceptance data; therefore, either the test data are suspect or the telemetry of the differential current is still not indicative of the actual thrust from the vernier engines. Because of the apparent inaccuracy of the telemetry commands, the premission thrust levels were used in the computer model for the main retro phase.

While telemetered thrust commands are not too useful for their steady-state values, they are valuable in analyzing system transients and, in particular, those caused by retro thrust misalignments. Any deviation of the retro thrust vector from the spacecraft center of gravity will cause moments that the vernier system must null out, causing uneven propellant consumption between engines. SC-3 data indicate relatively small misalignments resulting in a maximum thrust deviation about the nominal of about 3 pounds for engine 1. The maximum resulting impulse deviation about the nominal is approximately 22 lb-sec or 0.08 pound of propellant. Because this deviation was so small, the propellant results in Table 5.12-2 assume all engines thrusted at the same level during the retro phase.

Vernier Phase

To compute propellant consumption during the vernier phase, the computer model was initialized with the present best estimate of burnout conditions. A simulated descent of the spacecraft to touchdown was run, and discrete time events were compared with telemetry data as a measure of model accuracy. Table 5.12-5 presents time comparisons for first segment intercept, segment end points, 10-fps mark, and first touchdown. As will be noted, all time points compare within 0.7 second, indicating a good fit. In particular, the excellent correspondence in times from initial segment intercept to end of the first segment indicates that the simulated velocity at intercept must be accurate. In addition, the combination of accurate velocity at intercept with good time correspondence in first segment intercept points out that the initial conditions of altitude and velocity are also accurate.

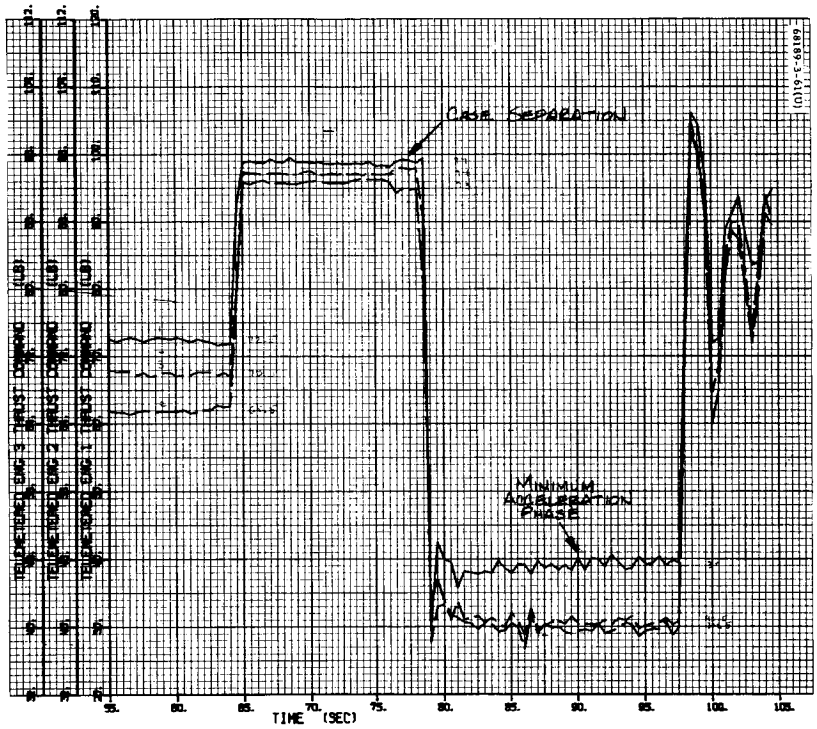

Figure 5.12-7. Vernier Engines Thrust Commands Versus Time

Retro separation phase – minimum acceleration phase

TABLE 5.12-4. VERNIER ENGINE THRUST DETERMINATION DURING RETRO PHASE

Telemetry Data	Thrust	Thrust Differences
Preflight		
High thrust phase	$T_1 = 91.12$	$\Delta T_{12} = -1.03$
	$T_2 = 92.15$	$\Delta T_{23} = -0.98$
	$T_3 = 93.13$	$\Delta T_{13} = -2.01$
Total	276.4	
Minimum acceleration phase	$T_1 = 38.11$	$\Delta T_{12} = -0.43$
	$T_2 = 38.54$	$\Delta T_{23} = -0.41$
	$T_3 = 38.95$	$\Delta T_{13} = -0.84$
Telemetry data (Figure 5.12-7)		
High thrust phase	$T_1 = 99.0$	$\Delta T_{12} = 7.0$
	$T_2 = 92.0$	$\Delta T_{23} = -1.2$
	$T_3 = 93.2$	$\Delta T_{13} = 5.8$
Minimum acceleration phase	$T_1 = 39.0$	$\Delta T_{12} = -1.0$
	$T_2 = 40.0$	$\Delta T_{23} = -0.5$
	$T_3 = 40.5$	$\Delta T_{13} = -1.5$
In-flight calibrated telemetry data		
High thrust phase	$T_1 = 95.4$	$\Delta T_{12} = 4.9$
	$T_2 = 90.5$	$\Delta T_{23} = -4.9$
	$T_3 = 95.4$	$\Delta T_{13} = 0.0$
Minimum acceleration phase	$T_1 = 42.2$	$\Delta T_{12} = 4.8$
	$T_2 = 37.4$	$\Delta T_{23} = 0.6$
	$T_3 = 36.8$	$\Delta T_{13} = 5.4$

TABLE 5.12-5. ACTUAL VERSUS MODEL TIME COMPARISONS

Event	Time From Start of Vernier Phase (Start RADVS-controlled Descent), seconds	
	Telemetry	Computer Model
First segment acquisition	19.2	19.3
End first segment	43.7	43.3
End second segment	98.3	98.3
End third segment	107	106.6
10-fps mark	115.9	115.2
First touchdown	123.4	123.2

The almost perfect time correlation of points along the trajectory to first touchdown give added confidence in the model's accuracy. It would take a very unlikely combination of abnormal spacecraft performance and erroneous initial conditions to give as good a fit as indicated in Table 5.12-5.

One of the obvious spacecraft functions that the computer model cannot simulate in detail is individual vernier engine thrust fluctuations caused by completely random radar noise. However, the model does simulate average thrust levels as indicated by the accurate time correspondence and, since the vernier engines specific impulse is relatively flat with thrust, a randomly varying thrust gives the same total impulse as its average thrust when integrated over time.

Another simplification in the model which could have been simulated but was not considered important enough is the change in the center of gravity offset caused by propellant depletion. Depending on the phase of the mission, the change in the center of gravity initial offset would be less than 0.1 inch. The maximum effect of this offset would cause variations in propellant consumption between engines up to 0.1 pound, but would have no effect on total propellant consumption.

The model accuracy, excluding the above two considerations, may be described in terms of the total effective velocity change, that is, the sum of burnout velocity and gravitational losses ("gt" term). With total time in the gravitational field known to 0.1 second, the uncertainty in gt is less than 1 fps. Since the uncertainty in burnout velocity is probably less than 5 fps, and the total differential velocity is 1137 fps, the probable error in the final results is less than 0.5 percent. As a comparison, this is equivalent to an error or uncertainty in vernier specific impulse of 1.5 seconds.

Total vernier propellant consumption based on the above model and best estimate of burnout conditions is 91.37 pounds as compared to the pre-retro prediction of 90.3 pounds.

Propellant Margin

During the mission, propellant margin figures are based on computing the amount of usable propellant on board at touchdown with a probability of 50 percent. In practice, the computation is done by taking the results of running the operational terminal descent computer program (similar to the program used in the previous computations) and combining this with median shift results obtained from a Monte Carlo simulation of the terminal descent. The median shift, based on specified values of retro moment and mixture ratio dispersions, is the amount of additional propellant that must be loaded to allow for uneven consumption between vernier tanks rather than variations in total propellant consumption. During the mission, 5.5 pounds of propellant were allowed for this effect, resulting in a predicted propellant margin of 33.69 pounds. Based on postmission analysis, it is clear that there was very little moment to correct during the retro phase and, therefore, very little or none of the 5.5-pound allowance was necessary for this purpose. In addition, vernier propellant temperatures were not extreme and, therefore, the 3σ mixture ratio variation allowance of 0.1 is probably far greater than the actual. While postmission data do not allow too accurate a prediction of quantitative consumption, a postflight "engineering" guess at the necessary allowance for uneven consumption would be 1.0 pound.

Item 11 of Table 5.12-3 gives a best estimate of 37.54 pounds for the nominal propellant margin at touchdown. Therefore, the best estimate of propellant margin with a 50 percent probability would be this value less 1.0 pound or 36.54 pounds. To compute the 99 percent minimum propellant margin, a value must be placed on the vernier specific impulse variations.

Propellant Consumption During Multiple Touchdowns

An attempt is made here to determine the total propellant consumption during the multiple touchdowns on the lunar surface due to failure of the 14-foot mark to occur. The propellant used between the first and second touchdown was computed to be 10.27 pounds and was obtained from the following equation,

$$\Delta W = \int \frac{T}{I_{sp}} dt$$

with T being the sum of the telemetered thrust commands to the engines. Telemetry errors were removed from the thrust commands by comparing steady-state thrust commands (after oscillations due to first bounce had damped out) to those obtained from the six-degree-of-freedom simulation.

Since telemetry data were not available after the second touchdown, the propellant consumption of 4.51 pounds from second touchdown to engine cutoff was computed assuming a nominal spacecraft thrust acceleration of 4.88 ft/sec^2 (nominal inertial mode acceleration without RADVS). The total propellant consumed from the first touchdown to engine cutoff is then $\Delta W = 10.27 + 4.51 = 14.78$ pounds. Beginning with the weight at first touchdown of 674 pounds obtained from the six-degree-of-freedom, the weight after engine cutoff is

$$W = 674 - 14.78 = 659.22 \text{ pounds}$$

From Table 5.12-3, the propellant margin at first touchdown is 37.54 pounds. The total propellant consumed during the multiple touchdowns of 14.78 pounds results in a final expected total propellant margin of 22.76 pounds.

5.12.4.8 Spacecraft and Retro Case Landing Location

The spacecraft landed near the center of a small lunar crater as determined from Surveyor TV camera photos and Lunar Orbiter IV photos. The Lunar Orbiter photos of the surface region places the spacecraft at a longitude of 23.34°W and a latitude of 2.977°S. The predicted landing site resulting from a midcourse correction of 4.19 m/sec was 2.92°S latitude and 23.25°W longitude. Based on the best available postflight orbit determination of the spacecraft position at retro ignition and a 6DOF simulation of the powered flight phase, the best estimate in the touchdown location of the spacecraft would have been 23.40°W and 2.91°S if the Lunar Orbiter data had not been available. The comparison between the Lunar Orbiter location determination and the computed value differs by only 2.49 kilometers. A large part of this difference may be attributed to two major error sources: orbit determination and uncertainties in the lunar grid system.

The retro-rocket case traveled beyond the spacecraft touchdown location another 947 feet and impacted with a velocity of 785 fps. The location is out of sight of the Surveyor camera (beyond the rim of the touchdown crater whose diameter is estimated at 650 feet).

Figure 5.12-8 shows the relative location of the spacecraft, retro case, and ignition point. Both the case and spacecraft are shown out of the preretro trajectory plane (approximately 1500 feet). This is because there was some out-of-plane thrust alignment error during retro burn. During the vernier descent phase, the spacecraft steering moved the spacecraft an additional 176 feet left of the plane of the free falling retro case.

A summary of positions shown in Figure 5.12-8 is given in Table 5.12-6.

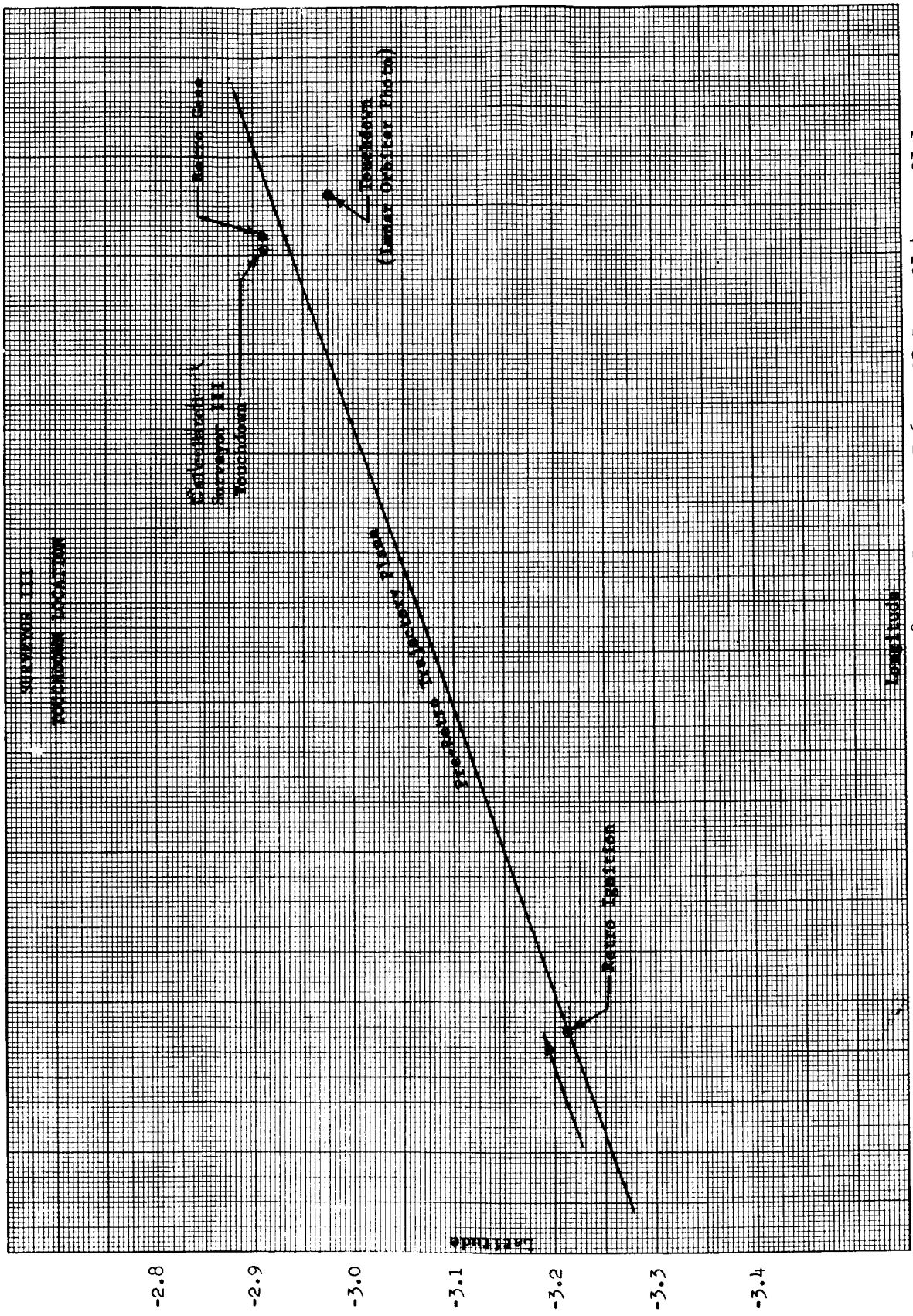

Figure 5.12-8. Surveyor III Touchdown Location

TABLE 5.12-6. SPACECRAFT POSITION SUMMARY

Latitude, degrees	Longitude, degrees	Item
-3.214	-24.194	Computed ignition
-2.909	-23.395	Touchdown (computed)
-2.908	-23.386	Retro case
-2.977	23.34	Touchdown (Lunar Orbiter photo)
Angle of trajectory plane (preretro) = 70.691°N		

5.12.4.9 Trajectory Reconstruction

This subsection essentially reconstructs the vernier phase of the terminal descent trajectory to provide a best estimate of the actual trajectory parameters. This reconstruction is accomplished by utilizing the 6DOF program. Initial conditions at vernier ignition of velocity, altitude, and retro thrust vector misalignment (while maintaining retro phase burn time equal to telemetry indication) are perturbed until the start of the vernier phase coincides with the calibrated telemetry RADVS parameters as indicated in subsection 5.12.4.1.

Prior to the above perturbations, the nominal predicted initial conditions determined from tracking data and the nominal Surveyor III system parameters determined from preflight assessment were inputs to the program. The nominal command descent segments were altered to match preflight test data. The nominal predicted retro thrust-time curve was modified such that the time from retro ignition to the 3.5 g mark corresponded to the telemetered time discrete. The thrust and specific impulse were modified to preserve the total impulse and total retro propellant weight.

Arriving at the burnout conditions of V_x, V_y, V_z and slant range corresponding to telemetry, the time during the minimum acceleration phase did not match the telemetered time determination. From premission assessment and postflight analysis, the telemetry of V_x, V_y, and V_z is accurate to within 1 percent. Therefore, the telemetry of slant range became suspect. Further perturbations were conducted until the V_x, V_y, and V_z matched the telemetry data and the time from burnout to first segment acquisition and the time to the 10-fps mark agreed with the telemetered times.

This resulted in a difference in slant range of approximately 1500 feet at the start of the RADVS-controlled descent phase between the 6DOF and the telemetry data (Figure 5.12-9). The 6DOF velocities of V_x, V_y, and V_z

agree almost identically with the calibrated raw telemetry data along the entire terminal phase (Figure 5.12-10). With the telemetry data of slant range being suspect, justification of the apparent true slant range as determined by the 6DOF program is indicated by the close correspondence of discrete time events as listed in Table 5.12-7 and by numerical integration of the telemetry velocity. Numerical integration of the telemetry velocity from first segment corner (about 13,000 feet telemetry data) up to sometime prior to the end of steering during the minimum acceleration phase (about 30,500 feet slant range) disagreed with the telemetry slant range by approximately 660 feet; however, it agreed within 80 feet of the 6DOF reconstruction. The telemetry slant range matched fairly well with the 6DOF within the resolution of the telemetry signal (Figure 5.12-11) after the first segment corner of the command descent contour. It could not be determined whether the telemetry or radar system was in error during the minimum acceleration phase, causing the apparent discrepancy in the telemetered data of slant range. However, further investigation is being undertaken to determine the cause for the discrepancy.

POSTPR Program Plots

Figures 5.12-9 through 5.12-17 are plots of important parameters for trajectory reconstruction. The processed telemetry data from PREPRO (solid lines) and the best-fit 6DOF trajectory (dashed lines) are superimposed on the plots. The time scale starts at 20 seconds, which corresponds to a GMT of 110:00:1:15.994 ±0.05. From Table 5.12-1, vernier ignition starts at 21.9 seconds on these figures; first touchdown corresponds to 202.056 seconds on these figures (GMT 110:04:18:05). After 202.056 seconds, the magnitude changes in the telemetry curves are a direct result of the spacecraft touchdown.

Table 5.12-7 lists the time occurrences of pertinent events as determined by the 6DOF program and PREPRO data as referenced to the time scale on Figures 5.12-9 through 5.12-17 with their respective conversion to GMT based on the referenced GMT time given above for the 20-second point.

Figure 5.12-9 shows the discrepancy mentioned previously between telemetry data and the best-fit 6DOF trajectory. The two spikes of telemetry data at 73 and 78 seconds are caused by loss of lock.

Figures 5.12-10a and b show an almost identical V_x and V_y reconstruction between the 6DOF and telemetry data. From Table 5.12-7, start of RADVS-controlled descent occurred at 78.53 seconds. It took approximately 11 to 12 seconds to steer out the V_x and V_y components of velocity developed by the retro burn phase. Approximately 2 seconds after vernier ignition, the RADVS is turned on, resulting in the spikes in the V_x and V_y telemetry plots at the time scale of approximately 24 seconds.

Figure 5.12-10c indicates a difference between the telemetry data and the 6DOF around the 60-second point. This is due to the RADVS tracker sweep limit of about 800 fps.

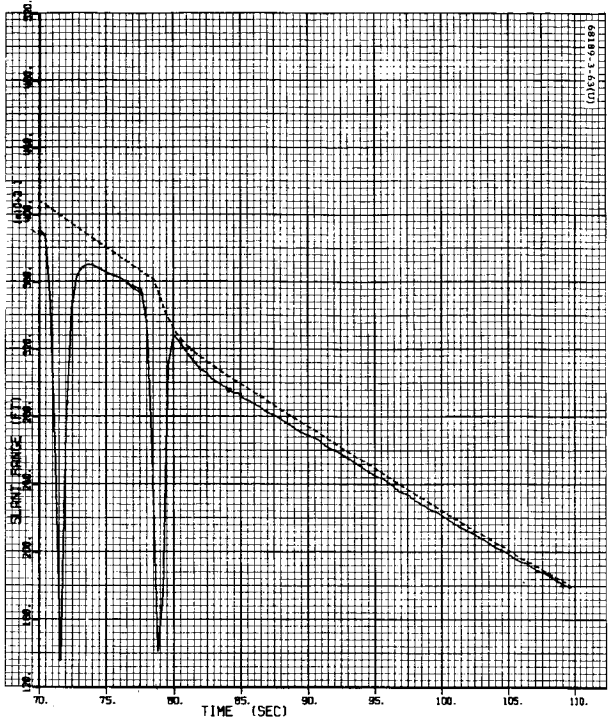

Figure 5.12-9. Slant Range Versus Time

Start of RADVS-controlled descent

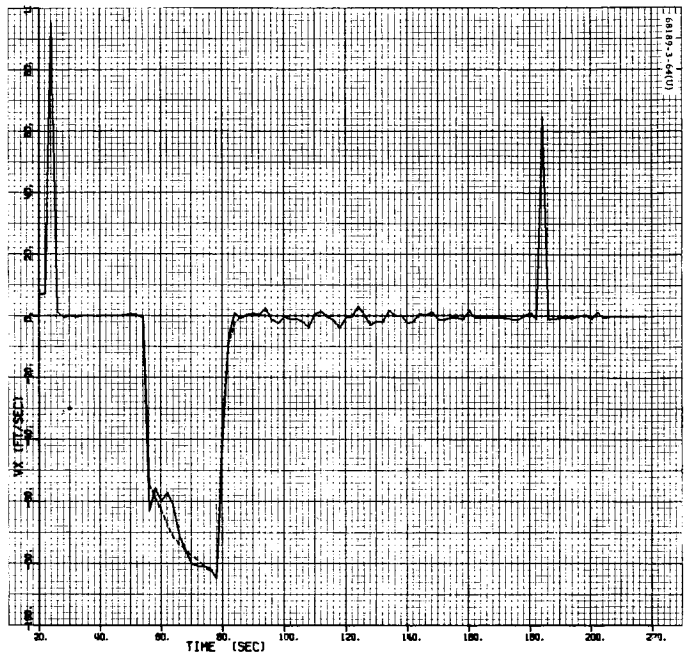

a) X-axis

b) Y-axis

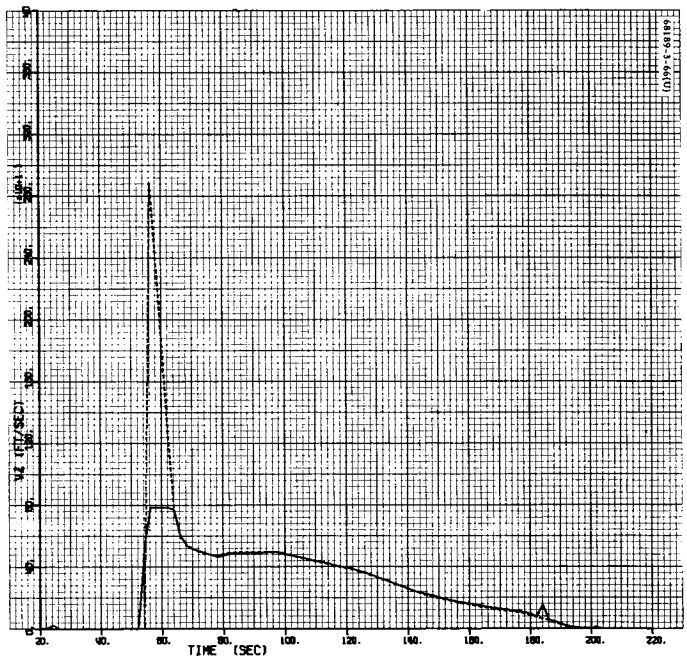

c) Z-axis

Figure 5.12-10. Spacecraft Velocity

TABLE 5.12-7. 6DOF DISCRETE TIME EVENTS VERSUS TELEMETERED

Event	6DOF (Figures 5.12-9-17), seconds	Time	
		Converted Figure Time to GMT, min:sec	Actual GMT at DSS, min:sec
Vernier engine ignition	21.9	01:17.92	01:17.922
Retro engine ignition	23.01	01:19.03	01.19.023
3.5-g mark	64.36	02:00.38	02:00.322
Retro eject	76.37	02:12.39	02:12.492
Start RADVS controlled descent	78.53	02:14.55	02:14.642
First segment acquisition	97.71	02:33.73	02:33.816
End of first segment	123.21	02:59.23	02:58.415
End of maximum acceleration during second segment	143.91	03:19.93	03:17.5±0.5
1000-foot mark	176.97	03:52.99	03:53.013
10-fps mark	194.88	04:10.9	04:10.613
Drop lock beam 3	197.33	04:13.8	04:13.275
First touchdown	202.06	04:18.0	04:18.050

The spikes at 184 seconds shown in Figure 5.12-10 were caused by a parity error in FC-77. The FC-77 correction is made within the PREPRO program to the telemetered signals of V_x, V_y, and V_z. Figure 5.12-10 shows essentially zero telemetry bias in the V_x, V_y, and V_z data before RADVS lockon. However, from looking at the TELTAB output (this program tabulates the processed telemetry data in engineer units per telemetry frame), the following biases existed:

$$V_x = +0.60 \text{ fps}$$

$$V_y = +0.099 \text{ fps}$$

$$V_z = +1.566 \text{ fps}$$

which indicates the telemetry calibration of these signals to be very accurate. The plots show that Beams 1, 2, and 3 locked on to a reliable signal at approximately 54 seconds.

Figure 5.12-11 shows the slant range as a function of time. The telemetry data from 20 to approximately 70 seconds show sporadic readings. This is due to the radar altimeter tracker sweep limit equivalent to about 40,000 feet.

Figures 5.12-12a and b show the telemetry gyro error signals to be biased about -0.45 degree beyond that determined by preflight calibration. The spikes on both plots at approximately 80 seconds are due to the start of steering. The spike at approximately 144 seconds on Figure 5.12-12a was found to be due to a parity error in the original telemetry data.

Figures 5.12-13a and b are the pitch and yaw precision commands. The increase in commanded rates occurs approximately at 78 seconds. The duration of the command rates compare favorably with the elimination of the V_x and V_y components during steering phase. From Figure 5.12-13a it can be seen that the pitch precision command saturates; this is due to the large y velocity component at burnout. Both figures show telemetry biases of 0.4 and 0.3 deg/sec in pitch and yaw, respectively. The 6DOF assumed a pitch and yaw rate limit of 6.5 deg/sec.

Figure 5.12-14 shows the vernier engine thrust commands. The telemetry data are determined from the differential current commands which are nonsensitive to temperature. As was previously indicated in subsection 5.12.4.7, the telemetry data are suspect. The telemetry data are oscillatory due to RADVS noise. The 6DOF is smooth since the RADVS noise is not simulated. However, the 6DOF curve appears to be an average of the actual spacecraft thrust commands, with an apparent bias and scale factor error in the calibrated telemetry data.

Figure 5.12-15 shows the same 6DOF signal as Figure 5.12-14, superimposed with the processed vernier engine strain gage data. The telemetry data here also seem to follow the same trend as the 6DOF program. The rapid change in slope of the telemetry data between 20 and 60 seconds is caused by the retro thrust.

Figure 5.12-16 compares the retro accelerometer with the 6DOF Z-axis acceleration. The telemetry data are apparently biased by 15 ft/sec^2. The peak acceleration occurs at 62 seconds which compares with the strain gage telemetry data. Figure 5.12-17 shows slant range versus velocity. The spike in Figure 5.12-17a at a V_z of 140 fps is due to a parity error in the V_Z telemetry data.

5.12.5 ACKNOWLEDGMENTS

Victor Marelia, Coordinator.

This section was compiled through the efforts of many individuals. The assistance of E. White is especially appreciated. He was solely responsible for utilization of the one-way doppler data in determining the retro and vernier phase velocity change and the velocities and times of the multiple touchdowns. He was also responsible for the retro thrust-time curve reconstruction. The six-degree-of-freedom program trajectory reconstruction was determined by Edward Kopitzke. The spacecraft and retro case landing site locations were analyzed by Vernon George. The plots presented here are the direct result of Nancy Krupa's efforts. Appreciation is also given to Leonard Davids for his general assistance.

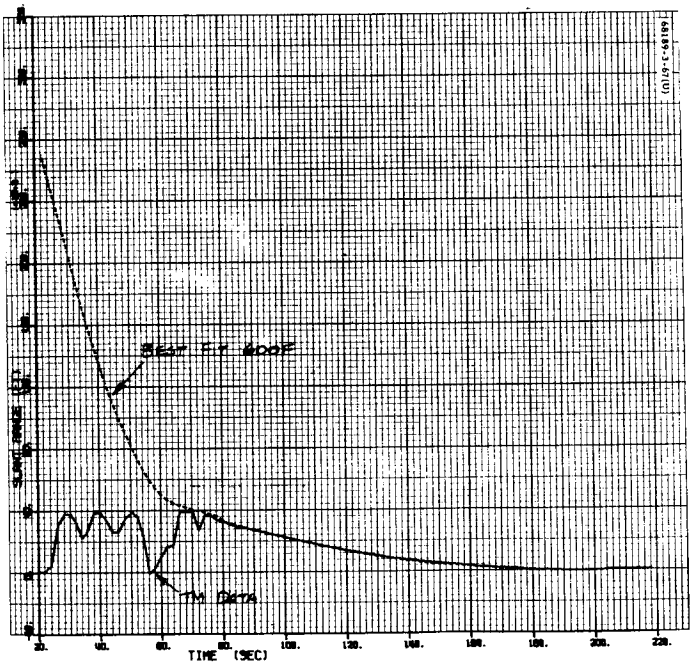

Figure 5.12-11. Slant Range Versus Time

Reference time, GMT-110:00:1:15.994

a) X-gyro

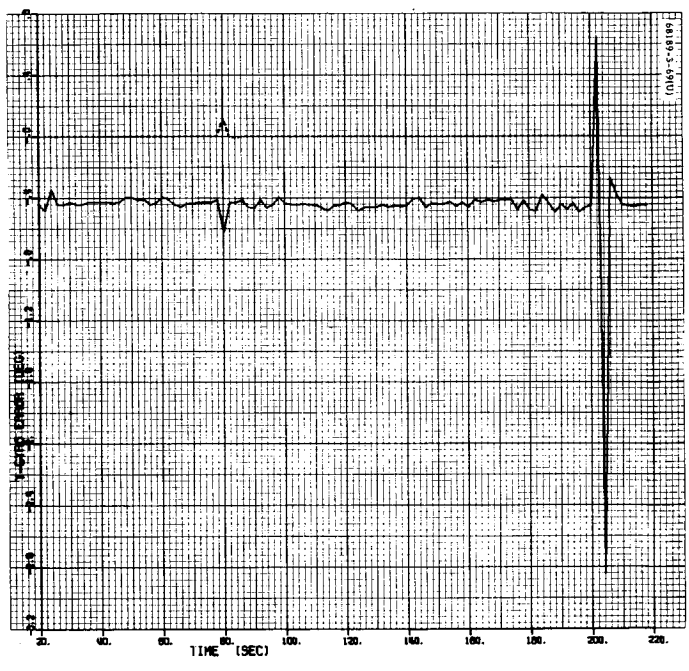

b) Y-gyro

Figure 5.12-12. Spacecraft Error Signal

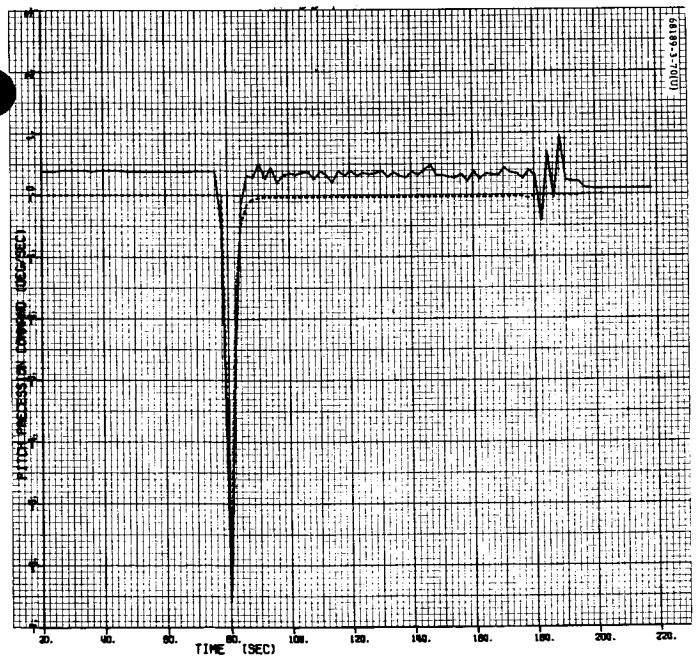

a) Pitch

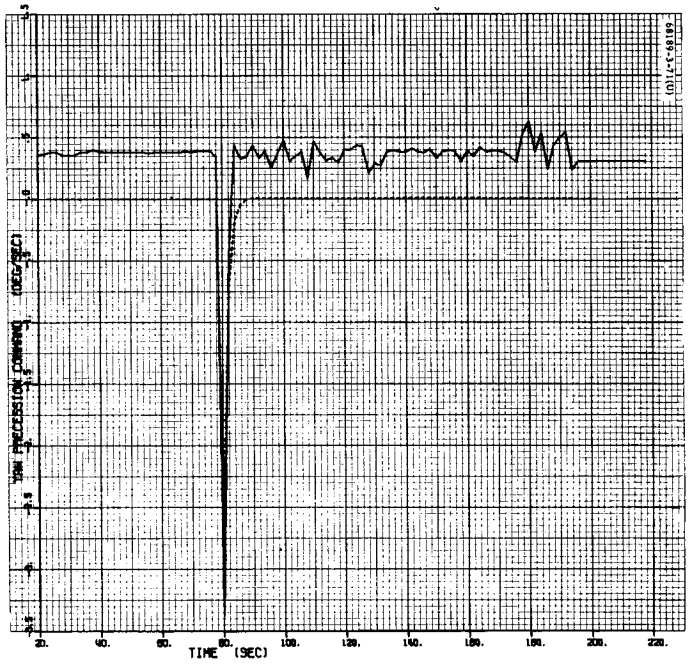

b) Yaw

Figure 5.12-13. Spacecraft Precession Commands

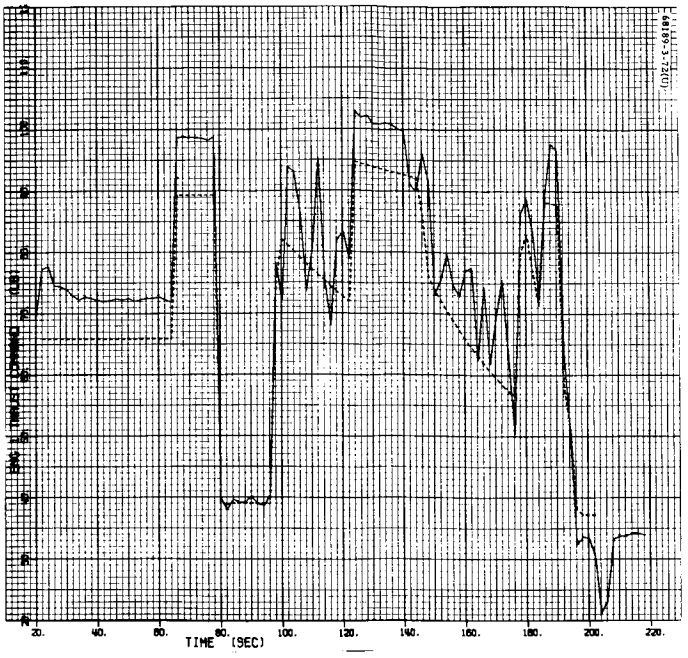

a) Engine 1

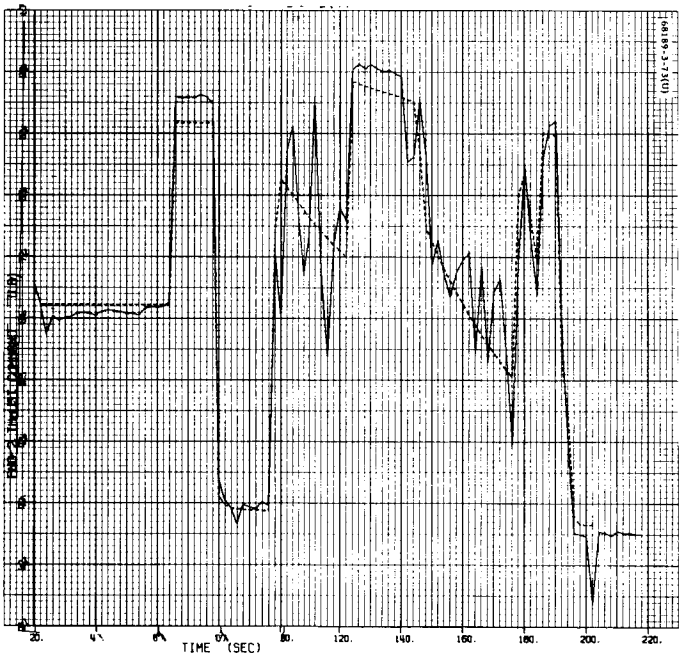

b) Engine 2

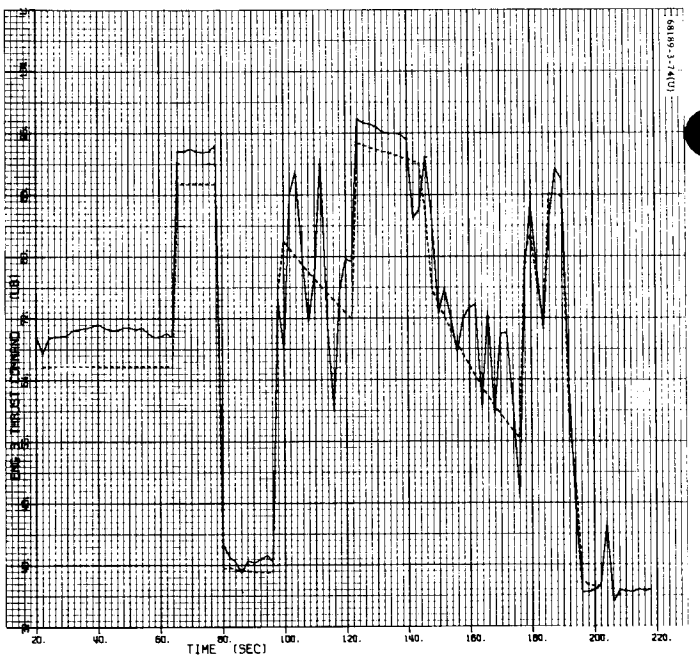

c) Engine 3

Figure 5.12-14. Vernier Engine Thrust Command

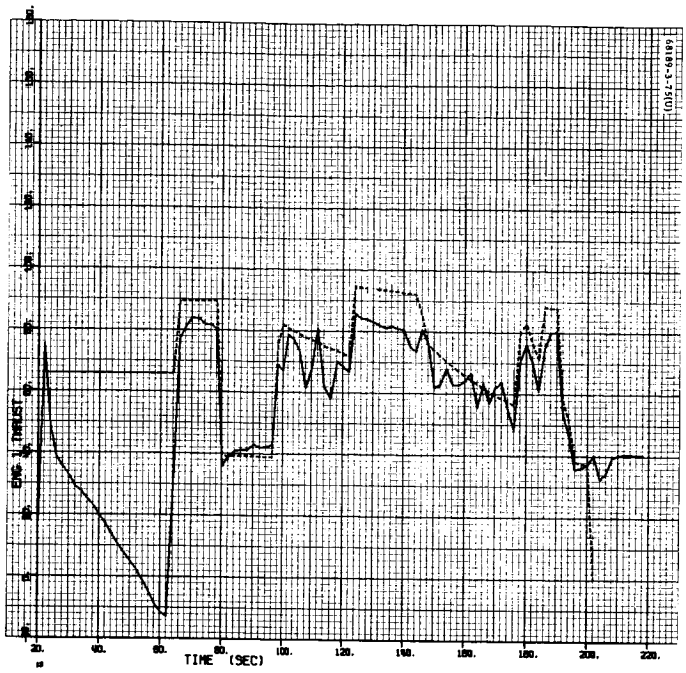

a) Engine 1

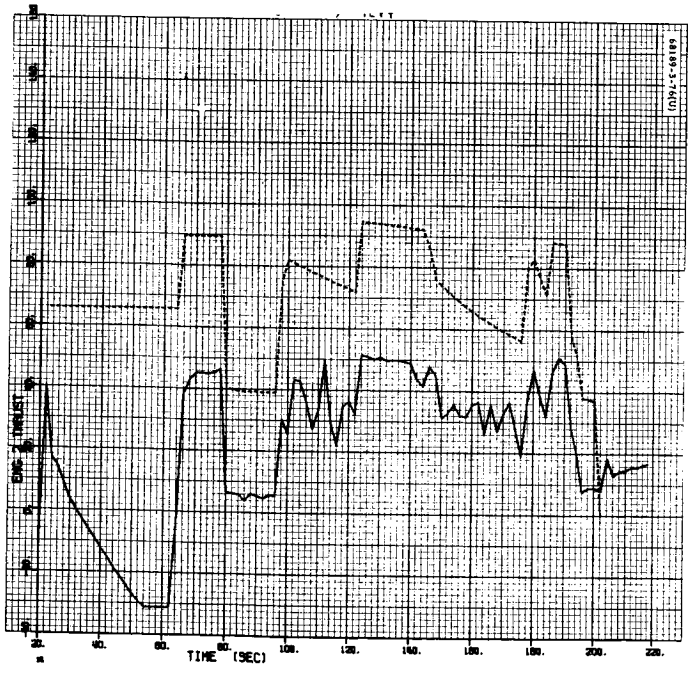

b) Engine 2

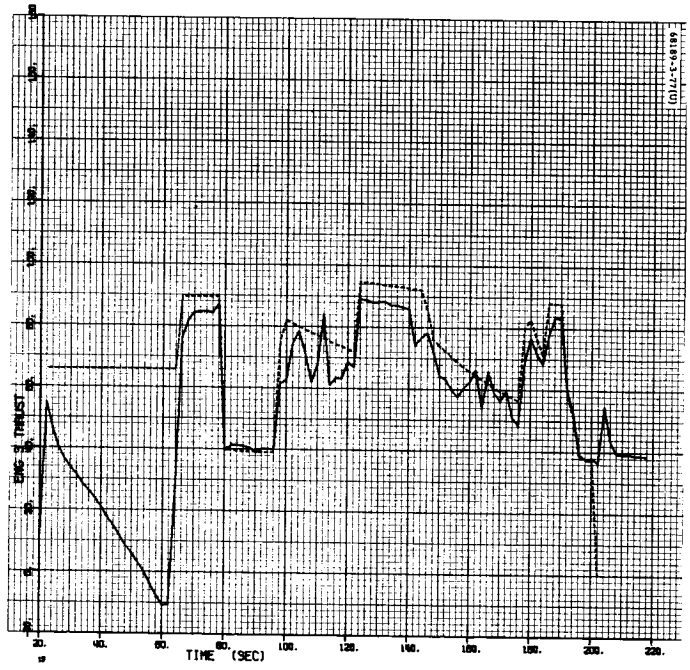

c) Engine 3

Figure 5.12-15. Telemetry Engine Strain Gage Data and 6DOF Thrust Command Versus Time

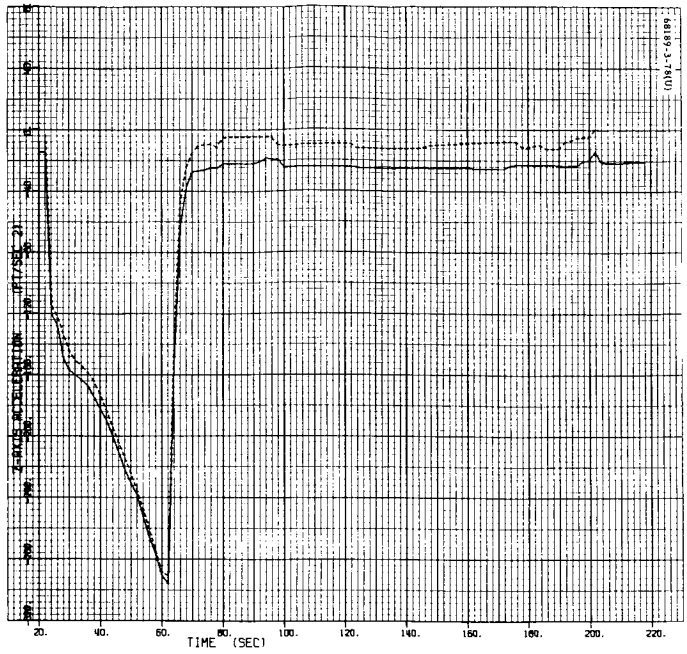

Figure 5.12-16. Telemetry Retro Accelerometer Data and 6DOF Z-axis Acceleration Versus Time

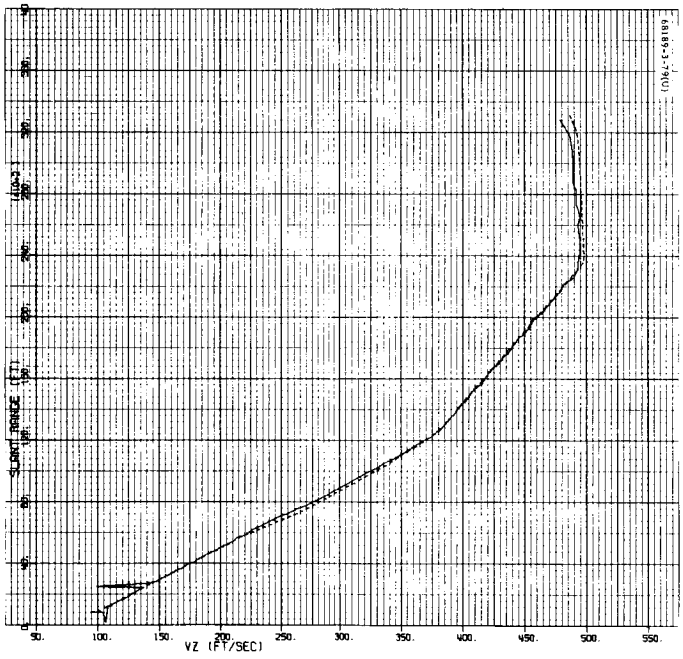

a) Start of RADVS-controlled Descent to 1000-foot Mark

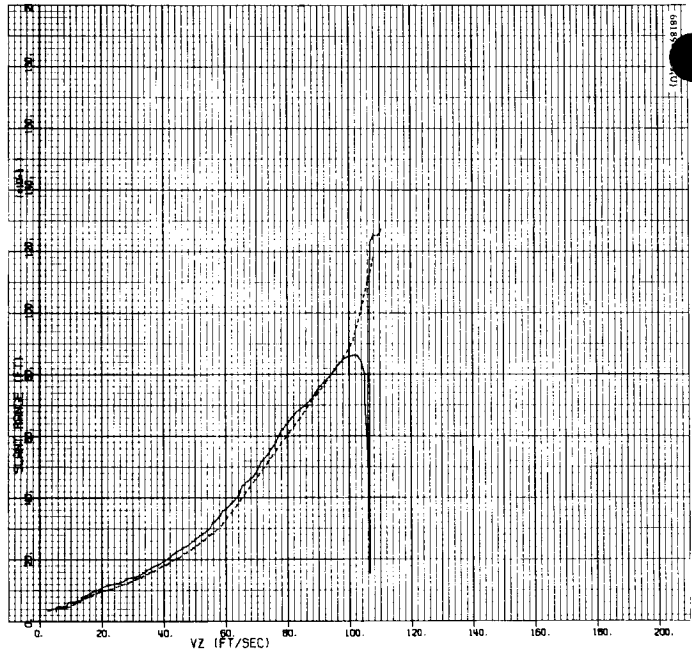

b) 1000-foot Mark to Loss of Radar Beam 3

Figure 5.12-17. Slant Range Versus Z-axis Velocity

5.13 TELEVISION

5.13.1 INTRODUCTION

Between 19 April and 3 May 1967, the television system aboard Spacecraft III returned 6315 pictures of the lunar environment. May of these photographs were of the soil mechanics/surface sampler. Near real-time analysis of the TV pictures indicated that the spacecraft was on a 10-degree slope inside a crater approximately 650 feet in diameter. Comparison of these TV pictures with Lunar Orbiter photographs allowed the pinpointing of the spacecraft location in this crater.

5.13.2 ANOMALIES

Mirror azimuth, elevation, and filter wheel readout failures were evident. The mirror failed to respond to 430 step right commands, 2 step left commands, and 65 step down commands. Figure 5.13-1 plots azimuth failure rate with time, and Figure 5.13-2 plots elevation failure rates. Table 5.13-1 gives the mirror stepping history.

The filter wheel readout failed on day 123, the last Goldstone visibility period before lunar night. While imagery showed the filters to be sequencing properly, the telemetry consistently indicated the blue filter.

Severe glare problems were encountered when the sun illuminated the mirror and filter wheel. This was particularly evident just after touchdown.

Because of soil mechanics/surface sampler operations, many photographs were taken of the lunar surface near the spacecraft. Parts of the spaceframe were in view in many of these scenes. The spaceframe was much brighter than the lunar soil, and up to 10 seconds were required between frames to properly erase saturated images.

Published calibrations for temperature readouts TV-9 (vidicon faceplate) and TV-10 (camera electronics) were inconsistent with the actual camera, so it initially appeared that camera temperatures were running radically high. Normally, TV-10 is calibrated in a camera to read out 5 volts (1023 BCD, the upper limit of the analog-to-digital converter) with a temperature of 165°F. Because of camera rework, however, the upper

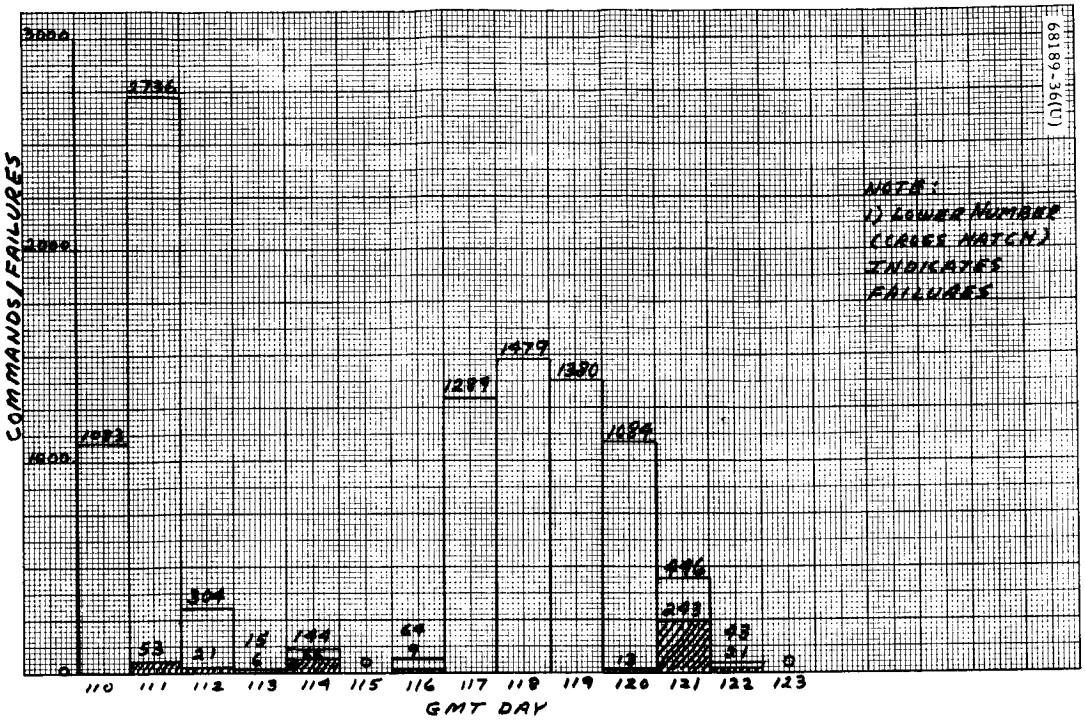

Figure 5.13-1. Mirror Azimuth Command and Failure History

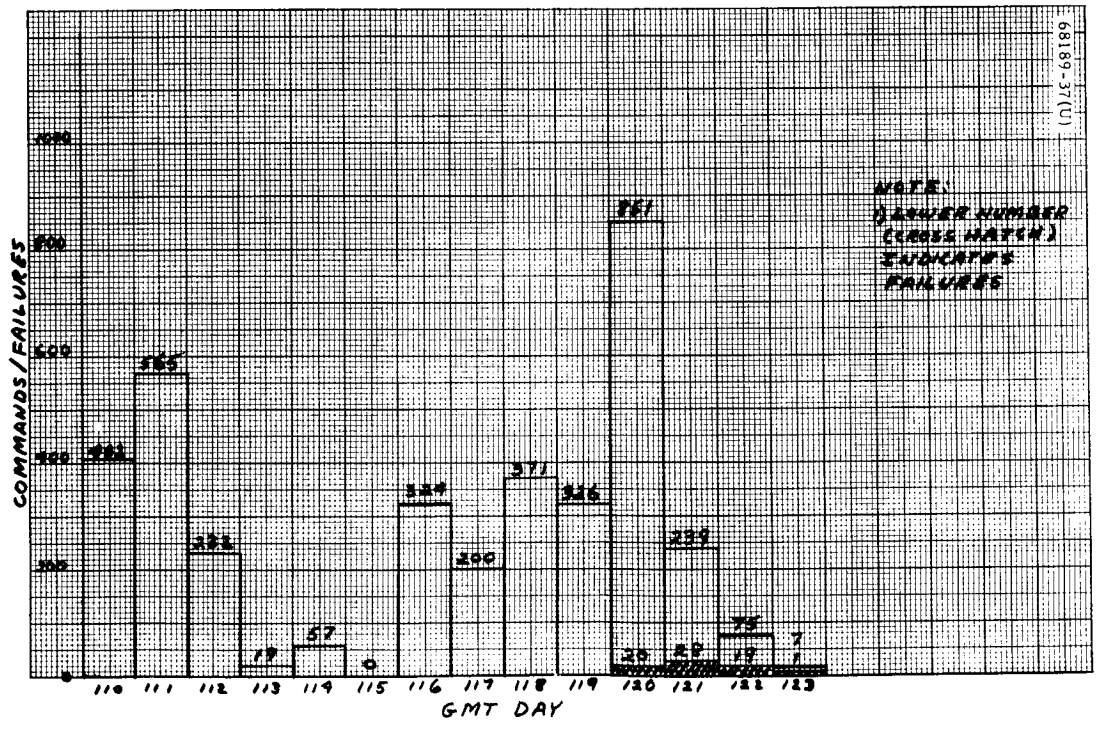

Figure 5.13-2. Mirror Elevation Command and Failure History

TABLE 5. 13-1. MIRROR HISTORY*

Day	Azimuth Steps This Day	Total Azimuth Steps to Date	Azimuth Failures This Day	Elevation Steps This Day	Total Elevation Steps to Date	Elevation Failures	Start Frame This Day	Total Start Frames to Date
110	1083	1083	0	402	402	0	380	380
111	2683	3766	53	565	967	0	1089	1469
112	283	4049	21	232	1199	0	187	1656
113	9	4058	6	19	1218	0	30	1686
114	78	4156	66	57	1275	0	118	1804
115	0	4126	0	0	1275	0	0	1804
116	55	4191	9	324	1599	0	276	2080
117	1289	5480	0	200	1799	0	800	2880
118	1479	6959	0	371	2170	0	752	3632
119	1380	8339	0	326	2496	0	994	4626
120	1071	9410	13	831	3327	20	861	5487
121	202	9612	243	211	3588	25	289	5776
122	22	9634	21	56	3594	19	261	6037
123	0	9634	0	6	3600	1	222	6259

*Steps taken during soil mechanics/surface sampler operation = 411; 9634 total azimuth steps on day 123 + 411 = 10,045 grand total azimuth steps.

readable limit was 145°F, causing some minor operational difficulty near lunar noon. An upper limit of at least 155°F would be required to permit continuous operation.

5. 13. 3 SUMMARY AND RECOMMENDATIONS

5. 13. 3. 1 Summary

The mirror elevation failures follow a pattern of motor wearout resulting in reduced output torque. Mirror azimuth problems appear to be the result of at least three failure modes: motor wear, binding of the azimuth journal bearing due to thermal gradients, and deformation of azimuth ring gear teeth.

All indications of the filter wheel failure analysis point to a loose set-screw holding a gear to the filter wheel readout potentiometer shaft.

Glare problems were almost undoubtedly caused by contamination of the exposed optics during the unusual landing.

Since SC-4 employs improved azimuth and elevation drive motors lubricated with Lubeco 905, it is expected that the increased motor torque and longer service life in the hard vacuum environment will offset azimuth bearing and ring gear deformation problems.

Corrective action is presently under way to ensure that the temperature readouts for TV-9 and 10 will conform to mission requirements.

5.13.3.2 Recommendations

The interface between television and soil mechanics/surface sampler was proven, and it is recommended that the same system, in which TV data is inhibited when the soil mechanics/surface sampler power is on, be used for the SC-4 sampler experiment.

Operational aspects should be improved since postflight data reduction was made more difficult by anomalies in the JPL ground data handling system. Anomalies were noted with the 3070 telemetry printer, the CCN (command) teletype, and command generator/tape unit. The latter sent extra commands at least twice, making it appear that the camera had taken extra steps. On one occasion during a tape survey, the CCN printout did not indicate an elevation step which the camera took. However, the camera stayed on sequence, indicating that the command was transmitted but not recorded on the CCN teletype.

In order to reduce glare problems resulting from a contamination layer (dust), the mirror should be positioned during launch and transit flight to aleviate possible contamination.

5.13.4 SUBSYSTEM PERFORMANCE ANALYSIS

In taking 6315 pictures, the camera scanning mirror was stepped 10,045 times in azimuth and 3600 times in elevation. When included with the number of preflight steps incurred by the mirror (34,300 azimuth and 34,400 elevation), the total mirror steps are 44,345 and 38,000, respectively. Azimuth failures were both temperature and time dependent. Severe azimuth stepping problems were first encountered during the lunar eclipse on day 114 (Surveyor III touched down on day 110). Stepping again became almost impossible during the last three visibility periods of the lunar day; however, the corresponding first three earth days of the lunar day were relatively trouble free. The probable cause of the problems was binding of the azimuth journal bearing during periods when the mirror was colder than the camera support structure. It was calculated that a 20° to 40°F difference could cause these difficulties, which correspond to temperatures actually experienced at the time of the failures.

The fact that comparatively few problems were encountered during the first part of the lunar day indicates that the drive torque was decreasing with time, most likely due to failure of motor lubricants in the hard vacuum.

The numerous azimuth stepping failures at 3 degrees may be indicative of a deformed azimuth ring gear, but limited data exist because of restricted stepping through this position. After the original failure, the 3-degree position was avoided and stepped through only four more times during the mission. Therefore, a definite conclusion cannot be formed as to ring gear integrity.

Elevation failures appear independent of thermal conditions. All problems occurred during the last four visibility periods before lunar sunset. Since all failures were in the step down direction, which is against the anti-backlash spring, degradation of the drive torque is indicated. The most likely cause of this degradation is motor wearout. Failure first occurred on day 120 when the mirror was at the upper elevation end stop. The mirror did not respond to down commands. The mirror was at the upper stop also on day 114 during the lunar eclipse and stepped out satisfactorily.

The filter wheel readout failure on day 123 was preceded by several minor filter anomalies which might have been indicative of the final trouble. Just prior to launch, filter clear next to green pot ratio read 0.0432. During the final launch pad system readiness test, the clear next to green pot ratio was 0.0470; at touchdown, the ratio was 0.0244. In addition, on day 114 at 05:02:16 GMT, the filter apparently missed one or two commands. The system was in the surface sampler mode at the time and no TV telemetry was being received, so full analysis is not possible. It is postulated that the potentiometer drive gear was turning on the pot shaft because of a loose gear setscrew. This assumption explains the failure quite well with the exception that it is not understood why the gear did not slip down the pot shaft and jam in the filter wheel web.

Glare problems rendered many pictures relatively useless. The contamination layer on the optics was apparently quite thin, so excellent photos were obtained as long as the mirror and filter wheel were not directly illuminated by the sun or surfaces reflecting high intensity light.

A review of the vidicon evaluation data for the tube in the camera shows that the difficulty encountered in erasure would be expected. Erasure of highly saturated images takes many times longer than erasure of an optimally exposed image. The fact that more pictures of the spaceframe were taken because of the soil mechanics/surface sampler accentuated this effect.

After correction, camera temperatures correlated quite well with Surveyor I. The original high temperature readings were rationalized by the fact that Surveyor III was in a crater, therefore increasing lunar heating of the spacecraft. Subsequent data correction indicated that this additional thermal loading was negligible.

5.13.5 ACKNOWLEDGEMENTS

The following people contributed to the television subsection:

J. Oicles, Coordinator

W. Drake

5. 14 SOIL MECHANICS/SURFACE SAMPLER

5. 14. 1 INTRODUCTION

The soil mechanics/surface sampler (SM/SS) subsystem has two major units: a mechanism (P/N 3024700) and an auxiliary (P/N 3024536). In addition, there are three cables that interconnect the auxiliary to the mechanism (P/N 3025707), the auxiliary to the squib pin puller (P/N 3025706), and the auxiliary to the spacecraft, as well as the mounting hardware that connects the mechanism and (P/N 3025708) auxiliary to the spaceframe.

The basic SM/SS mechanism consists of a bucket or scoop attached to the end of a lazy-tongs extension arm. The arm is attached to a base that is pivoted in elevation and azimuth, with respect to the spaceframe, and is manipulated by three motors that control the azimuth, elevation, and extension motions. A fourth motor opens and closes the scoop door. The lazy-tongs extension mechanism joints include torsion springs that provide the extension force, while the retraction force is provided by a motor that winds up a steel tape which is attached to the scoop. The elevation drive motor includes a positive latching clutch which can be disengaged from the gear train by actuation of a solenoid and allows the elevation torsion spring to drive the mechanism downward.

The purpose of the SM/SS subsystem is to manipulate the lunar surface, via the mechanism, within a sector that lies between the auxiliary battery and leg 2. The mechanism (upon receipt of command sequences from the auxiliary) has the capability of picking, digging, scraping, and trenching the lunar surface, transporting lunar surface material from one point to another within the space envelope of operation, and applying downward forces to the lunar surface. Picking is accomplished by elevating the scoop to a predetermined point (storing torsional spring energy) and then releasing the elevation drive train clutch, allowing the scoop to impact the lunar surface. Digging, retaining, transporting, and dumping samples of the lunar surface is accomplished by sequentially operating the four motors (extension/retraction, azimuth, elevation, and scoop door), while scraping and trenching is accomplished by opening the scoop door, applying a downward force to the surface, and operating the extension/retraction motor. The downward force is obtained by pressing the scoop to the lunar surface by selective operation of the elevation motor.

5.14.2 ANOMALIES

One anomaly was reported during the Surveyor III mission: TFR 18257 noted that the SM/SS auxiliary temperature during transit fell below -4°F. The predicted temperature limits for transit were -4° to +158°F and the survival limits were -67° to +185°F. Actual temperatures experienced during transit varied from approximately -12° to -35°F after initial cool-down. This is well below the predicted transit temperature range but above the lower bound for survival and therefore not a failure. During the SC-3 flight, the heater was on continuously, and did not bring the temperature up to the automatic turnoff point.

The temperature prediction was based upon performance during solar thermal vacuum testing. Due to the decollimation effects, the solar thermal vacuum environment was not identical to the actual environment, resulting in an erroneous prediction. In any event, if the compartment had experienced the predicted temperatures, the heater would still have been full-on since the lower turn-on temperature is -4°F.

5.14.3 SUMMARY AND RECOMMENDATIONS

5.14.3.1 Summary of Results

The SM/SS subsystem was operated for 18 hours and 22 minutes during 10 earth days. In this period, the mechanism responded to 1898 auxiliary commands which were decoded from 5879 spacecraft commands. Five hundred thirty-six television pictures were taken to monitor the operation and performance. The operating times and summary of operations for each earth day are tabulated in Table 5.14-1.

5.14.4 ACKNOWLEDGMENTS

Summary flight data were obtained from Floyd Roberson of JPL, and the section was compiled by E. R. Zinn.

TABLE 5. 14-1 OPERATING SYNOPSIS FOR SM/SS

Earth Day Number	Operating Time, Minutes	Operating Summary
111	71	Fired squib pinpuller, operated in extension/retraction, azimuth, and elevation to deploy mechanism to initial position.
112	59	First bearing test made, first trench (3-1/2 to 4 inches deep and 18 inches long) dug. Started second trench (3-1/2 to 4 inches deep and 22 inches long).
113	182	Continued second and third pass in second trench. Sighted what appeared to be rock or dirt clod in foot of second trench.
114	–	No operation.
115	–	No operation.
116	48	Picked up clod (no rock) in second trench and transported it to footpad 2. Ran color survey of dirt on footpad.
117	86	Ran two bearing tests in vicinity of footpad 2. Dug third trench in stop action mode, i. e., retract and take photo.
118	168	Picked up pebble and placed it on footpad. Residual material from scoop covered and obscured it. Widened third trench with two parallel sweeps. Made bearing test in trench at depth of 2-1/2 to 3 inches. Impacted base of trench (picking mode).
119	90	Conducted twelve impact tests: Six at 18- to 24-inch heights, one at 6 inches, two at 12 inches, and three at 20 to 22 inches. No-load calibration test conducted.
120	96	Ran three bearing tests near auxiliary battery, and conducted four impact tests: two at 12-inch height and two at 20 to 24 inches. Discovered rock in third trench.
121	153	Picked up rock, moved in close, and ran color TV survey of it. Lost rock after survey. Picked at bottom of second trench to loosen material to attain greater depth.
122	149	Constrained operation near footpad 2 due to TV mechanism jamming; poor photos due to low sun angle. Four impact tests in trench bottom and on undisturbed surface. Started new trench, then turned on touchdown strain gages and, after stalling in the elevation down mode, sent 15 continuous retract commands. Monitored strain gages, but received no apparent indication. Telemetry dropout occurred during the operation. SM/SS extended to 55 inches and elevated to final position for lunar night.